

AD-A214 174 REPORT DOCUMENTATION PAGE

2

2a. SECURITY CLASSIFICATION AUTHORITY		1b. RESTRICTIVE MARKINGS	
2b. DECLASSIFICATION/DOWNGRADING SCHEDULE OCT 25 1989		3. DISTRIBUTION/AVAILABILITY OF REPORT Approved for public release; distribution unlimited.	
4. PERFORMING ORGANIZATION REPORT NUMBER(S)		5. MONITORING ORGANIZATION REPORT NUMBER(S) ARO 25560.1-MS-CF	
6a. NAME OF PERFORMING ORGANIZATION Univ. of California, Davis	6b. OFFICE SYMBOL (If applicable)	7a. NAME OF MONITORING ORGANIZATION U. S. Army Research Office	
6c. ADDRESS (City, State, and ZIP Code) Davis, California 95616		7b. ADDRESS (City, State, and ZIP Code) P. O. Box 12211 Research Triangle Park, NC 27709-2211	
8a. NAME OF FUNDING/SPONSORING ORGANIZATION U. S. Army Research Office	8b. OFFICE SYMBOL (If applicable)	9. PROCUREMENT INSTRUMENT IDENTIFICATION NUMBER DAAL03-88-G-0031	
8c. ADDRESS (City, State, and ZIP Code) P. O. Box 12211 Research Triangle Park, NC 27709-2211		10. SOURCE OF FUNDING NUMBERS	
		PROGRAM ELEMENT NO.	PROJECT NO.
		TASK NO.	WORK UNIT ACCESSION NO.
11. TITLE (Include Security Classification) Combustion and Plasma Synthesis of High Temperature Materials			
12. PERSONAL AUTHOR(S) Zuhair A. Munir			
13a. TYPE OF REPORT Final	13b. TIME COVERED FROM 7/1/88 TO 6/30/89	14. DATE OF REPORT (Year, Month, Day) October 1989	15. PAGE COUNT 771
16. SUPPLEMENTARY NOTATION The view, opinions and/or findings contained in this report are those of the author(s) and should not be construed as an official Department of the Army position, policy, or decision, unless so designated by other documentation.			
17. COSATI CODES		18. SUBJECT TERMS (Continue on reverse if necessary and identify by block number)	
FIELD	GROUP	SUB-GROUP	
		Solid State Combustion, Combustion, Plasma Synthesis, Materials, High Temperature Materials.	
19. ABSTRACT (Continue on reverse if necessary and identify by block number) The preparation and processing of well characterized materials, including ceramic and composite phases continue to be the focus of widespread research and development activities in the United States and elsewhere. As in other sub-disciplines of Materials Science, and aside from the route of journal publication, a need exists for the exchange of ideas among investigators in this area. This need is especially strong in areas which are rapidly			
(continued on reverse side)			
20. DISTRIBUTION/AVAILABILITY OF ABSTRACT <input type="checkbox"/> UNCLASSIFIED/UNLIMITED <input type="checkbox"/> SAME AS RPT. <input type="checkbox"/> DTIC USERS		21. ABSTRACT SECURITY CLASSIFICATION Unclassified	
22a. NAME OF RESPONSIBLE INDIVIDUAL		22b. TELEPHONE (Include Area Code)	22c. OFFICE SYMBOL

UNCLASSIFIED

SECURITY CLASSIFICATION OF THIS PAGE

developing or those that represent emerging technologies. It became evident to us and to many of our colleagues that Combustion and Plasma Synthesis are examples of these emerging techniques and that an international meeting would be highly desirable. The meeting would not only facilitate the exchange of ideas and discussion of findings but would also help focus on the important problems and their potential solutions in this area of materials processing.

The symposium was held as scheduled and stressed the areas of solid state combustion synthesis and plasma and gas phase synthesis.

→ Key words -

UNCLASSIFIED

SECURITY CLASSIFICATION OF THIS PAGE

Combustion and Plasma Synthesis of
High Temperature Materials

Z. A. Munir and J. B. Holt, Editors

Accession For	
NTIS CRA&I	<input checked="" type="checkbox"/>
DTIC TAB	<input type="checkbox"/>
Unannounced	<input type="checkbox"/>
Justification	
By	
Distribution /	
Availability Codes	
Dist	Avail and/or Special
A-1	

(Proceedings of First International Symposium on Combustion and Plasma Synthesis of High Temperature Materials, October 23-26, 1988, San Francisco, California, USA)

Forward

The preparation and processing of well characterized materials, including ceramic and composite phases continue to be the focus of widespread research and development activities in the United States and elsewhere. As in other sub-disciplines of Materials Science, and aside from the route of journal publication, a need exists for the exchange of ideas among investigators in this area. This need is especially strong in areas which are rapidly developing or those that represent emerging technologies. It became evident to us and to many of our colleagues that Combustion and Plasma Synthesis are examples of these emerging techniques and that an international meeting would be highly desirable. The meeting would not only facilitate the exchange of ideas and discussion of findings but would also help focus on the important problems and their potential solutions in this area of materials processing.

Our proposal to hold an International Symposium on Combustion and Plasma Synthesis of High Temperature Materials was met with enthusiasm by a number of organizations and government agencies whose support has been crucial to the success of this symposium. The American Ceramic Society was the official sponsor of this meeting which was held in San Francisco, California, on October 23-26, 1988, as part of the Pacific Coast Regional Meeting (PCRM) of the Society. We are grateful to the American Ceramic Society and to many of its officers who played a major role in facilitating the arrangements for this meeting.

Financial support for the organization of this meeting was provided through grants from the following U.S. government agencies and private organizations:

The National Science Foundation
Department of Energy
Lawrence Livermore National Laboratory
Army Scientific Research Office
Standard Oil Company
Corning Glass Works

We are grateful to these agencies for their support which has contributed measurably to the success and effectiveness of this meeting.

We extend our thanks to the following individuals who kindly devoted their time and effort in the capacity of members of the Symposium Organizing Committee:

Dr. Mark D. Allendorf (Sandia National Laboratory, Livermore)
Professor John S. Haggerty (MIT)
Dr. Kathy V. Logan (Georgia Tech Research Institute)
Dr. James W. McCauley (Army Materials and Technology Laboratory)
Dr. E. Pfender (University of Minnesota)
Professor Stanislaw Wojcicki (Washington State University)
Dr. G. Vogt (Los Alamos National Laboratory)

We are also grateful to the following individuals who accepted the responsibilities of co-chairing the technical sessions of the Symposium:

Dr. M. D. Allendorf (Sandia National Laboratory, USA)
Professor R. Flagan (California Institute of Technology, USA)
Professor J. S. Haggerty (MIT, USA)
Professor V. Hlavecek (SUNY - Buffalo, USA)
Professor J. L. Katz (Johns Hopkins University, USA)
Professor M. Koizumi (Ryukoku University, Japan)
Dr. K. Logan (Georgia Tech Research Institute, USA)

Professor Y. Miyamoto (Osaka University, Japan)
Professor J. J. Moore (University of Auckland, New Zealand)
Dr. A. Niller (US Army Ballistic Research Laboratory, USA)
Professor O. Odawara (Tokyo Institute of Technology, Japan)
Professor P. Pampuch (Institute of Materials Science, Cracow, Poland)
Professor E. Pfender (University of Minnesota, USA)
Dr. R. Rice (W. Grace Co., USA)
Professor Stanislaw Wojcicki (Washington State University)
Professor T. Yoshida (University of Tokyo, Japan)
Dr. G. Vogt (Los Alamos National Laboratory, USA)

We are indebted to all the contributors to this symposium. We had a truly international participation of individuals, both as speakers and audience. We are especially thankful to our Keynote Speaker, Professor Alexander G. Merzhanov (USSR Academy of Sciences) for his elucidating presentation. Although Plasma Synthesis as a topic has been addressed in previous meetings the topic of Combustion Synthesis, particularly Solid-State Combustion Synthesis, has not been the subject of an international forum such as this one. In this regard, the proceedings of this Symposium as they appear in this volume, are the first of their kind.

Finally, we extend our sincere thanks to our able staff at the University of California at Davis (UCD) and the Lawrence Livermore National Laboratory (LLNL) for their valuable support and contributions. We would like particularly to thank Barbara Haff, Pat Blondheim, Jane Hamiel, and Cathy McCullom for their help in the organization of the Symposium and the editing of its proceedings.

Z. A. Munir
University of California
Davis, CA 95616, USA

J. B. Holt
Lawrence Livermore National Laboratory
Livermore, CA 94550, USA

TABLE OF CONTENTS

Paper Number

KEYNOTE ADDRESS

SELF-PROPAGATING HIGH-TEMPERATURE SYNTHESIS: TWENTY YEARS OF SEARCH AND FINDINGS A. G. Merzhanov	1
--	---

SOLID STATE COMBUSTION SYNTHESIS

RECENT PROGRESS IN COMBUSTION SYNTHESIS OF HIGH PERFORMANCE MATERIALS IN JAPAN M. Koizumi and Y. Miyamoto	2
MODELING AND NUMERICAL COMPUTATION OF A NONSTEADY SHS PROCESS A. Bayliss and B. J. Matkowsky	3
NEW MODES OF QUASI-PERIODIC BURNING IN COMBUSTION SYNTHESIS S. B. Margolis, B. J. Matkowsky, and M. R. Booty	4
MODELING OF SHS OPERATIONS V. Hlavacek, P. Dimitriou, J. Degreve, and J. Scholtz	5
COMBUSTION THEORY FOR SANDWICHES OF ALLOYABLE MATERIALS R. Armstrong and M. Koszykowski	6
OBSERVATIONS ON THE COMBUSTION REACTION BETWEEN THIN FOILS OF NI AND AL U. Anselmi-Tamburini and Z. A. Munir	7
COMBUSTION SYNTHESIS OF INTERMETALLIC COMPOUNDS Y. Kaieda, M. Otaguchi, and N. Oguro	8
COMBUSTION SYNTHESIS OF NICKEL ALUMINIDES B. H. Rabin, A. Bose, and R. M. German	9
SELF PROPAGATING HIGH TEMPERATURE SYNTHESIS (SHS) OF NiTi INTERMETALLICS H. C. Yi and J. J. Moore	10
SHOCK-INDUCED CHEMICAL SYNTHESIS OF INTERMETALLIC COMPOUNDS S. Work, L. H. Yu, and N. N. Thadhani, M. A. Meyers, R. A. Graham, and W. F. Hammett	11
ADVANCED CERAMICS VIA SHS T. P. DeAngelis and D. S. Weiss	12

	<u>Paper Number</u>
IN SITU FORMATION OF SiC AND SiC-C BLOCKED SOLIDS BY SELF-COMBUSTION SYNTHESIS S. Ikeda, H. Izawa, K. Urabe, and M. Koizumi	13
POWDER PURITY AND MORPHOLOGY EFFECTS IN COMBUSTION SYNTHESIS REACTIONS L. J. Kecskes, T. Kottke, and A. Niiler	14
SIMULTANEOUS SYNTHESIS AND DENSIFICATION OF CERAMIC COMPONENTS BY THE SHS PROCESS UNDER THE GAS PRESSURE Y. Miyamoto and M. Koizumi	15
THE USE OF SELF HEATING HIGH TEMPERATURE SYNTHESIS FOR PRODUCTION OF HIGH DENSITY TITANIUM DIBORIDE P. D. Zavitsanos, J. J. Gebhardt, and A. Gatti	16
METAL-CERAMIC COMPOSITE PIPES PRODUCED BY A CENTRIFUGAL-THERMITE PROCESS O. Odawara	17
SIMULTANEOUS COMBUSTION SYNTHESIS AND DENSIFICATION OF AlN S. Dunmead, J. B. Holt, and D. D. Kingman	18
FABRICATION OF A FUNCTIONALLY GRADIENT MATERIAL BY USING A SELF-PROPAGATING REACTION PROCESS N. Sata, N. Sanada, T. Hirano, and M. Niino	19
COMBUSTION SYNTHESIS OF OXIDE-CARBIDE COMPOSITES L. L. Wang, Z. A. Munir, and J. B. Holt	20
HETEROGENOUS REACTION MECHANISMS IN THE Si-SYSTEM UNDER CONDITIONS OF SOLID COMBUSTION R. Pampuch, J. Lis, and L. Stobierski	21
EXPERIMENTAL MODELING OF PARTICLE-PARTICLE INTERACTIONS DURING SHS OF TiB_2/Al_2O_3 K. V. Logaň, J. T. Sparrow, and W. J. S. McLemore	22
COMBUSTION SYNTHESIS IN THE Ti-C-Ni-Al SYSTEM S. D. Dunmead and Z. A. Munir, J. B. Holt, and D. D. Kingman	23
COMBUSTION SYNTHESIS DYNAMICS MODELING T. Kottke, L. J. Kecskes, and A. Niiler	24
ELEMENTARY PROCESSES IN SiO_2 -Al THERMITE-TYPE REACTION ACTIVATED OR INDUCED BY MECHANOCHEMICAL TREATMENT G. T. Hida and I. J. Lin	25
COMBUSTION SYNTHESIS OF CERAMIC PREFORMS FOR MOLTEN-METAL INFILTRATION D. C. Halverson, Z. A. Munir, and B. Y. Lum	26

Paper Number

COMBUSTION CHARACTERISTICS OF SOLID-SOLID SYSTEMS EXPERIMENT
AND MODELING

S. Kumar, J. A. Puszynski, and V. Hlavacek 27

MICROSTRUCTURE OF TiB_2 SINTERED BY SELF COMBUSTION METHOD

K. Urabe, Y. Miyamoto, and M. Koizumi 28

A LASER IGNITION STUDY OF GASLESS REACTIONS USING THERMOGRAPHY

C. T. S. Chow and J. H. Mohler 29

SHOCK-INDUCED REACTION SYNTHESIS ASSISTED PROCESSING OF CERAMICS

R. Ward, N. Thadhani, and P. Persson 30

SUMMARY ASSESSMENT OF THE APPLICATION OF SPS AND RELATED REACTION
PROCESSING TO PRODUCE DENSE CERAMIC

R. W. Rice 31

SHOCK CONSOLIDATION OF COMBUSTION SYNTHESIZED CERAMICS

A. Nijler, L. J. Kecskes, and T. Kottke 32

HIGH PRESSURE BURNING RATE OF SILICON IN NITROGEN

M. Constantino and J. B. Holt 33

PLASMA AND GAS PHASE SYNTHESIS

PREPARATION OF TiC SINGLE CRYSTAL FROM SELF-COMBUSTION ROD BY
FLOATING ZONE METHOD

S. Otani, T. Tanaka, and Y. Ishizawa 34

THERMAL PLASMA SYNTHESIS OF CERAMIC POWDERS AND COATINGS

T. Yoshida 35

A THEORETICAL COMPARISON OF CONVENTIONAL AND HYBRID RF PLASMA REACTORS

J. W. McKelliget and N. El-Kaddah 36

HOMOGENEOUS NUCLEATION AND PARTICLE GROWTH IN THERMAL PLASMA SYNTHESIS

S. L. Girshick and C. Chiu 37

FORMATION OF REFRACTORY AEROSOL PARTICLES

R. C. Flagan, H. V. Nguyen, and S. Rogak 38

CERAMIC POWDER SYNTHESIS IN AN AEROSOL REACTOR

M. K. Alam, C. Wiseman, and Q. Azeez 39

	<u>Paper Number</u>
SILICA PARTICLE FORMATION USING THE COUNTERFLOW DIFFUSION FLAME BURNER J. L. Katz, D. Chin, S. Chung, M. R. Zachariah, H. G. Semerjin	40
SYNTHESIS AND PROPERTIES OF LOW-CARBON BORON CARBIDES C. L. J. Adkins, A. N. Campbell, and T. J. Headley	41
SYNTHESIS OF Si, SiC AND Si ₃ N ₄ POWDERS UNDER HIGH NUMBER DENSITY CONDITIONS J. S. Haggerty and J. H. Flint	42
RAPID PREPARATION OF TITANIUM AND OTHER TRANSITION METAL NITRIDE AND CARBIDE POWDERS BY A CARBO-REDUCTION METHOD USING ARC IMAGE HEATING M. Yoshimura, M. Nishioka, and S. Somiya	43
MICROWAVE PLASMA DENSIFICATION OF ALUMINUM NITRIDE S. M. Knittel and S. H. Risbud	44
PLASMA SYNTHESIS OF FINE POWDERS BY COUNTER-FLOW LIQUID INJECTION P. C. Kong and E. Pfender	45
APPLICATION OF NON-EQUILIBRIUM GAS DYNAMIC TECHNIQUES TO THE PLASMA SYNTHESIS OF CERAMIC POWDERS J. S. McFeaters and J. J. Moore	46
DEVELOPMENT OF TIN OXIDE COATINGS FOR USE AS ELECTRODES IN MERCURIC IODIDE PHOTODETECTOR APPLICATIONS A. K. Hays and R. C. Hughes	47
REFINING AND NITRIDING OF Si AND Ti WITH A PLASMA TORCH P. Humbert, D. Morvan, J. F. Campion, P. Jolivet, and J. Amouroux	48
PLASMA SYNTHESIS OF IRON AND CHROMIUM CARBIDES BY CARBOTHERMIC REDUCTION OF THEIR MINERAL OXIDES J. J. Moore	49
LASER DIAGNOSTICS OF PLASMA SPECIES IN PACVD PROCESS FOR HARD FACE COATING DEPOSITION W. C. Roman, J. H. Stufflebeam, A. C. Eckbreth and C. J. Ultee	50

SELF-PROPAGATING HIGH-TEMPERATURE SYNTHESIS:
TWENTY YEARS OF SEARCH AND FINDINGS*

Alexander G. Merzhanov
The Institute of Structural Macrokinetics
USSR Academy of Sciences
Chernogolovka, Moscow, USSR

Abstract

A historical account of the development of the SHS method in the Soviet Union is presented. Accomplishments along theoretical and applied directions in the synthesis of a large number of materials are described. The uniqueness and advantages of the SHS process and its adability in the processing of materials are discussed.

*Keynote Address

1. Introduction

The aim of this paper is to show how the research and development activity in the field of self-propagating high-temperature synthesis (SHS) has been originated and been developed in the USSR, consider the main trends and periods in this work, demonstrate the most important achievements in our studies, and outline future directions of our research.

SHS is one variety of combustion. In the updated interpretation SHS is a combustion process of any chemical character resulting in the formation of valuable condensed products (materials) for practical purposes. The medium which is able to interact under the SHS regime may be in various states: solid, liquid, gaseous and mixed. It is important that after cooling the combustion product it should be a solid substance in order to be further utilized. Nevertheless, the first experiments which led to the notion "Self-propagating High Temperature Synthesis" were of a rather specific characteristic, i.e., the initial solid substances reacted in self-propagating regime with high self-heating and formed hard refractory products even at high combustion temperatures.

Borovinskaya, Shkiro, and the author, all members of the Institute of Chemical Physics, USSR Academy of Sciences, discovered the phenomenon of self-propagating high-temperature synthesis in 1967 [1,2] when studying the combustion of cylindric compacts, consisting of the titanium-boron mixture. Figure 1 (a historical relic now) presents one of the first SHS processes. There is clearly a luminous front separating the initial reactant mixture from white-hot but solid combustion product (titanium boride in this case, a valuable heat-resistant compound).

Processes in which the initial substances and the products are solid at

the combustion temperature, were recently called "Solid Flame". This term is now used for the description of primary SHS process to distinguish it from a vast variety of modern SHS processes. The discovery of "solid flame" attracted much attention. It became a new objective of the combustion theory because of the contradiction to low velocities of mass-transfer in the solid phase, great heat capacity of the produced condensed products since they were not gaseous as in the case of fuel combustion. However, it should be noted that the combustion products became no less a matter of interest than the process itself. The most valuable refractory compounds (borides, carbides, silicides, and the like) are not easily produced by conventional production methods. This was a new method of synthesis which later received a large development effort.

It is worthy to say a couple of words about the discovery of solid flame and the SHS method. The authors, the specialists in combustion, were engaged in the study of the combustion mechanism in gasified systems, analogous to explosives and propellants. The search for simple gasless systems, capable of burning practically without gas evolution, was undertaken to verify original theoretical assumptions in modeling one of the combustion stages. It led to the observation mentioned above regarding the titanium-boron system. However, the products produced in the first experiments appeared to be unexpectedly hard, which prompted the probability of a new approach to the problem of refractory compounds synthesis. It also became a crucial point of combustion mechanism and factors affecting the combustion products. A special group headed by Borovinskaya was organized in the laboratory of macrokinetics at the Institute to study the SHS processes. The author, who was the laboratory chief at that time, took an active part in the research. Though there were, of course, moments of deep uncertainty, this was an exciting period of our

activity, full of thrilling anticipations and discoveries which strengthened our interest in the problem. The investigation of the combustion of metal porous substances in nitrogen (gaseous and liquid) led to the theory of filtration combustion. Oscillatory and spin waves, discovered at that time, became an important contribution to the general theory of chemical stability processes.

At the end of the 1960's, i.e., at the very start, the finding of every new system consistent with the SHS process seemed to be a great success. However, it soon became clear that they were numerous. The formation of a refractory compound of metal and non-metal stable at high temperatures is accompanied by heat evolution. Consequently, it may be produced by the SHS method. Self-propagating high-temperature synthesis turned out to be a viable method for industrial production of valuable compounds applicable in industrial technology.

Since 1972 technological investigations have been developing to produce large amounts of SHS products. A pilot installation was created at the Institute. The first SHS production (10-20 tons a year) was for refractory compound powders (carbides, nitrides, diborides and carbonitrides of titanium; boron and aluminum nitrides; titanium and molybdenum silicides, etc.). Their successful application in sintering and gas-thermic sputtering in powder metallurgy, and in particular, as abrasive powders, stimulated further development of technological work. However, it should be noted that SHS products differ from their furnace-counterparts in purity and structure. Therefore, their application required somewhat different processing conditions. At the early stage, the lack of understanding of this circumstance aroused a cautious attitude towards the SHS method from specialists in the traditional

materials science, thus restraining practical development of the problem.

In 1975 at the Institute the work on the direct synthesis of SHS materials and articles without an intermediate stage of powder synthesis was started. A set of original processes was designed in which SHS itself was combined with the traditional methods of metallurgy and technology of machine building (sintering, hot pressing, extrusion, rolling, explosive compaction, deposition by welding, centrifugal casting, electrowelding). By that time our attention had been shifted to multicomponent materials of complex structure, parts and articles of required shape and size with desired operational properties, and coatings with high adhesiveness. The synthesis of the material components, the process of structurization, the formation of shape of the article or its coating, being combined into one process showed the way to the realization of SHS vast potential. Many results obtained in this direction have not been elucidated in the literature. It is a pity that the scientific community is unaware of some rather important achievements.

The industrial production of SHS materials was brought to life at the Kirovakan Plant of High Temperature Heating Elements at the end of the 1970's. The production of molybdenum disilicide powder and MoSi_2 -based heating elements demonstrated the advantages of the new technology - the increase in productivity, the decrease in material and labor costs and the improvement of the product quality. It is of interest that for some time there coexisted both old and new technologies at the plant. Later the former was forced out and SHS-based manufacture increases steadily to higher technical and economical levels.

The commercial realization of SHS processes suffered from continuous opposition by supporters of conventional approaches which had already been in

production. In their opinion, the SHS-processes could not be controlled and hence could not provide the required quality of products, needed costly raw materials and could not find wide application in technology. However, time and experience showed that there was no foundation for such fear.

A large research experience allowed deep and complete understanding of the combustion of processes going on in SHS and led to a new approach to the theory of SHS at the end of the 1980's, which was termed "Structural Macrokinetics". The objective of its research became direct and indirect relations among the rates of the chemical reactions, heat- and mass exchange and structural transformations. This approach allows the entire transition from the destruction of initial reactants structure to a new structure formation in the products and gives the possibility of controlling the properties of the synthesized materials. Currently, structural macrokinetics is the main direction of the fundamental research in the field of SHS. The center of the SHS investigations is the Institute of Structural Macrokinetics of the USSR Academy of Sciences, organized in Chernogolovka in 1987. Its staff is mainly composed of the scientific workers of the Institute of Chemical Physics whose work was largely concerned with the problems pertinent to the SHS processes.

The main contributors to the development of the SHS theory and practice are Borovinskaya and coworkers, Aldushin, Grigoriev, Maltsev, Rosenband, Stolin, Khaikin, Steinberg, Stessel, and their colleagues Maksimov, Itin (Tomsk University), Dolukhanyan and Kharatyan (Erevan, Institute of Chemical Physics), Karyuk (Kiev, Institute of Materials Science), and others.

For almost half the time (more than 10 years) the problem of SHS was mainly investigated in the Soviet Union. Only in the early 1980's did it become multi-national. To my mind, it was an interesting review by J. Crider

"Self-propagating High-temperature Synthesis - A Soviet method of Producing Ceramic Materials", which stimulated an interest in the SHS processes in a number of countries. The most active research and development has been initiated in the USA and Japan. Also, the "DARPA" program (1984-1986) involved some organizations and scientists in the solution of the problems pertinent to the SHS technology. The names of Holt, Munir, Matkowsky (USA), Koizumi, Miyamoto, Odawara (Japan) and their work are well known to the Soviet scientists. The world recognition of the SHS as a new scientific and technological field is a reliable ground for international collaboration on this problem.

Following are the main aspects of the SHS problem. These are: the combustion theory, chemical synthesis and materials science, technology and structural macrokinetics. Because of the great amount of the experimental research material which had accumulated over the years, only the statement of conceptions and description of some interesting examples will be dealt with in this paper.

2. Combustion Theory*

The SHS problem took its source from combustion and developed towards materials science. Therefore, it is not a surprise that it's combustion part was studied the most thoroughly during investigations.

We will consider some problems in the theory of SHS-system combustion. With respect to the oscillatory processes (such as SHS) they can be summarized

*The term "theory" in our consideration involves qualitative interpretations of the process with the quantitative apparatus for their description independent of the way they were obtained - experimentally, analytically or by calculations.

as follows: The laws of combustion front propagation; The structure of the combustion wave (zone); The mechanism of the combustion process. It is noteworthy that in our study of the SHS processes we made extensive use of the Soviet school of combustion founded by Semenov, Zeldovitch, Frank-Kamenetsky, Belyaev and, in particular, of the methodology of investigations developed for the combustion of gases and gasified condensed systems [3-8].

2.1. The Laws of Combustion Front Propagation

In the majority of SHS processes the combustion front presents a smooth surface (planar or slightly curved), which propagates layer-to-layer with a constant velocity. The study of the combustion velocity's dependence on various parameters is the most popular and simplest task in the investigations. A large number of them have been conducted presently. Some of their results are summarized recently by the author [9]. There should be two groups of parameters outlined. One of them characterizes the initial reactant mixtures (chemical composition, shape and size of reactant particles, and shape, size, and density of samples). The other characterizes the combustion conditions (composition and pressure of the environment, initial temperature of the compact, the method and intensity of combustion initiation, or additional external effects). The laws of the combustion front propagation differ for the two most typical SHS-systems. These are: a) mixed system, which consists of the reactant particles mixture (gasless combustion [10]), and b) hybrid system, in which burning is accompanied by gaseous reactant participation (filtration or permeation combustion [11-13]). It should be noted that in the latter case the laws are more interesting and diverse. At present the influence of one or another parameter on the combustion velocity is almost clear. Rare anomalous cases are thoroughly studied.

For the SHS processes the exact value of the combustion velocity is commonly of no importance. However, the quantitative study of its dependence on various parameters is useful, since it contains valuable information on the process. Stationary layer-to-layer regime of combustion is not always realized. Sometimes, during SHS reactions there arise situations in which the combustion front propagates with time or spatial inhomogeneities (unsteadiness). An important event in the combustion theory was the discovery of oscillatory and spin regimes of the front propagation [14]. In the former case, the layer-to-layer nature of combustion is retained, however, the front propagation proceeds in an oscillatory regime, i.e., it consists of successions of rapid displacements and stops, flashes and extinctions. In the latter case, the layer-to-layer regime is distorted, the combustion reaction is located in the hot spot which propagates at constant velocity along a definite trajectory (in cylinder samples along a helical path).

Oscillatory combustion often results in a layered structure of the product [15,16]. The products of gasless oscillatory combustion consist of wafers (layers) of the same composition, their number being equal to the number of flashes. One may observe a more complicated pattern in the permeation (filtration) oscillatory combustion. The layers are of different composition and twice as many as the number of flashes. The product consists of alternating layers of silicon nitride and elemental silicon. The former results from the combustion at the flash; the adjacent silicon layer does not react with nitrogen because of sintering which occurs during extinction. Figure 2 represents one of the first cinegrams of spin combustion [14]. It is clearly seen that the combustion hot spot appears from the far (invisible) side of the cylinder compact, moves in a transverse path to the main direction of

the front propagation, and then disappears again.

Oscillatory and spin combustions were considered for some time as quite different phenomena. Then it became clear [18] that they are different manifestations of unstable combustion, i.e. when the steady-state layer-to-layer regime was unable to maintain the process propagation. Oscillations result from the process sensitivity to the longitudinal minor perturbations. while spin result from sensitivity to transverse perturbations. In both cases burning out of the heated layer, formed ahead of the combustion front due to the heat transfer, takes place. However, in the former case the layer burns out in the longitudinal direction and then is formed again. In the spin case, it burns out in the transverse direction. In the course of long-duration transverse combustion a new heated layer is formed, thus providing the conditions for the continuous displacement of the hot spot. The unstable, though ordered combustion was subjected to a thorough experimental and theoretical study [19-24]. This phenomenon has attracted the attention of specialists in mathematical physics (Volpert et al. [25,26], Matkowsky, Sivashinsky et al. [27-29]).

2.2 The Combustion Wave Structure

The combustion front is the "fire" part of the wave and is followed by extended zones of chemical reactions and various physico-chemical conversions. These processes in their general case presuppose the applicability of the laws of the front propagation. Therefore, the study of the zone wave structure is an important problem for the SHS investigations.

The temperature profiles of the combustion wave carry valuable information. A great number of works is devoted to their measurements. The greatest contribution to the problem solution was made by Zenin [30-32] and

Maltsev [33-35]. They used microthermocouple and optico-spectral methods for the determination of temperature profiles. The investigations showed that SHS temperature profiles are of a complicated character and consist of elementary patterns of four types. They are presented schematically in Figure 3 and discussed below.

TYPE I is a classical case. The combustion wave consists of a heated layer and a reaction zone (shadowed in Figure 4), which is narrower than the former. The concept of a narrow reaction zone, developed by Zeldovitch and Frank-Kamenetsky [36], was the base for the classical combustion theory and allowed a creation of the fine analytical technique. Profiles of a wide reaction zone belong to TYPE II. There are two subzones termed "propagation" and "post-combustion" in this case. Only the propagation sub-zone promotes the combustion front displacement. Wide reaction zones are typical of such essentially heterogeneous heavily activated processes as SHS. It is interesting that their existence was first predicted theoretically and then studied by Khaikin, Aldushin, and the author [37-40]. TYPE III is characterized by a clearly seen point of inflection in the temperature profile curve which may have a zero derivative. The presence of two zones of chemical reactions is essential for its existence, the front propagation being affected only by the first zone. Such profiles are realized with complicated reactions occurring in the combustion wave. Khaikin et al. [41-42] contributed much to the development of the theory of such structures. Finally, profiles of TYPE IV are characterized by the presence of an isothermal region. The isothermal region (plateau) screens the thermal action of the profile high temperature regions from the combustion front. Such an action is determined by the zone adjacent to the plateau from the lower temperature zones. The temperature

plateau results from the simultaneous action of the chemical reaction and phase transition (e.g., reactant melting). The theoretical analysis of such cases has been undertaken in previous studies [43-44]. The combustion thermogram of the Ti-Si systems [45] is depicted in Figure 4. The variety of effects belonging to the elementary types described above are seen in the temperature profiles.

Types II-IV differ considerably from Type I. The wave velocity in Type I is determined by complete conversion of the substance, and the highest combustion temperature is evaluated from thermodynamic calculations assuming negligible heat losses. The combustion waves of such a classical mode were referred to as waves of the first kind. Sometimes they are called Zeldovitch waves. In the other types (II-IV) the front velocity is determined by the partial conversion of the substance at some intermediate temperature lower than the adiabatic value. These intermediate values cannot be evaluated by thermodynamic calculations and should be taken from additional macrokinetic conditions. Such non-classical waves are called combustion waves of the second kind. Their existence and theoretical considerations were the objectives of the author's study for a number of years [7,16,43,46,48]. It should be noted that waves of the second kind are associated with heat losses such that the degree of incomplete conversion of the initial reactants may be considerable. This important fact should always be taken into account when setting up SHS processes. As for the classical combustion theory, the complete conversion of reactants (until extinction) may always have a place due to the narrow reaction zones.

An important achievement in the combustion theory of SHS systems is the generalized expression describing the dependence of the wave velocity on the

parameters of the main stage of combustion, i.e.

$$u = A(T_*, \eta_*) \exp(-E/RT_*) \quad (1)$$

where

u is the velocity of the combustion front;

T_* is the temperature of the main combustion stage;

η_* is the degree of the substance conversion at T_*

E is the activation energy of the process

The function A is weaker than the exponential one and can have different profiles in various cases. Its interpretation, as well as T_* and η_* determination allow the description of the combustion laws observed in practice using this expression. The relationships defining the parameters T_* and η_* for the four types discussed above are:

$$\text{Type I: } T_* = T_0 + Q/\bar{C}; \eta_* = 1 \quad (2)$$

where

T_0 is the initial temperature of the burning sample

Q is the reaction enthalpy

\bar{C} is the average value of the specific heat capacity of the combustion product.

$$\text{Type II: } \left(\frac{d \ln \phi}{d \eta} \right)_{\eta_*} + \frac{QE}{CRT_*^2} = 0; \eta_* = \frac{\bar{C}(T_* - T_0)}{Q} \quad (3)$$

where $\phi = \phi(\eta)$ is the function describing the relation between the reaction rate and the conversion degree;

The values of T_* and η_* are obtained by solving the two above equations after a substitution of a particular function (for example, $\phi = e^{-m\eta}$).

$$\text{Type III: } T_* = T_0 + Q_1/\bar{C}_1; \eta_* = 1 \quad (4)$$

(for the case of zero derivative in the point of inflection)

The values of Q_1 and \bar{C}_1 refer to the first stage of the chemical reaction.

$$\text{Type IV: } T_* = T_p; \eta_* = \frac{\bar{C} (T_p - T_0)}{Q} \quad (5)$$

where T_p is the temperature of the phase transition.

As can be seen from the above considerations, thermodynamic methods do not always give complete information about the process temperature for the SHS systems. Nevertheless, they are widely used in the general SHS theory. Combustion temperatures are currently calculated for almost all systems with known thermodynamic functions [48,49]. In simple cases with definite composition of the combustion products the calculations are plain and can easily be performed [10,50]. For more complicated systems the combustion temperatures are calculated using computers on the universal program. The comparison of calculations and experimental data obtained under adiabatic conditions are listed in Table 1 [51], the agreement between the results is seen to be so high that the usefulness of thermodynamic calculations becomes obvious.

As for the wave structure, it cannot be described by temperature profiles only. Concentration distribution of all the substances involved in the process is also of importance. However, there are some methodological difficulties which cannot be avoided in the experiments though some attempts have been already made [52-54]. The calculations of concentrational fields for certain systems have been performed by Nekrasov [55,56].

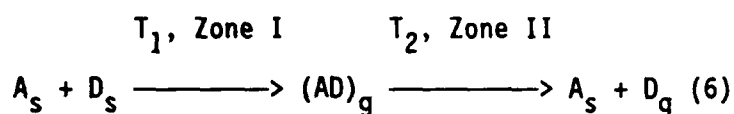
2.3. The Combustion Mechanism

The diagnostics of the combustion mechanism is of great importance in the study of each particular system. In other words, it is the determination of the combination of the processes (chemical reactions, physico-chemical

conversions, transfer processes and their interrelations) occurring during combustion which help to reveal the principal leading processes and understand how the substance undergoes conversions under the complicated conditions of the combustion waves. There is no end of work on this problem. Only results for some binary elemental systems, e.g. $A + B$ (where A and B are chemical elements) have been obtained. The combustion mechanism of compositions which contain chemical compounds as reactants has been poorly studied.

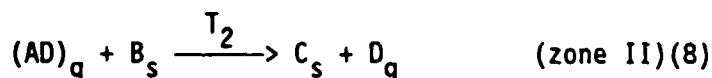
Let us consider first mixed systems (powder mixtures). An ideal ultimate case for such systems is the combination of clad two-component powders. They consist of particles of one substance covered by a layer of the other, providing a rather large reacting surface if the particles are relatively small. Micrometer-sized particles under such conditions are quite sufficient. If the particles do not melt, the solid-phase reaction takes place under the reactive diffusion mode. Low values of mass transfer constants in solid-state reactions may be compensated by the large contact surface. High combustion temperature is an important factor promoting a high-rate combustion. In such an ultimate case the regime of purely solid flame can be realized, i.e., all the substances (not only initial and final, but intermediate as well) are in the solid state.

Real mixtures consisting of particles of two kinds are much more complicated. Their main salient feature is a small surface of contact between the particles, failing to provide a purely solid-phase combustion regime in the majority of cases. Some additional agents are needed to raise the rate of the combustion wave propagation. Gas-transport agents (gaseous carriers of the matter) are some examples of the above. The traditional scheme of gas-transport action is as follows:



It presupposes the presence of two zones at T_1 and T_2 , respectively. The temperature difference $\Delta T = T_1 - T_2$ is a driving force for the solid substance A_s to transfer from Zone I to Zone II. For exothermic and endothermic reactions of A_s with the gaseous carrier D_g the relation between the two temperatures is $T_1 > T_2$ and $T_1 < T_2$, respectively. Since temperature gradients in the combustion wave are extremely high, the transfer of some reactant from the preheating zone to the reaction zone and vice versa can take place.

The transferred reactant can condense on the surface of the other reactant and react with it according to the following scheme:



where C_s is a solid product of A_s and B_s interaction and $T_1 \neq T_2$. Thus, gas-transport in the SHS wave can be considered as one of the stages in the mechanism of solid phase reactions:



Isothermal nontraditional transfer in the gas phase ($T_1 = T_2$) is of certain interest. The transfer is realized in the combustion wave in a microscopic scale, between the reactant particles with micrometer sizes. The difference between the partial pressures of gaseous carrier over the surface of heterogeneous particles rather than the temperature difference is a driving force in this case. Thus, gaseous carriers somewhat increase the efficient contact surface between the reactant particles. The conceptions about the role

of regenerated gas molecules in solid phase reactions are developed in the theory of furnace syntheses [57] and can be applied to the SHS processes. The chemical nature of the gaseous carriers may be different for various reactants: carbon can be transferred by hydrogen, metals by halogens.

The role of contact melting which also raises the rate of the process of solid phase reaction through the formation of readily melting eutectics formation is elucidated in a recent publication [58]. The strong rate-raising effects due to melting of one of the reactants were discovered by Shkiro and Borovinskaya [59] in the study of the combustion of a mixture of titanium and carbon black. They showed that a readily melting compound (titanium in this case) could melt in the preheating zone and, due to the carbon wettability and under the action of capillary forces, spread over the surface of carbon black particles. An illustration to this process is shown in Figure 5. This figure shows that in the combustion products there are cavities (pores) instead of the titanium particles, which melted and spread during the combustion process. The phenomenon of capillary spreading leads to a drastic change in the heterogeneity scale of the reacting mixture (from large titanium particles to very small particles of carbon black). As the result of this change, the rate of the combustion process is considerably raised.

The effect of capillary spreading explained the mystery of high velocities of gasless combustion as it seemed a first sight. Thus, under certain conditions, the combustion velocity reaches up to 20 cm/s in the titanium-boron powder mixtures ($\sim 100 \mu\text{m}$ and $\sim 0.1 \mu\text{m}$ in size, respectively), which cannot be explained in the terms of diffusional saturation of the titanium particles. The attempts to affect the velocity of capillary spreading by ultrasound look rather interesting. The combustion in the Ti + 2B system was studied in the

ultrasonic field [60,61]. Figure 6 presents the dependence of the combustion velocity on the specimen density in the presence and absence of ultrasound. The combustion intensity in the ultrasonic field is seen to sharply increase at certain density values, when capillary spreading is likely to be hindered. The interaction between the carbon black particles and the titanium melt (or non-metal particles and metal melt in general) is a particular case for investigations. One of the recent results is the observation that the rate of heat evolution is temperature-inactivated, i.e., independent of temperature, in a certain temperature range [62].

The influence of physical and chemical conversions is important for the hybrid systems, but their manifestation can be of a different character. Thus, the reactant melting may lead to coalescence of the particles or to the complete loss of dispersity [11,53,64], which hinders the possibility of the reactants interaction. The experimental observations on the quenched silicon specimens after being combusted in nitrogen showed that in the heated layer the size-distribution of particles differed from that in the initial state. The distribution maximum is shifted towards larger particles (Figure 7) [17]. The authors attributed this effect to the melting and coalescence of the silicon particles. It is of interest that the process can be readily affected by the introduction of inert non-melting additions into the silicon green mixture [17]. Their presence prevents coalescence. Figure 8 depicts the dependence of the silicon particles average size in the preheated layer and the combustion velocity on the degree of dilution of the green mixture by the combustion product, silicon nitride. The increase in the degree of dilution is seen to decrease the particle size to the initial one, whereas the combustion velocity increases despite the dilution of the active green mixture by inactive filler.

Polymorphous transformations in hybrid systems, unlike those in mixed systems, can noticeably promote the combustion. At the phase transformation there appear some additional channels in the destroyed lattice which are filled with the gas molecules moving to the surface of the solid, thus increasing the reacting surface. The study of the combustion of the ferroalloy Fe-V in nitrogen gave interesting data on the process [65]. The combustion velocity was shown to decrease with an increase of the iron content of the alloy (see Figure 9). It is evident that iron, being an inert filler in this case, is not nitrided in the combustion wave. However, the situation becomes quite different for the systems when the initial composition of the alloy gets into the region of the σ -phase which is unstable at high temperatures. On crossing the boundary of this region the combustion velocity increases because of the disordering of the initial phase in the combustion wave.

Under normal conditions one of the components of the combustion product in the hybrid system is gaseous. Therefore, the processes of the dissociation of products at high combustion temperatures may be of great importance. This problem is described in detail for the metal combustion in hydrogen [66-68]. What is interesting are physico-chemical effects in the hybrid system combustion, the most important for the process is the access of the gaseous reactant to the combustion zone. With gas starvation shortage (in the combustion zone, rather than in the reactor volume) the process will either stop or if it continues will lead to incomplete conversion or clearly seen heterogeneity. The gaseous reactant contained in the initial pores of the powder charge or pressed specimen is not enough for the combustion, unless, of course, it is the case of very high pressures of the order of kilobars. The gas gets inside the specimen by permeation from the environment. That is where

another name for hybrid systems conduction comes from - permeation (filtration) combustion.

The combustion of a permeation character is associated with numerous effects. The transition from surface to layer-to-layer combustion, prolonged bulk post-combustion, repeated combustion, reflection and splitting of combustion waves and others are among them. They have all been studied in detail in experimental and theoretical works [11, 69-73]. Let us consider one of the most important cases of permeation combustion, namely concurrent forced permeation studied by Aldushin and Seplyarsky in their theoretical works [72-73]. This is the case when the gas and the combustion front propagate in one direction, i.e. the gas passes through the combustion products before entering the reaction zone, its temperature is increased while that of the product is decreased. In such a process the temperature profile of the combustion wave is determined not only by the heat conductivity through the porous base but also by convective heat exchange between the gas and the particles of the solid reactant. The authors cited above found that both ordinary combustion waves (with hot reaction products) and so-called inverse waves (with an anomalously wide preheated layer and cool reaction products) to be parameter-dependent (Figure 10). In the former case the maximum combustion temperature is higher than the adiabatic value and therefore such combustion is called superadiabatic. The combustion of low-temperature (weakly exothermic) compositions can be performed under such regimes. In the latter case the combustion temperature is lower than the adiabatic value and this can be used to moderate the combustion regime when the reaction heat is extremely high. A wide heated zone in the inverse wave can be rather useful for the heat treatment of the initial substance and also for rapid cooling of the product

resulting in quenching of the high-temperature zones formed. This example provides convincing evidence for the importance of understanding of the mechanism of the SHS processes. Therefore, the combustion theory always played an important role in the SHS research and development.

As a result of laborious study there have been developed theory-based techniques for the control of combustion rate, temperature, and degree of conversion in SHS systems.

The experience we obtained in the investigations of the combustion processes permits us to identify new systems efficiently and to find the shortest routes to get the necessary information. But SHS methods, it should be emphasized here, have been not indebted to the combustion theory, since SHS gave birth to such directions as gasless combustion, permeation combustion, unsteady wave propagation, and others in the combustion theory.

3. Structural Macrokinetics

At the initial stage of investigations the combustion theory was thought to be the theory of self-propagating high-temperature synthesis, since SHS process is one of the varieties of combustion and the final product formation is not only the consequence but also the cause of combustion. The reactive diffusion processes mainly considered in the first SHS theories [40,74,75] seemed to prove this idea. In other words, the final product formation was thought to proceed in the heat evolving zone related to the combustion velocity.

Another point of view was first reported by Borovinskaya at the (Soviet) Fourth All-Union Symposium on Combustion and Explosion in 1975 [76]. She supposed that the combustion reactions might result in solutions (solid or liquid, binary or multicomponent, saturated or oversaturated), rather than

final products (refractory compounds), which are formed far from the combustion front as the result of further transformations of the solutions (for example, during the decomposition of oversaturated solutions). Borovinskaya came to this idea accidentally in one of the routine experiments on boron combustion in nitrogen at pressures up to 5 kbar and analyzing boron nitride samples synthesized in the experiments. In one of the series immediately after combustion there took place a spontaneous pressure drop in the reactor, resulting in drastic cooling of the product. Its analysis did not show any presence of the boron nitride phase despite the fairly high nitrogen content in the product. It was in the amorphous state and that suggested an idea of possible formation of oversaturated solid solutions of nitrogen in boron as an intermediate combustion product (such a mechanism was discussed in detail for the titanium-zirconium combustion in nitrogen [63,64]. Later, both aforementioned concepts of the final product formation in the SHS processes were analyzed and an interpretation of the two ultimate mechanisms - equilibrium and nonequilibrium was developed [18]. There is a simplified scheme of the adiabatic structure for both cases in Figure 11.

In the first case (Khaikin-Merzhanov-Aldushin, equilibrium mechanism) chemical and structural transformations proceed simultaneously in the common zone of heat evolution. Both chemical and phase compositions are formed immediately behind the combustion front. All phases existing in the phase diagram of the studied system are realized in the process and can be identified as intermediate combustion products. In other words, there is a state of local equilibrium of the substance in the combustion wave which corresponds to the isothermal cross-sections in the phase diagram. Such a process is mainly typical for solid-phase reactions (in solid flame) at extremely low combustion

velocities.

In the second case (Borovinskaya, non-equilibrium mechanism) the structural transformations take place far behind the combustion front, when the chemical reactions have been completed. The substances formed are in metastable state in the zone of heat evolution and are able to decompose to form the product final structure. The phase diagram does not directly reflect this process, the equilibrium phases existing in the studied system may not be formed (except those corresponding to the final composition). Such a non-equilibrium mechanism is characterized by the rapid SHS processes. The validity of these interpretations is confirmed by numerous experimental results [53,54,62,63,77]. From the above-stated it becomes clear that the combustion theory is not able to describe the formation of the final state of the SHS products (their phase composition, structure), therefore, the SHS theory should combine the considerations of combustion mechanism and processes of structure formation. Thus, there appeared a new scientific trend, "structural macrokinetics."*

3.1 Ideology of Structural Macrokinetics

Structural macrokinetics (SMK) studies the evolution of the medium structure in the course of chemical conversions taking into account heat and mass transfer processes. The notion of "medium structure" involves the wide

*This term was introduced by the author in his key talk "Macroscopic Kinetics and Their Role in Modern Chemistry Development" at the (Soviet) First All-Union Symposium on Microscopic Kinetics and Chemical Gas Dynamics (Alma-Ata, 1984).

range of characteristics, among them are the following:

- macrostructure (composition distribution, macroscopic defects);
- microstructure (phase interlocation, medium graininess, impurity localization, porosity);
- crystal structure (symmetry and parameters of the crystal lattice, its distortion, ordering with superstructure formation, number and distribution of dislocations).

Below are given two formulas which determine the SMK place in macroscopic kinetics:

$$\begin{array}{lcl} \text{classical} & & \text{chemical} \\ \text{macrokinetics} & = & \text{kinetics} \quad + \quad \text{theory of mass and} \\ & & & \text{heat transfer} \\ \\ \text{structural} & & \text{classical} \\ \text{macrokinetics} & = & \text{macrokinetics} \quad + \quad \text{kinetics of} \\ & & & \text{structural conversions} \end{array}$$

The principal concept of the SMK in its general form is presented in Figure 12. It is based on the Borovinskaya non-equilibrium mechanism where in chemical conversions the decomposition of the old structure and the formation of a new one can occur sequentially and are accompanied by the formation of a disordered state of the substance (amorphous, liquid, and gaseous in some cases). The situations of decomposed old structures and new ones not yet formed are more probable for high temperature rapid processes due to the high values of chemical activation energy.

It is obvious that the SMK ideology is of interest not only for SHS investigations but also for all chemical processes with structural conversions. There are basic differences in SMK for various processes. Thus, during thermal decomposition and combustion of gasified condensed systems of an explosive or propellant type the disintegration of the old structure is not followed by the formation of a new one. In gas-phase chemico-condensational processes there is

no initial structure and structural effects become evident only in the reaction products. A diversity of structural conversions is characteristic of solid phase processes yielding solid products (such as in the SHS process), since the chemical reaction from its beginning to completion is accompanied by structural conversions which continue even after the reaction is completed.

The sequence of conversions shown in Figure 12 has its characteristic times t_c , t_p , and t_{rec} . For non-isothermic processes with heat losses (such as the SHS process) there also exists a characteristic time of thermal relaxation, t_r . Both macrokinetic characteristics of the process and structural distinctive properties of the product formed are dependent on the characteristic times ratio (complicated and various processes being seen behind their values). Relations (conditions) between these characteristic times are given below as applied to SHS processes:

Wave-like Regimes

Wave propagation: $t_c \ll t_r$

Splitting of the combustion and structurization zones: $t_c \ll t_{ph}, t_{rec}$

Confluence of the combustion and structurization zones $t_c \gg t_{ph}, t_{rec}$

Product Structure

Amorphous product: $t_c \ll t \ll t_{ph}$

Crystalline product of a non-equilibrium structure: t_c and $t_p \ll t_r \ll t_{rec}$

Crystalline product of an equilibrium structure: $t_c, t_{ph},$ and $t_{rec} \ll t_r$.

From the above, it is seen that the combustion itself is an initial step in the SHS process and consequently, the combustion theory should be taken as a section in SMK. At the same time it would be erroneous to consider combustion and structurization independent of each other. The combustion regimes are known to directly affect the product structure. For slow processes a reverse

relation takes place, i.e., the structurization may affect the combustion velocity via its kinetic and thermo-diffusional characteristics. The cases of complete separation of the combustion and structurization processes (the former determining only the initial conditions) i.e. for processes of structurization without reverse influence, are called ultimate. Unfortunately (however, fortunately for the beginners in this fascinating field of science), SMK is not so far supported by developed scientific techniques since it is a newly-born discipline. These techniques have yet to be developed. By now, just the SMK ideology has been accepted and the process of accumulation experimental observations is in progress. These observations will form a base for the creation of a certain system of concepts.

3.2 Structural Statics and Structural Dynamics

A large pool of information on the relationship between the structural characteristics of the final product and the green mixture parameters and combustion conditions has been accumulated. Vast empirical observations have been summarized having no claim on the interpretation of the mechanism and dynamics of structural formation. Structural characteristics of the products were obtained by different methods (metallography, local chemical analysis, x-ray analysis, electron microscopy, neutronography, etc.). Such an approach was called "Structural Statics".

The results of investigations of structural characteristics of the combustion products obtained in various conditions have been described in the literature. The most studied aspects are morphology and porosity of the samples [2,11,16,59], chemical and phase macro-inhomogeneity [76,78], and microstructure [79-81]. Interesting structural effects have been observed. The study of combustion of porous metal samples in nitrogen showed the

possibility of product formation of two types, purely inhomogeneous and completely homogeneous [63,78]. Figure 13 exemplifies the longitudinal cross-sections of tantalum compacts after the surface combustion in nitrogen. There are two regions in the first sample, which was quenched: the central region which is almost without nitrogen, and the surface region which consists of a mixture of $\gamma\text{-Ta}_2\text{N}$ and $\epsilon\text{-TaN}$. The other sample cooled without quenching consists of $\zeta\text{-TaN}$ (at the surface), $\epsilon\text{-TaN}$, $\gamma\text{-Ta}_2\text{N}$ layers, and nitrogen solid solution in tantalum (in the center). The increase in time for the reaction completion or transition to the layer-to-layer combustion is the way to obtain homogeneous samples containing one of the possible products. The effect of macro-inhomogeneity of products produced by the layer-to-layer and surface regimes was explained in the theory of permeation combustion.

The investigations devoted to the study of the laws of gasless combustion [20,82,83] showed that with an intentional decrease in the combustion temperature (in different ways) the homogeneous, dense product spontaneously begins to separate into layers and thus becomes a combination of flat flakes. One of them (continuous) formed at a combustion temperature of $\sim 3000\text{K}$ while the other (layered) formed at $\sim 2000\text{K}$. It is of interest that layered samples readily break up into flakes. Shkiro, Galtchenko, and coworkers studied the flake structure and found them to be inhomogeneous across their thickness. The product segregation is attributed to the appearance of the oscillatory regime of combustion. In the works by Rogatchev, Pityulin, Gordopolov, and the author, the dependence of the size of the carbide phase grains on the pressure applied to the sample was studied in the combustion of complex compositions, yielding solid alloys. In Figure 14 there are photographs of metallographic cross-sections of the samples produced by static and shock densification (other

conditions being equal). The figure shows the grains of shock densification to be much smaller. The changes in the process conditions may affect the formation of grain microstructure of the product. Bloshenko and coworkers studied the porous structure of combustion products, the relationship between open and closed porosity, and the possibility of affecting the pore characteristics.

One of the recent results in structural statics is the observation of anisotropic effects [84], which reveal the dependence of physical properties of some polycrystalline combustion products on the direction, and, in particular, on the orientation towards the direction of the combustion front propagation. The results of the measurements of dielectric permeability and electroresistivity of some oxides obtained under the combustion regime show differences in these properties. The measurements were taken on the samples cut along (\parallel) and transverse (\perp) to the combustion front. The difference, particularly in the electroresistivity values, is noteworthy.

The samples of oxide and metal mixtures converted by combustion into ferrites are weak permanent magnets, primary (spontaneous) magnetization being of 200 oersteds. They establish the magnetic field and attract iron shavings. It is of interest that the point of ignition always becomes the magnetic south pole, i.e., the effect does not depend on the magnetic field of the earth.

Anisotropy of mechanical properties was observed in boron nitride samples. The effect is related to the crystallites orientation along the direction of combustion front propagation due to the existence of the axial temperature gradients. The origin and localization of anisotropic effects are under study now.

The resources of structural statics permit us to obtain some information

pertinent to the mechanism of structure formation, and to the theoretical SMK models, since the combustion products often contain traces of the processes occurring in the SHS zones. However, this information is indirect and, therefore, may be not always completely and conclusively interpreted. Structural dynamics has more reliable techniques for the continuous registration of physical parameters in the course of the SHS process in all its zones. The most developed thermographic techniques are used for temperature measurements and, consequently, thermal effects of combustion and structure formation. The interpretation of structural effects according to the temperature - time - composition curves has been provided [32]. The dependence of the average product composition (determined gravimetrically) on temperature during the process of cooling is depicted in Figure 15. The curve is superimposed on the phase diagram of for the Ti-H system. Isothermal regions are seen to correspond to the phase transformations in the zone of structurization.

Boldyrev, Aleksandrov, and coworkers suggested an interesting and promising approach in their works [53,54]. They used the ability of synchrotronous radiation to produce diffractograms with a small time lag (operational time is 0.5-1.0 s), thus studying the dynamics of changes in the phase composition of the substance during the SHS process. Figure 16 shows the data on the phase formation kinetics in the Ni-Al system. The main achievement of this work is that the formation of the final product (nickel monoaluminide, NiAl) begins far from the combustion front in accordance with the Borovinskaya non-equilibrium mechanism [76]. The investigations resulted in finding two earlier unknown intermediate phases which are not identified so far. This is more evidence for the non-equilibrium character of conversions in the SHS

processes. Synchrotronous radiation can become one of the main methods in the investigations of structural dynamics.

Currently, a combined approach to the study of the structural conversions in SHS processes has been developed. It is based on the rapid arrest of the process allowing quenching of the intermediate substance in the SHS wave and further layer-to-layer analysis. Rogatchev, Mukasyan, and the author [77] carried out the quenching of burning reactants mixture through the use of a copper wedge. The quenching rate under such conditions is low ($\approx 10^3 - 10^4$ K/s), nevertheless it allows a qualitative view of the dynamics of chemical and structural conversions in SHS. The Ti-C system has been studied in detail. Three principal stages of the process have been highlighted as follows:

- titanium melting, capillary soaking of carbon black layers and simultaneous carbon dilution in titanium, accompanied by considerable heat evolution;
- the formation of the product primary structure by the nucleation of titanium carbide crystallites at the carbon - melt interface and in the melt bulk;
- recrystallization and growth of titanium-carbon grains which become an order of magnitude larger with sizes reaching tens of micrometers.

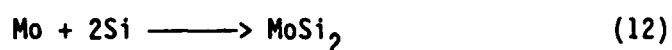
The first two stages relate to the combustion and determine its velocity, the latter relates to the structure formation of the final product. Analogous results were obtained in the study of the titanium - boron system. The SHS processes in solid-phase systems of the Ta-C type and hybrid systems of the Si-N₂ (gas) type are currently studied using the quenching technique.

Some information about SMK can be obtained from the study of self-purification and outgassing (evolution of volatile impurities) in the course of

the SHS process (see Bloshenko et al. [85-89], Steinberg et al. [90], and Filonenko et al. [91]). We may expect that the development of the fundamental aspects of the structural macrokinetics will lead to the creation of the set of science-based approaches to the formation of new generation of complex SHS materials with unique properties.

4. Chemical Synthesis

Structural macrokinetics and in particular, the combustion theory, forms the foundation for a better understanding and description of the SHS processes. The major objective of the SHS processes is the synthesis of materials through chemical reactions by combustion. From the time of discovery of the SHS method as a physico-chemical phenomenon, investigations have been carried out to determine the feasibility of material synthesis. The first papers reported on the direct synthesis of refractory compounds of various elements. Among the simplest reactions, the following types were considered:



These compounds (borides, carbides, nitrides, silicides, and others) seem to ideally fit the SHS reaction conditions. They are thermally stable at high temperatures, the values of their chemical bond energies are high, which means that during their formation much heat is released. Hence the application of SHS to the synthesis of these compounds is necessary rather than advantageous.

4.1 Elemental Systems

Synthesis undertaken in the elemental systems during the earlier stages of SHS studies showed the close dependence between the synthesis conditions and

macrokinetic factors. This allowed the SHS processes to be divided into three main groups:

(i) gasless synthesis: When pure components are used the gas evolution is not practically observed (small gas evolution is usually caused by self-purification from impurities). The product composition is weakly influenced by changes in the parameters of the external medium (vacuum, inert gases). The major factors controlling the synthesis are concentration ratios, reactant particles size, green density, and combustion temperature.

The gasless synthesis yields borides, carbides, silicides, and other compounds consisting of elements stable at high temperatures. The SHS method is used to perform direct synthesis of nonstoichiometric carbides, to obtain various phases in the metal-boron, metal-metal, and metal-silicon systems. Controlling the level of impurities composition (oxygen inclusions, in particular) is a rather skillful operation in the gasless synthesis. The problem of self-purification from the impurities became the subject of the series of investigations by Bloshenko et al. [85-89]

(ii) gas consumption of permeation synthesis is carried out in the hybrid metal-gas systems. Their main salient feature is a strong dependence of the product composition on the composition and pressure of the gas medium. In practice the way the gas is supplied to the combustion zone is of great importance (spontaneous permeation blowing through). The discovery of the principle of changing the combustion conditions by dilution of a green mixture or a reacting gas by inert products [11] became an important achievement in the theory and practice of gas-absorbing synthesis. The decrease in temperature and combustion rate, which appeared to increase both the amount of bound gas in the product and the uniformity of its distribution in the compact, was found to

be an essential controlling procedure in the permeation processes.

The most common scheme of gas-absorbing synthesis could be applied to the production of nitrides and hydrides, the former being the first synthesized by SHS (see the works by Borovinskaya et al. [63,64,69,76]. Much effort was spent to overcome the main problem, i.e., incomplete combustion so as to obtain homogeneous nitrides with large required contents of nitrogen in the products. The synthesis of high-quality products by the methods of this group requires the combination of the following criteria:

homogeneity	$t_f/t_c \ll 1$
stability	$k = d \ln u / dT_B \leq 3.9-4.0$ [92]
post-combustion	$t_c/t_r \ll 1$

where t_f , t_c , t_r are specific times of permeation, chemical reactions, and product thermal relaxation, respectively; k is the temperature coefficient of the combustion rate; u is the combustion velocity; and T_B is the combustion temperature.

The SHS method appeared to be efficient in the synthesis of nonstoichiometric nitrides and, solid solutions in the metal-nitrogen systems. The permeation factors which are important in the nitride synthesis are of a less importance in the synthesis of hydrides because of the high hydrogen diffusivity which provides the requirement of the first criterion. The problems of product (hydride) dissociation are of greater significance in this case. Self-propagating high-temperature synthesis of hydrides was first performed in 1976 [66]. It was further developed by the researchers of the Armenian School of SHS (Dolukhanyan et al. [93-96], Kharatyan et al. [67,68]). In the beginning there was a great deal of surprise because of the SHS feasibility in producing such thermally unstable compounds as hydrides. In all

the systems studied by that time the combustion temperature was in the range 2000-3500°C, whereas that of hydride dissociation is known to be much lower (e.g., it is only 800° for titanium dihydride at atmospheric pressure). The hydride phenomenon seemed to contradict the main idea of the SHS method.

The explanation can be found in Figure 17 [68]. The figure it shows a plot of equilibrium composition of titanium hydride (the hydrogenation completeness) vs. temperature at constant pressure and a plot of the adiabatic temperature-composition line. Their intersection determines the state realized during combustion. There are two sites, low-temperature (for nonstoichiometric titanium dihydride) and high-temperature (for hydrogen solid solution in β -titanium) and high-temperature (for hydrogen solid solution in β -titanium). From Figure 17 it is seen that at $T > 650^\circ\text{C}$ there is no hydride phase and a solid solution instead of titanium dihydride is formed in the combustion wave. The completeness of hydrogenation is ~25%. The hydride phase is formed during cooling of the product at the expense of the shift of the thermodynamic equilibrium. The cooling temperature should not be too high, otherwise the quenching of the solid solution would take place. A similar mechanism exists in the synthesis of some other metal hydrides.

(iii) gas-evolving synthesis forms the third group discovered in the study of the elements interaction in SHS mode. It involves the systems with highly volatile components, e.g., mixtures of metal powders with sulfur, selenium, tellurium, phosphorus, and liquified gases (liquid nitrogen) [51,97-102]. The main difficulty of this synthesis is caused by the reactant leakage into the atmosphere which, requires that certain precautions to be taken when performing the process. The use of gas-tight vessels filled up with the green mixture is the simplest solution to this the problem. In this case, the evaporating

reactant just fills cavities, staying in the reaction bulk and participating in the process. The reactant losses in the open systems can be decreased in various ways, e.g., by using inert gas pressure.

High quality sulfides, selenides, tellurides, phosphides and other compounds of the required chemical and phase composition can be obtained by changing the initial mixture composition and combustion conditions taking account the volatile reactant evaporation. Unfortunately, the investigations of systems with two readily volatile reactants had no further development. An example to such synthesis ("condensate syntheses" as they were termed by the author [9,103]) is the formation of magnesium sulfide from the elements.

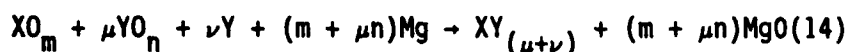
The results of direct synthesis from the elements under the SHS regime are well-known [9,102,104,106]. Therefore, there is no need to dwell on the characteristics or the particular products in the present paper. Their common property is high purity as compared with the products of furnace synthesis. This is explained by a lower content of impurities (due to the process of self-purification) and the amount of unreacted elements (due to the higher temperature with the possibility creating optimum conditions to provide reaction completeness).

4.2 Extension of Chemical Foundations of the SHS Method

That was the development of the synthesis direction in the SHS processes which inevitably led to the extension of chemical foundations of the process and raw materials basis for the synthesis. Apparently the synthesis from elements cannot completely fit the requirements of industry. Therefore, it was quite natural that in 1974-75 an active search for new resources for the SHS started which resulted in the establishment of new synthesis directions. Syntheses using metal and non-metal oxides as reactants, metal-reducers

(magnesium, aluminum, etc.), and reacting and controlling additives are of great importance among various chemical classes of SHS systems. There are two general chemical types of combustion in such systems, i.e., the reduction to the element from oxides and the interaction of the reduced elements to form refractory compounds. They were called self-propagating high-temperature synthesis with a reduction stage. They are essentially a combination of well-known chemical reactions.

The SHS processes with the reduction stage were described in detail by Borovinskaya, Mayan, Yukhvid, et al. [107-113], who found magnesium and aluminium thermite SHS processes to have essential differences. The chemical scheme of Mg thermite SHS processes in its general (simplified) form can be written as follows:



where X, Y are chemical elements of refractory compounds, Mg and O are magnesium and oxygen, respectively, and μ , ν , m, and n are stoichiometric coefficients.

In Mg thermite synthesis the combustion product is at least a two-phase compound which consists of the final product and MgO by product. They are uniformly distributed in the combustion product in the common case. Therefore, the phase separation of the combustion product is an additional task for the industrial synthesis. However, the necessity of phase separation is compensated by the high quality of the products synthesized and low costs and availability of raw materials. The metallothermic SHS processes are mostly applied to the synthesis of boron carbides and nitrides, borides, some carbides, nitrides and silicides of transition metals. Aluminium thermite SHS processes can be described by the chemical scheme analogous to the above (Eq.

14) with the only difference of Al and Al_2O_3 taken instead of Mg and MgO , respectively, and different coefficient ratio. The distinctive feature of many Al thermite processes under study is their temperature which is higher than the melting point of all the products formed. Multicomponent high temperature melt is the combustion product in these systems. The phase separation (light Al oxide comes to the surface whereas the heavy refractory compound sinks) takes place in the melt under gravity. The process of phase separation is well known for the simple process of Al thermite reduction, in which the problem of final product separation is solved when it forms an ingot after the stages of phase separation and crystallization. It is seen that the final product yield (the relative weight of the ingot) depends on the whole diameter [108, 114, 115] and the process is of a critical character. At low diameter values the phase separation is not observed (crystallization of unsegregated melt takes place); at high values the degree of the phase separation is equal to 100%, the process being affected by some other parameters (centrifugal acceleration, combustion temperature, gas pressure, heat losses and the like) [107, 110, 112, 113]. The critical conditions relate to the ratio between the characteristic times of segregation processes and the product cooling. The Al thermite synthesis method is realized in the production of cast carbides, borides, and silicides of transition metals of groups VI and VIII of the periodic table. The main problem of the decrease in aluminum admixtures in the product is solved by the addition of special additives. Aluminum thermite approach is most efficient in the aluminides synthesis.

The azide direction based on the use of solid nitrogen carriers as reactants is an interesting direction in the SHS research and development. Nitrogen introduction into the green mixture in the form of readily decomposing

compounds makes it possible to overcome the problem of permeation and to increase the amount of bound nitrogen in synthesized nitrides. The work on azide use as a reactant in the SHS processes was started at the Kuibyshev Polytechnical Institute under Professor Kosolapov guidance in 1977 [116]. Two substances, ammonium nitride, NH_4N_3 and sodium azides, NaN_3 , appeared to be the most suitable reactants. Ammonium nitride yields more pure nitrides, and NaN_3 is more applied in handling. The azide variant is used in fine synthesis and in general cases. It cannot compete with a simpler nitrogen one.

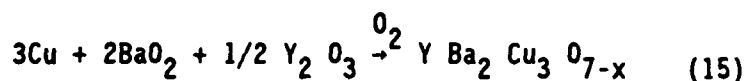
In SHS method there are numerous directions based on the use of various reactants. Besides those discussed above, hydrides [117], alloys [118], polymers [119], intermetallides [95], and mineral raw materials can be used in the green composition. The SHS chemistry is so rich, there are no limitations in the reactants used, if you are able to compose necessary exothermic complexes for desired products. An important contribution to the development of the SHS chemistry was made by Holt (azide synthesis of nitrides, SHS-magnitermicity, oxide-carbon materials) [106,120-128].

Among new directions in the field of the SHS chemistry the oxide one should be noted, i.e., synthesis of complex oxides under the combustion regime, which was underestimated for a long time. Burning metals in oxygen (or in the air) with the oxide formation was considered trivial and not efficient. The emphasis was made to the systems of nonoxygen combustion as more original ones. However, the paper by Boldyrev et al. [129] elucidated the usefulness of the SHS methods in the problem of complex oxide synthesis. They became the impetus to the new publications in this branch [130-132].

A series of investigations have been undertaken in the Institute of Structural Macrokinetics by Nersesyan and Borovinskaya, et al. The list of

complex oxides obtained by SHS is given in Table 2. There are compounds of a very complicated structure (perovskites, etc.). It is evidence for the vast synthetic feasibility of the method. The oxide purity is high, e.g., in lithium niobate the contents of impurities is at a level of $10^{-3} - 10^{-5}$ wt%. Both solid oxidants and air oxygen are used for the oxide synthesis. The combustion velocity in multicomponent green compacts is only 0.1 - 2 cm/s, and the combustion temperature is in the range 850-1500°C.

The greatest success in this direction is likely to be connected with the synthesis of high temperature superconductors (so called oxide ceramics). The discovery of such compounds is known to be a most important finding in modern physics. All over the world the synthesis of high temperature superconductors, which are the most complicated oxides, have been undertaken, whereas the group of Nersesyan has carried out the combustion reaction synthesis according to the science:



where Cu is the fuel, BaO_2 is a solid oxidant, Y_2O_3 is an active filler, and O_2 is gaseous oxygen. Figure 18 shows the temperature dependence of the resistivity and magnetic susceptibility of the product obtained in SHS. The superconducting parameters of the SHS products correspond to the level of this class compounds. SHS-superconductors have some peculiarities, which make them the best products among analogous ones. All high temperature superconductors known so far can be obtained by the SHS method, including bismuth and thallium ceramics.

4.3 Thermodynamic Analysis and Chemical Stages

As stated above the search for the optimum conditions for the synthesis of

the product of desired chemical and phase composition is in progress. Along with the methods of combustion theory and structural macrokinetics those of combustion chemistry, particularly thermodynamic analysis of the SHS reactions, play an important role in the solution of this search.

The development of the thermodynamic branch is based on the estimations of both temperature and equilibrium compositions of the combustion product. Thermodynamic analysis is especially important for the multicomponent systems, when the combustion product composition is not apparent because of competing side reactions and phase transformations. The thermodynamic diagram of the combustion product in the TiO_2 - B_2O_3 - Mg system [54] is given as an illustration to this approach (Figure 19). The end product of the reaction is titanium boride, the main (obligatory present) by-product is magnesium oxide. Magnesium boride, unreacted titanium boron, and magnesium can be found among the combustion products. The problem is to find the optimum initial composition to produce one boride phase only. Such a region for TiB_2 is shadowed in Figure 26. It is important to note that it is a region and, not a point in the ternary diagram. It was formed due to the side process leading to the gas phase appearance and ununiqueness of the optimum conditions. It is rather curious that the stoichiometric point calculated from the reaction:



lies beyond the optimum area, which confirms the necessity of thermodynamic calculations.

Knowledge of the kinetics and mechanism of chemical reactions in SHS processes is essential in the understanding of the difference between real and thermodynamically calculated conditions. The knowledge of the sequence and velocity of chemical transformations helps to create the conditions for the

synthesis of intermediate compounds, i.e. products of incomplete transformation and metastable phases. The synthesis of cubic modification of TaN is an instructive example. It had been observed in the thin films and later obtained by the SHS method [134]. The study of the tantalum combustion mechanism in nitrogen [78,135-137] revealed the following rules (see also the flow diagram in Figure 20) only tantalum half-nitride (Ta_2N) is formed in the combustion wave. This compound is an intermediate product of Ta interaction with nitrogen. This product can be obtained as a single phased if the process is quenched after the combustion wave has passed. If the sample, heated by the combustion wave, in nitrogen, repeated combustion will take place with the formation of the tantalum mononitride phase, TaN. Remember that the experiments held at ambient nitrogen pressure (~40 atm) produce the hexagonal modification of TaN, those at high pressures (~3000 atm) yield a cubic one. The cubic modification is synthesized through the combustion of Ta in liquid nitrogen [138].

In the study of the structural dependence of the nitride formed on the combustion conditions it was possible to determine the homogeneous region of the TaN_x cubic modification ($x=0.9 - 1.2$). The superstoichiometry was shown to be connected with the defects in the metal sublattice. The specially performed annealing allowed production of the ordered phase, Ta_5N_{6-x} [139,140]. Ordering of the nonstoichiometric phases is one of the most interesting problems closely connected with the SHS facilities. The series of neutron diffraction investigation on the ordering in the Me-C, Me-N, Me-C-N, etc. systems was carried out by Karimov et al. [139,141-144] on SHS products. Recently Guzhko and co-workers [145] have obtained an ordered phase Ta_4C_3 by special annealing of the nonstoichiometric SHS product. It is of interest that ordered phases

can be obtained by the direct SHS method without further annealing when the process of product cooling is conducted under control. The kinetic laws and SHS reaction constants are necessary for a better understanding of the synthesis conditions. High temperature (up to 3000°C) interactions between metals and gases (nitrogen, oxygen, hydrogen) are studied in the original electro-thermographic experiments by Grigor'ev, Kharatyan et al. [146-154].

The development of the synthetic branch of the SHS problem becomes more complicated. There is a tendency to solve more complicated synthetic tasks connected with certain structural requirements to the products obtained. It can be expected that developing structural macrokinetics methods and combinations of chemical and macrokinetic approaches will contribute much to the solution of the problems of SHS.

5. Technology and Materials

If structural macrokinetics and the combustion theory are the brain of the SHS process, technology is its heart which secures the problem its vital ability. These are technologies and materials obtained in the chemical synthesis that played the most important role in the establishment of SHS as a new active field of scientific and technical progress. Even now, twenty years after the SHS emergence, one must sometimes provide evidence for the practical application of SHS. The first evaluation of SHS by many specialists is inconsistent. "The process is magnificent, however, it won't work in practice. It won't give efficient and reliable production," - these are the most common conclusions. The only convincing argument in the discussion is satisfactory operation properties of final product obtained by SHS method. When the author realized this, active development of the technological direction of the SHS process began. At present the stock of the technological methods in SHS is

great. It allows the solution of the industrial tasks in obtaining:

- chemical products of a desired composition;
- simple and multicomponent materials of a desired structure;
- parts of the definite form and size (including parts with coating);
- articles with the required combination of operation characteristics.

These tasks are probably of different complexities, their degree decreasing down the above sequence. In the same order the potential and current scope of the research and development activities decrease. Most of the actual problems of the present state of SHS development are the products shape formation and, direct production of parts and articles by SHS method and their direct coating. The solution of the problems is expected to bring about drastic changes in the technology of inorganic materials.

More than 30 original technological methods have been developed in the USSR by now. They can be divided into six technological types (TT).

5.1: SHS Technology of Compacts and Powders (TT-1)

This is the simplest of the technological variety of SHS. It is based on the green compact burning under ambient conditions. The most common procedure is the condition of SHS in the reactors up to 30 liter capacity. They can be evacuated or work used for under the pressure of inert or reacting gases. The SHS product obtained in such reactors is a sinter or ingot of a shapeless mass, which can directly find practical application. For example, nitrid ligatures obtained by ferro-alloys burning in nitrogen are used for the addition of nitrogen to steel [155]. However, the reactor SHS products are mostly used for the powder production. Two approaches are realized in this case:

- (a) mechanical grinding of SHS products to obtain one-phase or composite powders;

(b) thermochemical (hydrometallurgical) processing of multiphase product to isolate powders of desired composition (for example, to remove MgO in Mg thermite products).

High quality powders are obtained by the SHS technology in much simpler ways than by furnace synthesis. As has been shown, SHS products are quite competitive and are of a certain interest in the commercial aspects.

SHS powders are used as raw material for sintering of ceramic and metal-ceramic articles, depositing protecting coatings, production of abrasive pastes and tools, etc. High quality of S.S powders under the optimum technological conditions provide high quality level of the final product. Abrasive properties of TiC powders obtained by different methods have been in [156]. SHS powders have the best abrasive ability. Thus highly efficient abrasive pastes of KT and KTIOL trade mark have been produced with the collaboration of the USSR Academy of Sciences Institutes of Chemical Physics and Materials Science. They allow the combination of grinding and polishing into a one-stop operation in the processing of ferrous and non-ferrous metals [157]. The application of SHS powders is making a lot of progress [158]. One of new results is the development of sintered tungstenless cemented carbides obtained from the SHS powder products of complex composition (Table 3). As seen earlier, the use of pure SHS powders in the problem of the cemented carbides can lead to a considerable increase in the physico-mechanical properties of the materials. The use of SHS powders of Si_3N_4 (α and β), SiC (β), BN, B_4C , AlN, and sialones for the production of structural, tool-making and dielectric ceramics is rather promising. A great contribution to the preparation and development of the SHS powder technology was made by Borovinskaya, Ratnikov, Prokudina, Mamyán, and their co-workers. At present work on the development of

industrial technological lines and SHS facility sites have begun.

5.2: SHS Sintering (IT-2)

Powder production is far from being an optimum version of technological realization of SHS. Its use is justified only for the cases when SHS products are used as starting materials for sintering or as abrasive. One of the promising technological tasks is the sintering of the solid product during SHS for the production of articles of desired form and size. The realization of this task is in the molding of the green compact and the retention of its configuration during the SHS process. The size correlation can be investigated in a preliminary way.

The problem of the SHS product sintering is not studied well. It is evident that

$$\eta_e = \eta_v + \eta_p; \eta_e = \frac{v_2 - v_1}{v_2} \quad (17)$$

where η_v , η_p are the degrees of sintering in the synthesis wave and in the time during which the product is still at high temperatures, respectively, η_e is the net degree of sintering in the SHS process, v_2 is the sample volume; and v_1 is the volume of pores in sample. The η_v value is decreased by the admixture gas-evolution, η_p can be changed to some extent by varying the rate of cooling of the SHS product. The first work concerning the production of SHS sintered articles [79] was followed by the development of the problem in three directions, in which sintering is realized: (i) in air, (ii) in vacuum chambers, and (iii) in special gas environments. Accuracy of the retention of sample configuration, sufficient for practical applications, can be provided. Porosity of the sintered product can be easily realized in 5-70% limits.

Some characteristics of SHS refractories are listed in Table 4. In spite

of its technological simplicity SHS sintering of high melting articles yields high quality materials. SHS sintering have been developed in connection with ceramic materials based on oxygen-free refractory compounds. We have succeeded in the production of articles suitable for practical use. A number of new ceramic materials has been obtained (Table 5). Ceramics based on boron, aluminum, and silicon carbides and nitrides are known to difficult to sinter. Activators introduced to facilitate the formation of low porosity articles, however, make the material less stable at high temperatures. Ceramics obtained by SHS sintering possess a remarkable peculiarity. There is no sintering activators in their composition, their strength does not depend on temperature.

The use of thermovacuo SHS technology help to obtain highly porous articles of high structural strength. Thus articles from titanium carbide with 55% porosity have ultimate compression strength of 100-120 MPa, which is much higher than the corresponding value for articles obtained by powder metallurgical methods. Porous parts obtained by SHS sintering are used as workpiece to be soaked, as filters, catalyst supports, etc. The work by Borovinskaya, Bloshenko, Nersesyan, and their co-workers promoted the investigations on the use of SHS sintering.

5.3: SHS Densification (TT-3).

SHS sintering fails to give products of sufficiently low porosity. In some cases the value of 1% porosity has been achieved. A set of methods has been developed to obtain poreless parts when SHS products heated by the combustion wave is subjected to densification up the the poreless state. The most common way is to conduct SHS in special press forms in which the product obtains the properties and the form of a final material. The first results on the solid alloy synthesis in this important technological direction have been

reported [80]. They were further developed both in the investigative and technical engineering aspects. A time diagram of the process (Figure 21) has been utilized. The optimum ratios between t_1 , t_2 , etc. values are being determined in the process operation.

With references to Figure 22, the compact homogeneity is ensured under the following conditions:

$$t_1 \ll t_r$$

$$t_2 - t_1 \ll t_r$$

where t_r is the characteristic time of thermal relaxation of the compact and the other values, are as defined in Figure 34. Optimum conditions are needed to obtain materials and articles of low residual porosity. In general, these conditions can be stated as:

$$t_d = t_3 - t_2 = (t_d)_{\text{opt}}$$

$$t_p = t_4 - t_3 = (t_p)_{\text{opt}}$$

$$P = P_{\text{opt}} > P_{\text{crit.}}$$

where t_d , t_p are the delay and duration of pressing, respectively, P is the process pressure, and the subscript "opt" refers to the optimum conditions. A very important feature typical to the discussed process is the pressing delay, t_d . Figure 22 shows the dependence of the residual porosity on the pressing delay in one of the compositions of a solid alloy. It is seen that $t_d = (t_d)_{\text{opt}}$ is at a defined porosity minimum. The increase in porosity caused by the deviation from the optimum of pressing delay is connected with the incompleteness of outgassing, evolution of the impurity gases (at low t_d), and with the loss of the product elasticity, its "overcooling" (at high t_d). The determination of the optimum conditions from t_d and t_p as well as from P is an experimental task to be solved, since there is not yet a quantitative theory of

optimum ratios.

The method of SHS densification is of great importance for the creation of new materials due to its simplicity and efficiency. One of the most interesting directions is the synthesis of tungstenless solid alloys. A number of new compositions with a wide range of physico-mechanical properties has been designed in the USSR (both superhard and superstrong). As compared to the alloys obtained in powder metallurgy, the SHS alloys possess more perfect grain size distribution and a higher purity and, consequently, higher structural stability (at certain grain size and porosity). Because of the above properties the SHS alloys were referred to as synthetic hard tool materials (SHTM).

The technology of SHS densification is used for direct manufacture of hard-alloy articles: rollers, drawing blocks, pressing equipment, cutting plates, and the like. Some of these industrially produced items are shown in Figure 23. Their high operational characteristics and the advantages of their production technology led to the demand for the method of SHS densification in engineering. Investigations undertaken by Borovinskaya, Ratnikov, Pityulin, Kvanin, and co-workers contributed much to the creation and realization of SHS densification technology. An interesting variety of this technology is SHS extrusion developed under the guidance of Stolin. Densification in this case is completed by pressing the SHS product through a drawing block. SHS extrusion is especially effective in the production of long-sized articles. In

Interesting investigations on the combination of the SHS process with the shock wave action were started in 1980. Adadurov, then Gordopolov et al. showed that it is possible to obtain suitable materials through the use of SHS shock densification rather sound process [159,160]. The explosion action in

the SHS hard alloy production is one of the procedures of grain refining. Microstructures of SHTM alloys, obtained with pressure application and with explosion densification under similar conditions are shown in Figure 14. It is seen that the grain size of the explosion case is noticeably smaller.

5.4 SHS Metallurgy (TT-4).

The technology of SHS melt plays an important role in the general complex of SHS processing techniques. The fruitfulness of the idea of choosing highly exothermic green mixture to provide the combustion temperatures exceeding that of the melting temperature of the products is evident. This is the way to synthesize melts of refractory substances. High temperature melt can be subjected to all known metallurgical procedures (though with serious technical difficulties) to obtain ingots, cast articles, to perform surfacing by welding. That is why this direction was called SHS metallurgy which involves two stages:

- (i) melt obtained by SHS, and
- (ii) the treatment of the melt by metallurgical methods. The processes of Al thermite reduction accompanied by extremely high temperature (up to 4500°C) became widely spread in the SHS metallurgy.

Three technological directions have been developed under the guidance of Yukhvid and Borovinskaya:

- SHS technology of ingots and cast articles;
- centrifugal SHS casting;
- SHS deposition by welding.

With reference to the first direction, technological regimes of producing the ingots of chromium, molybdenum, and tungsten carbides and borides with alumina by-product were worked out.

The realization of the SHS processes in the field of centrifugal forces is

rather efficient for the melt formation. They strongly affect the process of phase separation providing their completeness and in some cases intensify combustion itself. To develop the technology of centrifugal SHS casting the results of Maksimov, Maksimov, Yukhvid and the author on the influence of centrifugal action upon the combustion process of various systems were used [161-162]. In 1975 centrifugal casting was carried out in cylindrical chambers rotating around their axes to obtain pipes (see patents [107]). Depending on the centrifugal acceleration and some other factors these conditions produced two-layer pipes (metal or refractory compound formed the external layer, aluminum oxide formed the internal one) or monolayer pipes, and mineral ceramics (without phase separation). Such articles offer various applications (metal laying, pipes for the transport of corrosive media roller sleeves, etc.). Centrifugal SHS casting was further developed in the investigations of Odawara [164-169] who conducted his work in nitrogen (normal pressure), in air flow, and in vacuum. The coating of curved pipes (5.5 m in length, is evidence for technical triumph of this research [169].

The SHS melt obtained on the metal surface is used in the technology of SHS deposition by welding. Besides the stages of synthesis and phase separation, there is also the process of interaction of the high temperature melt with the cold metal base, resulting in a deposited layer. High adhesion of the layer with the metal base is caused by the intermediate gradient zone which gradually changes its composition. Figure 24 shows the changes in the element contents in the lateral microsection of the system steel-substrate-deposited layer and the hardness distribution in the same cross-section. The thickness of the transition zone is 0.5-1.0 mm. The main component of the layer is titanium-chromium carbide. The wear resistance of SHS deposited layer

is 4-5 times higher than that of castings from the alloy "Sormite", widely used in the USSR. SHS deposition by welding begins to find its application in the technology of wear-resistant parts (bits, ploughshares, mixer blades, and the like). Materials produced by "SHS metallurgy" are diverse, but their specific feature is the presence of traces of the way they were produced. In their physico-mechanical properties they are behind the materials of the SHTM group. Some characteristics of SHS cast materials are summarized in Table 6.

5.5 SHS Welding (TT-5).

This direction of the SHS-technology headed by Steinberg is aimed at the creation of strong one-piece connection of the refractory parts of uniform and nonuniform materials by SHS processes and products. The process itself is a source of exothermicity and high temperatures since the SHS product is a welding material [170]. SHS welding is usually carried out in a clearance between the parts to be joined by making a high temperature melt which forms a strong bond. To increase heat evolution, electric current is usually passed through the green mixture bringing about the so-called "electro-heat" explosion [62]. SHS welding is somewhat intermediate between electro- and thermite welding. Its main advantage is the possibility of making one-piece connection between high-temperature materials not easily welded by other methods. Carbon, titanium, steel, tungsten, molybdenum, and others can be welded with each other and to themselves by this method. Investigations on SHS welding are in progress.

5.6 SHS Technology of Gas-Transport Coatings (TT-6)

This direction in SHS technology deals with new processes in which thin coatings are deposited onto various surfaces. For such processes to be realized, gas-transport additions and the parts to be coated are introduced

into the SHS mixture. The process is fulfilled by gas-transport transfer to the surface where chemical reaction (the same as in the main mixture) takes place and the desired SHS product is formed as a coating. The thickness of the coating can be regulated from 5 to 150 μm . Its homogeneity is conditioned by the gas phase site.

Table 7 gives some data on the gas-transport SHS coatings which have high operational value. There are no requirements to their form. The part size and its composition are of more importance. It is of interest that there is no problem, in the majority of cases, in producing good adhesion between the coating and the substrate because of the formation of gradient transition layers (the elemental distribution is shown in Figure 25). The process of gas-transport SHS coatings is, in principle, intermediate between gas-phase condensation and diffusional saturation (bonding). Shtessel, the head of investigations in this area, considers this variant of SHS technology to be beyond any competition when used to deposit coatings onto small parts of complicated shape.

The six types of SHS technology discussed above are almost developed at present. Some other variants based on the SHS principles (gas combustion and detonation or gas suspension combustion) are being developed. Despite the variety of SHS technological processes, in particular the structure and application of the resulting product, they have much in common. Figure 26 shows the generalized scheme of SHS technology. It consists of three stages: preparation of the SHS mixture, the realization of the SHS process, and the treatment of the resulting product. The main differences between technological processes are details concerning these stages.

One of the most important tasks of modern technology and science is a

careful comparison of various technological processes and the determination of more efficient fields of their application. The same problems can be solved by modern technologies based on powder metallurgy, plasma and laser techniques, combustion, etc. Therefore, it is no surprise that there is a competition between technologies. We are not always sure whether we use the most efficient one. SHS methods being among the most up-to-date technologies looks ahead with confidence.

The use of cheap chemical energy instead of electrical, fast bulk self-heating rather than slow heating through the substance surface, and simple devices rather than complicated higher temperature ones are features of the progressive technological principles of the SHS process, as an alternative to the traditional approaches.

"To burn, not to warm up", this simple motto can lead to fundamental changes in modern SHS technology (being persistantly and universally realized).

6. CONCLUSIONS

About twenty years have passed since the first experiments were carried out which brought to life the notion of "self-propagating high-temperature synthesis". An extraordinary idea has grown up into a modern field of science and technology with its own structure, trends in investigations and applications. The deliberate search for new SHS systems, the study of their combustion mechanisms and synthesis conditions, and the development of new SHS-based technological processes became a routine job. A start has been made to bring these processes to a commercial level. So far it proceeds slowly, but accelerating with every new achievement. Despite conservative attitudes towards the process from some specialists in materials science and process

engineers - the classics of their business - the SHS method worked its way to recognition.

A new stage, rather era, in the SHS development is approaching. In the near future we expect will face the following:

The development of scientific principle of SHS processes will proceed along the path of structural macrokinetics which will get firmly established and will involve related processes close to their scientific techniques.

The development of the investigations in the mathematical modeling of SHS processes proceeding under various (including technological) conditions with the use of modern supercomputers for the solution of the most complicated three dimensional and non-steady nonlinear tasks to predict the course of SHS processes in each particular case.

High temperature investigations in the interdisciplinary fields (chemical kinetics and thermodynamics, heat and mass transfer, rheology and hydrodynamics, and others) which will supply the initial data necessary for the quantitative description of SHS process.

The SHS technology will proceed along the path of automation at the sufficient level of computerization and robotization which allows the creation of radically new SHS processes based on the continuous combustion resulting in "people-free" production and realizing technological cycles procedures.

SHS expansion into various fields of modern engineering will be continuing and cause fundamental technological reconstruction ("perestroika") in many manufacturing techniques with significant technical and economic advantages.

Certainly such an optimistic forecast can be realized only under the conditions of close scientific cooperation all over the world.

The author is cherishing hopes that his presentation at the Symposium

organized by the American Ceramic Society will be his modest contribution to the development of fruitful international collaboration.

ACKNOWLEDGMENTS

The author gratefully acknowledges Dr. I. P. Borovinskaya for her fruitful twenty-year collaboration. Also, Dr. A. S. Rogatchev is gratefully acknowledged for his help in the selection of material for this work. The author wishes to thank Dr. S. N. Sklyarov for his translation of this paper.

7. REFERENCES

1. Merzhanov, A. G., Shkiro, and V. M., Borovinskaya, I. P. Synthesis of Refractory Inorganic Compounds. - Certif. No 255221, 1967, Appl. No. 1170735. "Invest. Bull.", 1971, No. 10. France Patent No. 2088668, 1972. U. S. Patent No. 3726643, 1973. U. K. Patent No. 1321084, 1974. Japan Patent No. 1098839, 1982.
2. Merzhanov, A. G., and Borovinskaya, I. P., Dokl. Akad. Nauk SSSR, (1972), 204, No. 2, p. 366-369 (in Russ.).
3. Frank-Kamenetsky, D. A. Diffusion and Heat Transfer in Chemical Kinetics, "Nauka", 1987, 483 p. (in Russ.).
4. Zeldovich, Ja. B., Berenblatt, G. I., Librovich, V. B., and Makhviladze, G. M. Mathematical Theory of Combustion and Explosion, "Nauka", 1980 (in Russ.).
5. Bakhman, N. N., and Belayev, A. F. Combustion of Heterogeneous Condensed Systems, "Nauka", 1967 (in Russ.).
6. Merzhanov, A. G., and Averson, A. E., Combustion and Flame, (1971), 16, 89-124.
7. Merzhanov, A. G., Combustion and Flame, (1969), 13, 143-156.
8. Merzhanov, A. G., and Khaikin, B. Ja. Theory of Combustion Waves in Homogeneous Media. - Progress in Energy and Combustion Science. 1988.
9. Merzhanov, A. G. Self-Propagating High Temperature Synthesis. - Modern Problems. Ed. by Ja. M. Kolotirkin. "Chemistry", 1983, p. 5-45 (in Russ.).
10. Merzhanov, A. G. Archiw. Procesow Spalania, (1974), 5, No. 1, 17-39 (in Russ.).
11. Merzhanov, A. G., Borovinskaya, I. P., and Volodin Yu. E., Dokl. Akad. Nauk SSSR, (1972), 206, No. 4, 905-908 (in Russ.).

12. Aldushin, A. P., and Merzhanov, A. G. Filtration Combustion Theory: General Ideas and Investigations. Preprint. Branch of the Institute of Chemical Physics USSR Academy of Sciences. 1987, Chernogolovka, 48 p.
13. Aldushin, A. P. Filtration Combustion of Metals. Ibid. 22 p. (in Russ.).
14. Merzhanov, A. G. , Filonenko, A. K., and Borovinskaya, I. P. Dokl. Akad. Nauk SSSR, (1973), 208, No. 4, 892-894 (in Russ.).
15. Borovinskaya, I. P., Merzhanov, A. G., Novikov, N. P., and Filonenko, A. K. Fizika Gorenia i Vzriva, (1974), No. 1, 4-15 (in Russ.).
16. Merzhanov, A. G., Archivum Combustionis, (1981), 191, No. 1/2, 23-48.
17. Mukasyan, A. S., Merzhanov, A. G., Martinenko, V. M., Borovinskaya, I. P., and Blinov, M. Yu., Fizika Gorenia i Vzriva, (1986), No. 5, 43-49 (in Russ.).
18. Merzhanov, A. G., Bull. Akad. Nauk SSSR, (1976), No. 10, 76-84 (in Russ.).
19. Filonenko, A. K., Archiwum Termodynam i spal, (1975), 6, No. 1, 23-35 (in Russ.).
20. Maksimov, Yu. M., Merzhanov, A. G., Pak, A. T., and Kuchkin, M. P., Fizika Gorenia i Vzriva, (1981), No. 4, 51-58 (in Russ.).
21. Merzhanov, A. G., Dvoryankin, A. V., and Strunina, A. G. Dokl. Akad. Nauk SSSR, (1982), 267, No. 4, 869-872 (in Russ.).
22. Shkadinskiy K. G., and Khajkin, B. I., Fizika Gorenia i Vzriva, (1971), No. 1, 19-28 (in Russ.).
23. Ivleva, T. P., Merzhanov, A. G., and Shkadinskiy, K. G., Dokl. Akad. Nauk SSSR, 239, No. 5, 1086-1068 (in Russ.).
24. Sherbak, S. B., Fizika Gorenia i Vzriva, (1983), No. 5, 9-12 (in Russ.).
25. Volpert, V. A., Volpert, A. I., and Merzhanov, A. G., Dokl. Acad. Nauk SSSR, (1982), 262, No. 3, 642-645 (in Russ.).

26. Volpert, V. A., Volpert, A. I., and Merzhanov, A. G. Dokl. Akad. Nauk SSSR, (1982), 262, No. 3, 642-645 (in Russ.).
27. Matkowsky, B. J., and Sivashinsky, G. I. SIAM. J. Appl. Math., (1978), 35, No. 3, 465-478.
28. Margolis, S. B., Kaper, H. G., Leaf, G. K., and Matkowsky, B. J., Combust. Sci. Technol., (1985), 43, No. 3-4, 127-165.
29. Kaper, H. G., Leaf, G. K., Margolis, S. B., and Matkowsky, B. J. Combust. Sci. Technol., (1987), 53, 289-314.
30. Zenin, A. A., Merzhanov, A. G., and Nersisyan, G. A. Dokl. Acad. Nauk SSSR, (1980), 250, No. 4, 880-884 (in Russ.).
31. Zenin, A. A., Merzhanov, A. G., and Nersisyan, G. A., Fizika Gorenia i Vzriva, (1981), No. 1, 79-90 (in Russ.).
32. Zenin, A. A., Nersisyan, G. A., and Nesesyanyan, M. D., Fizika Gorenia i Vzriva, (1982), No. 4, 66-73 (in Russ.).
33. Azatyan, T. S., Maltsev, V. M., Merzhanov, A. G., and Seleznev, V. A., Fizika Gorenia i Vzriva, (1974), No. 3, 445-446 (in Russ.).
34. Azatyan, T. S., Maltsev, V. M., and Seleznev, V. A., Fizika Gorenia i Vzriva, (1976), No. 2, 286-287 (in Russ.).
35. Andreev, V. A., Maltsev, V. M., and Seleznev, V. A., Fizika Gorenia i Vzriva, (1980), No. 4, 18-23 (in Russ.).
36. Zeldovich, Ja.B., and Frank-Kamenetskiy, D. A., Dokl. Akad. Nauk SSSR, (1938), 19, 693 (in Russ.).
37. Khaikin, B. I., and Merzhanov, A. G., Dokl. Akad. Nauk SSSR, (1967), 173, No. 6, 1382-1385 (in Russ.).
38. Aldushin, A. P., Merzhanov, A. G., and Khaikin, B. I., Dokl. Acad. Nauk SSSR, (1972), 204, No. 5, 1139-1142 (in Russ.).

39. Aldushin, A. P., Martemianova, T. M., Merzhanov, A. G., Khaikin, B. I., and Shkadinskiy, K. G., Fizika Gorenia i Vzriva, (1972), No. 2, 202-212 (in Russ.).
40. Khaikin, B. I., Combustion Propagation in Systems Forming Condensed Reaction Products. - Combustion and Explosion. Proceedings of the Fourth All-Union Symposium on Combustion and Explosion, "Nauka", 1977 (in Russ.).
41. Khaikin, B. I., Filonenko, A. K., and Khudjaev, S. I., Fizika Gorenia i Vzriva, (1986), No. 4, 591-599 (in Russ.).
42. Merzhanov, A. G., Rumanov, Ed. N., and Khaikin, B. I., J. Appl. Mechanics and Techn. Phys., (1972), No. 6, 99-105 (in Russ.).
43. Merzhanov, A. G., Dokl. Acad. Nauk SSSR, (1977), 233, No. 6, 1130-1133 (in Russ.).
44. Aldushin, A. P., and Merzhanov, A. G., Dokl. Akad. Nauk SSSR, (1977), 236, No. 5, 1133-1136 (in Russ.).
45. Zenin, A. A., and Nersisyan, G. A., Mechanism and Macrokinetics of Titanium and Zirconium Silicides Formation in SHS Wave. - "Chem. Phys. of Comb. and Expl. - Combustion of Condensed and Heterogeneous Systmes", 1980, Chernogolovka, p. 63-67 (in Russ.).
46. Merzhanov, A. G., and Dubovitskiy, F. I., Dokl. Acad. Nauk SSSR, (1959), 129, No. 1, 153-156 (in Russ.).
47. Merzhanov, A. G., Dokl. Acad. Nauk SSSR, 135, No. 6, 1439-1441 (in Russ.).
48. Mamyan, S. S., Borovinskaya, I. P., and Merzhanov, A. G., Thermodynamical Analysis of Titanium, Zirconium and Tantalum Carbides and Nitrides by SHS. Preprint of Inst. of Chem. Phys. USSR Acad. of Sci., 1977, Chernogolovka, 20 (in Russ.).
49. Mamyan, S. S., and Merzhanov, A. G., Thermodynamicla Analysis. - Preprint

- of Inst. of Chem. Phys. (Branch) USSR Acad. Nauk. Chernogolovka. 1978-79 (in Russ.).
50. Novikov, N. P., Borovinskaya, I. P., and Merzhanov, A. G., Thermodynamical Analysis of SHS. - "Combust. Processes in Chem. Techn. and Metallurgy". Chernogolovka, 1975, p. 174-188 (in Russ.).
 51. Maslov, V. M., Borovinskaya, I. P., and Merzhanov, A. G., Fizika Gorenia i Vzriva, (1978), No. 5, 79-85 (in Russ.).
 52. Shkiro, V. M., Doronin, V. N., and Borovinskaya, I. P., Fizika Gorenia i Vzriva, (1980), No. 4, 13-18 (in Russ.).
 53. Boldirev, V. V., Aleksandrov, V. V., Korchagin, M. A., Topochko, B. P., Gusenko, S. N., Sokolov, A. S., Sheromov, M. A., and Lakhov, N. Z., Dokl. Akad. Nauk SSSR, (1981), 259, 1127-1129 (in Russ.).
 54. Aleksandrov, V. V., Korchagin, M. A., Topochko, B. P., and Sheromov, M. A. Fizika Goreniz i Vzriva, (1983), No. 4, 65-66 (in Russ.).
 55. Nekrasov, E. A., Smolykov, V. K., and Maksimov, Yu. M., Fizika Gorenia i Vzriva, (1981), No. 5, 39-46 (in Russ.).
 56. Smolyakov, B. K., Nekrasov, E. A., Maksimov, and Yu. M., Fizika Gorenia i Vzriva, (1984), No. 2, 63-73 (in Russ.).
 57. Shefer, G., Chemical Transport Reactions, (1964) (in Germ.).
 58. Maksimov, Yu. M., Merzhanov, A. G., Raskolenko, L. G., Pak, A. G., and Lepakova, O. K., Dokl. Akad. Nauk SSSR, (1986), 286, No. 4, 911-914 (in Russ.).
 59. Shkiro, V. M., and Borovinskaya, I. P., Fizika Gorenia i Vzriva, (1976), No. 6, 945-948.
 60. Kirdyashkin, A. I., Maksimov, Yu. M., and Merzhanov, A. G., Fizika Gorenia i Vzriva, (1981), No. 6, 10-15 (in Russ.).

61. Maksimov, Yu. M., Kirdyashkin, A. I., Merzhanov, A. G., and Raskolenko, L. G. Fizika Gorenia i Vzriva, (1984), No. 6, 83-86 (in Russ.).
62. Kniazik, V. A., Merzhanov, A. G., Solomonov, V. V., and Steinberg, A. S., Fizika Gorenia i Vzriva, (1985), No. 3, 69-73 (in Russ.).
63. Borovinskaya, I. P., and Loryan, V., Dokl. Akad. Nauk SSSR, (1976), 231, No. 4, 911-914 (in Russ.).
64. Borovinskaya, I. P., and Loryan, V., Powder Metallurgy, (1978), No. II (191), 42-45 (in Russ.).
65. Maksimov, Yu. M., Merzhanov, A. G., Ziatdinov, M. X., Rascolenko, A. S., and Lepakova, O. K., Dokl. Akad. Nauk SSSR, (1982), 264, No. 3, 629-632 (in Russ.).
66. Dolukhanyan, S. K., Nersesyan, M. D., Nalbandyan, A. B., Borovinskaya, I. P., and Merzhanov, A. G., Dokl. Akad. Nauk SSSR, (1976), 231, No. 3, 675-678 (in Russ.).
67. Agababyan, Ed. V., Kharatyan, S. L., Nersesyan, M. D., and Merzhanov, A. G., Fizika Gorenia i Vzriva, (1979), No. 4, 3-9 (in Russ.).
68. Kharatyan, S. L., Agababyan, Ed. V., and Merzhanov, A. G., Archiwum Combustionis. (1985), 5, No. 7, 3-33 (in Russ.).
69. Borovinskaya, I. P., and Pitulin, A. N., Fizika gorenia i Vzriva, (1978), No. 1, 137-140 (in Russ.).
70. Aldushin, A. P., Merzhanov, A. G., and Khaikin, B. I., Dokl. Akad. Nauk SSSR, (1974), 215, No. 3, 612-615. (in Russ.).
71. Aldushin, A. P., Merzhanov, A. G., and Seplyarskiy, B. S., Fizika Gorenia i Vzriva, (1976), No. 3, 323-332 (in Russ.).
72. Aldushin, A. P., and Seplyarskiy, B. S., Dokl. Akad. Nauk, SSSR, (1978), 241, No. 1, 72-75 (in Russ.).

73. Aldushin, A. P., and Seplyarskiy, B. S., Dokl. Akad. Nauk, SSSR, (1979), 249, No. 3, 585-588.
74. Khaikin, B. I., To the Theory of Combustion Processes in Heterogeneous Condensed Medium. - "Combustion Processes in Chemical Technology and Metallurgy". Chernogolovka, 1975, p. 227-244 (in Russ.).
75. Khaikin, B. I., Investigations on Heterogeneous Systems Combustion Theory. Theses. Chernogolovka, 1975 (in Russ.).
76. Borovinskaya, I. P., Refractory Compounds Formation during Combustion of Heterogeneous Condensed Systems. - "Combustion and Explosion". Proceedings of the Fourth All Union Symposium on Comb. and Expl. "Nauka", 1977, p. 138-148 (in Russ.).
77. Rogachev, A. S., Mukasyan, A. S., and Merzhanov, A. G., Dokl. Akad. Nauk SSSR, (1987), 297, No. 6, 1425-1428.
78. Borovinskaya, I. P., Merzhanov, A. G., Pitulin, A. N., and Shehtman, V. Sh., SHS of Tantal Nitrides. - "Combustion Processes in Chemical Technology and Metallurgy". Chernogolovka, 1975, p. 113-118 (in Russ.).
79. Borovinskaya, I. P., Vishnyakova, G. A., Maslov, V. M., and Merzhanov, A. G., The Possibility of Composites Production During Combustion.- "Combustion Processes in Chemical Technology and Metallurgy". Chernogolovka, 1975, p. 141-149 (in Russ.).
80. Merzhanov, A. G., Borovinskaya, I. P., Yuchvid, V. I., and Ratnikov, V. I., New Production Methods of High Temperature Materials Based on Combustion. - "Scientific Principles of Materials Science". M., "Nauka", 1981 (in Russ.).
81. Rogachov, A. S., Galchenko, Yu. A., Aslamazashvily, Z. G., and Pitulin, A. N., Bull. Akad. Nauk SSSR Inorganic Materials, (1986), 22, No. 11, 1842-

1844 (in Russ.).

82. Shkiro, V. M., and Borovinskaya, I. P., The Study of Combustion Regularities of Titanium and Carbon Mixtures. - Combustion Processes in Chemical Technology and Metallurgy. Chernogolovka, 1975, p. 253-258 (in Russ.).
83. Shkiro, B. M., Nersisyan, G. A., and Borovinskaya, I. P., Fizika Gorenia i Vzriva, (1978), No. 4, 58-64 (in Russ.).
84. Merzhanov, A. G., Borovinskaya, I. P., Nersesyan, M. D., Mkrtchan, S. O., Avakyan, P. B., Dokl. Acad. Nauk SSSR, (1989) (in press, in Russ.).
85. Bloshenko, V. N., Bokij, V. A., and Borovinskaya, I. P., Fizika Gorenia i Vzriva, (1984), No. 6, 87-90 (in Russ.).
86. Bloshenko, V. N., Bokij, V. A., Borovinskaya, I. P., and Merzhanov, A. G., Fizika Gorenia i Vzriva, (1984), No. 6, 90-94 (in Russ.).
87. Bloshenko, V. N., Bokij, V. A., and Borovinskaya, I. P., Fizika Gorenia i Vzriva, (1985), No. 1, 93-98 (in Russ.).
88. Bloshenko, V. N., Bokij, V. A., and Borovinskaya, I. P., Fizika Gorenia i Vzriva, (1985), No. 2, 81-88 (in Russ.).
89. Bloshenko, V. N., Bokij, V. A., and Merzhanov, A. G., Fizika Gorenia i Vzriva, (1988), No. 2, 102-111 (in Russ.).
90. Sherbakov, V. A., Sichev, A. E., and Steinberg, A. S., Fizika Gorenia i Vzriva, (1986), No. 4, 55-61 (in Russ.).
91. Filonenko, A. K., and Vershinnikov, V. I., Chem. Phys., (1984), No. 3, 430-434 (in Russ.).
92. Aldushin, A. P., and Kasparyan, S. G., Dokl. Akad. Nauk, SSSR, (1979), 244, No. 1, 70-76 (in Russ.).
93. Dolukchanyan, S. K., Nersesyan, M. D., and Borovinskaya, P. P., Combustion

- of Transitional Metals in Hydrogen. - "Chem. Phys. of Combust. and Expl. Processes, Combustion of Condensed Systems". Chernogolovka, 1977, p. 96-99. (in Russ.).
94. Dolukhanyan, S. K., Nersesyan, M. D., Martirosyan, N. A., and Merzhanov, A. G., Bull. of Akad. Nauk SSSR. Inorganic Materials. (1978), 14, 1581-1585 (in Russ.).
95. Dolukhanyan, S. K., Akopyan, A. G., and Merzhanov, A. G., Fizika Gorenia i Vzriva, (1981), No. 5, 50-55 (in Russ.).
96. Martirosyan, N. A., Dolukhanyan, S. K., and Merzhanov, A. G., Fizika Gorenia i Vzriva, (1985), No. 5, 53-57 (in Russ.).
97. Merzhanov, A. G., Borovinskaya, I. P., Ratnikov, V. I., Prokudina, V. K., Memelov, V. L., and Gluskin, Ja. A., Bull. of Akad. Nauk. SSSR, Inorganic Materials, (1977), 13, No. 5, 811-814 (in Russ.).
98. Prokudina, V. K., Kalikhman, V. L., Golubnichnaya, A. A., Borovinskaya, I. P., and Merzhanov, A. G., Powder Metallurgy, (1978), No. 6, (186), 48-52 (in Russ.).
99. Muchnik, S. V., Ivanchenko, V. B., and Linchak, K. A., Powder Metallurgy, (1979), No. 6, 7 (in Russ.).
100. Muchnik, S. V., Chernogorenko, V. B., Linchak, K. A., and Dubroz, A. N. Peculiarities of Phosphides Synthesis in Combustion Regime. - Problems of Technological Combustion, V. 1, Chernogolovka, 1981, p. 70-74 (in Russ.).
101. Chernogorenko, V. B., Muchnik, S. V., Linchak, K. A., Klimak, Z. A., and Ivanchenko, V. G., Mater. Res. Bull., (1981), 16, No. 1, 1-6 (in Russ.).
102. Borovinskaya, I. P., Archiwum Procesow Spalania, (1974), 5, No. 2, 145-162 (in Russ.).
103. Merzhanov, A. G., New Problems in Combustion Theory and Practice.

- "Problems of Chemical Kinetics", "Nauka", 1979, p. 92-100.
104. Merzhanov, A. G., and Borovinskaya, I. P., Journal of Mendeleev Chemical Society, (1979), 24, No. 3, 223-227 (in Russ.).
105. Frankhouser, N. L., Kieszek, M. G., et al, Gasless Combustion Synthesis of Refractory Compounds. Noyes Publication, Mill Rd., Park Ridge, N.J. 07656. 1985 - viii 125 pp. ISBN 08155-1015-2.
106. Holt, J. B., Mater. Res. Soc. Bull., (1987), 12, No. 7, 60-64.
107. Merzhanov, A. G., Kachin, A. R., Yuhvid, B. I., and Borovinskaya, I. P., Vishnyakova, G. A., Production of Cast Twolayer Tubes. USA, No. 4217, 19.08.80; FRG No 2837688 29.08.72; France, No. 2401771 29.08.78; Italy No. 1104078 14.10.85.
108. Bagramyan, A. P., Yuhvid, V. I., and Borovinskaya, I. P., Synthesis Regularities of Cast Chromium Borides during Combustion. Preprint. Chernogolovka, 1980, 24 p. (in Russ.).
109. Merzhanov, A. G., Yuhvid, V. I., and Borovinskaya, I. P., Dokl. Akad. Nauk. SSSR, (1980), 255, No. 1, 120-124 (in Russ.).
110. Kachin, A. R., Yuhvid, V. I., and Vishnyakova, G. A., Formation Regularities of Composition and Microstructure of Cast Hard Alloy on the Basis of Composite Titanium-Chromium Carbide in SHS Processes. - Problems of Technolog. Combust.", v. II, Chernogolovka, 1981, p. 22-25 (in Russ.).
111. Yuhvid, V. I., Okolovich, E. V., Vishnyakova, G. A., and Muratov, S. M., Formation Regularities of the Cast Tungsten Carbide in SHS Regime. Ibid, p. 18-22 (in Russ.).
112. Yuhvid, V. I., Borovinskaya, I. P., and Merzhanov, A., G., Fizika Gorenia i Vzriva, (1983), No. 3, 30-32 (in Russ.).
113. Karataskov, S. A., and Yuhvid, V. I., Fizika Gorenia i Vzriva, (1985), No.

- 6, 41-43 (in Russ.).
114. Bulaev, A. M., Galchenko, Yu. A., Vishnyakova, G. A., Yuhvid, V. I., Borovinskaya, I. P., and Merzhanov, A. G., Bull. of Akad. Nauk SSSR "Metals", (1986), No. 5, 178-182 (in Russ.).
115. Yuhvid, V. I., Bull. of Akad. Nauk SSSR "Metals", (1986), No. 6, 61-64 (in Russ.).
116. Kosolapov, V. T., Shmelkov, V. V., Levasov, A. F., and Markov, Yu. M., Synthesis of Al, Ti, Zr, Hf Carbides during Combustion, Proceedings of the Second All Union Conference on Technological Combustion, 1978, p. 129-130 (in Russ.).
117. Dolukhnyan, S. K., Aleksanyan, A. T., Nalbandyan, A. B., Seiranyan, G. B., and Agadzhanyan, N. N., Dokl. Akad. Nauk. SSSR., (1984), 276, No. 1, 131-140 (in Russ.).
118. Aslamazashvily, Z. G., Pitulin, A. N., and Oniashvily, G. Sh., Bull. of Akad. Nauk Gruz. SS. (1986), 124, No. 3, 581-584 (in Russ.).
119. Nersisyan, G. A., and Kcharatyan, S. L., Chemical Journal of Armenia, (1983), 36, No. 1, 54 (in Russ.).
120. Munir, Z. A., and Holt, J. B., J. Mater. Sci., (1987), 22, No. 2, 710-714.
121. Philpot, K. A., Munir, Z. A., and Holt, J. B., J. Mater. Sci. (1987), 22, No. 1, 159-169.
122. Holt, J. B., Adv. Ceram. (Ceram. Powders Sci.), (1987), 21, 301-10.
123. Holt, J. B., and Munir, Z. A., J. Mater. Sci., (1986), 21, No. 21, 251-59.
124. Holt, J. B., Kingman, D. D., and Bianchini, G. M., Mater. Sci. and Eng. (1985), 21, 321-327.

125. Holt, J. B., and Kingham, D. D., Mater. Sci. Res. (1984), 17, 167-175.
126. Holt, J. B., Ind. Res. and Deveopment, (1983), 25, No. 4, 88-91.
127. Holt, J. B., Synthesis of Refractory Materials. - US Pat., No. 4446242, 01 May, 1984.
128. Holt, J. B., Synthesis of Refractory Materials. - US Pat. No. 4459363, 10 Jul., 1984.
129. Boldirev, V. V., Aleksandrov, V. V., Novikov, N. P., and Smirnov, B. I. Dokl. Akad. Nauk SSSR, (1977), 233, No. 2, 395-397 (in Russ.).
130. Merzhanov, A. G., Popova, G. Ja., Semiletova, D. V., Toropov, A. N., Ulibin, V. B., Chervyakov, V. V., Shipilov, V. V., and Steinberg, A. S., Formation of Complex Oxides with Perovskite Structure During SHS. "Problems of Techn. Comb.", v. II, Chernogolovka, 1981, p. 15-18 (in Russ.).
131. Kosova, N. V., Aleksandrov, V. V., and Awakumov, E. G., Production of Molybdates and Tungstate Strontium or Lead. - Certificate 927753, 1982, Bull. of Inventions, 1982, No. 18 (in Russ.).
132. Vereshagin, A. A., and Sviridov, V. V., Dokl. Akad. Nauk SSSR, (1978), 240, No. 3, 602-604 (in Russ.).
133. Bednorz, J. G., and Muller, K. A., Z. Phys. B-Condensed Matter, (1986), 64, 189-193.
134. Terao, N., Jap. J. of App. Phys., (1971) 10, 2.
135. Kirpichev, E. P., Rubtsov, Yu. I., Sorokina, T. B., and Pitulin, A. N., J. Phys. Chem., (1976), 50, No. 7, 1907 (in Russ.).
136. Pitulin, A. N., Tantalum Nitrides Synthesis at High Nitrogen Pressures "Kinetics of Phys. - Chem. Reactions", Ed. by B. N. Condratjev, Chernogolovka. 1977, p. 91 (in Russ.).

137. Pitulin, A. N., Sherbakov, V. A., Borovinskaya, I. P., and Merzhanov, A. G., Fizika Gorenia i Vzriva, (1979), No. 4, 9-17 (in Russ.).
138. Borovinskaya, I. P., Merzhanov, A. G., Butakov, A. A., Rjabinkin, A. G., and Shehtman, V. Sh., Production of Tantal Mononitrides. - Certificate No. 264365, 1969, Appl. No. 131160, 1969, Bull. of Invent. 1970, No. 9 (in Russ.).
139. Molodovskaya, E. K., Petrunin, V. F., Karimov, I., Kalanov, M., Khaidarov, G., Borovinskaya, I. P., Pitulin, A. N., and Merzhanov, A. G., Phys. Metal. and Materials Science, (1975), 40, No. 1, 202-204 (in Russ.).
140. Petrunin, V. F., Sorokin, N. I., Borovinskaya, I. P., and Pitulin, A. N., Powder Metallurgy, 1980, No. 3, 62-64 (in Russ.).
141. Em, V. T., Karimov, I., Petrunin, V. F., Khidirov, I., Latergays, I. C., Merzhanov, A. G., Borovinskaya, I. P., and Prokudina, V. K., Crystallography, (1975), 20, No 2, 320-323 (in Russ.).
142. Khidirov, I., Karimov, I., Em., V. T., and Loryan, V. Ed, Bull. Akad. Nauk. SSSR. Inorganic Materials, (1986), 22, No. 4, 609-612 (in Russ.).
143. Khidirov, I., Karimov, I., Em., V. T., and Loryan, V. Ed., Physics of Metals and Metal Science, (1980), 49, No. 2, 409-412 (in Russ.).
144. Khidirov, I., Karimov, I., Em, V. T., and Loryan, V. Ed, Bull. Akad. Nauk. SSSR. Inorganic Materials, (1986), 22, No. 10, 1675-1678 (in Russ.).
145. Guzhko, R. K., private communication.
146. Vadchenko, S. G., Grigorjev, Yu. M., Phys. of Metals and Metal Science, (1975), 40, No. 6, 1204-1209 (in Russ.).
147. Grigorjev, Yu. M., Filament Usage for Studying the Kinetics of High Temperature Interaction of Metals and Gases. - Combustion Processes in Chemical Technology and Metallurgy, Chernogolovka. 1975, p. 199-210 (in

Russ.).

148. Merzhanov, A. G., Grigorjev, Yu. M., Kharatyan, S. L., Mashkinov, L. B. and Vartanyan, G. S., Phys. Comb. and Epl., (1975), No. 4, 563-568 (in Russ.).
149. Grigorjev, Yu. M., Khaikin, S. L., Andrianova, Z. S., Ivanova, A. I., and Merzhanov, A. G., Fizika Gorenia i Vzriva, (1977), No. 5, 713-721 (in Russ.).
150. Kharatyan, S. L., Grigorjev, Yu. M., and Merzhanov, A. G., Bull. Akad. Nauk SSSR. Metals, (1977), No. 3, 178-181 (in Russ.).
151. Vadchenko, S. G., and Grigorjev, Yu. M., Bull. Akad. Nauk SSSR. Metals, (1979), No. 1, 187-195 (in Russ.).
152. Vadchenko, S. G., Grigorjev, Yu. M., and Merzhanov, A. G., Bull. Akad. Nauk SSSR. Metals, (1980), No. 5, 223-229 (in Russ.).
153. Grigorjev, Yu. M., Kudryashov, V. A., Sarkisyan, A. A., and Merzhanov, A. G., Chem. Phys., (1985), No. 5, 714-720 (in Russ.).
154. Kharatyan, S. L., Sardaryan, Yu. S., Sarkisyan, A. A., and Merzhanov, A. G., Chim. Phys., (1984), No. 11, 1604 (in Russ.).
155. Maksimov, Yu. M., Ziatdinov, M. X., Merzhanov, A. G., Raskolenko, L. G., and Lepakova, O. K., Fizika Gorenia i Vzriva, (1984), No. 5, 16-21 (in Russ.).
156. Merzhanov, A. G., Karuk, G. G., Borovinskaya, I. P., Sharivker, S. Yu., Moshkovskiy, E. I., Prokudina, V. K., and Dyadko, E. G., Powder Metallurgy, (1981), No. 10, 50-59 (in Russ.).
157. Abrasive Paste KT/Akad. Nauk SSSR. Information List. 1982, 33p. (in Russ.).
158. Information on Lists of ISTC "Thermosynthesis": "Powders of SHS-Silicium

Nitride", "Powders, Materials from SHS-Sialons", "High Temperature Superconducting SHS-Materials", "High Temperature Oxygen Free SHS-Ceramics", "STIM-Synthetic Solid Instrumental Materials", "Refractory SHS-Materials", "Insulation Material", "Porous SHS-Materials and Products from Refractory Inorganic Compounds", "Cast Pink Corundum", "Niobate Litium Charge for Growing Monocrystals", "Products with SHS-Covering", "Electrodes for Metal Surface Hardening", etc. Central Inst. of Economy and Inform. M. 1988.

159. Gordopolov, Yu. A., Shikhverdiev, R. M., Molokov, I. V., Bogatov, Yu. V., Borovinskaya, I. P., and Merzhanov, A. G., The Study of Shock Wave Loading of Heated Reaction Products at Synthesis of Refractory Alloys in Combustion Wave. - Preprint Inst. Chem. Phys. (Branch), ISMAN. Chernogolovka, 1988.
160. Gordopolov, Yu. A., Shikhverdiev, R. M., Molokov, I. V., Bogatov, Yu. V., Borovinskaya, I. P., and Merzhanov, A. G., The Influence of Shock Wave on the Structural Formation of Refractory Solid Alloys, Synthesized by Combustion. - Proceedings of the VII International Symposium. Explosion Energy for Production of Metallic Materials with New Characteristics. Pardubiza, Czechoslovakia, 25-27, Oct. 1987.
161. Yuhvid, V. I., Maksimov, E. I., and Kozlov, V. S., Fizika Gorenia i Vzriya, (1974), No. 2, 162-168 (in Russ.).
162. Yuhvid, V. I., Maksimov, E. I., Merzhanov, A. G., and Kozlov, V. S., Fizika Gorenia i Vzriya, (1974), No. 1, 28-33 (in Russ.).
163. Yuhvid, B. I., Maksimov, E. I., and Matveev, S. I., To Combustion Theory of Fuel Comb. and Expl. Proceedings of the Fourth All Union Symposium on Comb. and Explosion, "Nauka", 1977, p. 236-243.

164. Odawara, O., and Ikeuchi, J., J. Amer. Ceram. Soc., (1986), 69, No. 4, 80-81.
165. Odawara, O., and Ikeuchi, J., J. Amer. Ceram. Soc. (1986), 69, No. 4, 85-86.
166. Odawara, O., Kaida, Y., Soseito Kako, (1987), 28, No. 312, 3-8.
167. Odawara, O., Soseito Kako, (1987), 28, No. 322, 1109-14.
168. Odawara, O., and Ikeuchi, J., Trans. Jpn. Inst. Met., (1986), 27, No. 9, 708-709.
169. Odawara, O., Ishii, Y., and Yamazaki, H., Lining of Steel Pipe by Centrifugal-Thermite of Steel Pipe by Centrifugal-Thermite Process. JP 61-238972-A2, 240 A. 1986, CL C23 C20/00 Appl. 85179575, 15 April, 1985.
170. Merzhanov, A. G., Borovinskaya, I. P., Steinberg, A. S., Kochetov, O. A., Ulibin, V. B., Shipilov, V. V., Chervyakov, V., V., and Makrovskiy, S., Materials Connection Certificate No. 747661, 1980, Appl. No. 2350713, 1976. Bull. of Inventions, 1980, No. 26.



Figure Captions

- Figure 1 The combustion wave in a titanium boron mixture
- Figure 2 Spin combustion of hafnium in nitrogen (Source: A. K. Filonko, et al., 1975)
- Figure 3 Elementary temperature profiles of SHS waves
- Figure 4 Thermogram of the combustion of the 5Ti + 3Si system
(Source: A. A. Zenin, G. A. Nersesyan, and A. G. Merzhanov, 1980)
- Figure 5 Capillary spreading in the titanium-carbon system
(Source: V. M. Shkuro and I. P. Borovinskaya, 1976)
- Figure 6 The effect of ultrasound on the combustion of the Ti + 2B system
- Figure 7 The size distribution of silicon particles combusted in nitrogen: (Source: S. D. Mukasyan, I. P. Borovinskaya et al., 1986)
- Figure 8 Effect of dilution on the combustion of the silicon-nitrogen system (Source: A. S. Mukasyan, I. P. Borovinskaya et al., 1986)
- Figure 9 Fe-V alloy combustion rate in nitrogen
- Figure 10 The temperature profiles of normal and inverse waves
- Figure 11a Adiabatic structures of combustion waves: Equilibrium mechanism
- Figure 11b Adiabatic structures of combustion waves: Non-equilibrium mechanism
- Figure 12 The principal concept of structural macrokinetics
- Figure 13 Cross section of tantalum samples combusted in nitrogen
(1) quenched (2) slowly cooled
- Figure 14 Microstructural features of static and shock-densified titanium carbide (Source: A. N. Pityulin, Yu.A. Gordopolov et al., 1987)
- Figure 15 Product formation in the Ti-H system
- Figure 16 Synchrotron radiation analysis on the Ni-Al system (Source: V. V. Boldyrev, V. V. Aleksandrov et al., 1981)
- Figure 17 Equilibrium composition and the adiabatic temperature of titanium hydride
- Figure 18 The temperature dependence of the electrical resistivity and magnetic susceptibility of SHS ceramics of $\text{MeBa}_2\text{Cu}_3\text{O}_{7-x}$

- Figure 19 Condensed phase equilibrium diagram in the $\text{TiO}_2\text{—B}_2\text{O}_3\text{—mg}$ system
- Figure 20 Schematic of product formation during the combustion of tantalum in nitrogen
- Figure 21 Time diagram of SHS densification
- Figure 22 The dependence of residual porosity on pressing time delay
(Source: A. N. Pityulin et al., 1985)
- Figure 23 Industrially produced hard-alloy articles
- Figure 24 Compositional and hardness variations in the cast titanium-chromium carbide based coating
- Figure 25 The elemental distribution of a transition layer between the coating and the substrate
- Figure 26 Generalized scheme of SHS technology

Table 1. Comparison of Calculated and Experimental Combustion
Temperatures in SHS Systems

Reaction	$T_{\text{calc}}(\text{K})$	$T_{\text{exp}}(\text{K})$
$\text{Ni} + \text{Al} \rightarrow \text{NiAl}$	1910	1910
$\text{Co} + \text{Al} \rightarrow \text{CoAl}$	1900	1880
$\text{Ti} + \text{Si} \rightarrow \text{TiSi}$	2000	1850
$\text{Ti} + 2\text{Si} \rightarrow \text{TiSi}_2$	1800	1770
$\text{Nb} + 2\text{Si} \rightarrow \text{NbSi}_2$	1900	1880
$\text{Mo} + 2\text{Si} \rightarrow \text{MoSi}_2$	1900	1920
$5\text{Ti} + 3\text{Si} \rightarrow \text{Ti}_5\text{Si}_3$	2500	2350
$\text{Nb} + \text{C} \rightarrow \text{NbC}$	2800	2650
$2 \text{Ta} + \text{C} \rightarrow \text{Ta}_2\text{C}$	2600	2550

Table 2. Complex SHS Oxides

Aluminates	Bismuth-containing Compounds	GarnatesNiobates
$YAlO_3$	$Bi_4V_4O_{11}$	$Y_3Al_5O_{12}LiNbO_3$
$MgAl_2O_4$	$Bi_4Fe_2O_9$	$Y_3Fe_5O_{12}NaNbO_3$
	$Bi_4Ti_3O_{12}$	$GdGa_5O_{12}KNbO_3$
	Bi_3TiNbO_9	$NaBa_2Nb_5O_{13}$
	Bi_3TiTaO_9	$KBa_2Nb_5O_{15}$
	$BaBi_2Nb_2O_9$	$BaNb_2O_6$
	$PbBi_2Ta_2O_9$	$Ba_5Nb_4O_{15}$
	Bi_4O_{12}	

Table 3. Physico-Mechanical Properties of SHS-Based Alloys

Carbide Base Composition	Flexural Strength (MPa)	Hardness (HRA)	Density (g/cm ³)	Binder
TiC	1200-1300	90-91	5.5-5.6	Ni-Mo
TiC _{0.5} N _{0.5}	1300-1400	90-91	5.8-5.9	Ni-Mo
Ti _{1-x} Mo _x C	1400-1800	90-92.3	-	Ni
Ti _{1-x} Mo _x N _{0.5} C _{0.5}	1600-1800	90.91.5	-	-

Table 4. Characteristics of Some Refractory Materials

Dolomite and Magnesite-Based		
Characteristics	Dolomite-Based	Magnesite-Based
Refractoriness (°C)	2150	2200
Porosity (%)	40-60	45-55
Adhesion shear strength with a brick base (MPa)	3-5	2-4
Depth of slag corrosion (mm)	2.0-2.5	1.3-1.9
Depth of slag impregnation (mm)	1.1-1.3	1.1-1.4
Depth of steel penetration (mm)	4.2-4.8	4.6-5.2
Chromium-Ore-Based		
Refractoriness (°C)	1750-1850	
Porosity (1%)	40-65	
Compression strength (MPa)	40-80	
Thermal expansion coefficient (K^{-1})	9×10^{-6}	
Thermal conductivity (J/m.s.K)	0.5-1.1	
Thermal shock resistance (900°C-water)	up to 25 thermocycles	

Table 5. Physico-Mechanical and Thermal Properties of SHS Ceramics
of Si_3N_4 -SiC-TiN Composition

Density ($\text{kg}\cdot\text{m}^{-3}\cdot 10^3$)	3.05-3.25
Porosity (%)	8-15
Modulus of Elasticity (GPa)	
dynamic	194-200
static	200
Hardness	
Rockwell (HRA)	85-93
Vickers (GPa)	6.1-11.3
Ultimate flexural strength* (GPa)	300-430
The critical value of stress	2.5-4.9
intensity coefficient ($\text{MN m}^{1/2}$)	
Weibull modulus	5.8
Thermal conductivity coefficient	18
($\text{J/m}\cdot\text{s}\cdot\text{K}$)	

*The value of the ultimate flexural strength is retained up to 1670K.

Table 6. Characteristics of Some Cast Coatings

Coating Material	Nonmetal Content (wt%)		Al (wt%)	O ₂ (wt%)	Phase Composition	Unannealed Specimens Microhardness (kg/mm ²)
	<u>total</u>	<u>free</u>				
Tungsten carbide	3.8	0.05	0.2	0.05	WC-W ₂ C	2300-2800
Vanadium carbide	15.4	0.05	0.7	0.4	VC	2100
Molybdenum carbide	5.9	0.05	0.4	0.05	Mo ₂ C	2000-2500
Chromium boride	30	0.05	0.3	0.05	CrB ₂	2500
Cobalt boride	15.5	0.1	-	0.05	CoB	1150
Vanadium silicide	15.8	0.2	-	0.1	V ₃ Si	1950

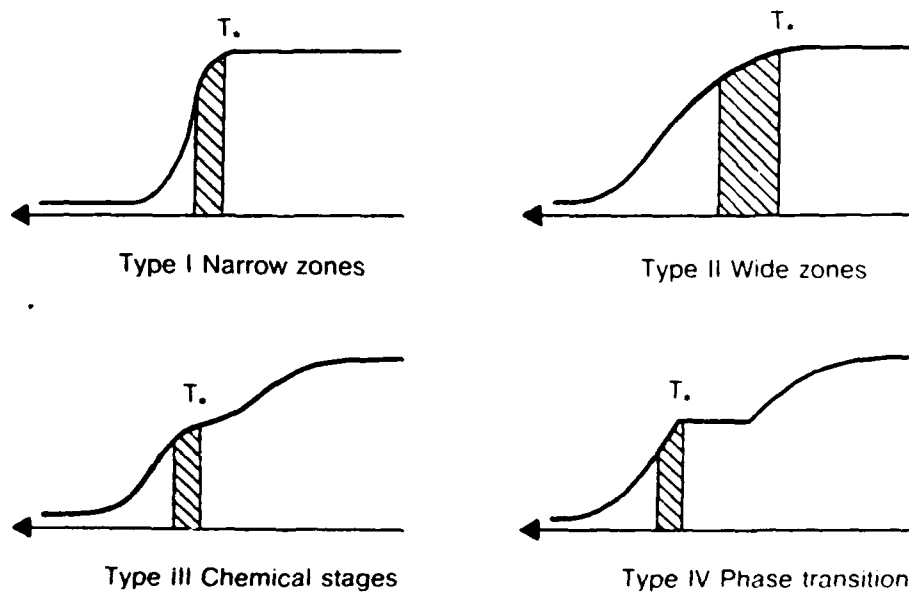
Table 7. Characteristics of Some Gas-Transport SHS-Coatings

Coated Articles	Article Materials	Aim of Coating	Coating Composition	Coating Thickness	Improvement in Operational Characteristics (times)
Jig bushing	Steel 45	Enhanced wear-resistance	Fe-Cr-B	60	6-8
Die parts	Steel HVC	Enhanced wear-resistance	Fe-Cr-B-Al	40	3-4
Hard-alloy tools	Hard alloy VK-6, VK-8	Enhanced wear-resistance	Ti, TiCN, TiN	12	3-3.5
Hot-pressing matrix	Graphite	Enhanced wear-resistance	Cr-Ni-Al-Y	70	2-3

Fig. 2



Fig. 3



T_0 is the temperature affecting wave propagation

Fig. 4

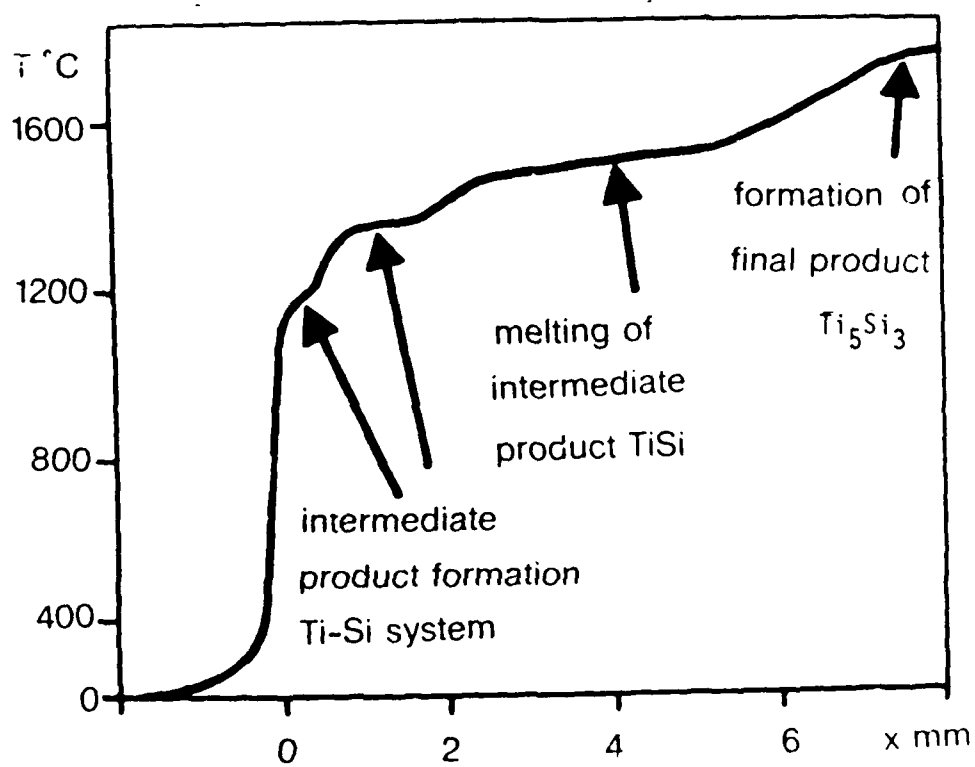


Fig. 5



Initial mixture

Reaction zone

Combustion product

Fig. 6

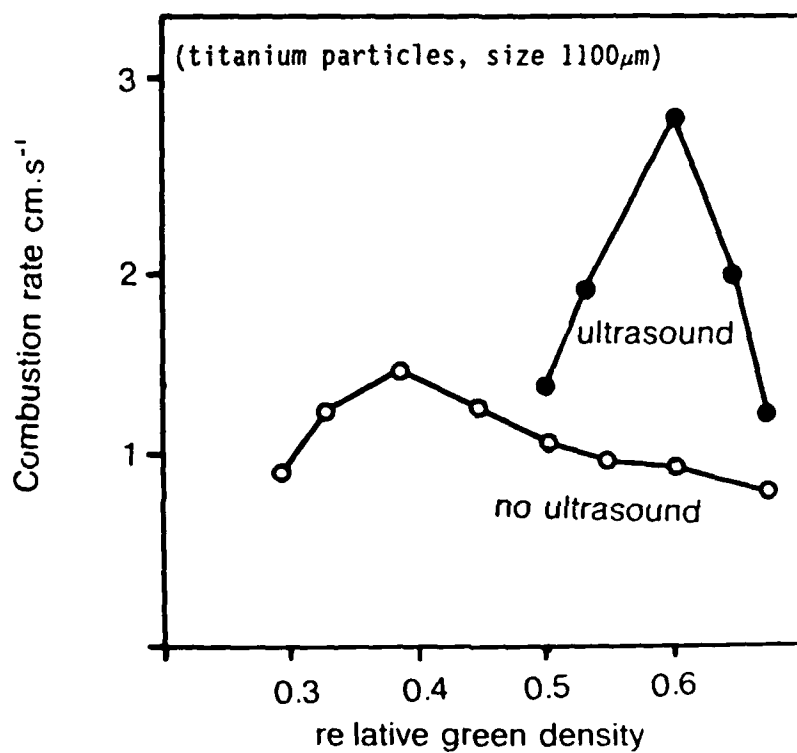


Fig. 7

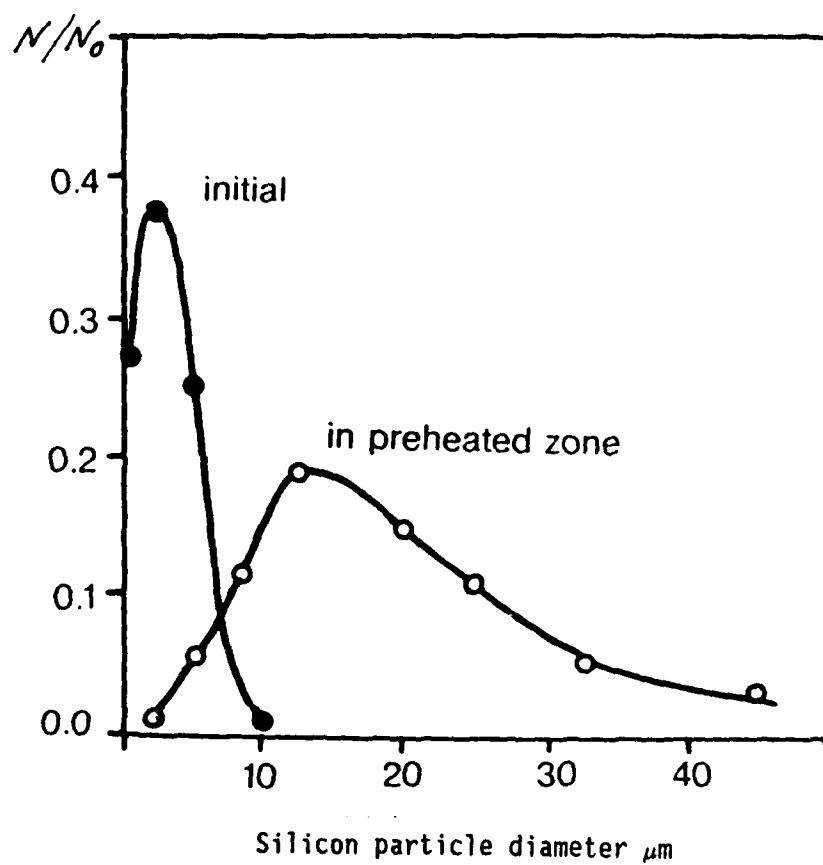


Fig. 8

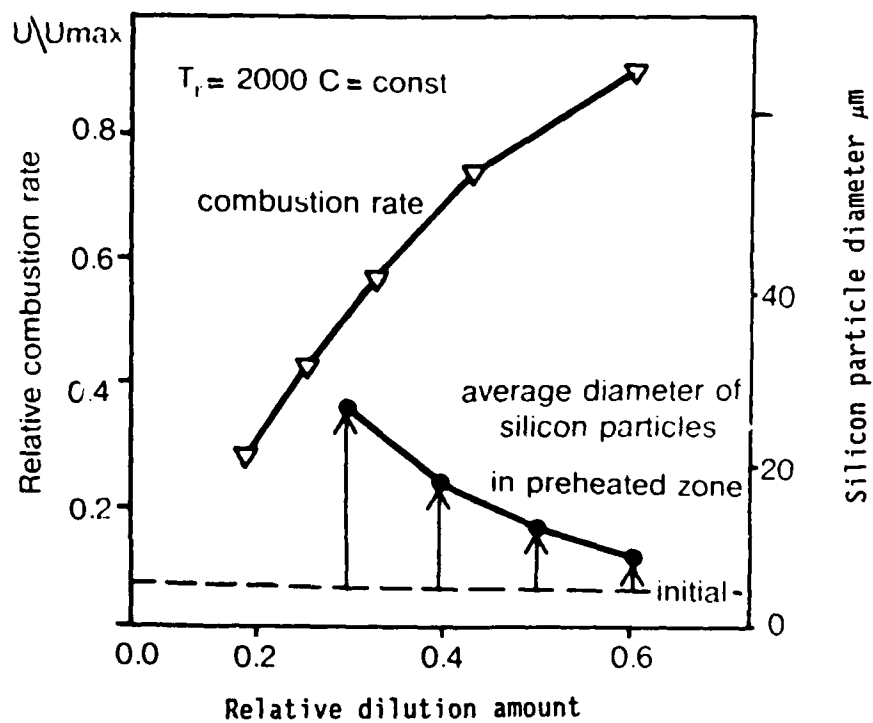


Fig. 9

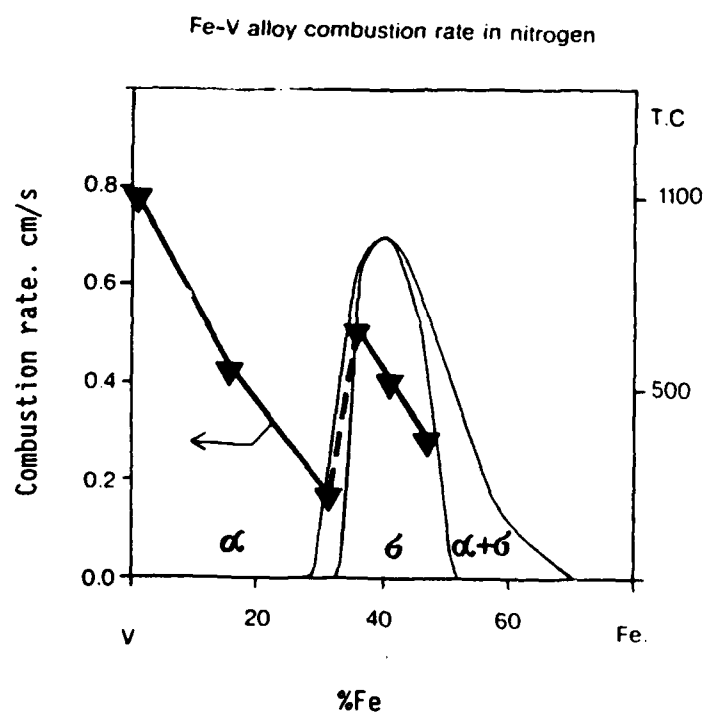


Fig. 10

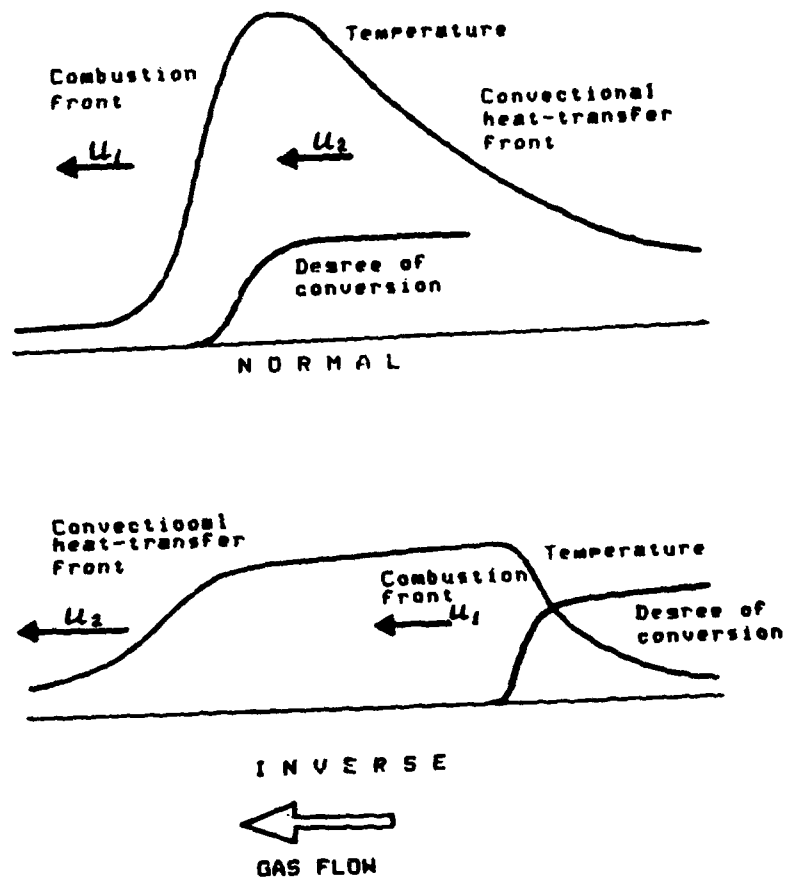
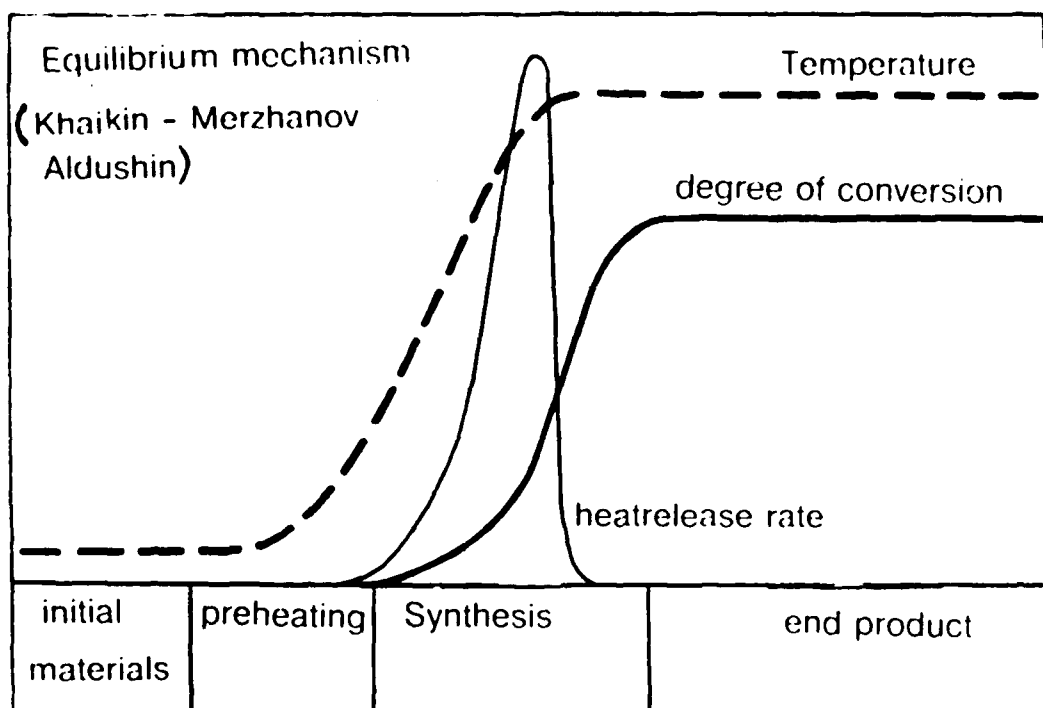


Fig. 11a



100

Fig. 11b

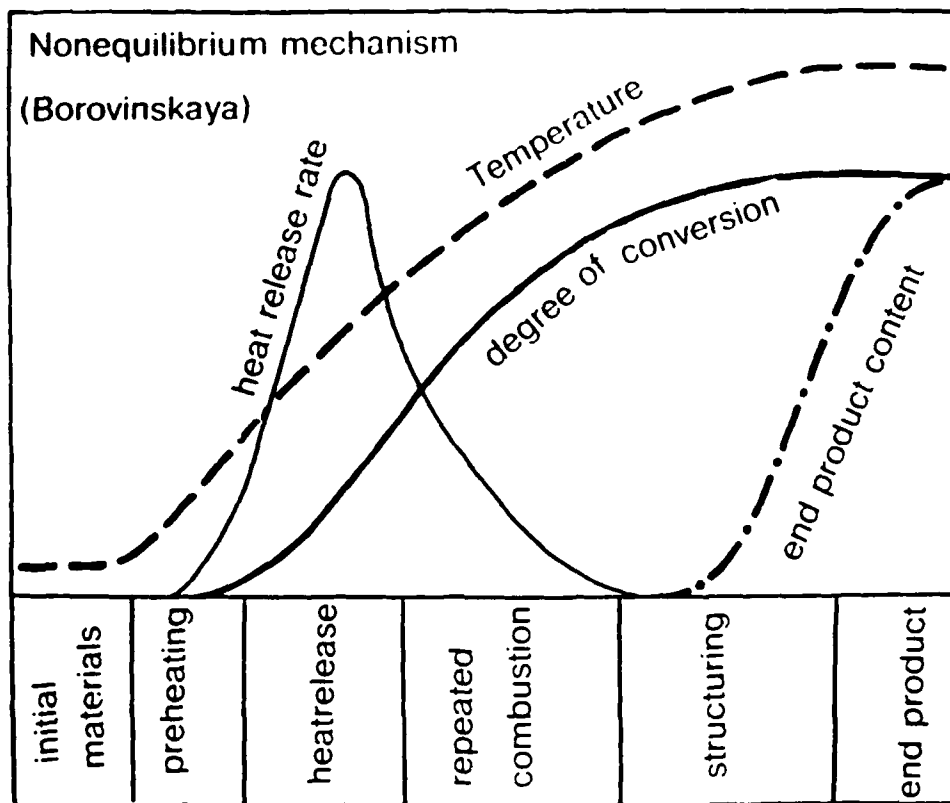


Fig. 12

The Principal Concept of Structural Macrokinetics

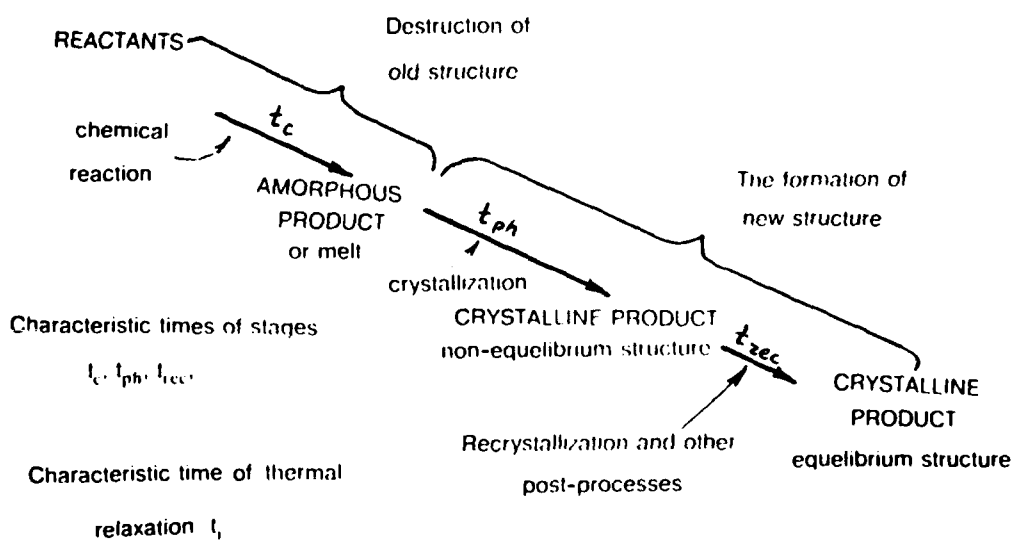


Fig. 13

1



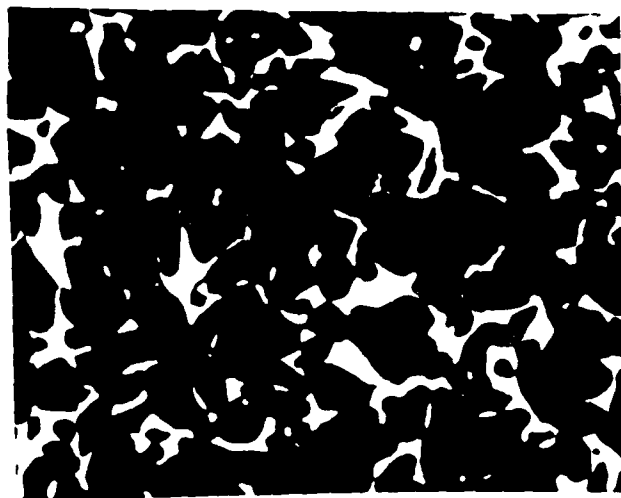
2



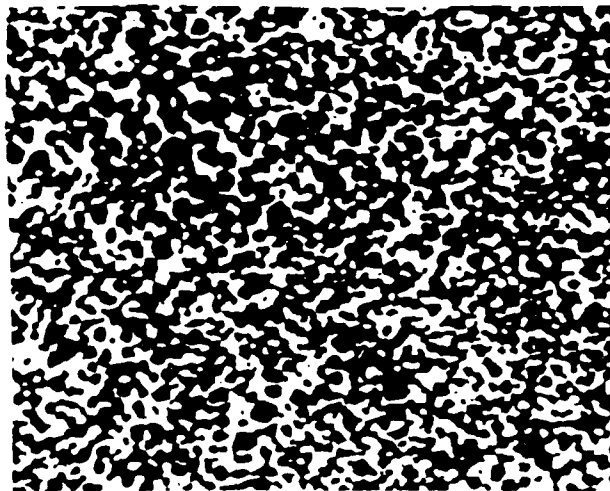
Doc. 1, 27
S. 1

103

Fig. 14



static loading



dynamic loading

Fig. 15

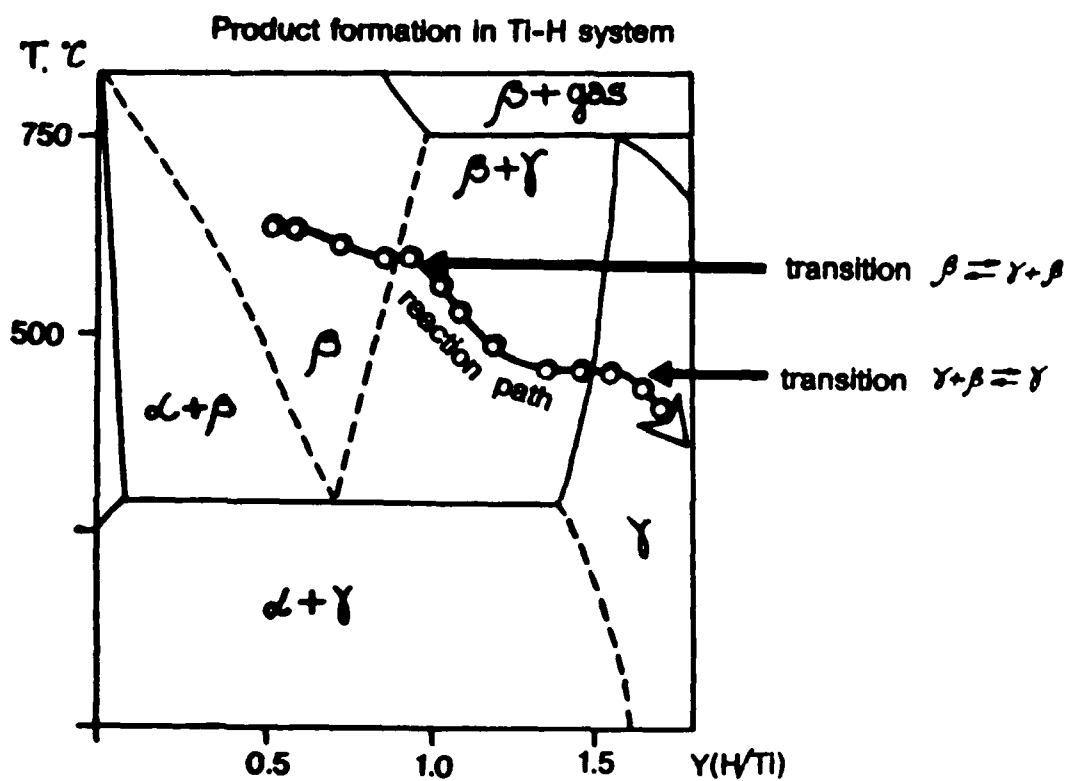


Fig. 16

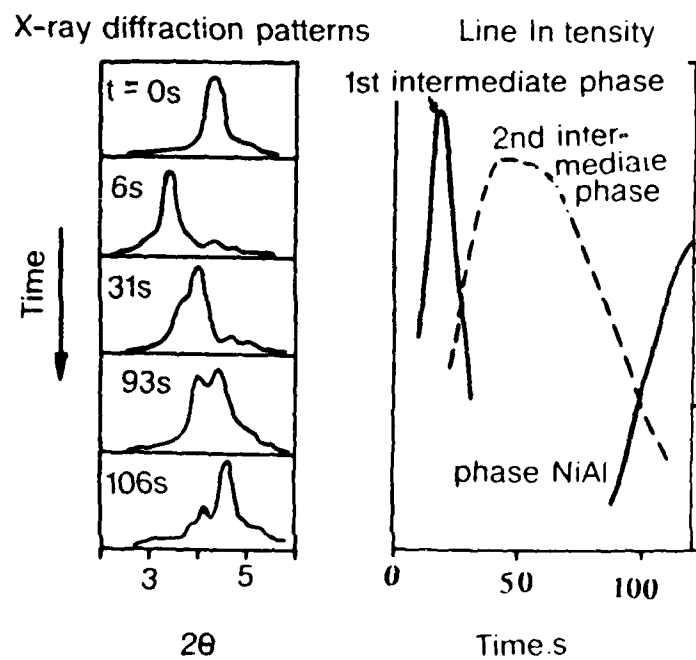


Fig. 17

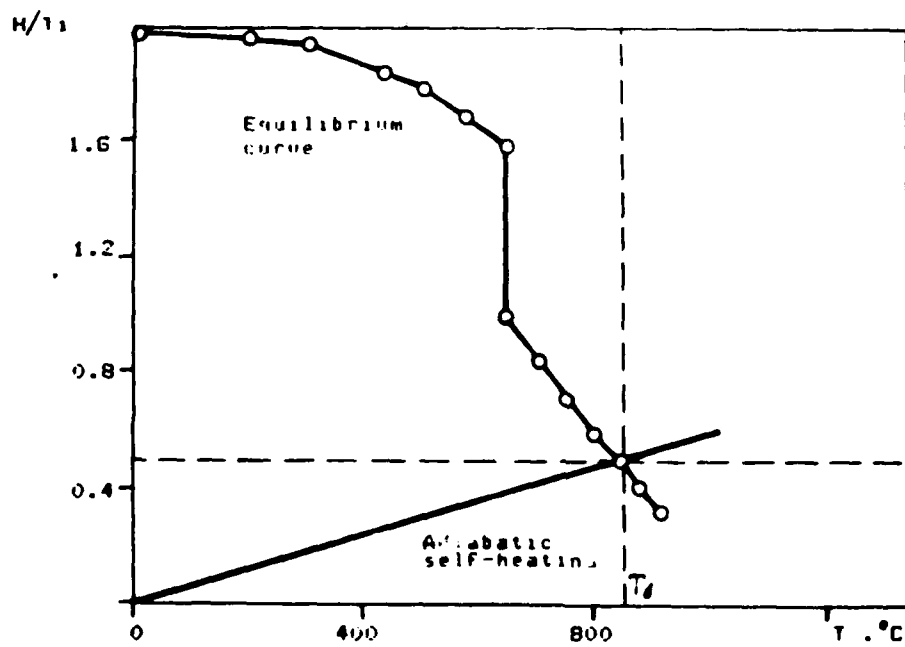


Fig. 18

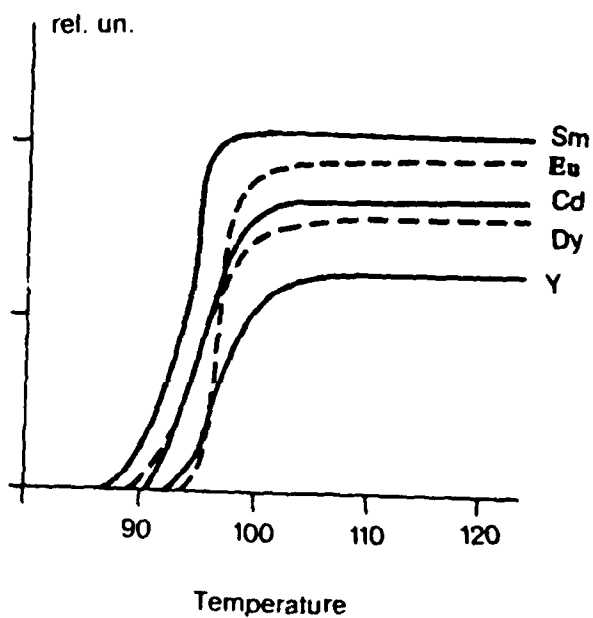
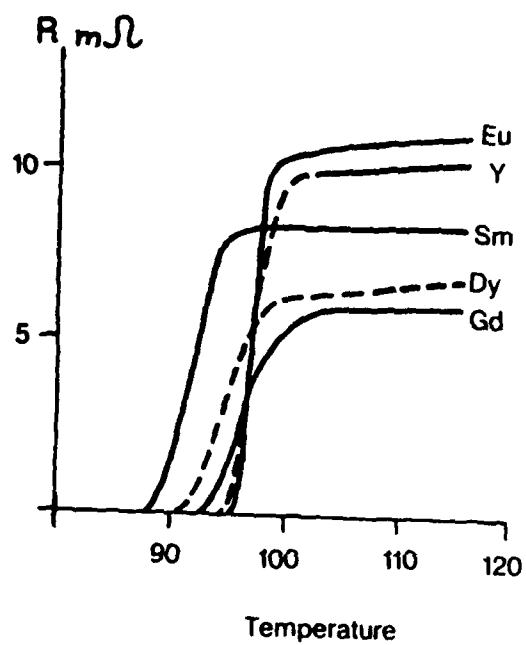


Fig. 19

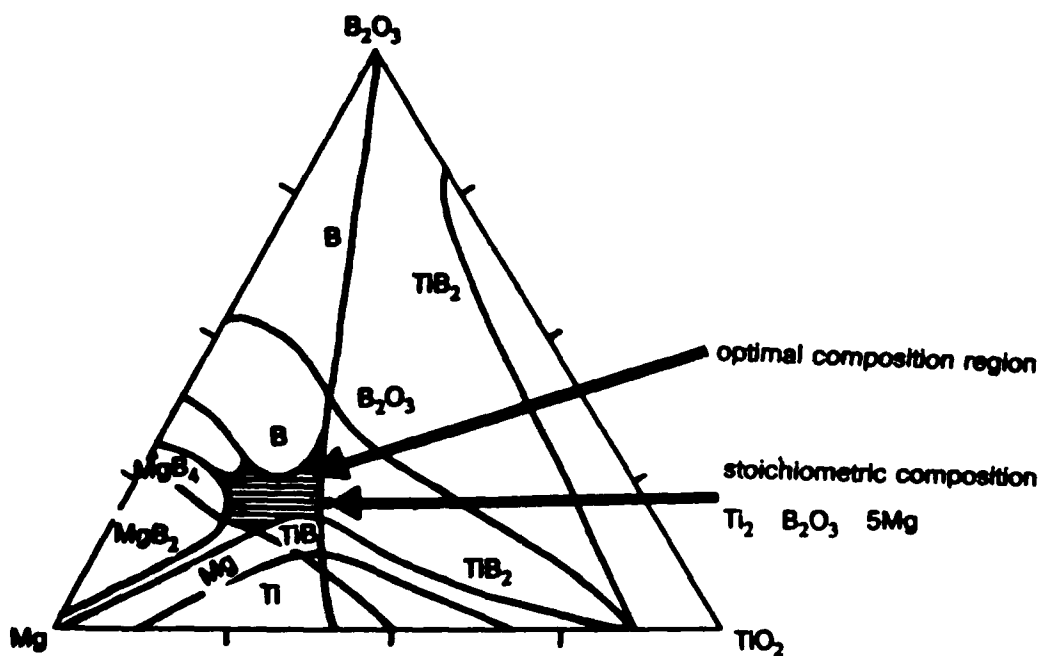


Fig. 20

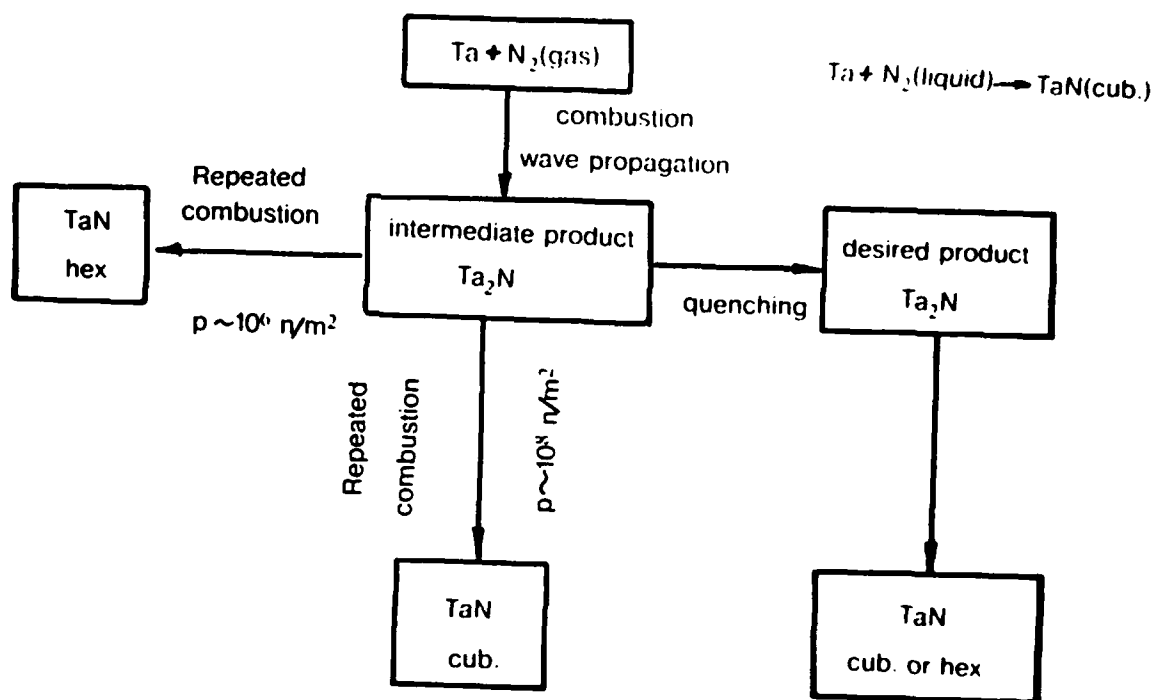
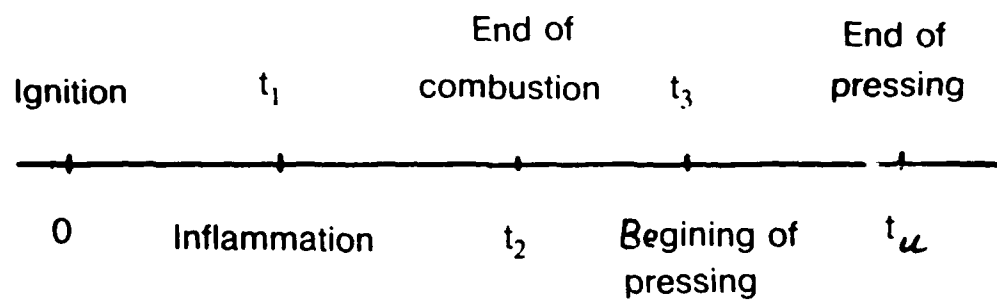


Fig. 21



Homogeneity and nonporosity conditions

$$t_1 < t_2$$

$$t_2 - t_1 < t_z$$

$$t_d = t_3 - t_2 = (t_d)_{opt}$$

$$p > p_*$$

$$t_p = t_4 - t_3$$

Fig. 22

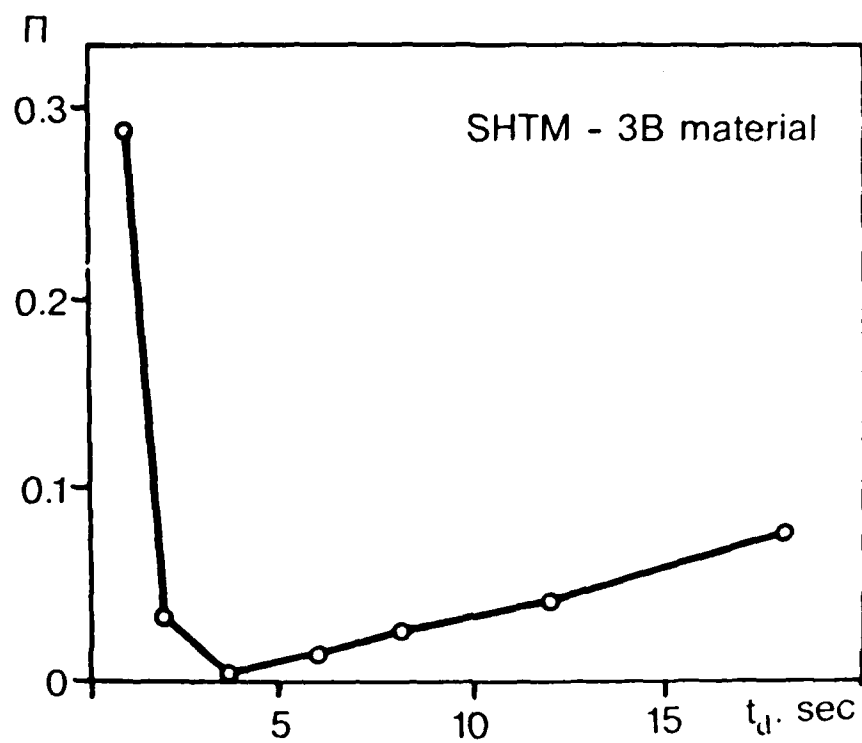
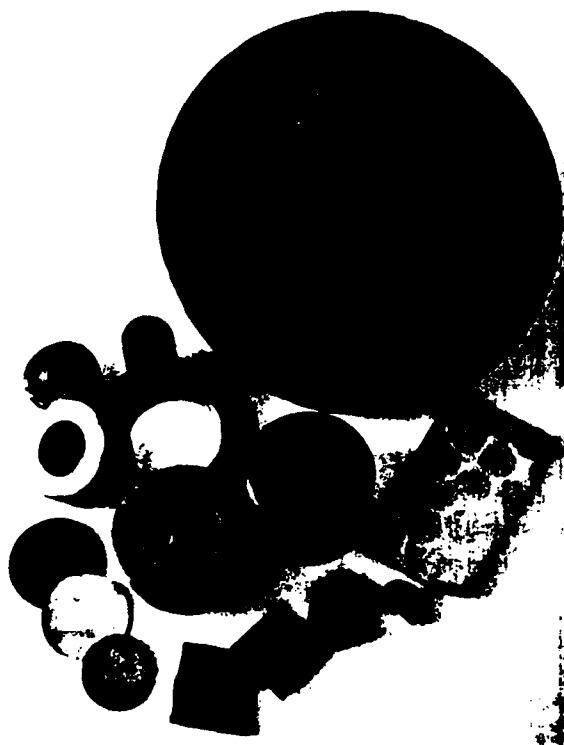


Fig. 22

12

Fig. 23



1B

Fig. 24

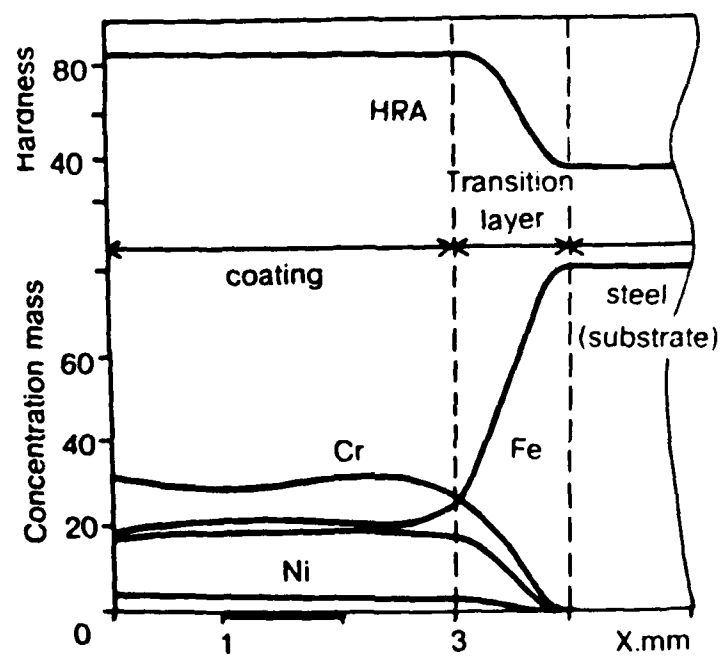


Fig. 25

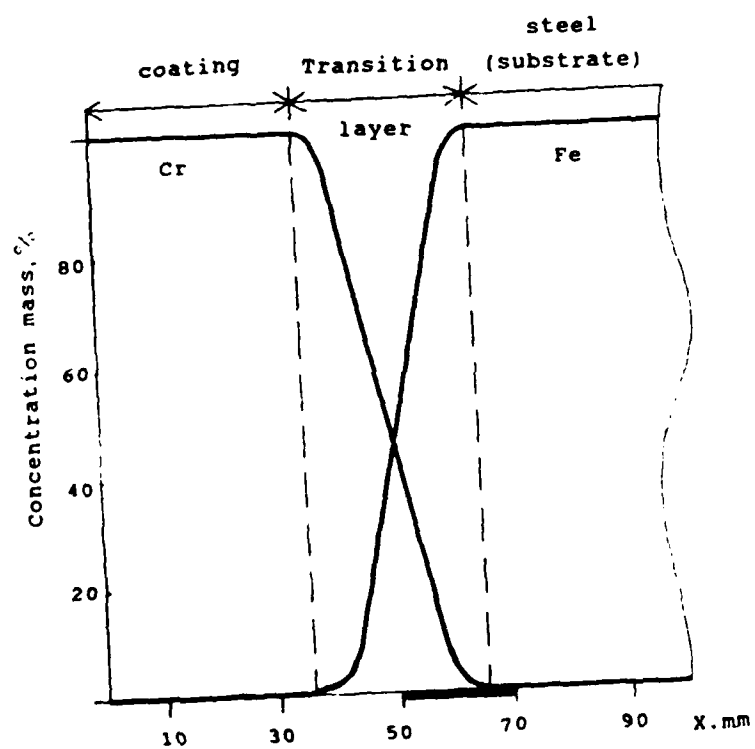
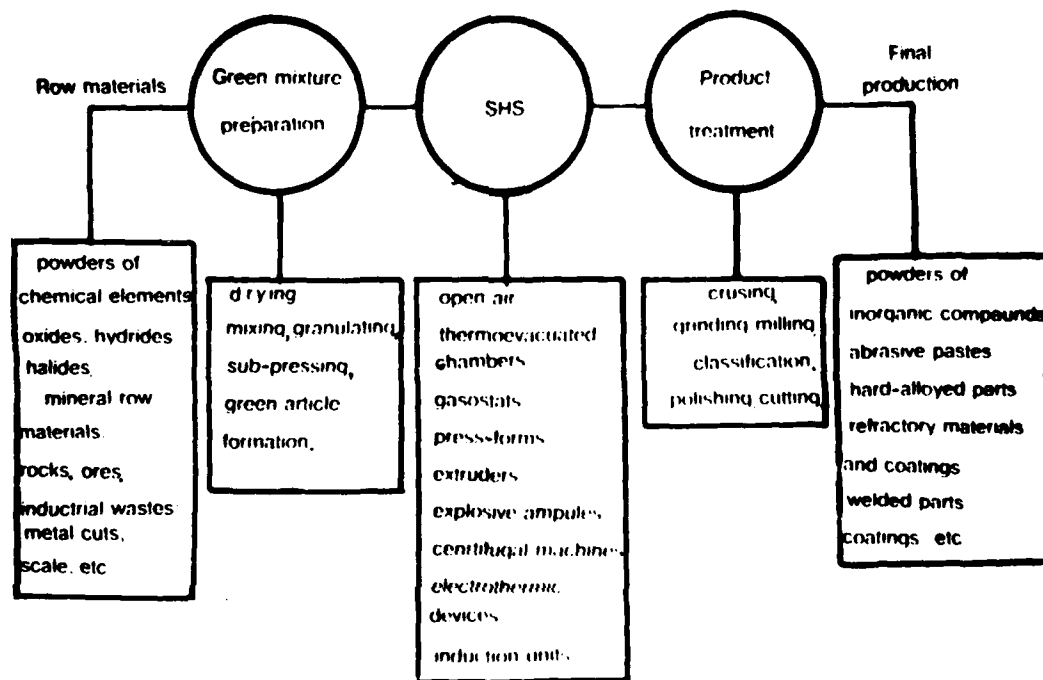


Fig. 26



RECENT PROGRESS IN COMBUSTION SYNTHESIS OF HIGH PERFORMANCE
MATERIALS IN JAPAN

Mitsue KOIZUMI

Institute of Science and Technology, Ryukoku University,
Fukakusa, Fushimi-ku, Kyoto 612, Japan
and

Yoshinari MIYAMOTO

Processing Research Center for High Performance Materials, The
Institute of Scientific and Industrial Research, Osaka
University, Ibaraki, Osaka 567, Japan

Key words : Combustion synthesis, Combustion sintering,
Centrifugal-thermit process

ABSTRACT

Research and development on the SHS is actively expanding in Japan. The trend is oriented to the process developments for a variety of high performance materials. This paper reports the current status of R&Ds in combustion synthesis for ceramic powders and intermetallic alloys, combustion sintering for ceramics, centrifugal-thermit process for ceramic coating, and single crystal growing from the polycrystalline rod prepared by SHS.

INTRODUCTION

In Japan, R&Ds on the SHS¹⁾ have started in 1984, when Osaka University group demonstrated that the refractory ceramics such as TiB_2 ²⁾, TiC ³⁾ and SiC ⁴⁾ can be synthesized and simultaneously densified by the High-Pressure Combustion Sintering (HPCS) method which was developed as a combined process of the SHS and high pressure technique. Now, at least five universities, five national institutes and eight companies are engaged in R&Ds of SHS aiming at the developments of a variety of high performance materials. The examples are ceramic powder synthesis, intermetallic alloy formation, simultaneous synthesis and consolidation for ceramics and composites, ceramic coating, joining, single crystal growth of carbides, and so on. In this paper the current status of R&Ds on SHS in Japan is reviewed.

COMBUSTION SYNTHESIS OF CERAMICS

Various ceramic powders of carbides, borides, nitrides and silicides have been produced by the SHS since 1984. Fine silicon carbide powders are produced from mixed powders of silicon and carbon in traveling through a tunnel kiln by the exothermic synthesis reaction, and commercially supplied as raw materials for SiC ceramics, refractory bricks and abrasives. These are the examples that the SHS or the exothermic synthesis reaction has been applied to industrial production in Japan.

The basic study on the combustion synthesis of nitrides and the reaction analysis has been performed in Osaka University. The process is the nitridation combustion reaction for elemental metal powders in pressurized nitrogen atmosphere below 10 MPa,

and high purity nitride powders of TiN, NbN, ZrN, TaN, Si_3N_4 and AlN are synthesized. Appropriate amount of the same powders as product are added to the raw metal powders within a few ten percent in order to complete the nitridation by reducing too high reaction temperatures and preventing the agglomeration of molten metal particles.

The value of activation energies for the nitridation reactions obtained for TiN (370kJ/mol), NbN (290kJ/mol) and TaN(140kJ/mol) suggest that the synthesis reactions are controlled by the diffusion of nitrogen atom through the solid nitrided layer of each metal particle⁵⁾. On the other hand, it is considered that Si_3N_4 ^{6,7)} and AlN⁸⁾ are formed by the vapor phase reaction of Si and Al vapors with nitrogen gas at the nitriding combustions respectively.

The niobium nitride synthesized has a NaCl type B1 phase structure and shows superconductivity at the transition temperature of 17.3K. which coincides with the highest reported value for NbN prepared by sputtering. Recently, it was found that the solid solution system of $\text{NbN}_{1-x}\text{C}_x$ ($0 \leq x \leq 0.8$) can be synthesized from the mixed powders of Nb and C by the nitridation combustion. The superconducting transition temperatures varied depending on the composition and showed a peak value of 18.8K at $x=0.4$ as shown in Fig.1, which is 0.9K higher than the highest reported value for this system. B1 phase NbN is a high temperature equilibrium form above 1300°C and usually not easy to be synthesized. The rapid cooling effect of the combustion reaction seems to affect to quench the high temperature form. It is also possible to synthesize $\text{Si}_3\text{N}_4+\text{SiC}$ composite powders in

a wide composition range by igniting the mixed powders of Si and C under nitrogen gas pressure. The SHS is expected to develop as a synthesis process to produce new materials of composite powders and solid solutions which are difficult to be prepared by the conventional synthesis methods.

INTERMETALLIC ALLOY FORMATION

The intermetallic compounds such as TiAl, NiTi, Ni₃Al and ZrNi alloys can be synthesized by the combustion reaction of their constituent elements. The R&Ds are promoted in the following institutions—National Research Institute for Metals, Tokyo; Government Industrial Research Institute, Hokkaido; Tohoku University, Sendai; Tokyo Institute of Technology, Yokohama; and others.

Titanium aluminum alloy which was consolidated for the synthesized powders by HIPing shows mechanical properties equivalent to the centrifugally atomized alloy. Nickel titanium alloy with less oxygen content is synthesized and formed to wire and thin plate via processes of HIPing, hot-rolling, cold-rolling and drawing. The shape memory effect and the superelasticity equal to the commercial NiTi alloy are obtained. These technologies have been developed by Y. Kaieda in National Research Institute For Metals⁹⁾. Some products of NiTi alloy are shown in Fig. 2.

COMBUSTION SINTERING PROCESS

Synthesis and densification for ceramics can be achieved simultaneously by combining the SHS and high pressure techniques.

The first experiment was conducted by igniting the mixed powders of Ti and B under the ultra high pressure of 3GPa by using a cubic anvil device, and a sintered body of TiB_2 with 95% density was obtained. Other dense ceramics of ZrB_2 , TiC and SiC were fabricated by this method, but its practical application was limited because of small sample size and pressure loading system of GPa order. As a useful process to solve these problems, a new method of the gas-pressure combustion sintering has been devised by Y. Miyamoto in 1987¹⁰⁾ as illustrated in Fig. 3.

In this method, the reactant is vacuum sealed into a glass capsule just like the capsule method for HIPing and embedded into the combustion agent such as the mixed powders of Ti and C. The reaction is initiated by the high heat release from the combustion agent which is ignited at the glass softening temperature under Ar gas pressures below 100MPa. Nearly full dense TiB_2 , TiC, and their composites with metals and with ceramics have been fabricated by this process. If this new process is fully developed, the mass production of near-net shape components of ceramic composites will be available.

Another pressure loading systems are being developed for simultaneous synthesis and consolidation of ceramics by N. Sata at Government Industrial Research Institute, Tohoku¹¹⁾. One is a uniaxial loading system by a spring and another is an isostatic loading system by water pressure. Using these methods, the so called Functionally Gradient Materials (FGM) for TiB_2 -Cu system are now being developed. The FGM is a new composite material consisting of a surface layer of refractory ceramics with a metal phase continuously increasing within the ceramic matrix,

eventually forming a metal base ¹²⁾. Such materials are expected to have high-temperature resistance with low internal stress, good fracture toughness, and enhanced metal bonding capabilities. The combustion consolidation method enables to change continuously the metal composition to a certain content in the ceramic matrix because the initial arrangement of compositional constituents in the green body remains in the product due to the rapid wave propagation of combustion reaction. Two research groups of GIRI, Tohoku, and Osaka University are being engaged in developing FGM by the pressurized combustion sintering and consolidation methods.

Recently a reaction sintering process to fabricate new composite material of SiC and C without pressure loading has been developed at Osaka Cement Co., Ltd.¹³⁾. In this process, the exothermic reaction for Si and C mixture enables to form β -SiC particles and to make them distribute homogeneously in the carbon matrix. The products exhibit excellent properties in surface hardness, lubrication, electric and thermal conductivities as well as wear and oxidation resistances. Various shaped components, as shown in Fig.4, are being produced with the trade name of "CARBO-SIC".

OTHER UNIQUE APPLICATIONS OF SHS

Centrifugal-thermit process, which is a new technique of a kind of SHS, has been devised for lining the ceramic-metal composite layer on inner surface of pipes by O. Odawara¹⁴⁾. By inducing the following thermit reaction, $3\text{Fe}_3\text{O}_4 + 8\text{Al} \rightarrow 4\text{Al}_2\text{O}_3 + 9\text{Fe} - 3265\text{kJ}$, in a hollow metal pipe rotating at high speed, the

inner surface of the pipe melts and forms a composite with the reaction product. Since the density of the produced ceramic such as alumina is normally smaller than that of the produced metal, the thick ceramic layer can be coated with the intermediate metallic layer on the inner surface of pipe as shown in Fig. 5. A metal-ceramic composite pipe as long as 5m can be produced by the centrifugal-thermit process and this technique was transferred to Kubota Iron Works Co., Ltd..

In National Institute for Research in Inorganic Materials, high-quality large single crystals of TiC were prepared from the feed rod synthesized by SHS. S. Ohtani has succeeded to grow a large single crystal from a TiC feed rod formed by igniting the rod of Ti and C mixed powders in vacuum, using the floating zone method as shown in Fig. 6¹⁵⁾. The application of SHS to prepare the feed rod of high purity TiC leads to growing of single crystal with high crystal perfection compared with the crystal prepared from the commercial TiC powders. Single crystal of TiC can be used as an efficient field emitter and a substrate material for high temperature SiC semiconductor with less thermal expansion mismatch. These new material processings are noted as the unique applications of SHS.

SUMMARY

As described in the previous chapters, SHS research and development are actively expanding in Japan. The SHS is characterized as the rapid and economical process with generating high heat. It is expected, therefore, that further ideas, combinations with other processes as well as fundamental

investigations to develop the process merits, will lead to a variety of new processings for material science and technology, especially in the field of ceramics and metals.

REFERENCES

1. A. G. Merzhanov and I. P. Borovinskaya, "Self-Propagating High Temperature Synthesis of Refractory Inorganic Compounds", Dokl. Chem. (Engl. Trans.), 204, 429-32 (1972)
2. Y. Miyamoto, M. Koizumi and O. Yamada, "High-Pressure Self-Combustion Sintering for Ceramics", J. Am. Ceram. Soc., 67, C224-5 (1984)
3. O. Yamada, Y. Miyamoto and M. Koizumi, "High-Pressure Combustion Sintering of Titanium Carbide", J. Am. Ceram. Soc., 70 C206-8 (1987)
4. O. Yamada, Y. Miyamoto and M. Koizumi, "High-Pressure Self-Combustion Sintering of Silicon Carbide", Bull. Am. Ceram. Soc., 64 319-21 (1985)
5. K. Hirao, Y. Miyamoto and M. Koizumi, " Reaction Analysis of Nitrides", Proc. Int. Symp. on "Sintering '87", Tokyo ,Elsevier Science Publishing Co.Inc., vol.1, 551-556 (1988)
6. K. Hirao, Y. Miyamoto and M. Koizumi, "Combustion Reaction Characteristics in the Nitridation of Silicon", Adv. Ceram. Mat. 2 780-83 (1987)
8. K. Tanihata and Y. Miyamoto, "Combustion Synthesis of AlN", in preparation
9. A. Takahashi, O. Yamada, M. Koizumi and Y. Miyamoto, "Combustion Synthesis of Superconducting $\text{NbN}_{1-x}\text{C}_x$ ", in

preparation

10. K. Hirao, Y. Miyamoto and M. Koizumi, " Sintering of Si_3N_4 Powders Synthesized by a Combustion Reaction", J. Ceram. Soc. Jpn. Int. Ed. 95 905-10 (1987)
9. Y. Kaieda, M. Otaguchi, O. Odawara, M. Nakamura, T. Oie and S. Shite, "Self-propagating High-Temperature Synthesis of Intermetallic Compounds", Proc. Int. Conf. on " Sintering '87", Tokyo (1987) in press
10. Y. Miyamoto and M. Koizumi, "Potentiality of High Pressure Combustion Sintering to Produce Ceramic Based Multi-Phase Components" Proc. Int. Symp. on "Sintering '87", Tokyo (1987) in press
11. N. Sata and J. Ikeuchi, "Simultaneous Synthesis and Forming of Ti-B System by Self-Propagating Reaction", J. Ceram. Soc. Jpn, 95 243-47 (1987)
12. M. Niino, "Design of Functionaly Gradient Materials Utilizing Process Technologies of Micro-Elements", Function & Materials, 7 31-43 (1987)
13. S. Ikeda, H. Izawa, K. Urabe and M. Koizumi, "In-Site Formation of SiC and SiC-C Blocked Solids by Self-Combustion Synthesis", this symp. proc.
14. O. Odawara and J. Ikeuchi, "Ceramic Composite Pipes Produced by a Centrifugal-Exotheric Process", J. Am. Ceram. Soc., 69 C80-81 (1986)
15. S. Ohtani, T. Tanaka and Y. Ishizawa, "Preparation of TiC Single Crystal from Self-Combustion Rod by Floating Zone Method", J. Cryst. Growth, 83, 481-84 (1987)

Figure Captions

- Fig. 1. Superconducting transition temperatures of $\text{NbN}_{1-x}\text{C}_x$ solid solutions synthesized by the SHS under 10 MPa nitrogen pressure.
- Fig. 2. Various products of NiTi alloy prepared by the SHS.
(Courtesy, Dr. Y. Kaieda, Institute for Metals, Tokyo.)
- Fig. 3. A model process of the gas-pressure combustion sintering for future production system.
- Fig. 4. SiC-C Components, "CARBO-SIC", produced by the exothermic reaction sintering at Osaka Cement Co., Ltd..
- Fig. 5. Metal-ceramic (alumina) composite pipe produced by the centrifugal-thermit process. (Courtesy, Prof. O. Odawara, Tokyo Institute of Technology)
- Fig. 6. TiC single crystal prepared from the self-combustion rod of polycrystalline TiC by floating zone method.
(Courtesy, Dr. S. Ohtani, National Institute for Research in Inorganic Materials, Tsukuba)

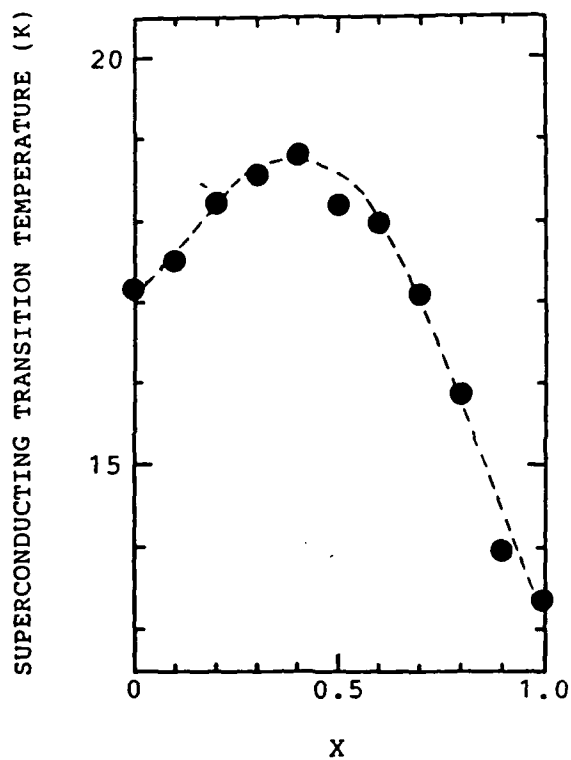


Fig. 1 Superconducting transition temperatures of $\text{NbN}_{1-x}\text{C}_x$ solid solutions synthesized by the SHS under 10 MPa nitrogen pressure.



Fig. 2

Various products of NiTi alloy prepared by the SHS. (Courtesy, Dr. Y. Kaieda, Institute for Metals, Tokyo.)

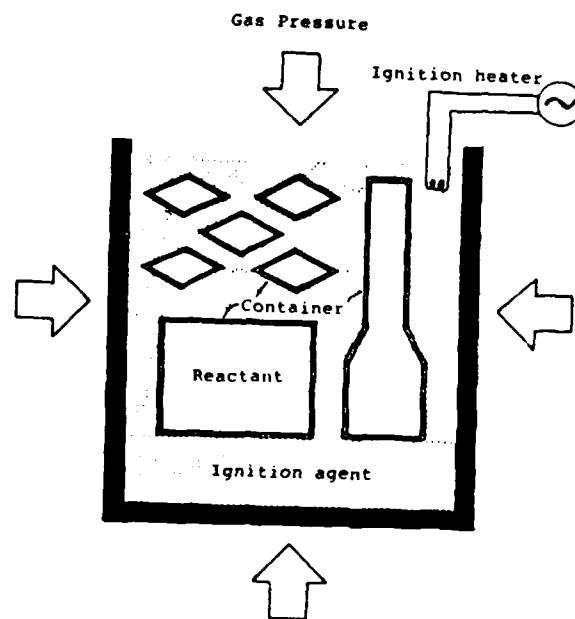


Fig. 3

A model process of the gas-pressure combustion sintering for future production system.

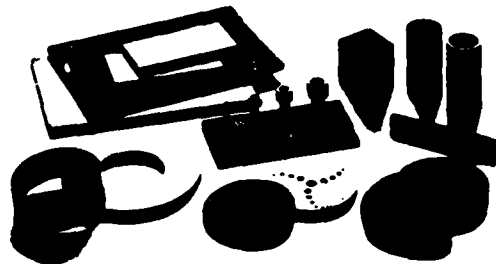


Fig. 4 Components, "CARBO-SIC", produced by the
exothermic reaction sintering at Osaka Cement Co., Ltd..



Fig. 5

Metal-ceramic (alumina) composite pipe produced by the centrifugal-thermit process. (Courtesy, Prof. O. Odawara, Tokyo Institute of Technology)



Fig. 6

TiC single crystal prepared from the self-combustion rod of polycrystalline TiC by floating zone method. (Courtesy, Dr. S. Ohtani, National Institute for Research in Inorganic Materials, Tsukuba)

MODELING AND NUMERICAL COMPUTATION OF A NONSTEADY SHS PROCESS

A. Bayliss and B. J. Matkowsky

Department of Engineering Sciences and Applied Mathematics

Northwestern University

Evanston, Illinois 60208

Abstract Analytical and numerical methods are employed to study the SHS process. In particular, solutions to equations modeling the process which describe observed modes of propagation are obtained. Predictions of new modes of propagation, exhibiting yet more complex behavior, not yet reported experimentally are also made.

1. INTRODUCTION Combustion synthesis, or self propagating high temperature synthesis (SHS), is a new and innovative method for the fabrication of high tech ceramic and metallic materials. In this method a sample (say a cylindrical sample) consisting of a compacted powder mixture is ignited at one end. A thermal wave then propagates through the sample, converting unburned reactants to products. This process was pioneered by Merzhanov and colleagues in the U.S.S.R. (see e.g. [1-6]), and has been extensively investigated by J. B. Holt and colleagues in the U.S. [7], as well as by others throughout the world. The SHS process is important not only because of its technological implications, but also from the point of view of basic science. Modeling and analysis of the process involves the study of complex dynamical systems. The mathematical model consists of a system of highly nonlinear partial differential equations. Studies of this system not only lead to a greater understanding of the combustion process, but the theoretical problems describing the process pose serious challenges which require the development of new mathematical methods for their resolution. Finally, the insight gained from these studies helps us to understand the behavior of the process, which is a necessary prerequisite to our ability to effectively control the process.

Thus we consider a reaction front (so-called solid flame) propagating through a cylindrical sample. Experiments have revealed a variety of modes of

propagation through the sample. In addition to the uniformly propagating planar front, there have been observations of (i) pulsating combustion, in which a planar front propagates with an oscillatory velocity, (ii) spin combustion, in which one or more hot spots (luminous points) are observed to move in a helical motion along the surface of the sample, and (iii) multiple point combustion, in which the hot spots appear, disappear, and reappear repeatedly. Finally, experiments indicate that in certain cases burning occurs throughout the sample, while in other cases burning occurs only on the surface of the sample and not in its interior.

We employ both analytical and numerical methods to study the SHS process. In particular we obtain solutions to equations modeling the process, which describe the above mentioned observed modes of propagation, as well as predict new modes of propagation, exhibiting yet more complex behavior, not yet reported experimentally.

2. MATHEMATICAL MODEL The nondimensional model we consider is given by

$$(2.1) \quad \theta_t - \phi_t \theta_z + \nabla^2 \theta + \left[\frac{1}{\alpha(1+\gamma)} \right] \Lambda Y \exp \left\{ \frac{N(1-\sigma)(\theta-1)}{\sigma+(1-\sigma)\theta} \right\}, \quad \begin{matrix} z < 0 \\ z > 0 \end{matrix}$$

$$(2.2) \quad Y_t - \phi_t Y_z - \left[\frac{1}{\alpha} \right] \Lambda Y \exp \left\{ \frac{N(1-\sigma)(\theta-1)}{\sigma+(1-\sigma)\theta} \right\}, \quad \begin{matrix} z < 0 \\ z > 0 \end{matrix}.$$

Here θ and Y denote nondimensional temperature and concentration respectively, N is the activation energy, σ is the ratio of unburned to burned temperature, $z = x_3 - \phi(x_1, x_2, t)$ is a coordinate moving with the front ϕ , and Λ , the solid flame speed eigenvalue, is determined from the solution corresponding to the uniformly propagating planar front. The model accounts for melting, which causes the reaction rate to increase by the factor $\alpha > 1$. The condition at the melting surface is

$$(2.3) \quad (1 + (\nabla \phi^2)) [\theta_z] + \gamma Y(t, z=0) \phi_t = 0,$$

where $[q]$ denotes the jump in the quantity q across the melting surface, and γ is the heat of fusion. The boundary conditions are

$$(2.4) \quad Y = 1, \quad \theta = 0 \quad \text{as} \quad z \rightarrow -\infty,$$

$$(2.5) \quad Y = 0, \quad \theta = 1 \quad \text{as} \quad z \rightarrow +\infty.$$

134

We consider this problem in each of the geometries corresponding to (i) one dimensional propagation, (ii) burning on the surface of a cylinder, and (iii) burning throughout the cylinder. In addition, we consider the problem both for finite activation energies, where the reaction occurs over a zone whose width is inversely proportional to N , with rate given by the Arrhenius kinetics, and for very large activation energies (the so called flame sheet model), in which case the reaction zone collapses to a moving surface (the reaction front) and the Arrhenius reaction rate is replaced by delta-function kinetics on the reaction surface. The flame sheet model is employed in our analytical studies, while the Arrhenius kinetics is employed in our numerical studies. Finally, in case (iii) of burning throughout the cylindrical sample, we impose the insulated boundary condition

$$(2.6) \quad \frac{\partial \theta}{\partial r} - \frac{\partial \phi}{\partial r} \frac{\partial \theta}{\partial z} = 0, \quad \text{at } r = R,$$

and in cases (ii) and (iii) we impose the periodicity conditions

$$(2.7) \quad g(\psi + 2\pi) = g(\psi)$$

where g denotes θ , Y and ϕ .

3. ANALYTICAL AND NUMERICAL RESULTS A theoretical analysis of the one-dimensional case was undertaken by Matkowsky and Sivashinsky [8] who considered the flame sheet model without melting. They showed that the self-oscillatory mode arose as a Hopf bifurcation from the uniformly propagating planar front, as a critical parameter $\mu_c = 2 + \sqrt{5}$, of the system, was exceeded. Here $\mu = N(1-\sigma)/2$, Matkowsky and Sivashinsky showed that the uniformly propagating planar front is stable for $\mu < \mu_c$. For $\mu > \mu_c$ they showed that the uniform front is unstable and perturbations evolve to the bifurcated state, i.e., to the pulsating propagating state. In their bifurcation analysis, they calculated the amplitude, frequency and velocity of the pulsating front.

Bifurcation analysis is valid locally, in a neighborhood of the bifurcation point. To determine more global behavior, i.e., to determine the behavior of the system beyond this neighborhood, it is necessary to determine the bifurcation branch(es) numerically. To do so, Bayliss and Matkowsky [9]

introduced an adaptive Chebyshev pseudo-spectral method for the numerical solution of the one-dimensional problem, which was subsequently extended in [10]. Employing this method [9,11] for the model with Arrhenius kinetics, with melting included, they showed how the sinusoidal oscillations predicted by bifurcation theory developed into relaxation oscillations as μ is increased. Note that the definition of μ is now modified to account for melting, so that $\mu = N(1-\sigma)/2(1-M)$, where the melting parameter M is defined as $M = (1 - (1+\gamma)/\alpha) \exp(N(1-\sigma)(\theta_m - 1))$, where θ_m denotes the melting temperature. They were then able to numerically identify a period doubling secondary bifurcation at $\mu = \mu_2$. The oscillations exhibit sharp narrow spikes alternating with longer slowly varying behavior. The peaks of the oscillations become progressively sharper and steeper as μ is increased. In addition the temperature profiles change very rapidly in a very narrow region (reaction zone) in space. The resolution of this behavior in space and in time, poses a serious challenge to numerical computations, and makes adaptive techniques particularly attractive. Our adaptive pseudo-spectral method was introduced to meet this challenge of accurately and efficiently computing solutions exhibiting this behavior. As μ is increased beyond μ_3 , the doubly periodic solution can no longer be computed, and the solution returns to the singly periodic branch. There is an interval of bistability where the singly and doubly periodic branches stably coexist, each with its own domain of attraction.

In our numerical approach we solve the problem as an initial boundary value problem, integrating in time until a stable oscillatory steady state is achieved. Thus we necessarily compute only the stable branches of the bifurcation diagram. Generally the solution reaches its steady state after a relatively short period of time, except near bifurcation points where much longer times are required to reach steady state conditions.

In the numerical computations we employ the parameter values $N = 50$, $\alpha = 1.7$, $\gamma = 0.5$, $\theta_m = 0.8$. In Figures 1a-1f we exhibit plots of the computed temperature at a fixed value of z , for increasing values of μ . We observe the

transition from the steadily propagating front to the bifurcated oscillatory front for $\mu > \mu_1$, where μ_1 lies between 4.27 and 4.28. This compares well with the analytical prediction of $\mu_c = 4.236$ [8], which was computed for the flame sheet model. The oscillations rapidly develop into relaxation oscillations with progressively sharper spikes of increasing amplitude, as μ increases. Then a period doubling secondary bifurcation occurs at μ_2 which lies between 4.454 and 4.459. The growth of the larger spike is very rapid along the secondary branch. As μ is increased beyond μ_3 , with $4.521 < \mu_3 < 4.523$, solutions are again singly periodic. In Figure 2 we exhibit temperature profiles at selected times in the cycle for $\mu = 4.519$.

Theoretical analyses of the cases in which burning occurs on the surface of a cylindrical sample, as well as throughout the sample, were considered in [12] and [13] respectively. In each case the flame sheet model, with melting included, was considered, and a basic solution corresponding to a uniformly propagating planar front was identified. A linear stability analysis of that solution then led to a neutral stability curve, which separated the region in parameter space in which the uniformly propagating solution is stable from the region in which it is unstable. Perturbations in the form of modes $\phi \sim \exp(i(\omega t \pm n\psi))$ in the case of surface burning, and of the form $\phi \sim J_n(kr) \exp(i(\omega t \pm n\psi))$ in the case of burning throughout the sample were considered (with similar perturbations of the temperature field, suitably modified to account for their dependence on z). For surface burning, the wave number k is given by $k = n/R$, while for burning throughout the sample, k is determined by $J'_n(kR) = 0$. Thus only discrete points or modes on the neutral stability curve are realized. We note that if the radius R of the cylindrical sample is sufficiently small, then the most unstable mode corresponds to $n = 0$, so that as μ is increased beyond the value $\mu_c = 2 + \sqrt{5}$, the uniformly propagating solution becomes unstable and a transition to planar pulsating propagation occurs. As R is increased, the discrete points on the neutral

stability curve move to the left. Thus for larger R , the most unstable modes correspond to $n > 0$. First the mode $n = 1$ becomes the most unstable, then $n = 2$ and so on as R is increased. In the nonlinear analysis we derived equations for the amplitudes of the most unstable modes and found solutions corresponding to (i) spinning waves, which travel clockwise or counter-clockwise around the cylinder, while propagating forward in the $-z$ direction, thus resulting in a helical motion, and (ii) standing waves whose points of maximum temperature periodically rise, fall and rise again, thus describing multiple point combustion. In addition, we found solutions corresponding to various modes of quasi-periodic burning. We presented formulae for the amplitude, frequency and average velocity of the nonsteadily propagating solutions. When the uniformly propagating solution becomes unstable, a transition to a stable spinning or stable standing wave will occur. The spinning (standing) wave will be one headed ($n=1$), two headed ($n=2$) or n headed, depending on the size of R . The quasi-periodic modes of propagation that we predict are new and experimental observations of these modes have not yet been reported.

We now present some results of numerical computations of the surface burning problem, for the model with Arrhenius kinetics, with melting included. The analysis, described above, predicts that the uniformly propagating solution becomes unstable at $\mu = 4$, $k = 1/2$. For $\mu > 4$, both traveling wave solutions (spinning combustion) and standing wave solutions (multiple point combustion) exist. The stability of these solutions depends on the parameters of the problem.

First we describe solutions corresponding to standing waves. In these computations we employ the parameter values $N = 50$, $\alpha = 2.3$, $\gamma = 0.18$, $\theta_m = 0.8$. In Figure 3 we present a plot of the location of the melting surface at a sequence of time values, for the case $\mu = 4.207$. As μ is increased the solution exhibits relaxation oscillations in time and a progressive narrowing of the location of the luminous point in ψ . In Figure 4 we illustrate the temperature θ as a function of time t , at $z = 0.4$, at angles $\psi = 0$, $\psi = \pi/2$,

$\psi = \pi$, and $\psi = 3\pi/2$ respectively, for $\mu = 4.07$ and for $\mu = 4.16$. In Figures 5a,b, perspective plots of $\theta(z, \psi)$ are shown for $\mu = 4.16$ at two different times. The figures show the formation of the luminous point, and its subsequent reappearance on the other side of the cylinder. We have also computed solutions describing spinning waves. An example of such a solution is shown in Figure 6. This computation corresponds to the parameter values $N = 50, \alpha = 2.0, \gamma = 0.05, \theta_m = 0.8$.

Finally, we remark that in addition to the problems described above, we have also considered the problems of (i) non-adiabatic propagation [14], which describes the effects of heat losses, (ii) the interaction of various modes of pulsating and spinning combustion [15,16], and (iii) the effect of a sequential reaction mechanism [17] to more realistically account for the chemical kinetics occurring in the problem. Finally, we have begun an investigation of the problem of filtration combustion, in which gas under high pressure is introduced into the porous powder mixture, to enhance the combustion process.

Supported in part by DOE grant DEFG02-87ER25027 and NSF grant DMS87-01543.

REFERENCES

1. A. G. Merzhanov, A. K. Filonenko, I. P. Borovinskaya, Dokl. Phys. Chem. 208 (1973), 122.
2. Yu. M. Maksimov, A. T. Pak, G. B. Lavrenchuk, Yu. S. Naibodorenko, A. G. Merzhanov, Comb. Expl. and Shock Waves 15 (1979), 415.
3. Yu. M. Maksimov, A. G. Merzhanov, A. T. Pak, M. N. Kuchkin, Comb. Expl. and Shock Waves 17 (1981), 393.
4. A. V. Dvoryankin, A. G. Strunina, A. G. Merzhanov, Comb. Expl. and Shock Waves 18 (1982), 134.
5. A. G. Strunina, A. V. Dvoryankin, A. G. Merzhanov, Comb. Expl. and Shock Waves 19 (1983), 158.
6. A. G. Merzhanov, Arch. Comb. 1 (1981), 23.
7. J. B. Holt, Mat. Res. Soc. Bull. 12 (1982), 60.
8. B. J. Matkowsky, G. I. Sivashinsky, SIAM J. Appl. Math. 35 (1978), 465.
9. A. Bayliss and B. J. Matkowsky, J. Comp. Phys., 71 (1987), 147.
10. A. Bayliss, D. Gottlieb, B. J. Matkowsky and M. Minkoff, J. Comp Phys. 81 (1989), 421.
11. A. Bayliss, B. J. Matkowsky and M. Minkoff, SIAM J. Appl. Math., to appear.

12. M. Garbey, H. G. Kaper, G. K. Leaf and B. J. Matkowsky, submitted.
13. S. B. Margolis, H. G. Kaper, G. K. Leaf and B. J. Matkowsky, Comb. Sci. and Tech., 43 (1985), 127.
14. H. G. Kaper, G. K. Leaf, S. B. Margolis and B. J. Matkowsky, Comb. Sci. Tech. 53 (1987), 289.
15. M. R. Booty, S. B. Margolis and B. J. Matkowsky, SIAM J. Appl. Math., 46 (1986), 801.
16. S. B. Margolis, B. J. Matkowsky, SIAM J. Appl. Math., 48 (1988), 828.
17. M. R. Booty, J. B. Holt and B. J. Matkowsky, submitted.

Figure Captions

- 1a. θ at $z = 0.25$, $\mu = 4.426$, steady solution branch.
- 1b. θ at $z = 0.5$, $\mu = 4.294$, singly periodic solution branch.
- 1c. θ at $z = 0.2$, $\mu = 4.454$, singly periodic solution branch.
- 1d. θ at $z = 0.026$, $\mu = 4.466$, doubly periodic solution branch.
- 1e. θ at $z = 0.026$, $\mu = 4.51918$, doubly periodic solution branch.
- 1f. θ at $z = 0.026$, $\mu = 4.51918$, singly periodic solution branch.
- 2. Spatial profiles of θ at four different times, $\mu = 4.51918$, singly periodic solution branch.
- 3. Location of the melting surface at different times, standing wave solution; $\mu = 4.20$.
- 4. $\theta(t, z = 0.4, \psi)$ at angles $\psi = 0, \pi/2, \pi, 3\pi/2$. Standing wave solution; $\mu = 4.16$.
- 5a. $\theta(t, z, \psi)$ at $t = 30.5$. Standing wave solution; $\mu = 4.16$.
- 5b. $\theta(t, z, \psi)$ at $t = 32.25$. Standing wave solution; $\mu = 4.16$.
- 6. Location of the melting surface at different times, spinning wave solution; $\mu = 4.11$.

Key Words: combustion synthesis, nonlinear stability, quasi-periodic, bifurcation

NEW MODES OF QUASI-PERIODIC BURNING IN COMBUSTION SYNTHESIS

Stephen B. Margolis,[†] Bernard J. Matkowsky[‡] and Michael R. Booty[§]

[†]Combustion Research Facility
Sandia National Laboratories, Livermore, California 94551 USA

[‡]Department of Engineering Sciences and Applied Mathematics
Northwestern University, Evanston, Illinois 60201 USA

[§]Department of Mathematics
Southern Methodist University, Dallas, Texas 75275 USA

ABSTRACT

In combustion synthesis, the steady, planar burning of a propagating reaction front is unstable to time-periodic modes of burning for sufficiently large values of the activation energy and the melting temperature. At critical values of the radius of a long cylindrical sample, *two* sets of modes, which correspond to pulsating and spinning combustion waves, are neutrally stable simultaneously. A nonlinear stability analysis in the neighborhood of such a radius then leads to the prediction of additional stable solution branches that correspond to new quasi-periodic modes of gasless combustion.

§1. Introduction

It is now well known from both experimental and theoretical studies that the propagation of reaction fronts in condensed phase combustion can exhibit a rich variety of nonsteady bifurcation phenomena. The physical process is often referred to as *self-propagating high-temperature synthesis (SHS)*, since it consists of the propagation of a highly exothermic chemical reaction through a mixture of finely ground metal powders to form an alloy product. Nonuniform reaction zone temperatures, which occur in nonsteady, nonplanar modes of combustion, may result in corresponding nonuniformities in the synthesized product. Thus, a knowledge of the various types of stable nonsteady, nonplanar modes which can exist may have important practical applications.

In a cylindrical geometry (Fig. 1), for example, there have been numerous experimental documentations of spinning and so-called "multiple-point" modes of propagation.¹⁻³ In the case of spin combustion, a spiraling motion of a nonplanar front occurs, and one or more luminous points are observed to move in a helical fashion along the surface of the cylindrical sample. (A special case of spin combustion is sometimes referred to as "self-oscillatory combustion," in which a front with

no angular dependence propagates in a pulsating fashion). In multiple-point combustion, one or more luminous spots are observed to appear, disappear, and reappear on the sample surface. However, these two categories are very broad, and the analysis presented in the present study indicates that mode interactions within and between these two categories can produce a variety of complex quasi-periodic behavior.

The model, which we have employed in several studies⁴⁻⁶ to analyze the transition to nonsteady condensed combustion, is based on the realistic assumptions that the activation energy of the intermetallic reaction is large and that at least one component of the mixture melts during the reaction process.^{7,8} For sufficiently large activation energies, the reaction zone collapses to a thin sheet which separates the unburned mixture from the burned product, and the solutions on each side of the front are related by a nonlinear jump condition which depends on local conditions. This jump condition also depends on a modified activation energy parameter Δ and a melting parameter M . The latter ranges from zero in the limit that the melting temperature is sufficiently lower than the adiabatic reaction temperature, to unity in the limit that the melting temperature approaches the adiabatic reaction temperature and chemical reaction prior to melting is negligible. Stability of the steadily propagating planar solution is lost when the parameter ratio $2\Xi = \Delta/(1 - M)$ becomes sufficiently large, and thus the effect of nonzero M is to make the neutral stability threshold more accessible. This result is consistent with experimental results which indicate that a decrease in the adiabatic reaction temperature (which increases Δ) by means of dilution or a decrease in preheating, or an increase in the amount of inert but meltable binding material, can effect a transition to nonsteady combustion. However, the nature of the bifurcation depends crucially on Δ and M separately.

Previous analyses which have sought to determine the nature of combustion synthesis above the stability threshold have been one-dimensional,⁹⁻¹¹ and except for the last of these, have also neglected melting, which is equivalent to setting $M = 0$ in the models discussed above. Owing to the nonmonotonicity in the neutral stability boundary for the multidimensional problem (Fig. 2), the basic solution is in general more unstable to nonplanar disturbances. Thus, for sufficiently large sample radii, stability of the steady, planar mode would first be lost to a nonsteady, nonplanar mode of propagation. In [4], a bifurcation analysis in a cylindrical geometry was performed for values of the sample radius such that a simple eigenvalue of the linear stability problem occurred at the minimum of the neutral stability boundary at $\Xi = \Xi_0 = 4$. Employing Ξ as the bifurcation parameter, three solutions were shown to bifurcate from the basic solution at that point, corresponding to a clockwise spinning mode, a counterclockwise spinning mode, and a standing (multiple-point) mode formed from a superposition of the other two modes. For the special case of a zero angular wavenumber these three solutions collapse to a single "radial" (self-oscillatory) mode. However, it was found that only for a realistic range of M greater than zero were either the spinning or standing wave solution branches stable. Consequently, a local bifurcation analysis which neglected melting was not able to describe the observed phenomena.

In the present work we summarize the results of two recent studies^{5,6} in which we consider the possibility of secondary and higher-order bifurcations arising from various mode interactions. In particular, we analyze the the problem in the neighborhood of a multiple bifurcation point. This

occurs for values of the sample dimensions such that two sets of modes correspond to the same value of Ξ ; one set lies to the left and the other set to the right of the minimum in the neutral stability boundary (Fig. 2). By varying the sample radius, we "split" the multiple bifurcation point into two simple primary bifurcation points and a number of secondary, tertiary and quaternary bifurcation points. The resulting bifurcation diagrams thus display considerable structure and predict new stable quasi-periodic modes of propagation.

§2. The Mathematical Model

We now consider a specific problem; namely the propagation of a reaction front through a solid combustible mixture contained in a long cylindrical channel of radius \bar{R} with insulated boundaries (Fig. 1). To describe this process we employ an asymptotic model valid for either homogeneous or heterogeneous reaction rate laws.^{7,8} This model assumes a large, but finite, activation energy for a one-step Arrhenius chemical reaction in which two finely ground metallic powders combine to form an alloy product. The model accounts for melting of the limiting component of the reaction at temperatures near the adiabatic flame temperature, although the final product is assumed to be solid at the adiabatic flame temperature.

For large activation energy, the reaction zone becomes a thin sheet whose location in nondimensional cylindrical (r, ψ, z) coordinates is given by $z = \Phi(r, \psi, t)$, where Φ is to be determined as a function of its arguments. Then, introducing the moving coordinate system

$$r = r, \quad \psi = \psi, \quad z = z - \Phi(r, \psi, t), \quad (1)$$

the asymptotic model for Φ and the nondimensional temperature Θ is given by

$$\frac{\partial \Theta}{\partial t} - \frac{\partial \Phi}{\partial t} \frac{\partial \Theta}{\partial z} = \nabla^2 \Theta - \frac{\partial \Phi}{\partial t} \delta(z) \quad (2)$$

$$\frac{\partial \Phi}{\partial t} = - \left[1 + \left(\frac{\partial \Phi}{\partial r} \right)^2 + \frac{1}{r^2} \left(\frac{\partial \Phi}{\partial \psi} \right)^2 \right]^{1/2} \left\{ \frac{\exp \{ \Delta [\Theta(r, \psi, z = 0, t) - 1] \} - M}{1 - M} \right\}^{1/2} \quad (3)$$

$$\Theta = 0 \text{ at } z = -\infty, \quad \Theta = 1 \text{ at } z = +\infty \quad (4)$$

$$\frac{\partial \Theta}{\partial r} - \frac{\partial \Phi}{\partial r} \frac{\partial \Theta}{\partial z} = 0 \text{ at } r = R, \quad (5)$$

where $\delta(z)$ is the Dirac delta function and ∇^2 is the Laplacian in the moving coordinate system. The (large) modified activation parameter Δ is defined in terms of the dimensional activation energy \bar{E} , unburned temperature \bar{T}_u , adiabatic burned temperature \bar{T}_a , and the gas constant R_g as

$$\Delta = (\bar{E}/\bar{R}_g \bar{T}_a)(1 - \bar{T}_u/\bar{T}_a). \quad (6)$$

The melting parameter M is defined in terms of the dimensional melting temperature $\bar{T}_m < \bar{T}_a$, the ratio $\gamma > 0$ of the heat of fusion of the melting reactant to the heat of reaction of the (solid) product relative to the (solid) unburned powder, and the factor α by which the reaction rate jumps upon melting, as

$$M = \left(1 - \frac{1 + \gamma}{\alpha} \right) \exp \left[\frac{\bar{E}}{\bar{R}_g \bar{T}_a} \left(\frac{\bar{T}_m}{\bar{T}_a} - 1 \right) \right], \quad (7)$$

144

and is less than unity since $\tilde{T}_m < \tilde{T}_a$. In the heterogeneous model,⁸ it was assumed that no chemical reaction occurred prior to melting and thus $\alpha = \infty$. The special case $\alpha = 1$, $\gamma = 0$ corresponds to the limiting case ($M = 0$) of no melting; i.e., there is no change in the reaction rate coefficient and the heat of fusion is zero. In this limit, as well as in the limit $\tilde{T}_m \ll \tilde{T}_a$, the present model collapses to a single-phase model with the single parameter Δ .

§3. The Basic Solution and its Linear Stability

A one-dimensional, time-independent solution of Eqs. (2) - (5), which exists for all values of the parameters Δ and M , and which we refer to as the basic solution, is

$$\Phi^0(t) = -t, \quad \Theta^0(z) = \begin{cases} e^z, & z < 0 \\ 1, & z > 0. \end{cases} \quad (8)$$

Thus, in nondimensional units, the basic solution describes a planar reaction front which moves normal to itself with velocity $d\Phi^0/dt = -1$.

We now consider the linear stability of the basic solution. We introduce the perturbation quantities

$$\phi(r, \psi, t) = \Phi - \Phi^0(t), \quad \theta(r, \psi, z, t) = \Theta - \Theta^0(z) - \phi \frac{d\Theta^0}{dz}, \quad (9)$$

and find that the only solutions of the linear stability problem which can render the basic solution unstable are multiples of the modes

$$\phi \sim J_n(k_{n,m} r) e^{i(\omega t \pm n\psi)}, \quad (10)$$

where the discrete radial wavenumber $k_{n,m}$ is the m th root of $J'_n(kR) = 0$ and J_n is the Bessel function of the first kind of order n . We note that the values of the admissible wavenumbers $k_{n,m}$ thus depend on the radius R of the channel. The dispersion relation $\omega(k)$, $k = k_{n,m}$, is determined by

$$4(i\omega)^3 - (i\omega)^2(1 - 4\Xi - \Xi^2 + 4k^2) - (i\omega)\Xi(1 - 4k^2) + \Xi^2 k^2 = 0, \quad (11)$$

where

$$\Xi = \Delta / [2(1 - M)]. \quad (12)$$

The basic solution (8) is unstable (stable) if $\text{Re}(i\omega) > (<) 0$. On the neutral stability boundary, $\text{Re}(i\omega) = 0$, and Eq. (11) possesses a nontrivial solution which corresponds to a time-periodic motion. On this boundary (Fig. 2),

$$\Xi^2(1 - 4k^2) - 4\Xi(1 - 3k^2) - (1 + 4k^2)^2 = 0, \quad \omega^2 = \Xi(1 + 4k^2)/4. \quad (13)$$

Another solution, $\omega = k = 0$, $\theta = d\Theta^0/dz$, corresponds to a linear translation of the basic solution. We note from Eq. (13) that the neutral stability boundary depends only on the ratio Ξ of Δ to $2(1 - M)$. However, in the bifurcation analysis which follows, each of the two parameters Δ and M enters separately.

For a given channel radius R , there exists a discrete set of admissible wavenumbers $k_{n,m}$ determined from the roots of $J'_n = 0$. Consequently, from Eq. (13), there exists a discrete set of eigenvalues $\Xi_{n,m}$ of the linear stability problem, the smallest of which is the critical value Ξ_0 at which the basic solution loses stability. In general, Ξ_0 will be a simple eigenvalue (i.e., only a unique member of the set $\Xi_{n,m}$ is identified as the smallest eigenvalue), which was the case considered in [4]. However, for certain values R_0 of the channel radius, Ξ_0 is a double eigenvalue. That is, two members of the set $\Xi_{n,m}$ are equal and smaller than all the other members of that set, as illustrated in Fig. 2. As we vary the channel radius, the double eigenvalue "splits" into two simple eigenvalues, resulting in a much more complex bifurcation diagram. However, we note that at least for nonzero angular wavenumber n , a set of modes is associated with each wavenumber $k_{n,m}$. These modes correspond to clockwise spinning, counterclockwise spinning, and standing combustion waves, as discussed below.

We denote the first set of modes to the left of the minimum in the stability boundary by the subscript "1" with mode numbers n_1 , m_1 , radial wavenumber k_{n_1,m_1} , and frequency ω_1 . Similarly, the first set of modes to the right of the minimum is denoted by the subscript "2" with mode numbers n_2 , m_2 , radial wavenumber k_{n_2,m_2} , and frequency ω_2 . As discussed above, we consider the case in which Ξ_0 is a double eigenvalue. We note that to insure that Ξ_0 is indeed the smallest critical value of the parameter Ξ , there can be no other mode numbers (n_j, m_j) such that $k_{n_1,m_1} < k_{n,m} < k_{n_2,m_2}$. The ordering of the mode numbers (n_i, m_i) in the direction of increasing wavenumber $k_{n,m}$, is (0,1), (1,1), (2,1), (0,2), (3,1), (4,1), (1,2), (5,1), (2,2), (0,3), (6,1), (3,2), (1,3), (7,1), (4,2), (8,1), (2,3), Thus, by varying the radius of the channel, we can arrange for any two sets of adjacent modes to lie on opposite sides of the minimum in the neutral stability boundary (Fig. 2).

§4. The Bifurcation Branches and Their Linear Stability

We employ a perturbation analysis in the neighborhood of $\Xi = \Xi_0 = \Delta_0/[2(1-M)]$ by introducing the scaled bifurcation parameter σ and the splitting parameter μ , according to

$$\Delta \sim \Delta_0(1 - \sigma\epsilon^2 - \dots), \quad R \sim R_0(1 - \mu\epsilon^2 - \dots), \quad (14)$$

where R_0 is a value of the radius such that Ξ_0 is a double eigenvalue. The value of the small expansion parameter ϵ is defined by specifying σ and/or μ . Here, we consider the case in which the splitting parameter μ is nonzero. Setting $\mu^2 = 1$ without loss of generality, ϵ is then defined as

$$\epsilon = \sqrt{R - R_0/R_0}. \quad (15)$$

Consequently, the bifurcation parameter σ is related to Δ according to $\sigma \sim \epsilon^{-2}(\Delta - \Delta_0)$.

We now seek solutions for the perturbation quantities ϕ and θ in the form of power series expansions in ϵ . The result of this analysis⁵ is that, to a first approximation, the solution for the reaction front $\Phi(r, \psi, t)$ has the long time behavior

$$\begin{aligned} \Phi(r, \psi, t) \sim & -t - \epsilon^2 b_1 (|A_{1,1}|^2 + |A_{1,2}|^2) - \epsilon^2 b_2 (|A_{2,1}|^2 + |A_{2,2}|^2) t \\ & + \epsilon \left[|A_{1,1}| e^{i(\omega_1 t + \epsilon^2 \varphi_{1,1} t + n_1 \psi)} + |A_{1,2}| e^{i(\omega_1 t + \epsilon^2 \varphi_{1,2} t - n_1 \psi)} \right] J_{n_1}(k_{n_1,m_1} r) + \text{c.c.} \\ & + \epsilon \left[|A_{2,1}| e^{i(\omega_2 t + \epsilon^2 \varphi_{2,1} t + n_2 \psi)} + |A_{2,2}| e^{i(\omega_2 t + \epsilon^2 \varphi_{2,2} t - n_2 \psi)} \right] J_{n_2}(k_{n_2,m_2} r) + \text{c.c.}, \end{aligned} \quad (16)$$

where "c.c." denotes the complex conjugate. Equations for the coefficients b_1, b_2 and the complex amplitudes $A_{i,j} e^{i\epsilon^2 \varphi_{i,j}}$ (the latter are complicated functions of the bifurcation and splitting parameters), are obtained from solvability conditions at $O(\epsilon^2)$ and at $O(\epsilon^3)$, respectively. In particular, the magnitudes of the amplitudes $|A_{i,j}|$ are determined as solutions of

$$\frac{d|A_{1,1}|}{d\tau} + (c_1\sigma + c_2\mu)|A_{1,1}| + |A_{1,1}|(c_3|A_{1,1}|^2 + c_4|A_{1,2}|^2 + c_5|A_{2,1}|^2 + c_6|A_{2,2}|^2) = 0, \quad (17)$$

$$\frac{d|A_{1,2}|}{d\tau} + (c_1\sigma + c_2\mu)|A_{1,2}| + |A_{1,2}|(c_3|A_{1,2}|^2 + c_4|A_{1,1}|^2 + c_5|A_{2,2}|^2 + c_6|A_{2,1}|^2) = 0, \quad (18)$$

$$\frac{d|A_{2,1}|}{d\tau} + (d_1\sigma + d_2\mu)|A_{2,1}| + |A_{2,1}|(d_3|A_{2,1}|^2 + d_4|A_{2,2}|^2 + d_5|A_{1,1}|^2 + d_6|A_{1,2}|^2) = 0, \quad (19)$$

$$\frac{d|A_{2,2}|}{d\tau} + (d_1\sigma + d_2\mu)|A_{2,2}| + |A_{2,2}|(d_3|A_{2,2}|^2 + d_4|A_{2,1}|^2 + d_5|A_{1,2}|^2 + d_6|A_{1,1}|^2) = 0, \quad (20)$$

where the slow time $\tau = \epsilon^2 t$, and the coefficients c_k, d_k are functions of the parameters Δ_0, M, R_0 and the mode numbers n_1, m_1, n_2, m_2 . The conditions (17) - (20) determine the number and stability of the bifurcation branches in the neighborhood of the double eigenvalue Ξ_0 . In particular, counting the basic solution $A_{1,1} = A_{1,2} = A_{2,1} = A_{2,2} = 0$, there exist up to 16 nontrivial *steady* solutions of the amplitude equations for a given set of parameter values. Solutions Ia,b,c,d have one nonzero amplitude, solutions IIa,b,c,d,e,f have two nonzero amplitudes, solutions IIIa,b,c,d have three nonzero amplitudes, and solution IV has all four amplitudes nonzero. We remark that the type I solutions represent time-periodic spinning modes of combustion, whereas solutions IIa ($|A_{1,1}| = |A_{1,2}| \neq 0$) and IIb ($|A_{2,1}| = |A_{2,2}| \neq 0$) represent time-periodic standing (pulsating) modes. The remaining solutions represent various quasi-periodic modes of propagation, since they correspond to the superposition of two or more spinning waves with incommensurate frequencies ω_1 and ω_2 . We also note that the phases $\varphi_{i,j}^0$ are perturbations of the spinning or pulsation frequency ω_i through the slow time $\epsilon^2 t$. The linear stability of these various solutions are easily obtained from a linear stability analysis of Eqs. (17) - (20).

We may now obtain bifurcation diagrams by plotting the amplitude of the perturbation from the basic solution as a function of the scaled bifurcation parameter σ . Since the splitting parameter μ is nonzero, the double eigenvalue Ξ_0 is split into two simple eigenvalues, and the single multiple bifurcation point Ξ_0 splits into two primary and a number of secondary, tertiary and quaternary bifurcation points. Thus, as we vary Ξ in a neighborhood of Ξ_0 by varying σ , we predict transitions among the various modes of propagation. The periodic solutions Ia, Ib, IIa (frequency $\approx \omega_1$) emanate from one of the primary bifurcation points, and the periodic solutions Ic, Id, IIb (frequency $\approx \omega_2$) emanate from the other. For $\mu > 0$, corresponding to a radius R larger than R_0 , the basic solution first loses stability to one or more of the primary modes Ic, Id, IIb at a value of σ which is less than zero (the other primary branches emanate from a positive value of σ). Similarly, for $\mu < 0$, corresponding to $R < R_0$, the basic solution first loses stability to one or more of the primary modes Ia, Ib, IIa. In Fig. 3 we exhibit a representative bifurcation diagram for particular values of M and adjacent mode numbers (n_1, m_1) and (n_2, m_2) . It indicates considerable variety and complexity, predicting various cascades of bifurcations, exchanges of stability, and mode-jumping phenomena as we vary the bifurcation parameter σ .

The amplitude equations (17) - (20) also admit *nonsteady* solutions.⁶ In particular, since the amplitude equations are differential equations with respect to the slow time τ , there exist time-periodic solutions in addition to the steady solutions discussed above. These additional solutions, which, from Eq. (16) represent new modes of quasi-periodic combustion, appear as closed, stable branches when the melting parameter M is above a critical value M_c . This is shown by the dotted curves in Fig. 4, which differs from Fig. 3 only in the value of M , which was less than M_c in that figure. As M approaches M_c from above, the two (Hopf) bifurcation points on solutions IIIc and IIIId, between which these solutions are unstable, coalesce into a single degenerate point. For M in a neighborhood of M_c , we employ a perturbation method to show that these new solution branches appear as ellipses on IIIc and IIIId. Alternatively, we have also determined these branches from a numerical integration of the amplitude equations for arbitrary values of $M > M_c$.

§5. Concluding Remarks

The analysis that we have employed has shown that many different periodic and quasi-periodic modes of combustion synthesis are possible in the parameter regime for which steady planar burning is unstable. In this regime, the time-averaged propagation velocity is readily obtained from Eq. (16) as

$$\lim_{T \rightarrow \infty} \frac{1}{T} \int_0^T \frac{\partial \Phi}{\partial t} dt = -1 - \epsilon^2 b_1 \left(\overline{|A_{1,1}|^2} + \overline{|A_{1,2}|^2} \right) - \epsilon^2 b_2 \left(\overline{|A_{2,1}|^2} + \overline{|A_{2,2}|^2} \right) + o(\epsilon^2), \quad (21)$$

where $\overline{|A_{i,j}|}$ denotes the time-averaged value of $|A_{i,j}|$. Thus, whether the nonsteady, nonplanar modes propagate slower or faster than the steadily propagating planar solution depends on the coefficients b_j , on the amplitudes $|A_{i,j}|$, and on the mode numbers n_j and m_j . Nonsteady combustion tends to decrease the propagation speed; however, the wrinkling of the reaction front can overcome the slowing effects of nonsteady combustion if the spatial wavenumber is sufficiently large.^{8,12} In the regimes where the primary branches are supercritical (i.e., bend to the right), the propagation speed is usually less ($b_1 < 0$, $b_2 < 0$) than that of the basic solution.

Acknowledgement. This work was supported by the Applied Mathematical Sciences Research Program, Office of Energy Research, U. S. Department of Energy.

REFERENCES

1. A. G. Merzhanov, A. K. Filonenko and I. P. Borovinskaya (1973), *New phenomena in combustion of condensed systems*, Dokl. Phys. Chem. **208**, pp. 122-125.
2. A. V. Dvoryankin, A. G. Strunina and A. G. Merzhanov (1982), *Trends in the spin combustion of thermites*, Combustion, Explosion and Shock Waves **18**, pp. 134-139.
3. A. G. Strunina, A. V. Dvoryankin and A. G. Merzhanov (1983), *Unstable regimes of thermite system combustion*, Combustion, Explosion and Shock Waves **19**, pp. 158-163.
4. S. B. Margolis, H. G. Kaper, G. K. Leaf and B. J. Matkowsky (1985), *Bifurcation of pulsating and spinning reaction fronts in condensed two-phase combustion*, Combust. Sci. Technol. **43**, pp. 127-165.

5. M. R. Booty, S. B. Margolis and B. J. Matkowsky (1986), *Interaction of pulsating and spinning waves in condensed phase combustion*, SIAM J. Appl. Math. **46**, pp. 801 - 843.
6. S. B. Margolis and B. J. Matkowsky (1988), *New modes of quasi-periodic combustion near a degenerate Hopf bifurcation point*, SIAM J. Appl. Math. **48**, pp. 828-853.
7. S. B. Margolis (1983), *An asymptotic theory of condensed two-phase flame propagation*, SIAM J. Appl. Math. **43**, pp. 351-369.
8. S. B. Margolis (1985), *An asymptotic theory of heterogeneous condensed combustion*, Combust. Sci. Technol. **43**, pp. 197-215.
9. K. G. Shkadinsky, B. I. Khaikin and A. G. Merzhanov (1971), *Propagation of a pulsating exothermic reaction in the condensed phase*, Combustion, Explosion and Shock Waves **7**, pp. 15-22.
10. B. J. Matkowsky and G. I. Sivashinsky (1978), *Propagation of a pulsating reaction front in solid fuel combustion*, SIAM J. Appl. Math. **35**, pp. 465-478.
11. A. Bayliss and B. J. Matkowsky (1987), *Fronts, relaxation oscillations, and period doubling in solid fuel combustion*, J. Comp. Phys. **71**, pp. 147-168.
12. S. B. Margolis and B. J. Matkowsky (1985), *Flame propagation in channels: Secondary bifurcation to quasi-periodic pulsations*, SIAM J. Appl. Math. **45**, pp. 93-129.

FIGURE CAPTIONS

1. Condensed phase combustion in a long cylindrical channel. In the limit of large activation energy, the reaction zone, which contains the isotherm on which melting occurs, collapses to an infinitesimally thin sheet.
2. The neutral stability boundary. The sets of discrete modes denoted by square markers are for a case ($R = R_0$) in which $\Xi = \Xi_0$ is a double eigenvalue of the linear stability problem. When the channel radius R is perturbed from R_0 , the double eigenvalue Ξ_0 splits into two simple eigenvalues $\hat{\Xi}_1$ and $\hat{\Xi}_2$, as indicated by the circular markers.
3. Bifurcation diagram near a double eigenvalue for a given pair of mode interactions and a value of the melting parameter $M < M_c$. Solid (dashed) curves denote stable (unstable) solutions. The labels refer to the various steady solutions of the amplitude equations (17) - (20).
4. Same as Fig. 3, but with a value of the melting parameter $M > M_c$. The solid dotted curves denote stable periodic solutions of the amplitude equations (17) - (20).

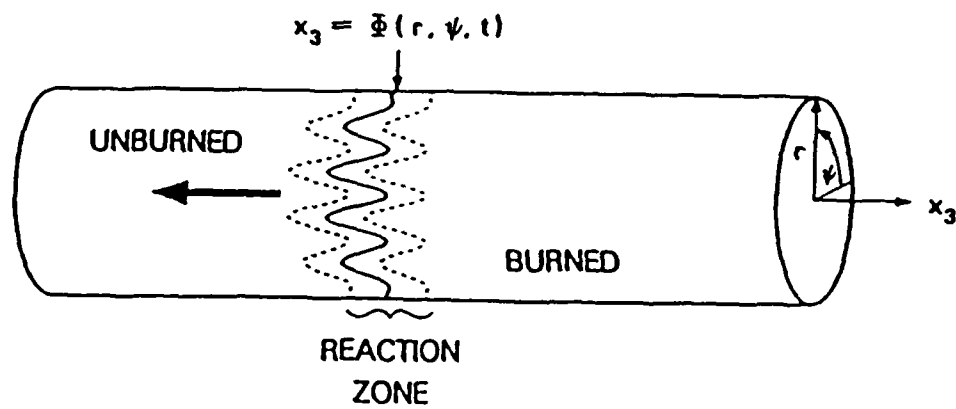


Figure 1

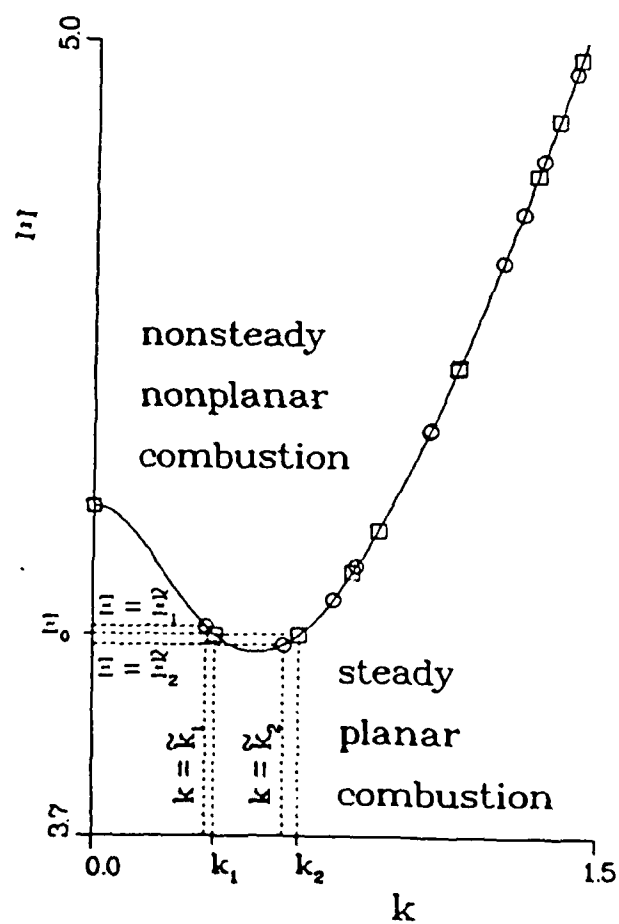


Figure 2

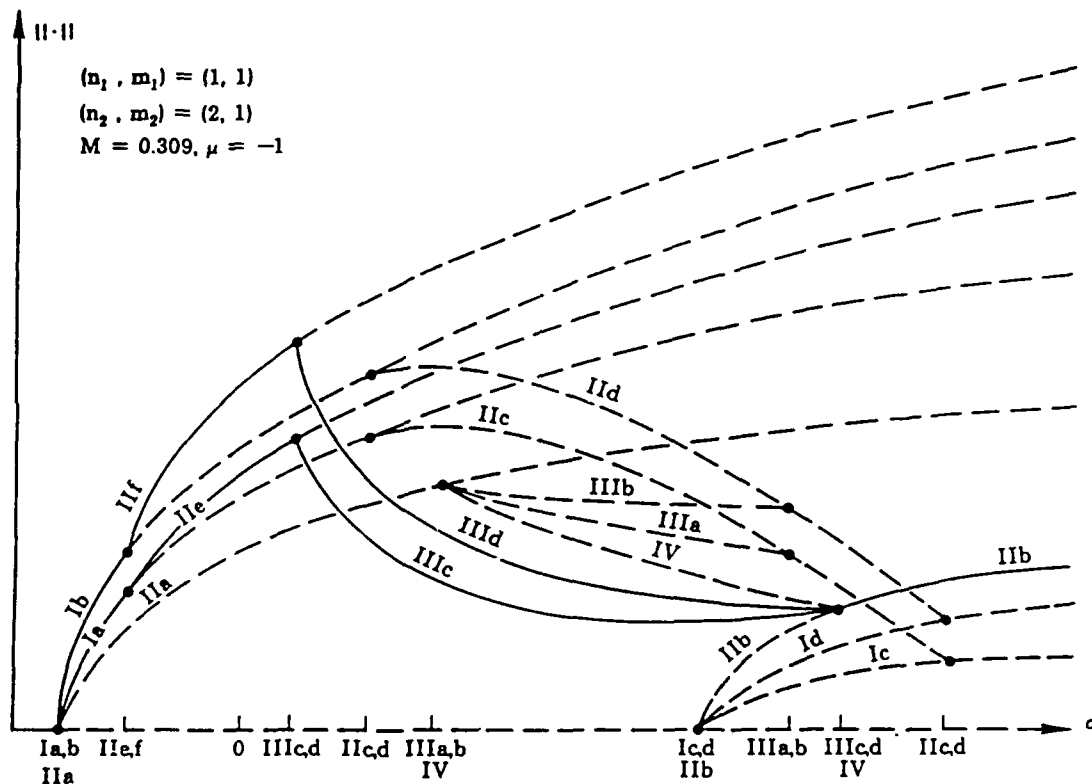


Figure 3

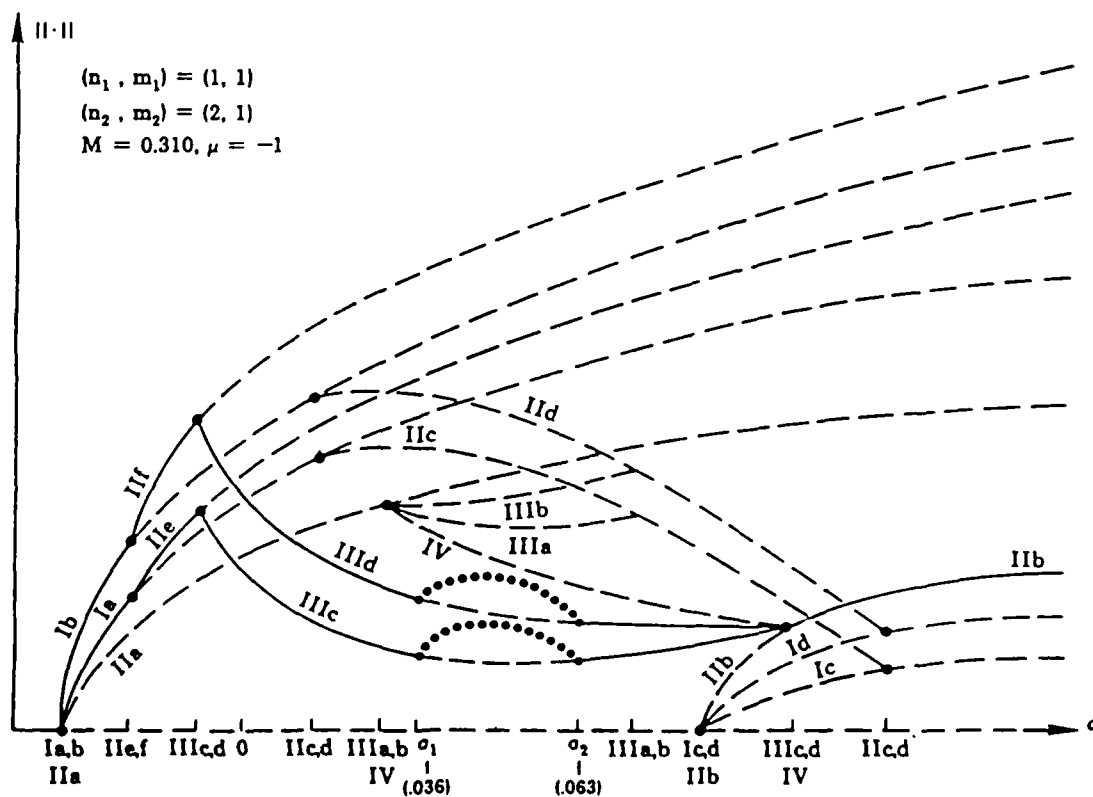


Figure 4

Modeling of SHS Operations

V. Hlavacek, P. Dimitriou, J. Degreve, and J. Scholtz

Chemical Engineering Department

State University of New York at Buffalo

Amherst, NY 14260, USA

Abstract

SHS processes are described by transport equations whose solution features very thin reaction boundary layers. A two dimensional regridding algorithm was employed which makes it feasible to perform numerical solutions.

Key words : Condensed phase combustion, adaptive grid.

1. Introduction

Advanced ceramic materials are a relatively new class of high performance materials with significant potential for future economic impact. Because of their special properties, advanced ceramic materials are expected to be used increasingly in a number of high-performance commercial applications ranging from heat and wear resistant parts to electronic and optical devices.

Several methods of manufacturing of ceramic materials have been developed. This paper attempts to analyze two important classes of methods:

- (i) preparation by a direct combustion reaction (solid-solid or solid-gas combustion), and
- (ii) preparation of oxide ceramic powders in a hydrogen-oxygen flame.

Governing equations describing each process are developed and ways of simulation of these models described. Since both methods of synthesis take advantage of strongly exothermic processes a sophisticated mathematical software must be used to cope with occurrence of steep gradients and instabilities.

2. Modeling of SHS Operations

Combustion in condensed systems is an efficient method of synthesis of many high performance ceramic materials such as carbides, borides, nitrides, silicides, etc [1,2,3,4,5,6,7]. The process utilizes the heat released by an exothermic reaction between the precursor components. After ignition of the exothermic reaction by an energy source with a short term service, a reaction front forms which is self-sustaining and propagates throughout the unreacted sample as long as fresh material is available. This process, sometimes referred to as Self-Propagating High-Temperature Synthesis, is a unique technology for preparing advanced ceramic materials. Major advantages over conventional processes are: fast processing of the material, self-purification and generation of temperatures in excess of 2000°C so that an expensive furnace is not necessary [1]. Initiation of the chemical reaction is obtained by conductive heat exchange or by a flow of radiant energy [8].

The modeling of SHS operations involving reaction between two solids (solid-solid) or a solid and a gas (gas-solid) is based on the following assumptions:

- a. The heterogeneous system consisting of a mixture of two different powders or powder and reacting gas is treated as though it were homogeneous.
- b. A heterogeneous noncatalytic reaction occurs between the solid S and the gas G (or the solid M):



The reaction rate is represented by the following equation:

$$r_s = k f(p_s) p^v \quad (2)$$

and the temperature dependence of reaction rate constant is in the Arrhenius form:

$$k = k_0 \exp(-E/RT) \quad (3)$$

c. The mass diffusion and heat conduction processes are described in terms of Fick's and Fourier's law, respectively.

d. All physical properties (solid density, heat of reaction, diffusion coefficient, effective thermal conductivity and heat capacity) are assumed constant.

e. The porosity of the system remains constant.

f. The equation of state of the gas is described by the ideal gas law.

g. The gas flow in the permeable medium is governed by Darcy's law.

Based on the above assumptions, the modeling equations are as follows (see [9] for definition of symbols):

a. Mass balance in gas and solid phases :

$$\epsilon \frac{\partial \rho_g}{\partial t} = -\epsilon \nabla \cdot (\underline{u} \rho_g) - \mu r_s \quad (4)$$

$$(1-\epsilon) \frac{\partial \rho_s}{\partial t} = -r_s \quad (5)$$

where :
$$\mu = \frac{g M_g}{s M_s}$$

b. Energy balance:

$$\frac{\partial}{\partial t}(\rho C_p T) = -\epsilon \nabla \cdot (\underline{u} \rho_g C_p T) + \bar{\lambda} \nabla \cdot (\nabla T) + (-\Delta H) r_s \quad (6)$$

c. Momentum balance:

$$\underline{u} + k_f \nabla p = 0 \quad (7)$$

d. Equation of state:

$$p = \frac{\rho_g R T}{M_g} \quad (8)$$

In the case of solid-solid SHS reaction, equations (4), (7) and (8) are not considered and the porosity ϵ is taken to be zero.

The solution of these diffusion-reaction (solid-solid) and diffusion-convection-reaction (solid-gas) equations presents a real challenge. The difficulties associated with the numerical solution of SHS problems are due to the occurrence of a very thin reaction zone or propagating front. An accurate simulation will require the resolution of this boundary layer where very high temperature and concentration gradients are present [10]. Discretization therefore will generally result in a large set of algebraic equations. The size of this set can be reduced by the use of an adaptive mesh [11].

Some results of the numerical simulation of SHS operations based on the above model are presented in Figs. 1 to 3.

A typical one dimensional simulation of reaction front propagation in a solid-solid system is shown in Fig. 1. The system considered has an activation energy $E = 60,000$ cal/mol and a heat of reaction $(-\Delta H) = 170$ cal/g. The initial temperature T_0 is 720K (preheated system) and the adiabatic temperature rise ΔT_{ad} is 1280K. Temperature profiles at different times after ignition are shown. As can be seen, this system exhibits oscillatory combustion with peak temperatures higher than the adiabatic temperature [12]. The inverted triangles correspond to the adaptively placed positions of the moving mesh points used in the calculations.

The above system was also studied in two dimensions since a planar front can be unstable to perturbations and become corrugated. Isotherms on the lateral surface of a thin annulus are presented in Figs. 2a,b. The reaction front propagates in the form of a two head rotating wave. In Fig. 2b, the two heads a and b are shown after almost a full rotation. The maximum temperature in the hot spots is 2600K and this is higher than the highest temperature observed in the one dimensional calculations ($T_{max} = 2250K$).

The mesh point distribution, used in the simulation of the front propagation shown in Figs. 2a and 2b, is shown in Figs. 2c and 2d, respectively. Grid points concentrate around the two rotating heads where the steepest temperature and mass gradients occur.

Results of simulation for a gas-solid system characterized by $\mu = 0.3$, $E = 33,000$ cal/mol, $(-\Delta H) = 210$ cal/g, $\Delta T_{ad} = 1350$ K and being operated under very high pressure (≈ 1000 atm) are shown in Figs. 3a and 3b for temperature and gas density respectively.

References

1. W.L. Frankhouser, K. Brendley, M. Kieszek and S. Sullivan, "Gasless Combustion Synthesis of Refractory Compounds," Noyes Publications, N.J. (1985).
2. A.G. Merzhanov and I.P. Borovinskaia, "A New Class of Combustion Processes," *Combustion Science and Technology*, 10, 195 (1975).
3. A.G. Merzhanov, "A Method for Obtaining Refractory Compounds of Borides or Carbides," U.S.S.R. Patent 556,110 (April 1977).
4. A.G. Merzhanov, "Process for Preparing Titanium Carbide," U.S. Patent 4,161,512 (July 1979).
5. A.G. Merzhanov, "Method for Obtaining Borides of Transition Metals," U.S.S.R. Patent 465,544 (April 1973).
6. A.G. Merzhanov, "Method of Producing Refractory Carbides, Borides, Silicides, Sulfides and Nitrides of Metals of Groups IV, V and VI of the Periodic System," U.S. Patent 3,726,643 (April 1973).
7. Z. Munir, "Synthesis of High Temperature Materials by Self-Propagating Combustion Methods," *Ceramic Bulletin*, 67, 342 (1988).
8. A.G. Merzhanov and A.E. Averson, "The Present State of the Thermal Ignition Theory : an Invited Review," *Combustion and Flame*, 16, 89 (1971).
9. A.P. Aldushin, A.G. Merzhanov and B.S. Seplyarskii, "Theory of Filtration Combustion of Metals," *Fizika Goreniya i Vzryva*, 12, 323 (1976).
10. M. Smooke, "Use of Adaptive Methods in Premixed Combustion," *AIChE Journal*, 32, 1233 (1986).
11. J. Degreve, P. Dimitriou, J. Puszynski, V. Hlavacek, S. Valone and R. Behrens, "Use of 2D Adaptive Mesh in Simulation of Combustion Front Phenomena," *Computers and Chemical Engineering*, 11, 749 (1987).
12. J. Puszynski, J. Degreve and V. Hlavacek, "Modeling of Exothermic Solid-Solid Noncatalytic Reactions," *Industrial Engineering Chemical Research*, 26, 1424 (1987).

Figure captions

- Fig. 1 1D solid-solid oscillatory combustion.
Temperature profiles at four different times.
- Fig. 2 2D solid-solid spinning combustion.
a, b. Isotherms at two different times.
c, d. Adaptive grid.
- Fig.3 Gas-solid oscillatory combustion.
a. Temperature profiles at four different times.
b. Density profiles at four different times.

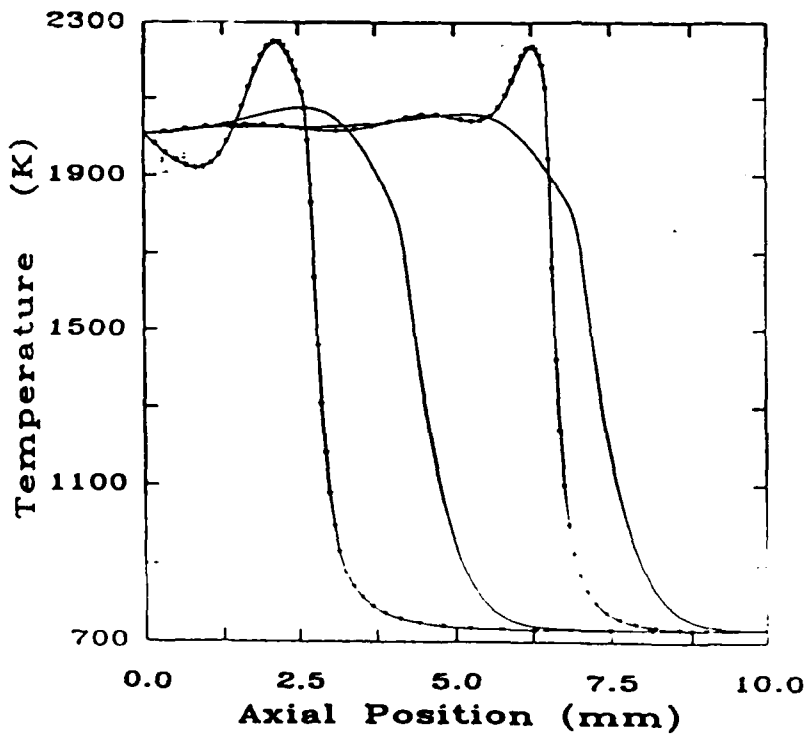


Fig. 1

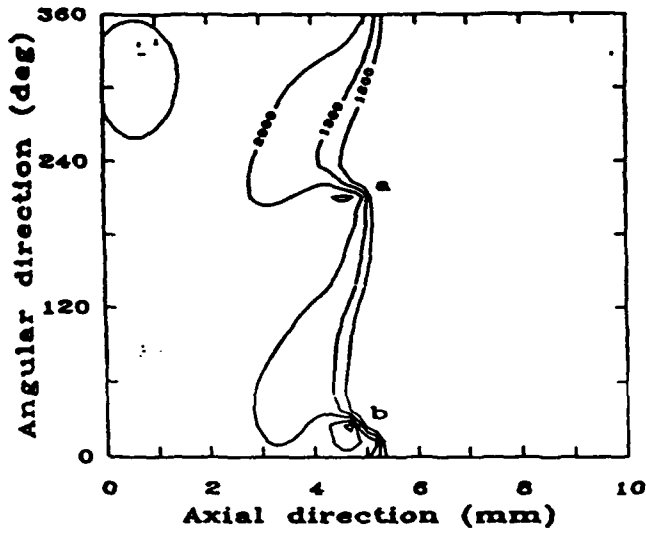


Fig. 2a

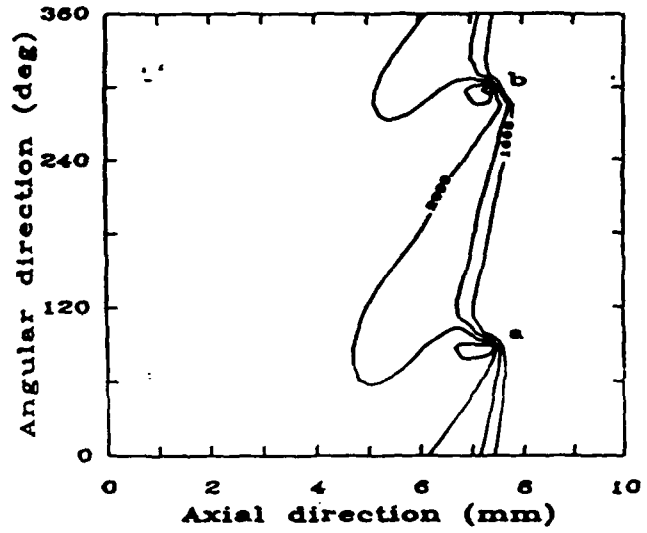


Fig. 2b

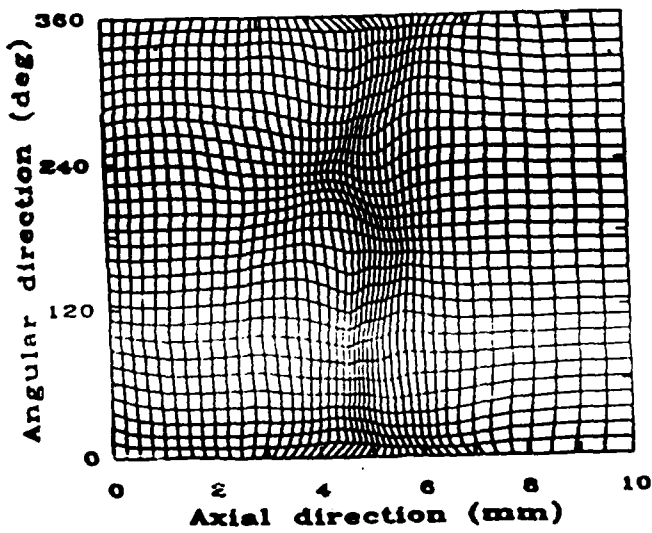


Fig. 2c

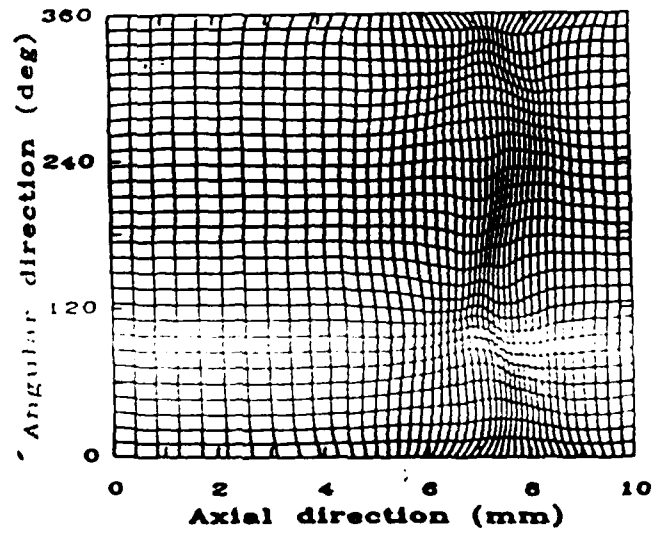


Fig. 2d

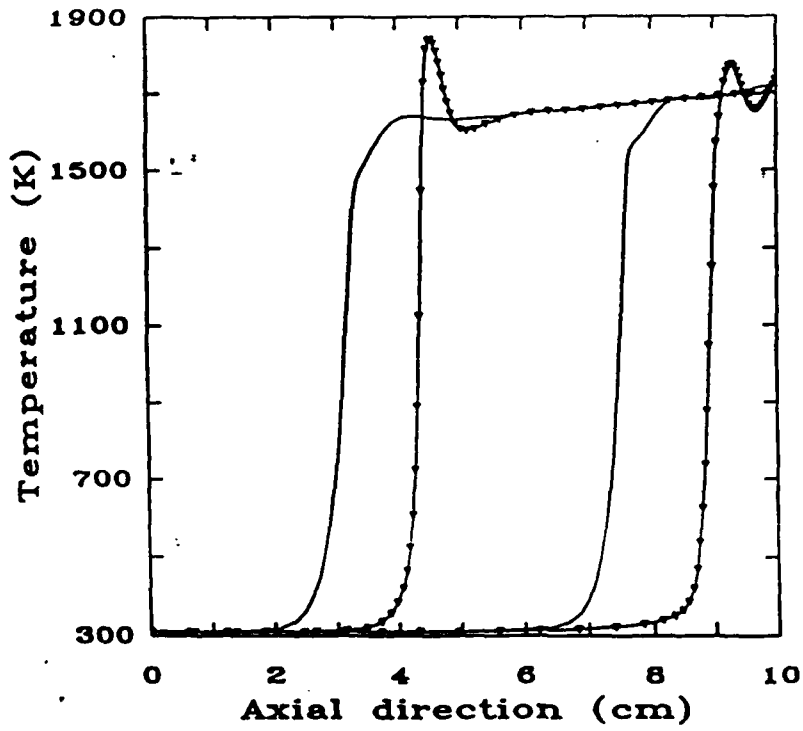


Fig. 3a

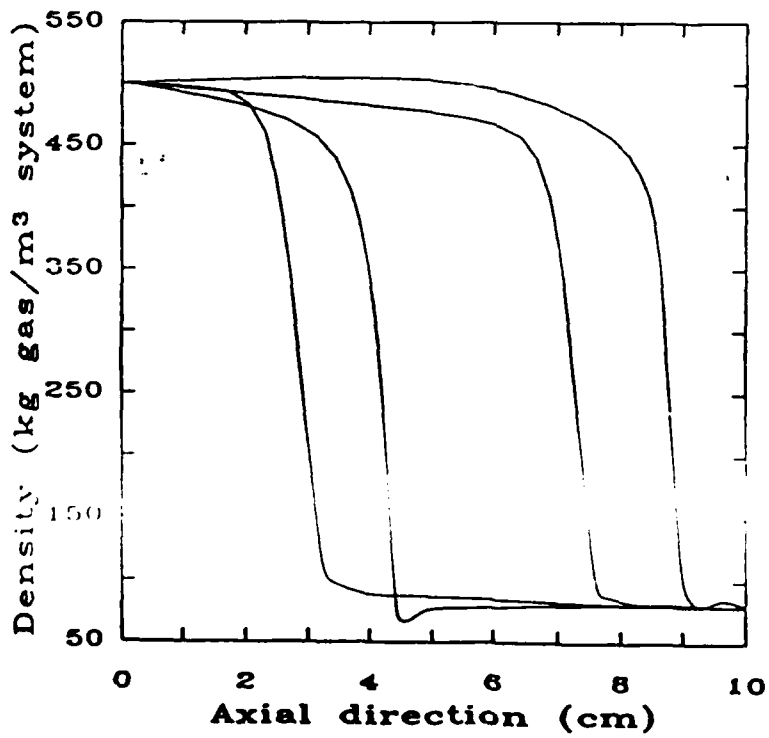


Fig. 3b

Combustion Theory for Sandwiches of Alloyable Materials*

Robert Armstrong
and
Mike Koszykowski
Combustion Research Facility
Sandia National Laboratories
Livermore, CA 94551, USA

Abstract

It is generally assumed in this work, as elsewhere, that the diffusion coefficient has an Arrhenius temperature dependence which allows a combustion wave propagated by thermal conduction, to develop similar to more conventional combustion systems. It is found that for realistic systems the problem must involve a three length scale analysis. Similar to the classic theory on premixed, gas-phase flames, the largest scale is identified with thermal conduction and a "reaction zone" scale proportional to the inverse of the diffusion activation energy is associated with a small length over which significant diffusion is possible. Unlike classic flame theory a still smaller scale is identified with the length over which diffusion takes place (i.e., the size of a typical domain of alloyable constituent). The flame speed is derived for a geometric configuration similar to a sandwich for a binary system using a singular perturbation analysis. The constituents are arrayed in alternating lamina stacked perpendicular to the flame propagation direction. We find that the flame speed is proportional to the inverse of the lamina thickness. This is the same as would be predicted by the "parabolic" law, often used to explain experimental data.

*This work supported by the U.S. Department of Energy, DOE, under Contract DE-AC04-76DP00789.

Introduction

This paper is principally concerned with the flame propagation induced by the exothermic interdiffusion of two substances (usually metals). Systems of this class are potentially important to the production of high quality ceramics and belong to the larger topic of combustion synthesis. In classical premixed, gas-phase flame theory an activation energy barrier prevents the cold gas from burning until a self-propagating thermal wave unleashes the exothermic chemistry. In this case, a fine powder mixture of exothermically alloyable substances interdiffuse, releasing heat, in a thin flame zone that propagates at a speed determined by the mechanics of the interdiffusion process. An activation energy barrier to interdiffusion keeps the differentiated particles of alloyable material distinct until the thermal wave raises the temperature to the point that interdiffusion can occur and contribute to its propagation. Though both of these systems can have aspects of diffusion and reaction, the gas flame derives its propagation mechanism from exothermic, locally-homogeneous chemical reaction, while the alloying reaction relies on mixing one constituent with another.

This phenomenon has been of intense interest in the Soviet Union for many years and is recently of greater concern in the West. Ceramics have desirable properties for use in combustion machinery, such as turbine blades in jet engines. However they are notoriously difficult to reform (by grinding, etc.) and thus it would be of considerable use to form the shape of the desired product first and then undergo a combustion process to the desired ceramic *in situ*¹. The final strength and other properties are dependent on the details of the interdiffusion process during the time that the flame passes². The flame thickness typical to alloying reactions is no larger than those found in gas flames and the materials participating in the flame do not lend themselves to sophisticated diagnostics such as lasers and thus theoretical investigations are indispensable.

There are a number of investigations that treat the powder media in a "mesoscopic" fashion deriving global behavior of the rate of conversion mechanics of reactants by simplifying the microscopic geometry of the powder.^{3,4} Aldushin and coworkers⁵, on the other hand, have studied the "flat particle" problem in which the geometry of the alloying system is idealized. Their model consists of assuming that the powdered media is equivalent to alternating laminae of alloyable material. This simplification allows the analytic calculation of a flame speed while keeping all of the microscopic detail of the interdiffusing laminae. This is the type of theory most closely associated with the work to be presented here. Aldushin's theory and others with less clearly defined microscopic-physical underpinnings have been used in models for gauging the stability of alloying systems, in filtration combustion and examination of the so-called "burn out" phenomenon.

Oscillatory instabilities are often observed in experiment⁽¹⁾ because the length of thermal interaction (which defines the size of the instability) is much larger than more common systems involving solids (e.g. solid propellants^{6,7}). Margolis and coworkers⁸ have extended stability analyses to get bifurcation results that give a good geometric description of these instabilities.

Filtration combustion⁹ involves percolation of a reactive gas to the flame zone where it reacts with the solid powder to yield a useful material (e.g. titanium nitride can be formed in this way). Models for this system generally consist of an overall reaction rate and a detailed accounting for the gas percolation to the reaction zone.

The "burn out" (an unfortunate translation of a Soviet-coined term which tends to connote the opposite of its meaning) phenomenon refers to the general characteristic exhibited by these systems that after the thin flame zone has passed a residual quantity of material continues to react long after. This has been modeled by using an exponential inhibition to the phenomenological relation for the reaction rate¹⁰.

The purpose of this paper is to look at idealized situations and attempt to relate the global flame speed to the physical and chemical configuration of the alloyable constituents. Rather than use some of the well known phenomenological constitutive relations we seek an exact understanding of the microscopic structure for idealized model systems that could in principle exist and are, in at least one instance, similar to systems in commercial use. For instance the model developed in the next section will consider layers of two alloyable constituents stacked perpendicular to the flame propagation direction (the seams parallel to the flame propagation). A cylindrical version of this ideal already exists in the form of PyrofuzeTM, used for timing and electrical fuses. It consists of an aluminum wire codrawn with a palladium tube to form a wire-sandwich that supports a combustion wave and has the desirable property of highly reproducible flame velocity and heat release in the presence or absence of oxygen (it burns nicely underwater).

Theory

The following analysis proceeds in ways similar to premixed, gas-phase, activation-energy asymptotics but the physics of the combustion process is very different. In classical flame theory a locally homogeneous reaction is activated by the temperature approaching close to the flame temperature, where "close" is gauged by the inverse activation energy. Here we expect that the diffusion processes will be activated in the same fashion, however diffusion, by its very nature, cannot occur homogeneously but must have another length associated with it.

Here two constituents will be considered, labeled "A" and "B", which will codiffuse releasing heat simply by virtue of mixing on the molecular scale. Typically the Lewis number for these systems is extremely large ($> 10^3$ is common at the flame temperature^{11,(5)}), even compared with more common condensed-phase systems like propellants. This is due to the fact that the reactants are often metals with a much larger thermal conductivity than organic constituents of propellants. Though often the Lewis number is considered infinite in condensed phase reactions in propellant systems¹², here mass transport is the only vehicle for heat release and thus we require the characteristic dimension over which diffusion will occur to be very small compared to thermal transport dimensions. In addition, the Lewis number is so small even at the flame temperature that, to a good approximation, this diffusion distance will be much smaller than the flame thickness. As we shall see, this thickness is characterized by an inverse Zeldovich number, not due to an homogeneous-reaction activation energy, but from an activation energy with lattice or viscous diffusion⁽¹¹⁾.

We assume that "A" and "B" form a solution and that all compositions are traversed in the progress of "reaction" from domains of pure "A" and pure "B" to a homogeneous 50-50 mixture (see Conclusion). This situation is physically most like a system that either never melts (forms a solid solution) or where all constituents melt (forms a liquid solution). Anselmi-Tamburini and Munir¹³ have reported on experiments that bear out these assumptions: alternating lamina of Ni and Al stacked perpendicular to the flame

direction (similar to Fig. 2), apparently burn as a flame only after both constituents melt. In addition, it is assumed that the thermal diffusivity and mass diffusivity are composition independent and that thermal diffusivity is independent of temperature as well. It is clear however, that the mass diffusivity must be temperature dependent. Moreover, it is also assumed that there is no substantial volume change with composition.

Choosing C as the mass concentration of "A", the general diffusion equation translating in the negative \bar{x} direction at a velocity \bar{u} can be written:

$$\frac{\partial \bar{C}}{\partial \bar{t}} + \bar{u} \frac{\partial \bar{C}}{\partial \bar{x}} - \bar{\nabla} \cdot \bar{D} \bar{\nabla} \bar{C} = 0 \quad (1)$$

Since there is no volume dependence on concentration, the presence of "A" indicates the absence of "B" and the concentration of "B" is $\bar{C}_0 - \bar{C}$, where \bar{C}_0 is the concentration of pure "A". The volumetric heat generation rate can be obtained from the enthalpy as a function of composition which must have a maximum somewhere between $\bar{C} = 0$ and $\bar{C} = \bar{C}_0$. The enthalpy of the system is presumed of the form:

$$\bar{H} = \bar{\rho} \bar{c} (\bar{T} - \bar{T}_0) - \bar{\Delta}(\bar{C}) + \bar{H}_0 \quad (2)$$

The volumetric heat generation due to interdiffusion can be written:

$$\left. \frac{\partial(-\bar{H})}{\partial \bar{t}} \right|_{\bar{T}} = \frac{\partial \bar{\Delta}(\bar{C})}{\partial \bar{t}} \quad (3)$$

\bar{H} is the enthalpy of the system, assumed to be only a function of composition at constant temperature, and $\bar{\Delta}$ is the negative of this, the heat release.

The thermal transport equation may be written down:

$$\bar{c} \bar{\rho} \left\{ \frac{\partial \bar{T}}{\partial \bar{t}} + \bar{u} \frac{\partial \bar{T}}{\partial \bar{x}} - \bar{\lambda} \bar{\nabla}^2 \bar{T} \right\} = \frac{\partial \bar{\Delta}(\bar{C})}{\partial \bar{t}} + \bar{u} \frac{\partial \bar{\Delta}(\bar{C})}{\partial \bar{x}} \quad (4)$$

where \bar{T} is the temperature and $\bar{\lambda}$ is the thermal diffusivity. \bar{c} is the heat capacity (assumed constant) and $\bar{\rho}$ is the density. A constant flame speed \bar{u} can be anticipated and the concentration, \bar{C} can be normalized by $\frac{1}{2} \bar{C}_0$. In addition, the spatial coordinates are nondimensionalized by the thermal length ($\bar{\lambda}/\bar{u}$) and time by the thermal time ($\bar{\lambda}/\bar{u}^2$) while the temperature is normalized by the flame temperature and mass concentration is normalized by its maximum (see the List of Symbols and Figure 1):

$$\frac{\partial C}{\partial t} + \frac{\partial C}{\partial x} - \nabla \cdot L e^{-1} \nabla C = 0 \quad (5)$$

$$\frac{\partial T}{\partial t} + \frac{\partial T}{\partial x} - \nabla^2 T = \left\{ \frac{\partial}{\partial t} + \frac{\partial}{\partial x} \right\} \Delta(C) \quad (6)$$

$C = 1$ is the state at which everything has completely interdiffused or equivalently: totally reacted. [The term "interdiffusion" and reaction are for the purposes of this paper semantic

equivalents. Since $1 - |1 - C|$ is a tacit measure of the extent of reaction, $\Delta(C)$ can be considered to be the total heat released at the present extent of reaction.

It is expected that the Lewis number, $Le = \tilde{\lambda}/\tilde{D}$ will exhibit an Arrhenius dependence and will be defined here as:

$$Le^{-1} = A \exp \left(-\frac{\tilde{E}}{\tilde{R}\tilde{T}} \right) \quad (7)$$

$$Le_0^{-1} = A \exp \left(-\frac{\tilde{E}}{\tilde{R}\tilde{T}_f} \right) \quad (8)$$

where Le_0^{-1} is the maximum that Le^{-1} attains at the flame temperature. In the next section we will seek a steady state so that the time dependence in Equations (5) and (6) can be neglected, however in the later sections it will be necessary to include the time dependence.

Lamina Stacked Perpendicular to the Flame Direction

For this situation the diffusion direction is perpendicular to the flame direction which demands a truly two dimensional model, though a steady solution can be expected. Note that an outwardly similar system consisting of striations of gaseous components that interdiffuse and undergo a locally homogeneous, high-activation reaction is mechanistically different than the system considered here (see Linan and Crespo¹⁴). Figure 2 shows the general scheme of the semi-infinite lamina problem and serves as a definition sketch. The diffusion equation of "A" into "B" is:

$$\frac{\partial C}{\partial x} - \left\{ \hat{x} \frac{\partial}{\partial x} + \hat{y} \frac{\partial}{\partial y} \right\} \cdot Le^{-1} \left\{ \hat{x} \frac{\partial}{\partial x} + \hat{y} \frac{\partial}{\partial y} \right\} C = 0 \quad (9)$$

where \hat{x} and \hat{y} are the unit vectors in the x and y direction. It should be recognized that, by taking advantage of symmetry, one-half of a single "B" lamina is sufficient to determine the entire system (again see Figure 2). Here the boundary conditions are stated in terms of limits far in front of and in back of the flame:

$$C \rightarrow 0 \text{ as } x \rightarrow -\infty, y \in (0, \delta] \quad (10)$$

$$C \rightarrow 1 \text{ as } x \rightarrow +\infty, y \in (0, \delta] \quad (11)$$

$$C = 1 \text{ at } y = 0, \forall x \quad (12)$$

Similar to Maksimov¹⁵ we choose the heat release to be just a weighted version of the extent of reaction:

$$\Delta(C) = \begin{cases} (1 - T_0)(2 - C), & 1 \leq C \leq 2; \\ (1 - T_0)C, & 0 \leq C \leq 1 \end{cases} \quad (13)$$

which is a form simple enough for illustration while retaining the energy conservation relation: $(2\Delta(1) - (\Delta(2) + \Delta(0)))/2 = 1 - T_0$, resulting from the choice of $T = 1$ to represent the flame temperature. Since the heat is released over a length much smaller

than the thermal scale, it is assumed that the y variation in temperature is negligible and can be replaced by an average over the y :

$$\frac{\partial \bar{T}}{\partial x} - \left(\frac{\partial}{\partial x} \right)^2 \bar{T} = \frac{\partial \bar{\Delta}(C)}{\partial x} \quad (14)$$

where the overbar denotes the y -direction average:

$$\bar{\Delta}(C) = \lim_{L \rightarrow \infty} 1/2L \int_{-L}^L dy \Delta(C) = (1 - T_0) \frac{1}{\delta} \int_0^\delta C = (1 - T_0) \bar{C}$$

taking advantage of symmetry.

Anticipating that most of the diffusion, and hence heat generation, will occur where Le^{-1} attains its maximum Le_0^{-1} at the flame temperature, it is posited that the distance over which diffusion occurs is much thinner (call it $O(\epsilon)$, to define a scaling variable) than the thermal length. It is necessary in order for a flame to exist at all that $Le_0^{-1} \sim \delta^2/\epsilon$, that is, diffusion must occur appreciably over the thickness of the lamina in a length of time of order ϵ . From the before mentioned typical magnitude for Le_0^{-1} we expect $\delta \ll \epsilon$. To obviate this scaling we redefine the Lewis number:

$$Le^{-1} = \Lambda \frac{\delta^2}{\epsilon} \exp \left(- \frac{\bar{E}}{\bar{R}\bar{T}_f} \left(\frac{1}{T} - 1 \right) \right) \quad (15)$$

where Λ is an "eigenvalue" to be determined and from which the flame speed will be derived. Since diffusion only exists in a small ϵ sized region, external to this region there is an outer solution identical to the classical, chemical-reaction flame results (locating the flame at $x=0$):

$$\bar{T} = \begin{cases} x < 0, & T_0 + (1 - T_0) \exp(x); \\ x \geq 0, & 1. \end{cases} \quad (16)$$

where T_0 is the initial unburned temperature. Behind this ϵ -sized flame front everything is reacted and in front of it nothing is reacted:

$$C = \begin{cases} 0, & x < 0, \text{ for } y \in (0, \delta], 1 \text{ for } y = 0 \\ 1, & x \geq 0, \forall y \end{cases} \quad (17)$$

For the inner region, using the reasoning above, x should be scaled on a length ϵ :

$$x = \epsilon \xi \quad (18)$$

while diffusion in y occurs over its whole range $(0, \delta)$ suggesting the new scaling:

$$y = \delta \eta \quad (19)$$

Choosing:

$$\epsilon = \left(\frac{\bar{E}}{\bar{R}\bar{T}_f} \right)^{-1} \quad (20)$$

and

$$\bar{T} = 1 - \epsilon \bar{\theta} \quad (21)$$

the equations for the inner region can be written down:

$$\frac{1}{\epsilon} \frac{\partial C}{\partial \xi} - \left\{ \bar{x} \frac{1}{\epsilon} \frac{\partial}{\partial \xi} + \bar{y} \frac{1}{\delta} \frac{\partial}{\partial \eta} \right\} \cdot \Lambda \frac{\delta^2}{\epsilon} e^{(-\bar{\theta})} \left\{ \bar{x} \frac{1}{\epsilon} \frac{\partial}{\partial \xi} + \bar{y} \frac{1}{\delta} \frac{\partial}{\partial \eta} \right\} C = 0 \quad (22)$$

$$-\frac{\partial \bar{\theta}}{\partial \xi} + \frac{1}{\epsilon} \left(\frac{\partial}{\partial \xi} \right)^2 \bar{\theta} = \frac{1}{\epsilon} (1 - T_0) \frac{\partial \bar{C}}{\partial \xi} \quad (23)$$

Remembering that $\delta \ll \epsilon$, choose the coordinate transformation:

$$\mathcal{F} = \int_{-\infty}^{\xi} d\xi e^{-\bar{\theta}(\xi)} \quad (24)$$

Keeping the lowest order terms, Equations (22) and (23) can be solved using fourier series and the conditions of Equation (17). Recasting in terms of \mathcal{F} :

$$\frac{\partial \mathcal{F}}{\partial \xi} = B - \frac{8(1 - T_0)}{\pi \Lambda} \sum_{n \in \{1, 3, 5, \dots\}} \frac{1}{n^2 \pi \left(\frac{n\pi}{2} \right)^2} e^{-\mathcal{F} \left(\frac{n\pi}{2} \right)^2 \Lambda} \quad (25)$$

where B is an arbitrary constant. The boundary conditions matching the outer problem:

$$\lim_{\xi \rightarrow -\infty} \mathcal{F} = 0; \quad \lim_{\xi \rightarrow -\infty} \frac{\partial \mathcal{F}}{\partial \xi} = 0 \quad (26)$$

$$\lim_{\xi \rightarrow \infty} \mathcal{F} = \xi; \quad \lim_{\xi \rightarrow \infty} \frac{\partial \mathcal{F}}{\partial \xi} = 1 \quad (27)$$

Using the first boundary condition to define B and the second to find the eigenvalue, the flame speed in dimensional terms is given by:

$$\tilde{u}^2 = 3 \frac{A \exp \left(-\frac{\tilde{E}}{RT_f} \right) \frac{RT_f}{\tilde{E}} \tilde{\lambda}^2}{\tilde{\delta}^2 \frac{\tilde{T}_f - \tilde{T}_0}{\tilde{T}_f}} \quad (28)$$

Similar to Aldushin⁽⁵⁾, we obtain the "parabolic law" and the interesting result that the activation energy for diffusion appears in the same role as a chemical reaction activation energy would. For this reason the "constitutive" relationship between a so-called "reaction" rate and a process involving pure diffusion can become blurred. By choosing a parabolic definition for $\Delta(C)$ (not related to the "parabolic" law): $\Delta(C) = (1 - (1 - C)^2)(1 - T_0)$ one obtains exactly twice the right hand side of the above and consequently an increase in the flame speed by a factor of $\sqrt{2}$ (see Figure 1).

Conclusion

In this paper the fundamental properties of mass diffusion, thermal conduction and geometric configuration have been related to the dynamics of alloying reactions. The flame speeds for lamina arranged perpendicular to the propagation direction of the flame were calculated for two different heat release parameters $\Delta(C)$. It was assumed that the two constituents formed a solid or liquid solution and that heat release was an artifact of mixing caused by an Arrhenius-dependent interdiffusion. It is notable that Aldushin⁽⁵⁾ derived a flame speed identical in form to that of the case of the model considered here. His model is geometrically the same as this one, however the interdiffusion took place through a growing layer of reaction products, using the so-called "parabolic law" and "flat particle" assumptions. It is significant that the results here are in agreement with models employing parabolic law by virtue of the fact that flame speeds generated from such models are generally successful at correlating data⁽¹⁾.

Thus there is strong reason to believe that the flame speeds of this work can be applied to systems that do not strictly form solutions. A parallel analogue of the perpendicular model, in which the lamina are stacked along the flame direction, given here has also been done. Not surprisingly, the flame speed is identical to that of this paper. This is true because the length-scale over which diffusion occurs is much smaller than the width of the flame "reaction" zone (i.e. heat release zone). The lamina influence only their nearest neighbors and the length over which temperature, and hence diffusivity, increase is so broad as to appear homogeneous.

In the case studied here the flame speed is inversely proportional to the square root of the time for mass diffusion multiplied by the thermal diffusivity. The time for mass diffusion is identified with Lewis number, evaluated at the flame temperature times thermal diffusivity divided by the distance over which diffusion has to occur (δ). This diffusion time effectively takes the place of the reaction time in the standard asymptotic result for premixed, gas-phase flames.

In addition to predictions of flame speed behavior, the results suggest that the particles making up a powder must necessarily have a size much less than the inverse of the normalized activation energy in order to develop a single thin flame:

$$\delta \ll \epsilon \quad (29)$$

Also a mechanistic requirement demands that significant mass diffusion must occur over the width of the flame:

$$\frac{\delta^2}{\epsilon} \sim Le_0^{-1} \quad (30)$$

This paper has centered on flames that result in 100% conversion within the flame zone. Other cases exist where some of the particles are larger than can be admitted by external boundary conditions. Consider the above equation rewritten:

$$\frac{\delta^2 \bar{u}^2}{\epsilon \bar{\lambda}^2} \sim Le_0^{-1} \quad (31)$$

or rearranging:

$$\bar{u} \sim \frac{\bar{\lambda}}{\delta} \sqrt{Le_0^{-1} \epsilon} \quad (32)$$

which implies:

$$\bar{\epsilon} \sim \frac{\bar{\delta}\epsilon}{\sqrt{Le_0^{-1}\epsilon}} \quad (33)$$

where $\bar{\epsilon} = \epsilon\bar{\lambda}/\bar{u}$ is the dimensional flame thickness. All of the above equations differ by only an order 1 factor from the flame speed relation (Equation (28)). As the physical thickness of the lamina ($\bar{\delta}$) grows while all other parameters are held constant, the flame velocity (\bar{u}) decreases keeping δ , the nondimensional thickness, constant. Also the flame thickness increases along with $\bar{\delta}$ such that $\bar{\delta} \ll \bar{\epsilon}$ remains true no matter how large $\bar{\delta}$ becomes. However there is a circumstance where $\bar{\lambda}/\bar{u}$, the thermal induction length of the flame, becomes larger than a significant dimension of the container in which the combustion occurs. This may correspond to a case (observed experimentally¹⁶) where the powder cannot support a propagating flame but can be made to undergo a homogeneous explosion. Another possibility that this circumstance suggests is a mixture of the two sizes: some particles meeting conditions for flame propagation (Equation (30)) and some meeting the proposed thermal explosion condition. This may result in the "burn out" or "after burning" condition, where an initial flame passes through the powder igniting a homogeneous explosion subsequently⁽¹⁾. The current research on the "burn out" phenomenon is phenomenological in nature and is usually characterized with an exponential decay in extent of reaction for an overall expression representing the interdiffusion rate.

The principal original result of this work is to show that Arrhenius-dependent, diffusion-controlled processes produce a flame speed in which the activation energy for mass diffusion plays a role similar to that of the chemical-reaction in premixed, gas-phase flames. Moreover this remains true to within a numerical factor for a several radically different configurations. The most likely future extension to this paper would be to investigate and characterize this "burn out" phenomenon.

References

1. Merzhanov, A.G., *Archiwum Procesow Spalania*, **5**, 17, (1974).
2. Budnikov, P.P., and A.M. Ginstling, *Solid State Chemistry*, p.391 & ff., Gordon and Breach (1968).
3. Margolis, S.B., *Combust. Sci. Technol.*, **43**, 127 (1985).
4. Hardt, A.P. and P.V. Phung, *Combustion and Flame*, **21**, 77, (1973).
5. Aldushin, A. P. and B.I. Khaikin, *Combustion, Explosions and Shock Waves*, **10**, 273, (1974).
6. Price, E.W., *Fundamentals of Solid Propellant Combustion-Progress in Astronautics and Aeronautics*, **90**, 733, (1984).
7. Margolis, S.B. and R.C. Armstrong, *Combust. Sci. Technol.*, **47**, 1, (1986).
8. Margolis, S.B., H.G. Kaper, G.K. Leaf and B.J. Matkowsky, *Combust. Sci. Technol.*, **43**, 127, (1985).
9. Aldushin, A.P. and B.S. Septyarskii, *Sov. Phys. Dokl.* **23**, 483, (1978).
10. Aldushin, A.P., A.G. Merzhanov, and B.I. Khaikin, *Dokl. Akad. Nauk SSSR*, **204**, 1139, (1978).
11. Budnikov, P.P., and A.M. Ginstling, *Solid State Chemistry*, p. 1 & ff., Gordon and Breach (1968).
12. Margolis, S.B., F.A. Williams and R.C. Armstrong, *Combust. and Flame*, **67**, 249, (1987).
13. U. Anselmi-Tamburini and Z.A. Munir, *Observations on the Combustion Reaction between Thin Foils of Ni and Al*, Proceedings of the International Symposium on the Combustion and Plasma-Synthesis of High-Temperature Materials, San Francisco, Oct 23-26, 1988, to appear.
14. Linan, A. and A. Crespo, *Combust. Sci. Technol.*, **14**, 95, (1976).
15. Maksimov, Yu.M., V.K. Smolyakov, and E.A. Nekrasov, *Combustion, Explosions and Shock Waves*, **20**, 479, (1983).
16. J. B. Holt, Lawrence Livermore Laboratories, Livermore CA, 94550, Personal Communication.

List of Symbols

A	Arrhenius prefactor defined in (7)
C	nondimensional concentration (\bar{C}/\bar{C}_0)
\bar{C}	concentration [=] g/cm ³
\bar{C}_0	concentration of pure "A" [=] g/cm ³
\bar{c}	heat capacity [=] cal/g
\bar{D}	mass diffusivity [=] cm ² /sec
\bar{E}	activation energy for mass diffusion [=] cal
\mathcal{F}	convenient time-like coordinate defined in (24)
\bar{H}	enthalpy of reaction [=] cal/cm ³
Le	Lewis number, ratio of thermal diffusivity to mass diffusivity, $\bar{\lambda}/\bar{D}$
Le_0	Lewis number evaluated at the flame temperature
\bar{R}	gas constant [=] atm cm ³ / gmol k
T	nondimensional temperature: \bar{T}/\bar{T}_f
T_0	nondimensional initial unburned temperature: \bar{T}_0/\bar{T}_f
\bar{T}	temperature [=] deg K
\bar{T}_f	flame temperature
\bar{T}_0	initial unburned temperature
t	nondimensional time
\bar{t}	time [=] sec
\bar{u}	flame speed [=] cm/sec
x	x coordinate $x = \frac{\bar{x}}{\bar{\lambda}}$
\bar{x}	x coordinate [=] cm
\hat{x}	unit vector in the x direction
y	y coordinate $y = \frac{\bar{y}}{\bar{\lambda}}$
\bar{y}	y coordinate [=] cm
\hat{y}	unit vector in the y direction
δ	length scale of diffusion $\delta = \frac{\bar{u}\bar{\delta}}{\bar{\lambda}}$
Δ	nondimensional heat release, $\Delta = \frac{\bar{\Delta}}{\bar{\rho}\bar{c}}$
$\bar{\Delta}$	heat release [=] cal/cm ³
ϵ	scaling factor for the reaction zone $\epsilon = \frac{\bar{R}\bar{T}_f}{\bar{E}}$
η	scaled diffusion distance in the y direction defined by Equation (19)
θ	temperature perturbation in the flame zone
Λ	flame speed eigenvalue
$\bar{\lambda}$	thermal diffusivity [=] cm ² /sec
ξ	scaled reaction zone thickness in the x direction $x = \epsilon\xi$
$\bar{\rho}$	density of the burning media [=] g/cm ³
σ	standard deviation of $1 - C$ in the random media

Figure Captions

Figure 1: Gives the nondimensional heat release versus the nondimensional concentration. The initial state is considered to be made of equal quantities of $C = 0$ (pure "B") and $C = 2$ (pure "A") while $C = 1$ is the completely interdiffused or reacted state. Shown here are the two heat release functions use in this paper. Note that the heat release is always larger for the parabolic case and that it always yields a faster flame speed (Equation (28)).

Figure 2: Shows a series of laminae stacked in the y direction (perpendicular to the flame direction) for Section (i) and the three different length scales under which the analysis proceeds. The diffusion coefficient is assumed to have an Arrhenius temperature dependence and requires a temperature sufficiently close to the flame temperature for the interdiffusion of the lamina to proceed.

At the top of the drawing is the domain of thermal variation where all conversion of reactants to products occurs on a much smaller length scale. Here the flame is considered an infinitesimally thin heat source and proceeds from left to right. To the right ($+x$ direction) everything is reacted (interdiffused) and to the left ($-x$ direction) the temperature has not yet reached a point where significant diffusion is possible.

The middle of the drawing depicts the size over which conversion of reactants ("A" and "B") to products ("AB") occurs. At this scale ($\propto \epsilon \sim$ inverse activation energy for diffusion) the temperature is sufficiently close to the flame temperature to activate diffusion. Yet, to be consistent with physically realistic diffusion coefficients, diffusion itself must occur over considerably smaller distances.

The bottom of the drawing depicts plots of the concentration at three different positions in the reaction zone scaled by a quarter thickness of the laminae ($\equiv \delta$). On the left is the initial condition: a square wave in the y direction. In the middle is a partially reacted (interdiffused) example taken from the the center of the reaction zone. On the right is a completely reacted example taken from the left boundary of the reaction zone. The dashed lines give the boundaries for the diffusion analysis in Section (i), taking advantage of symmetry inherent in the initial condition.

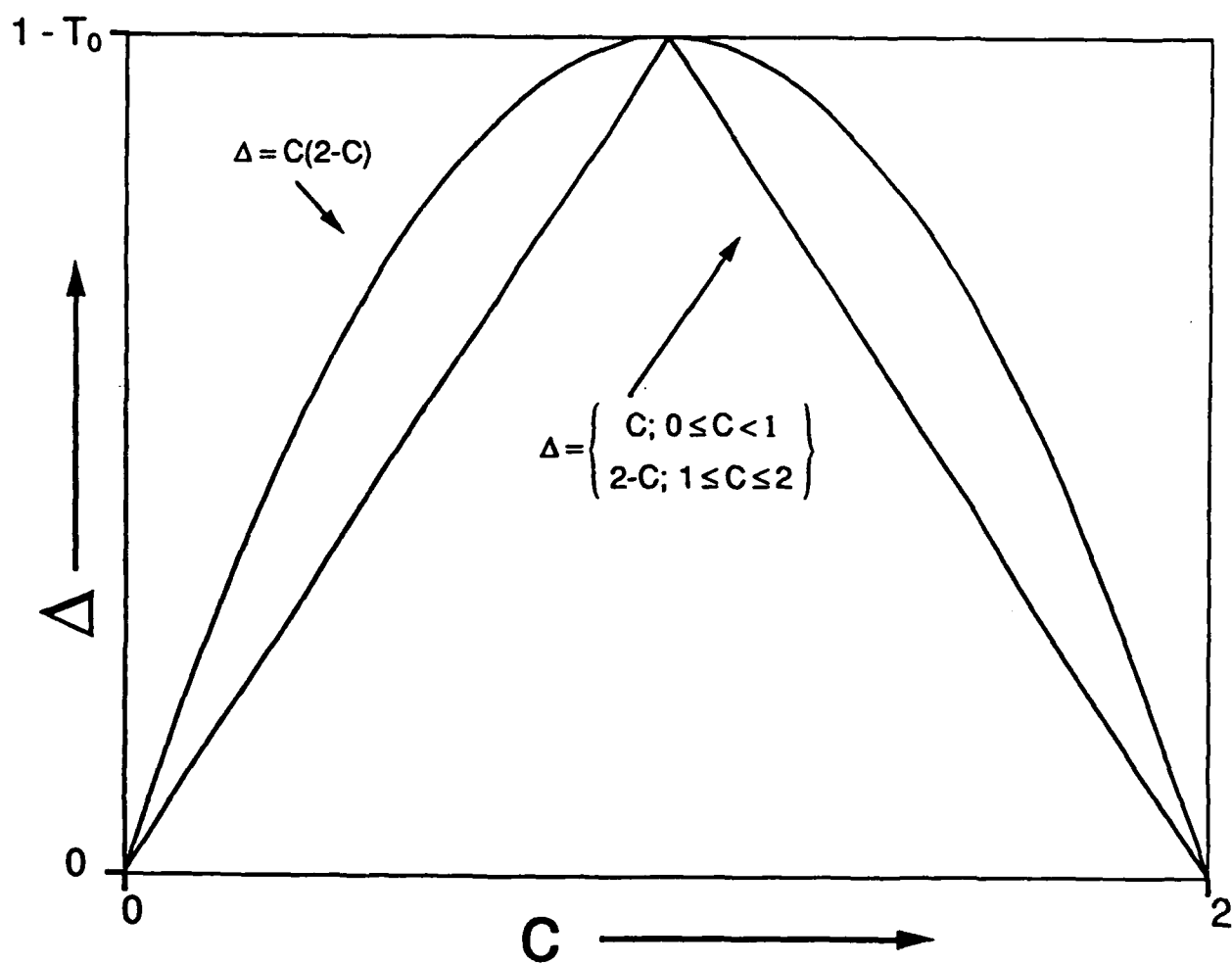
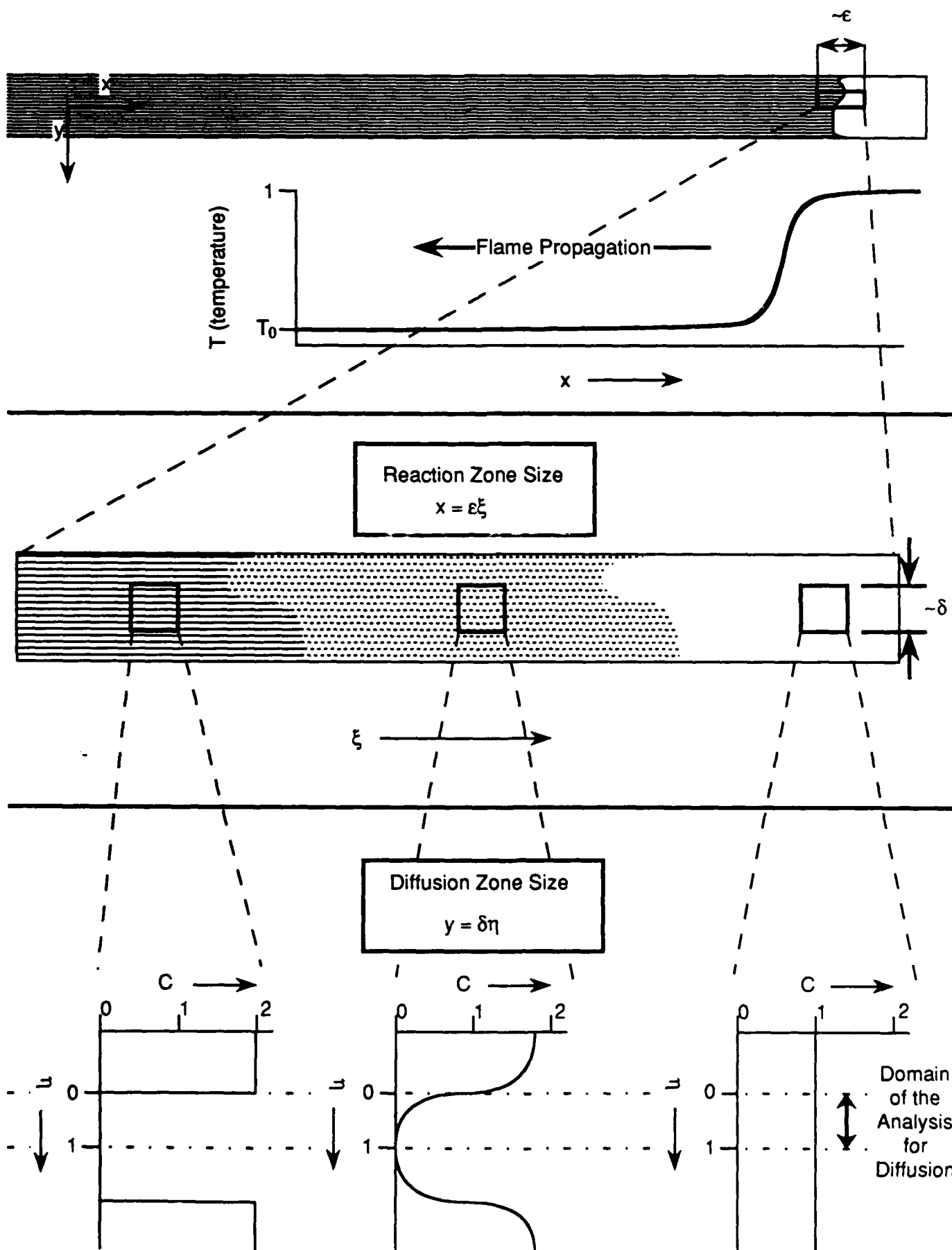


Fig. 1



Observations on the Combustion Reaction Between Thin Foils of Ni and Al

Umberto Anselmi-Tamburini* and Zuhair A. Munir

Division of Materials Science and Engineering
University of California
Davis, California 95616, U.S.A.

ABSTRACT

The combustion reaction between Ni and Al was studied using sandwiches of thin foils (125 and 12.5 μm thick) instead of powders. The temperature of ignition, combustion and the combustion rate were determined for compositions corresponding to the four intermetallic compounds present in this system. The phase evolution was studied on quenched samples. Combustion was found to take place after melting of both metals. Dissolution of solid Ni in melted Al was found to be the main process ahead of the reaction front. The advantage of using simple starting geometry in the study of combustion reaction is shown.

*NATO Postdoctoral Fellow. Permanent address: Dipartimento di Chimica Fisica, viale Taramelli 16, 27100 Pavia, Italy.

Introduction

The study of combustion synthesis of refractory materials has focused on the reactivity of fine powders [1]. Because of their technological importance, powders allow easy control of some macroscopic parameters of reactants and offers the possibility of obtaining high contact surface between the reacting phases. But their microstructural nature complicates investigations on the basic steps of combustion synthesis and the lack of a well-defined starting geometry makes it difficult to develop reliable theoretical models.

Hardt and Phung [2] first proposed the use of thin foils instead of powders for the study of gasless combustion and applied it to the system Pd-Al. More recently, Vadchenko et al. [3] used wires of Ti coated with Ni which were ignited by passing an electrical current through them. The present work was formulated to explore the possibilities offered by a different approach to the gasless combustion processes through the use of sandwiches of thin foils in the system Ni-Al.

The combustion reaction between powders of nickel and aluminum was the object of several studies in the last 20 years [4-7]. All four intermettalic compounds (AlNi_3 , AlNi , Al_3Ni_2 , and Al_3Ni) have been synthesized in this way. The influence of the particle size of reactants, porosity, sample size, and composition on the macroscopic features of the combustion process and on the microstructure of the product was investigated. Some significant insight on the reaction mechanism was also provided by studies of reactive sintering and combustion synthesis using the thermal explosion method [8,9].

Experimental

In contrast to powders, the reaction between foils of Ni and Al is not self-sustaining due to the high thermal conductivity of the foils. A method, often referred to as the "chemical oven," was used in this work to initiate a self-propagating reaction in the laminated foils. Foil ensembles are embedded vertically in a pellet of Ni and Al powders (the chemical oven) with 1:1 molar ratio, as shown in Figure 1(a). The relative porosity of the chemical oven was approximately 35%. The reaction was started at the top using a tungsten coil and an igniter. The igniter was used to obtain a flat combustion front in the pellet. The sandwich was made using high purity sheets of Ni and Al. Ni foils of two different thicknesses (125 and 12.5 μm) were utilized.

To obtain information about the phase evolution at the reaction front, the combustion reaction in foils was sometimes stopped before completion. In this experiment, the setup was modified as shown in Figure 1(b). A pellet of inert material (Al_2O_3) was placed at the bottom of the chemical oven, and the sandwich extended through the pellet. In some cases, the sample was quenched in water immediately after the end of the reaction. The cooling time was 2-3 minutes for naturally cooled and 10-15 seconds for quenched samples. All experiments were performed in a cylindrical metallic vessel filled with argon gas at one atmosphere pressure. The combustion temperature was measured using a two color pyrometer and, in a few cases, by a 75 μm thick W5%Re-W26%Re thermocouple. In the latter case, the thermocouple was connected to one of the Ni foils inside the sandwich. The combustion rate was evaluated using a video recorder. The products of combustion were characterized using X-ray diffraction, optical microscopy, scanning electron microscopy, and microprobe analysis.

Results and Discussion

A delay of a few seconds induction period between the arrival of the wave in the chemical oven to the top of the foils and the initiation of a reaction in the foils was observed. Once the reaction in the foils began, it propagated rapidly through the sandwich, leaving behind a melted product. Although the extent of the induction period appeared to be related to the thickness of the foils and the sandwich, no quantitative evaluation of this parameter was made.

X-ray diffraction showed that the combustion of foil sandwich with starting compositions Al+3Ni, 3Al+2Ni led to the formation of single-phased products. In contrast, when samples with composition 3Al+Ni were combusted, the product showed the presence of two phases (Al_3Ni and Al_3Ni_2). A similar result for the combustion of powders was reported by Naiborodenko, et al. [7].

Figure 2 shows the ignition temperature for the foil sandwich for compositions corresponding to the four intermetallic compounds present in the phase diagram [10]. The temperature appears to be constant and coincide with the melting temperature of Ni. This implies that, at least under these experimental conditions, the combustion reaction propagates only after the melting of both metals.

Some interesting insight on the mechanism of the combustion process was obtained when the reaction was stopped before completion, as discussed earlier.

Figure 3 shows the typical morphology of one of these samples, with the combustion product at the top and the partially unreacted part of the sandwich at the bottom. The light regions correspond to the remnants of the nickel foils. Between them is a complex microstructure which is the result of the crystallization of an aluminum rich liquid alloy. The sample reproduced in the picture had a starting composition close to 50 at% Ni. Samples with higher Ni

content (e.g. 75% at%) had a markedly different microstructure. In fact, such showed features resembling the intermixing pattern of two liquids [11]. The final product, AlNi_3 , formed at a considerable distance behind the reaction front. These features suggest that the kinetic of the process of intermixing of the two melted metals plays a key role in the overall combustion process. As Figure 4 indicates, a steady decrease in the velocity of combustion in foils can be found when the amount of nickel in the starting sandwich is increased.

Due to the low melting point of Al and to the high heating rate, the main process ahead of the reaction front is an interaction between liquid aluminum and solid Ni. A considerable amount of Ni had reacted with liquid aluminum in this region. The thickness of Ni foils decreases by about 10-20% and the concentration of Ni in the liquid alloy can reach 25 at%. During cooling, this alloy crystallizes and produces the observed characteristic microstructure. Figure 5 is an example of the microstructure of the region ahead of the wave in a naturally cooled sample. Four phases can be identified: Ni, Al_3Ni , Al_3Ni_2 and an Al-rich eutectic. The nickel content decreases with distance from the center of the Ni layer. This morphology is homogenous along all the unreacted part of the sandwich. Only in the area very close to the reaction front is there a rapid decrease of thickness of Ni foils. Their disappearance coincides with the reaction front and the formation of the final product.

Acknowledgements

One of us (U.A.T.) is grateful to the Italian National Research Council (CNR) for the financial support provided during his stay at the University of California, Davis, in the form of a NATO Postdoctoral Fellowship.

This work was supported by a grant from the Basic Energy Sciences of the U. S. Department of Energy.

References

1. A. G. Merzhanov, Archiv. Combustionis, **1**, 23 (1981).
2. A. P. Hardt and P. V. Phung, in: Proc. 5th International Pyrotechnic Seminar, Vail, Co., July 1976, p. 223 (1976).
3. S. G. Vadchenko, A. M. Bulaev, Y. A. Gal'chenko, and A. G. Merzhanov, Comb. Explos. Shock Waves, **23**, 706 (1987).
4. Y. S. Naiborodenko, V. I. Itin, B. P. Belozarov, and V. P. Ushakov, Sov. Phys. J., **16**, 1507 (1973).
5. Y. S. Naiborodenko, V. J. Itin, A. G. Merzhanov, I. P. Borovinskaya, Y. P. Ushakov, and V. M. Maslov, Sov. Phys. J., **6**, 872 (1973).
6. Y. S. Naiborodenko and V. I. Itin, Comb. Explos. Shock Wave, **11**, 293 (1975).
7. Y. S. Naiborodenko and V. I. Itin, Combust. Explos. Shock Wave, **11**, 626 (1975).
8. V. M. Maslov, I. P. Borovinskaya, and A. G. Merzhanov, Combust. Explos. Shock Wave, **12**, 631 (1976).
9. K. A. Philpot, Z. A. Munir, and J. B. Holt, J. Mater. Sci., **22**, 159 (1987).
10. P. D. Desai, J. Phys. Chem. Ref. Data, **16**, 109 (1987).
11. U. Anselmi-Tamburini and Z. A. Munir, J. Appl. Phys., in press (1989).

Figure Captions

- Fig. 1 Schematic representation of the experimental set-up.
- Fig. 2 The dependence of the ignition temperature on composition of the foil sandwich. (The four points correspond to the compounds Al_3Ni , Al_3Ni_2 , AlNi , and AlNi_3).
- Fig. 3. Partially combusted sandwich with an initial composition of 50 at% Ni and an Ni foil thickness of 125 μm (naturally cooled).
- Fig. 4 The effect of composition on the combustion rate in foils. (The four points correspond to the compounds Al_3Ni , Al_3Ni_2 , AlNi , and AlNi_3).
- Fig. 5 The microstructure of a region in advance of the reaction front.

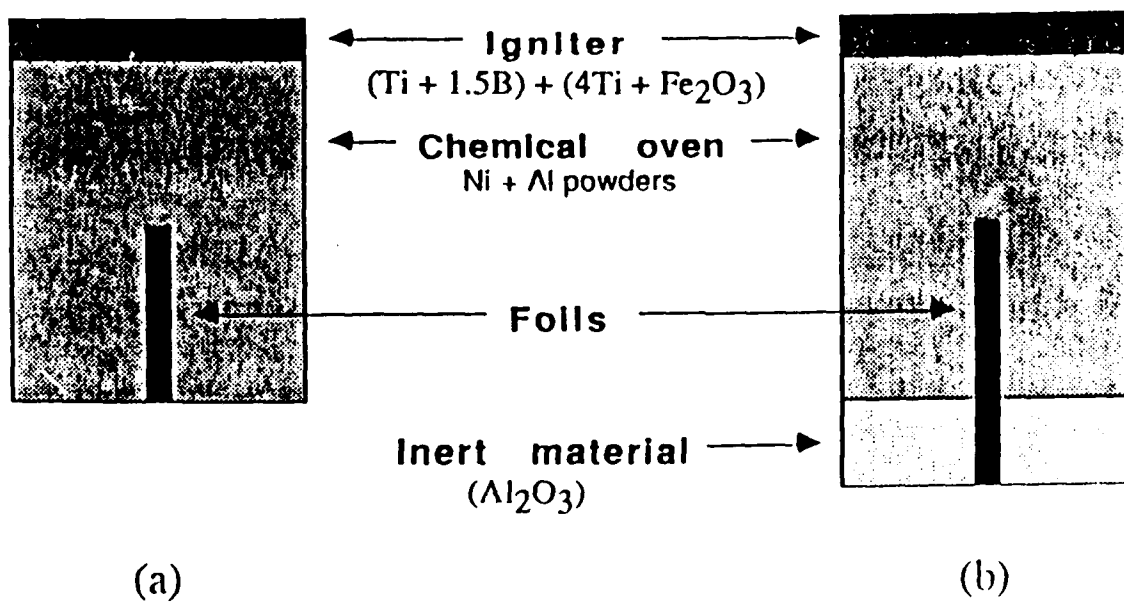


Fig. 1

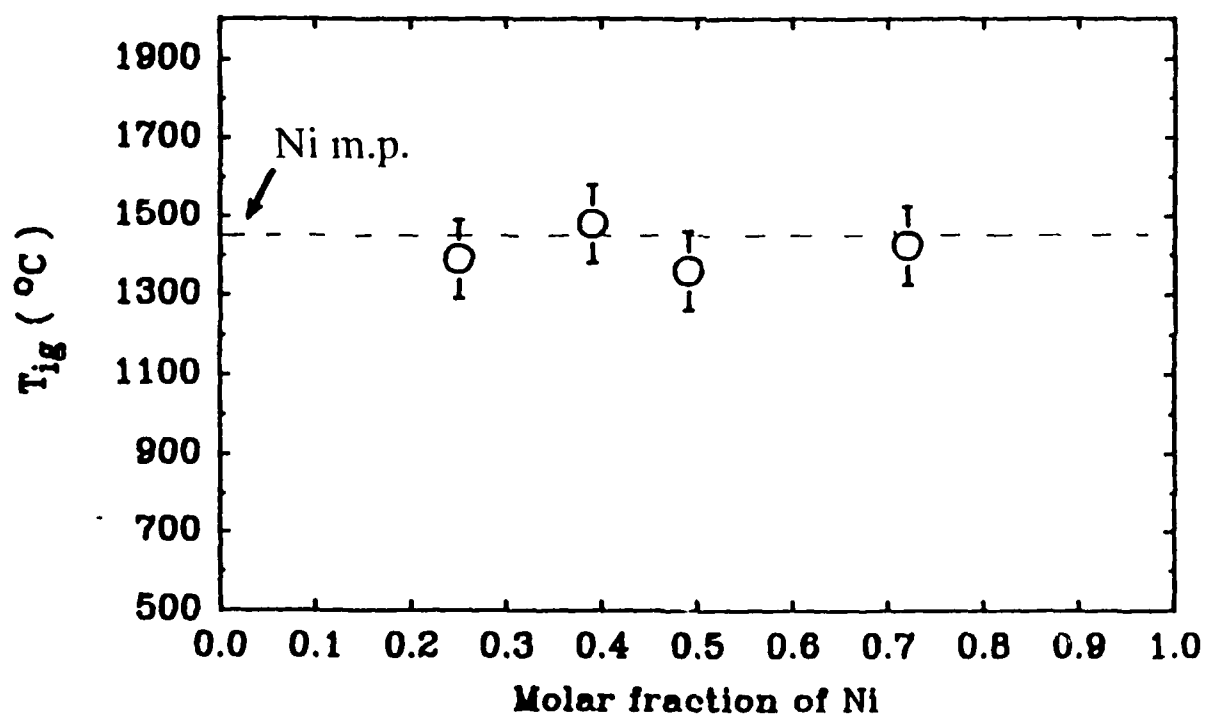


Fig. 2

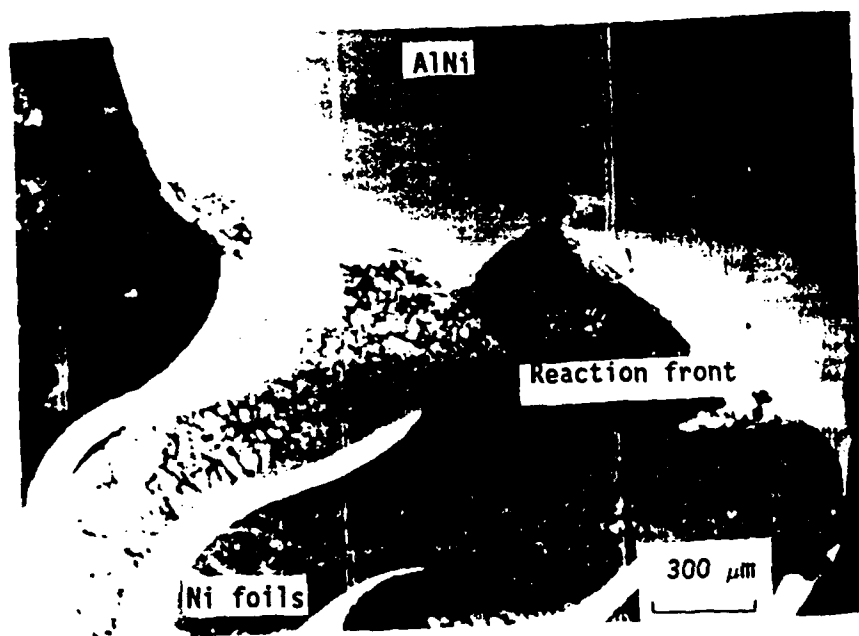


Fig. 3

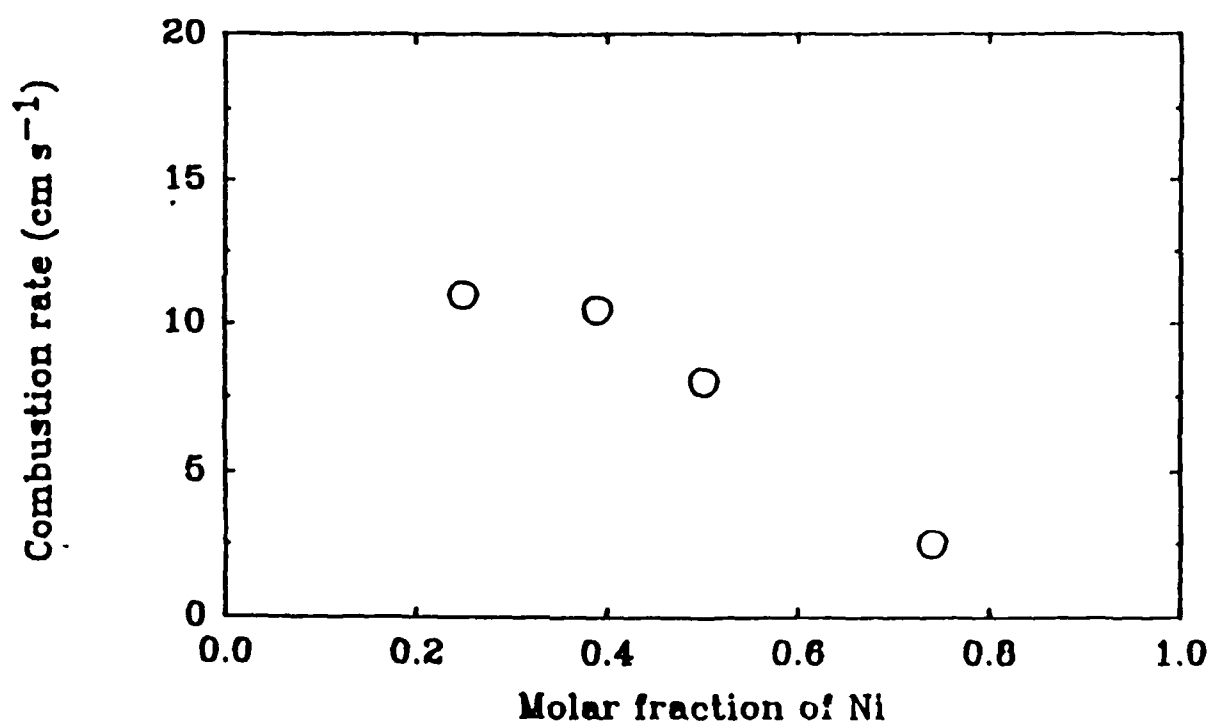


Fig.4

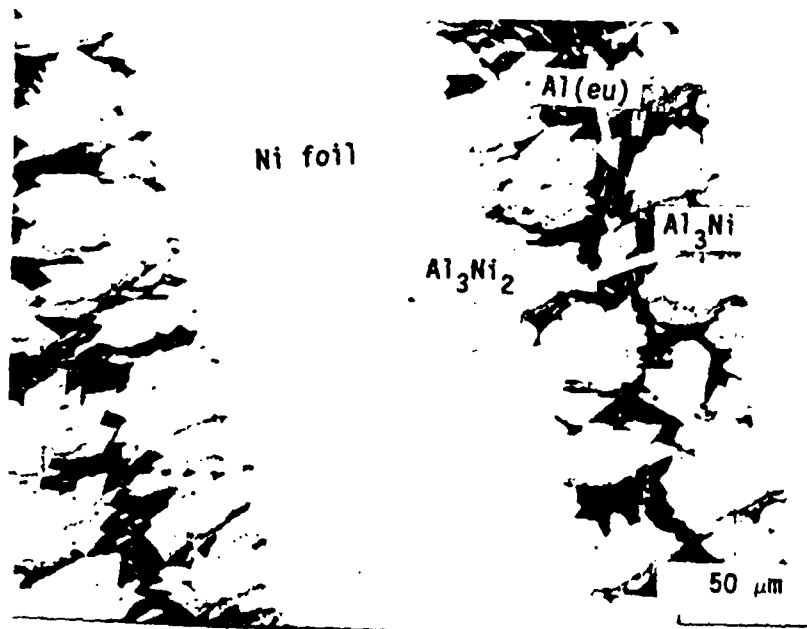


Fig. 5

COMBUSTION SYNTHESIS OF INTERMETALLIC COMPOUNDS

YOSHINARI KAIEDA, MINORU OTAGUCHI and NOBUTAKA OGURO

National Research Institute for Metals, 2-3-12 Nakameguro,
Meguro-ku, Tokyo 153, Japan

ABSTRACT

We applied the combustion synthesis method to the production of some intermetallic compounds such as TiAl, NiAl, ZrNi, CoAl, etc. We report the production of NiTi particularly in the present paper because NiTi is a very useful intermetallic compound as a shape memory and superelastic material. We produced not only the stoichiometric NiTi intermetallic compound but also nonstoichiometric NiTi having various amounts of Ni content (Ni=53wt.% - 57wt.%). We developed a manufacturing process of NiTi wire, tube and sheet. This process consisted of mixing of elemental powders, forming of mixed powders with a cold isostatic press (CIP), combustion synthesis, sintering with a hot isostatic press (HIP), and plastic working.

INTRODUCTION

NiTi shape memory alloy is usually manufactured at present using conventional metallurgical processes which consist of melting, casting, hot forging, hot rolling, and drawing. The disad-

vantages of the conventional method lie in the gravity segregation of Ni and Ti during the melting and casting process and the non-uniformity of the chemical compositions of Ni and Ti. These cause variations in the martensitic transformation temperature and mechanical properties. Powder metallurgical processes were tried to solve these difficulties. Pre-alloyed powder was produced using inert gas atomization following the arc melting process and was consolidated by HIP and drawn into wire. This process was successful but the cost of the production of the pre-alloyed powder was expensive and not yet commercialized. Many trials were conducted to produce the NiTi alloy from the elemental powder, but failed because the oxygen content could not be reduced and plastic working of the product into wires and sheets became impossible.

We made many kinds of ceramics such as borides, nitrides, carbides and silicides and several intermetallic compounds such as TiAl, NiAl, ZrNi and NiTi, using elemental powders with the combustion synthesis method [1,2]. Among these materials, the production of NiTi using the combustion synthesis of elemental powders is particularly reported in the present paper, since this process offers considerable potential for making high quality NiTi shape memory alloys cost-effective. We tried to make not only the as combustion-synthesized NiTi bulk material but also the NiTi wire, tube and sheet from the elemental powders.

EXPERIMENTAL

The heat of formation of NiTi was utilized to produce the NiTi shape memory alloy using the combustion synthesis method. Fig.1 shows the heat of formation of NiTi and the change in enthalpy of Ni and Ti mixture and the NiTi intermetallic compound. The heat of formation of the NiTi intermetallic compound is approximately 68 kJ/mol. This value was enough to ignite and to propagate the exothermic chemical chain reaction. We developed the production process of the NiTi shape memory alloy from the elemental powders using the combustion synthesis method as shown in Fig.2. Various ratios of Ni and Ti powder were mixed, pressed with a cold isostatic press (CIP) and synthesized with the combustion synthesis method. The combustion synthesized NiTi was encapsulated in a steel can and evacuated and sealed, then hot-isostatically pressed (HIP). If the weight of the HIP'ped NiTi was under 10 kg, it was hot-extruded at 900°C and drawn to the 1.0-0.1mm diameter wires. When the weight of HIP'ped NiTi was over 10 kg, it was forged at 900°C as shown in Fig.3 and Fig.4, and then the forged NiTi billet was hot rolled as shown in Fig.5 and drawn into wire as shown in Fig.6. The chemical compositions of the mixed powder, combustion synthesized NiTi and the drawn wire were examined. The transformation temperatures (A_s , A_f , M_s , M_f) of each wire were measured by differential scanning calorimetry (DSC) and electrical resistance. The mechanical properties of these wire were also measured.

RESULTS AND DISCUSSION

The weight of the mixture of Ni and Ti powder for the combustion synthesis method was varied from 50 g to 100 kg in the present experiments. The combustion synthesis method to produce the NiTi shape memory alloy was successful in all weights of the powder mixtures. The oxygen content of each combustion synthesized NiTi was less than 400 ppm. Fig.7 shows the added Ni content and the found Ni content in the mixed powder and in the combustion synthesized NiTi. The found Ni content against the added Ni content exhibited a good linear relationship. This fact indicates that we can predict the chemical compositions of the products accurately. Fig.8 shows an example of the differential scanning calorimetry (DSC) chart and the transformation temperatures of the NiTi shape memory wire produced by this process. Fig.9 shows the Ms temperatures of the present experimental NiTi wires measured with the DSC method and electrical resistance method compared with the reference of a conventionally produced NiTi. The Ms temperatures of the combustion synthesized and drawn NiTi wires are in good agreement with that of the conventional NiTi.

Fig.10 shows the result of a tensile test of the superelastic 1.0 mm diameter NiTi wire with high Ni content produced with the combustion synthesis process. The Ms temperature of the wire was 181 K. The loaded and unloaded stress-strain curves exhibit good superelastic behavior. From these experimental results, the

manufacturing process including the combustion synthesis method shows good potential for producing the NiTi shape memory alloy from the elemental powders.

CONCLUSIONS

We propose a new production process of shape memory alloy from the elemental powder in the present paper. The process is probably the first successful trial to produce NiTi wire, tube and sheet from elemental powders. The mechanical properties and the shape memory effect of the wire are similar to the conventionally produced NiTi wire. We have started the mass production of the NiTi shape memory alloy with this process including the combustion synthesis method and supplying them to the market.

REFERENCES

1. Y. Kaieda, M. Otaguchi, O. Odawara, M. Nakamura and S. Shite, presented at the SINTERING '87, Tokyo (to be published).
2. Y. Kaieda, M. Otaguchi and N. Oguro, presented at 1988 MRS International Meeting on Advanced Materials, Tokyo (to be published)

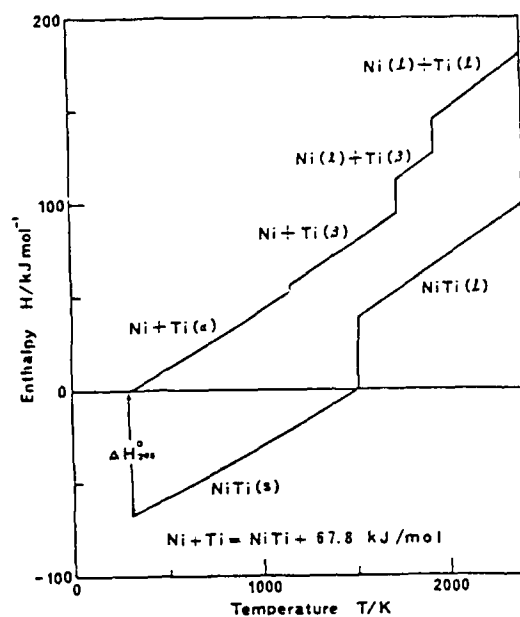


Fig. 1 Change in enthalpy of Ni, Ti and NiTi and heat of formation of NiTi.

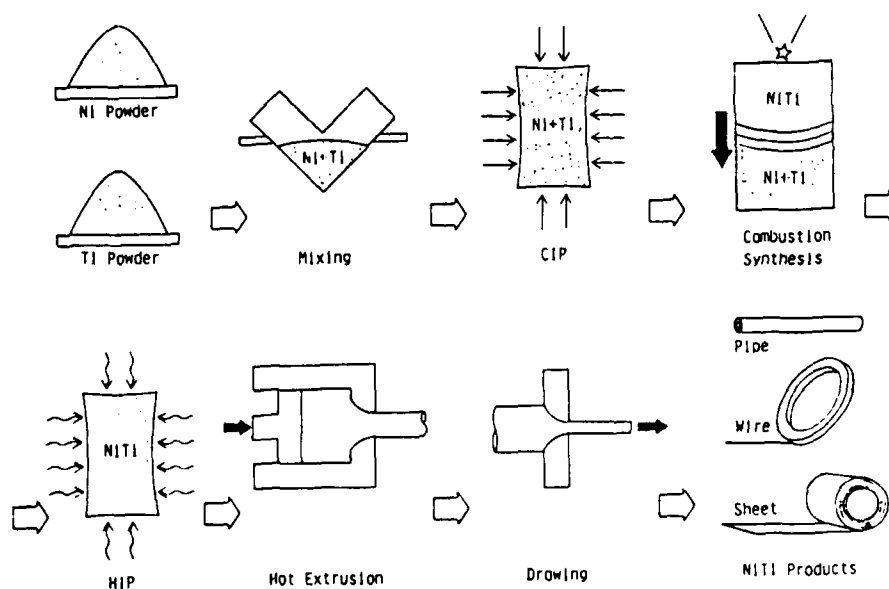


Fig. 2 Flow chart of the production process including the combustion synthesis of NiTi from the elemental powder.

MB



Fig. 3 Hot forging of 70 kg combustion-synthesized and HIP'ped NiTi.



Fig. 4 Forged bar of NiTi. The weight of the bar is 70 kg.

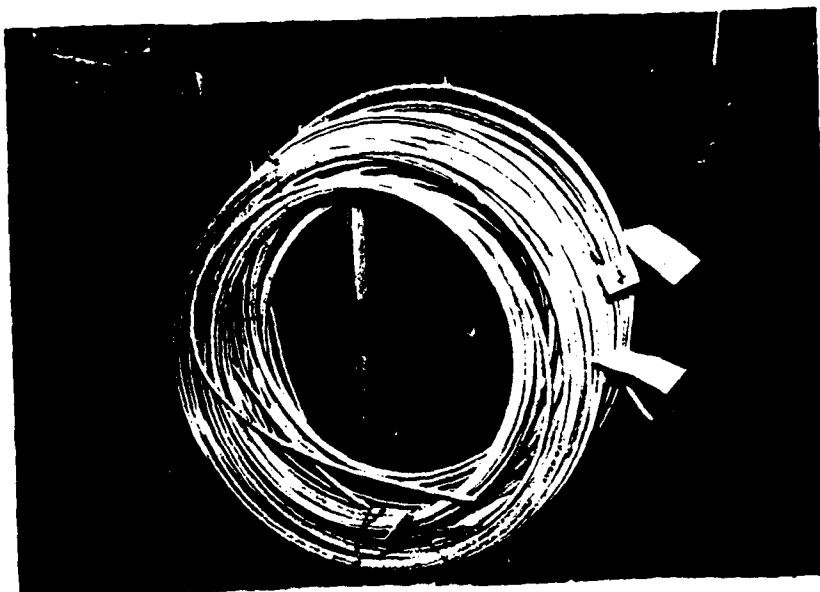


Fig. 5 Hot rolled coil of NiTi after forging. The diameter of the bar is 9.5 mm. The weight of the coil is 70 kg.



Fig. 6 The NiTi shape memory alloy produced with the present process including combustion synthesis. From left to right HIP'ped ingots, tube, sheet and wires.

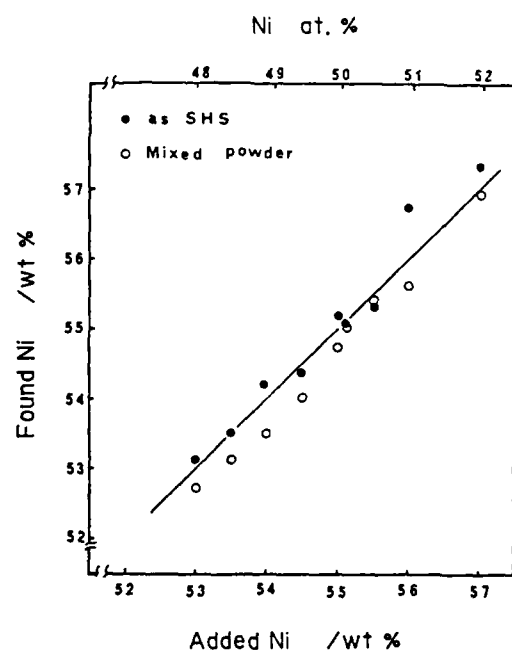


Fig. 7 Found Ni content in the mixed powder and combustion-synthesized NiTi, against added Ni content.

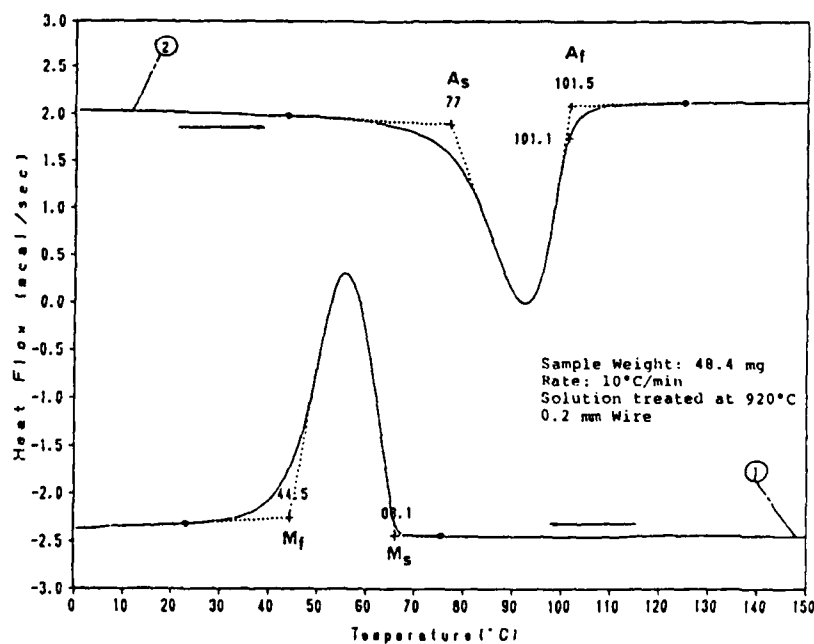


Fig. 8 An example of the differential scanning calorimetry (DSC) chart and the transformation temperatures.

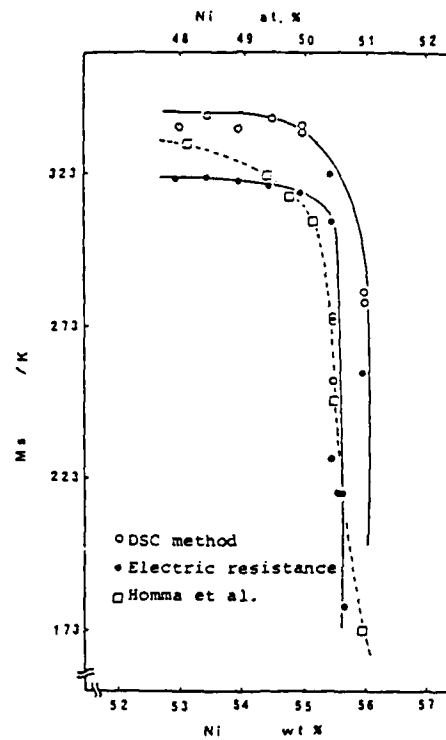


Fig. 9 Ms temperature of NiTi wire produced by the present process against Ni content.

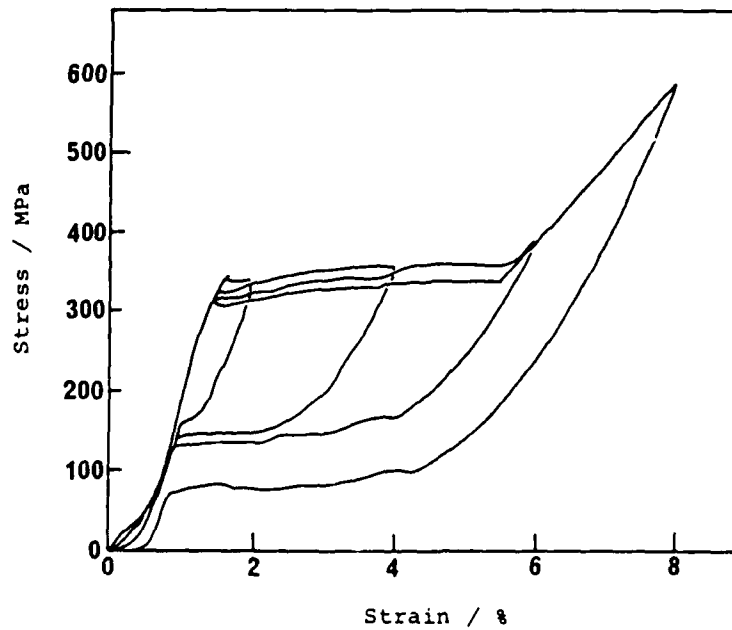


Fig. 10 Stress-strain curves of the superelastic NiTi wire having 181K of Ms.

COMBUSTION SYNTHESIS OF NICKEL ALUMINIDES

B. H. Rabin¹, A. Bose² and R. M. German²

¹Materials Technology Group
Idaho National Engineering Laboratory
P. O. Box 1625, Idaho Falls, ID 83415-2218, USA

²Materials Engineering Department
Rensselaer Polytechnic Institute
Troy, NY, 12180-3590, USA

Abstract

Nickel aluminides near the Ni_3Al stoichiometry were fabricated by combustion synthesis of mixed elemental powders. Densification mechanisms and the effects of powder and process variables on sintered density were studied. Densification was controlled by the amount and distribution of the transient liquid phase which forms during rapid exothermic heating. Density of the combustion product is sensitive to aluminum content, aluminum to nickel particle size ratio, heating rate and atmosphere. Through careful control of these variables it is possible to fabricate near full density alloys in very short times. Mechanical properties of the materials appear promising and a variety of unique microstructures are possible.

Keywords: exothermic, densification, transient liquid.

Introduction

Alloys based upon the compound Ni_3Al possess an attractive combination of mechanical and physical properties which makes them ideal candidates for a number of high temperature applications [1]. Of the available processing routes, powder metallurgy is proving to be an effective method for producing high performance, near net shape intermetallic parts [2].

Typically, powder metallurgy fabrication of intermetallics involves consolidation of prealloyed powders via hot isostatic pressing or hot extrusion. This approach, although

successful, is time and energy intensive, involving considerable expense. As an alternative, combustion synthesis of intermetallics offers several advantages including the use of elemental powders, short processing times and low energy input (see reviews in 3 and 4). In spite of these attributes, problems such as porosity and lack of process control have prohibited widespread use of combustion methods.

To realize the potential of this novel processing technique, a deeper understanding of the factors which control densification and microstructural development is required. Toward this goal, we summarize here our previous findings [5,6] concerning fabrication of the intermetallic compound Ni_3Al . It is anticipated that the mechanisms of densification in this system have a generic applicability and will prove useful for predicting and controlling behavior in other intermetallic systems.

Experimental

The characteristics of the powders used are listed in Table 1. Powders were mixed in a turbula mixer for about 30 min and then pressed into green compacts 12 mm in diameter by approximately 6 mm high using a compaction pressure of 300 MPa and zinc stearate as a die wall lubricant. Green densities were near 70% of theoretical.

Combustion synthesis was carried out in a horizontal tube furnace with either dry hydrogen, dry argon, or vacuum of 7×10^{-3} Pa as the sintering atmosphere. The maximum temperature studied was 750°C and the heating rate was varied between 3 and 30 K/min. Holding time at the maximum furnace temperature was 15 min.

The combustion process was monitored by differential thermal analysis and dilatometry. After sintering, samples were analyzed for density and selected mechanical properties. Microstructural characterization was performed using optical metallography, x-ray diffraction and electron microscopy.

Results

Figure 1 shows a plot of shrinkage versus temperature along with a differential thermal analysis scan obtained by heating a stoichiometric Ni_3Al powder compact (Ni-13.3 wt.% Al). During heating there is an initial expansion of the compact; above 400°C gradual shrinkage begins. Examination of samples quenched from these temperatures indicated that the intermetallic compounds NiAl_3 and Ni_2Al_3 had formed

by solid state reaction at the nickel-aluminum interparticle contacts, in agreement with previous reports [7]. A large exothermic reaction begins at a temperature near 600°C. Within seconds the compact temperature rises to over 1300°C. At the onset of the large exotherm, the compact undergoes a very rapid (less than 0.5 s) expansion of a few percent followed immediately by rapid shrinkage. The total time between the onset of the exothermic reaction and the completion of densification was less than 3 s; no further densification occurred upon continued heating. The reaction initiation temperature was lower for smaller aluminum particle sizes, faster heating rates and higher green densities.

Figure 2a shows a green compact of a stoichiometric sample containing 15 μm aluminum powder. The unetched structure after heating at 30 K/min in vacuum, shown in Figure 2b, contains a small amount of porosity and a second phase tentatively identified as Ni_5Al_3 by electron microprobe analysis. Figure 2c shows the microstructure after etching; an equiaxed grain structure is apparent with a grain size of approximately 30 μm . After annealing at 1350°C for 1 h, transmission electron microscopy confirmed that the sample was composed of single phase, ordered Ni_3Al . Chemical analysis of the combustion synthesized material gave the composition as 12.2% Al, 87.6% Ni, with 0.02% Fe, 0.01% Si, 482 ppm O and 420 ppm C.

Initial experiments [5,6] showed the highest sintered densities were obtained in vacuum using the highest heating rate investigated, 30 K/min, regardless of the aluminum particle size or stoichiometry. Therefore subsequent densification studies were carried out under these conditions. The effect of aluminum particle size on porosity was studied for the Ni_3Al stoichiometry. The best densification was achieved with an intermediate aluminum particle size of 15 μm , giving under 3% porosity in the product.

The effect of stoichiometry was investigated using 10 μm aluminum powder; the results are shown in Figure 3. For alloys which are hyperstoichiometric in Al, a two phase NiAl - Ni_3Al microstructure is obtained. When the aluminum content was greater than about 14% the alloys did not show improved densification, rather the compacts

exhibited slumping as a result of excess liquid phase formation. Alloys with less than about 12.5% Al show high porosity and unreacted nickel in the microstructure.

Discussion

Figure 4 is a schematic diagram of the events which take place during combustion synthesis of Ni_3Al . During heating, solid state diffusion leads to the formation of Al-rich intermetallic compounds at the interparticle contacts. Due to the exothermic nature of the solid state reactions, the lowest eutectic temperature of 640°C is reached locally, thus initiating the combustion reaction before the furnace temperature reaches the melting point of aluminum. Once a small amount of eutectic liquid forms, rapid dissolution takes place and solid Ni_3Al precipitates directly from the saturated liquid. Initial compound formation generates heat which further accelerates the reaction leading to extensive liquid formation. The liquid quickly spreads throughout the structure and compound formation continues until the reactants are consumed.

The observation that highest sintered densities were obtained in vacuum can be attributed to the negative influence of entrapped gases on densification. Volatilized species and the sintering atmosphere can limit densification when they are sealed off inside closed porosity. Vacuum aids in the removal of gases from the compact, thus allowing higher densities to be achieved.

All other densification results can be explained by the process of transient liquid phase sintering for which the sintered density is determined by the amount, distribution and duration of a wetting liquid [8]. These factors are strongly influenced by material and processing variables as explained below.

Higher densities are achieved with rapid heating rates because less interdiffusion takes place in the solid state, allowing more liquid phase to form at the eutectic temperature. Higher liquid contents are also achieved with greater aluminum concentrations in the starting mixture. For less than about 12.5% Al there is insufficient liquid present to provide an interconnected liquid structure and, in the absence of long range capillary action, low sintered densities result. For Al contents greater than 13.3% there is an excess of liquid over that required to form Ni_3Al , and slumping and shape loss are observed.

Long range capillary action is promoted by an interconnected network of liquid. At the stoichiometric composition, aluminum constitutes 34 vol% of the solid structure. For this percentage, an interconnected network is predicted for a particle size ratio of at least 2.4:1 (major phase diameter to minor phase diameter) [9]. In the green compact the nickel agglomerates had an intercept length of about 30 μm , or an actual diameter of 45 μm . Thus, an aluminum particle size of less than 19 μm is required to form an interconnected liquid structure at the eutectic temperature. This value is in agreement with the observation that 15 μm aluminum gave the best densification. Figure 5 shows the role of minor phase connectivity in promoting long range densification. This concept is particularly important for combustion synthesis where densification is primarily dependent upon the capillary action of a liquid which persists for only a few seconds. In contrast to conventional sintering treatments, maximum furnace temperature (above the initiation temperature) and time at temperature have no influence on densification.

Finally, it is noteworthy that combustion synthesis offers considerable flexibility in terms of alloying and microstructure control. For example, it is possible to add boron or other additions directly to the reactant powder mixture. As well as their effects on the alloy properties, these additions will influence the densification behavior through their effects on the transient liquid phase. We have also investigated using the HIP to assist densification, particularly as a method of preparing nickel aluminide matrix composites [10].

Initial assessments of the mechanical properties of the combustion synthesized materials are promising. For example, a sample of Ni_3Al containing 0.06% boron fabricated using HIP to assist densification gave a room temperature tensile strength of 722 MPa and a ductility of 10% in the as-prepared condition. Future studies will aim to improve and characterize properties with emphasis on metal matrix composites. In addition, studies are aimed at extending the current understanding to other intermetallic systems.

Conclusions

Combustion synthesis of nickel aluminides has been shown to be a viable alternative to current powder metallurgy fabrication approaches. Near full density alloys have been

prepared directly from elemental powders by careful control of material and process variables. The effects of several variables on sintered density were determined and the results are explained by the role of the transient liquid phase in promoting capillary induced densification.

Acknowledgments

This research was performed at Rensselaer Polytechnic Institute under sponsorship of the Defense Advanced Research Projects Agency through the Office of Naval Research. The manuscript was prepared with funding from the Department of Energy under DOE contract No. DE-AC07-76ID01570. The authors thank D. Sims and B. Lograsso for their assistance with this work.

References

1. C. C. Koch, C. T. Liu and N. S. Stoloff (eds.), High-Temperature Ordered Intermetallic Alloys, Materials Research Society Symposium Proceedings, vol. 39, Materials Research Society, Warrendale, PA, 1985.
2. W. M. Schulson, "Structure, Properties and Potential Applications of Intermetallic Compounds Produced from Powders," Intern. J. Powder Met., vol. 23, 1987, pp. 25-32.
3. W. L. Frankhouser, K. W. Brendly, M. C. Kieszek and S. T. Sullivan, Gasless Combustion Synthesis of Refractory Compounds, Noyes Publications, Park Ridge, NJ, 1985.
4. Z. A. Munir, "Synthesis of High Temperature Materials by Self-Combustion Methods," Ceram. Bull., vol. 67(2), 1988, pp. 342.
5. D. M. Sims, A. Bose and R. M. German, "Reactive Sintering of Nickel Aluminide," Prog. Powder Met., vol. 43, 1987, pp. 575-596.
6. A. Bose, B. H. Rabin and R. M. German, "Reactive Sintering Nickel Aluminide to Near Full Density," Powder Met. Int., vol. 20(3), 1988, pp. 25-30.
7. K. A. Philpot, Z. A. Munir and J. B. Holt, "An Investigation of the Synthesis of Nickel Aluminide," J. Mater. Sci., vol. 22, 1987, pp. 159.
8. R. M. German, Liquid Phase Sintering, Plenum Press, New York, NY, 1985.
9. D. M. Biggs, Metal Filled Polymers, S. K. Bhattacharya (ed.), Marcel Dekker, New York, NY, 1986, pp. 165-226.

10. A. Bose, B. Moore, R. M. German and N. S. Stoloff, "Elemental Powder Approaches to Ni_3Al Matrix Composites," J. Metals, vol. 40(9), 1988, pp. 14-17.

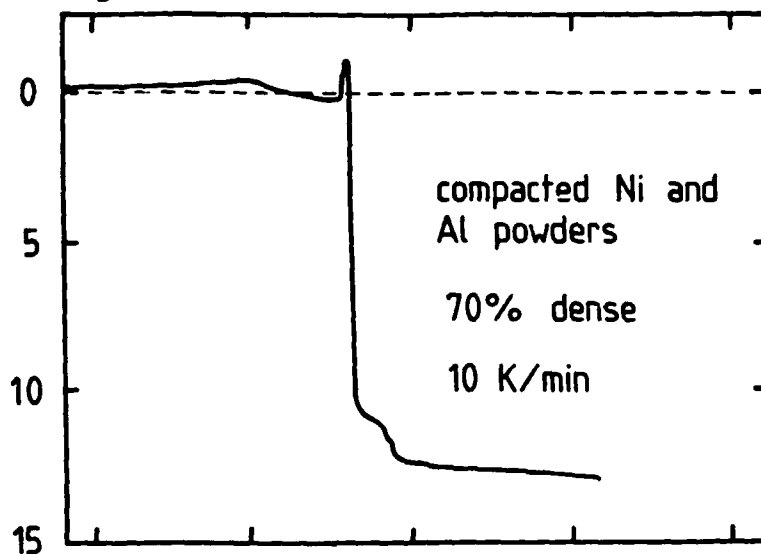
List of Figures

- Figure 1. A plot of shrinkage versus temperature for a stoichiometric Ni_3Al sample heated in a dilatometer along with a typical differential thermal analysis scan.
- Figure 2. Microstructure of Ni_3Al before (a) and after combustion (b) and (c).
- (a) Green compact
 - (b) Unetched sample of Ni_3Al showing a small amount of porosity and second phase
 - (c) Etched sample showing grain structure of Ni_3Al
- Figure 3. The effect of stoichiometry on the final porosity of combustion synthesized nickel-aluminum powder mixtures.
- Figure 4. Schematic diagram showing the sequence of events which take place during heating of a stoichiometric mixture of nickel and aluminum powders.
- Figure 5. Schematic diagram illustrating the particle size effect on capillary induced densification during combustion synthesis.

TABLE 1. NICKEL AND ALUMINUM POWDER CHARACTERISTICS

<u>Property</u>	<u>Nickel</u>	<u>Aluminium</u>
Vendor	INCO	Valimet
Designation	123	H-3, H-10, H-15, H-30 and H-90
Powder type	carbonyl	gas atomized
Purity, %	99.99	99.7
FSSS size, μm	2.8	3, 10, 15, 30, 95
Apparent density, g/cm^3	2.2	---
Major impurities, ppm	Ca = 10 Fe = 30	Fe = 1200 Volatiles = 200

shrinkage, %



heat flow
mJ/s

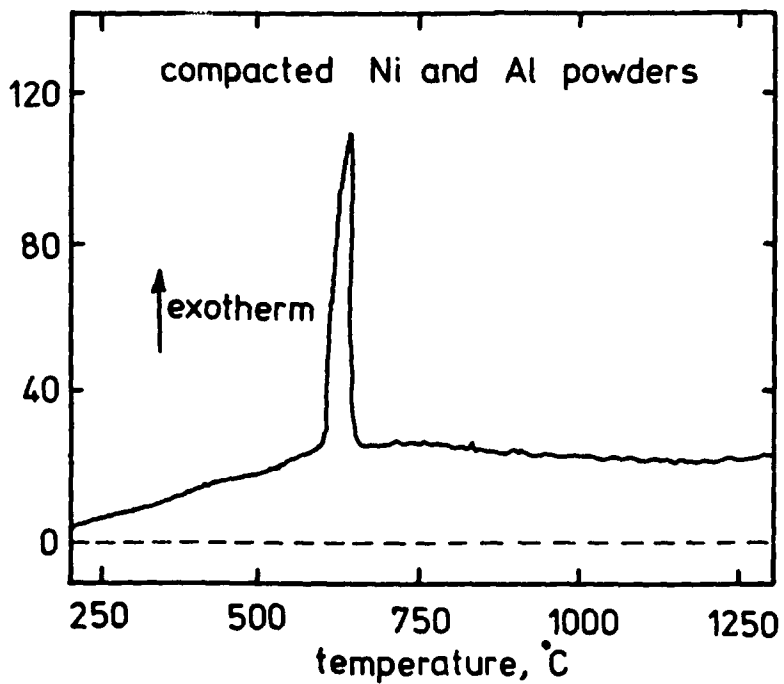


Figure 1

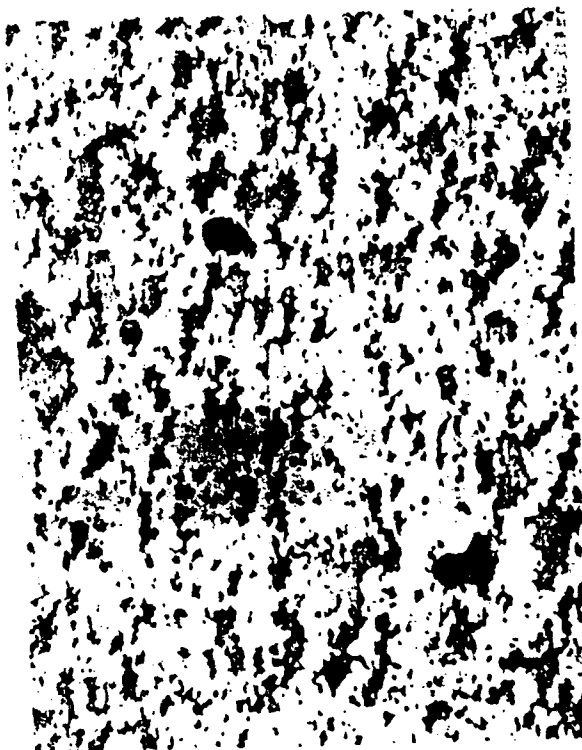


Fig. 2a



Fig. 2b

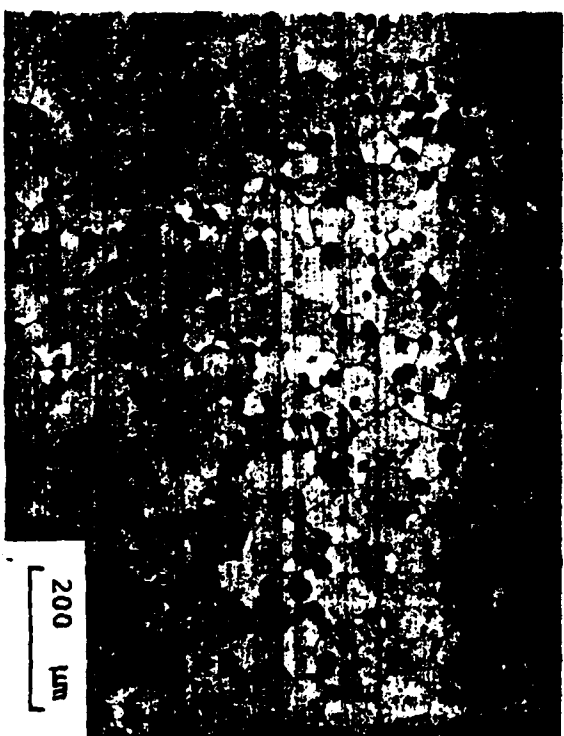


Fig. 2c

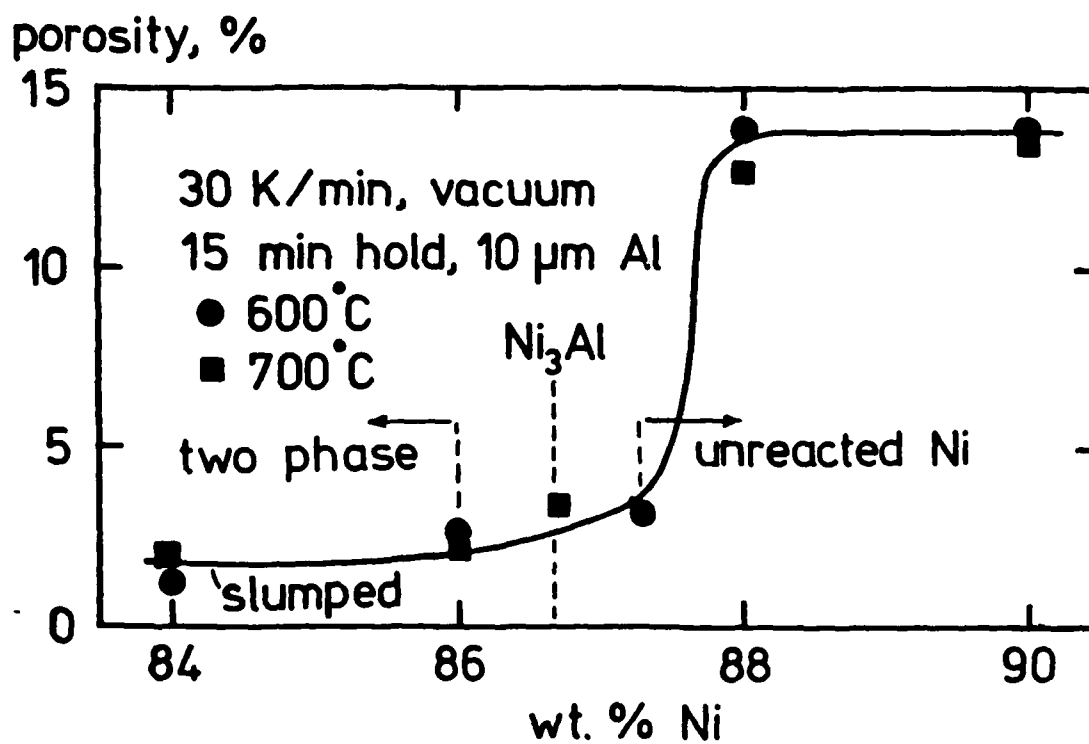


Fig. 3

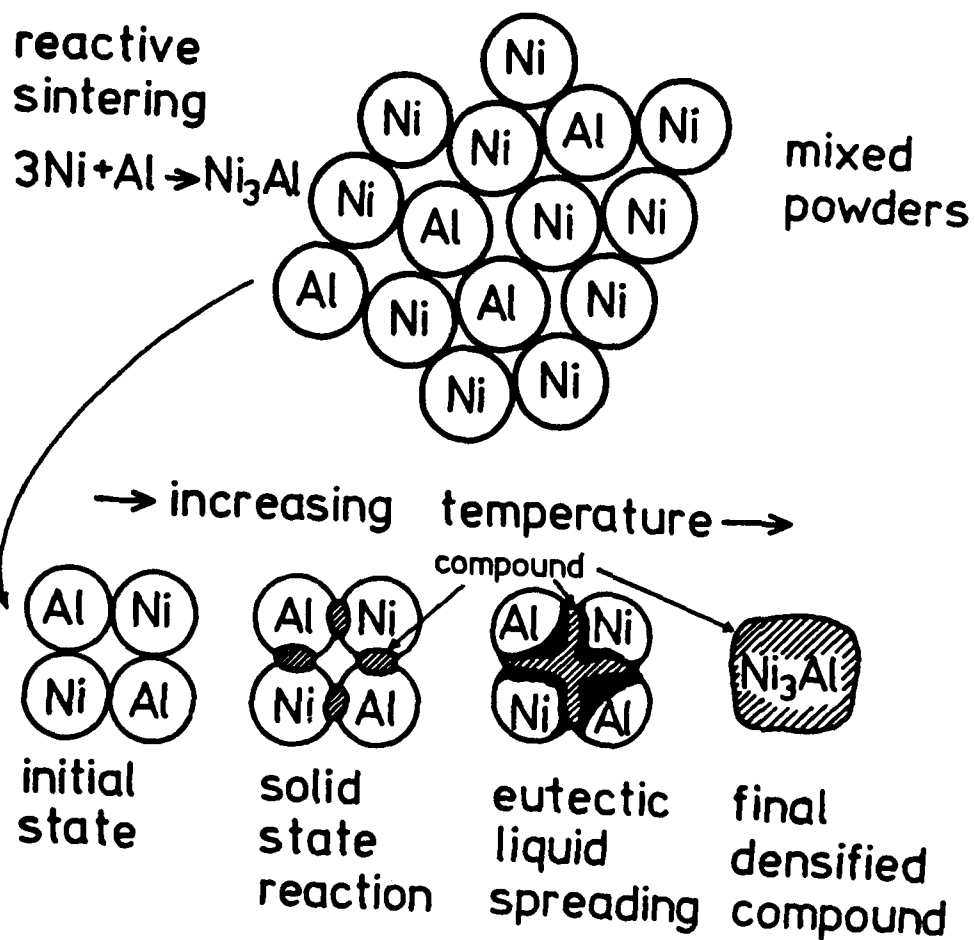


Fig. 4

202

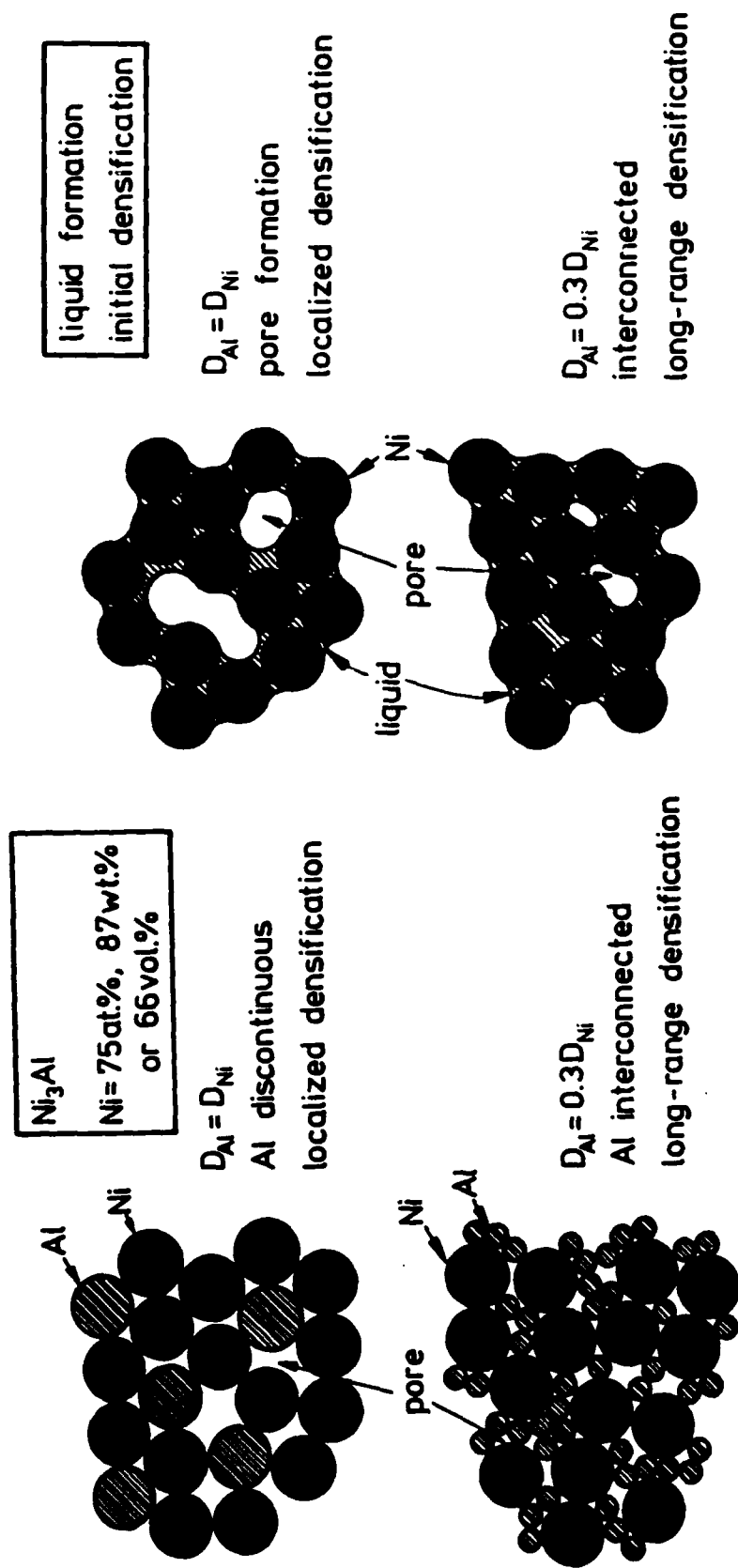


Fig. 5

Self Propagating High Temperature Synthesis (SHS) of NiTi Intermetallics

*H.C.Yi and +J.J.Moore

*Department of Chemical & Materials Engineering
University of Auckland, Auckland, New Zealand

+Department of Metallurgical & Materials Engineering
Colorado School of Mines, Golden, Colorado, 80401

Introduction

The near equiatomic nickel-titanium intermetallic compound (Figure 1) is an established shape memory alloy¹ (SMA) and is normally produced using conventional melting techniques. Recently, combustion synthesis, or self-propagating high temperature synthesis (SHS), has been used²⁻⁴. In the current investigation the thermal explosion mode of SHS has been used to successfully synthesize the NiTi intermetallic compound⁴ via the liquid phase.

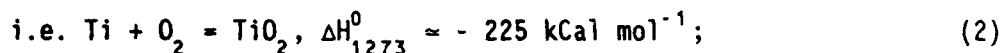


where (s) and (l) refer to solid and liquid states respectively. A "trigger" mechanism associated with TiO_2 formation was investigated by conducting the synthesis reaction in air was investigated and the shape memory characteristics of the alloy were identified after hot rolling.

2. Experimental Procedure

Irregularly shaped Ti powder ($<44\mu\text{m}$) and spherical Ni powder (44-150 μm), in equiatomic stoichiometry, were tumbled in a mechanical shaker for 5-10 minutes and pressed into cylindrical 7.94 mm diameter pellets 67 \pm 2% theoretical density. The pellets were heated at different rates in a tube furnace set at different temperatures i.e. 873-1573K, for heating rates in excess of 300 K/min, or using a programmable controller for lower heating rates.

The formation of TiO_2 from Ti in air is highly exothermic at 1273K.



equilibrium partial pressure of $\text{O}_2 = 10^{-40}$ at.

The use of this as a "trigger" reaction was investigated as was the dilution of the reactants with previously reacted NiTi ($<120\mu\text{m}$) and Ni particle size on Tig and Tc.

Experimental Results

Figure 2 schematically compares the combustion reaction conducted in (a) air and (b) argon. In both cases the maximum combustion temperature, Tc, was greater than the melting point, Tcr, of NiTi, while both the ignition (Tig) and combustion (Tc) temperatures were lower in air. Figure 3 shows the effect of heating rate on Tc and Tig for both argon and air atmospheres. At heating rates below 500 Kmin^{-1} the Tc values (1628K) in air or argon were approximately the same. At higher heating rates, Tc in argon, (1773K), was 150K higher than in air. The Tig (argon) remained relatively constant (1183K), whereas Tig (air) decreased linearly as heating rate increased.

No reaction occurred in air below 823K, i.e. $<300\text{K/min}$, or heating at 20 K/min between 298-1200K, suggesting that a minimum critical heating rate is required to ignite reaction (1) in air. From Figure 4, Tc and Tig were independent of Ni particle size, ($20\mu\text{m}$ - $130\mu\text{m}$). This indicates that heat dispersion was not affected by Ni particle size, the heat needed to generate reaction (1) is a constant, and Tig (1183K) is an intrinsic value for the Ni + Ti synthesis reaction in argon. Tc decreased sharply with dilutions greater than 12% of the charge weight

and no reaction occurred at dilutions of more than 35%.

The NiTi product (Figure 5) is mainly NiTi parent phase (white) with a dendritic second phase of NiTi_2 (dark). Increased porosity was evident in reactions using a NiTi diluent. The NiTi_2 was present in a branch-like morphology and more evenly distributed in the non-diluted reacted sample. Figures 6 and 7 show the exothermic nature of reaction (2). The maximum temperature obtained by the Ni + Ti pellet (Figure 7) was 1081K, 208K higher than the furnace temperature. X-ray diffraction data on the products indicated a mixture of Ti + Ni + TiO_2 , with the TiO_2 as a thin outside layer. Also, heating the Ni + Ti pellet between the Tig(air) and Tig(argon), (Figure 3), with an argon flow rate of 3 litre/min. no reaction took place until the pellet was pulled out of the furnace into the air.

The microstructure of NiTi synthesised in air (Figure 8) and argon are similar, except that in the latter product some of the NiTi_2 is in a coarser dendritic form. A eutectic NiTi + Ni_3Ti structure (Figure 8b and c) is evident towards the outer edge with NiTi_2 mainly present between the NiTi and the eutectic areas. Table 1 lists the Tig, Tc and shape recovery range for pellets synthesised with different Ni particle size ranges and Ti powder of $-44\mu\text{m}$. The twinned domains of the shape memory R-phase were observed under polarised light (Figure 9) immediately after the reaction was complete.

The solidified alloys were subsequently hot-rolled at approximately 800°C into plates of 0.5mm thickness and then annealed at 600°C for 2

hours followed by air cooling. These specimens were subsequently deformed into an arc at 0°C and the shape-recovery temperatures were determined during reheating. These results are given in Table 1 and Figure 10 where l_T , l_0 and l_u are chord lengths of the arc at temperatures T, 0°C and total length of the sample respectively.

$$\%R = \frac{l_T - l_0}{l_u - l_0} \times 100\% \quad (3)$$

The morphology of the four variants of R-phase^{5,6} were clearly observable after hot rolling and annealing (Figure 11, indicated by arrow). An increased amount of NiTi₂ was thought to be the reason for poor hot ductility in some samples (Table 1, Sample 1).

TABLE 1. Characteristics of Reactants and Products
After Hot rolling at Approximately 800°C.

Sample No.	Ni particle size (μm)	T _{ig} (°C)	T _c (°C)	Shape-recovery range °C	Comments
1	125-149*	880	1482	30-95	Difficult to hot roll (increased amount of NiTi ₂) Easier to hot roll than sample 1
2	90-125*	910	1496	17-45	
3	10-20 ⁺	912	1470	45-85	

* by sieve analysis

+ roughly estimated by optical microscopy

Discussion

In the thermal explosion mode, the whole pellet is heated by an ambient heating source and as such is more likely to provide adiabatic conditions than the combustion mode. This provides a possible explanation as to why the T_c obtained in the present investigation was 260K higher than that reported by Itin et al^{2,3,7,8} who used the combustion mode and who found T_c to be more dependent on process

factors (e.g. diameter⁹, density of pellets).

Assuming adiabatic conditions using the thermal explosion mode for reaction (1) (T_c adiabatic temperature):

$$-\Delta H_f^0(T_{ig}) = \int_{T_{ig}}^{T_m} C_{p_s}(\text{NiTi})dT + \Delta H_m(\text{NiTi}) + \int_{T_m}^{T_c} C_{p_l}(\text{NiTi})dT \quad (4)$$

where $\Delta H_m(\text{NiTi})$ is the heat of fusion and $C_{p_s}(\text{NiTi})$ and $C_{p_l}(\text{NiTi})$ ¹⁰ are the heat capacities for NiTi solid and liquid respectively. Since the decrease of T_{ig} in air (Figure 3) must be due to heat generated by reaction (2) the different amounts of TiO_2 needed to initiate or "trigger" reaction (1) at different heating rates can be calculated. The total amount of TiO_2 formed is α , where:

$$\alpha = \alpha_1^d + \alpha_2^r \quad (5)$$

in which α_1^d is the fraction of TiO_2 whose ΔH_f is dissipated into the furnace atmosphere and α_2^r the heat used to initiate reaction (1). Assuming adiabatic conditions and constant T_c (1628K), the theoretical T_{ig} in air is 1019K (Figure 12¹⁰). This corresponds to a certain critical heating rate, T_1 , beyond which the heat generated by reaction (2) is transferred to the pellet and can be used to "trigger" reaction (1). Heating rates greater than T_1 lower T_{ig} , air, in the direction indicated in Figure 12 which also gives the corresponding $\Delta H_f(\text{TiO}_2)$. At heating rates lower than T_1 some of the heat generated by TiO_2 formation is dissipated into the furnace atmosphere.

Thus when $T \gg T_1$, $\alpha_2^r \gg \alpha_1^d$ and $\alpha \approx \alpha_2^r$
 when $T = T_1$, $\alpha_1^d \approx \alpha_2^r$ and $\alpha = \alpha_1^d + \alpha_2^r$
 when $T \ll T_1$, $\alpha_1^d \gg \alpha_2^r$ and $\alpha \approx \alpha_1^d$, no reaction (1) occurred

From Figure 12 at any $T_{ig} < 1019K$ in air:

$$\Delta H_f(TiO_2, T_{ig}) + \Delta H_f(NiTi, T_{ig}, air) = \Delta H(NiTi, T_c, air) \quad (6)$$

i.e.

$$\left[\begin{array}{c} \text{heat generated} \\ \text{by formation of} \\ TiO_2 \text{ at } T_{ig} \end{array} \right] + \left[\begin{array}{c} \text{heat generated by} \\ \text{formation of NiTi} \\ \text{at } T_{ig} \text{ in air} \end{array} \right] = \left[\begin{array}{c} \text{Total heat generated} \\ \text{by synthesis of} \\ \text{NiTi to reach } T_c \end{array} \right]$$

The terms in equation (6) can be calculated by equating equations (4) and (6) and are plotted in Figure 13 for the corresponding heating rate. Substituting equation (5) and (6) gives:

$$\begin{aligned} \alpha_2^r \Delta H_f(TiO_2, T_{ig}) + (1-\alpha) \Delta H(NiTi, T_{ig}, air) &= \Delta H(NiTi, T_c, air) \\ &= \int_{T_{ig}}^{T_m} C_{p_s}(NiTi) dT + \Delta H_m(NiTi) + \int_{T_m}^{T_c} C_{p_l}(NiTi) dT \end{aligned} \quad (7)$$

since $\alpha = \alpha_1^d + \alpha_2^r$, $(1-\alpha)$ can be replaced by $(1-\alpha_1^d - \alpha_2^r)$.

Equations (7) and (5) and Figure 3 can now be used to calculate α_2^r for $T > T_1$ and α_1^d for $T < T_1$, (Figure 14) and T_1 , (673 K/min⁻¹).

From Figure 3, for the condition $T > 600$ K/min, $T_c(Ar) > T_c(air)$ may be due to less Ti being available for reaction (1) owing to TiO_2 formation. This corresponds approximately with T_1 (673 K/min) at which all the TiO_2 generated provides heat to "trigger" the NiTi reaction. Therefore, the value of α (equation 5) remains relatively constant for $T > 673$ K/min, at which rate the pellet is in the furnace for less than a minute prior to ignition. For $T < 500$ K/min produces a decrease in $T_c(Ar)$ probably due to longer pellet heating times and non-adiabatic conditions. Also, the use of commercially pure Ar may explain the decrease in T_c for the lower heating rates in that increased amounts of

Ti are consumed by TiO_2 formation (reaction 2) whose heat of formation was largely dissipated into the furnace atmosphere.

The shape memory characteristics of the NiTi product, after hot rolling at approximately 800°C , indicated some deterioration in both recovery and hot formability as the amount of NiTi_2 phase increased. The eutectic structure ($\text{NiTi} + \text{Ni}_3\text{Ti}$) lies on the Ni-rich side of the equiatomic stoichiometry (Figure 1). Since some Ti is consumed by reaction (2), the combustion synthesis product tended to be Ni-rich at the edges of the sample favouring the eutectic reaction at this position with TiO_2 at the surface and NiTi in the centre. The reason for Ni-lean, NiTi_2 phase between the NiTi and eutectic is not yet clear but may be due to poor powder mixing.

5. Conclusion

A shape memory NiTi intermetallic compound has been produced using the thermal explosion mode of combustion synthesis of Ti and Ni powder pellet mixtures combusted in either air or argon. T_c was lower in air (1628K) than in argon (1773K) but was always higher than the melting point of the NiTi compound. T_{ig} remained constant in an argon (1183K) but decreased on increasing the heating rate in air. This was found to be dependent on the prior formation of TiO_2 , the exothermic nature of which acted as a "trigger" for the NiTi reaction. A thermodynamic formulation was derived to estimate the required amount of TiO_2 needed to "trigger" the NiTi synthesis reaction. The triggering mechanism was more favourable when a certain critical heating rate, T_1 , was exceeded (673 K/min). The shape memory R phase was present in the NiTi

product. The formation of TiO_2 resulted in a thin outer layer of TiO_2 , a central area of NiTi and an intermediate outer layer of eutectic NiTi + Ni_3Ti . Some $NiTi_2$ was also observed in the outer layers of the product and tended to decrease the NiTi ductility.

References

1. W.J.Buehler and R.C.Wiley "Nickel-Base Alloys" U.S. patent 3,174,851, March 23, (1965).
2. V.I.Itin, V.N.Khachin, A.D.Bratchikov, V.E.Gyunter, E.F.Dudarev, T.V.Monasevich, D.B.Chernov, G.D.Timonin and A.P.Paperskii. Sov. Phys. J., 20,1631, (1977).
3. V.I.Itin, V.N.Khachin, V.E.Gyunter, A.D.Bratchikov and D.B.Chernov. Sov. Powd. Metall. Met. Ceram, 22 No.3 (243), 156, (1983).
4. H.C.Yi and J.J.Moore, J. Mat. Sci., in press.
5. S.Miyazaki and C.M.Wayman, Acta Metall., 36, No.1, 181 (1988).
6. H.C.Yi, M.Zhu and D.Z.Yang, Chinese Phys. Lett., 5, No.6 281 (1988).
7. Y.S.Naiborodenko, V.I.Itin and K.V.Savitskii, Sov. Powd. Metall. Met. Ceram. No.7 (91) p562 (1970).
8. V.I.Itin, A.D.Bratchikov, A.G.Merzhanov and V.M.Maslov, Comb. Explo. Shock Waves, 17 p293 (1981).
9. V.M.Maslov, I.P.Borovinskaya and A.G.Merzhanov: Comb.Explo.Shock Wave, 12 p631 (1976).
10. H.C.Yi and J.J.Moore: J.Mat.Sci. in press.

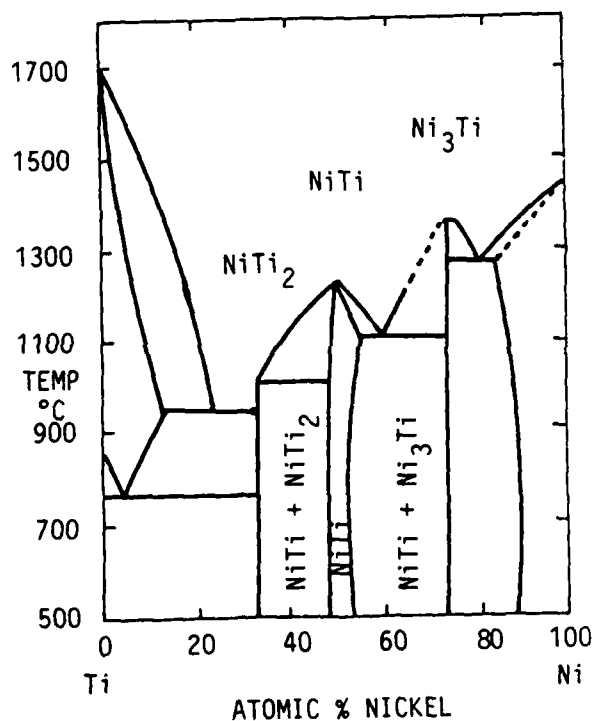


FIGURE 1. NiTi PHASE DIAGRAM

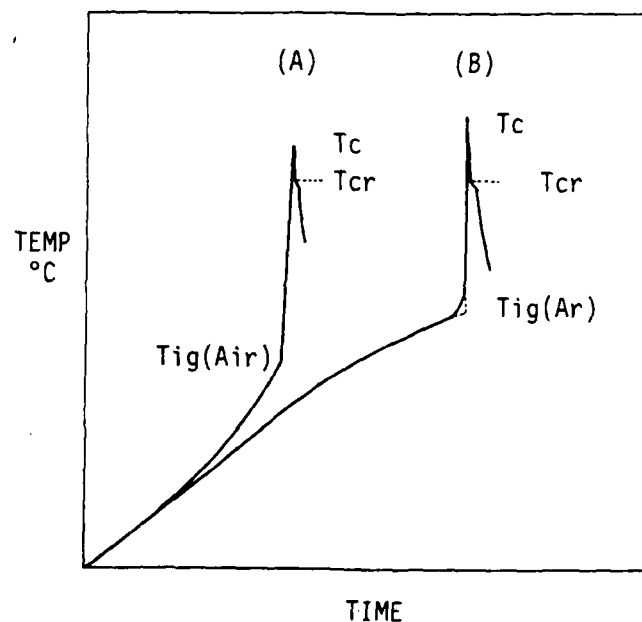


FIGURE 2. COMPARISON OF TEMP.-TIME PLOTS FOR THE COMBUSTION SYNTHESIS REACTION CONDUCTED IN (A) AIR, AND (B) ARGON AT THE SAME FURNACE TEMPERATURE

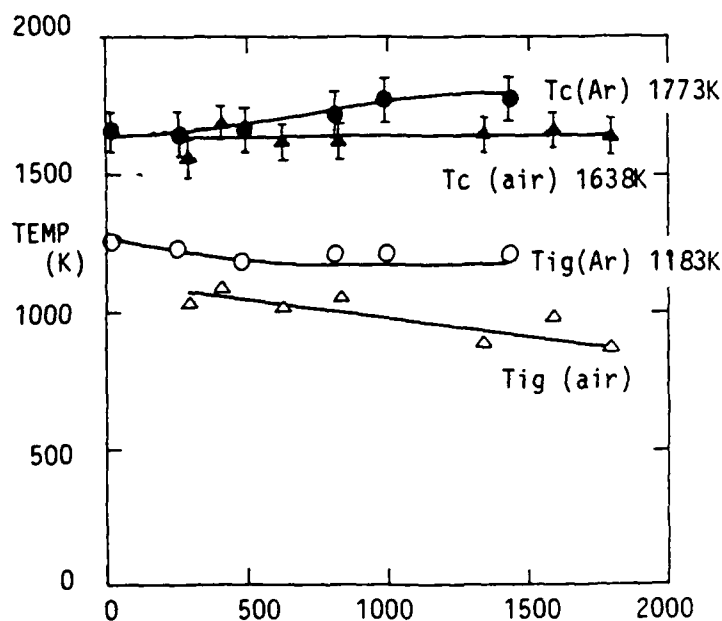


FIGURE 3. EFFECT OF HEATING RATE ON THE COMBUSTION (Tc) AND IGNITION (Tig) TEMPERATURES WHEN COMBUSTION CONDUCTED IN ARGON, (o, ●) AND AIR (Δ, ▲)

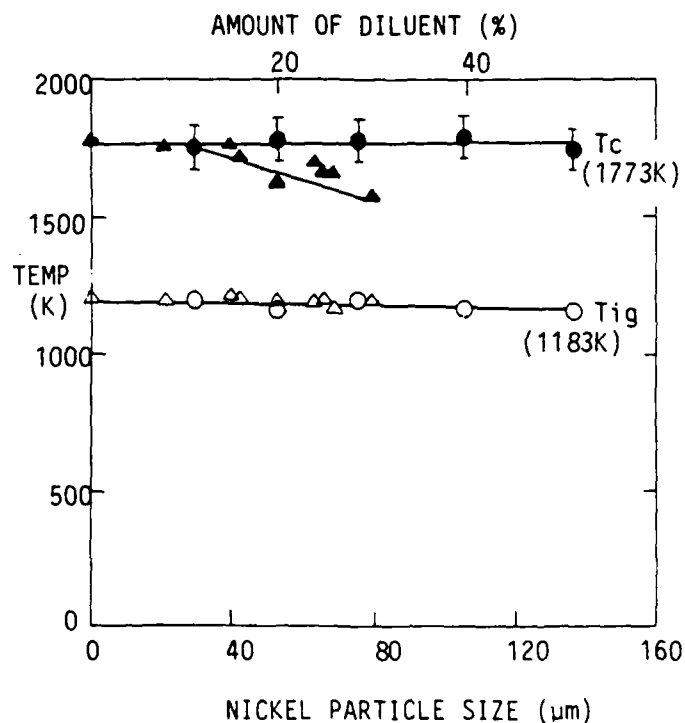


FIGURE 4. EFFECT OF MEAN NICKEL PARTICLE SIZE (o, ●) AND AMOUNT OF DILUTION (Δ, ▲) ON THE COMBUSTION (Tc) AND IGNITION (Tig) TEMPERATURES RESPECTIVELY IN AN ARGON ATMOSPHERE

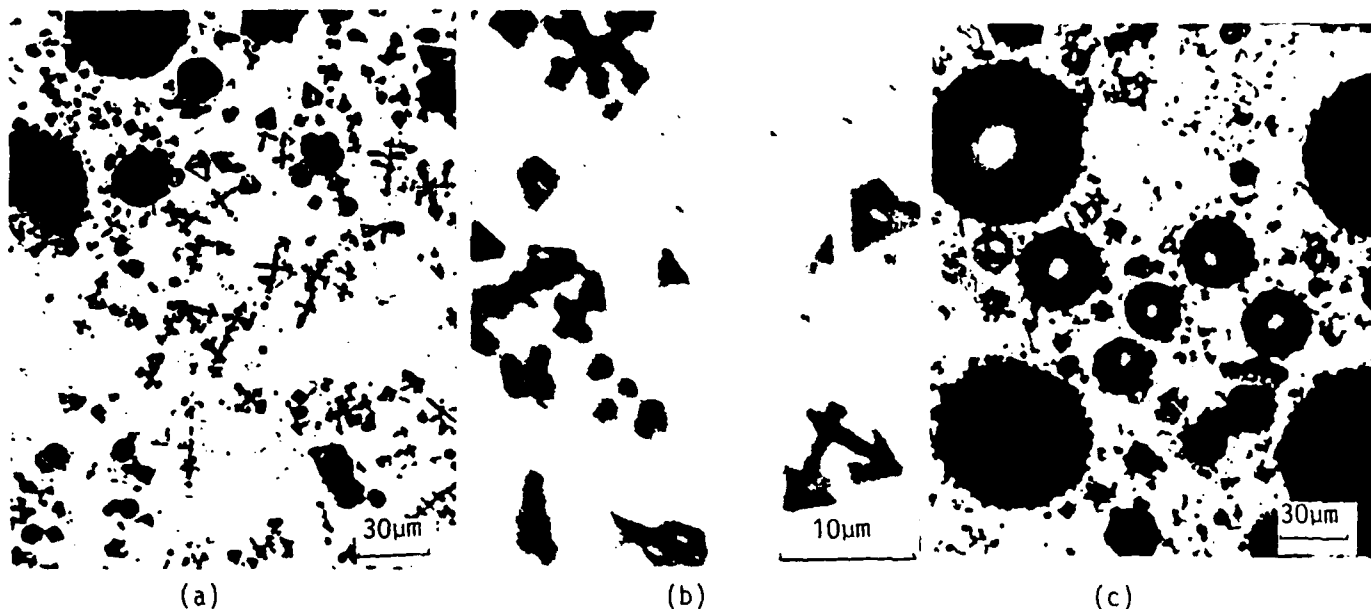


FIGURE 5. TYPICAL OPTICAL (a) AND SEM (b) PHOTOMICROGRAPHS OF NiTi PRODUCT REACTED IN ARGON. THE BLACK PHASE IS NiTi, EXCEPT FOR THE LARGER BLACK AREAS IN (a) WHICH IS POROSITY.

(c) OPTICAL PHOTOMICROGRAPH OF THE DILUTION-REACTED SAMPLE (30% DILUTION) SHOWING A HIGH DEGREE OF POROSITY.

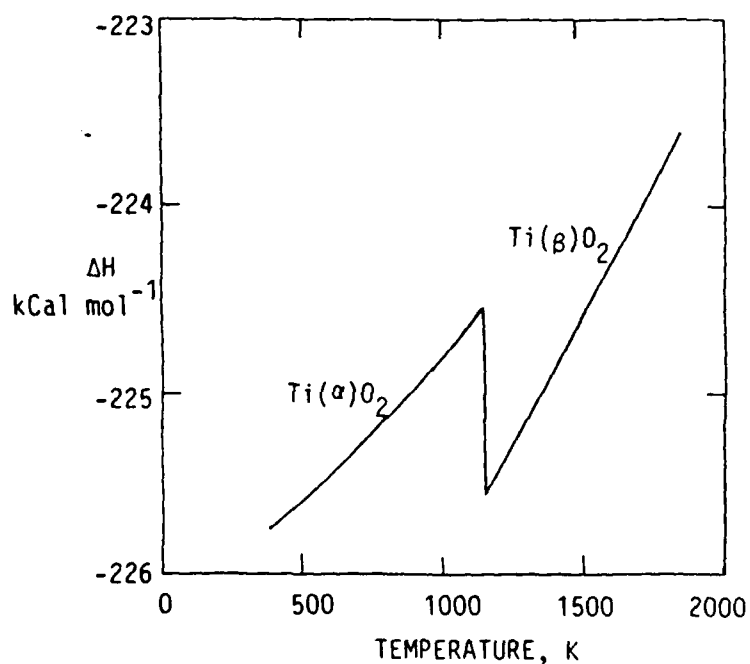


FIGURE 6. CHANGE OF ENTHALPY WITH TEMPERATURE FOR $\text{Ti} + \text{O}_2 \rightarrow \text{TiO}_2$ REACTION (2).

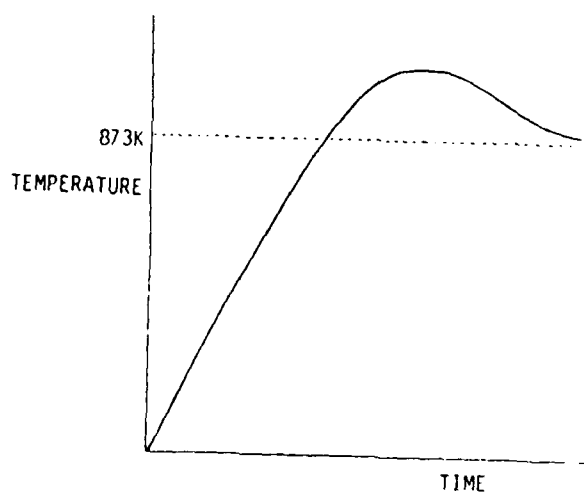
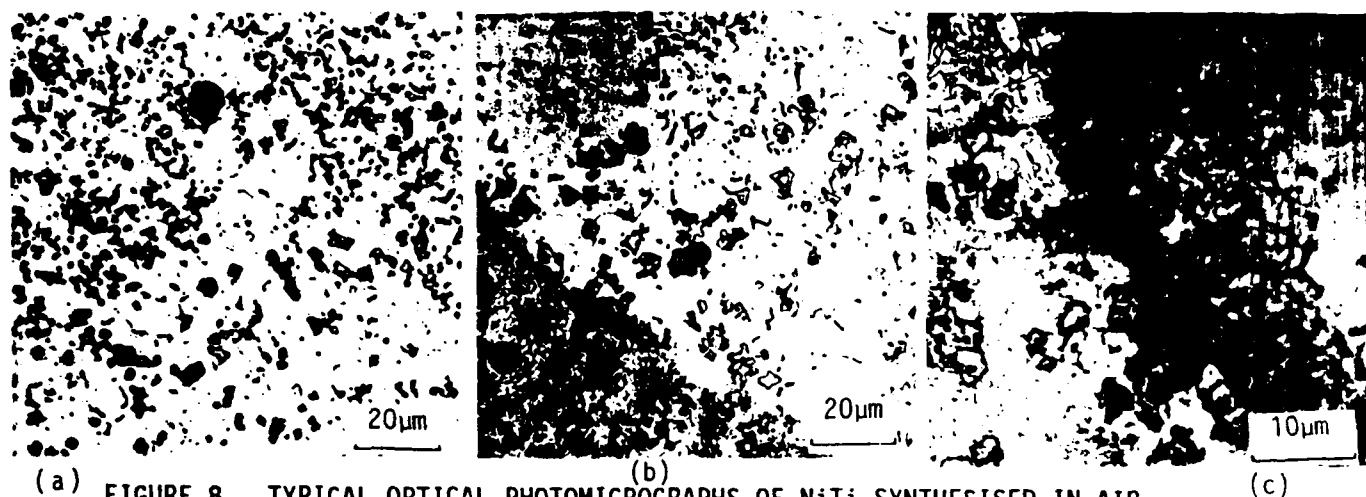


FIGURE 7. THE TEMPERATURE-TIME PLOT FOR HEATING THE Ni + Ti POWDER PELLET WITH THE FURNACE CONTROLLED AT 873K.



(a) FIGURE 8. TYPICAL OPTICAL PHOTOMICROGRAPHS OF NiTi SYNTHESISED IN AIR
(a) CENTRAL REGION OF SAMPLE
(b) AND (c) SAMPLE TAKEN FROM SURFACE REGIONS OF THE PRODUCTS

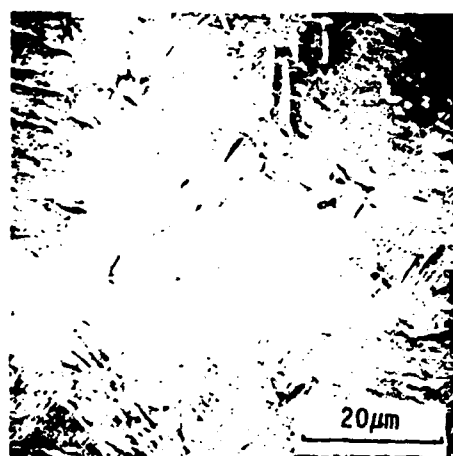


FIGURE 9. PHOTOMICROGRAPH OF SAMPLE 2 (TABLE I) IN AS-CAST STATE.

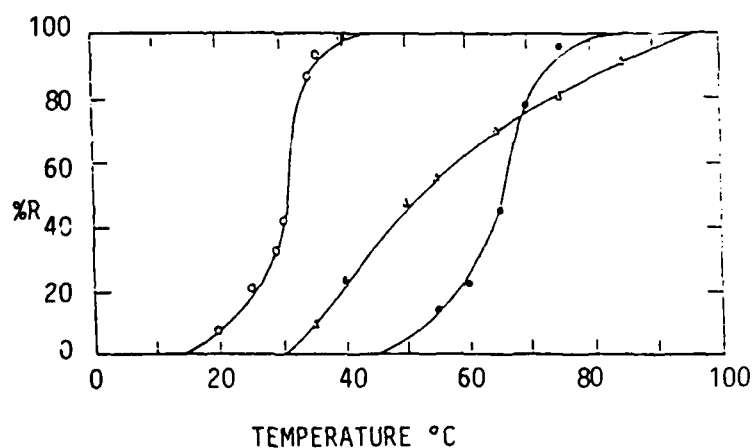


FIGURE 10. EXTENT OF SHAPE-RECOVERY %R AS A FUNCTION OF THE REHEATING TEMPERATURE OF THE HOT-ROLLED SAMPLES.
Δ - SAMPLE 1; ○ - SAMPLE 2;
◻ - SAMPLE 3. (TABLE I)

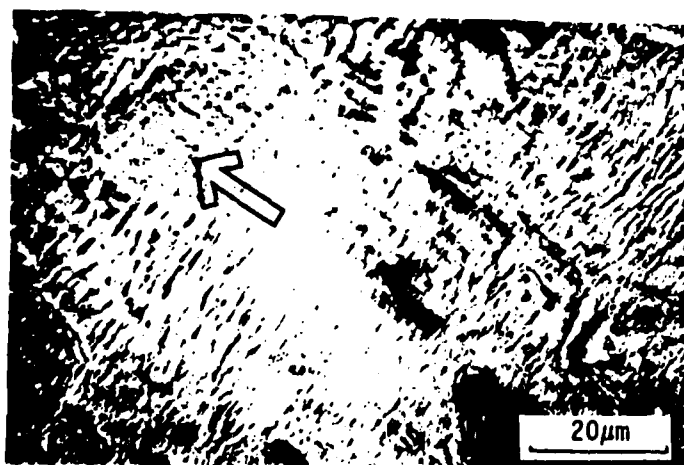


FIGURE 11. PHOTOMICROGRAPH OF SAMPLE 2 (TABLE I), AFTER HOT ROLLING AND ANNEALING TREATMENT.

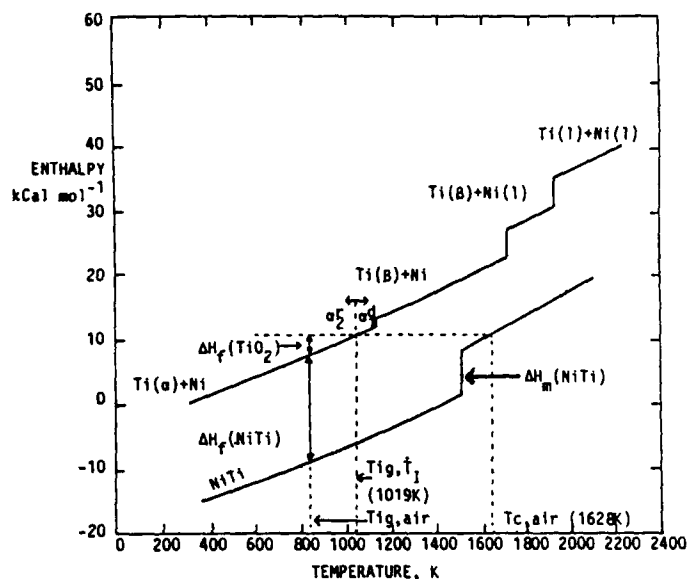


FIGURE 12. ENTHALPY-TEMPERATURE RELATIONSHIPS FOR REACTANTS (Ni + Ti) AND PRODUCT (NiTi). CONDITIONS WHICH PRODUCE Tig (AIR) $\dot{T} < \dot{T}_1$ (i.e. $\dot{T} > \dot{T}_1$), THE HEAT PRODUCED BY TiO_2 FORMATION (i.e. $\Delta H_f(\text{TiO}_2)$), IS USED TO "TRIGGER" THE Ni + Ti COMBUSTION SYNTHESIS REACTION (α_2^r). CONDITIONS WHICH PRODUCE Tig (AIR) $\dot{T} > 1019\text{K}$ (i.e. $\dot{T} < \dot{T}_1$) THE HEAT PRODUCED BY TiO_2 FORMATION IS LARGELY DISSIPATED (α_1^d)

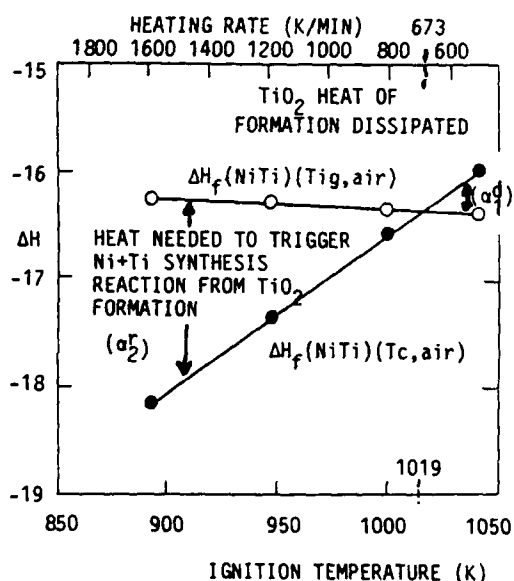


FIGURE 13. HEAT OF REACTION VERSUS TEMPERATURE RELATIONSHIPS.

$\Delta H(\text{NiTi}), (T_c, \text{AIR})$ IS THE TOTAL ENTHALPY CHANGE FOR THE COMBUSTION SYNTHESIS REACTION ($\text{Ni} + \text{Ti} = \text{NiTi}$) IN AIR TO REACH T_c . $\Delta H_f(\text{NiTi}), (Tig, \text{AIR})$ IS THE ENTHALPY CHANGE FOR THE FORMATION OF NiTi AT Tig IN AIR.

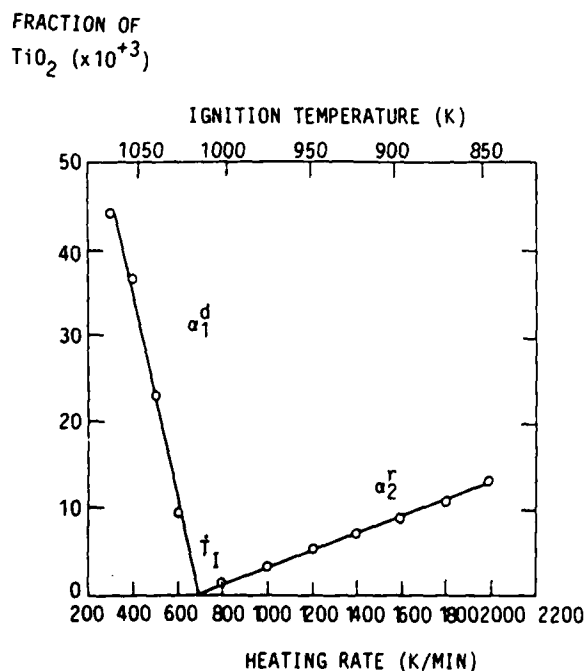


FIGURE 14. FRACTION OF TiO_2 (α_2^r) PRODUCED WHICH IS NEEDED TO TRIGGER Ni+Ti COMBUSTION SYNTHESIS WHEN $\dot{T} > \dot{T}_1$ AND AMOUNT OF TiO_2 (α_1^d) WHEN $\dot{T} < \dot{T}_1$, WHOSE HEAT OF FORMATION IS LARGELY DISSIPATED INTO SURROUNDINGS.

SHOCK-INDUCED CHEMICAL SYNTHESIS OF INTERMETALLIC COMPOUNDS

S.J. Work¹, L.H. Yu¹, N.N. Thadhani¹, M.A. Meyers², R.A. Graham³ and W.F. Hammetter³

¹ Center for Explosives Technology Research, New Mexico Tech, Socorro, New Mexico (USA)

² Department of Applied Mechanics and Engineering Sciences, University of California at San Diego, La Jolla, California (USA)

³ Sandia National Laboratories, Albuquerque, New Mexico (USA)

Key Words: shock-synthesis nickel aluminides
 morphological effects shock-induced mixing
 niobium aluminides DTA characterization

ABSTRACT

Shock synthesis experiments were performed on elemental powder mixtures of Ni-Al and Nb-Al, to study the effect of material parameters on solid-state chemical synthesis. Elemental powders of different morphologies were pre-mixed in a proportion of ~65 wt% Ni, or Nb, and 35 wt% Al. Shock-compression loading experiments were conducted on Ni-Al mixtures at 19-22 GPa pressures using the Sandia Bear fixtures, and on Nb-Al mixtures at 30-40 GPa pressures using a 12-capsule Sawaoka recovery fixture. In the case of Ni-Al mixtures the starting powder morphology plays a significant role in determining the extent of reaction. The Nb-Al powder mixtures shock processed at higher pressures underwent complete reaction.

1. INTRODUCTION

In the work presented here, explosively generated shock compression waves were used to synthesize aluminides of Ni and Nb from elemental powder mixtures, and at the same time induce bonding between the powder particles. This shock-induced chemical synthesis, involving the simultaneous application of very high pressure and high-strain-rate deformation, is a non-equilibrium processing

technique, to produce new materials with special microstructures. The technological potential of shock processing was first demonstrated by the pioneering work of DeCarli and Jamieson,^{1,2} in 1961, namely the synthesis of diamond from rhombohedral graphite. Since that time shock-induced chemical synthesis has been successfully used, not only to induce phase changes, but also synthesize compounds from elements in ceramic³⁻⁷ as well as metallic systems.⁸⁻¹⁴

The first systematic investigation of shock-induced chemical synthesis in intermetallics was conducted by Horie, et al⁸⁻¹². They synthesized aluminides of Ni and Ti, starting with mechanically mixed powders of the respective elemental constituents, in ratios appropriate to form stoichiometric Ni_3Al and Ti_3Al . In the case of the Ni-Al powder mixtures, they observed that the nickel aluminide products were readily synthesized and controlled by the shock conditions (peak pressure and mean bulk temperature). Large yields of Ni_3Al were produced and the material had a hardness similar to that of cold worked Ni_3Al even though the material had low defect concentration. In contrast, the reaction yield was very limited in the case of Ti-Al powder mixtures. The present work is an extension of the work conducted by Horie, et al. Instead of concentrating on optimizing the processing parameters (pressure, temperature), the emphasis of this effort was on determining the influence of material parameters on the extent of the reaction and nature of reaction products.

2. EXPERIMENTAL PROCEDURE

Shock-compression experiments were conducted on mixtures of Ni and Al powders of different morphologies (shape and size). Table I lists the five types of powders used in the study. The powder particle sizes ranged from 1 to 45 micrometers for Al and from 3 to 45 micrometers for Ni. The morphology of the powders was either flaky or spherical. Characteristic scanning electron

micrographs of the powder mixtures containing, flaky and spherical Ni particles, and rounded Al powders are shown in Figure 1(a) and (b), respectively.

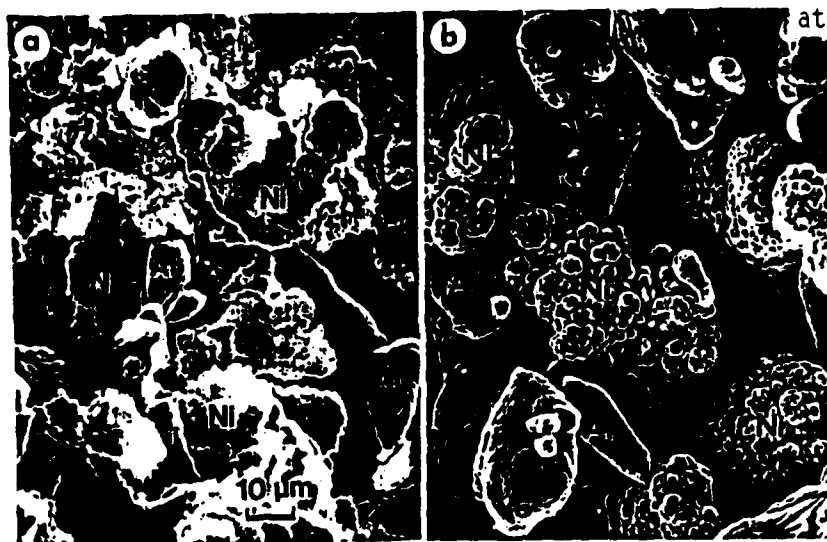


Fig. 1 (a) and (b) Characteristic scanning electron micrographs of the powder mixtures containing flaky and spherical Ni particles and rounded Al particles.

The pre-mixed Ni-Al powders, prepared by combining the pure elemental powders (65 wt % Ni and 35 wt % Al) under an argon atmosphere and then mixing in a ball mill, were packed into copper capsules at approximately 65% theoretical density. These were then sealed and placed in the Sandia Momma Bear A Fixture¹⁵ for shock compression loading. Composition B was used as a high explosive to generate the shock waves (shock pressure of 19-22 GPa), which were transmitted through the driver plate and into the powder. For the Nb-Al system only one type of powder was used, namely, Nb (irregular, -325 mesh) and Al (irregular, -325 mesh). The powder mixture (65 wt % Nb and 35 wt % Al) prepared by hand mixing in argon atmosphere was packed into stainless steel capsules at 65% of theoretical density. The capsules were embedded in a 12-capsule recovery fixture backed by a momentum trap, which was impacted by an explosively driven flyer

plate at a velocity of 1700 m/s.¹⁶ The planar/parallel impact of the flyer plate creates high amplitude shock waves (30-40 GPa shock pressure) that transmit through the powder.

After shock loading, the compacts of both Ni-Al and Nb-Al powder mixtures were recovered from the shock recovery fixtures and characterized by differential thermal analysis, microscopy and x-ray diffraction analysis.

TABLE I - CHARACTERISTICS OF MIXTURES OF Ni AND Al POWDERS

POWDER LOT # SNL-	SHOT #	NICKEL POWDER			ALUMINUM POWDER			GREEN DENSITY (g/cm ³)
		shape	size (μ m)	purity (%)	shape	size (μ m)	purity (%)	
0887-1	35G876	spher.	3-7	99.9	round	1	99.9	4.090
0887-2	38G876	spher.	10-20	99.9	spher.	10-20	99.5	4.147
0887-3	39G876	spher.	-40+20	99.9	spher.	-44	99.8	4.154
0887-4	6G876	flaky.	-44	99.9	spher.	-44	99.8	4.20
0887-5	41G876	spher.	-45+20	99.9	spher.	5-15	99.9	4.164

3. SHOCK PROCESSING OF Ni-Al

3.1 Ni-Al Compact Characterization by Microstructural Analysis

Optical microscopy observations revealed that in the case of the fine powder mixture compact (Shot #35G876), and the one containing flaky Ni powder (Shot #6G876), complete reaction had occurred. The recovered compact from Shot #35G876 was very poorly bonded together and almost fragmented whereas the compact of Shot #6G876 remained well bonded. Figure 2 shows a corner and central cross-section region of the recovered compact of Shot #6G876. Compacts from Shot #38G876, 39G876, and 41G876, exhibited practically identical characteristics, but unlike the fine or flaky powder compact, the bulk of the material remained unreacted.

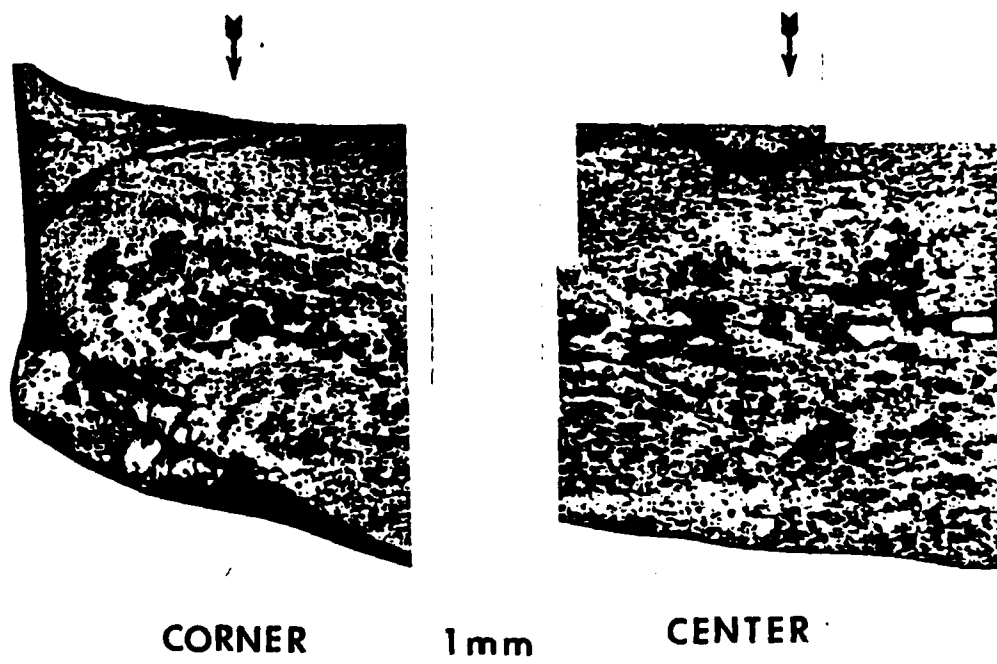


Fig. 2 Optical micrograph of the central and corner region along the cross-section of Sample No. 6G876 showing fully reacted regions, with spherical voids.

The fully reacted regions in these compacts were observed to be isolated along the circumference (or actually in a triangular area located near the corners) as observed in micrographs of cross-sectional planes of the compacts. These, in fact, are regions subjected to maximum shock-induced mean bulk temperature, as predicted by numerical simulations performed using the two-dimensional CSQ code.¹⁵ No unreacted Ni and Al was detected in this triangular region. Figure 3(a) is an optical micrograph of part of the cross-section of Sample #39G876, showing a typical triangular reaction region. The etching contrast generated reveals five dissimilar phase regions (A, B, C, D, and E, as shown in the figure). These regions correspond to the following phases and structures: regions A and B correspond to unreacted Ni and Al powders; Region C shows a reacted Ni_3Al compound; Region D is a reacted, melted and rapidly resolidified amorphous material; Region E is also a reacted, melted and resolidified compound possessing fine dendritic or microcrystalline structure. A scanning electron micrograph of one of the interface regions is shown in Figure 3(b). The bright

contrast of the Ni particles and dark contrast of the Al particles is clearly observed in this micrograph. A transition area approximately 150 μm thick between totally unreacted material and bulk reaction products appears to contain an Al-rich compound (with dendritic grains) between the Ni particles. The bulk reaction product on the other hand is contrast free and has Ni_3Al stoichiometry.

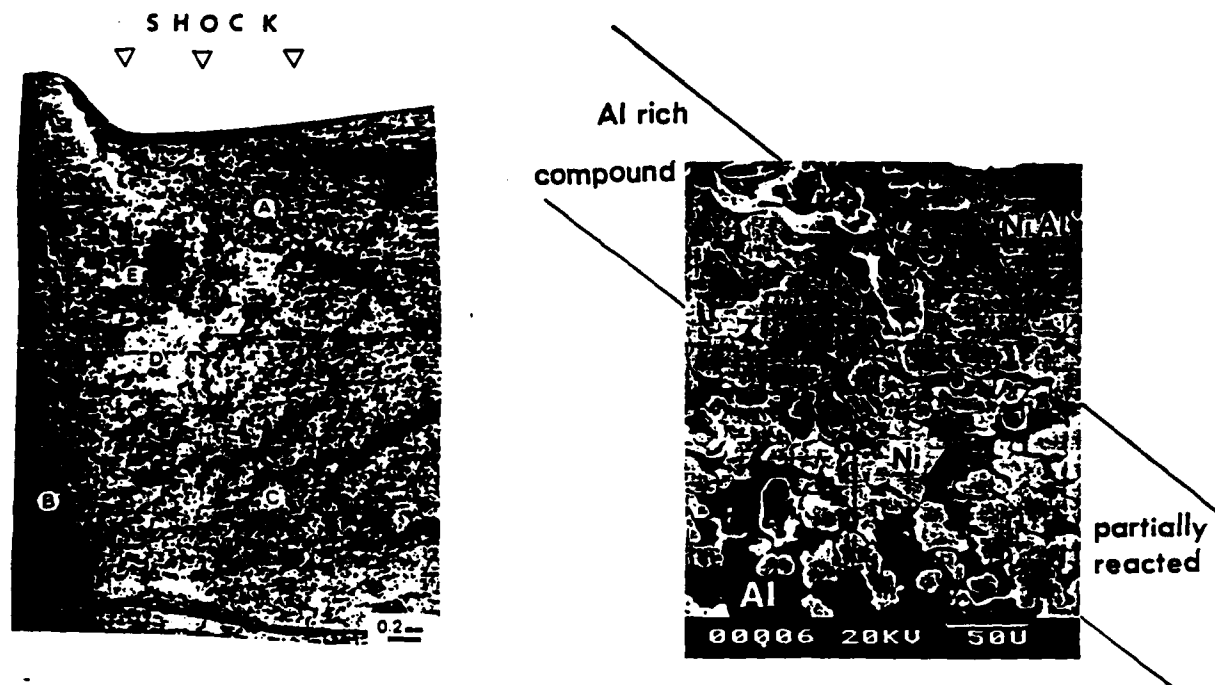


Fig. 3 Optical and scanning electron micrograph of a part of the cross-section of Sample No. 39G876 showing reacted and unreacted regions.

3.2 DTA Characterization of Powders

Samples of each of the five powder mixtures were run in a DuPont 9900 Differential Thermal Analyzer (DTA) to observe any variation in the powder reactivity before shock compression processing. The DTA scans of the powders are compiled in Figure 4. Ni and Al powders react together at 640°C (slightly below the melting temperature of Al) resulting in an exothermic self-sustaining reaction.¹¹ From the DTA scans shown in Figure 4, it is observed that the powder mix #SNL-0887-4 (325 mesh flaky Ni and spherical Al) shows maximum reactivity,

which arises from the efficient mixing of the Ni (flaky) and Al (spherical) powders. The fine powder mixture, in spite of possessing maximum surface area, shows lower reactivity. This is attributed to improper mixing of the powders, in particular because of the tendency of the very fine powders to agglomerate with like particles.

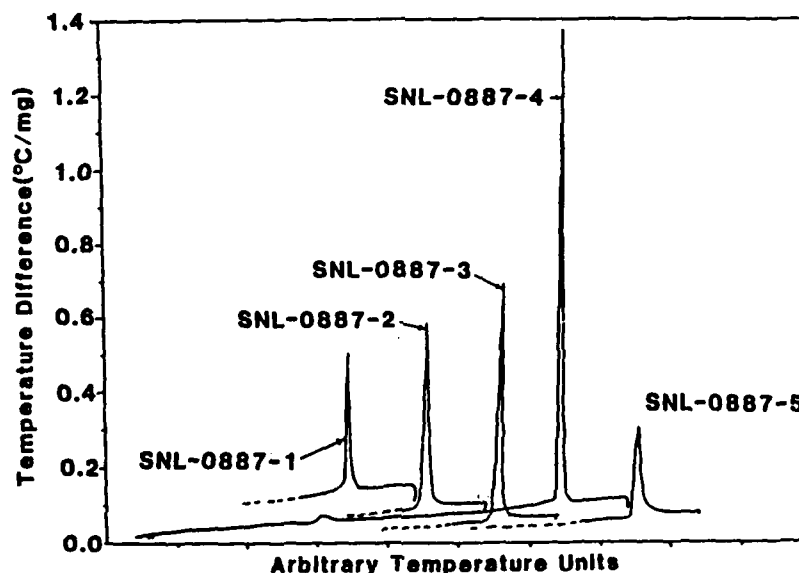


Fig. 4 DTA scans showing exotherms of reaction between different grades of Ni and Al powders.

In order to verify the reaction regions, as evidenced by different etching contrast in the optical micrographs, small samples were taken from different areas of the shocked compacts and analyzed in the DTA. Typical DTA traces are shown in Figure 5(a) and (b). Samples from the fully reacted regions of all compacts show a smooth trace in the DTA (Curve (a) in Figure 5) indicating no subsequent reaction while heating in the DTA, whereas, the samples from unreacted regions exhibit two exothermic peaks as shown in Curve (b) in Figure 5.

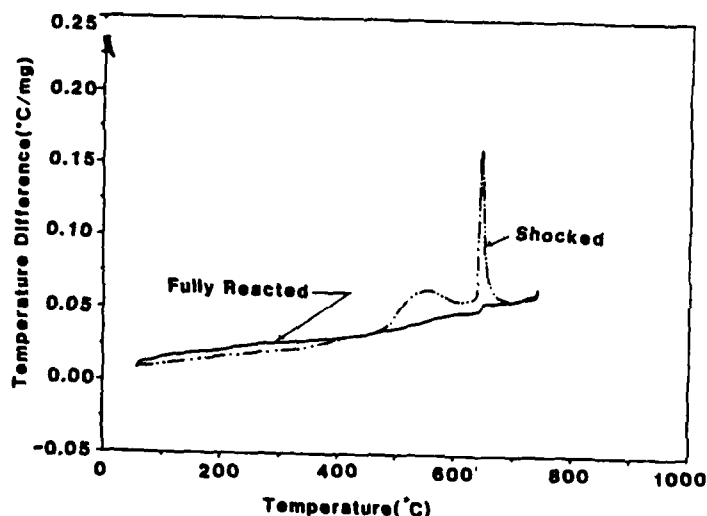


Fig. 5 Typical DTA traces from small samples from (a) reacted regions and (b) non-reacted regions of a recovered compact.

The first peak in Curve (b) is believed to be a "pre-ignition" phenomenon. This phenomenon was not observed in the unshocked powder mixtures heated in the DTA (Figure 4), and is characteristic of shock-induced processes. The latter peak is the exotherm corresponding to the complete reaction between Ni and Al. Similar observations were also made by Hammett et al.¹¹ They conducted x-ray diffraction studies at elevated temperatures and observed the formation of Al-rich compounds in shock-treated samples which had undergone no reaction.

From DTA analysis performed on shock processed powders, it was concluded that the bulk of the material in Samples #35G876 and 6G876 had been reacted. Shocked samples #38G876, 39G876, 41G876 had undergone only partial reaction with the reaction regions being confined along the outer circumference of the disk.

3.3 X-ray Diffraction Analysis

In order to identify the compounds and the structure of the bulk products formed during shock-induced chemical synthesis, x-ray diffraction analysis was performed on the mechanically blended Ni and Al powder mixtures and entire cross-sectional surfaces of the various shock processed Ni-Al compacts. The x-ray diffraction results are summarized in Figure 6. Curve (a) shows the Ni and Al diffraction peaks obtained on the blended powder (Mix #SNL-0887-1). X-ray

diffraction scans obtained from the central cross-sectional surfaces of the different compacts are given as Curve (b) - Shot #35G876; Curve (c) - Shot #38G876; Curve (d) - Shot #39G876; Curve (e) - Shot #41G876, and Curve (f) - Shot #6G876.

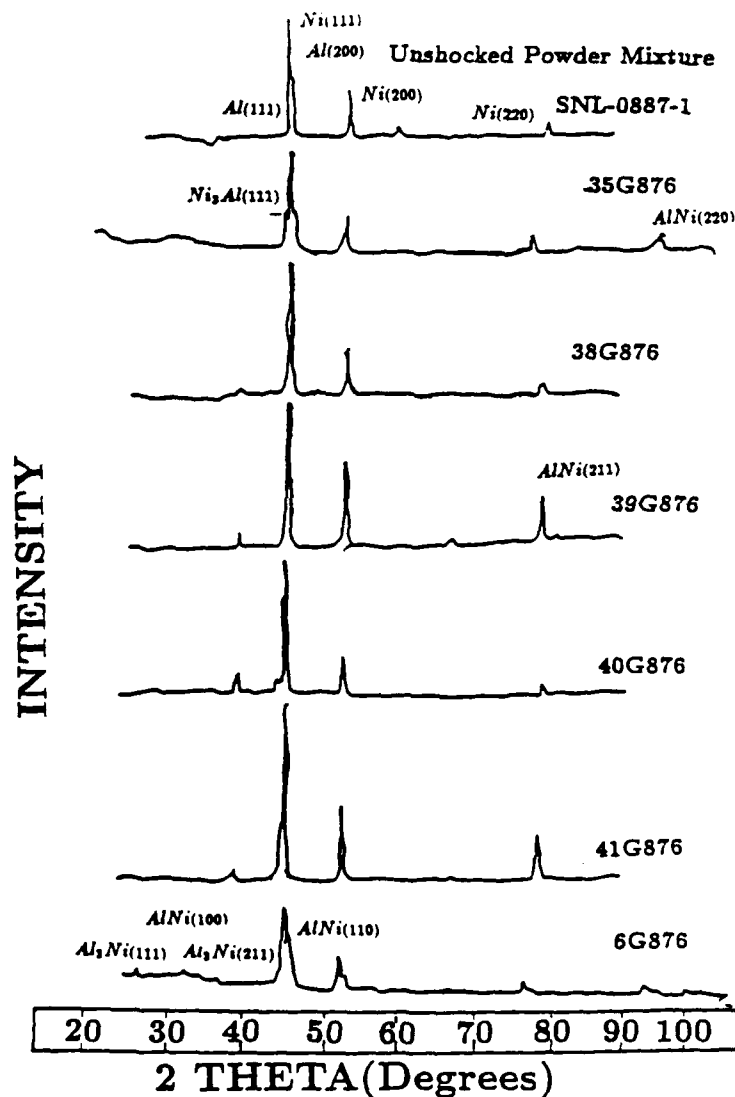


Fig. 6 X-ray results showing diffraction peaks obtained from the unshocked powder mixtures and recovered compacts.

It can be seen from these x-ray diffraction results that all of the recovered compacts show at least some degree of reaction, and the reaction products formed range from Al-rich to Ni-rich compounds. It is obvious that in Curves (b) and (f), which correspond to Samples #35G876 and 6G876; the Al(111) peak is totally missing, implying complete depletion of Al particles in the reaction process (within limits of detectability). The x-ray diffraction trace of the 6G876 compact indicates the presence of an AlNi compound along with elemental Ni and some Ni_3Al , whereas the traces for 35G876 show Ni_3Al as the predominant reaction product.

4. SHOCK PROCESSING OF Nb-Al

Shock processing of Nb-Al powders resulted in small disks 12 mm diameter x 5 mm thick. Although the disk was almost totally fragmented at the shock pressures produced in the powders upon impact at 1700 m/s, it could be established that most of the powder mixture had undergone reaction. Figure 7(a) shows a macrophotograph of the cross-section of a recovered Nb-Al powder compact. Most of the section had a microdendritic structure except the upper left hand corner, where no reaction took place. The Vickers microhardness measurements are shown in Figure 7(a). The reacted region had a higher hardness (800-900 kg/mm^2) than the unreacted region ($\sim 100 \text{ kg/mm}^2$). Figure 7(b) shows the microdendritic structure at a high magnification. The heat generated from the exothermic reaction between Nb and Al was enough to melt the reaction products, which solidified to a microdendritic structure. Shrinkage voids formed during solidification are also seen in Figure 7(a).

X-ray diffraction analysis was performed on the unshocked Nb-Al powders, as well as on the cross-section of the recovered shock-processed compacts.

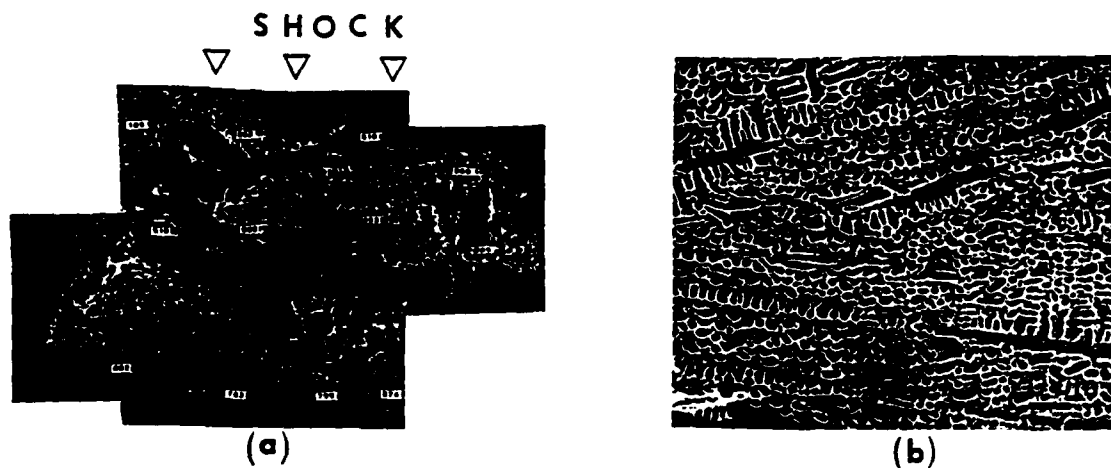


Fig. 7 (a) Macrophotograph of cross-section of fragmented powder compact containing 65 wt % Nb and 35 wt % Al powders (b) optical micrograph showing a dendritic structure at high magnification.

The Nb-Al powder mixture is shown in trace (a), while the shock synthesized material is shown in trace (b) in Figure 8. Two intermetallic compounds, Al_3Nb and AlNb_2 , can be identified from the x-ray diffraction analysis of the shocked compacts.

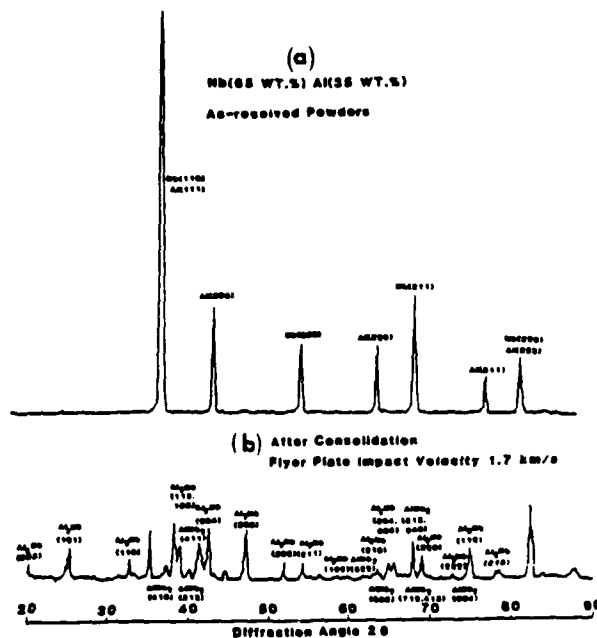


Fig. 8 X-ray diffraction results obtained from a Nb-Al powder mixture and shock synthesized compact.

5. SUMMARY OF RESULTS

Shock compression processing is used to chemically synthesize nickel and niobium aluminides, starting with the constituent elemental powders. In the case of Ni-Al mixtures the starting powder morphology plays a significant role in determining the extent of reaction. Very fine and flaky powders undergo intimate shock-induced mixing, and thereby result in complete reaction. The shock-induced reaction products formed range from an equiatomic NiAl compound with the use of flaky nickel morphology, and a Ni_3Al compound with fine powders.

Nb-Al powder mixtures upon being shock processed at higher pressures undergo almost complete reaction to Nb_2Al and NbAl_3 compounds with a microhardness of 800-900 kg/mm^2 .

6. ACKNOWLEDGEMENTS

The Ni-Al work has been funded by the Sandia National Laboratories under the Sandia/University Research Program. Support for the Nb-Al work was provided by McDonnell Douglas Research Corporation. The scanning electron microscopy was performed at University of New Mexico with the help of Mr. George Conrad. The assistance of Mr. Edward Binasiewicz of Sandia National Laboratories with the DTA work is also acknowledged.

REFERENCES

1. P.S. DeCarli, "Method of Making Diamond," U.S. Patent No. 3,238,019, March 1, 1966.
2. P.S. DeCarli and J.C. Jamieson, *Science*, 133 (1961) 821.
3. Y. Kimura, *Japan. J. Appl. Phys.* 2 (1963) 312.
4. Y. Horiguchi and Y. Nomura, *Bull. Chem. Soc., Japan*, 36 (1963) 486.
5. Y. Horiguchi and Y. Nomura, *J. Less-Common Metals*, 11 (1966) 378.
6. H. Suzuki, H. Yoshida and Y. Kimura, "Effect of Detonation Shock Waves on Powder Materials," *Yogyo Kyokaishi*, 77 (1969) 36 (in Japanese); Translation in Sandia National Laboratories Report RS3140/81/169, Oct. 1981.
7. R.A. Graham, B. Morosin, E.L. Venturini and M.J. Carr, *Ann. Rev. Mater. Sci.*, 16 (1986) 315.
8. Y. Horie, R.A. Graham and I.K. Simonsen, *Materials Letters*, 3(9,10) (1985) 354.
9. Y. Horie, R.A. Graham and I.K. Simonsen, "Observations on the Shock Synthesis of Intermetallic Compounds," in Metallurgical Applications of Shock-Wave and High-Strain-Rate Phenomena, L.E. Murr, K.P. Staudhammer, and M.A. Meyers, eds., Marcel Dekker, Inc. New York, p. 1023.
10. I.K. Simonsen, Y. Horie, R.A. Graham, and M.J. Carr, *Materials Letters*, 5 (1987) 75.
11. W.F. Hammetter, R.A. Graham, B. Morosin and Y. Horie, "Effects of Shock - Modification on the Self-Propagating High Temperature Synthesis of Nickel Aluminides," in Shock Waves in Condensed Matter, S.C. Schmidt and N.C. Holmes, (eds.), North-Holland Publications, (1987) 431.
12. R.A. Graham, B. Morosin, Y. Horie, E.L. Venturini, M. Boslough, M. Carr, and D.L. Williamson, "Chemical Synthesis Under High Pressure Shock Loading" in Shock Waves in Condensed Matter, Y.M. Gupta (ed.), Plenum Press, New York, (1986).
13. B. Ohlinger and L.R. Newkirk, *Solid State Comm.*, 37 (1981) 613.
14. A.R. Miller, J. Hao, A. Gehris, and P. Wolf, *Jap. Journal of Industrial Explosives*, June 1988.
15. R.A. Graham, "High Pressure Explosive Processing of Ceramics", R.A. Graham and A. B. Sawaoka, eds, TransTech Publications, Switzerland, 1986, p. 26.
16. A.B. Sawaoka and T. Akashi, "High Density Compacts," U.S. Patent 4,655,830 (1987).



FIGURE 1

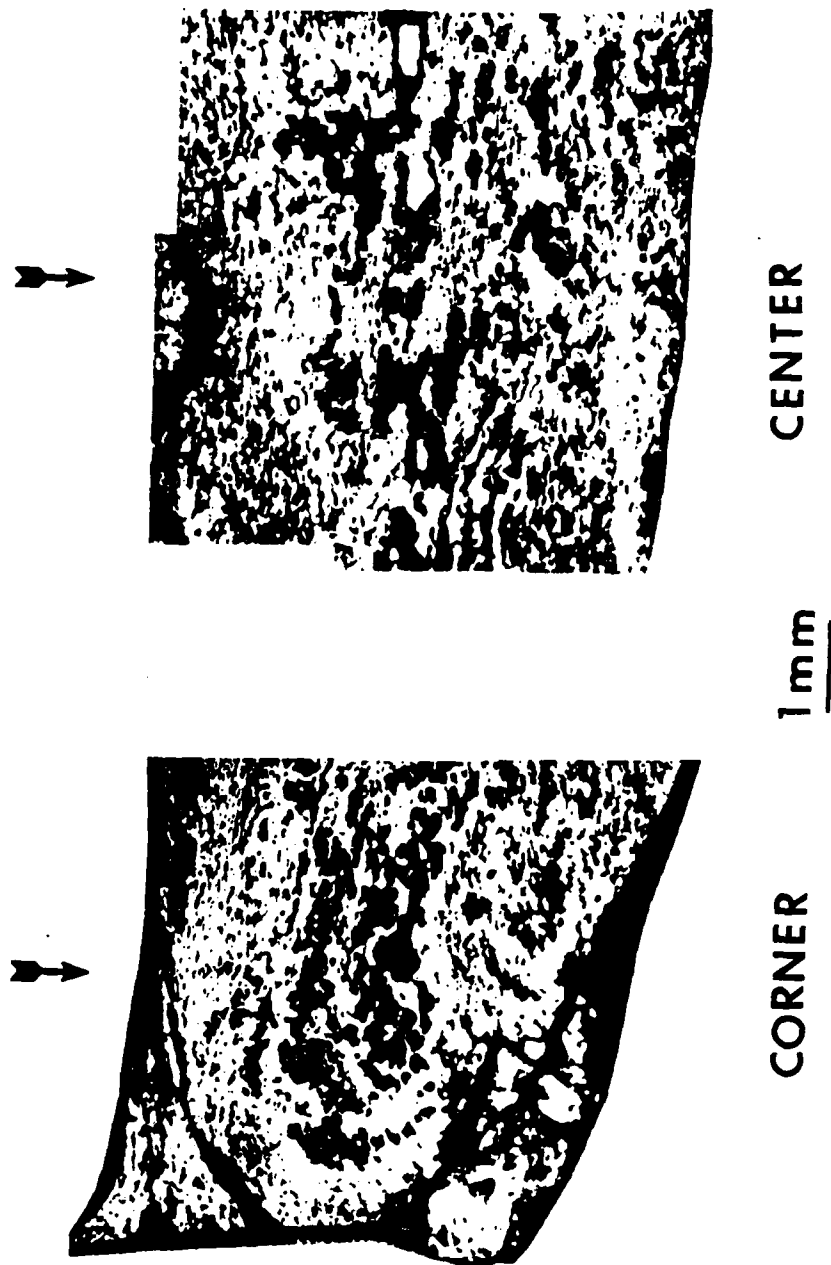


Figure 2

S H O C K



Figure 3

234

237

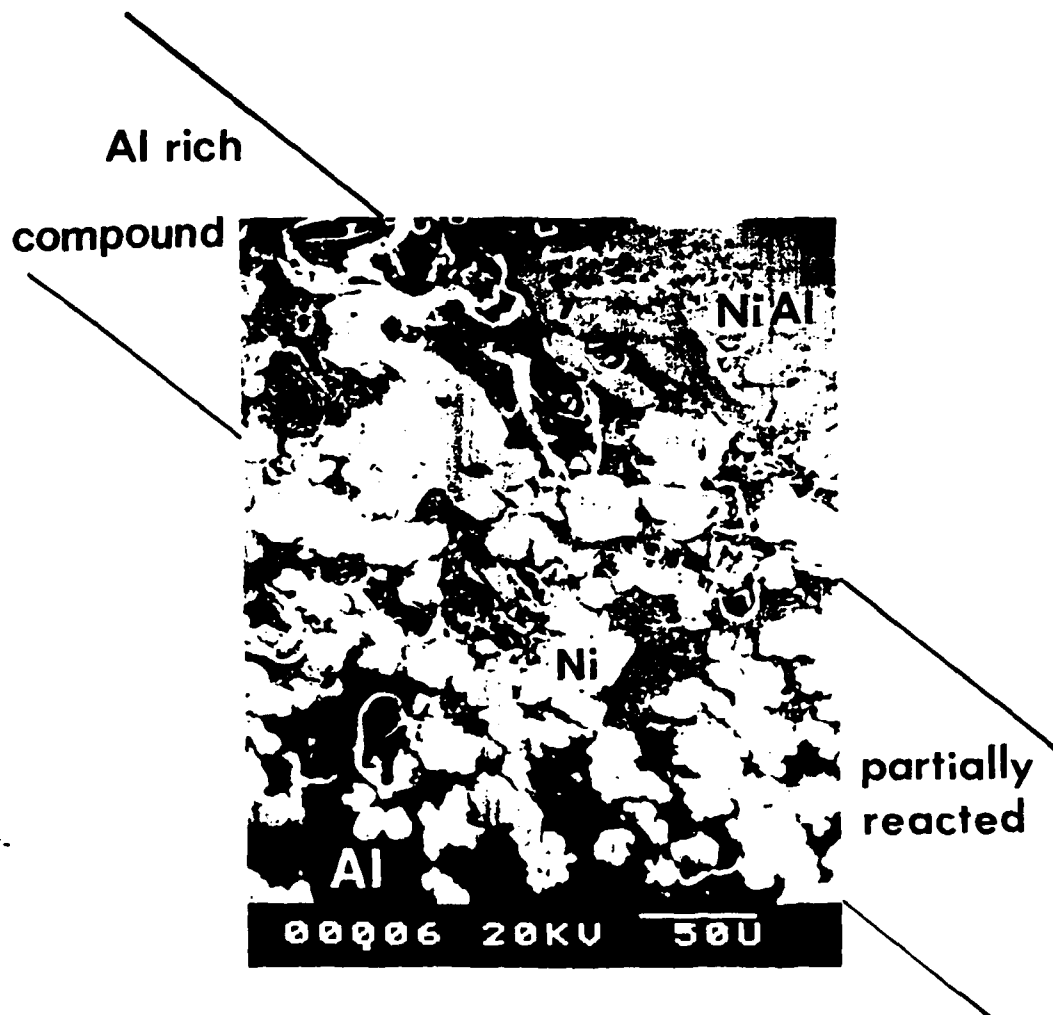


Figure 3

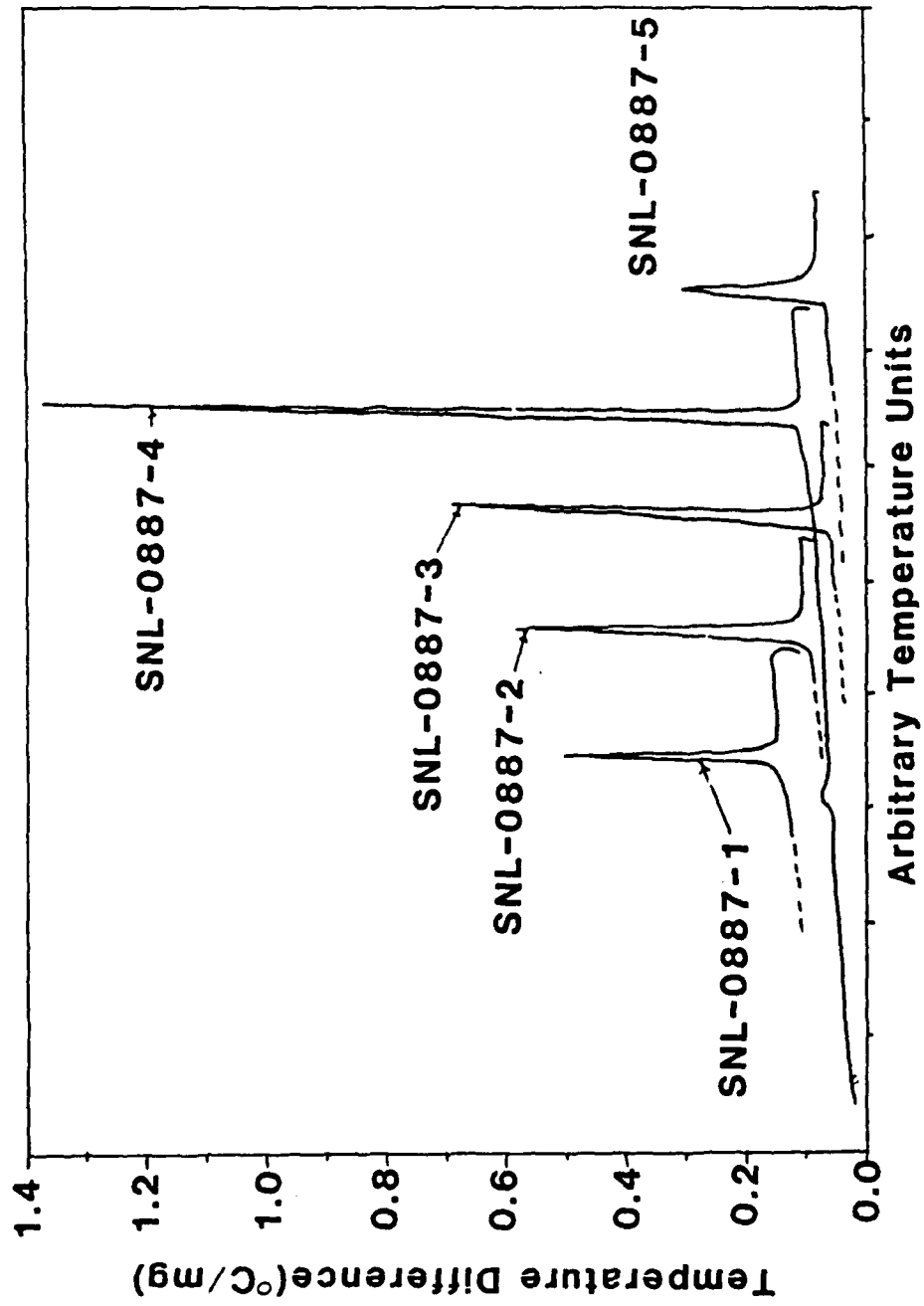


Figure 4

100-105#11 ~ 260

OTC

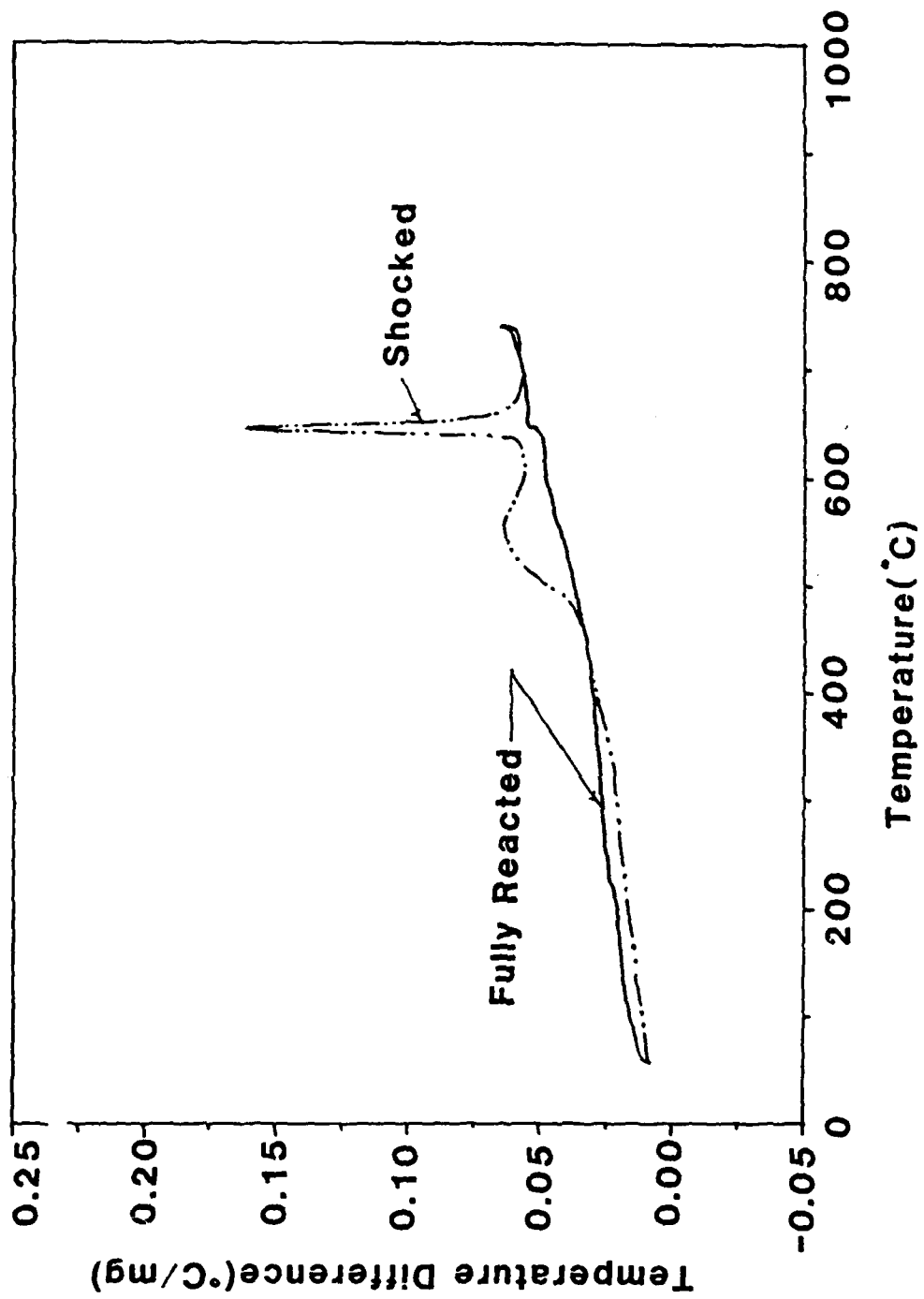


Figure 5

work in SF/1
222

INTENSITY

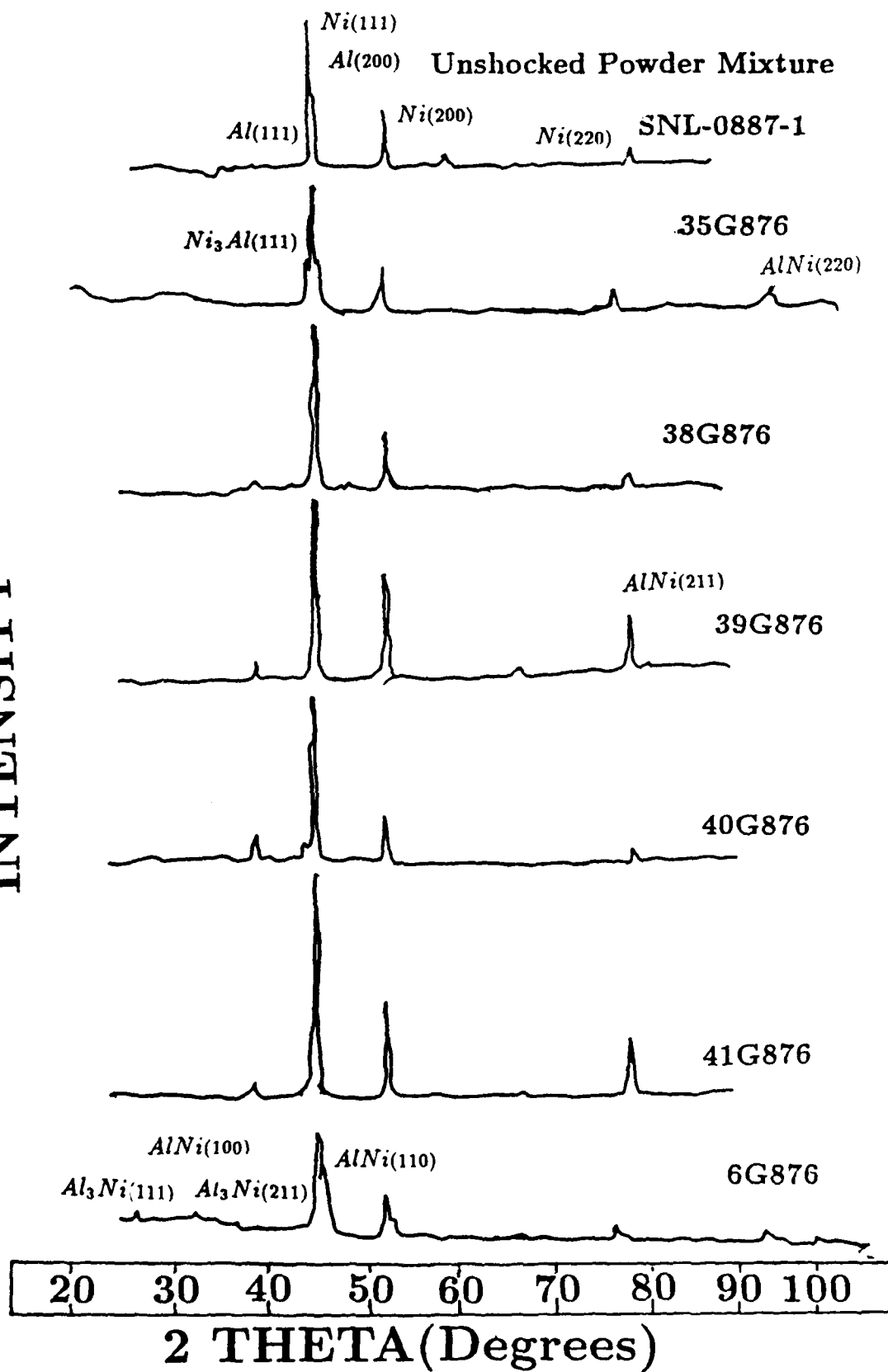


Figure 6

241

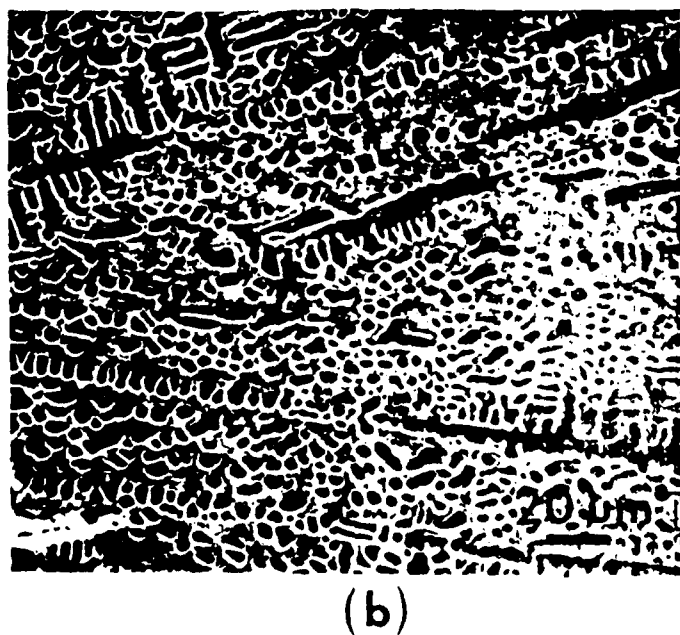
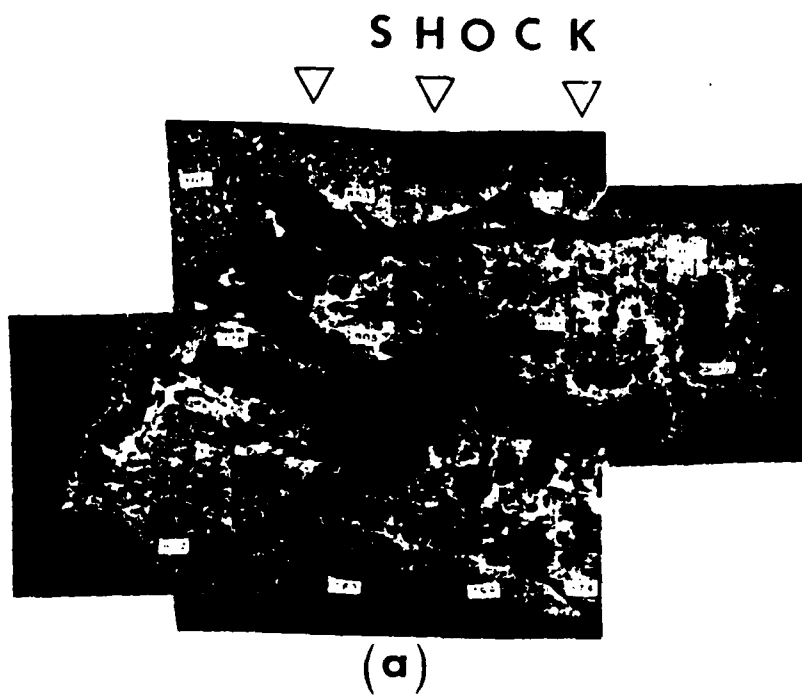


Figure 7

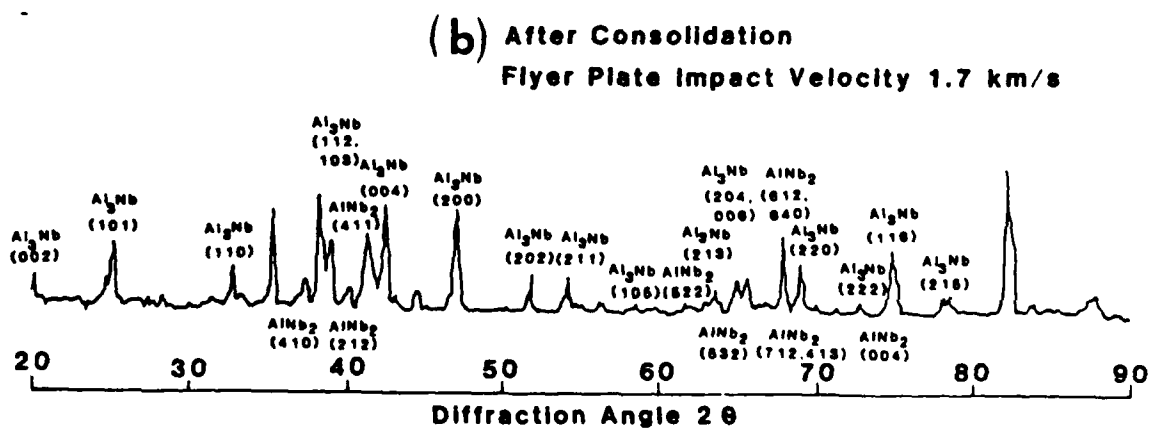
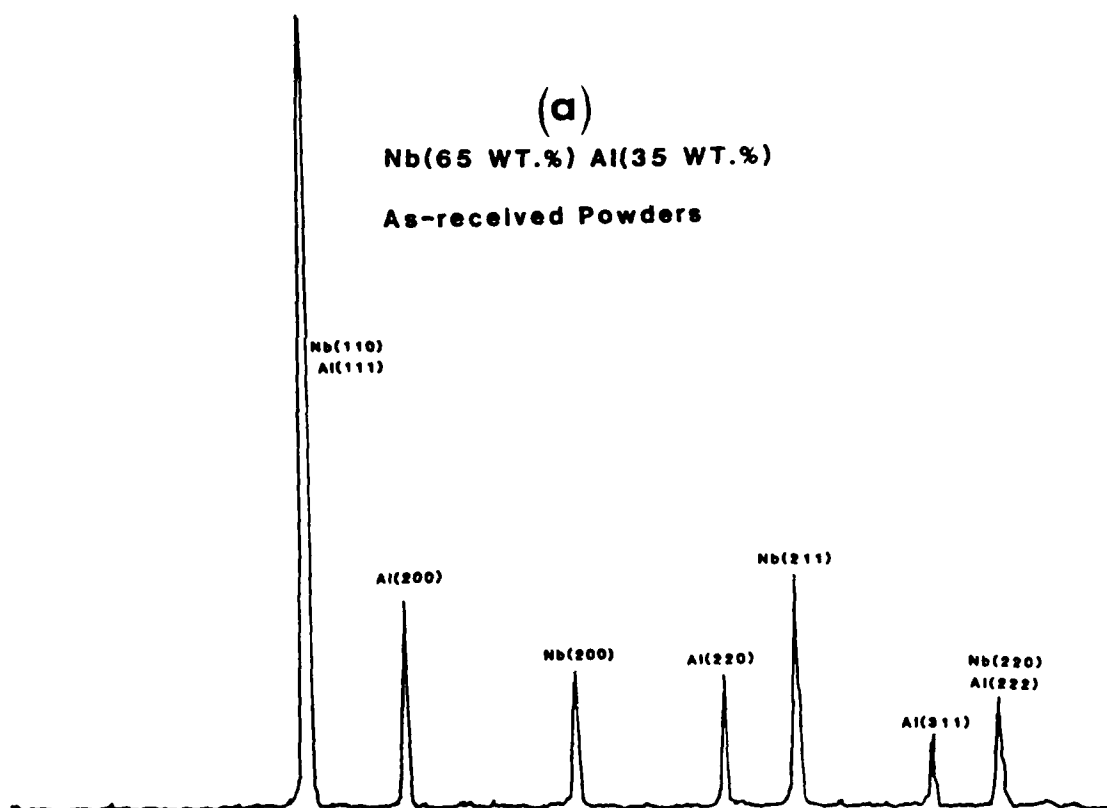


Figure 8

Advanced Ceramics Via SHS

T. P. DeAngelis and D. S. Weiss
Corning Incorporated, Corning, NY 14831, U.S.A.

ABSTRACT

Advanced ceramic materials can be made by several techniques known in the industry today. This paper discusses the use of reaction hot pressing via SHS as an advantageous process for producing a broad range of dense ceramic bodies. The preparation of several examples are described along with their physical and microstructural characterization. Some industrial applications are presented.

INTRODUCTION

Advanced ceramic materials can be classified as those high-tech ceramics possessing particularly useful properties under severe operating conditions such as high temperatures, high stress fields, high wear areas, or corrosive environments.

This paper gives an overview of some of the work done at Corning on reaction hot pressing (RHP) using self-propagating high-temperature synthesis (SHS) as an advantageous process for producing a very broad range of advanced ceramic materials.

PROCESS OVERVIEW

In this work on RHP, a multiphase ceramic material is formed by a chemical reaction between elements of two separate components resulting in a body which consists of at least two phases, both of which are the result of the chemical reaction.¹ The chemical

reaction is initiated by uniform external heating of the reacting powders in a graphite mold under pressure. RHP allows one to produce bodies at lower temperatures (with lower total porosity) than with conventional techniques. Not only can this process be used to make monolithic parts, but it can also be used to make multilayer ceramics, coatings, and bonded materials.

RESULTS

Titanium Diboride - Aluminum

The cermet composed of TiB_2/Al was of interest as a cathode for electrowinning aluminum metal. The nominal reaction for the formation of TiB_2/Al is $\text{TiH}_2 + \text{AlB}_2 \rightarrow \text{TiB}_2 + \text{Al} + \text{H}_2 \uparrow$. It was found that large samples react at about 670°C while small samples react at about 1100°C . The DTA for a small sample of this reaction is shown in Figure 1. It shows the reaction to form TiB_2 occurs at about 1090°C (the decomposition point of AlB_2). This was confirmed by X-ray analysis. It turns out that the reaction at 670°C is the reaction of aluminum contaminant in AlB_2 with titanium starting material forming an intermetallic intermediate. In making an actual sample (30 g and larger), this reaction at 670°C is sufficiently exothermic to ignite the reaction at 1090°C , thus the reaction appears to ignite at 670°C . In the DTA experiment, sample size is 15 mg and the true reaction is elucidated.

The density of the TiB_2/Al material was strongly dependent on the hot pressing pressure and soak temperature as shown in Figure

2. At higher temperatures, aluminum metal could be squeezed out of the sample, resulting in raising the cermet density.

A scanning electron micrograph (SEM) of the TiB_2 fractured surface is shown in Figure 3. The small relatively uniform grain size and intergranular fracture pattern are demonstrated.

Titanium Diboride - Nickel

TiB_2/Ni is of interest because it has higher density, hardness, Young's modulus and temperature capability than TiB_2/Al . TiB_2/Ni is formed by the reaction of NiB , TiH_2 , and B . The microstructure of an etched polished section TiB_2/Ni is shown in the SEM in Figure 4. TiB_2 grain size is about 1-2 μm with nickel concentrated at the triple points.

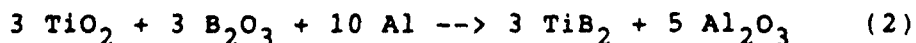
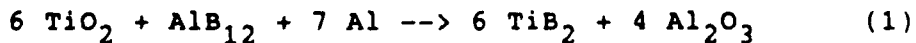
Titanium Diboride - Aluminum Nitride

A composite of TiB_2/AlN can be formed by the reaction of $\text{TiN} + \text{AlB}_2 \rightarrow \text{TiB}_2 + \text{AlN}$. This is a well behaved reaction, not violently exothermic and very good samples are routinely made.

A property comparison of conventionally hot pressed TiB_2/AlN and RHP/SHS TiB_2/AlN , shows, in all cases, that the properties of the RHP/SHS TiB_2/AlN are superior to the conventionally formed TiB_2/AlN .

Titanium Diboride - Alumina

There is much interest in $\text{TiB}_2/\text{Al}_2\text{O}_3$ compositions due to their hardness and wear resistance. Two reactions, shown below, have been used to successfully make $\text{TiB}_2/\text{Al}_2\text{O}_3$ bodies:



The work reported here used the first reaction shown above.

Typical microstructure (SEM) of a fracture surface is shown in Figure 5.

Multilayer Materials

One of the advantages of the RHP process is the ability to make other than monolithic materials; for examples, multilayer compositions, coated parts, graded compositions. Also, the process can be used to bond together similar and dissimilar materials.

One example of a multilayer material is RHP $\text{TiB}_2/\text{Al}_2\text{O}_3$ layer with non RHP zirconia toughened alumina (ZTA). Tape cast sheets, 0.015 inches thick are layered and pressed, the binder burned out at 550°C , and hot pressed at 1450°C . An SEM photomicrograph of a polished section of a layered material is shown in Figure 6. Note that layers can be of different thicknesses and that the layers are well bonded to one another.

An example of a coated sample is shown in Figure 7. The coating is $\text{TiB}_2/\text{Al}_2\text{O}_3$, and it was reaction hot pressed onto an already sintered piece of zirconia.

Figure 8 shows photograph of several parts made by the RHP process. It demonstrates various sizes and shapes which can be made.

SUMMARY

It has been demonstrated that a broad range of materials with potentially useful properties can be made RHP/SHS. Sample size, powder purity and particle size, heating rate, presence of non-reacting species, and atmosphere affect the reaction ignition temperature, reaction rate, and maximum temperature achieved.

These factors ultimately control the phases which are formed, grain size of each phase, sample density and porosity, and the physical and mechanical properties.

REFERENCES

- ¹ U.S. Patents 4,746,363; 4,514,268; 4,605,634; 4,540,475; 4,605,633; and 4,534,835.

ACKNOWLEDGMENTS

The authors gratefully acknowledge the very capable assistance of L. Manfredo, S. Hagg, L. Marks, and S. Solsky during the course of this work.

FIGURE CAPTIONS

- Figure 1. DTA of the $\text{TiH}_2 + \text{AlB}_2$ reaction.
- Figure 2. Density of TiB_2/Al as a function of hot pressing pressure and soak temperature.
- Figure 3. SEM photomicrograph of a fracture surface of TiB_2/Al .
- Figure 4. SEM photomicrograph of an etched polished section of TiB_2/Ni .
- Figure 5. SEM photomicrograph of a fracture surface of $\text{TiB}_2/\text{Al}_2\text{O}_3$.
- Figure 6. SEM photomicrograph of a polished section of $\text{TiB}_2/\text{Al}_2\text{O}_3$ - ZTA
- Figure 7. Photograph of $\text{TiB}_2/\text{Al}_2\text{O}_3$ coating on ZrO_2 .
- Figure 8. Photograph of several parts made by the RHP/SHS process.

DIFFERENTIAL THERMAL ANALYSIS
OF
 $\text{TiH}_2 + \text{AlB}_2$

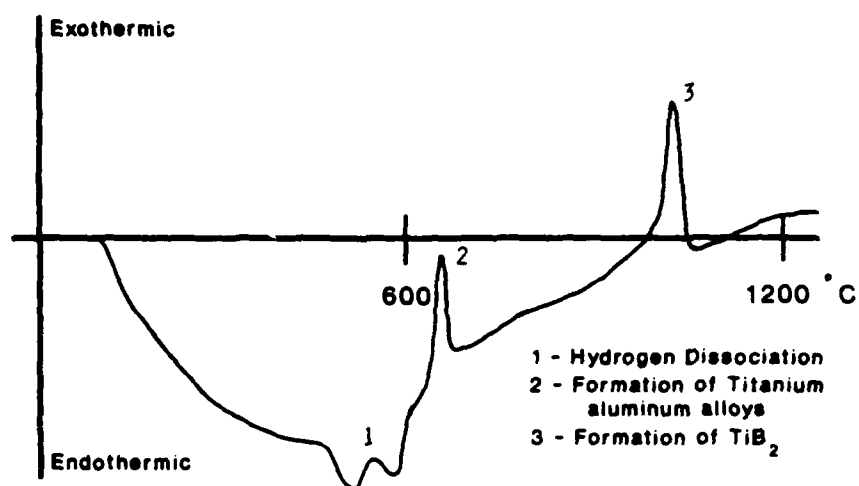


Figure 1

#12

247

247

TITANIUM DIBORIDE - ALUMINUM

Density as a Function of Hot Pressing Pressure
and Soak Temperature

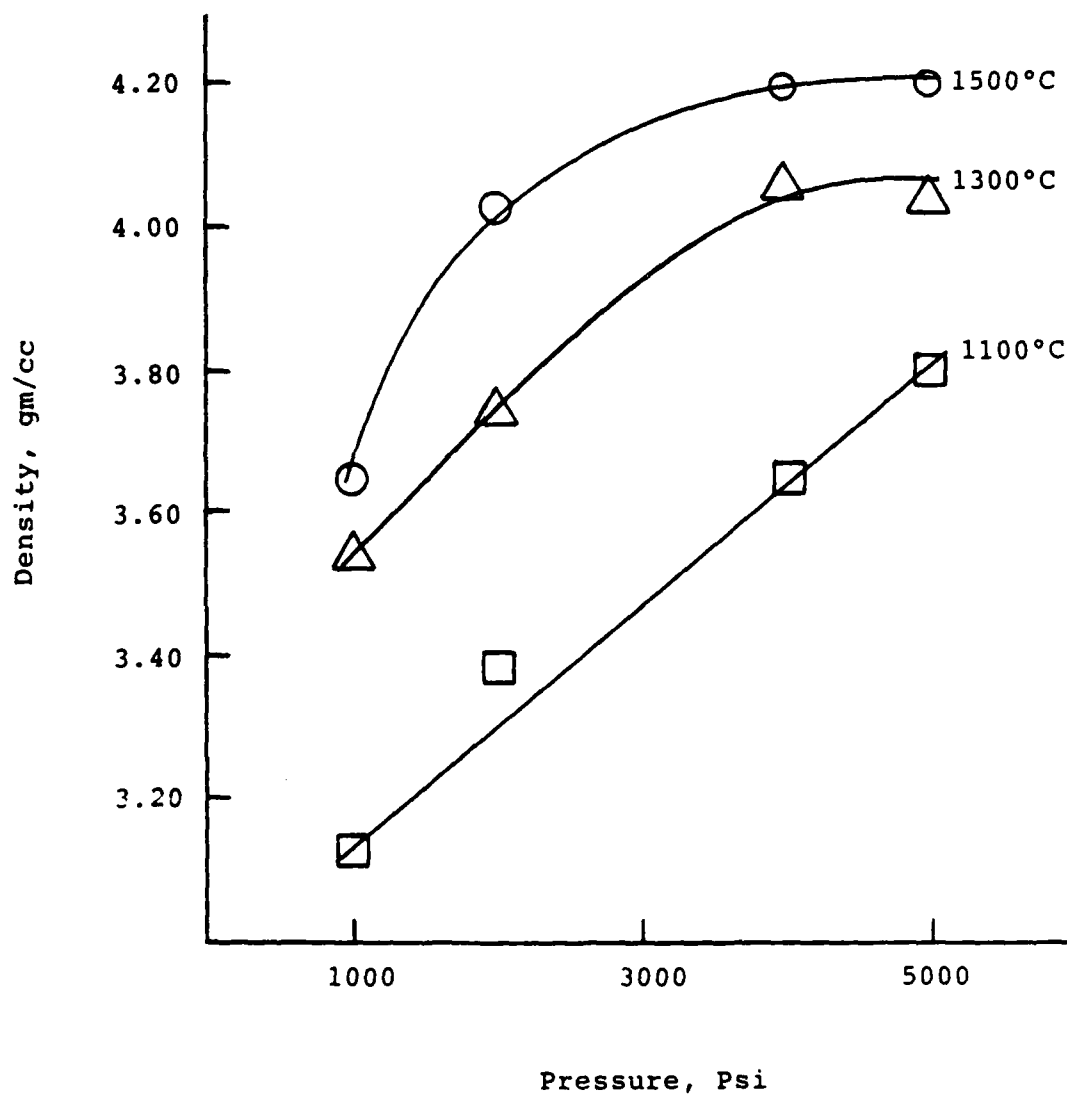


Figure 2

12 T. Chung

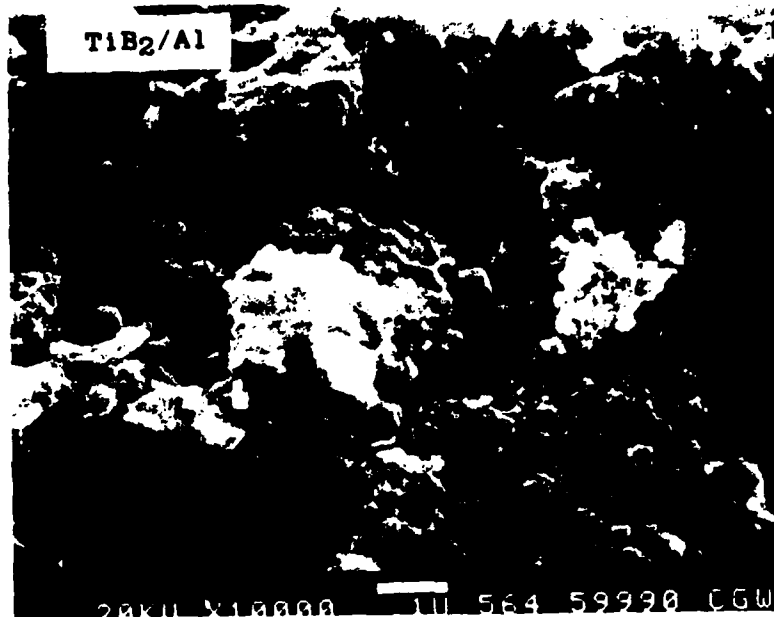


Figure 3

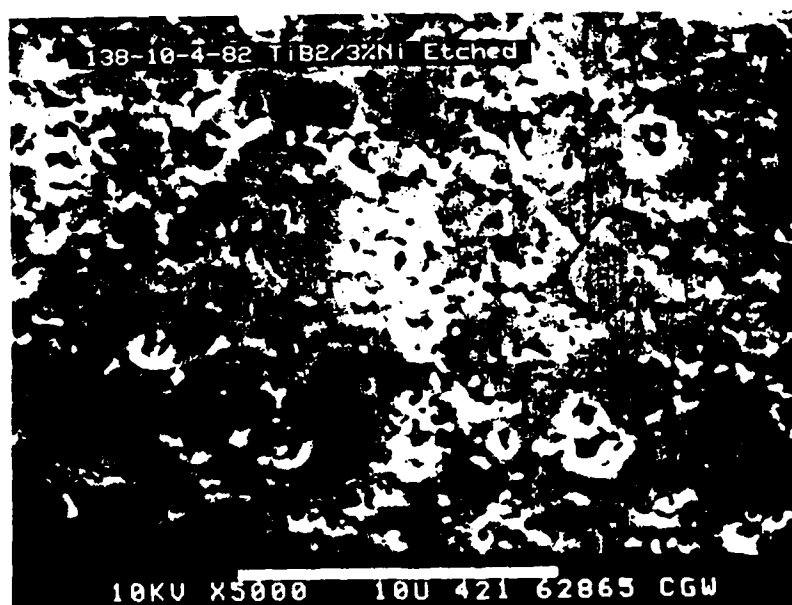


Figure 4



Figure 5

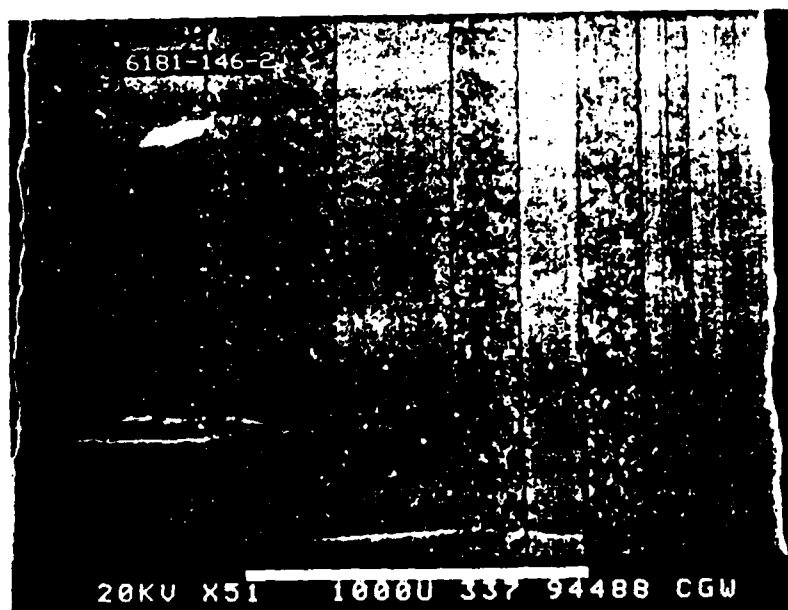


Figure 6

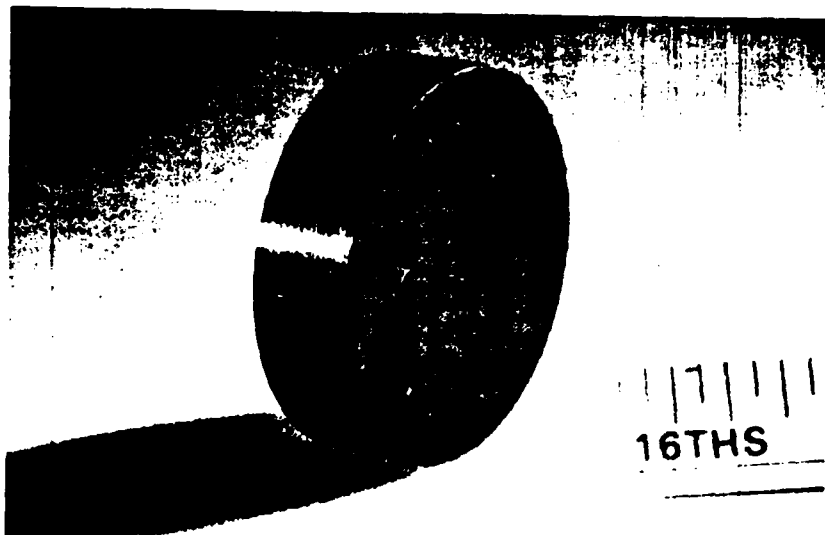


Figure 7

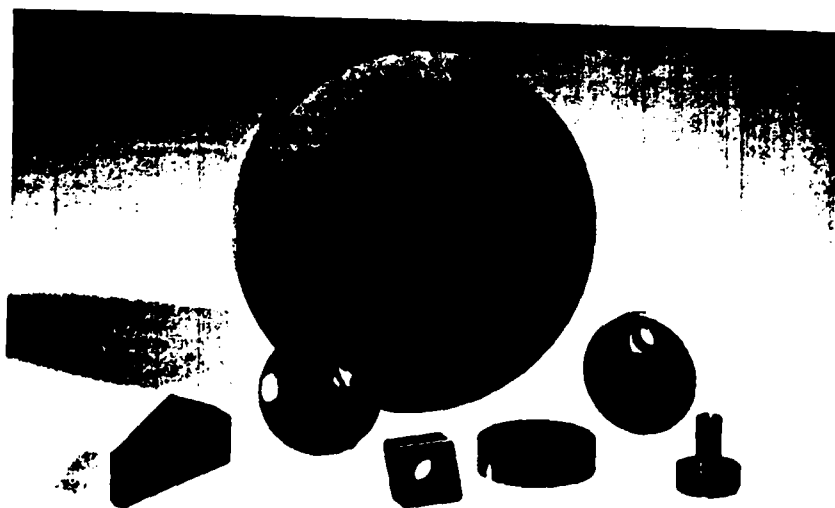


Figure 8

In Situ Formation of SiC and SiC-C Blocked Solids
by Self Combustion Synthesis

S. Ikeda, H. Izawa*, K. Urabe and M. Koizumi

Institute of Science & Technology, Ryukoku Univ., Kyoto, Japan

*Reserch Laboratory, Osaka Cement Co., Ltd., Osaka, Japan

ABSTRACT

A macroscopically homogenous SiC-C solid block was obtained by the SHS reaction of a previously shaped carbon material and molten silicon. The product contained about 30 mol% of β -SiC. The shape and the size of the composite were almost the same as those of the starting carbon material. Improvements in the mechanical properties were attributable to the formation of SiC by the SHS reaction.

In Situ Formation of SiC and SiC-C Blocked Solids
by Self Combustion Synthesis

S. Ikeda, H. Izawa*, K. Urabe and M. Koizumi

Institute of Science & Technology, Ryukoku Univ., Kyoto, Japan

*Reserch Laboratory, Osaka Cement Co., Ltd., Osaka, Japan

1. Introduction

Carbon materials not only have high electric and thermal conductivity, high heat and corrosion resistance, but also good lubricative nature and good machinability. These superior properties have been the basis for practical use of these materials in applications such as electrodes, molds, crucibles, refractory materials, and so on (1). However, the materials have low mechanical strength and low resistance in abrasion and oxidation. In order to improve these weak points, carbon-ceramic composites, especially C-SiC composite, have been studied recently (2). On the other hand, self-propagating High temperature Synthesis (SHS) (3-6) has been utilized for producing SiC. In these processes, SiC was formed by the direct reaction between powdered Si and C.

This paper deals with in situ formation of a C-SiC composite by the SHS process by reacting a blocked solid of carbon with molten silicon. The purpose of this study is to describe a process to form a C and SiC composite which maintains a shape of a blocked solid of carbon used as a starting material.

2. Experimental Procedure

Properties of carbon and silicon materials used were shown in Table 1 and Fig. 1. A piece of silicon was put on the cubic carbon material with 7 by 7 by 7 mm in size, the weight ratio of Si and C being 0.7. The specimen was put in a heating apparatus shown in Fig. 2. Arc discharge was made between a graphite electrode and the specimen, argon being flowed at 0.1 MPa during heating. The reaction was able to be observed through a window with a glass which was equipped in the heating apparatus. Crystal phases of the product were characterized by X-ray diffraction (Rigaku Co./ Rotaflex RAD-RC System using $\text{CuK}\alpha$ radiation). The amount of SiC in the product was estimated gravimetrically by heating the product at 1000 °C in air for one day.

Microstructures of the product were observed by SEM (JEOL Co./ JSM-T20), and chemical compositions were analyzed using EPMA (HORIBA. LTD./ NEWMAX 1500). Pore distribution in the starting carbon material and the product was measured by mercury porosimeter (CARLO ERBA STRUMENTAZIONE).

3. Results and Discussion

The reaction proceeded from the top to the bottom of the specimen as schematically represented in Fig. 3. The silicon lump and the carbon cube were heated by the arc discharge (Fig. 3 (1)), and then the silicon lump was melted as shown in Fig. 3 (2). The molten silicon seemed to be viscous at first. Additional heating lowered the viscosity. Subsequently, the molten silicon started to be soaked into the carbon cube (Fig. 3

(3)). The top of the carbon cube began to glow and the glowed part was propagated toward the bottom(Fig. 3 (3)). The arc discharge was stopped when the glowed front reached to the bottom of the cube(Fig. 3 (4)). It took about two seconds for the glowed front passing the cube.

The properties of the product were compared with those of a carbon material and a sintered silicon carbide in Table 2. The color of the product was grayish black. The shape and the dimensions of the product were almost the same as those of the starting carbon cube. The density was about 2.40 gcm^{-3} . The product had a relatively high Mohs' hardness(8-9) comparing with the carbon material(2-3) as shown in Table 2. X-Ray diffraction diagrams of the starting carbon material and the product were depicted in Fig. 1. Intense 002 line of graphite was observed at $2\theta=26.1^\circ$ on the diagram of the carbon material. Three weak lines were also observed at $2\theta=42.5, 53.9$ and 77.5° . On the other hand, sharp diffraction lines of β -SiC were observed at $2\theta=35.6, 41.4, 60.0, 70.8$ and 75.5° with the 002 line of graphite on the diagram of the product. Very weak lines of silicon were also detected at $2\theta=28.4, 47.3$ and 56.1° . These results showed that the product consisted of C, β -SiC and a small amount of Si. A surface and a cross section of the product were observed by SEM and EPMA(Fig. 4). The results are shown in Figs. 4 (1) and 4 (2). Fig. 4 (2) showed that the molten silicon was soaked thoroughly into the inside of the carbon cube. The Si distribution in the product was not homogeneous microscopically as shown in Figs. 4 (3) and 4 (4). Silicon concentrated in the pore walls making a network-structure in the carbon material.

The Si component should combine with carbon to form β -SiC which was detected by X-rays. The amount of β -SiC in the product was roughly estimated to be 30 mol% by oxidizing carbon in the product at 1000 °C in air for 1 day.

Pore distributions were measured on the starting carbon material and the product. The number of pores 750-7500 nm in size decreased markedly after the reaction. The total pore volume was reduced to less than 1/10. From those evidences mentioned above, the reaction process was considered to be as follows. The molten Si soaked into a carbon material along the open pores and reacted with carbon at the surface layer of the pores. The product (SiC-C blocked solid) expanded 0.6 % in length after the reaction although the volume per mol of β -SiC is about 2.4 times as large as that of carbon (7). No visible cracks were observed on the surface of the product. The increased volume was able to be calculated to be comparable to the volume of open pores in the carbon material. This result suggests that the amount of SiC in the product depends on the pore volume of the carbon materials.

References

- (1) T. Ishikawa and T. Nagaoki, "Shin Tanso Kogyo", pp.1-10, Kindai Henshu, Tokyo (1980).
- (2) H. Honda and K. Kobayashi, "High Tech Tanso Zairyo", pp.113-163, Kogyo Chosa Kai, Tokyo (1987).
- (3) O. Yamada, Y. Miyamoto and M. Koizumi, Am. Ceram. Soc. Bull., 64, 319 (1985).
- (4) R. Pampuch, J. Bialoskorski and E. Walasek, "High Tech Ceramics" edited by P. Vincenzini, pp.217-227, Elsevier Science Publishers B.V., Amsterdam (1987).
- (5) Z. A. Munir, Ceramic Bulletin, 67, 342 (1988).
- (6) J. B. Holt and Z. A. Munir, J. Mater. Sci., 21, 251 (1986).
- (7) T. Hase and H. Suzuki, Yogyo Kyokai Shi, 83, 594 (1975).

Figure Captions

Fig. 1 X-ray diffraction diagrams of carbon material and product.

Fig. 2 Schematic drawing of heating apparatus

Fig. 3 Schematic representation of reaction process

Fig. 4 SEM and EPMA photographs of a cross section of product.

(1) and (2) and (3) and (4) are the same field. Bright points on
(2) and (4) show Si.

Table Captions

Table 1 Some properties of starting materials

Table 2 Properties of product, carbon material and sintered silicon carbide

Table 1. Some properties of starting materials.

1. carbon material

form	density /gcm ⁻³	c-lattice parameter /nm	open pore /vol. %
solid block	1.45	0.6818	29.3

2. silicon material

form	purity / %
lump	>99.99

262

Table 2. Properties of product, carbon material and sintered silicon carbide.

	product	carbon material	sintered silicon carbide
composition	SiC + C	C	SiC
color	black	black	black
bulk density	gcm^{-3} 2.40	1.45	3.15
Mohs' hardness	8-9	2-3	9.2

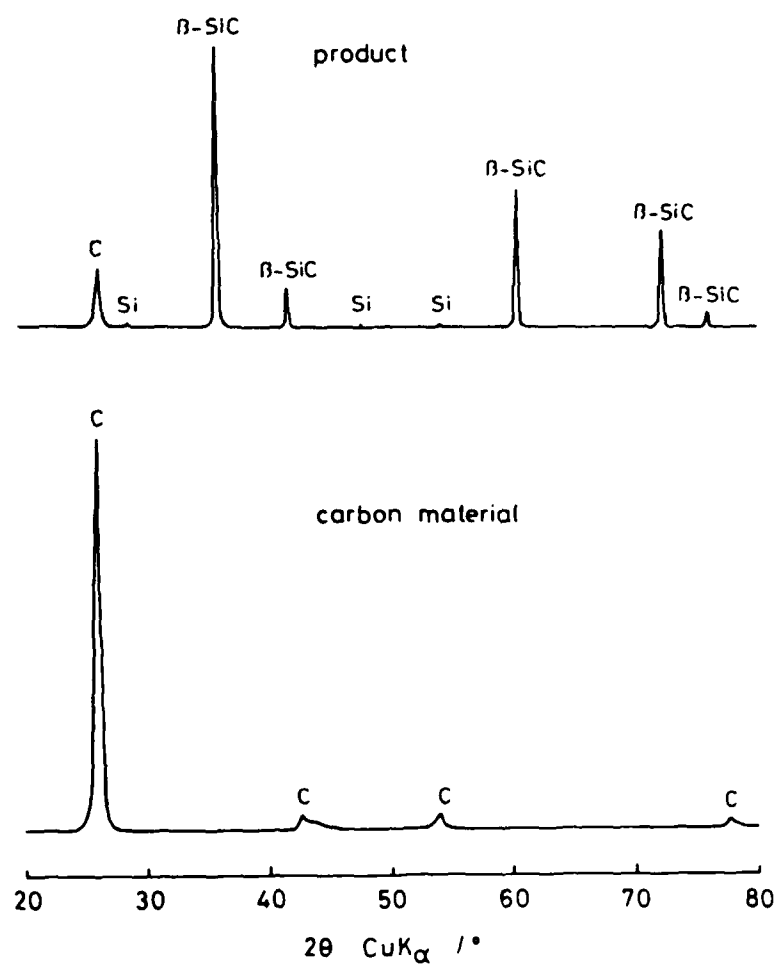


Fig. 1. X-Ray diffraction diagrams of carbon material and product.

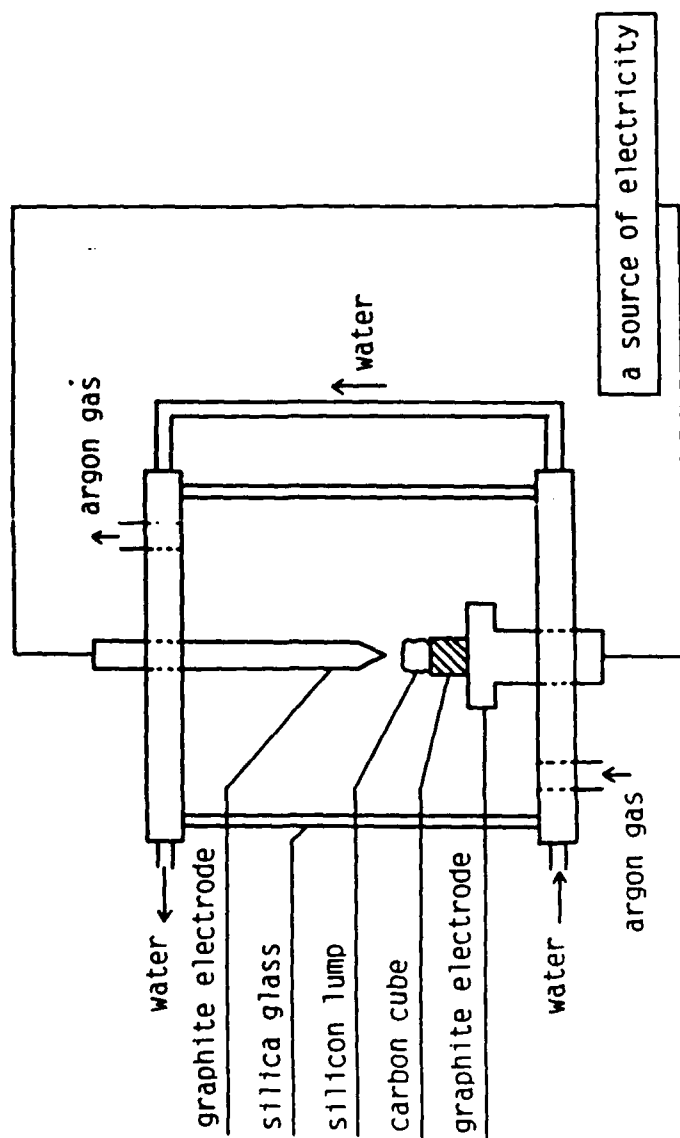


Fig. 2 . Schematic drawing of heating apparatus.

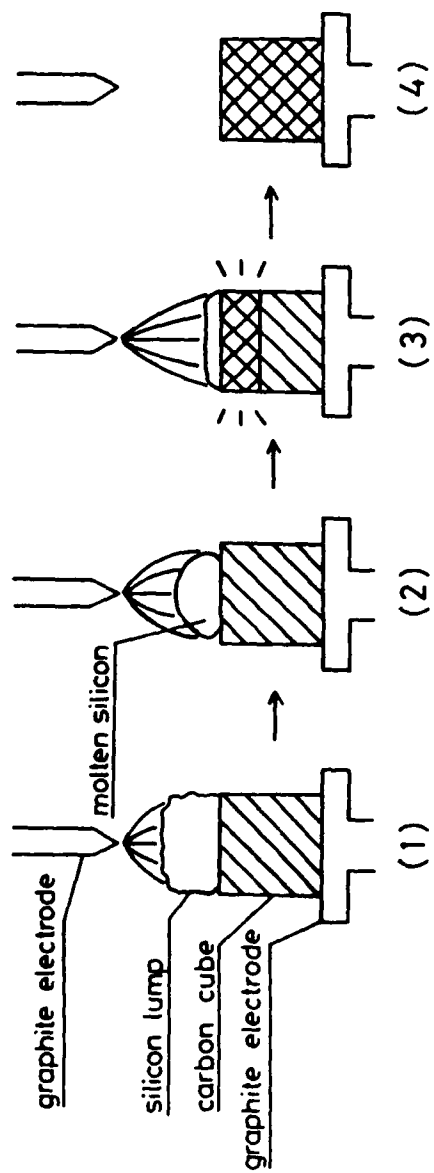
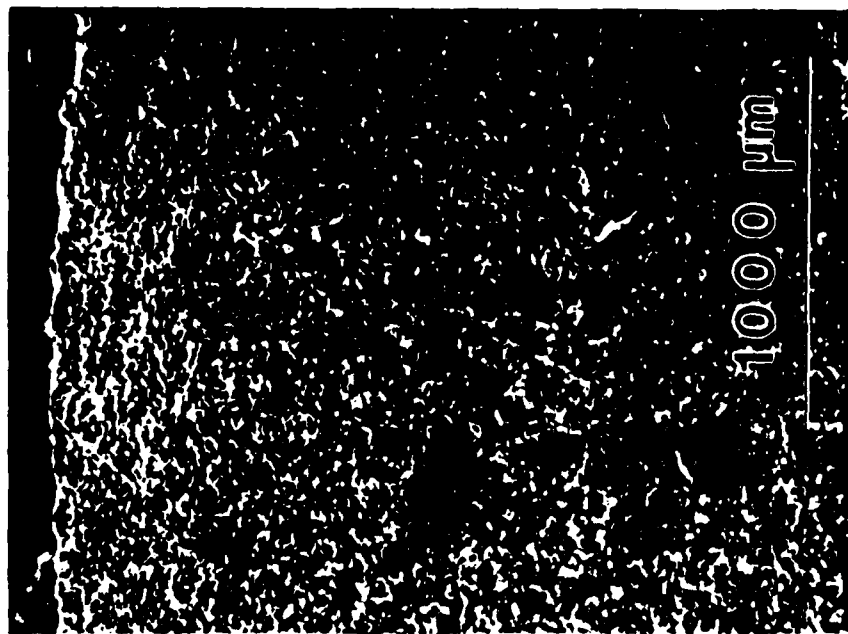


Fig.3 . Schematic representation of reaction process.

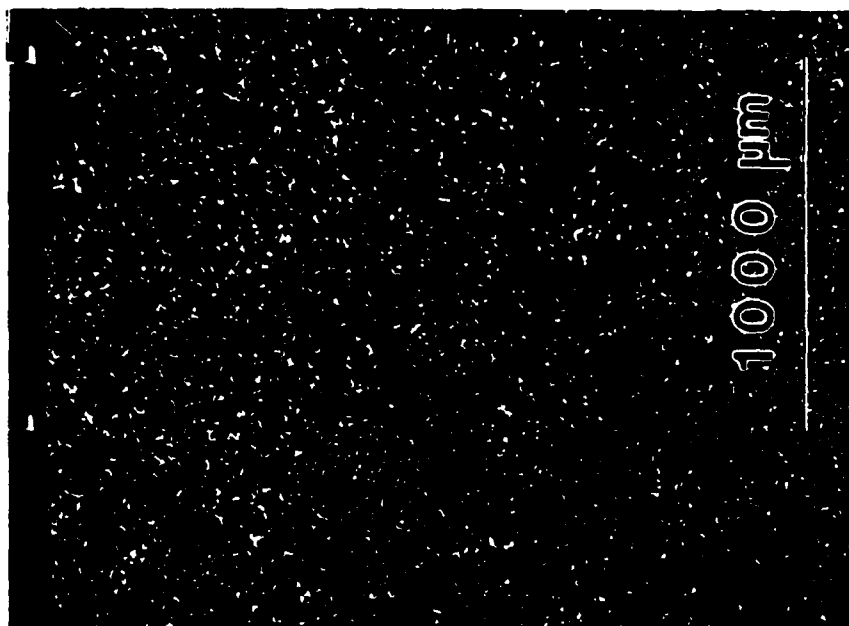
)

Blank
200



(1) SEM

← surface →

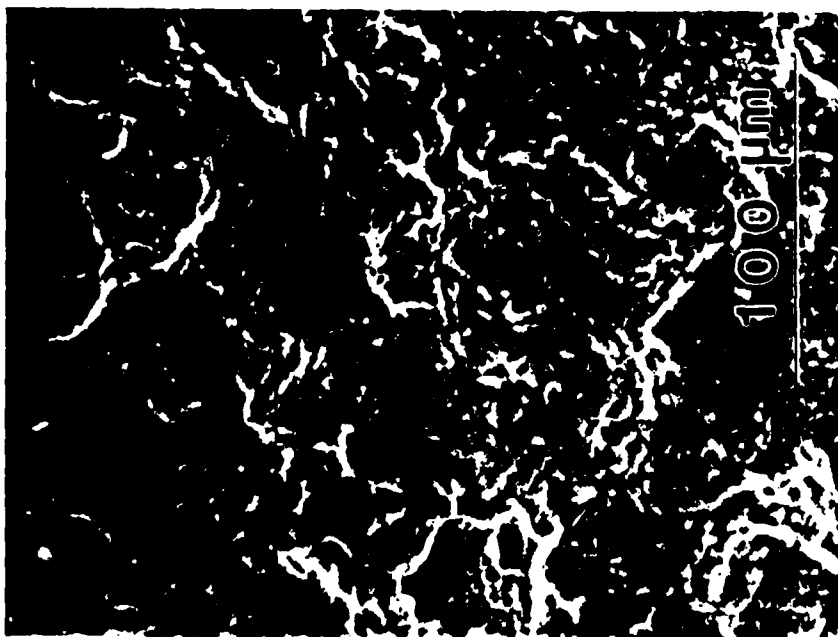


(2) EPMA

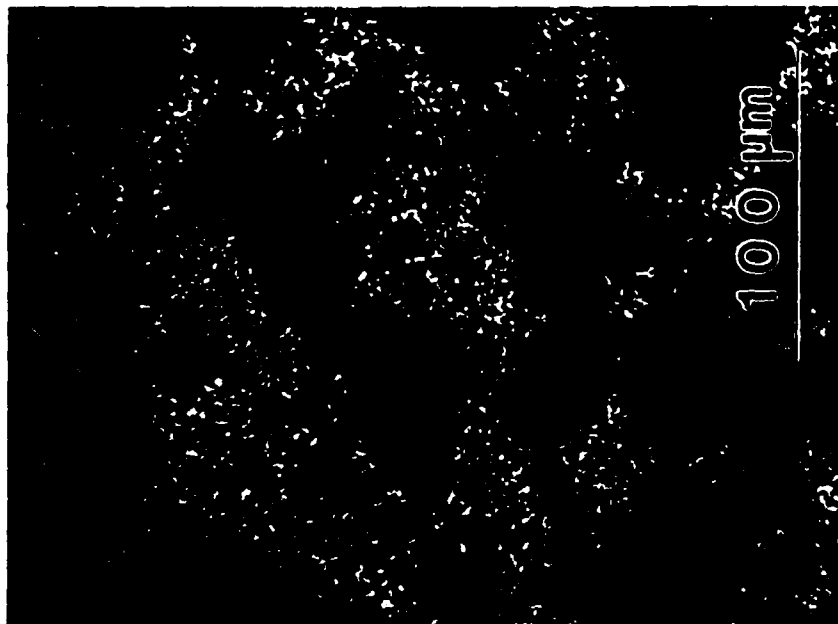
Fig.4 . SEM and EPMA photographs of a cross section of product.

(1) and (2), and (3) and (4) are the same field.

Bright points on (2) and (4) show Si.



(3) SEM



(4) EPMA

Fig. 4

POWDER PURITY AND MORPHOLOGY EFFECTS IN COMBUSTION SYNTHESIS REACTIONS

L.J. Kecskes, T. Kottke, and A. Niller
Ballistic Research Laboratory, Aberdeen Proving Ground, MD. 21005, USA

ABSTRACT

Solid and gaseous impurities evolved during combustion synthesis reactions were measured for green compacts made with as-received and vacuum outgassed Ti+C powders. The purity and morphology of these powders affect both the reaction dynamics and the properties of the product. Vacuum baking was found to improve interparticle bonding and reduce sample porosity.

INTRODUCTION

Combustion Synthesis is a well known method of producing ceramic materials from their constituent powders. Once ignition is achieved, the heat release from such exothermic combustion processes is sufficient to propagate a combustion front through the powder compact and to completely consume the reactant powders. Such reactions occur at a temperature above 2000 C which is high enough to cause the evolution of most impurities found on the reactants. The evolution is visible in the form of a prominent flame that consists of both condensable and non-condensable reactant impurities. At the high reaction temperatures, the evolution process may be so violent that it can have deleterious effects on the structural integrity of the final ceramic product.^{1,2}

The objectives of this investigation have been to determine the identities of the reactant impurities and the effect that their volatilization has on the reaction dynamics as well as on the product structure. These objectives were accomplished by measuring both non-condensable and condensable species given

off by the reacting Ti-C system.

EXPERIMENTAL PROCEDURE

Cylindrical Ti+C green compacts were made from stoichiometric mixtures of as-received titanium and graphite powders. The compacts were reacted in a chamber fitted with a removable collection chamber to allow the measurement of the non-condensable impurities given off during the reaction. A tungsten filament was used to both vacuum bake and initiate the reaction. Prior to ignition, the reaction and collection chambers were pumped down to a base pressure of 13 mPa and then backfilled with argon to a pressure of 130 Pa. The argon provided an absolute standard against which the amounts of non-condensing species could be calibrated. The experimental details are described in Ref. 3.

Two types of experiments to measure the non-condensables were carried out in the reaction chamber. In the first experiment, the compacts were ignited without previous outgassing. In the second experiment, the compacts were first vacuum baked for 10 minutes, allowed to cool to room temperature, and ignited after the argon backfill. After each reaction, the non-condensed gases in the collection chamber were analyzed with a Residual Gas Analyzer (RGA). Experiments to measure the condensing species were also carried out in the chamber. The solid residue, ejected from the reacting samples, was collected as coatings on aluminum targets placed 3 to 4 cm away from the sample. This collection took place during the reaction of both unbaked and baked samples.

The condensate morphology and the interior microstructure and fracture characteristics of the TiC reaction products were examined with scanning electron microscopy. Additionally, three Ion Beam Analysis methods were used on the coatings produced by the reactions from the baked and unbaked samples. The

first, Proton Induced X-Ray Excitation (PIXE), was used for a qualitative elemental identification. The second, Rutherford Backscattering Spectroscopy (RBS), was used to quantitatively depth profile the structure of the coatings. The third method was Nuclear Reaction Spectroscopy (NRS). The description of the RBS and NRS techniques, along with the computer code PROFILE used to analyze the raw data, are given in Ref. 4.

RESULTS AND DISCUSSION

1. Non-Condensable Impurities from the Reaction

The impurity gases ejected during the reaction consisted predominantly of H_2 , CO, O_2 , CO_2 , and hydrocarbons. These results agree with previous investigations that find H_2 and CO as the major contaminant species.⁵ While baking considerably reduces the amount of evolved gas, the impurities detected in the reaction are identical to those detected on the reactant powders.⁶ The origin of these gases is almost certainly the evolution of impurities from the reactants rather than any synthesis reaction occurring during the SHS process. H_2 is from the decomposition of TiH_2 and O_2 is from the TiO_2 in the Ti powder. The CO, CO_2 , and hydrocarbons are mainly from the graphite.

2. Condensable Impurities from the Reaction

Figure 1 shows the morphology of the reaction ejecta from the unbaked and baked reactions. The coating from the unbaked sample contains two types of particles. The first type consists of extremely fine and uniform soot-like particles (~50 nm). The second is irregular, about 10 to 30 μ m in size. The larger particles are probably reacted TiC fragments that are ejected by the violent gas flow. The coating from the baked sample, however, is made up of soot-like particles only. Since the soot-like particles from both samples are

identical in appearance, the absence of larger reacted particles from the baked sample is most likely caused by the gentler reaction in that case.

The PIXE spectra for the two samples show the elements Na, Al, Si, S, Cl, K, Ca, Ti, Cr, Mn, Fe, Ni, Cu, and W. The sources of these elements are: the precursor powders, the filament, the aluminum substrate, and the specimen stage holding the green compact. Results of the Ion Beam Analysis for the baked sample is summarized in Fig. 2 with the NRS(2b) and RBS(2c) data along with the computed fits to these data using the concentration profiles of the elements shown in Fig. 2a. Similar data and fits were obtained for the unbaked sample.

The elements of oxygen, carbon, titanium, calcium, and chlorine appear on the coating's surface. The atomic ratios of Ti and O are 1 to 2 which is right for TiO_2 with the excess oxygen being tied up as Al_2O_3 . If, however, the assignment of the titanium went to TiC , a possibility which seems in line with the Ti and C concentration numbers, the oxygen on the outer surface layers must be explained. Since oxygen cannot remain unbound, the assignment of the oxygen to the titanium is the only possibility. The TiO_2 may originate in one of two ways. First, it may be simply the oxide layer blowing off the Ti powder during the reaction and attaching to the aluminum target. Second, it may be due to the oxidation of any titanium that was blown out of the reacting sample and remaining on the aluminum surface. The source of oxygen for this second case would be either the dissociated oxide from the Ti powder or from the small amount of residual oxygen in the reaction chamber. The carbon can now be attributed to some of the carbon powders in the sample being blown to the aluminum substrate by the action of the volatile gases during the reaction.

3. Sample Structures

TiC samples resulting from the baked and unbaked compacts were examined

for interior microstructure and fracture characteristics. Polished surfaces of the unbaked and baked samples do show some differences in their resultant microstructures (see Fig.3). In the figure, the light areas are void-free TiC and the darker areas are open pores. The unbaked sample shows TiC regions dispersed with open and interconnected porosity. An equivalent region of the baked sample shows larger areas of TiC with pores that are somewhat smaller than those in the unbaked sample. Several Knoop hardness measurements of fully dense areas of the baked sample yielded values at or above 12.7 GPa. This value approaches the hardness of fully dense hot pressed TiC.⁶ No successful hardness measurements could be made on the unbaked sample because the grains always collapsed under the indenter.

At room temperature, both TiC samples failed by transgranular fracture. As seen in Fig. 4, the structures are relatively coarse in character, however the intergrain bonding in the baked sample is improved. This is evident in the increased number of cleavage steps and the absence of pullouts. Further examination of pore interiors gives a better insight into the failure of these samples. In the unbaked sample, the grains lining pore walls are well defined with a small amount of sintering present. In the baked sample, however, the grains have sintered to a greater degree, giving an almost melted appearance. This difference between baked and unbaked samples can be explained as follows. When the precursors are contaminated with impurities, heat is lost as the impurity gases are heated to high temperatures and driven out of the reaction zone. Because of the greater amount of impurities in the unbaked sample, the net porosity due to the force of the exiting gases is greater and because less heat is retained, the sintering of particles is less effective. The relatively high hardness values of large TiC grains in the baked sample confirm that the inter-

particle bonds that result from more sintering and less disruption by gas flow improve the local strength of the material.

SUMMARY

This experiment has identified several impurities from the TiC combustion synthesis process. The non-condensable species, in their order of importance, are H_2O , H_2 , O_2 , CO , CO_2 , and a variety of hydrocarbons. The condensable species consist of TiO_2 and carbon. The evolution of contaminant species create internal pressures that not only counteract the sintering process but also increase the sample porosity, and as a result, degrade the mechanical properties of the ceramics. The structural disruption of the reacting sample may be prevented if most of non-condensable impurities are purged in a vacuum oven in several hours at temperatures in the 500 C range. However, the condensables of carbon and TiO_2 , as well as the oxygen released from the TiO_2 , cannot be purged at any reasonable bakeout temperature.

REFERENCES

1. W.F. Henshaw, A. Niiler, and T. Leete, "Self-Propagating High-Temperature Synthesis of Ceramics in Vacuum," Ballistic Research Laboratory Report ARBRL-MR-03354, Aberdeen Proving Ground, MD. (1984).
2. J.B. Holt, G.M. Bianchini, and D.D. Kingman, "Simultaneous Combustion Synthesis and Densification of Refractory Materials," UCRL-93467, Lawrence Livermore National Laboratory, CA. (1986).
3. L.J. Kecskes and A. Niiler, "A Study of Impurities in Combustion Synthesis Systems," Ballistics Research Laboratory Report BRL-MR-3658, Aberdeen Proving Ground, MD. (1988).

4. A. Niiler, R. Birkmire, and J. Gerrits, "PROFILE: A General Code for Ion Beam Analysis Spectra," Ballistics Research Laboratory Report ARBRL-TR-2233, Aberdeen Proving Ground, MD. (1980).

5. J.B. Holt and Z.A. Munir, "Combustion Synthesis of Titanium Carbide: Theory and Experiment," J. Mat. Sci., 21, [1] 251-259 (1986).

6. D.B. Miracle and H.A. Lipsitt, "Mechanical Properties of Fine Grained Substoichiometric Titanium Carbide," J. Amer. Cer. Soc. 66 [8] 592-597 (1983).

FIGURE CAPTIONS

Fig. 1. Microstructures of the particulates ejected during the TiC reaction, 1a for the unbaked and 1b for the baked samples.

Fig. 2. Elemental concentration, NRS, and RBS spectra for TiC reaction effluent.

Fig. 3. Polished surfaces of the TiC reaction products with 3a showing the unbaked sample and 3b showing the baked sample.

Fig. 4. Fractographs of the samples. 4a shows the fracture surface of the unbaked sample and 4b shows that of the baked sample.

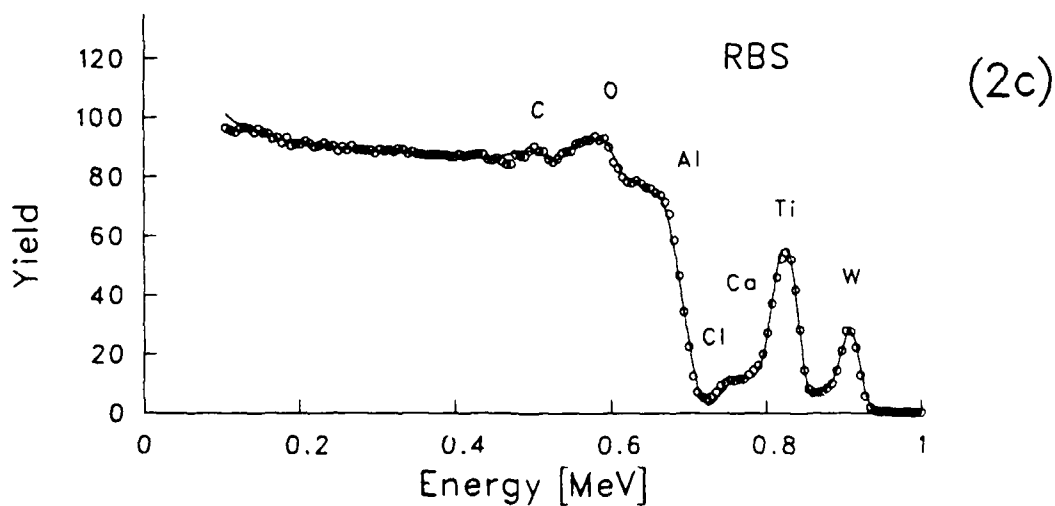
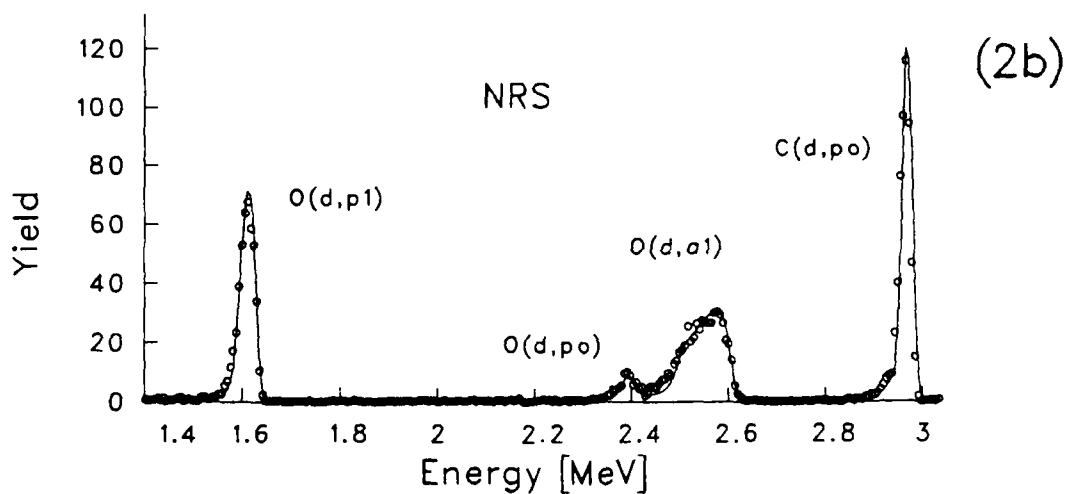
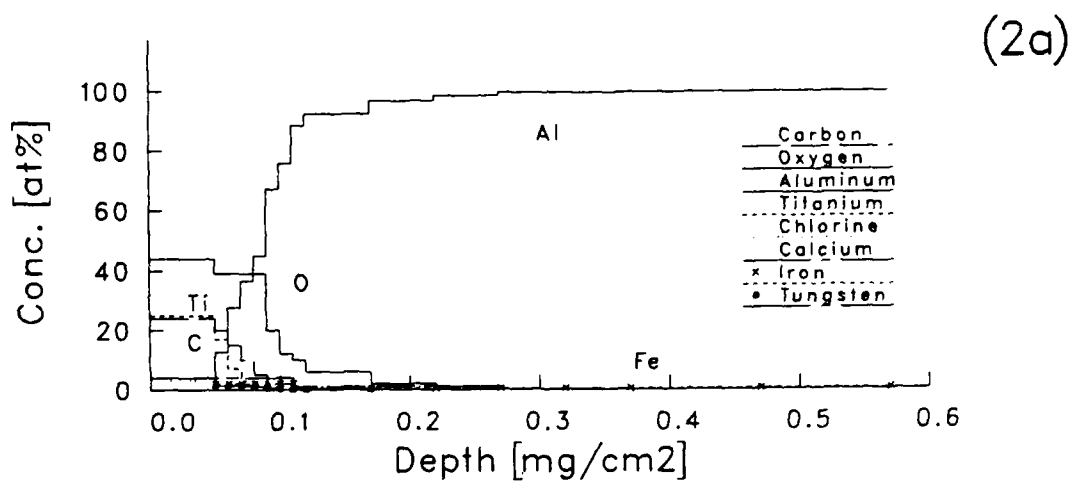
(1a)



(1b)



10 μm



Rec'd 7/1/1

642

(3a)



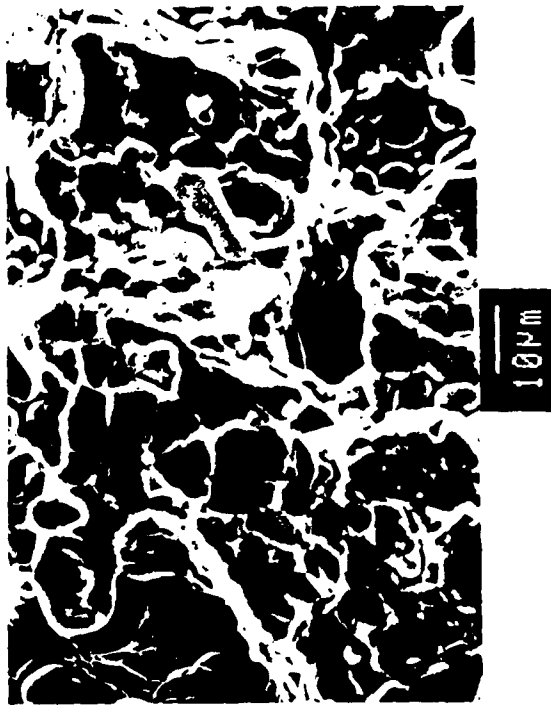
100 μm

(3b)

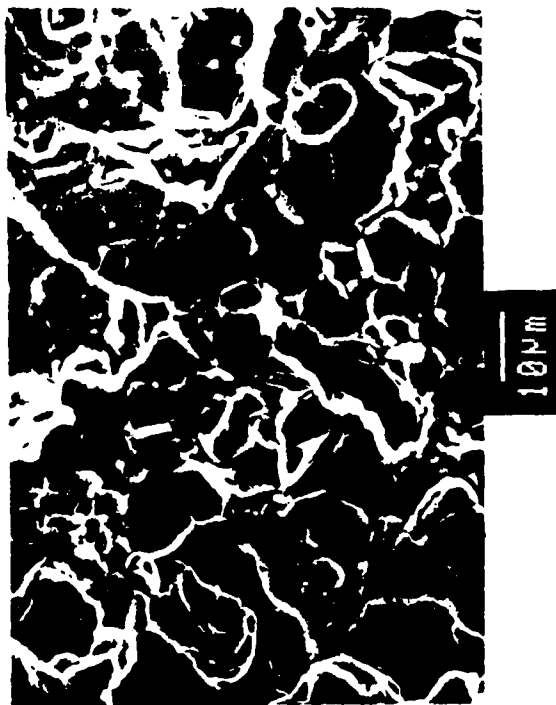


100 μm

(4a)



(4b)



SIMULTANEOUS SYNTHESIS AND DENSIFICATION OF CERAMIC COMPONENTS BY
THE SHS PROCESS UNDER THE GAS PRESSURE

Yoshinari MIYAMOTO

The Institute of Scientific and Industrial Research, Osaka
University, Ibaraki, Osaka 567, Japan

and

Mitsue KOIZUMI

Institute for Science and Technology, Ryukoku University,
Fushimi-ku, Kyoto 612, Japan

Key words: Gas-pressure combustion sintering, TiB_2 , TiC , Ceramic
alloying

ABSTRACT

The gas-pressure combustion sintering is a new reaction sintering process to synthesize and densify the ceramics simultaneously and rapidly under isostatic pressure. By this method, the dense ceramics of TiB_2 (Ti_3B_4 , TiB) and TiC_x ($x=0.5\sim 0.8$) and the composites of $TiC+Ni$ ($\geq 10wt\%$) have been fabricated from their elemental powders under Ar gas pressures below 100MPa. This process has large potentials not only for the mass production of near-net shape components but also for the production of a variety of new material complexes in the ceramic-ceramic and ceramic-metal systems.

Introduction

The self-propagating high temperature synthesis (SHS)¹⁾, also called combustion synthesis, is known as a highly exothermic reaction which is spontaneously propagating through the reactant

converting into the compound without gasification. Many refractory materials of borides, carbides, nitrides and silicides having high formation energies are easily formed by igniting the mixed powders of their constituent elements.

When the SHS is carried out under pressure, it is expected that the product can be densified simultaneously with the synthesis. Recently, a new process using gas pressure has been devised for the combustion sintering²⁾. The isostatic gas pressure is useful to offset disadvantages of the other pressurizing systems. In this paper, the process of gas-pressure combustion sintering and its application to materials development are described.

Process Development of Gas-Pressure Combustion Sintering.

Figure 1 shows a schematic of the interior of an autoclave for the gas-pressure combustion sintering. In this way, the reactant is vacuum-sealed into a glass container just like as the glass encapsulation method for HIP, and embedded into the ignition agent which is charged in a graphite crucible. This sample assemblage is placed at the center of the autoclave in which a furnace to heat the glass container and a heater to ignite the ignition agent are installed as seen in Fig.1. The combustion reaction of reactant is initiated by the exothermic heat of the surrounding ignition agent. The combustion sintering is carried out as follows. First, the inside of pressure vessel is heated to about 973K in order to make the container of pyrex glass soften. Then, the Ar or N₂ gas pressure is applied to an appropriate level usually below 100

MPa, and the ignition agent is burned by passing a current of 100 Amps for 3 seconds through an ignition heater.

The green compact of reactant and the glass capsule are coated with BN powder to protect the capsule from the reactions with reactant and ignition agent. As a material for ignition agent, the mixed powder which produces the strong combustion reaction is used. Many kinds of ignition agents would be available and the products can be used as ceramic powders. At present, a mixed powder of Ti and C is used, which produces high temperature of 3210K equivalent to the melting point of TiC.

Figure 2 is a photograph showing the green body, glass encapsulated sample and product for TiC+Ni (20wt%) composite. It is expected that the use of isostatic gas pressure and ignition agent would lead the combustion sintering to an economic process to realize mass production of near-net shape components.

Application to Materials Development

Nearly-full dense ceramics and ceramic composites of TiB_2 , TiC_x and TiC+Ni have been obtained from their elemental powders under Ar gas pressure of 100 MPa by the gas-pressure combustion sintering.

For TiB_2 ceramics, the reactant of Ti and B powders mixed with the stoichiometric 1 : 2 composition is difficult to be densified, but the addition of excess Ti enhances the densification. In this case, it is noted that Ti metal does not remain in the sintered body. The products are composed of TiB_2 with additional phases of Ti_3B_4 and TiB, which increase with

excess Ti. The liquid phases of Ti_3B_4 and TiB having lower melting points than TiB_2 seem to enhance the densification. Figure 3 shows the density of sintered bodies depending on the excess titanium when the combustion sintering was carried out at 100MPa. The relative density is calculated against the theoretical one for TiB_2 ($4.53g/cm^3$) since the densities of TiB_2 , Ti_3B_4 , TiB and Ti are almost the same value. The density reaches up to 99% when 20wt% excess Ti was added into the reactant. The titanium boride composites with excess Ti added more than 10wt% can be densified over 97% of theoretical at 40MPa.

These boride ceramics exhibit notable microstructures reflecting the unique sintering process. The detailed analysis is given in our separate report³⁾.

Figure 4 is a SEM photograph for the fractured surface of the compact with larger grains of a few μm size and smaller submicron ones dispersed, showing that the grains bonded tightly and the fracture occurred by both transgranular and intergranular modes. The sintered body had the Vickers microhardness of 19GPa and the fracture toughness of $5.6MPa\sqrt{m}$ when fabricated from the reactant with 10wt% excess Ti at 40 MPa.

In the case of TiC ceramics, the fully densified compacts were fabricated in the composition range of TiC_x ($0.5 \leq x \leq 0.8$) without additives at 100MPa. Figure 5 shows the relative densities depending on the starting compositions, which are calculated against the theoretical densities for each composition. Each reactant with $x \leq 0.8$ converted entirely into the single phase of TiC_x , but a small amount of carbon remained

at the grain boundary when reaching near to the unstable stoichiometric composition of $\text{TiC}(x=1)$, and the residual carbon inhibited the densification.

Metal addition is useful to densify the product and improve the toughness. Figure 6 shows the fractured surface of $\text{TiC} + \text{Ni}$ (10wt%) compacts which was densified to 99.6% of theoretical at 100MPa. Molten nickel scarcely reacted and located at the grain boundary, especially at the triple points. Figure 7 shows the dependencies of Vickers microhardness and fracture toughness on nickel content for the fully densified composites at 100MPa.

This is the cases that the metal composition is dispersed homogeneously in the sintered body. On the other hand, it is possible to change the metal composition heterogeneously in the ceramic matrix because the compositional configuration prepared in the green body remains due to the rapid wave propagation of combustion reaction. Figure 8 shows the dense product consisting of a surface layer of TiC with nickel concentration increasing to 30 wt% toward the other end of the compact. This ability of the gas-pressure combustion sintering can be applied to fabricate so-called Functionally Gradient Materials (FGM)⁴⁾ which is the new composite materials consisting of a surface layer of refractory ceramics with a metal phase continuously increasing within the ceramic matrix. The FGM is expected as a unique high temperature material having low internal thermal stress, toughened body and easiness in bonding to metal component.

Summary

The combustion sintering can produce the dense monolithic

ceramics of borides and carbides. However, it is better suited for the ceramic and ceramic-metal composites as mentioned before. The process melts at least a part of the reactant and product by the highly exothermic heat of $2000 \sim 3000^{\circ}\text{C}$ and consolidates or fuses the complex synthesized under pressure. This is just "Ceramic Alloying Process".

References

1. A. G. Merzhanov and I. P. Borovinskaya, "Self-Propagating High Temperature Synthesis of Refractory Inorganic Compounds", Dokl. Chem., (Engl. Trans.), 204 [2] 429-32 (1972)
2. Y. Miyamoto and M. Koizumi, "Potentiality of High Pressure Combustion Sintering to Produce Ceramic Based Multi-Phase Components", Proc. Int. Symp. on "Sintering '87", Tokyo, Elsevier Science Publishing Co.Inc., voll, 511-16 (1988)
3. K.Urabe, Y.Miyamoto, M.Koizumi and H.Ikawa, "Microstructure of TiB_2 Sintered Body by Self Combustion Method", this volume.
4. M. Niino, "Design of Functionally Gradient Materials utilizing process technologies of micro elements", Function & Materials, 7, 31-43 (1987), in Japanese.

Figure Captions

- Fig. 1. Schematic of the experimental apparatus for the gas-pressure combustion sintering.
- Fig. 2. Appearance of sample preparation and product, a green body (left), glass encapsulated sample (center) and sintered body (right) for $\text{TiC}+20\text{wt}\%\text{Ni}$ composite (99% density of theoretical).
- Fig. 3. Density of titanium boride composites as a function of starting composition. The samples were fabricated at 100MPa.
- Fig. 4. SEM photo of fractured surface of titanium boride composite fabricated from the reactant with 10wt% excess Ti at 100MPa.
- Fig. 5. Relative densities of titanium carbide ceramics depending on the starting compositions.
- Fig. 6. SEM photo of fractured surface of $\text{TiC}+10\text{wt}\%\text{Ni}$ composite fabricated at 100MPa.
- Fig. 7. Vickers microhardness and fracture toughness for $\text{TiC}+\text{Ni}$ composites as a function of nickel content. The samples were fabricated at 100MPa.
- Fig. 8. Dense TiC -based composite with heterogeneously distributed metal phase. The top surface layer consists of TiC and nickel concentration increases to 30wt% with 10wt% step toward the bottom end.

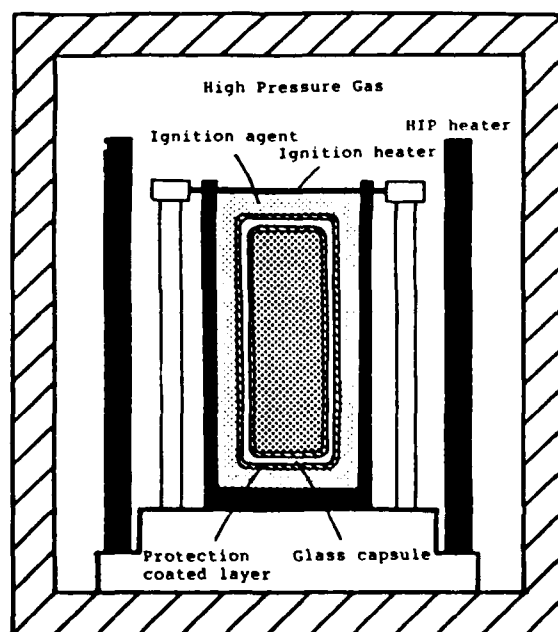


Fig. 1. Schematic of the experimental apparatus for the gas-pressure combustion sintering.

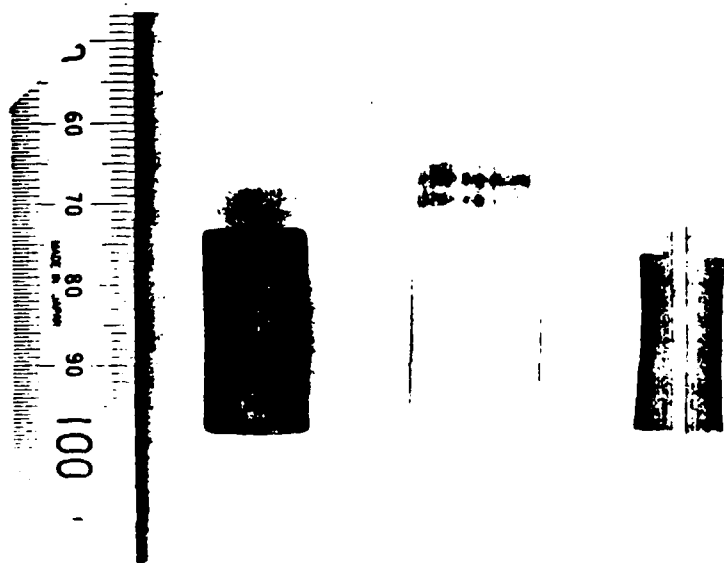


Fig. 2. Appearance of sample preparation and product, a green body (left), glass encapsulated sample (center) and sintered body (right) for $\text{TiC}+20\text{wt}\%\text{Ni}$ composite (99% density of theoretical).

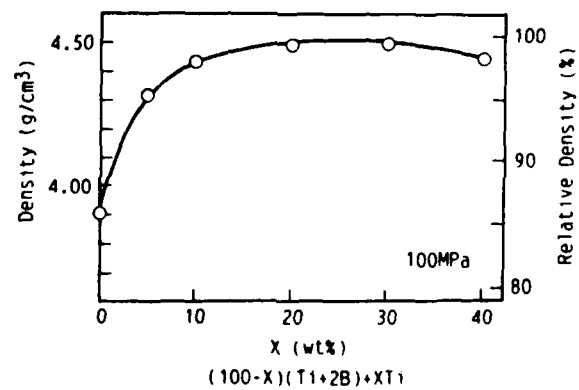


Fig. 3 . Density of titanium boride composites as a function of starting composition. The samples were fabricated at 100MPa.

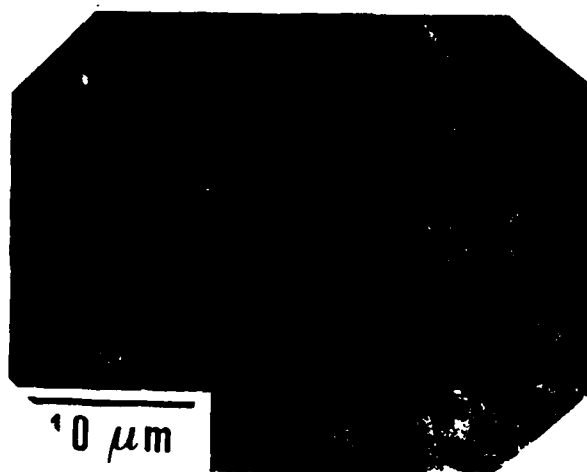


Fig. 4. SEM photo of fractured surface of titanium boride composite fabricated from the reactant with 10wt% excess Ti at 100MPa.

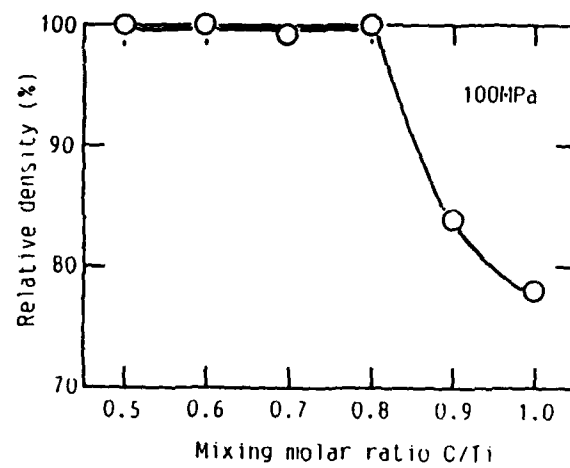


Fig. 5. Relative densities of titanium carbide ceramics depending on the starting compositions.

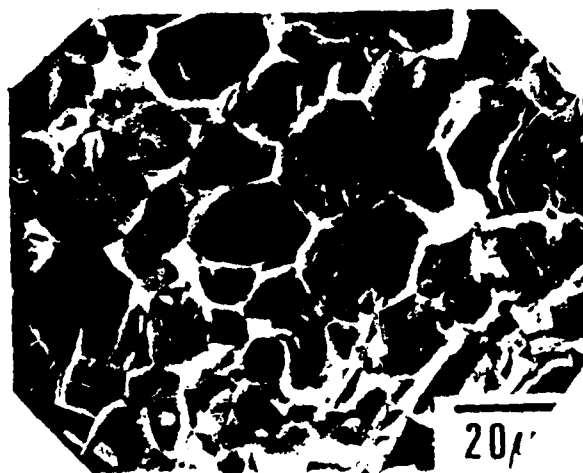


Fig. 6 . SEM photo of fractured surface of TiC+10wt%Ni composite
fabricated at 100MPa.

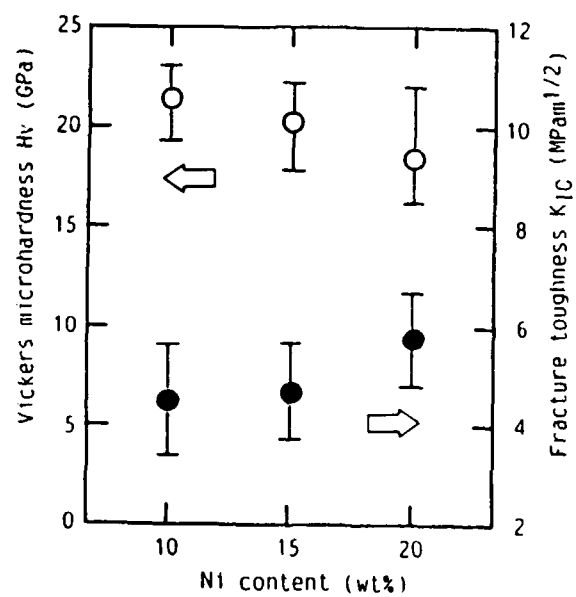


Fig. 7 . Vickers microhardness and fracture toughness for TiC+Ni composites as a function of nickel content. The samples were fabricated at 100MPa.

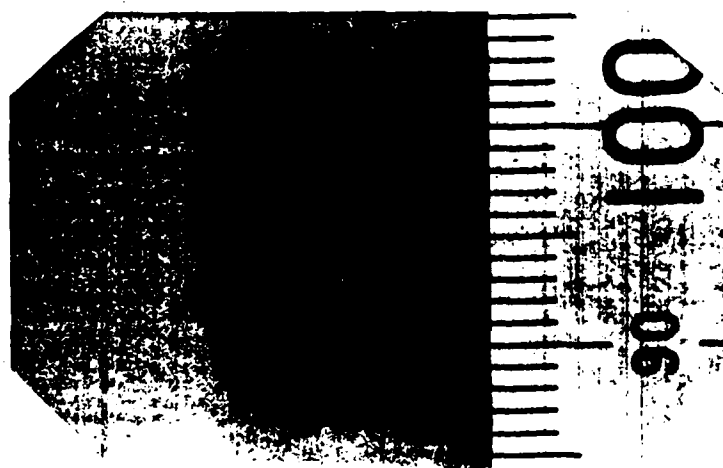


Fig. 8 . Dense TiC-based composite with heterogeneously distributed metal phase. The top surface layer consists of TiC and nickel concentration increases to 30wt% with 10wt% step toward the bottom end.

The Use of Self-Propagating High Temperature Synthesis of High Density Titanium Diboride

P.D. ZAVITSANOS, J.J. GEBHARDT, AND A. GATTI

General Sciences, Incorporated

655 South Gravers Road

Plymouth Meeting, PA 19462

Preliminary results of an experimental program aimed at synthesizing titanium diboride tiles up to one inch thick by SHS under uniaxial pressure are presented. Specimens up to 3" diameter and 4" x 4" with densities up to 95% were fabricated from mixed titanium, boron and nickel powders. The influence of experimental variables on integrity, uniformity, structure and related material properties will be discussed.

INTRODUCTION

Hard ceramics including TiB_2 produced by conventional methods such as sintering and hot pressing require expensive high temperature process steps and machining which add significant cost to the material.

The use of exothermic, self-propagating reactions (SHS), has recently received interest especially by the Soviets to form high purity refractory compounds especially in the boride and carbide systems. The cost effective production of abrasive compounds, cutting tools and hard, strong, and dense refractory materials has been claimed.

Most of the advantages of the SHS Process have been discussed by the Soviets as well as by the U.S. community and center on the following:

1. No significant process heat necessary.
2. Material can be shaped during the reaction and, therefore, requires minimum machining costs.
3. The temperatures generated during the reaction (~3900K as measured by radiometry in this laboratory) are higher than conventional techniques, and can thus, in principle, provide higher purity compounds.
4. The higher process temperature and melting in some cases, can favorably influence microstructure and other significant properties.

Lightweight ceramics which can be prepared by SHS reactions are being considered as candidates for armor, and limited testing to date has identified the generic properties which can maximize armor performance. They are as follows:

1. Highest Chemical Purity
2. High Microhardness
3. High Young Modulus
4. High Weibull Modulus (High Fracture Toughness)
5. Grain Size less than 20 μ m
6. Low Poisson's Ratio
7. Flexure Strength (does not correlate)

In the early 80's, Zavitsanos⁽¹⁾ and his group were the first to synthesize high density TiB₂ in relatively massive form using the self-propagating high temperature synthesis (SHS) by providing heat externally only for initiation of Ti/2B mixtures, and applying pressure simultaneously. The density was 97% of theoretical and the hardness exceeded that of commercially available hot pressed samples.

the work was continued with ARMY/MTL funds and a more comprehensive study was carried out on synthesis parameters and material characterization⁽²⁾.

The results of the reaction thermochemistry reported^(1,2) indicate that the calculated adiabatic temperature of 3600°K, obtained in the reaction



exceeds the melting point of TiB₂, reported as around 3200K⁽³⁾. Studies of the microstructure of the reaction pressings confirmed that a liquid phase is present during the process, and the reaction is in a liquid + TiB₂ phase field. Electron microprobe results confirm that liquid phases must be present and secondary phases (possibly TiB and Ti) and contaminants (Si, Fe), are rejected from the liquid as the mass cools and are located at pore surfaces and as inclusion in the TiB₂ matrix.

Stoichiometric and excess Ti powder mixes react to form TiB₂ with total metal impurities 0.57 to 0.75%. The formation of a liquid during the reactions is a desirable situation and rapid densification is readily accomplished.

Reaction pressing in graphite dies was used to form a finished sample 1.75" in diameter by at least 1/8" thick. The graphite die assembly with a carbon-carbon filament wound "strongback" retaining ring contained the compact during processing in a furnace atmosphere of flowing N₂ or argon and with an applied force of 15,000 pounds. Figure 1 shows a typical temperature-pressure-time profile used to synthesize and densify TiB₂ from the elemental powder mixes.

Properties of the TiB_2 obtained during these studies are listed in Table 1 and were sufficiently encouraging to exploit the possibility of utilizing the heat of reaction alone for densification and development of desirable structural properties. This would avoid the requirement of extensive furnace investment, associated energy expenditure and long processing times and enable a relatively low cost, big throughput fabrication process to be developed for TiB_2 tiles of useful size. The work described in this paper is directed toward that end.

EXPERIMENTAL PROCEDURE

Elemental powders used in fabricating SHS- TiB_2 have included the following:

Titanium	99.7%	325 mesh	AEE*
Boron (cryst)	99.5%	325 mesh	AEE
Boron (amorph)	94.5%	3-5 μ m	AEE
Boron (amorph)	>99%	<1 μ m	Gallery Chemical Co.
Nickel	99.5%	325 mesh	Chem-Alloy, Inc.

*Atlantic Equipment Engineers, Bergenfield, N.J.

Nickel is added in varying amounts (up to 12 W/O) to achieve a longer melting time and to improve bonding and toughness. The major impurity, aside from absorbed surface species, appears to be magnesium, present at 5.5%, in AEE amorphous boron according to the vendor's analysis. This may vary from batch to batch, however.

The procedure consists of loading the mixed and heat-treated powders into the mold, shown in Figure 2 and previously lined with grafoil®, inserting the fuse fixture consisting of a pyrotechnic wire compressing the charge to a selected pressure level using the comparison-load correlation shown in Figure 3 and igniting the mixture. To limit experimental complexity, a standard uniaxial pressure of about 1200 psi has been used. In certain cases, the piston has been stopped mechanically when it reaches a point predetermined to be about the thickness of a specimen with close to theoretical density. The fuse is located so that the piston covers the fuse hole as soon as possible after firing. The fuse is activated electrically and the reaction recorded on videotape for subsequent visual evaluation, particularly regarding overall performance, relative burning time and extent of material loss. After cooling, the specimen is removed by pressing the mold past it using a laboratory press, with the grafoil liner providing sufficient lubrication to recover the product. Specimens up to 3" diameter and 4" x 4" have been fabricated in varying thicknesses up to one inch, usually with the aim of obtaining plate material at least 0.5 in. thick for subsequent characterization.

RESULTS

Prior to incorporation of a two hour heat treatment at 500°C in flowing argon, most runs yielded low density, porous products or tiles that were dense but considerably thinner than would be expected from the quantity of powder placed in the die. This was due to entrapment of absorbed gases and oxides on both the boron and titanium or loss of part of the charge by explosive expulsion of the gas through gaps between the piston and cylinder of the die. After outgassing, loss of material was reduced and densities were usually above 90% of theoretical. In nearly all cases, the tiles were found to have broken into three or more parts; the presence of whiskers and oxidized regions on the fractured surfaces suggests fracture occurred at a temperature high enough for such growths to occur. Stringers or solidified small rivulets of a white glassy material were sometimes seen possibly the result of oxides on the titanium particles.

In several instances, regions of unreacted powder, probably boron, were found at the edges and corners of the tile farthest from the initiating charge. Addition of excess titanium overcame this in some cases, but was not universally helpful, suggesting that the balance between the rate of reaction, i.e., heat generation and loss of heat to the mold parts was not optimal. These regions were found to consist largely of boron, identified by inference from the large amorphous shoulder at the low mass end of the EDAX trace, plus magnesium, the major contaminant in the starting powder, as well as some titanium.

Examination of the microstructures of specimens suggests that grain size of the reacted material is related to the boron particle size as seen in Figure 4. The views on the right are from an area that contained Callery sub-micron boron as part of the initiation system while the structure on the left is from a region within the bulk of the specimen formed from AEE 3-5µm boron. No outgassing had been performed in this case and there is significant separation between grains, although density was measured as about 99% of theoretical. Figure 5 shows the structure of a specimen fabricated after heat treatment for two hours at 500°C in argon. Despite the outgassing, density was only about 88% of theoretical, taking the added nickel into account. Figure 6 shows the structure of another nickel-containing specimen, also fabricated without prior heat treatment. Some blowholes are clearly visible, while the titanium and nickel EDAX maps in Figure 6 show the latter to be concentrated at the grain boundaries. Density of this specimen was 90% of theoretical.

Portions of higher density runs were examined and specimens selected for three point flexure tests. Average values of 346,170 and 113 MPa from specimens of 98.88.5 and 85% theoretical density respectively were obtained with a maximum of 423 MPa for a specimen 97.8% dense. These compare well with results obtained in Ref. 2 but show greater scatter so that conditioning or heat treatment will be required after the initial reaction to improve intergranular bonding and uniformity.

Fracture of the reacted tiles appears to be the result of thermal shock in most cases and requires better management of the residual heat of reaction. This is currently being approached through improved mold design and insulation. Too rapid a release of pressure after reaction may also play a part and this is being addressed by the use of a more controllable pneumatic system.

CONCLUSIONS

Results to date show that reaction of titanium and boron to fabricate SHS-Ti₂ in relatively massive form is feasible and controllable in large batches. Optimization of the process, however, to produce a material of uniform quality routinely will require more precise temperature and pressure control during and after the reaction as well as improved outgassing and preparation of the green cake. Procedures to incorporate such improvements in the process are currently underway, as well as studies to evaluate the desirability of a post formation heat treatment step to improve uniformity.

ACKNOWLEDGEMENTS

This work was supported by the Army Materials Technology Laboratory under Contract No. DAAL04-87-C-0083. The authors express their appreciation to David Mark and Tom Landon for experimental assistance and to Dennis Viechnicki and Phillip Wong of AMTL for their support.

REFERENCES

1. P.D. Zavitsanos and J. Morris, "Synthesis of TiB₂ by a Self-Propagating Reaction", Ceramic Engineering Science Proc. pp 624-627, July-Aug. 1983.
2. P.D. Zavitsanos and J.F. D'Andrea, "Self-Propagating Reactions for Synthesis of High Temperature Materials "AMRC-TR-85-15, June 1985 Final Report Contract DAAG-83-C-0178.
3. G.V. Samsonov and G.V. Petrash, Met. Obrabotka Metallov, No. 4, 19 (1955)

TABLE 1
COMPARISON OF TiB₂ PRODUCED BY THE SHS-PROCESS

PROPERTY	TiB ₂ -HOT PRESSED	TiB ₂ -SHS (Ref. 2)
(1) Chemical Purity	98.5%	99.5%
(2) Microhardness (Knoop, 500g)	2345	2200-2800
(3) Young's Modulus (10 ⁶ psi)	60	(40-80)
(4) Weibull Modulus	28.7	58-85
(5) Grain Size		<20μm
(6) Density	98.5%	97%
(7) Poisson's Ratio	0.11	0.07

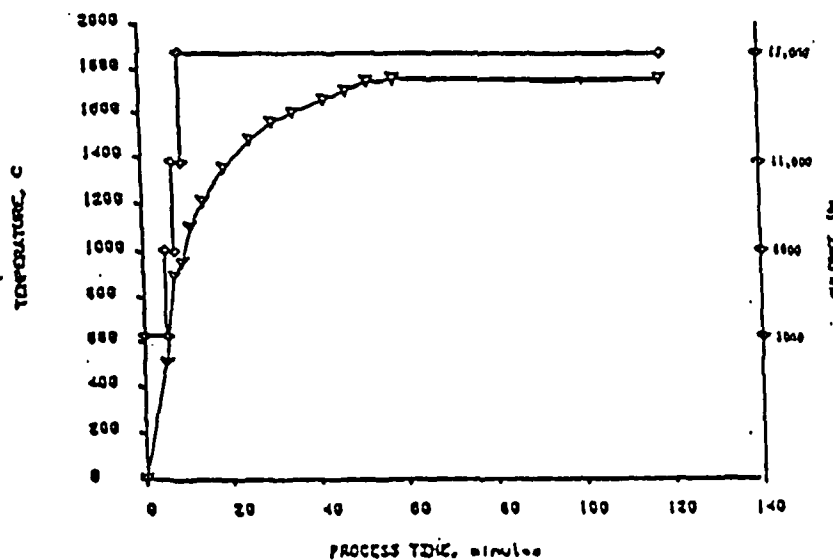
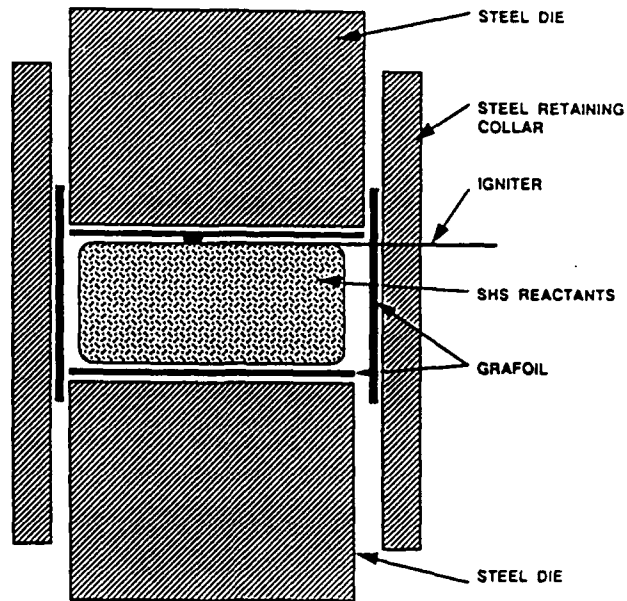


FIGURE 1. TEMPERATURE - PRESSURE - TIME PROFILE
(P.D. ZAVITSANOS & J.F. D'ANDREA, AMRC-TR-85-15, JUNE 1985)

FIGURE 2. Reaction pressing die configuration for spring loaded press.



CALIBRATION OF AF-15 SPRING DIE SET

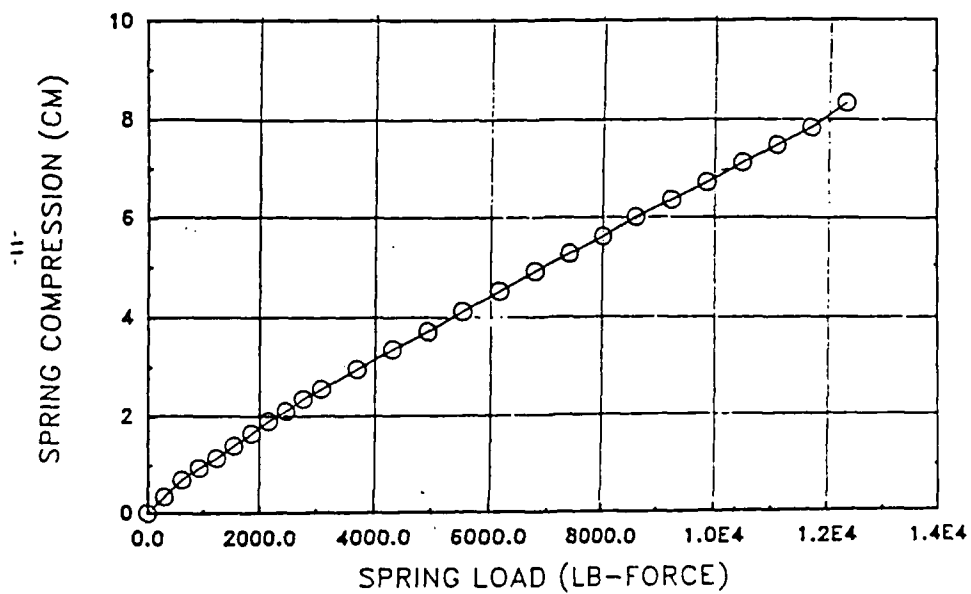


FIGURE 3

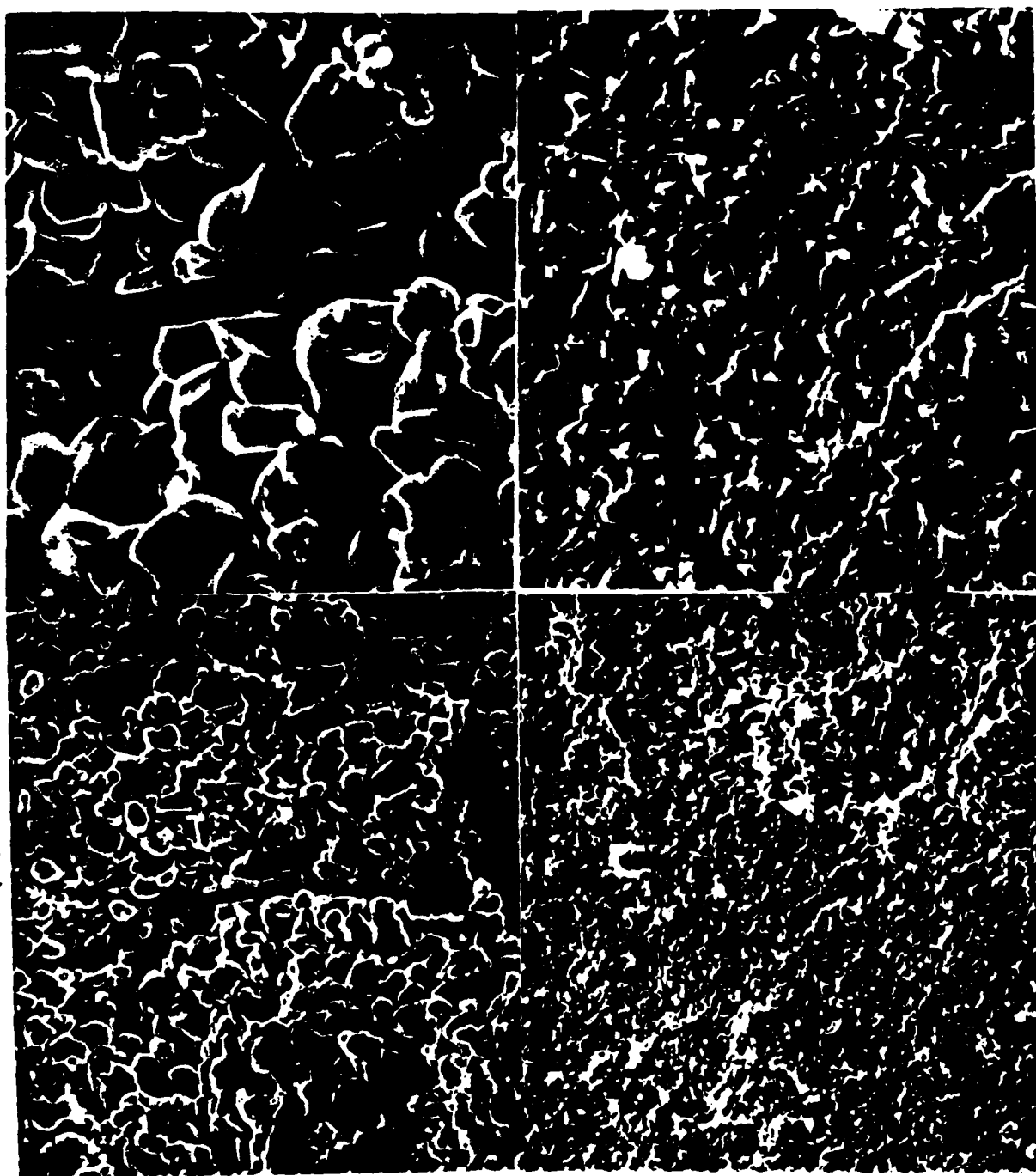


Fig. 4
SEM VIEWS OF TITANIUM BORIDE, SHOWING EFFECT OF VARIATION IN BORON PARTICLE
SIZE. NO NICKEL IN SPECIMEN. LINES = 10 MICROMETER (080988-2)

303
302



Fig. 5

SEM VIEWS OF TITANIUM BORIDE, SYNTHESIZED AFTER OUTGASSING. MIXED
AMORPHOUS AND CRYSTALLINE BORON, WITH NICKEL. LINES = 10 MICROMETER
(091488-1)

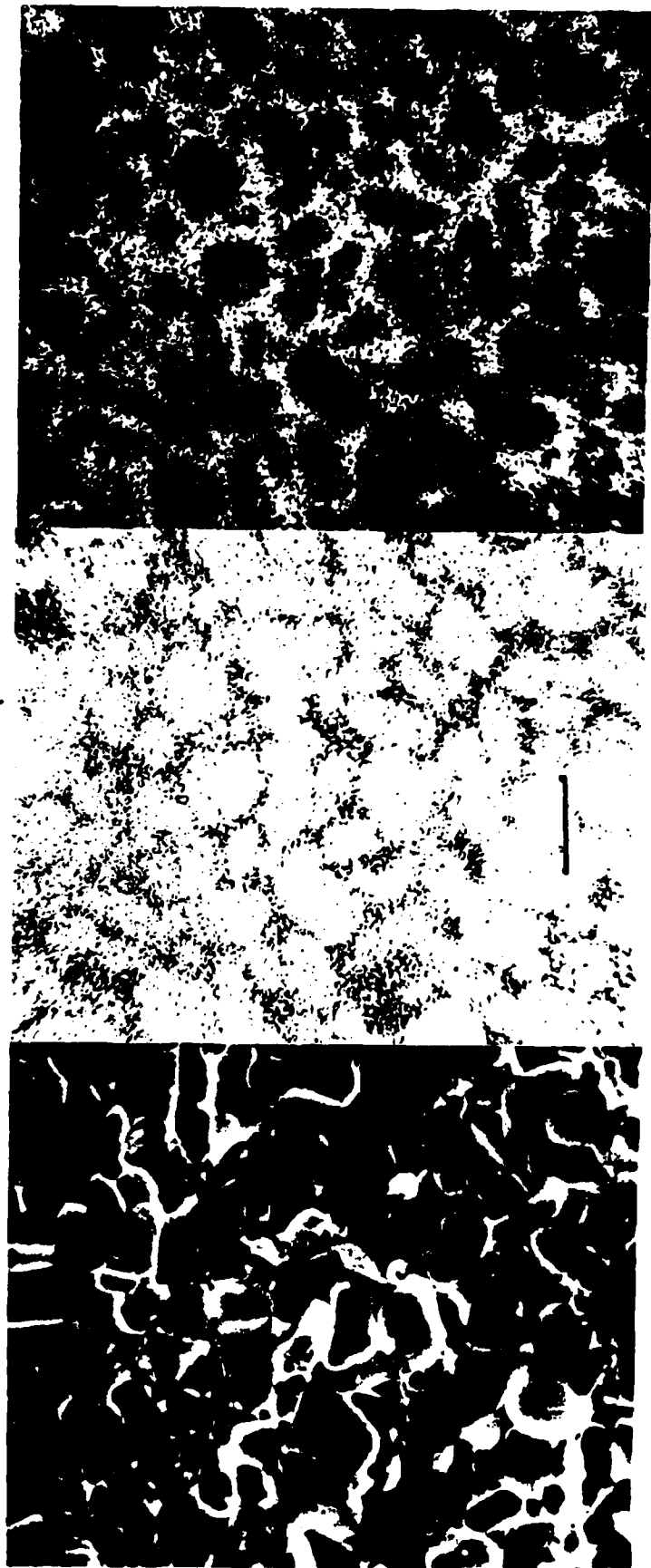


Fig. 6 SEM, TI AND NI MAPS OF TITANIUM BORIDE SPECIMEN CONTAINING NICKEL, SHOWING BLOWHOLES (LEFT). LINE = 10 MICROMETER (080988-1).

Metal-Ceramic Composite Pipes Produced by a Centrifugal-Thermit Process

Osamu Odawara

Department of Electronic Chemistry, Tokyo Institute of
Technology, Nagatsuta, Midori-ku, Yokohama 227, Japan.

ABSTRACT

Long-sized metal-ceramic composite pipes have been produced by means of a thermit reaction taking place under the influence of centrifugal force ("Centrifugal-Thermit Process"). The most important factor which made the production of long composite pipes possible is in the characteristics of thermit reaction propagation; when the reaction is applied to a hollow body, it propagates along the inner surface first and into the layer of the reactant subsequently. Therefore, by igniting only a part of the reactant the thermit reaction rapidly proceeds along the inner surface of the hollow body formed by centrifugal force and then into the layer simultaneously in the radial direction, resulting in producing the long composite pipes of homogeneous quality in the direction of pipe length. In this paper, the Centrifugal-Thermit process is discussed with particular reference to the propagation mechanism of thermit reaction in the process.

key words; exothermic reaction, centrifugal force, long pipe production,
reaction propagation

I. INTRODUCTION

Pipes and vessels with corrosion-, abrasion-, and heat-resistant ceramics bonded to the metallic body are required in many industrial applications. As a simple, rapid, and economical method for producing such metal-ceramic composite pipes, a Centrifugal-Thermit (C-T) process has been proposed and investigated^{1,2}. A thermit reaction under the influence of centrifugal force is an essential principle of the C-T process: The procedure of the process comprises the steps of (1) placing a powdery thermit mixture composed of a strongly reductive element, e.g. Al, and a reducible metal oxide, e.g. Fe_2O_3 , in a metal pipe, (2) rotating the pipe around the axis so as that the powdery thermit mixture is pressed against the inward surface of the pipe by centrifugal force to form a layer, (3) igniting the thermit mixture at one point under the influence of centrifugal force so that the thermit reaction takes place and the reducible metal oxide is reduced to the molten metal, e.g. Fe, while the strongly reductive element is oxidized to the molten oxide, e.g. Al_2O_3 , which forms the innermost layer with the molten metal forming the intermediate layer by the effect of centrifugal force, and (4) cooling the body having, on the inward surface, stratified layers of the metal and the ceramic oxide(see Fig. 1) .

In previous works, the influences affecting the composite pipes produced by the C-T process were mainly investigated by taking into consideration a large amount of reaction heat and centrifugal force applied to the reaction products; thermal insulation³, centrifugal force⁴, environmental gas content⁵ and pressure⁶, and the additives to thermit powders⁷.

The C-T process has recently been extended to the development of 5.5 m-long composite pipes. In the process of development, it was confirmed that the thermit reaction proceeded rapidly to produce composite pipes of homogeneous quality in the direction of pipe length under the conditions of proper amount of thermit powders and proper centrifugal force⁸. This fact was a great advantage in the production of long-sized composite pipes. In light of the fact, the propagation of the thermit reaction under centrifugal force plays an important role in the C-T process as well as a large amount of reaction heat and centrifugal force applied to the reaction products.

II. TEMPERATURE HYSTERISIS IN THE C-T PROCESS

The schematic illustration of temperature at a hollow surface measured by an infrared radiation thermometer through the C-T process is shown in Fig. 2. As shown in Fig. 2, the temperature first increased around the point of ignition(①), and, after some intervals with no indication of the temperature increase during the vaporization or dispersion process of reactant the temperature acutely rose with the start of reaction in the whole of the hollow surface. Then, it dropped rapidly in the fummy condition after the blowoff (②) following the inducement of reaction at the whole hollow surface. Subsequently, the highest temperature was reached after the reaction finished and was followed by the cooling process.

Since the reaction products were melted by the reaction heat, it is assumed that the emissivity would change drastically at the melting point of the

products. Therefore, the true peak would be much higher than 2400 K which was the highest one in Fig. 2. In the cooling stage, a plateau appeared at about 2300 K which was considered to be the melting point of the ceramic product. It is considered that the cooling in the C-T process occurs in the radial direction predominantly, so that the created heat was kept inside of the pipe in the reaction process and, once the heat is conducted to the metal mold, the system would be cooled down acceleratedly by the effect of centrifugal force.

With respect to the thermal expansion and shrinkage of each layer during the C-T process, some delay is expected in the outer metal layer compared to the product ones because of the delay in temperature increase; since the melting point of the produced ceramic is much higher than that of the metal and the heat propagation occurs in the radial direction, the outer pipe would be still in expansion when the produced ceramic starts to solidify and shrink. After the temperature of the outer pipe starts to cool down, the metal layer contracts much more than the ceramic with its higher coefficient resulting in the compression stress remaining in the ceramic layer. The size of the pipes produced is always a little smaller both in diameter and in length, so that the intermediate metal layer formed would play a role in balancing the residual stress of each layer.

III. PROPAGATION OF THERMIT REACTION IN THE C-T PROCESS

In Fig. 3, typical experimental data on the mechanical properties of 3 m-long composite pipes produced under 130 G are shown in the direction of pipe

length⁹, where ν , E , σ_p , σ_s , and P are Poisson's ratio, Young's modulus, compressive strength measured by a squeezing test, compression-shear stress, and porosity of the ceramic layer, respectively. As shown in Fig. 3, the difference of these properties in the direction of pipe length are negligibly small within the present testing precision, except the data near the pipe end. Therefore, the pipe is considered to be uniformly produced in the direction of pipe length. The deviation near the end of the pipe would be caused from the heat instability induced by the direct contact of a mold material.

If the reaction propagated from the point of ignition to the direction of pipe length through the cross section, homogeneous quality of the product layers would not be obtained because the products behind the reaction front solidify in turn causing non-uniform effect of centrifugal force in the direction of pipe length. Therefore, the products should solidify simultaneously in the direction of pipe length for obtaining such homogeneous quality. The present C-T process actually did perform this requirement by igniting only a part of reactant and provide composite pipes of homogeneous quality in the direction of pipe length.

In Fig. 4, typical results of time delays in temperature increase measured by thermocouples at fixed points(TC1; top end and TC2; bottom end) are shown in thermit reactions with different powder densities and shapes¹⁰. As shown in Fig. 4(A) and (B), the time interval between the change in TC1 and that in TC2 in the reaction with the density ratio of 0.32 is longer than that of 0.15. This result is comprehensible if considering high temperature gas diffusion as a predominant factor in the reaction; the diffusion of gas is hindered with the increase of the powder density because the free space be-

comes smaller, even the conduction of heat becomes better. On the other hand, the temperature increase of TC1 and TC2 occurs almost at the same time when reacting with a hollow body(Fig. 4(C)).

For making clear the mechanism of the reaction propagation in the C-T process, a radio(FM)-telemeter technique was set up as shown in Fig. 5. A low carbon steel pipe of 318.5 mm in outer diameter and 5500 mm in length was inserted in a pipe holder of 451 mm in outer diameter and 5890 mm in length placed on a roller-type centrifuge machine. Three thermocouples were attached to the surface of the pipe through the holes of a holder as shown in Fig. 5(A). Fe_2O_3 -Al thermit mixtures with 6.54 mass% of SiO_2 (total amount; 166.44 kg) were then distributed into the hollow part of the pipe and ignited under 69 G. Data on temperature increase measured by the thermocouples were transmitted from a sending antenna fixed to the rotating holder to a receiving one on the ground in FM wave. The temperature curves obtained by the FM-telemeter technique are shown in Fig. 6. The measurement was carried out from the point of the blowoff occurring in the process(refer to Fig. 2). Although the value of the temperature shown in Fig. 6 is not so reliable because the thermocouple contact with the surface of the pipe was not enough and stable during the process, e. g. in the case of TC1, the increasing point of temperature is reliable enough for further discussion. Fig. 6 shows that the deviation of the points in temperature increase among these three thermocouples is within one second. Since the distance between TC1 and TC3 was about 2400 mm, it is difficult to consider that heat propagates in the direction of pipe length from the part of ignition resulting in the temperature increase of three points within 1 s. With respect to the time delay in temperature increase at

each point, that of TC3 is a little shorter than that of TC2, which means that all the parts measured were heated up simultaneously. Therefore, the reaction should propagate simultaneously in the direction of pipe length. As a result, it is concluded that the C-T process proceeds along the inner surface of the hollow body first and then into the layer in the radial direction simultaneously resulting in producing the composite pipes of homogeneous quality in the direction of pipe length.

REFERENCES

- 1) O. Odawara: US Patent No.4363832(1982); JPN Patent No.144098(1983)
- 2) O. Odawara and J. Ikeuchi: J. Jpn. Inst. Metals, 45, 316(1981)
- 3) O. Odawara, J. Ikeuchi, Y. Ishii, H. Yamasaki and M. Sato: *ibid.*, 50, 763(1986)
- 4) O. Odawara and J. Ikeuchi: *ibid.*, 49, 801(1985)
- 5) O. Odawara, K. Nagata, K. S. Goto, Y. Ishii, H. Yamasaki and M. Sato: *ibid.*, 52, 116(1988)
- 6) O. Odawara and J. Ikeuchi: J. Am. Ceram. Soc., 69, C-85(1986)
- 7) O. Odawara and J. Ikeuchi: Trans. Jpn. Inst. Metals, 27, 702(1986)
- 8) O. Odawara, M. Shiraishi, J. Ikeuchi, Y. Ishii, H. Yamasaki and M. Sato: J. Jpn. Inst. Metals, 49, 806(1985)
- 9) O. Odawara: Proc. 30th Jpn. Congr. Mater. Res., 191(1987)
- 10) O. Odawara: Trans. Jpn. Inst. Metals, 26, 578(1985)

Captions of Figures

- Fig. 1 Principle of a Centifugal-Thermit Process.
- Fig. 2 Schematic illustration of temperature curves in a hollow surface measured by an infrared radiation thermometer in the C-T process.
- ①; ignition, ②; blowoff of fumes, (A); hollow surface propagation of reaction, (B); radial direction propagation of reaction, (C); cooling process.
- Fig. 3 Mechanical properties of a 3 m-long C-T pipe.
v; Poisson's ratio, E; Young's modulus, σ_p ;
compressive strength, σ_g ; compression-shear stress,
P; porosity of ceramic layer.
- Fig. 4 Typical propagation patterns of thermit reaction.
- Fig. 5 Schematic illustration of an FM-telemeter technique applied to the C-T process.
- Fig. 6 Temperature curves obtained by the FM-telemeter technique in the C-T process.

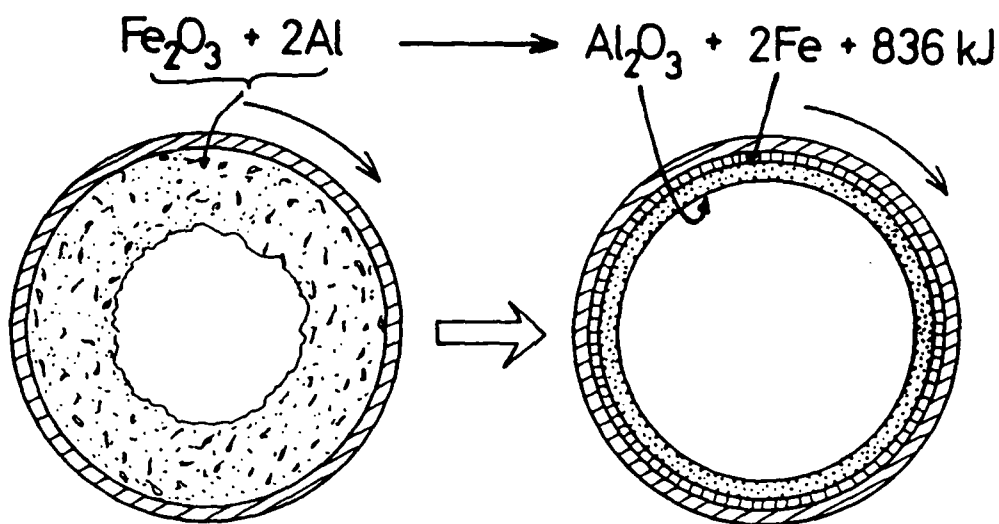


Fig. 1 Principle of a Centrifugal-Thermit Process

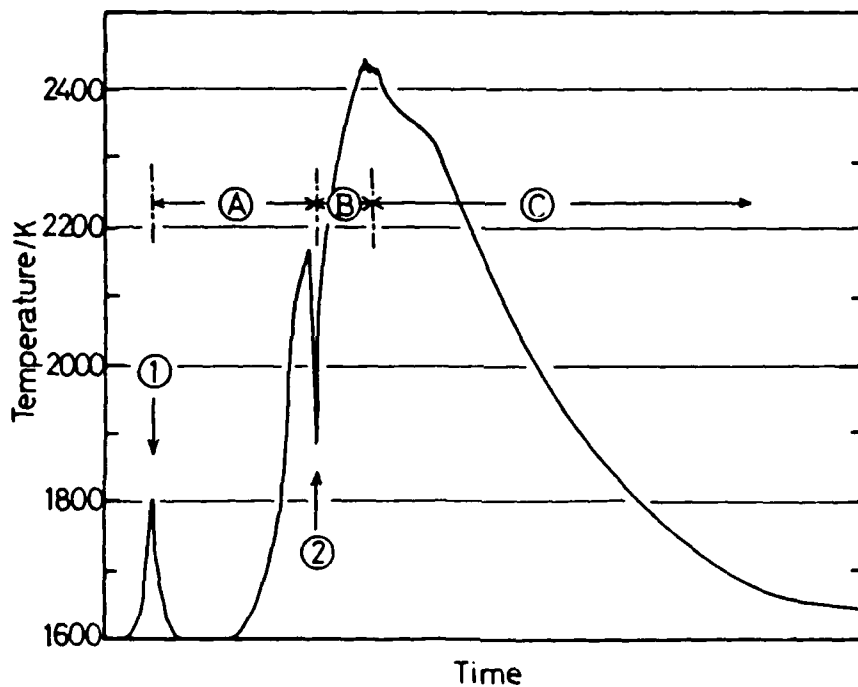


Fig. 2 Schematic illustration of temperature curves in a hollow surface measured by an infrared radiation thermometer in the C-T process.
 ①; ignition, ②; blowoff of fumes, (A); hollow surface propagation of reaction, (B); radial direction propagation of reaction, (C); cooling process.

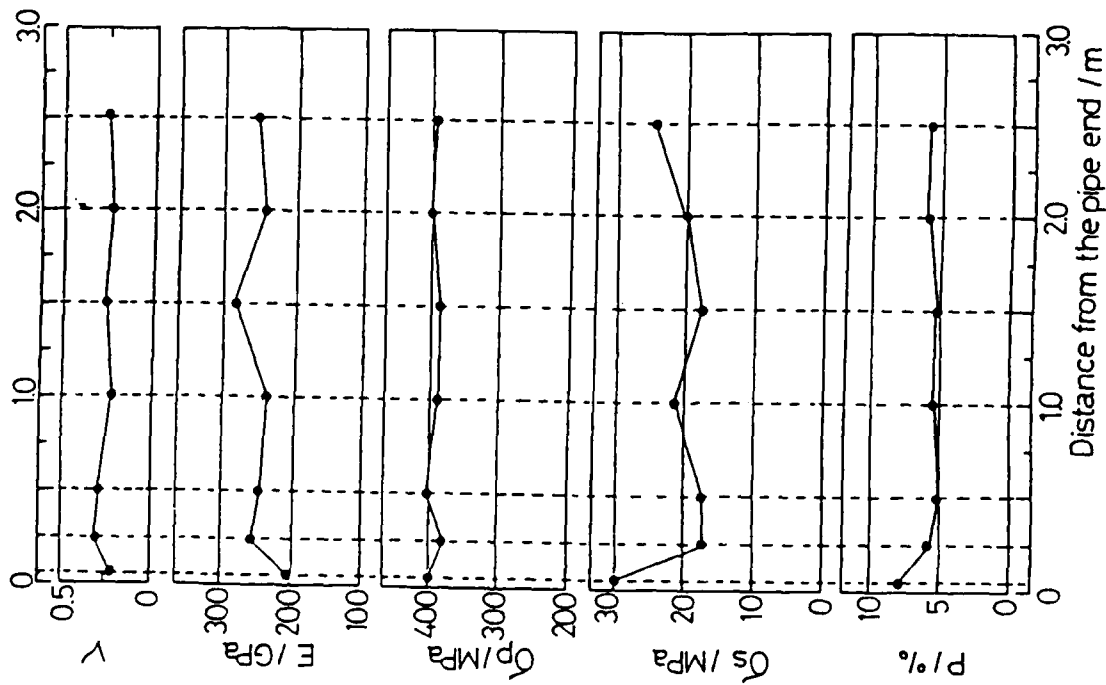


Fig. 3 Mechanical properties of a 3 m-long C-T pipe.
 ν : Poisson's ratio, E : Young's modulus, σ_p :
 compressive strength, σ_s : compression-shear
 stress, P : porosity of ceramic layer.

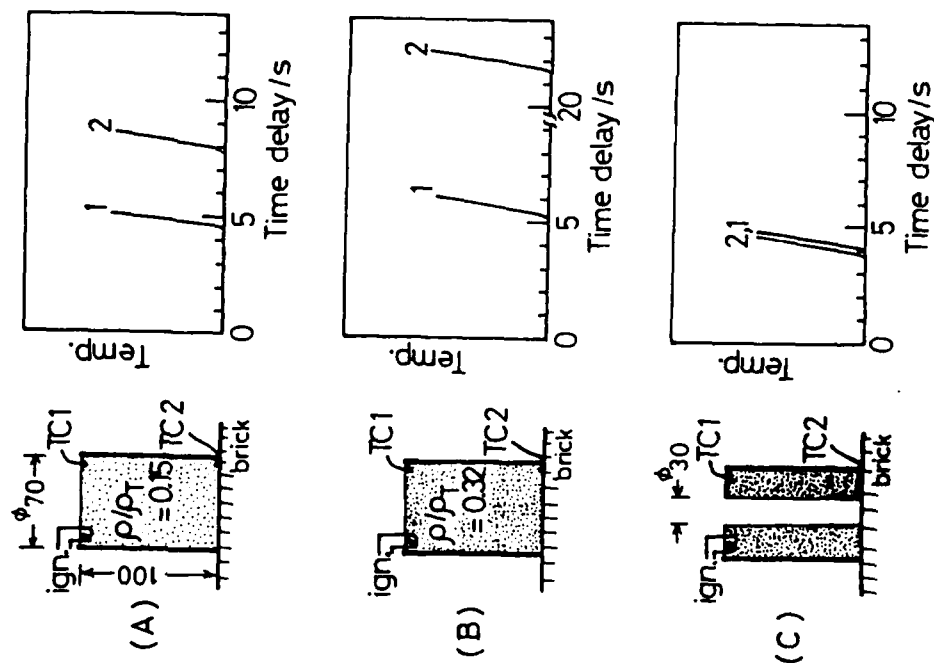


Fig. 4 Typical propagation patterns of
 thermit reaction.

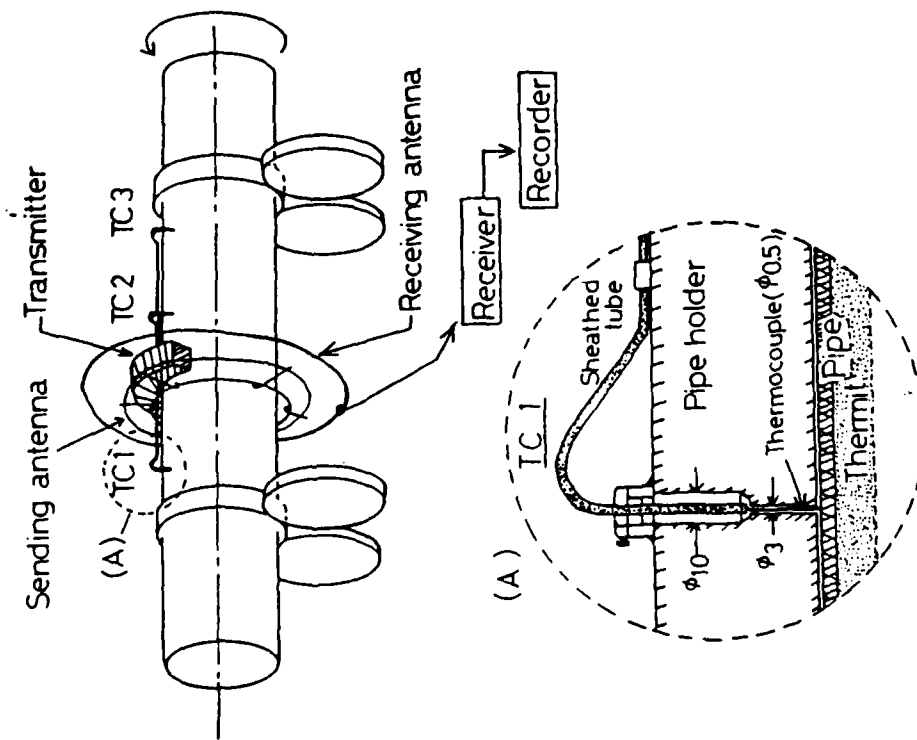


Fig. 5 Schematic illustration of an FM-telemeter technique applied to the C-T process.

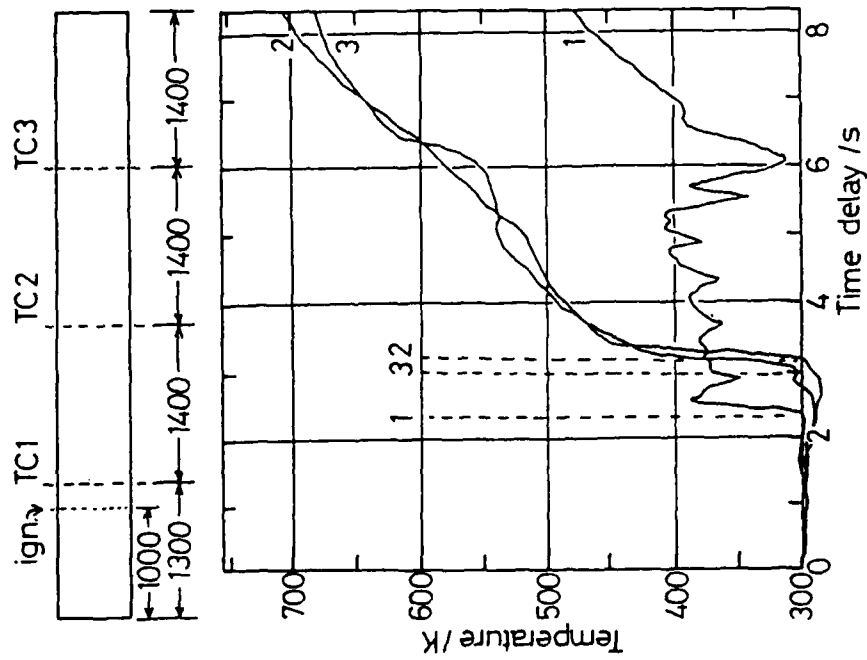


Fig. 6 Temperature curves obtained by the FM-telemeter technique in the C-T process.

Simultaneous Combustion Synthesis and Densification of AlN

by

Stephen D. Dunmead, J. Birch Holt, and Donald D. Kingman

Department of Chemistry and Materials Science

Lawrence Livermore National Laboratory

Livermore, California 94550 U.S.A.

1. Introduction:

AlN belongs to an important group of nitrogen ceramic materials. There has been rapid growth in the use of AlN in advanced ceramic components because of its excellent high temperature properties such as high strength, high hardness, wear resistance, high thermal conductivity, thermal shock resistance, etc... For these reasons, AlN is being considered for many applications such as electronic substrates, heat radiation fins, and a variety of structural components. Cermet materials often display enhanced physical properties when compared to the single phase ceramic. In the AlN-Al cermet material, the combination of the ceramic AlN phase with the metallic Al phase results in a material which has high hardness and strength due to the presence of AlN and increased toughness due to the presence of Al. The low density ($2.70\text{--}3.26\text{ gcm}^{-3}$) and superior properties of this cermet make it an ideal candidate for a variety of lightweight structural applications.

The fabrication of low porosity parts from AlN powder remains a challenging problem in ceramic technology. Powders of covalent compounds, such as AlN, are generally difficult to sinter because of the low rate of self-diffusion within the solid, even at elevated temperatures. In many cases to overcome this non-sinterable behavior, dopants are added to the powder prior to firing at high temperature. These dopants enhance the sintering process by either the formation of a liquid phase or by increasing the diffusivity in the solid state. Unfortunately, the presence of these sintering aids may seriously degrade the properties of the AlN product. The presence of the lower melting phase at the grain boundaries, for example, may cause a decrease in the high temperature mechanical strength of the sintered part. The addition of oxide dopants, on the other hand, serves to decrease the thermal conductivity and thus, the resistance to thermal shock.

Recognizing this problem, the more ideal production process might involve the simultaneous synthesis and densification of the product into near-net shapes without the use of dopants. We will discuss in this paper a method which has the potential to synthesize and densify AlN into dense parts in the same operation. This method is based on a combustion reaction in which aluminum powder compacts are combusted in a high pressure nitrogen environment. This reaction is characterized by self-generated high temperatures and a rapidly moving combustion front.

In the late 1960's, A.G. Merzhanov and his co-workers [1] began work on self-

propagating combustion reactions. This work led to the development of processes which the Soviet investigators refer to as 'Self-Propagating High Temperature Synthesis' (SHS) or more simply combustion synthesis. In these processes, materials with sufficiently high heats of reaction may be synthesized by a self-propagating combustion wave. These combustion synthesis reactions can be carried out with both solid-solid (TiC, TiB₂, TiC-Al₂O₃) and gas-solid (TiN, Si₃N₄, AlN) [2-11] systems. In this paper, a gas-solid type of combustion reaction to form AlN, in which the reactants are aluminum powder and nitrogen gas, has been described. The AlN combustion product may be in the form of a dense single phase compact or a dense AlN-Al cermet, depending upon the experimental parameters.

2. Experimental Procedures:

Small particle size aluminum powder was used for all of our combustion experiments. The aluminum powder, obtained from ALCOA, had an average particle size of 9.9 μm and a measured BET surface area of 1.10 m^2g^{-1} . The measured density of the powder was 2.68 gcm^{-3} which is very close to the theoretical value of 2.70 gcm^{-3} . The major impurities were found to be: Fe, 100 ppm and Si, 30 ppm. In some of the combustion experiments the aluminum was diluted with AlN powder. This AlN was obtained from Advanced Refractories Technology and had an average particle size of 2.9 μm and a measured density of 3.19 gcm^{-3} (theoretical density is 3.26 gcm^{-3}). The BET surface area was measured to be approximately 2.53 m^2g^{-1} . No attempt was made to obtain impurity information on this material.

Cylindrical compacts of the Al powder were formed using a stainless steel die with double acting rams. The compacts were 1.9 cm in diameter and approximately 2.0 cm in length. The exact dimensions and weights of the compacts were measured both before and after combustion so that the density and nitrogen uptake could be calculated. Ignitor pellets consisting of 72 wt%(Ti+1.5B) + 28 wt%(4Ti+Fe₂O₃) were placed on top of the Al powder compacts. The ignitor pellets were used because of difficulties in starting the nitriding reaction due to the high thermal conductivity of nitrogen gas in the selected pressure range. The aluminum powder compact and the ignitor pellet were placed into the testing chamber so that the tungsten coil used for ignition was approximately 4 mm from the top of the ignitor pellet.

3. Results and Discussion:

3.1 Conversion:

The effect of nitrogen pressure on the percent conversion of aluminum into its nitride is shown in Fig. 1. It can be seen in Fig. 1 that as the nitrogen pressure is increased from 20.7 MPa (3000 psi) to 103 MPa (15000 psi), the conversion of aluminum into its nitride increases as a function of 'green' compact density. This result can be explained by the fact that the local availability of nitrogen increases with increases in nitrogen pressure. Consequently, an increase in local availability of nitrogen causes an increase in the amount of conversion. In Fig. 1 it appears that for all three 'green' compact densities that the product is approaching full conversion in the 120-140 MPa nitrogen pressure range. This nitrogen pressure will later become important when attempting to determine the optimal parameters for producing fully converted AlN. Indeed when samples were combusted at 310 MPa (45000 psi), the products for all three green densities were fully converted.

An experiment was conducted in which an aluminum powder compact was ignited in a lower pressure (<1.4 MPa) combustion chamber where the sample could be viewed during the combustion reaction. The ignitor pellet easily ignited in the 1.0 MPa (145 psi) nitrogen atmosphere. As the combustion wave reached the aluminum powder compact, however, the sample appeared to boil off layer by layer. Finally, after approximately 4 mm of the sample had disappeared, the reaction ceased and the sample was removed. A very fine residue was found on the interior of the combustion chamber and X-ray diffraction analysis showed it to be finely divided aluminum powder. These observations indicate that the dissociation pressure of AlN at the combustion temperature is less than 1.0 MPa.

Fig. 1 also shows the effect of compact density on the extent of conversion of the aluminum specimens. At a given nitrogen pressure, the amount of conversion decreases with an increase in 'green' compact density. This is due to a decrease in the local availability of nitrogen as the pore volume decreases (compact density increases). As the nitrogen pressure increases, the amount of conversion for each of the three densities approaches the same level. This result illustrates the effect of compact density on degree of conversion due to availability of nitrogen.

3.2 Dilution:

The effect of dilution on the amount of conversion was also studied, and the results are shown in Fig. 2. It should be noted that all of the specimens shown in Fig. 2 had

approximately the same green compact density of $55 \pm 1\%$ of theoretical. For the specimens combusted at the highest pressure (310 MPa), the product was fully converted at all levels of AlN diluent content studied. As the nitrogen pressure is lowered to 103 MPa, however, it was found that the amount of conversion reaches a maximum at approximately 10 wt% diluent content. A similar phenomena was observed to occur at a nitrogen pressure of 20.7 MPa. The reason for the initial increase and subsequent decrease in the amount is not clearly understood. It is, however, likely due to interaction between the way in which changes in local nitrogen availability, changes in combustion temperature, and changes in wave velocity affect the degree of conversion. In an attempt to determine the effect of dilution on combustion temperature and wave velocity, thermocouples were placed into the aluminum powder compact. Experimental difficulties hampered this effort, however, and it is the topic of current research. It should be noted that a similar phenomena was observed for the combustion of NbN by both Dunmead, Munir, and Holt [4] and Munir and Zhang [11].

3.3 Product Characteristics:

While combusting aluminum samples in nitrogen, it was observed that the products were not as porous as the typical SHS products. Fig. 3, for example, shows the AlN product density plotted as a function of the green compact density for the samples combusted at 103 MPa. It should be noted that the density plotted in Fig. 3 is the bulk density of the entire AlN sample produced. Typical products from SHS reactions are on the order of 50-60% of theoretical density while these AlN products have bulk densities of 90% or greater, depending upon the nitrogen pressure and the 'green' density. Here, we see that as the green compact density increases, the AlN product density also increases. This is as expected because the porosity present in the unreacted sample is one of the main factors which result in the porous nature of SHS products [12].

In general, the small amount of porosity present in these specimens was not homogeneously dispersed throughout the entire product. In fact, the majority of the porosity was found in the upper quarter of the sample (end where ignition occurred). Because of this fact, the resulting products were sectioned, and the density of the bottom section of the sample was measured in addition to the bulk density of the entire sample (Fig. 3). The density of the bottom section will be referred to as the density of the part.

Fig. 4 shows an optical photomicrograph taken of the product of the combustion of a

54% dense aluminum compact combusted at 103 MPa nitrogen pressure. The measured density of the part was found to be 98% of theoretical with a residual aluminum content of 1.5 vol%. The average grain size of this material was approximately 5 μm . The microhardness of this product was measured to be 1260 kg/mm² which is in the range of the literature values for sintered AlN of 1200 - 1300 kg/mm²[13]. The microstructure and densification present in this sample as well as many others indicates that during the combustion reaction the AlN product is actually molten. Under ambient pressure, AlN does not melt on heating but undergoes dissociation. It is believed that under these high nitrogen pressures, it is possible to suppress the dissociation of AlN in favor of melting. At a representative nitrogen pressure of 103 MPa, the equilibrium dissociation temperature is approximately 3800 K.

While combusting samples at higher nitrogen pressures (310 MPa), it was noticed that the products generally consisted of a small (3-4 mm) cavity on the interior of the sample surrounded by a shell of nearly fully dense AlN. In between the cavity and the shell was a transition region in which the AlN was approximately 85-90% of theoretical density. Fig. 5 shows a SEM photomicrograph of the fracture surface of the transition region between the cavity and the fully dense AlN. This particular sample had a 'green' compact density of 55% of theoretical and was composed of fully converted AlN grains averaging 5 μm in diameter.

Observations made on products of combustion of aluminum at various nitrogen pressures led us to the conclusion that products with more uniform microstructures can be produced at lower nitrogen pressures. This is likely due to an increase in the combustion temperature as the nitrogen pressure is increased and a subsequent increase in the violentness of the combustion reaction. Coupling these results with the data shown in Fig. 1, we have determined that the optimum nitrogen pressure for producing dense, fully converted AlN should be in the range of 120-140 MPa. Further optimization of this production process will come from study of the effect of aluminum particle size and particle size distribution, cold pressing characteristics, pretreatment of the aluminum powder surface, etc... It is also possible to synthesize AlN powder by working with nitrogen pressures less than is used to form the solid AlN products.

The existence oxygen in AlN has very deleterious effects on the thermal conductivity

and thus, on the thermal shock resistance of this material. As a result, analysis of the oxygen content of both the reagent powders and the products is currently being done. The only two possible sources for oxygen contamination of the combustion synthesized AlN are the reagent aluminum powder and the nitrogen gas. It is possible to 'clean-up' the nitrogen gas by purification techniques and by increasing the volume to surface ratio in the reagent aluminum a decrease in the oxygen content should be possible. As a result, it should be possible to minimize the oxygen content of the AlN produced.

It is also possible to produce AlN-Al cermet materials by the SHS process. By lowering the nitrogen pressure, the amount of conversion decreases (Fig. 1) and thus, the possibility of forming cermets exists. Fig. 6 shows optical photomicrographs of an AlN-Al cermet produced by this method. The green compact density of this material was 55% of theoretical and it was combusted at a nitrogen pressure of 51 MPa. The material had a measured part density of 92% of theoretical and a residual aluminum content of 13.4 vol%. The average AlN grain size was measured to be 10 μm and the microhardness was approximately 1075 kg/mm^2 . The spherical AlN particles present in this material indicate that the product may be formed by a process which involves dissolution of nitrogen into liquid Al and subsequent precipitation of AlN from the melt.

4. Summary:

It has been shown that it is possible to synthesize AlN and AlN-Al composites using a high pressure combustion process. Furthermore, the composition of the product can be altered by changing the synthesis conditions. It was found that either an increase in nitrogen pressure or a decrease in green compact density resulted in an increase in the amount of conversion. The addition of pre-reacted AlN as a diluent caused an increase in the amount of conversion at low contents and a decrease in conversion at higher contents. The nature of the combustion process in this particular system allows the AlN and AlN-Al products to be synthesized and densified simultaneously without applying mechanical pressure or adding chemical dopants.

Acknowledgments:

This work was performed under the auspices of the U.S. Department of Energy by the Lawrence Livermore National Laboratory under contract number W-7405-ENG-48.

References:

1. A.G. Merzhanov and I.P. Borovinskaya, "Self-Propagating High Temperature Synthesis of Refractory Inorganic Compounds," *Dokl. Acad. Nauk USSR (Engl. Transl.)*, 204[2] 429-432 (1972).
2. Z.A. Munir, "Synthesis of High-Temperature Materials by Self-Propagating Combustion Methods," *Am. Ceram. Soc. Bull.*, 67(2) 342-49 (1988).
3. Z.A. Munir and J.B. Holt, "The Combustion Synthesis of Refractory Nitrides Part 1: Theoretical Analysis," *J. Mater. Sci.*, 22, 710-14 (1987).
4. S.D. Dunmead, Z.A. Munir, and J.B. Holt, "Gas-Solid Reactions Under a Self-Propagating Combustion Mode," *Solid State Ionics*, 32/33, 474-81 (1989).
5. J.B. Holt, D.D. Kingman, and G.M. Bianchini, "Combustion Synthesis of AlN and Si₃N₄," pp. 17-28 in *Proc. of the DARPA/Army Symposium on SHS*. Edited by K.A. Gabriel, S.G. Wax, and J.W. McCauley. Daytona Beach, FL (1985).
6. K. Hirao, Y. Miyamoto, and M. Koizumi, "Combustion Synthesis of Nitride Powders Under High Nitrogen Pressure," *Advances in Ceramics*, 21, 289-300 (1987).
7. K. Hirao, Y. Miyamoto, and M. Koizumi, "Combustion Reaction Characteristics in the Nitridation of Silicon," *Adv. Ceram. Mater.*, 2[4] 780-83 (1987).
8. I.P. Borovinskaya, and V.E. Loryan, "Self-Propagating High-Temperature Synthesis of Titanium Nitride Under High Nitrogen Pressure," *Sov. Powder Metall. Met. Ceram. (Engl. Transl.)*, 191[11] 851-853 (1979).
9. T.M. Maksimov, M.K. Ziatdinov, A.G. Raskolenko, and O.K. Lepakova, "Reaction of Vanadium with Nitrogen Under Combustion Conditions," *Combust. Explos. Shock Waves (Engl. Transl.)*, 15[4] 415-18 (1979).
10. J.B. Holt and Z.A. Munir, "The Fabrication of SiC, Si₃N₄, and AlN By Combustion Synthesis": pp. 721-28 in *Proceedings of the First International Symposium on Ceramic Components for Engines*. Edited by S. Somiya, E. Karnai, and K. Ando, Hakone, Japan, 1984.
11. Z.A. Munir and S. Zhang, unpublished results (1988).
12. J.B. Holt, "The Use of Exothermic Reactions in the Synthesis and Densification of Ceramic Materials," *MRS Bull.*, Oct./Nov. 60-64 (1987).
13. O.H. Krikorian, "Development of Accurate Estimation Methods for Calculating Thermal Expansivities of Hard Materials," Lawrence Livermore National Laboratory, Livermore, CA, UCRL-90189, July 1985.

Figure Captions:

- Figure 1.** Conversion data for the combustion of aluminum at various green compact densities in nitrogen gas.
- Figure 2.** Conversion data for the combustion of aluminum (at three different pressures) in nitrogen gas while diluted with varying amounts of pre-reacted AlN.
- Figure 3.** Bulk product densities for aluminum combusted at 103 MPa nitrogen pressure for varying green compact densities.
- Figure 4.** Optical photomicrograph of dense AlN produced by combustion of aluminum at 103 MPa nitrogen pressure.
- Figure 5.** SEM photomicrograph of the fracture surface of the relatively porous transition region for an AlN specimen combusted at 310 MPa nitrogen pressure.
- Figure 6.** Optical photomicrographs of AlN-Al cermet produced by combustion of aluminum at 51 MPa nitrogen pressure.

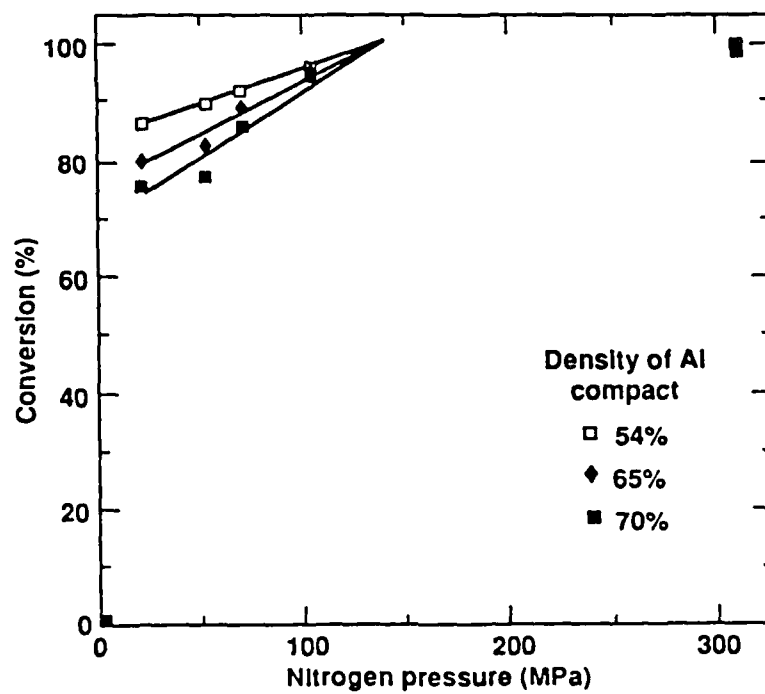


Fig. 1

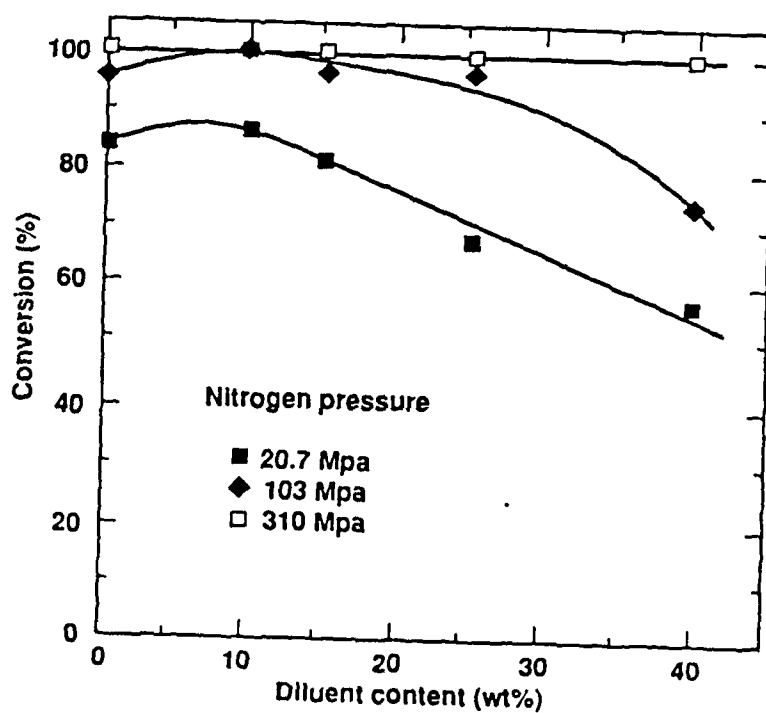


Fig. 2.

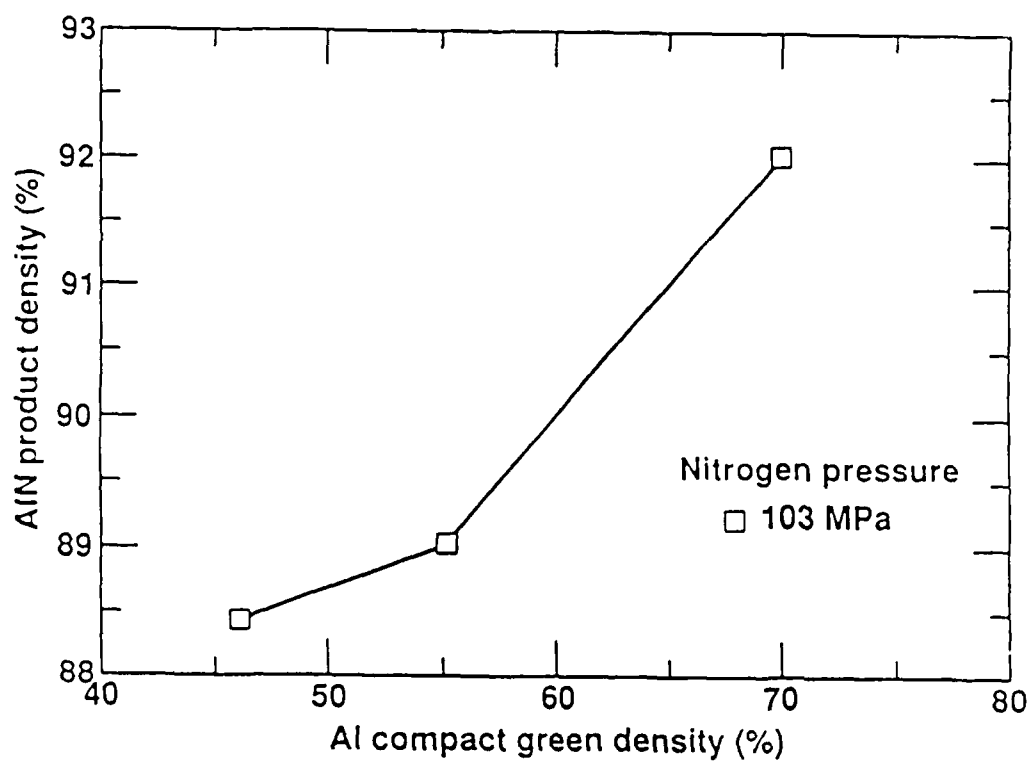


Fig. 3

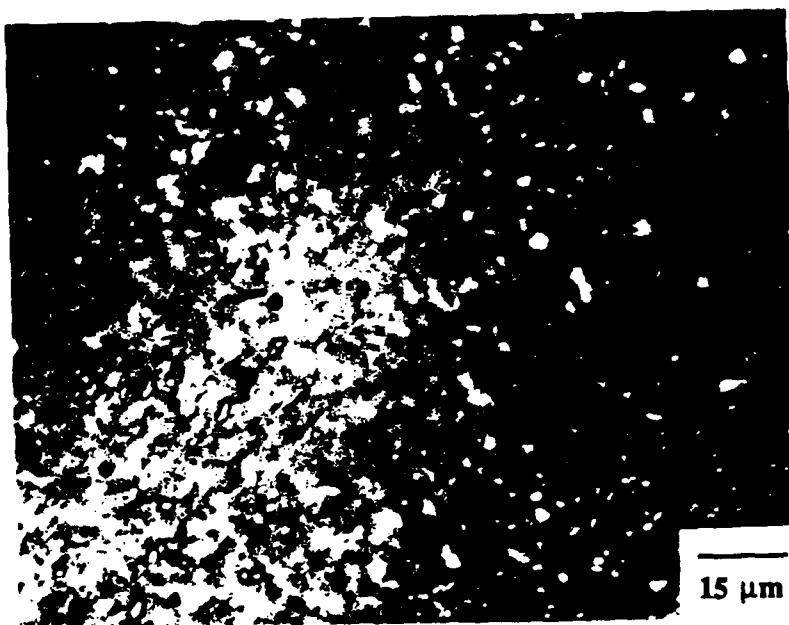


Fig. 4



Fig. 5

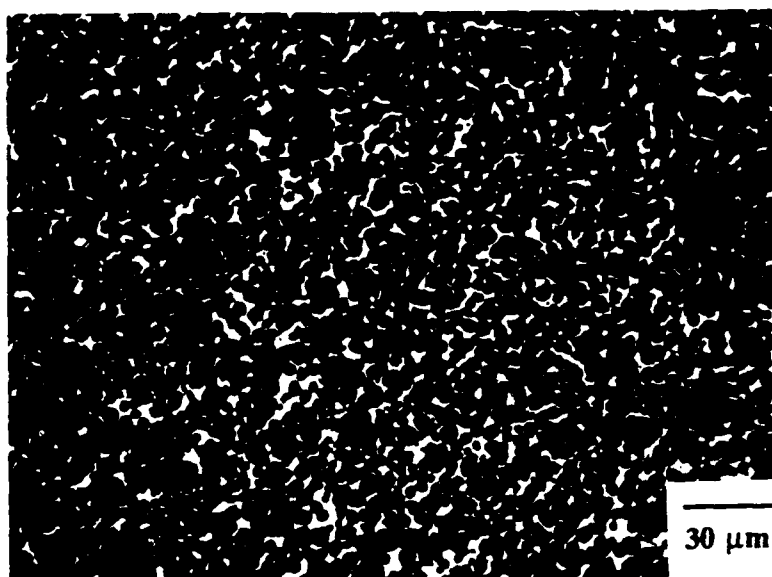


Fig 6.

FABRICATION OF A FUNCTIONALLY GRADIENT MATERIAL
BY USING A SELF-PROPAGATING REACTION PROCESS

NOBUHIRO SATA*, NORIO SANADA*,

TOHRU HIRANO**, and MASAYUKI NIINO***

*Government Industrial Research Institute, Tohoku, 4-2-1, Nigatake, Sendai,
983, Japan

**Daikin Industries, Ltd., 1304, Kanaoka-cho, Sakai, 591, Japan

***National Aerospace Laboratory, 1, Koganezawa, Kimikaya, Kakuta, 981-14,
Japan

ABSTRACT

The design and the production of a functionally gradient material (FGM) by using a self-propagating reaction process has been investigated. Cu/TiB₂ composites were fabricated with stepwise compact interlayers of Ti, Cu and B mixed powders. Maximum temperature of products (T_{max}) were calculated for adiabatic reaction and the reaction propagating regions were obtained, experimentally, for Ti-2B-TiB₂-Cu mixed powder.

INTRODUCTION

Functionally gradient material (FGM), a new type of metal/ceramic composite, can be fabricated with gradual compositional variations within the interlayers where thermal stresses are reduced, for heat-resisting and thermal barrier coatings[1] as shown in Fig.1-(1).

Self-propagating reaction process was developed by A.G.Merzhanov et al.[2] and the application studies have been reported.[3,4,5] Self-propagating reaction process is expected as one of the excellent methods for producing FGM.

This paper deals with the producing of a metal/ceramic composite, whose interlayers a compositional gradient as shown in Fig.1-(2), which was designed by using thermal and mechanical data as shown in Fig.1-(3) and (4). Large stress gaps remains at the interlayers in the case of producing 2 or 3 layered composite, though, such stress gap was disappeared in the case of FGM as shown in Fig.2. Samples of stepwise interlayers with controlled composition changing from pure metal (Cu) to pure ceramic (TiB_2) have been synthesized by using self-propagating reaction process. Microstructure of the interlayer was examined and the dependence on the characteristics of the reaction and the calculated T_{max} values was also discussed.

EXPERIMENTAL PROCEDURE

The producing process of FGM by using SHS is shown in Fig.3. Fig.4 shows two types of experimental apparatus for the fabrication of FGM by using SHS. The spring pressing method (a) have been used for the fundamental study and the hydrostatic pressing method (b) have been developed for practical use as a synthesizing materials with large scale and complicated shape.

The raw materials used in the test were titanium powder (-350mesh), amorphous boron powder (-0.5 μ m) and copper powder (-325mesh). The experimental method used in this work was the spring pressing method [5] with a spring constant of 2.5×10^4 N/m. The reactional vessel of the apparatus was filled with the mixed powders of about 2g. The powders were stacked in the vessel with the steps compositionally divided into 2, 4, 6, 11, 16 or 21 units, and held at a pressure of 50MPa for 30 minutes in vacuum. Then the compact powder was ignited at 25MPa. After the synthesis, samples were cooled and polished cross sections of the cylindrical products

were observed. X-ray line analysis by EPMA and microstructural observation by SEM have been done.

Maximum temperature of the products during the reaction (T_{max}) shown in equation (1) was calculated for an adiabatic condition and measured relative density, where a and b are the amount of TiB_2 and Cu respectively.

$$Ti + 2B + a \cdot TiB_2 + b \cdot Cu = (1+a) \cdot TiB_2 + b \cdot Cu \quad (1)$$

The reaction propagating region in which the self-propagating reaction occurs in Ti-2B- TiB_2 -Cu mixed powders has been measured by using homogeneously mixed powders. FGM has fabricated by using a composition of mixed powder, which relative density was higher at various Cu content.

RESULTS AND DISCUSSION

Fig.5 shows a microphotograph of the sample with 16 units of compacted powders in Ti-2B-Cu mixed powder. The right end is Cu rich and the left end is TiB_2 rich in Fig.5. Large amount of porosity existed in the center of the sample. Fig.6 shows the X-ray line analysis of Ti, Cu and B along the white line in Fig.5. Stacking mixed powders with 16 units made the compositional change gradually in the sample. TiB_2 and Ti-Cu alloy phases existed in the samples synthesized by using the self-propagating reaction process from mixed powders of Ti, Cu and B. The intermetallic compound, Cu_3Ti , was also detected in the Cu-rich parts by X-ray micro-diffraction analysis.

Fig.7 shows the profile of the maximum temperature of products calculated in adiabatic reaction (T_{max}) of Ti-2B- TiB_2 -Cu powder mixture. The profile of the T_{max} shown in Fig.7 suggested that the T_{max} reacted to the Cu boiling point of 2843K at the composition of 60wt%Cu and the Cu completely vaporized at the composition of 25wt%Cu on the powder mixture of

no TiB_2 addition. The T_{max} decreases with addition of TiB_2 powder into the raw materials. The porous structure in the center of the sample in Fig.5 suggested that some Cu vaporized and left out of the sample. However, a decrease of Cu concentration was not observed in the result of EPMA analysis. Therefore, it is presumed that Cu almost reacted with Ti and formed Ti-Cu alloy and only small amount of Cu vaporised. The existence of pores in the center of the samples is the result of the disturbance, during densification, caused by the pressure of Cu vapour in spite of synthesizing under compression. The formation of a high dense TiB_2 -rich is explained in terms of a thermal relaxation which is larger than the inner part of the sample.

The results of Fig.7 was reconstructed in Fig.8. The reaction propagating region obtained experimentally was also indicated in Fig.8. There remains a small region in the composition of mixed powders where the synthesizing is possible with no vaporizing of Cu. But on synthesizing in this region the densified samples might not be able to be gotten, because the temperature in the reaction is too low. Fig.8 also suggested that the porosity (relative density) in the composite could be controlled by controlling the amount of additives.(Fig.9) Fig.10 shows the relative density profile in the relation of Cu and TiB_2 content in the raw materials. The samples as shown in Fig.11, fabricated by using the composition of mixed powders (closed circle) which the relative densities were higher at various Cu and TiB_2 contents as shown in Fig.10, was crack free and nice for FGM compared with the sample (open circle) using the mixed powders of no addition of TiB_2 .

CONCLUSIONS

- (1) Functionally gradient material (FGM) of a Cu/TiB₂ composite was successfully fabricated by using the self-propagating reaction process.
- (2) The microstructure of interlayers in the FGM was related to the maximum temperature of products calculated in adiabatic reaction (T_{max}).

The authors thank to Mr. Yuji Matsusaki, Kawasaki Heavy Industries, Ltd., for his cooperation in synthesizing the samples and in EPMA analysis.

This study was performed through Special Coordination Funds of the Science and Technology Agency of the Japanese Government.

REFERENCE

1. Report of Feasibility Study on Functionally Gradient Materials, Science and Technology Agency, Japan (1986).
2. A. G. Merzhanov and I. P. Borovinskaya, Combustion Sci. and Tech., 10, 195 (1975).
3. O. Odawara and J. Ikeuchi, J. Japan Institute of Metals, 45, 316 (1981).
4. Y. Miyamoto, M. Koizumi and O. Yamada, J. Am. Ceram. Soc., 67, C224 (1984).
5. N. Sata and J. Ikeuchi, J. Ceram. Soc. Jpn, Inter. Ed., 95, 208 (1987).

#19
next
version

89-08-16 11:18 T-

#133-07

7/9

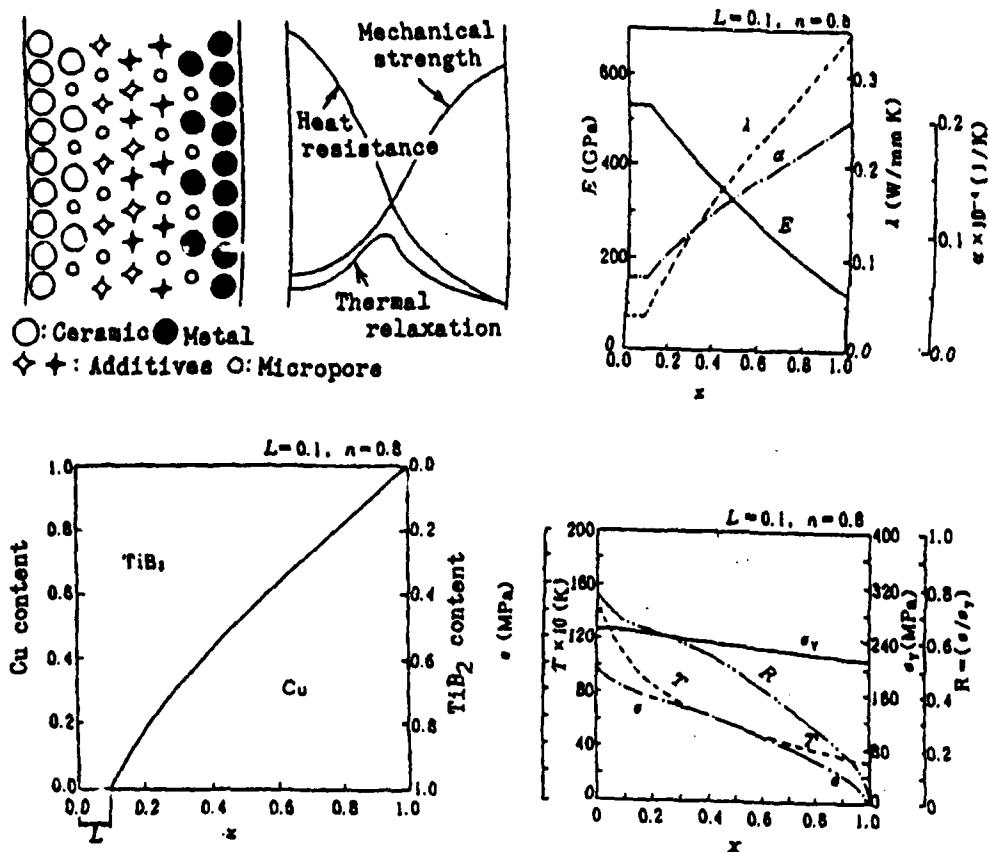


Figure 1. Concept and Design of Functionally Gradient Material

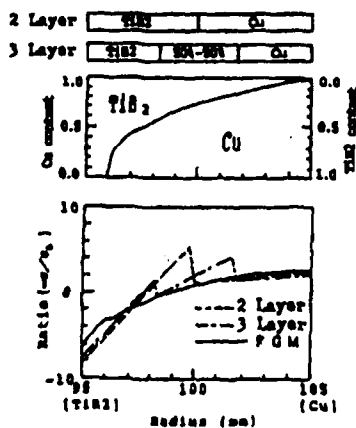


Figure 2. Effect of gradually compositional control in TiB_2 -Cu

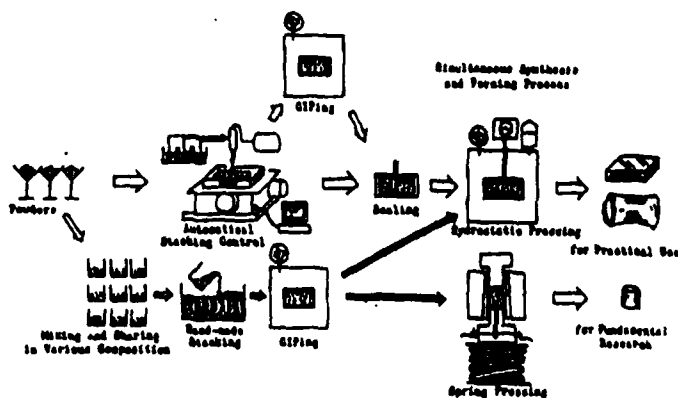


Figure 3. Producing process of FGM by using SHS

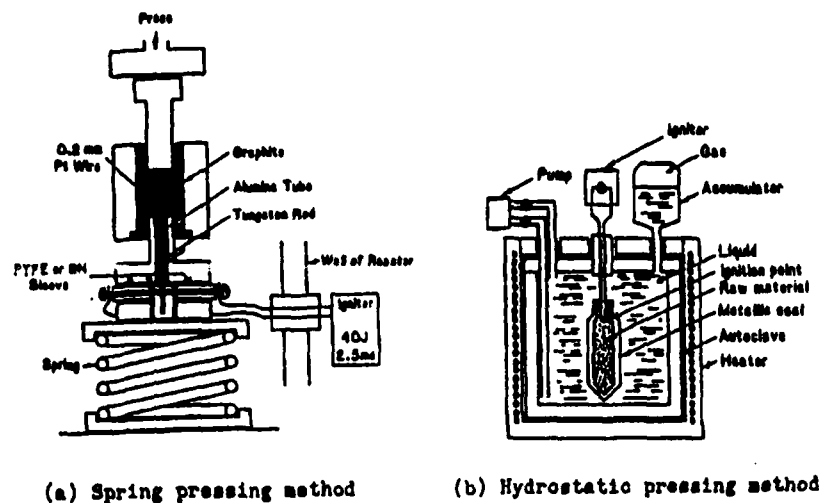


Figure 4. Experimental apparatus for the fabrication of FGM by using SHS-process



Figure 5. Microphotograph of 16 units sample.

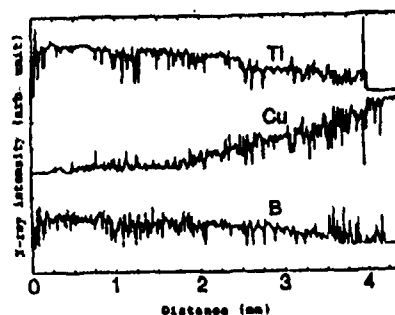


Figure 6. X-ray line analysis of Ti, Cu and B on the white line in Fig. 3.

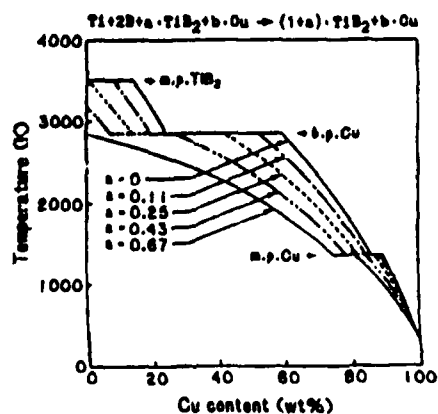


Figure 7. Profile of maximum temperature of products (T_{max}) in adiabatic reactions of Ti-28-TiB₂-Cu sized powders.

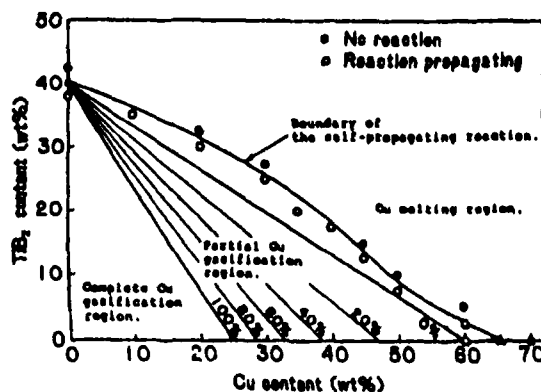


Figure 8. Reaction propagating region of Ti-28-TiB₂-Cu sized powders and the phase of Cu after reaction adiabatically.

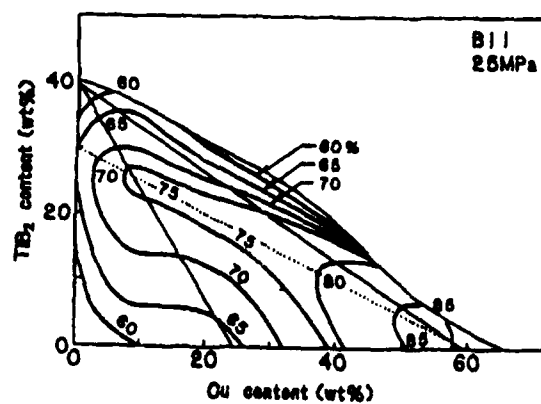
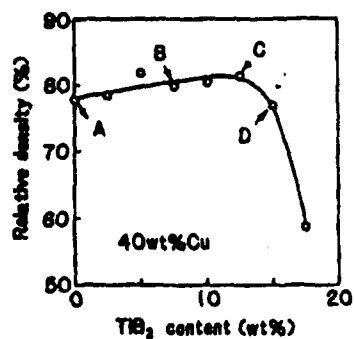
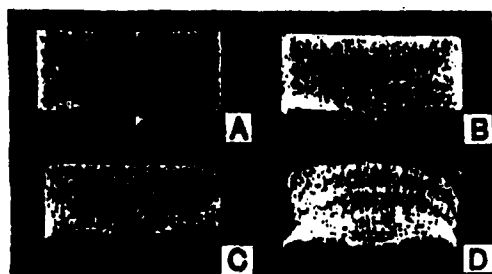


Figure 10. Relative density of TiB₂-Cu composite.

Figure 9. Relation between relative density and microstructure.

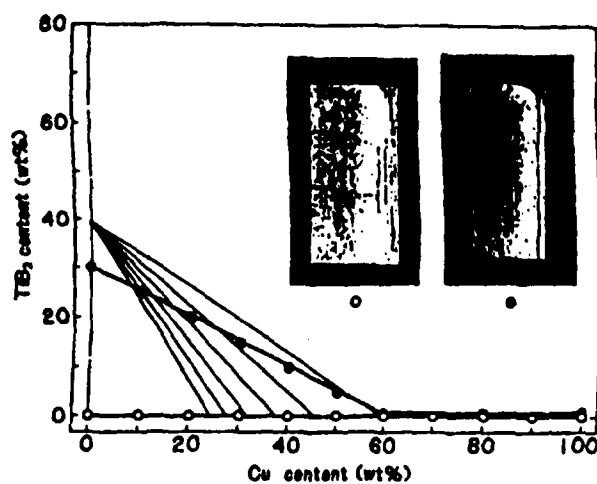


Figure 11. Two FOM samples synthesized from the different content of TiB₂ powder in the raw materials.

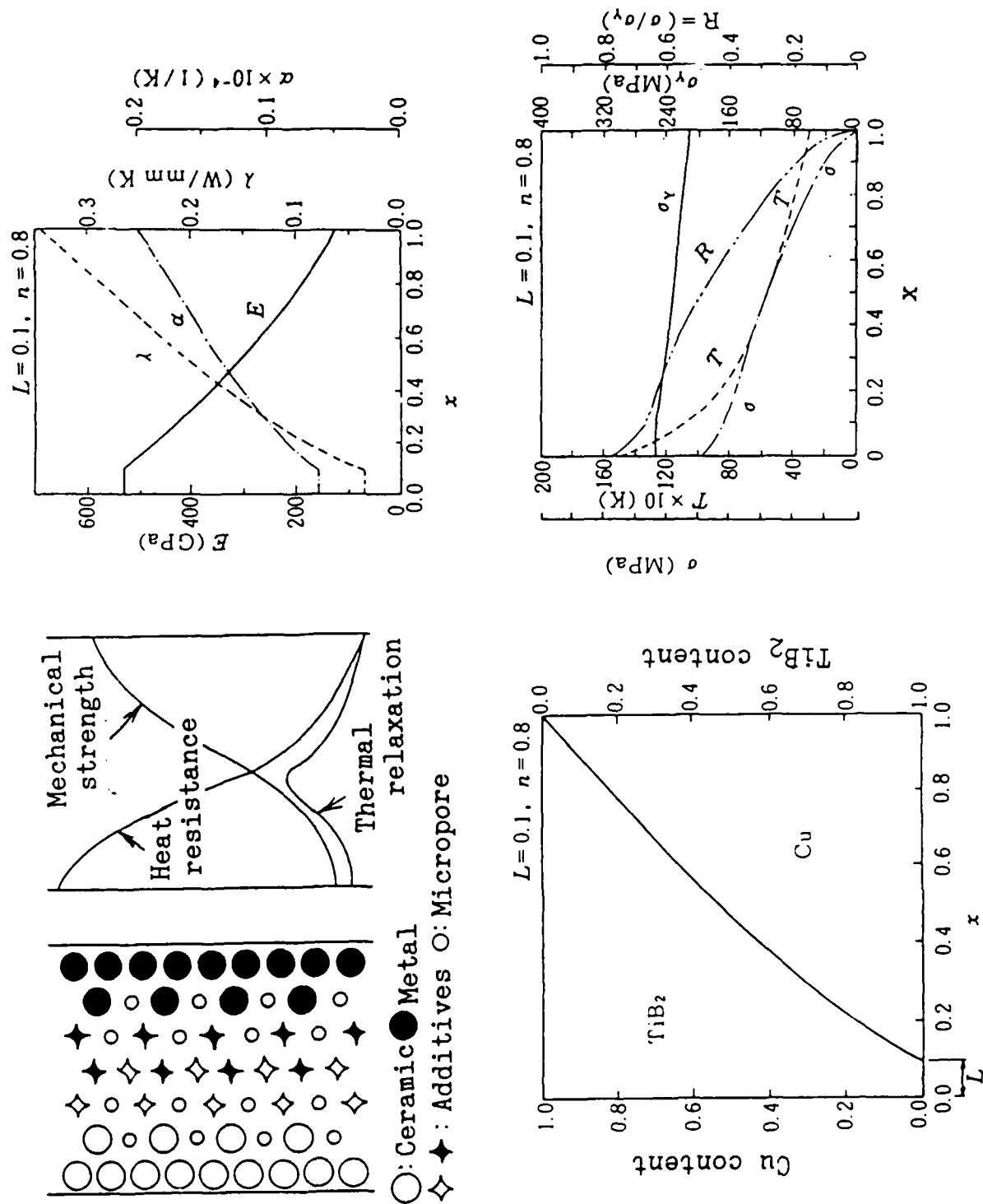


Figure 1. Concept and Design of Functionally Gradient Material

2 Layer

TiB ₂	Cu
------------------	----

3 Layer

TiB ₂	50%-50%	Cu
------------------	---------	----

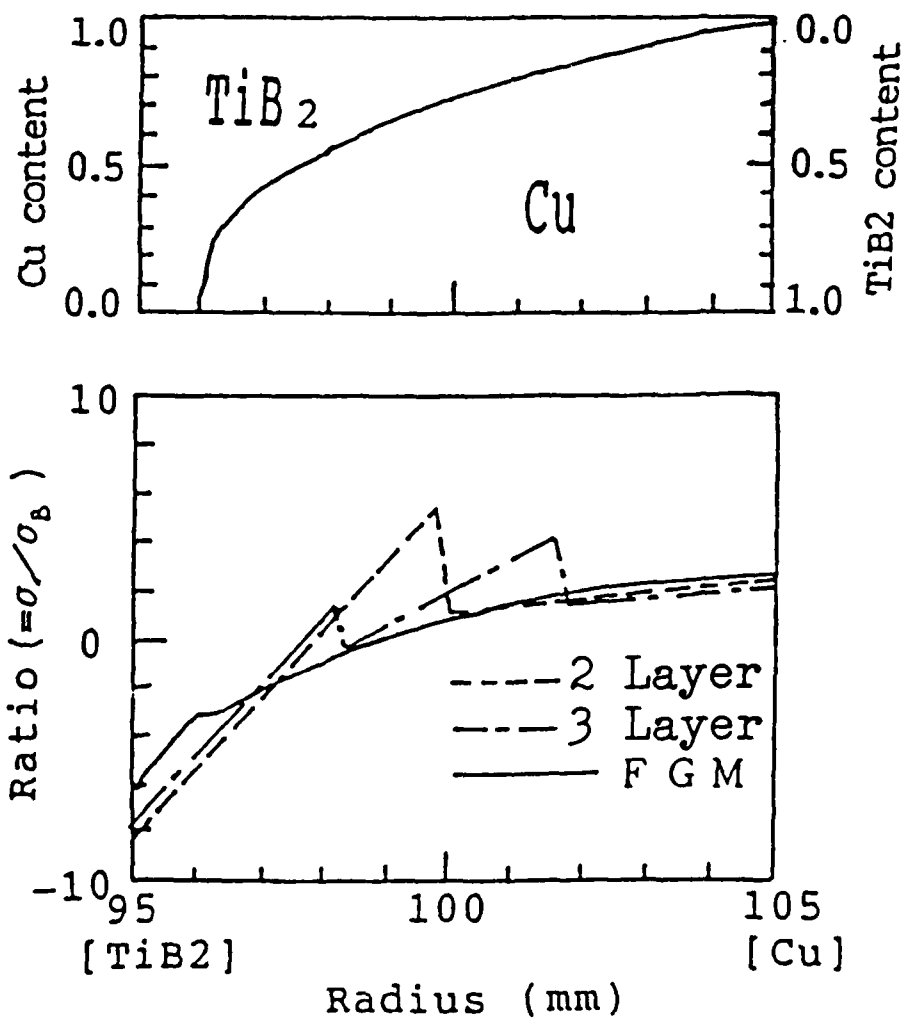


Figure 2. Effect of gradually compositional control in TiB₂-Cu

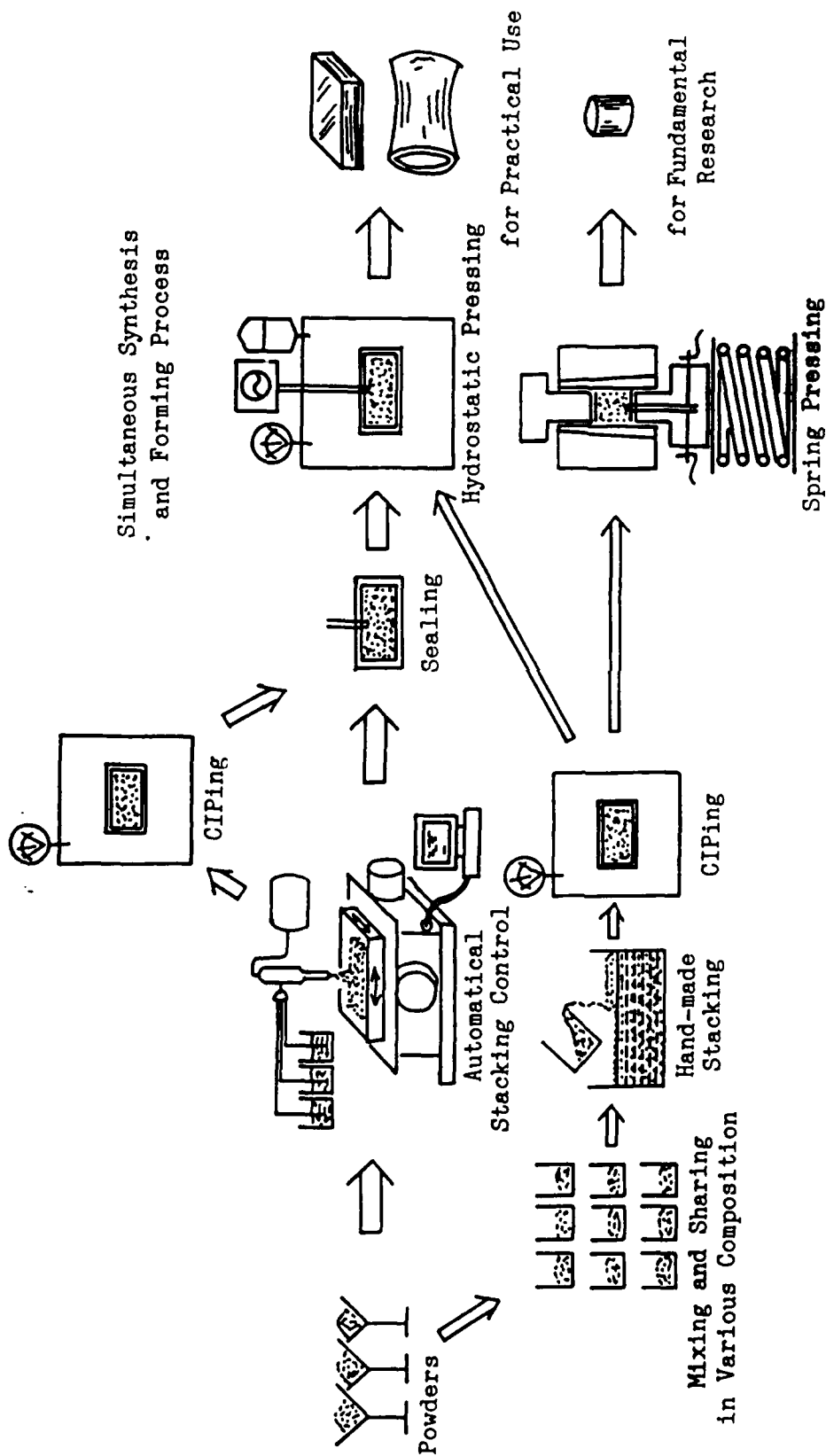
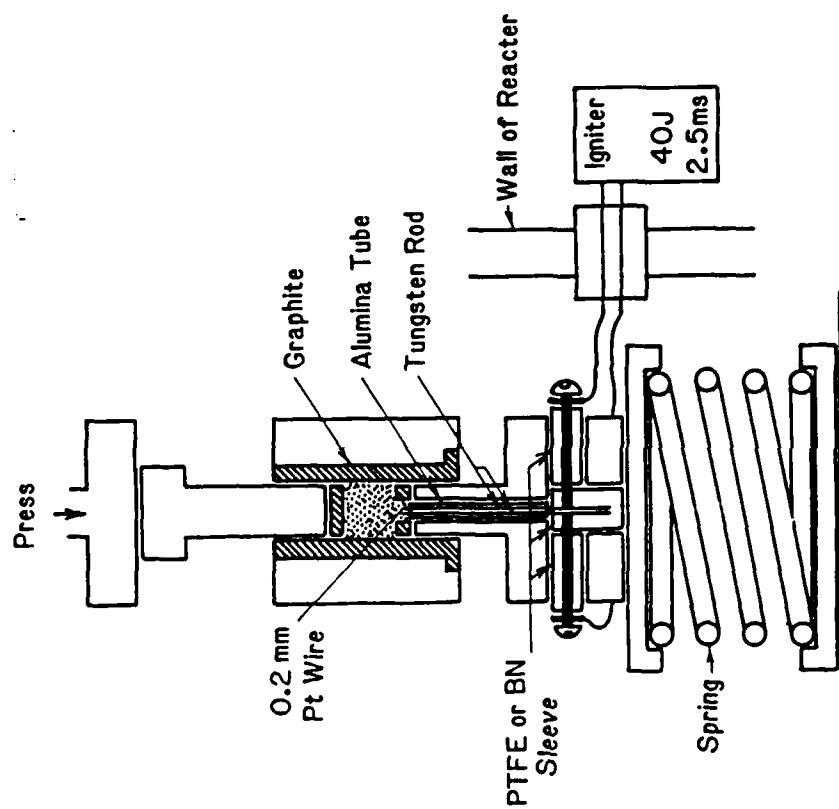
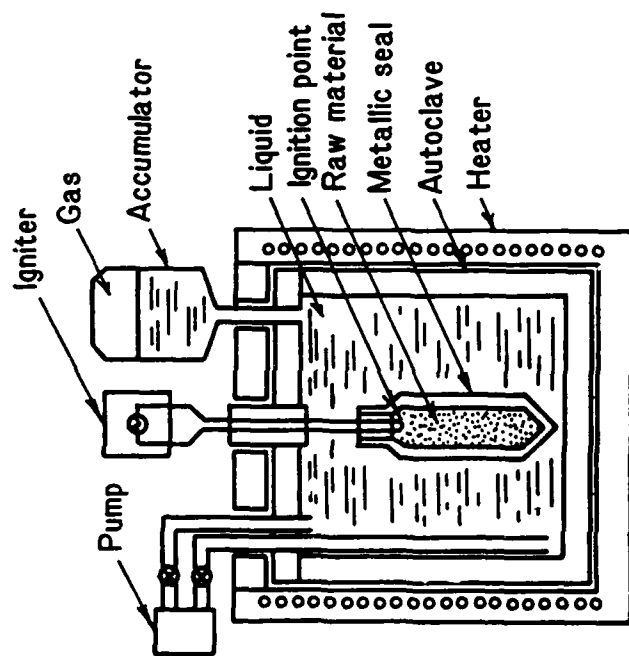


Figure 3. Producing process of FGM by using SHS



(a) Spring pressing method



(b) Hydrostatic pressing method

Figure 4. Experimental apparatus for the fabrication of FGM by using SHS-process

Combustion Synthesis of Oxide-Carbide Composites

Lily L. Wang
Zuhair A. Munir
Division of Materials Science and Engineering
University of California, Davis
Davis, CA 95616, U.S.A.

J. B. Holt
Department of Chemistry and Science
Lawrence Livermore National Laboratory
Livermore, CA 94550, U.S.A.
7/31/89

List of Key Words:

1. Al_2O_3
2. B_4C
3. MgO
4. Mechanism

Abstract

The process of forming $\text{Al}_2\text{O}_3\text{-B}_4\text{C}$ composite by combustion synthesis with Al, B_2O_3 and C as starting materials is proposed to involve a sequential mechanism. The highly exothermic thermite reaction between Al and B_2O_3 occurs first at a temperature higher than the melting point of Al, and the heat generated subsequently brings about the formation of B_4C between the carbon and the liberated boron. Once Al_2O_3 is formed, formation of aluminum borates becomes a competing reaction to the thermite reaction. As a comparison, the study of an alternate oxide-carbide composite system, $\text{MgO-B}_4\text{C}$, confirms the formation of B_4C and also reveals that the reaction mechanism in this case is dependent on the external pressure.

Introduction

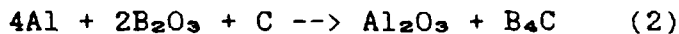
The synthesis of many high temperature materials using a metallothermic reduction reaction, i.e. a thermite reaction, has drawn much attention [1-9]. The general form of these thermite reactions can be described as follows:



where A and M are metallic elements, and MO and AO are their oxides. The exothermic energy released from these thermite reactions is typically large and is sufficient to raise the reaction temperature to 2000 to 3000 °C [10]. Weakly exothermic reactions such as the formation of some carbides and many intermetallic compounds from their elemental constituents are difficult if not impossible to initiate and sustain in the form of a combustion front. By coupling these weakly exothermic

reactions with a highly exothermic thermite reaction, the overall reaction can become self-sustaining and yield a product containing multiple phases, i.e. a composite.

The objective of this study is to investigate the mechanism of the combustion process that leads to the formation of an oxide-carbide composite. The composite system of particular interest is the $\text{Al}_2\text{O}_3\text{-B}_4\text{C}$ system. The overall reaction of this composite formation reaction is



Because of the difficulty in detecting the B_4C phase in the combusted $4\text{Al-2B}_2\text{O}_3\text{-C}$ samples, an alternate reaction system of $6\text{Mg-2B}_2\text{O}_3\text{-C}$ to form MgO and B_4C ,



was also investigated to confirm the formation of B_4C .

Experimental Procedure

The reactant powders used in this study were aluminum (Alcoa 1401), magnesium (Alfa Product 00871), boric oxide (B_2O_3) (Alfa Product 88290), and furnace process carbon black (Cabot Monarch 900). The reactant systems studied were $4\text{Al-2B}_2\text{O}_3\text{-C}$, $6\text{Mg-2B}_2\text{O}_3\text{-C}$ and as well as the thermite mixture $2\text{Al+B}_2\text{O}_3$. These powder mixtures were pressed into cylindrical pellets of 60-63 % of the theoretical density for differential thermal analysis (DTA) and combustion experiments, both of which were conducted in argon atmosphere.

The sample analyses included x-ray diffraction (XRD), scanning electron microscopy (SEM) and x-ray microanalysis. To

separate the B_4C phase, the combusted $6Mg-2B_2O_3-C$ sample was leached in 38% HCl solution to remove the magnesium compounds.

Results and Discussion

1. Differential Thermal Analysis (DTA)

As shown in Figure 1, the DTA curves of both the composite formation ($4Al-2B_2O_3-C$) and thermite reaction ($2Al-B_2O_3$) systems exhibited similar thermal characteristics. In the temperature range of 100 to 300 °C, an endotherm occurred corresponding to the dehydration of the B_2O_3 powder which is highly hygroscopic. No endotherm was observed at the melting point of B_2O_3 probably due to the B_2O_3 powder being partially amorphous.

Two exotherms occurred at temperatures higher than the melting point of aluminum (660 °C). In order to determine the corresponding reaction occurring in these exotherms, the samples heated at 25 °C/min to various critical temperatures along the DTA path were analyzed. After heating through the first exotherm, both the $4Al-2B_2O_3-C$ and $2Al-B_2O_3$ samples exhibited formation of an aluminum borate phase $Al_4B_2O_9$ (i.e. $2Al_2O_3 \cdot B_2O_3$, a phase that has been found to form from the reaction $2Al_2O_3(s) + B_2O_3(l) \rightarrow 2Al_2O_3 \cdot B_2O_3(s)$ [11]), but only in the $4Al-2B_2O_3-C$ sample small amounts of Al_2O_3 were detected. When both the $4Al-2B_2O_3-C$ and $2Al-B_2O_3$ samples were heated through the second exotherm, more of the $Al_4B_2O_9$ phase and as well as significantly more of the Al_2O_3 phase were formed. The absence of carbon in the thermite mixture (i.e. $2Al+B_2O_3$) affected the second exotherm which was resolved into two peaks at heating rates equal to or lower than 25 °C/min. For both mixtures heated at

this slow rate, reactions did not go to completion after the second exotherm for substantial amounts of Al and B_2O_3 were still present.

Difficulty was encountered in detecting boron carbide and boron phases in the DTA samples by the x-ray diffraction method. The reason can be attributed to that the x-rays diffracted by boron carbide and crystalline boron were likely absorbed before they escaped the sample due to the low x-ray absorption of these light-element phases, the amounts formed being small, and the fact the Al-O compounds having higher x-ray absorption. Moreover, boron existing in an amorphous form may be another reason for the lack of detection.

2. Combustion Mode

The results of the combustion experiments are summarized in Table 1. The combustion front of both the $4Al-2B_2O_3-C$ and $2Al-B_2O_3$ samples moved in a manner bordering pulsating and spiral (spin) modes. The combustion front of $2Al-B_2O_3$ moved at finer pulsating intervals and faster speed, see Table 1. In both systems, vaporization at or near the combustion front was observed. The vapor condensate was analyzed to be B_2O_3 , the most volatile component in the reactant mixture.

The combustion temperature of the $4Al-2B_2O_3-C$ system was about $100^\circ C$ lower than that of the $2Al-B_2O_3$ system, Table 1. The combusted samples of both mixtures were highly porous and friable. The cylindrical surface of the combusted samples of both systems showed rings of rippling effect which manifested

that melting had occurred at the combustion front to allow the reacting layer to sag.

As the DTA results have shown that the vigor of the reaction increases with increasing heating rate, Figure 1, higher heating rate is expected to bring the reaction process closer to completion. Thus the sample reacted through a combustion wave, which brings about an extremely high heating rate in the region in front of the combustion wave, should achieve a greater conversion to the final product. This is verified by the combusted $4\text{Al}-2\text{B}_2\text{O}_3\text{-C}$ and $2\text{Al}-\text{B}_2\text{O}_3$ samples containing mostly Al_2O_3 and small amounts of a more Al_2O_3 -rich borate, $\text{Al}_{18}\text{B}_4\text{O}_{33}$ (i.e. $9\text{Al}_2\text{O}_3 \cdot 2\text{B}_2\text{O}_3$, a phase that has been found to form from the reaction $9\text{Al}_2\text{O}_3(\text{s}) + 2\text{B}_2\text{O}_3(\text{l}) \rightarrow 9\text{Al}_2\text{O}_3 \cdot 2\text{B}_2\text{O}_3$ [11]). The presence of B_4C in the combusted $4\text{Al}-2\text{B}_2\text{O}_3\text{-C}$ sample was sometimes detected by x-ray diffraction.

In the $6\text{Mg}-2\text{B}_2\text{O}_3\text{-C}$ case, the combustion process involved a much greater release of vapors which clouded the chamber and prevented visual observation of the combustion process. The vapor condensates were analyzed to contain MgO , Mg , and WO_3 . The presence of the WO_3 phase is due to reactions with the tungsten ignition coil. Attempts to suppress the evaporation by increasing the argon pressure were conducted. At 13 atm pressure, the evaporation rate was reduced to a level that allowed visual observation of the combustion process. The combusted sample was intact but still exhibited a significant (38%) volume expansion. Further increasing pressure to 1020 atm, the sample shape was maintained, and, moreover, volume

expansion was reduced to 4%. Interestingly, at 13 atm the reaction temperature was measured to be 1450 °C, much lower than adiabatic combustion temperature which is 2467 °C, while at 1020 atm pressure, the combustion temperature was substantially higher (2180 °C). Increasing pressure also reduced weight loss of the sample from 3.9% observed at 13 atm to less than 0.3% at 1020 atm.

The types of crystalline phases present in the reacted $6\text{Mg}-2\text{B}_2\text{O}_3\text{-C}$ samples do not depend on the external pressure. All the reacted samples contained mostly MgO , and small amounts of $\text{Mg}_3(\text{BO}_3)_2$ (i.e. $3\text{MgO}\cdot\text{B}_2\text{O}_3$). Moreover, the formation of the B_4C phase in the combusted sample was definitely confirmed by the x-ray analysis of the product and the acid leached residue. The boron carbide obtained after acid leaching showed to have submicron particle size similar to that of the initial carbon particles.

The combusted samples becomes less porous and friable as the external pressure increases. Figures 2 and 3 present the morphology of the fractured surfaces of the $6\text{Mg}-2\text{B}_2\text{O}_3\text{-C}$ samples combusted at 1 and 1020 atm argon, respectively. The striated surfaces of the nodular particles in the sample combusted at 1 atm, Figure 2, indicate that the formation of these particles involved a vapor phase transport. Various reasons suggest that these striated particles are MgO . First Mg is the most volatile component in the reactant mixture. Secondly, the MgO is the predominant phase in the product, while the $\text{Mg}_3(\text{BO}_3)_2$ is present in minor amounts and would not show striated feature for it

would have melted at the combustion temperature (1450 °C) for the melting point of $\text{Mg}_3(\text{BO}_3)_2$ is 1356 °C [12]. Thirdly, the surrounding submicron particles can be identified to be B_4C from their similar appearance to the leached B_4C particles. In the sample combusted at 1020 atm, Figure 3, no striated feature is observed. The reacted phases appeared rounded and more tightly bonded and have smooth surfaces, indicative of formation from melt.

Conclusion

In the self-propagating combustion mode, the reactants are being heated up at an extremely fast rate. With the large sample condition being more conducive to heat retention, the extend of side reactions to form borates is reduced, and the reaction to form the product oxide is more complete. Moreover the reaction condition produces higher combustion temperatures. From DTA results, the combustion reaction is shown to initiate at a temperature substantially higher than the melting point of Al. Consistent with the DTA results, the combustion process shows evidence of melting of the reactants in the combustion zone. The lower combustion temperature and slower combustion velocity in the system containing carbon support the assumption that the reaction mechanism is sequential. The thermite reaction occurs first and subsequently brings about the formation of B_4C . With carbon added, the combustion temperature would be lower since the carbon acts as a diluent initially.

The cursory study of the $\text{MgO-B}_4\text{C}$ combustion synthesis reveals a noticeable difference in the reaction mechanism. The

formation of MgO appears to involve gaseous Mg and liquid B₂O₃, at least at one atm pressure. As the external pressure increases, the evaporation rate is reduced and the reaction changes to liquid-liquid interaction. Because materials loss due to evaporation is reduced at high pressures, more Mg participates in the reaction to achieve a higher combustion temperature.

References

1. J. D. Walton Jr., and N. E. Poulos, J. Am. Ceram. Soc., 42, 40-49 (1959).
2. O. Odawara and J. Ikeuchi, J. of Jpn. Inst. of Metals, 45 [3] 316-321 (1981).
3. A. G. Merzhanov, I. P. Boroviskaya, V. I. Iukhvid, and V. I. Ratnikov, in *Nauchnye Osnovy Materialovedeniia*. Moscow, 1981.
4. A. A. Shidlovskii, and V. V. Gorbunov, Combust. Explos. Shock Wave, 18 [4] 420-422 (1983).
5. K. V. Logan and J. D. Walton, Ceramic Engineering and Science Proceedings 5 [7-8] 735 (1984).
6. A. V. Dvoryankin, A. G. Strunina, and A. G. Merzhanov, Combustion Explos. Shock Wave, 21, [4] 421-425 (1985).
7. R. A. Cutler, A. V. Virkar and J. B. Holt, Ceram. Eng. Sci. Proc., 6 [7-8] 715-728 (1985).
8. R. A. Cutler, in *Proc. DARPA Symposium on SHS*. Daytona Beach, FL., Oct 21-23, 75-104 (1985).
9. R. A. Culter and K. R. Rigtrup, Ceramatec report no. 87012601, (1987).
10. W. L. Frankhouser, K. W. Brendley, M. C. Kieszek and S. T. Sullivan, *Gasless Combustion Synthesis of Refractory Compounds*. Noyes Publications, 6 (1985).
11. V. H. Scholze, Z. anorg. u. allgem. Chem., 284 272 (1956).
12. H. M. Davis and M. A. Knight, J. Am. Ceram. Soc., 28 [4] 100 (1945).

Table 1: Results of Combustion Experiments

Mixture	v cm/s	Tmax °C	Ar atm
4Al+2B ₂ O ₃ +C	0.19-0.22	1550-1600	1
2Al+B ₂ O ₃	0.26-0.31	1680-1680	1
6Mg+2B ₂ O ₃ +C	*	*	1
6Mg+2B ₂ O ₃ +C	0.93	1450	13
6Mg+2B ₂ O ₃ +C	0.56	2180	1020

* The combustion released much volatile which clouded the chamber immediately, and consequently temperature and velocity could not be measured.

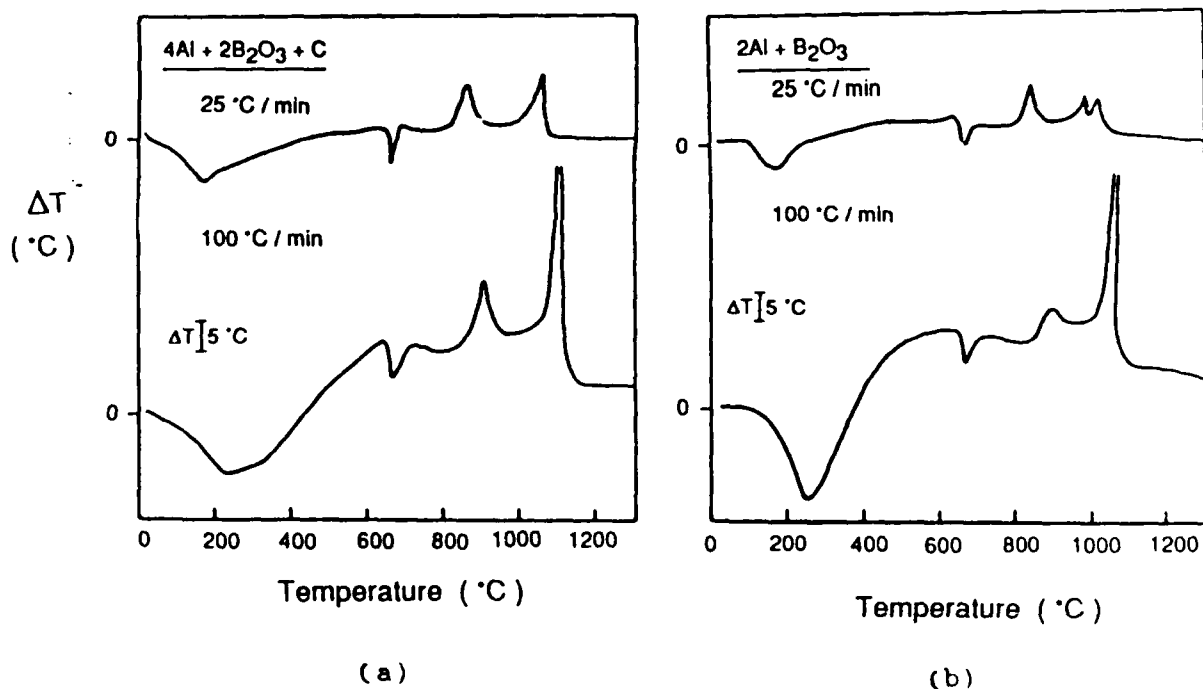


Figure 1: DTA curves of a) 4Al-2B₂O₃-C and b) 2Al-B₂O₃ samples.



Figure 2: Fractured surface of the $6\text{Mg}-2\text{BaO}_3\text{-C}$ combusted sample (reacted in 1 atm argon).

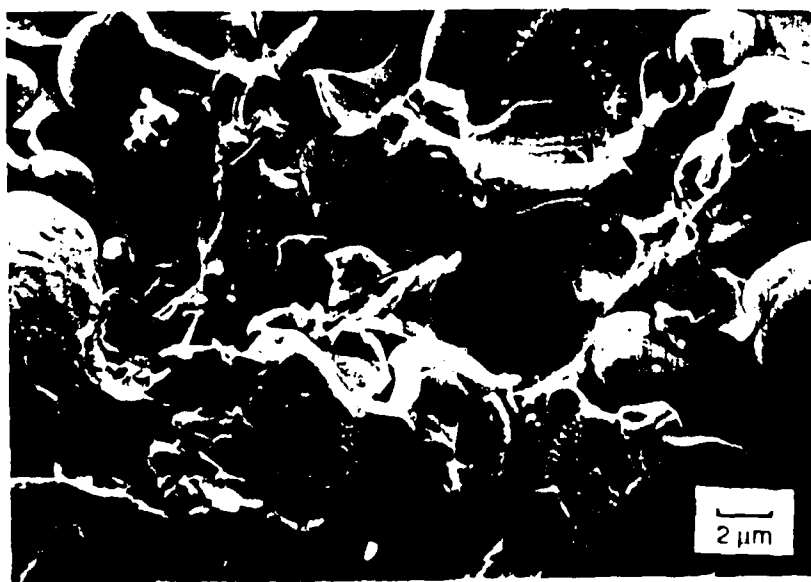


Figure 3: Fractured surface of the $\text{Mg-BaO}_3\text{-C}$ combusted sample (reacted in 1020 atm argon).

355
356

R.Pampuch, J.Lis, L.Stobierski
Institute of Materials Science, AGH Cracow (Poland)

Heterogeneous Reaction Mechanisms in the Si-C System
under Conditions of Solid Combustion

Abstract

The specific features of the mechanism and kinetics of heterogeneous reactions which occur on solid combustion in solid-solid and solid-liquid Si-C systems are discussed.

Introduction

Under the specific conditions of solid combustion also specific mechanisms of heterogeneous reactions should occur (1)-(3, rendering possible the high reaction rates and degrees of conversion to products observed here. This may be exemplified by heterogeneous reactions in the Si + C system under conditions of solid combustion.

Reactions at C/SiC Boundary and Ignition of the Si+C System

There is indirect evidence from combined DTA-DTG measurements, colour changes from black to grey, and from an increase of the oxidation resistance that in the Si+C particulate systems the carbon particles become covered by silicon layers during the last stages of preheating preceding the onset of reaction and ignition. Hence, it may be plausibly assumed that the leading reaction, responsible both for ignition and propagation of the heat wave on solid combustion in the Si-C system is the exothermic reaction between Si and C accompanied by a heat release which is able to rise the temperature of the system by some 900 to 1600 deg under adiabatic conditions. Since a thin SiC layer separating the substrates is formed at the initial reaction stages, conversion of further amounts of Si + C to SiC requires a diffusion through the SiC layer.

Diffusion coefficients in SiC are very low and diffusional transport to phase boundaries should be the rate-determining step of the reaction. When Si and C react with each other it is usually observed that Si diffuses into the carbon particles (4)(5) and that the diffusion coefficient of Si in SiC is ten times greater than the one of C (6). Hence, reactions at the C/SiC boundary due to diffusion of Si through SiC shall be now considered. In Fig. 1 the thick solid line shows the concentration profile of Si while r_0 and r_t denote, respectively, the radius of the carbon particles at time $t=0$ and after time t . When local equilibrium at the interface and consumption of the whole flux of diffusing silicon in formation of SiC at the C/SiC boundary are assumed, one obtains from Fick's law and the continuity condition:

$$-D_{SiC}^{Si} \left(\frac{dc^{Si}}{dr} \right)_{r_t} = (c_{r_t}^{Si} - c_c^{Si}) dr/dt \quad (1)$$

where: $c_c^{Si} = 0$; D_{SiC}^{Si} is the coefficient of diffusion of Si in SiC. Solution of Eqn (1) at boundary conditions $c_{r_0}^{Si} = g^{Si}/M^{Si}$ and $c_{r_t}^{Si} = g^{SiC}/M^{SiC}$, where g^i is the density and M^i the molecular mass of the given species, respectively, leads to an equation for the rate of increase of the thickness, y , of the SiC layer:

$$(dy/dt)_i = -(dr/dt) = \frac{D_{SiC}^{Si} X}{r_t \log(r_0/r_t)} \quad (2)$$

where: $X = (M^{SiC} g^{Si}/M^{Si} g^{SiC}) - 1$.

The degree of advancement of the reaction, α , in terms of carbon consumption and for spherical and cylindrical particles, may be expressed by:

$$\alpha = 1 - V_t/V_0 = 1 - (r_t/r_0)^2 \quad (3)$$

where: r_0 and r_t are the radius; V_0 and V_t are the volume of the particles at a time of $t=0$ and t , respectively. Taking into account Eqn.(3), the Eqn.(2) may be rewritten in form:

$$(dy/dt)_i = (D_{SiC}^{Si} X) / \{ -r_0 (1-\alpha)^{1/2} \log(1-\alpha)^{1/2} \} \quad (4)$$

Fig. 1

Taking $y=r_0 - r_t$, we obtain from Eqn.(3) and (4) after integration that:

$$\left\{ 1 - (1-\alpha) \left[1 - 2 \log (1-\alpha)^{1/2} \right] \right\} = \frac{4 D_{SiC}^{Si} X}{r_0^2} \cdot t \quad (5)$$

Fig. 2

Hence, a plot of the function of α which appears on the left-hand side of Eqn.(5) vs. time permits to check the model. Fig. 2 shows such a plot based on microscopic determinations of carbon not converted to SiC in the reaction with silicon of carbon fibres of two kinds, W and P, respectively (4). The carbon fibres had a circular section what enabled a use of Eqn.(3). The data in Fig. 2. indeed lie along straight lines predicted by Eqn.(5). From the slopes of the lines an effective diffusion coefficient of $2.10E-9 \text{ cm}^2/\text{s}$ has been obtained for both fibre types. This value is in a good agreement with the effective coefficient of diffusion of Si in SiC estimated in Ref.(5) for a temperature of 2050°C which is the peak temperature on solid combustion in the Si+C system (4). Assuming the above mechanism of reactions at the C/SiC boundary, the conditions favourable to ignition of the Si+C particulate mixtures shall now be discussed. In order to do this let us substitute in Eqn.(4) the relative thickness of the layer $y'=y/r_0$, for the degree of advancement of the reaction (expressed in terms of carbon consumption). For cylindrical particles $(1-\alpha)^{1/2} = 1 - y'$ and $dy' = dy/r_0$. From equations (1), (2) and (4) one obtains, after suitable rearrangements:

$$j_{C/SiC}^{Si} = (D_{SiC}^{Si} X g^{SiC}) / [M^{SiC} r_0 (1-y') \log (1-y')] \quad (6)$$

where: j_{SiC}^{Si} is the flux density of silicon at the C/SiC boundary. On hand of the Eqn.(6) a diagram may be constructed in which j_{SiC}^{Si} (in arbitrary units) is plotted vs. the reciprocal temperature and the relative thickness of the SiC layer. The plot is shown in Fig. 3.

Fig. 3

In deriving the plot a temperature dependence of D_{SiC}^{Si} such as found in Ref.(5) was taken into account. The conclusions from Fig.3 are trivial but important for further analysis. According to thermal balance, ignition of the reactive mixture of C+Si should occur when the product of heat effect of the reaction, Q , (in J/mole) and flux density of Si at the C/SiC boundary, j_{SiC}^{Si} , is equal or greater than the heat losses:

$$Q j_{SiC}^{Si} \geq -\lambda \left(\frac{dT}{dr} \right)_{C/SiC} \quad (6)$$

where: λ is the coefficient of thermal conductivity, and dT/dr is the temperature gradient at the phase boundary. Eqn.(6) indicates that a high flux density of Si at the C/SiC boundary is necessary for ignition of the mixture. According to Fig.3, this requirement is met only when the SiC layer is thin, even at elevated temperatures. Such a conclusion is the counterpart, for heterogeneous reactions, of the conclusion drawn in case of homogeneous reactions that most favourable conditions for ignition of a reactive mixture should occur at low degrees of advancement of the reaction only.

Reactions at the SiC/Si(l) Boundary and Formation of the Final Product

A high flux density at the C/SiC boundary is also necessary for high reaction rates at higher degrees of advancement of the reaction. In terms of the model proposed, this means that the initially thin SiC layer should remain constant over the whole solid combustion process. This may take place when due to an increase of temperature of the system after ignition silicon melts and dissolution of the SiC layer at the SiC/Si(l) becomes possible. Let us consider the concentration profile of carbon at the SiC/Si(l) boundary, shown in Fig.4.

Fig. 4

Fick's law and continuity condition lead to an equation:

$$\left(\frac{dy}{dt}\right)_2 = -\left(\frac{dr}{dt}\right) = \frac{D_{Si(l)}^C}{(c_0^C - c_{eq}^C)} \left(\frac{dc}{dx}\right) \quad (8)$$

where: $D_{Si(l)}^C$ is the coefficient of diffusion of carbon in liquid silicon; x is the distance from the SiC/Si(l) boundary in the liquid. At $x=0$ $c^C = c_0^C$ in the solid and $c^C = c_{eq}^C$ in the liquid, respectively, where c_{eq}^C is the equilibrium concentration of carbon in liquid silicon (a local equilibrium is thus assumed at the SiC/Si(l) boundary). The concentration of C in liquid silicon in function of distance, x , and time, t , is:

$$c^C(x, t) = \left[\operatorname{erfc} \left(\frac{x}{2(D_{Si(l)}^C t)^{1/2}} \right) \right] (c_{eq}^C - c_{\infty}^C) \quad (9)$$

where: c_{∞}^C is the concentration of carbon far away from the SiC/Si(l) boundary. Let us denote $x / \{2(D_{Si(l)}^C t)^{1/2}\} = z$. Since $\operatorname{erfc}(z=2) \approx 0$:

$$x = 4 (D_{Si(l)}^C t)^{1/2} \quad (10)$$

and

$$\left(\frac{dy}{dt}\right)_2 = \frac{1}{4} \left(\frac{c_{eq}^C - c_{\infty}^C}{c_0^C - c_{eq}^C} \right) \left(\frac{D_{Si(l)}^C}{t} \right)^{1/2} \quad (11)$$

Substituting a function of the degree of advancement of reaction (in terms of carbon consumption) for time t , and noting that $c_{\infty}^C = 0$ one obtains from Eqns. (4) and (11):

$$\left(\frac{dy}{dt}\right)_2 = \frac{1}{2} \left(\frac{c_{eq}^C}{c_0^C - c_{eq}^C} \right) \left[\frac{D_{Si(l)}^C D_{SiC}^{Si} x}{\{1 - (1-\alpha)[1 - 2 \log(1-\alpha)^{1/2}]\} r_0^2} \right]^{1/2} \quad (12)$$

Growth of the primary-SiC layer at the C/SiC boundary and its dissolution at the SiC/Si(l) boundary may lead to three types of behaviour:

a. growth rate higher than the dissolution rate; comparing Eqns. (4) and (12) this should be the case when:

$$\left(\frac{dy}{dt}\right)_1 > \left(\frac{dy}{dt}\right)_2 ; \quad \frac{D_{Si(l)}^C}{D_{SiC}^{Si}} < F(\alpha) \quad (13)$$

where:

$$F(\alpha) = \frac{4x}{\{c_{eq}^C / (c_0^C - c_{eq}^C)\}} \cdot \frac{\{1 - (1-\alpha)[1 - 2 \log(1-\alpha)^{1/2}]\}}{\{-(1-\alpha)^{1/2} \log(1-\alpha)^{1/2}\}^2}$$

b. growth rate at the SiC/C boundary equal to the dissolution rate at the SiC/Si interface; this should occur when:

$$(dy/dt)_1 = (dy/dt)_2 ; \frac{D_{SiC}^C}{D_{SiC}^{Si}} = F(\alpha) \quad (14)$$

c. growth rate at the SiC/C boundary lower than the dissolution rate at the SiC/Si boundary; this should occur when:

$$(dy/dt)_1 < (dy/dt)_2 ; \frac{D_{SiC}^C}{D_{SiC}^{Si}} > F(\alpha) \quad (15)$$

The behaviour a. corresponds to the one predicted by the classical model of heterogeneous reactions under nearly isothermal conditions; the behaviour c. is a simple dissolution of the product layer and/or of the solid substrate in the liquid. The behaviour b. corresponds to a constant thickness of the product layer. Together with behaviour of type c. it may ensure high rates of reaction up to the total conversion to products, such as occurs on solid combustion.

Experimental data are known for all quantities which appear in Eqns. (4) and (12). Inserting into Eqns. (4) and (12) data taken from Ref. (5), (7)-(10), and taking into account an average experimental error of determinations of the diffusion coefficients in SiC (see Ref. (11)), a plot of $\log(D_{SiC}^C/D_{SiC}^{Si})$ and of $\log F(\alpha)$ vs. reciprocal temperature may be constructed. The plot, shown in Fig. 5, enables to estimate the range of temperatures at which a given type of behaviour should predominate. According to the Figure, the classical mechanism of continuous growth of primary SiC layer should predominate at temperatures below about 1900 °C and the one of dissolution of SiC and/or of carbon in silicon at temperatures above 2100 °C. Owing to similar rates of growth and of dissolution of the layer, a thin layer of SiC of a constant thickness is expected to occur in the intermediate range of temperatures,

Fig. 5

between about 1900 and 2100°C . It may be noted that this is the very range of peak temperatures estimated to occur on solid combustion in the Si-C system (12). The occurrence of a primary-SiC layer of a constant thickness is tantamount to a mechanism, shown in Fig.6, in which a thin layer of SiC moves into the carbon substrate owing to its simultaneous growth at the C/SiC boundary and its dissolution at the SiC/Si(l) boundary. The moving layer thus pulls a solution of C in liquid silicon in its wake and the final product, i.e. secondary SiC, is eventually formed by crystallisation from the supersaturated solution. The mechanism explains rationally the morphology of SiC formed by reaction of Si and C under conditions of solid combustion. It has been, namely, found that the SiC particles are here the metamorphoses of the original carbon particle, be it a fibre, carbon black, charcoal, or natural graphite (13)-(15).

Conclusions

A mechanism of heterogeneous reactions in the Si-C particulate system on solid combustion has been proposed, according to which a constant small thickness of the primary SiC is retained due to simultaneous growth and dissolution at opposite phase boundaries and the formation of the final product, secondary SiC, occurs by crystallization from the supersaturated liquid solution. It has been assessed that this mechanism occurs in the Si-C system at temperatures between 1900 and 2100°C which are the peak temperatures on solid combustion in the Si+C system. At lower temperatures the classical mechanism of heterogeneous reactions, characterised by a continuous growth of thickness of the SiC, should predominate and hamper the ignition, lower the reaction rate, and overall conversion.

The latter behaviour has been observed earlier by us in Si-C particulate system at slower rates of temperature increase during the preheating stage (14). The mechanism proposed in the present paper for the Si-C system probably also occurs on solid combustion in C,B-metal systems, other than Si-C, what follows from direct microscopic observations of the behaviour of the latter systems reported in Ref.(1).

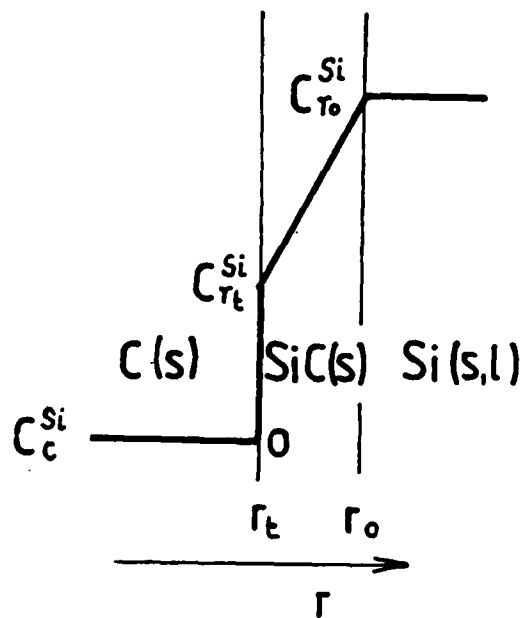
References

1. Aleksandrov V.V., Korchagin M.A., O mekhanizme i makrokine-tike reaktsiy pri gorenii SVS-sistem, Fiz.Goreniya i Vzryva (Russ.) 5 (1987), 55-63
2. Pampuch R., Lis J., Stobierski L., SHS Synthesis of Ceramic Powders, in Science of Ceramics 14, D.Taylor (Ed). Inst.of Ceramics, Shelton, 1988, pp.15-26
3. Pampuch R., Walasek E., Białoskórski J., Mechanizm reakcji węgiel-ciekły krzem w podwyższonych temperaturach (Polish), Inż.Mater.(Poland) 6 (1985) 132-138
4. Pampuch R., Walasek E., Białoskórski J., Reaction Mechanism in Carbon-Liquid Silicon System at Elevated Temperatures, Ceram.Intern. 12 (1986), 99-103
5. Fitzer E., Fritz W., Gadow R., Carbon Fibre Reinforced Silicon Carbide, in Proc.Intern.Symp.Ceram.Compon.for Engine, 1983, Japan, p.505-515
6. Ghoshtagore R.N., Coble R.L., Self-Diffusion in Silicon Carbide, Phys.Rev. 143 (1966) 623-26
7. Scace R.J., Slack G., Solubility of Carbon in Silicon and Germanium, J.Chem.Phys. 30 (1959) 1551-58
8. Kostikov V.Ya., Tarabanov A.S., in Silitsirovanniy Grafit (Russ.), Metallurgiya Publ. Moskva, 1977, 14
9. Kern E.L., Hamill D.W., Deam C.W., Sheets H.D., Thermal Properties of Beta-Silicon Carbide from 20 to 2000 C, in "Silicon Carbide-1968", Mater.Res.Bull. 4 (1969), pp.25-32
10. Gnesin G.G., Raychenko A.J., Poroshk.Metall. 5 (1973) 35-38
11. Birnie D.P., A Model for Silicon Self-Diffusion in SiC: Anti-Site Defect Motion, J.Am.Ceram.Soc. 69 (1986) C33-35
12. Pampuch R., Białoskórski J., Walasek E., in Reactivity of Solids, Nowotny J., Dyrek E., Haber J. (Eds) Elsevier Science Publ.Co., Amsterdam, 1983. p.567-572
13. Pampuch R., Białoskórski J., Walasek E., Mechanism of Reactions in the Si+C System and the SHS of Silicon Carbide, Ceram.Intern., 13 (1987) 63-68
14. Pampuch R., Stobierski L., Lis J., Rączka M., Solid Combustion Synthesis of SiC Powders, Mater.Res.Bull. 22 (1987) 1225-31
15. Fitzer E., Gadow R., Investigations of the Reactivity of Different Carbons with Liquid Silicon, in Proc. Intern. Symp. Ceram. Comp. for Engine, 1983, Japan, pp561-70

Captions of Figures

- Fig.1. Model of reactive diffusion at the C/SiC boundary
Fig.2 Plot of $4(1-\alpha)[1 - 2\log(1-\alpha)]$ vs time obtained in the case of two types of carbon fibres (W and P) of a different radius, reacting with silicon at a temperature around 2050°C.
Fig.3 Flux density of silicon at the C/SiC boundary (in arbitrary units) vs. reciprocal temperature and relative thickness of the SiC layer
Fig.4 Model of dissolution at the SiC/Si(l) boundary
Fig.5 Plot of $\log(D_{Si,C}^C/D_{Si,C}^{Si})$ and of $\log F(\alpha)$ vs. reciprocal temperature for the Si + C system
Fig.6 Model of reactions occurring in the Si+C system under conditions of solid combustion

Param. ... $AT \gg 1$



$$C_{r_o} = \frac{\rho^{Si}}{M^{Si}}$$

$$C_{r_t} = \frac{\rho^{SiC}}{M^{SiC}}$$

Figure 1

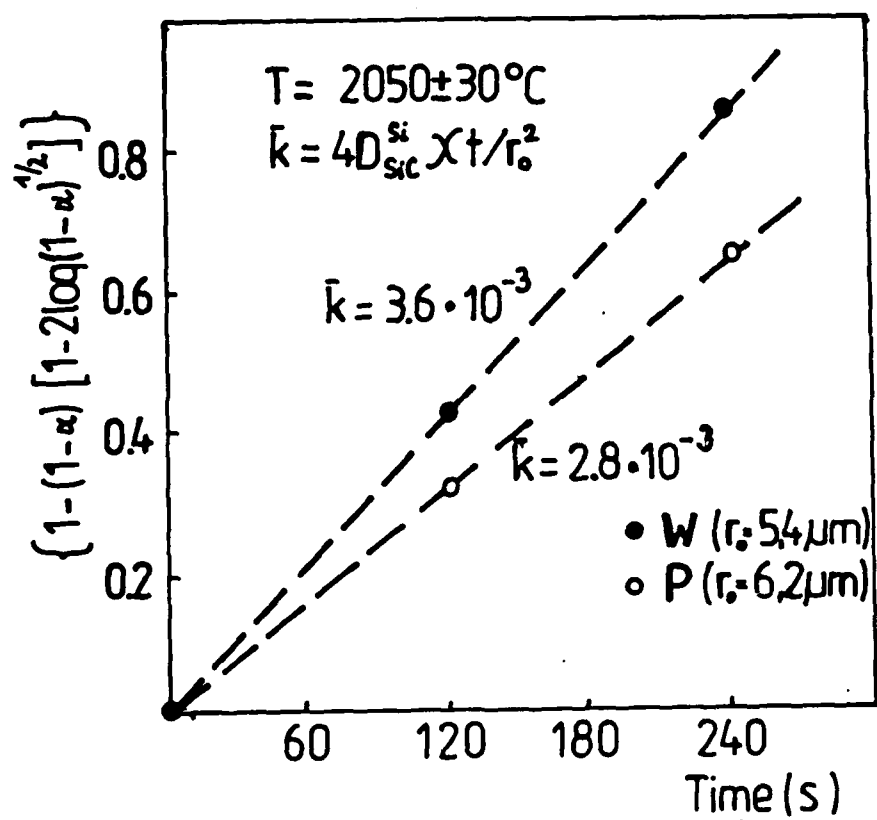


Figure 2

Figure 3

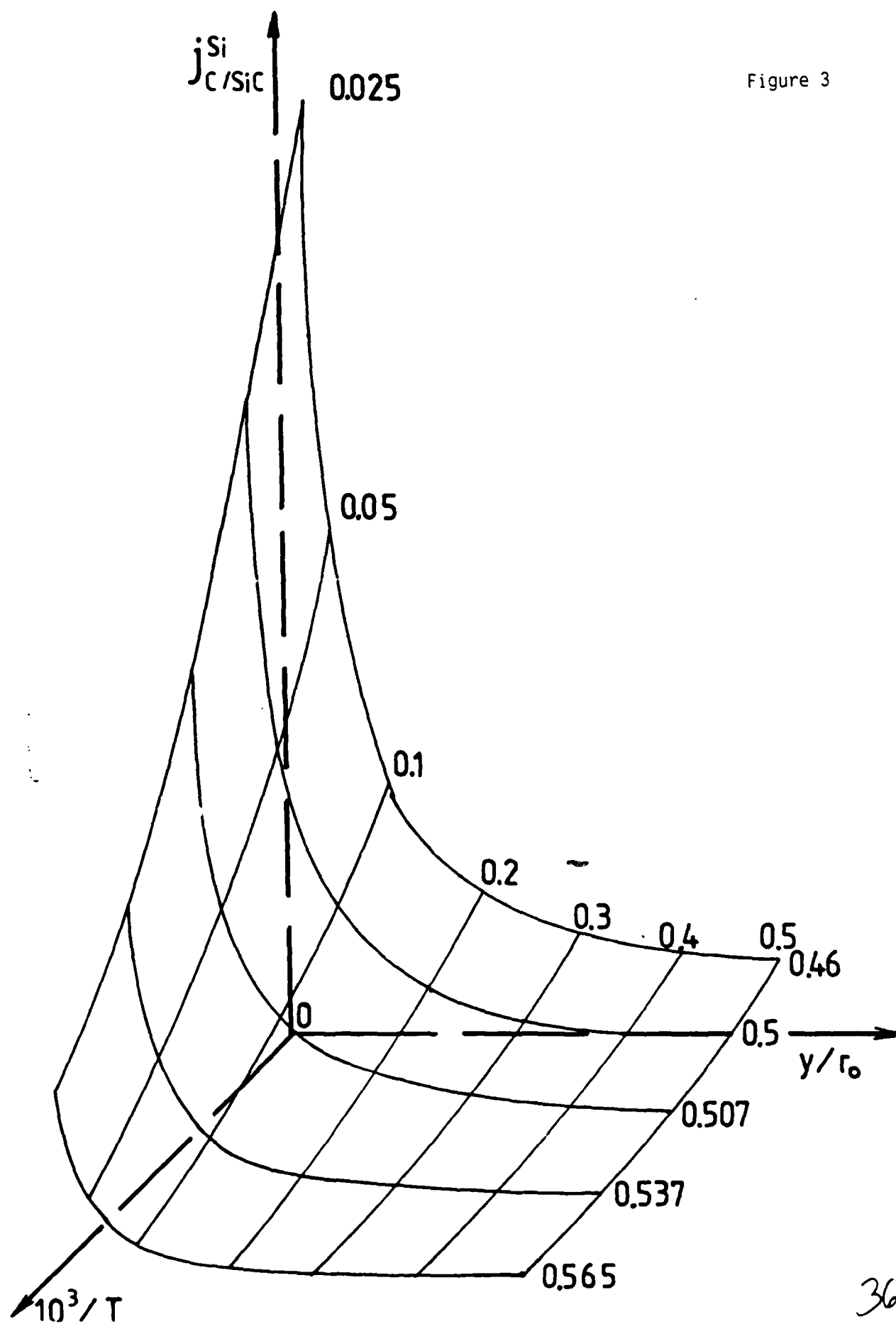


Figure 4

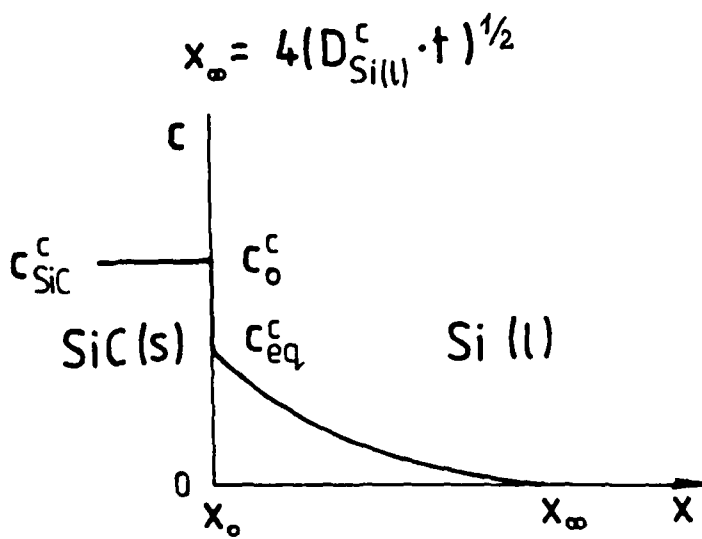


Figure 5

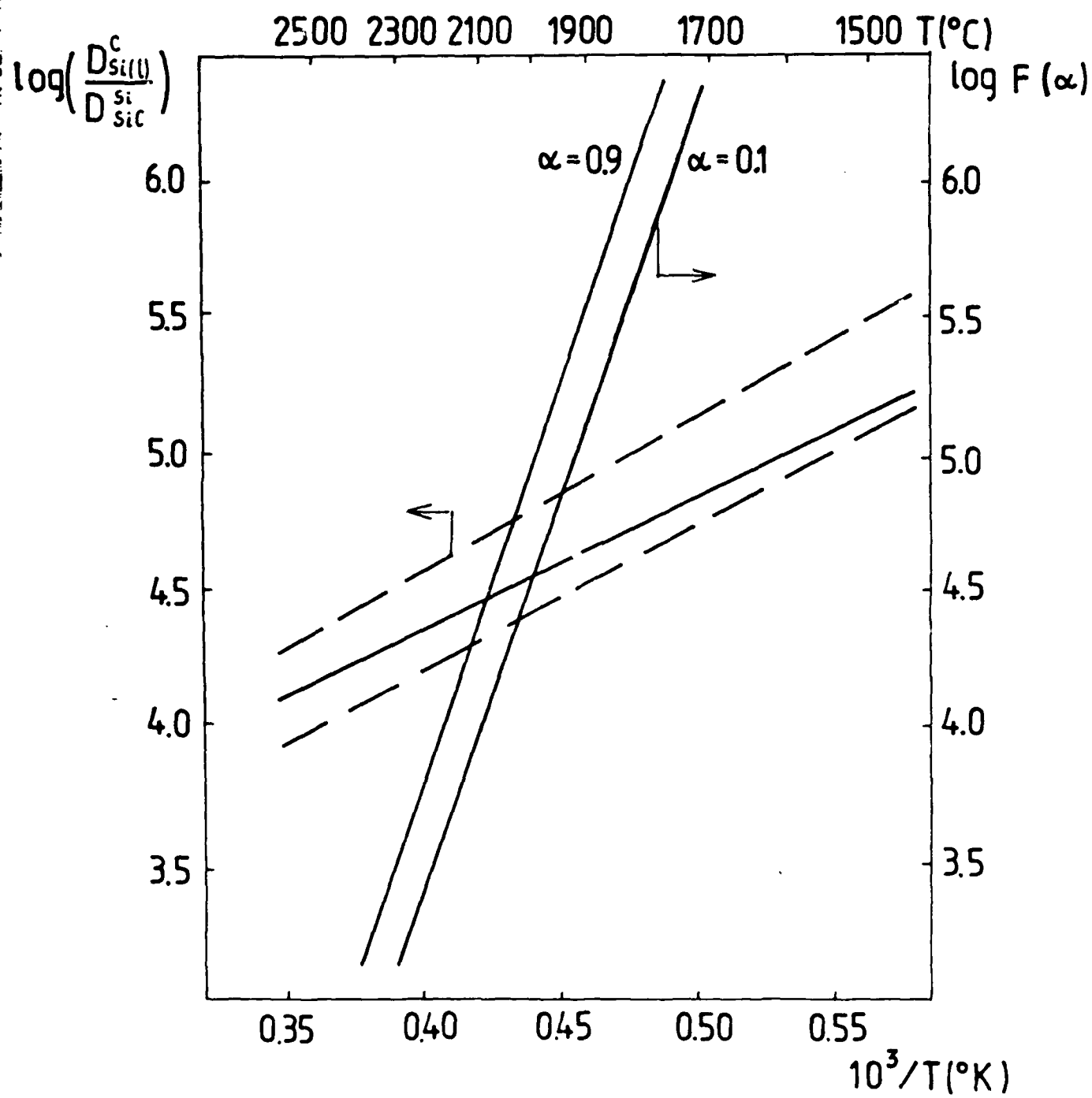
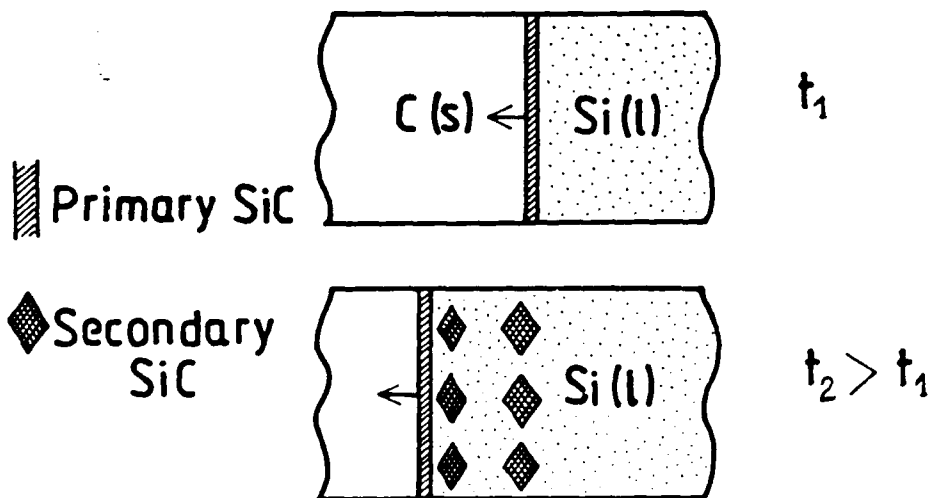


Figure 6



MS# 22

EXPERIMENTAL MODELING OF PARTICLE-PARTICLE INTERACTIONS DURING SHS OF
TiB₂/Al₂O₃.

K. V. Logan,* J. T. Sparrow, W. J. S. McLemore
Georgia Tech Research Institute, Atlanta, Georgia.

ABSTRACT

Simplistic, experimental models of the Al + B₂O₃ and Al + TiO₂ reactions are being developed. The interaction between aluminum and boron oxide in the two-component system began with the melting of B₂O₃. The reaction between aluminum and titanium dioxide occurred at a higher temperature than the Al/B₂O₃ reaction in their respective two-component reactions. The aluminum metal oxidized and reacted with titanium oxide forming titanium, titanium-aluminum alloys and Al₂O₃ through a series of intermediate steps depending on the relative amounts of aluminum and oxygen present.

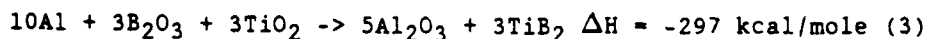
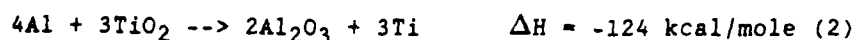
11 p

371

EXPERIMENTAL MODELING OF PARTICLE-PARTICLE INTERACTIONS DURING SHS OF TIB₂/AL₂O₃
K. V. Logan,* J. T. Sparrow, W. J. S. McLemore
Georgia Tech Research Institute, Atlanta, Georgia.

I. INTRODUCTION

Self-propagating high temperature synthesis (SHS) reactions have been successfully used to synthesize pure and composite materials. The reaction behavior and resultant product configuration, determined mainly by operator experience, can sometimes be uncontrollable and unpredictable. Prior research has shown the effects of various process parameters on the behavior and products of the reactions given by equations (1), (2) and (3).¹



An experimental, mechanistic model of the reaction depicted in equation (3) was begun using differential thermal analysis (DTA) as a means of identifying critical point temperatures and phase changes.² Next, interactions between aluminum and boron oxide were studied.^{3,4} This paper will discuss the continued development of the model.

II. EXPERIMENTAL APPROACH

The three-component reaction depicted in equation (3) is complex; therefore, individual components and possible intermediate reactions were studied separately. Enthalpy calculations indicated exothermic reactions could theoretically occur between $\text{Al}+\text{B}_2\text{O}_3$, $\text{Al}+\text{TiO}_2$ and $\text{Al}+\text{B}_2\text{O}_3+\text{TiO}_2$. The stoichiometric reactions are depicted in equations (1), (2) and (3). There are numerous intermediate reactions which could also occur; however, the present

modeling effort will consider only reactions following equations (1), (2) and (3). The raw material reactants consisted of ≤ 40 micron atomized aluminum metal, ≤ 40 micron boron oxide and ≤ 1 micron pigment grade titanium dioxide powders. Table I lists relevant melting points and crystal structures of possible reaction components and species.

Table I. Relevant Component/Product Properties

<u>Component</u>	<u>Melting Pt.</u> (°C)	<u>Vapor Pt.</u> (°C)	<u>Crystal Structure</u>
B ₂ O ₃	450	1860	Rhombohedral
Al	660	2618	FCC
AlB ₂	850	----	Hexagonal
Al ₂ O ₃ /B ₂ O ₃	1035-1950	----	----
Ti ₃ Al	1472	----	----
Ti	1660	3287	Hex. to 840, then BCC
TiO ₂	1830	2500-3000	Tetragonal
Al ₂ O ₃ /TiO ₂	1860	----	----
B	2027	2550	Rhombohedral
Al ₂ O ₃	2080	2980	Hexagonal
TiB ₂	3000	----	Hexagonal

Bulk powder reactions and individual particle-particle interactions were observed and documented using the following techniques:

1. Differential thermal analysis (DTA) was performed on aluminum powders and mixtures of Al/B₂O₃, Al/TiO₂ and Al/B₂O₃/TiO₂ powders. The samples were heated in static air and flowing argon atmospheres at 25 to 50°C/min. in a DTA using the differential scanning calorimetry (DSC) mode.

2. A resistance strip heating technique was used on small amounts of powders and mixtures of powders in tantalum boats clamped between electrical contacts. Sample heating was conducted under vacuum until a reaction occurred.

3. Room temperature/auto-ignitions were made on bulk quantities of two and three-component combinations of reactants. The room temperature ignitions were

initiated using a hot wire technique, and the auto-ignitions were made in a controlled environment furnace.

4. An optical hot stage microscope with an alumina stage was used to observe individual and multiple particle behavior when heated up to 1000°C.

5. A high temperature stage was used in a transmission electron microscope (TEM) in order to observe the Al/B₂O₃ interaction from room temperature to the melting points of boron oxide or aluminum. Thin section samples were prepared from aluminum particles, coated with B₂O₃ by thermal evaporation, then heated until a reaction occurred. Micrographs and selected area diffraction were used to document chemical/crystalline changes.

III. RESULTS

This section discusses the experimental results obtained from studying bulk powder reactions and individual particle-particle interactions.

Water: Reactions with water were possible with all three main components. At room temperature, aluminum adsorbed a small amount of water on the particle surfaces, and TiO₂ adsorbed a much larger amount because of the higher surface area. Boron oxide was extremely hygroscopic. Water was difficult to remove and keep removed once incorporated into the B₂O₃ structure. Extremely violent reactions occurred when the raw materials were allowed to acquire water; therefore, care was taken to use dry powders.

Aluminum/Aluminum Oxide: Resistance heating of single aluminum particles allowed documentation of the passivating aluminum oxide film morphology and behavior. Aluminum particles, as received, were coated by a relatively thin oxide film about 50 angstroms thick. As the particles were heated to the melting point of aluminum, the oxide film separated, exposing aluminum metal which continued to oxidize as the reaction progressed. Particles of aluminum

were pre-oxidized to document the characteristic behavior of thicker oxide films. Figure 1 shows the oxide formation on the surface of an aluminum particle exposed to oxygen eight hours. As the particle was heated, the oxide film parted and the oxide growth continued in a dendritic manner. Figure 2 shows a thicker oxidized coating which formed on an aluminum particle exposed to oxygen 24 hours. When the pre-oxidized aluminum particle was heated, the thick oxide coating cracked. The aluminum then expanded and pushed out of the alumina shell to be exposed to further oxidation. The thick oxide coatings remained as hollow spheres of Al_2O_3 after the reaction was completed.

Aluminum/Boron Oxide: Figure 3 shows the results of heating a bulk mixture of aluminum and boron oxide powders to a temperature just above the melting point of aluminum. Spherical, hollow shells covered with needle-like crystals remained after aluminum reacted with boron oxide. XRD analysis of the bulk material showed alpha-alumina and $9\text{Al}_2\text{O}_3 \cdot 2\text{B}_2\text{O}_3$.

A composite thin section of aluminum coated with boron oxide was heated in the TEM. Small needle-like crystals formed on the surface of the thin section similar to those formed in the bulk mixtures. Electron diffraction analysis indicated that the crystals were $9\text{Al}_2\text{O}_3 \cdot 2\text{B}_2\text{O}_3$.

Alumina/Boron Oxide: Acicular type crystals, similar to those shown in Figure 3, also formed when a mixture of alumina and boron oxide was heated. Figure 4 shows acicular crystals embedded in boron oxide. X-ray diffraction analysis confirmed the presence of $9\text{Al}_2\text{O}_3 \cdot 2\text{B}_2\text{O}_3$.

Aluminum/Titanium Dioxide: Figure 5 shows the results of heating a bulk mixture of aluminum and titanium dioxide powders to a temperature above the melting point of aluminum and to a point where a reaction with titanium dioxide occurred. SEM/EDXRA showed a melted mass in the central region composed of

titanium and some aluminum. It is not possible to determine whether the compound is an oxide or metal with the EDXRA system used for the analysis. However, based on prior determinations, the small, white spheres at the boundary of the mass are aluminum oxide shells. XRD of the product indicated titanium, a titanium-aluminum alloy and alpha-alumina. The interface between the spheres and melted mass was high in aluminum content, indicating absorption of aluminum oxide into the melted mass.

Alumina/Titanium Dioxide: Figure 6 shows the interaction between titanium dioxide and alumina. EDXRA indicated a melted area consisting only of a compound containing titanium. Apparent aluminum oxide crystals remained as discrete crystallites, indicating the probable temperature attained to be between the melting point of TiO_2 (1830°C) and Al_2O_3 (2080°C).

Aluminum/Boron Oxide/Titanium Dioxide: Interaction between the three main reactants can be seen in Figures 7 and 8. Figure 7 is a secondary image SEM showing a fibrous growth (white image) on the surface which is not visible in a back-scattered image SEM (Figure 8). The fibrous growth is probably a boron oxide compound since the fibers are not visible in the back-scattered image. Neither boron nor oxygen could be detected by the EDXRA system used for the observation. The small, whitish particles on the surface of the gray area were identified as a titanium compound, and the gray area as an aluminum compound.

Reaction Analysis

The as-received aluminum powder and mixtures of $\text{Al}+\text{B}_2\text{O}_3$, $\text{Al}+\text{TiO}_2$ and $\text{Al}+\text{B}_2\text{O}_3+\text{TiO}_2$ were analyzed by DTA in argon and air. Table II is a tabulation of the results. Temperatures correspond to peak onset and maximum, respectively.

Table II. Tabulation of Thermal Analysis Results

	Al		Al/B ₂ O ₃		Al/TiO ₂	
	Endo (Onset/Max)	Exo (Onset/Max)	Endo (Max)	Exo (Onset/Max)	Endo (Max)	Exo (Onset/Max)
Air (°C)	656/669	885/1074	660	998/1040	660	945/1010
cal/gm				86		330
Argon (°C)	650/667	None	660	1000/1030	660	1060/1110
cal/gm				77		90

Analysis of the aluminum metal in air and argon showed an endotherm which corresponded to the melting point temperature of aluminum. An endotherm occurred around 660°C in all of the mixtures at the melting point of aluminum. The exotherm in air was due to the oxidation of aluminum.

The exotherm which occurred during the analysis of Al/B₂O₃ in argon was the beginning of the oxidation of aluminum and reduction of the B₂O₃. The peaks and the onsets both in air and argon which occurred during the analysis of Al/B₂O₃ in air were generally the same. The cal/gm generated in air was only slightly larger, indicating that the oxidation exotherm was not strongly influenced by the oxygen or nitrogen present in air. Apparently the B₂O₃ melted and encapsulated the aluminum during the reactions, preventing the aluminum particles from reacting with the oxygen or nitrogen present in air.

The onset of the oxidation exotherm in air which occurred during the analysis of Al/TiO₂ began at a lower temperature and generated a significantly larger cal/gm than the oxidation reaction in argon, indicating a strong influence on the reaction from the oxygen or nitrogen present in air. Also, the onset of the reaction of Al/B₂O₃ in argon began at a lower temperature than the onset of the reaction of Al/TiO₂ in argon, indicating that the aluminum reduction of B₂O₃ occurred before the aluminum reduction of TiO₂.

XRD analysis for stoichiometric mixes of Al/B₂O₃ samples heated in air

indicated the presence of $\alpha\text{-Al}_2\text{O}_3$ and the aluminoborate, $9\text{Al}_2\text{O}_3 \cdot 2\text{B}_2\text{O}_3$. Apparently some of the aluminum was oxidized by the oxygen available in the air, allowing excess, unreacted B_2O_3 to react with the newly formed Al_2O_3 . XRD analysis for samples heated in argon showed peaks corresponding to $\alpha\text{-Al}_2\text{O}_3$, $9\text{Al}_2\text{O}_3 \cdot 2\text{B}_2\text{O}_3$ and elemental aluminum. The presence of aluminum can be explained by an incomplete reaction. Boron was not confirmed by XRD. It is possible that amorphous boron formed; or, any boron that formed during the reaction re-oxidized when the sample was ground for XRD analysis.

XRD analysis for stoichiometric mixes of Al/TiO_2 samples heated in air indicated the presence of $\alpha\text{-Al}_2\text{O}_3$ and titanium nitride. XRD analysis for samples heated in argon showed peaks corresponding to $\alpha\text{-Al}_2\text{O}_3$, elemental titanium and/or titanium-aluminum alloys, and titanium dioxide. The presence of titanium was confirmed by using SEM/EDXRA. XRD analysis of the three-component system showed the products to be titanium diboride and alpha-alumina.

IV. SUMMARY

The three-component experimental model is being developed as information is obtained from the observed and experimental analyses. Simplistic, experimental models of $\text{Al+B}_2\text{O}_3$ and Al+TiO_2 reactions are being developed first. The interaction between aluminum and boron oxide began with the melting of B_2O_3 . The presence of water lowered the melting point of boron oxide and added to the violence and unpredictability of the reaction. The aluminum metal began to expand, disrupting the continuity of the Al_2O_3 film covering the particles. The aluminum then reduced the boron oxide, forming boron, Al_2O_3 and $9\text{Al}_2\text{O}_3 \cdot 2\text{B}_2\text{O}_3$, depending on the relative amounts of oxygen and B_2O_3 present.

The reaction between aluminum and titanium dioxide in argon occurred at a higher temperature than the $\text{Al/B}_2\text{O}_3$ reaction. The aluminum metal oxidized and

reacted with titanium oxide forming titanium, titanium-aluminum alloys and Al_2O_3 through a series of intermediate steps depending on the relative amounts of aluminum and oxygen present.

In the $\text{Al}+\text{B}_2\text{O}_3+\text{TiO}_2$ reaction, boron and titanium became available through a series of intermediate steps. The free titanium then reacted with boron to form titanium diboride concurrently with aluminum oxide. Variations in the stoichiometry of the reactants and the presence of water, oxygen or nitrogen can determine or control the amounts and types of compounds produced by the reaction.

REFERENCES

1. K. V. Logan and J. D. Walton, "TiB₂ Formation Using Thermite Ignition," Ceramic Eng. and Science Proceedings, 5, No. 7-8, pp. 712-738, July-August 1984.
2. K. V. Logan, E. W. Price, W. J. S. McLemore, "Differential Thermal Analysis of the $\text{TiO}_2 + \text{B}_2\text{O}_3 + \text{Al}$ Thermite System/Development of an Experimental Model For Self-Propagating High Temperature Oxidation-Reduction Reactions," Materials Processing By Self-Propagating High Temperature Synthesis (SHS), Symposium Proceedings, DARPA/ARMY SHS Symposium, pp. 167-175, 1985.
3. K. V. Logan, W. J. S. McLemore, J. T. Sparrow, "Particle-Particle Interactions in the Aluminum Reduction of Boron Oxide," Proceedings AICHE Heat Transfer Symposium, pp. 59-68, 1988.
4. K. V. Logan, "The Use of Oxidation-Reduction (Thermite) Reactions to Produce Titanium Diboride," High Temperature Materials Chemistry-IV, Proceedings, Volume 88-5, pp. 584-589, The Electrochemical Society, 1988.

Acknowledgements

Dr. Andrew Crowson, Technical Monitor, U. S. Army Research Office, Contract No. DAAG29-85-K-0125; Mr. John L. Brown, hot stage transmission electron microscopy.

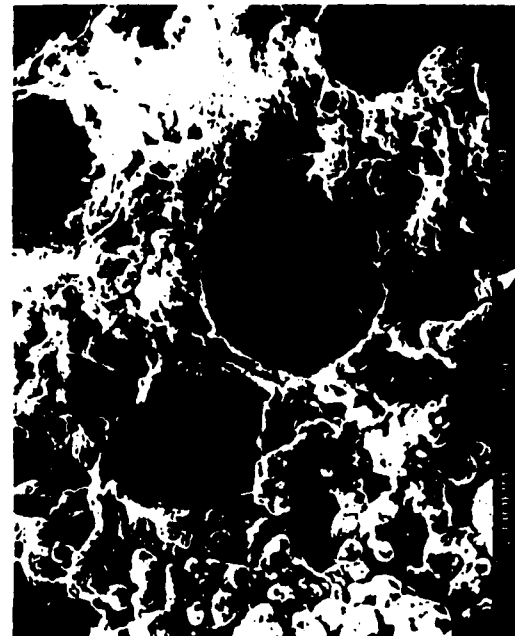


Figure 3. Aluminum Oxide Shells After Reaction of Aluminum with Boron Oxide.



Figure 4. Acicular Crystals Formed During Interaction Between Aluminum Oxide and Boron Oxide.



Figure 1. Aluminum Oxide Film Formed After an Eight-Hour Exposure to Oxygen.

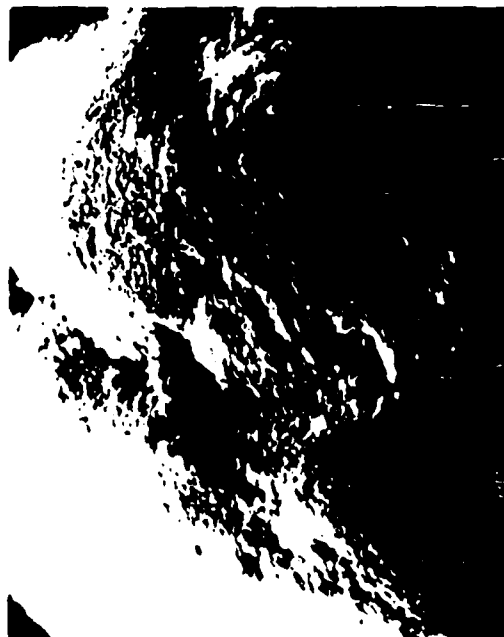


Figure 2. Thick Al_2O_3 Film Formed After a 24-Hour Exposure to Oxygen.



Figure 5. Alumina Being Absorbed Into the Titanium Compound.



Figure 7. Secondary Image SEM Showing Interaction Between the Three Main Reactants.



Figure 6. Interaction Between Alumina and Titanium Oxide.



Figure 8. Back-Scattered SEM Showing Interaction Between the Three Main Reactants.

Combustion Synthesis in the Ti-C-Ni-Al System

by

S.D. Dunmead and Z.A. Munir

Division of Materials Science and Engineering

University of California, Davis

Davis, California 95616, U.S.A.

J.B. Holt and D.D. Kingman

Department of Chemistry and Materials Science

Lawrence Livermore National Laboratory

Livermore, California 94550, U.S.A.

Abstract

The process of combustion synthesis was used to produce ceramic-metal composite materials consisting of titanium carbide (TiC) and an intermetallic alloy of the nickel-aluminum (Ni-Al) system. The samples were produced by rapidly heating a mixture of elemental titanium (Ti), carbon (C), Ni, and Al powders in a graphite die up to the ignition temperature. By applying mechanical pressure during or immediately following the combustion reaction, products of greater than 99% of theoretical density were obtained. By varying the combustion synthesis parameters, the properties of the product can be tailored to meet specific application needs. Apparent applications of such composites include cutting tools, wear parts, structural components, armor, etc...

1. Introduction

One of the major drawbacks in the combustion synthesis of refractory materials is the highly porous nature of the products. This porosity is caused by three basic factors: 1) the molar volume change inherent in the reaction, 2) the porosity present in the unreacted sample, and 3) adsorbed gases which are present on the reactant powders. In the reaction between Ti and C to form TiC, for example, the product is approximately 23% more dense than the reactants. Furthermore, the unreacted powders are generally cold pressed to the 50-70% density range. Thus, without densification occurring one could not expect to obtain a product of greater density than approximately 50%. Maksimov et al. [1] and Holt and Munir [2] have also found that adsorbed gases greatly contribute to the porosity of the final product. This is due to the massive expansion which takes place as these gases are rapidly heated from ambient temperature up to the combustion temperature. Because of the porosity of these products the majority of the materials produced are used in powder form. If dense materials are desired the powders then generally must undergo some type of densification process such as sintering or hot pressing. The ideal production process would combine the synthesis and densification steps into a one step process.

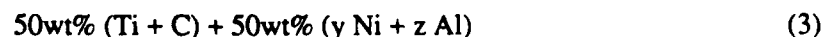
In this paper the use of a low-pressure hot pressing technique to produce dense

ceramic-metal composites will be demonstrated by results from work on the Ti-C-Ni-Al system. This system was selected because strongly exothermic reactions occur in both the Ti-C and Ni-Al systems and because of interest in composite materials consisting of TiC and an intermetallic alloy of the Ni-Al system for various structural, cutting tool, and armor applications.

2. Experimental Procedures

Small particle sizes of titanium, nickel, aluminum, and carbon were used in all of the combustion experiments. The titanium, obtained from Alfa Products, had an average particle size of $11\text{ }\mu\text{m}$ and a measured surface area of $0.5\text{ m}^2\text{g}^{-1}$. A spectrochemical analysis showed the principle impurities to be: Zr, 5000 ppm; Al, 2000 ppm; Ca, 1000 ppm; Si, 100 ppm; Mn, 100 ppm; and Mg, 100 ppm. The nickel powder, obtained from EM Scientific, had an average particle size of $83\text{ }\mu\text{m}$ and a measured surface area of $0.1\text{ m}^2\text{g}^{-1}$. The major impurities were found to be: Co, 100 ppm; Cu, 2 ppm; and Al, 1 ppm. The aluminum powder, obtained from ALCOA, had an average particle size of $9.9\text{ }\mu\text{m}$ and a measure surface area of $1.1\text{ m}^2\text{g}^{-1}$. The major impurities were found to be: Fe, 100 ppm; Si, 30 ppm; Ga, 10 ppm; Cu, 10 ppm; and Mn, 10 ppm. Amorphous furnace black was selected for use because this form of carbon is much more reactive than graphite. Monarch 905 furnace black was used, which is a very fine ($0.01\text{ }\mu\text{m}$) powder obtained from Cabot Corporation with a surface area of $230\text{ m}^2\text{g}^{-1}$.

Reagent powder mixtures were prepared for the following three basic reactions:



where x ranged from 12.5 to 75 wt% while y and z were such that the proper stoichiometry existed in the mixture to form each of the Ni-Al compounds known to exist. It should be noted that the Ni-Al part of both the reagents and products will be referred to as the 'binder'. The reagent powders were weighed out in the proper stoichiometric proportions keeping a constant equimolar ratio of titanium to carbon but varying both the amounts of Ni and Al and the ratio of Ni to Al in the binder. The powder batches were mixed in a glass

jar for 30 minutes on a mechanical shaker and were inspected periodically to insure that even mixing was occurring.

The powder mixture was then poured into a cylindrical graphite die that had been fitted with a 254 μm (10 mil) graphoil liner. This liner served both to protect the die and to promote the escape of gases during combustion. The graphite die was equipped with double acting graphite rams which were machined so that there was a clearance of 127 μm (5 mil) after insertion of the graphoil liner. The powder mixture was cold pressed at a pressure of 20.7 MPa (3000 psi) where it achieved a density of approximately 50 % of theoretical. The die assembly was then inserted into the hot pressing apparatus and resistively heated at approximately 1500 K/minute. A thermocouple was inserted into a hole in the side of the die so that the approximate die temperature at ignition could be monitored. When ignition occurred the hydraulic rams were compressed to the desired pressure. This pressure was held for approximately 1 to 2 minutes (until the die was not red hot).

3. Results and Discussion

3.1 Temperature Profile

Figure 1 shows a temperature profile measured during the combustion of the mixture shown in equation 1 where x has a value of 50wt%. It should be noted that this particular sample was free standing, that is it was not combusted in the hot pressing apparatus. In this experiment an 80 μm (3 mil) tungsten-rhenium thermocouple was placed into a small hole in the bottom of the sample opposite the end where ignition occurred. The output voltage of the thermocouple was monitored using a Hewlett Packard multiprogrammer system developed by Dunmead and Holt [3]. Here, it can be seen that this reaction between solids is typified by a relatively sharp rise from ambient temperature up to a peak combustion temperature of approximately 2473 K (2200°C) followed by cooling to a plateau at approximately 2073 K (1800°C), a slight increase in temperature and then further cooling back to ambient temperature. It is interesting to note that this secondary increase in temperature was not found by Dunmead et al. [4] in a similar reaction in which the Al was omitted. The heating rate realized in the zone of sharpest temperature increase

was calculated to be on the order of $5 \times 10^4 \text{ Ks}^{-1}$.

The temperature profile in Figure 1 indicates that the compact remains at an elevated temperature well after the combustion front has passed. The phase in the Ni-Al system with the highest melting point is the 1:1 compound, NiAl, which has a melting point of 1911 K (1638°C). The compact remains above this temperature for approximately 23 seconds, and thus a liquid phase must exist for at least this amount of time. As a result of the existence of this liquid phase the application of pressure during this time should result in the densification of the product.

3.2 X-ray Diffraction

Table I shows the results of x-ray diffraction work which was done on the products of combustion of the mixtures shown in Equation 3. It should be pointed out that all of these reactions were carried out in the hot pressing apparatus under a mechanical pressure of 20.7 MPa (3000 psi). In this series of experiments the Ni to Al ratio in the binder was varied so that the stoichiometric relationships of all 7 compounds of the Ni-Al system (Ni, Ni₃Al, Ni₅Al₃, NiAl, Ni₂Al₃, NiAl₃, and Al) were represented. As can be seen in Table I, when the binder composition was Ni, 3Ni+Al, Ni+Al, and 2Ni+3Al the product contained only TiC and the Ni-Al phase with the same stoichiometry as was in the reactants. When however, the binder composition was 5Ni+3Al, the product consisted of TiC, NiAl, and Ni₃Al. This can be explained by noting that Ni₅Al₃ decomposes on heating at approximately 973 K (700°C) into NiAl and Ni₃Al. As the compact cools the kinetics of the peritectoid reaction between solids NiAl and Ni₃Al to form Ni₅Al₃ are slow enough that the phases present in the higher temperature two phase field are quenched in. It is also apparent from Table I that the compositions with high Al content (Ni+3Al and Al) result in complex phase relationships including the formation of TiAl₃.

3.3 Binder Content

3.3.1 Residual Porosity

The effect of the amount of binder in the compact on the residual porosity of the final product was studied for two sets of samples in which the product was either a TiC-NiAl or

TiC-Ni₃Al composite. Figure 2 shows the results of this work for a set of experiments where a mechanical pressure of 20.7 MPa (3000 psi) was applied. Here, it can be seen that in general there is a slight decrease in the level of porosity as the amount of binder in the compact increases. This is likely a result of an increase in the quantity of liquid phase present during the reaction. From Figure 2 it is also evident that at low binder contents the identity of the binder has little effect on the residual porosity in the product. At higher binder contents however, the compacts which contain NiAl as the binder have consistently lower levels of porosity than those which contain Ni₃Al. This is likely due to differences in the heat of formation of NiAl (-71650 J mol⁻¹) and Ni₃Al (-37550 J mol⁻¹). The compacts which contain NiAl will have higher combustion temperatures which promotes the formation of liquid and thus, favors densification.

3.3.2 Microstructure

Figure 3 contains an optical photomicrograph of the product of combustion of 50wt%(Ti+C) and 50wt%(Ni+Al). This sample had a mechanical pressure of 20.7 MPa (3000 psi) applied immediately following combustion resulting in a residual porosity of 0.3%. The spherical TiC grains (55 vol%) in this sample were found to average 1.2µm and the microhardness was measured to be 930 kg/mm². It is interesting to note that the TiC grains in this sample appear as if they were precipitated from a melt. Figure 4 contains an optical photomicrograph of the product of combustion of 50wt%(Ti+C) and 50wt%(3Ni+Al). This sample was combusted under the same conditions as the one shown in Figure 3. Here, the product was found to have a residual porosity of 3.0%, an average grain size of 1.1µm, and microhardness of 1111 kg/mm². Figure 5 contains an optical photomicrograph of the product of combustion of 75wt%(Ti+C) and 25wt%(Ni+Al). Again the combustion was under the same conditions as the previous two samples resulting in a residual porosity of 5.7%. The average grain size of the TiC was found to be 5.9µm and the microhardness was measured to be 1916 kg/mm². It is interesting to note that the TiC grains in Figure 5 are much larger than those seen in Figure 3. This is due to the fact that as the TiC content is increased the combustion temperature increases and thus, grain growth is enhanced.

In order to gain some insight into the mechanism of formation of these composites a sample identical to that shown in Figure 5 was combusted in which graphite fibers were substituted for the carbon black. The reagent mixture was difficult to mix and the sample was harder to ignite than with the carbon black. When examining the microstructure, however, no evidence was found that the fibers had ever existed. The grain size, porosity, and microhardness were virtually identical in the two samples. These results indicate that during the reaction the carbon is dissolved into a melt and then the TiC precipitates out, but further research is needed in this area.

3.4 Applied Pressure

Figure 6 shows the effect of the amount of applied pressure on the level of porosity in the product for samples which contain 50wt% of either NiAl or Ni₃Al as the binder. Here, it can be seen that the application of pressures as low as 6.9 MPa (1000 psi) has dramatic effects on the level of porosity. This graph also shows that as expected an increase in the amount of applied pressure results in a decrease in the residual porosity for both binders.

4. Summary

By using a simple hot pressing apparatus certain refractory materials may be synthesized and densified in a one step combustion process. Specifically composite materials consisting of TiC-Ni, TiC-NiAl, and TiC-Ni₃Al can be produced at near theoretical density using a combustion synthesis process under relatively low mechanical pressures. It was also shown that very fine grained materials can be produced in this way and that the grain size can be controlled by changes in the amount of the binder. By adjusting the synthesis conditions it is possible to tailor the properties of the product and further to develop a viable materials production process.

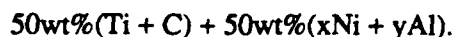
Acknowledgement

S.D. Dunmead and Z.A. Munir's work was supported by a grant for the Office of Basic Energy Sciences of the U.S. Department of Energy and is gratefully acknowledged. J.B. Holt and D.D. Kingman's work was performed under the auspices of the U.S. Department of Energy by the Lawrence Livermore National Laboratory under contract number W-7405-ENG-48.

References:

1. Y.M. Maksimov, A.G. Merzhanov, A.T. Pak, A.G. Raskolenko, and B.S. Braverman, "High-Temperature Synthesis in the System Ti-B-Fe," *Metally*, 2, 219-223 (1985).
2. J.B. Holt and Z.A. Munir, "Combustion Synthesis of Titanium Carbide: Theory and Experiment," *J. Mater. Sci.*, 21 251-259 (1986).
3. S.D. Dunmead and J.B. Holt, "Temperature Profile Analysis of Combustion Reactions," *Proc. of the DARPA/Army Symposium on SHS, Daytona Beach, FL, October 1985*, edited by K.A. Gabriel, S.G. Wax, and J.W. McCauley, pp. 113-121 (1985).
4. S.D. Dunmead, Z.A. Munir, and J.B. Holt, "Gas-Solid Reactions Under a Self-Propagating Combustion Mode," *Solid State Ionics*, 32/33 474 (1989).

Table I. X-ray Diffraction Results for Reactions of the form



Binder	TiC	Ni	Ni ₃ Al	Ni ₅ Al ₃	NiAl	Ni ₂ Al ₃	NiAl ₃	Al	TiAl ₃
Ni	M	M	-	-	-	-	-	-	-
3Ni+Al	M	-	S	-	-	-	-	-	-
5Ni+3Al	M	-	S	-	S	-	-	-	-
Ni+Al	M	-	-	-	S	-	-	-	-
2Ni+3Al	S	-	-	-	-	M	-	-	-
Ni+3Al	S	-	-	-	-	M	m	-	m
Al	m	-	-	-	-	-	-	m	M

M - Major Phase

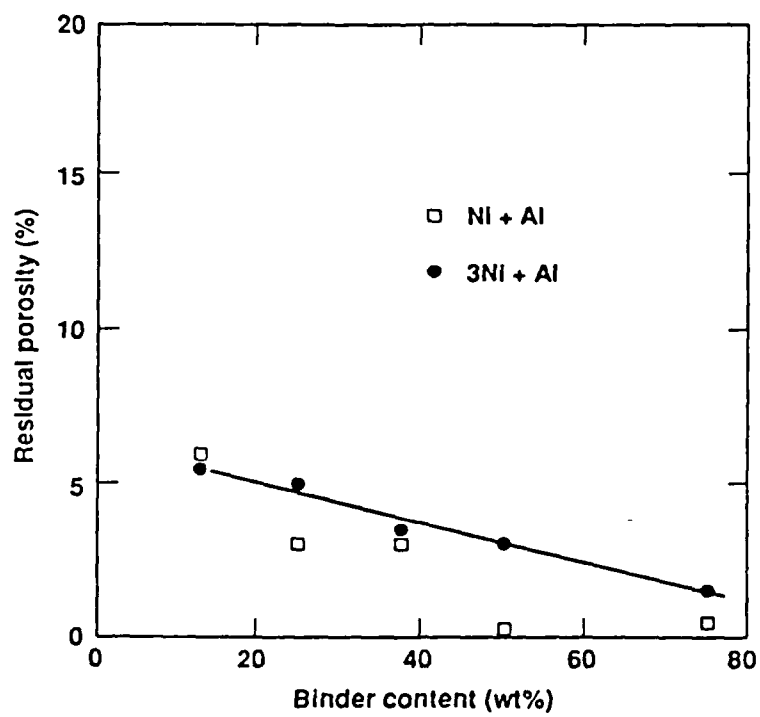
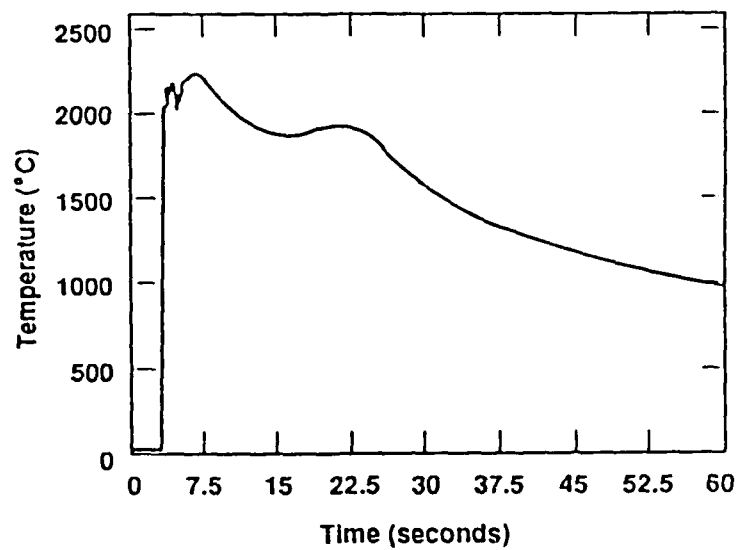
S - Secondary Phase

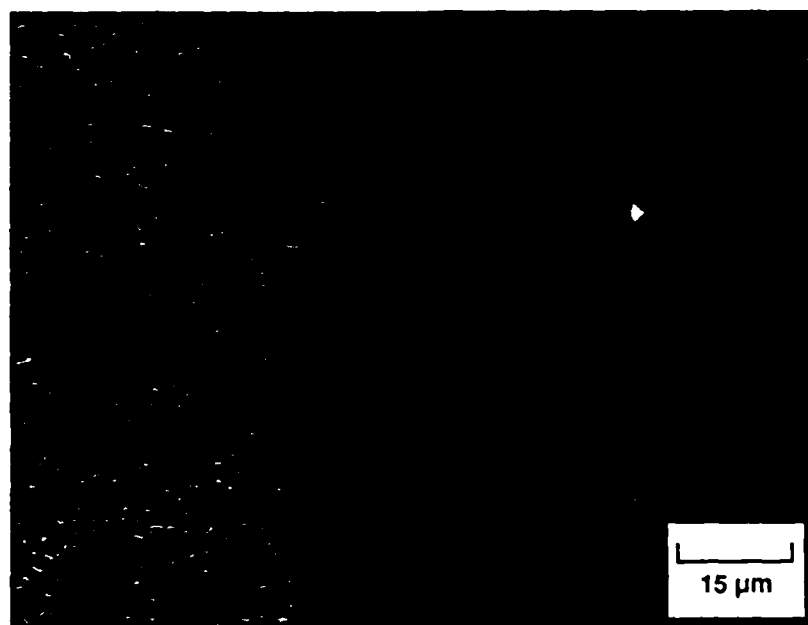
m - Minor Phase

t - Trace Phase

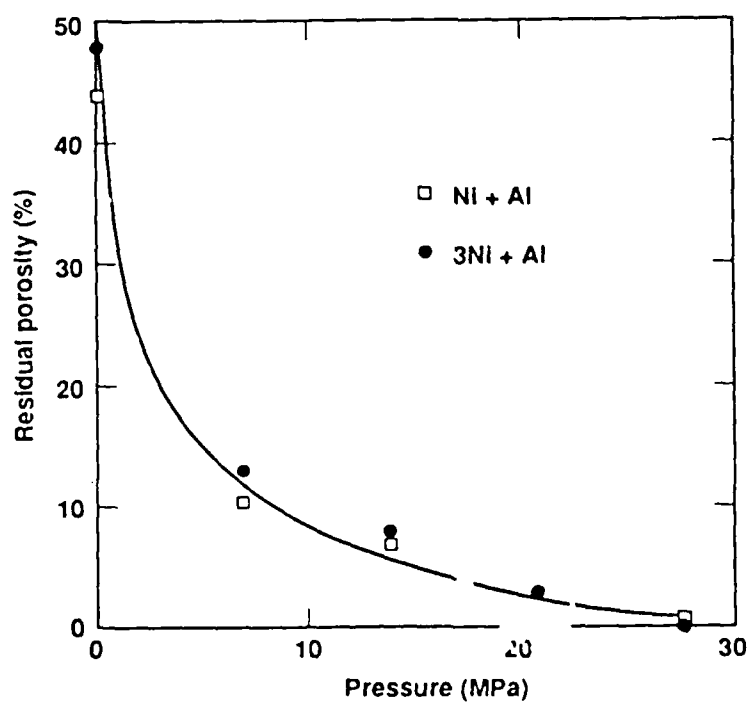
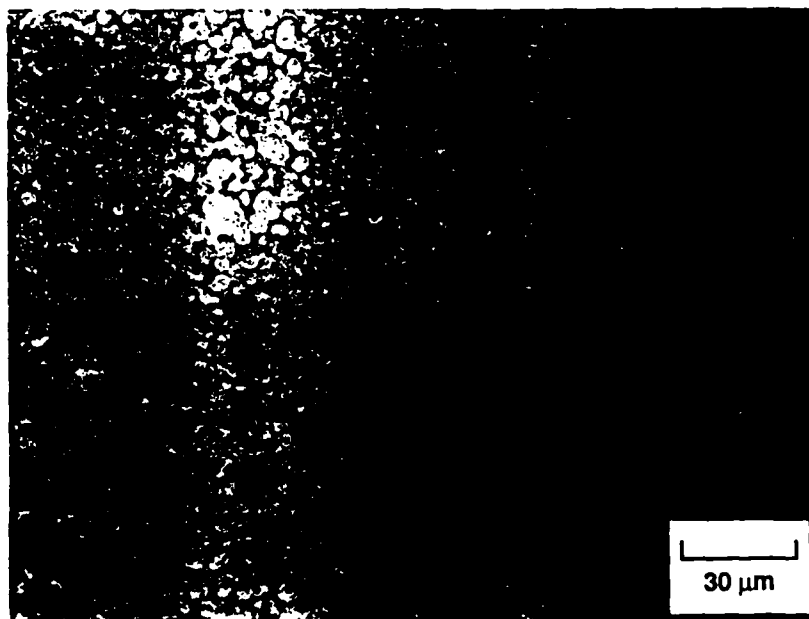
Figure Captions:

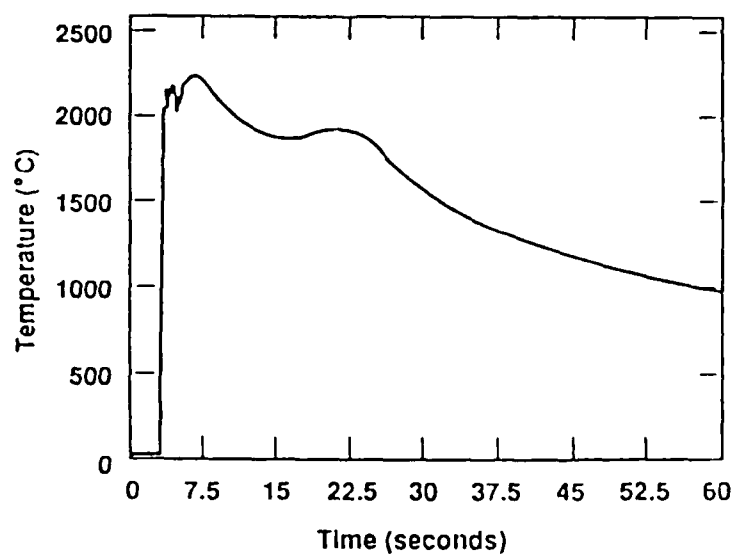
- Figure 1.** Temperature Profile Measured for the Combustion of 50 wt%(Ti+C) + 50wt%(Ni+Al).
- Figure 2.** Residual Porosity of Samples Containing Varying Amounts of (Ni+Al) or (3Ni+Al) as the Binder Combusted Under 20.7 MPa (3000 psi).
- Figure 3.** Optical Photomicrographs of the Product of Combustion of 50wt%(Ti+C) + 50wt%(Ni+Al) Under 20.7 MPa (3000 psi).
- Figure 4.** Optical Photomicrographs of the Product of Combustion of 50wt%(Ti+C) + 50wt%(3Ni+Al) Under 20.7 MPa (3000 psi).
- Figure 5.** Optical Photomicrograph of the Product of Combustion of 75wt%(Ti+C) + 25wt%(Ni+Al) Under 20.7 MPa (3000 psi).
- Figure 6.** Residual Porosity for Samples Containing Both (Ni+Al) and (3Ni+Al) as the Binder Combusted Under Various Pressures.

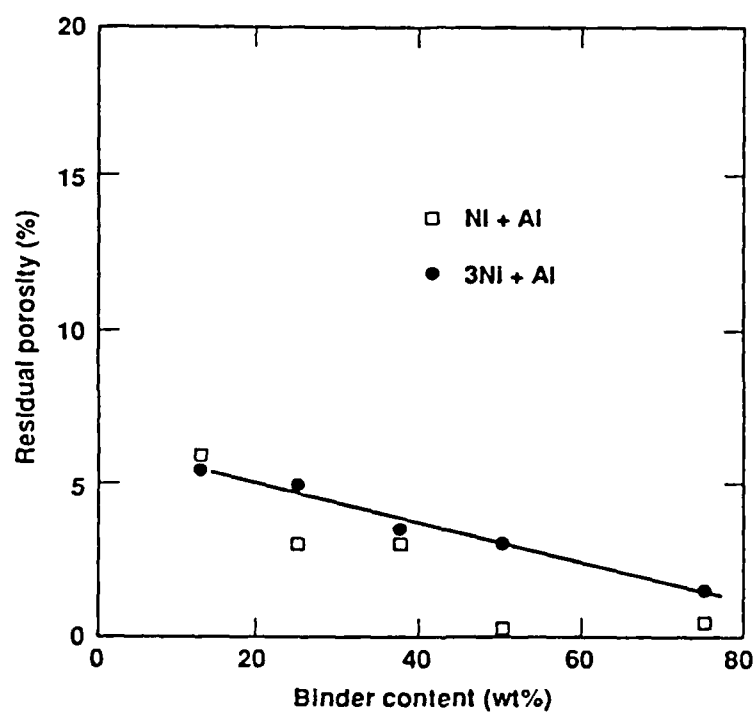




392







Combustion Synthesis Dynamics Modeling

T. KOTTKE, L. J. KECSKES and A. NIILER

Ballistic Research Laboratory, Aberdeen Proving Ground, MD 21005

Abstract - The limitations imposed on combustion synthesis dynamics by green compact thermal conductivity have been modeled for the Titanium-Graphite system. Powder compact thermal conductivities, required for dynamics modeling, were measured as functions of density and temperature. Combustion synthesis reaction initiation and propagation are both predicted to be dependent on the green compact thermal conductivity. Additional effects of sample containment vessels on post reaction sample temperatures are also investigated.

I. Introduction

During the past several decades, self-propagating high-temperature synthesis (SHS) has evolved from a basic research curiosity to a technique being applied to the production of a wide variety of ceramic, metallic and composite materials.¹ Recent research has been directed toward producing low porosity monolithic products in addition to powdered materials. Fabrication of low porosity SHS products often involves the application of external pressure to freshly synthesized material which is still above the ductile-brittle transition temperature. For this technique to work in a batch production scheme,^{2,3} the entire synthesized sample must be plastic at the time of the compaction event. This condition is obtained through rapid propagation velocities and highly exothermic reactions which result in high post reaction temperatures throughout the sample. For a continuous process scheme,⁴ where feedback and control must be established between the reacting sample and the compacting apparatus, reduced velocities may be more desirable but high temperatures are still necessary.

SHS propagation velocities can be controlled by a number of methods. The addition of a diluent, usually in the form of the powdered product, has been used to decrease propagation velocities through a reduction in the heat energy liberated per unit mass of precursor powder. This technique leads to reduced post synthesis sample temperatures which can make the compaction more difficult. Propagation velocities have also been varied through control of the size of the precursor powder particles with the larger particle sizes yielding lower velocities. In some systems, particle size variations have been shown to lead to potentially undesirable

variations in the combustion mode, final product stoichiometry and grain size as well as incomplete synthesis.⁵ The aim of this study was to investigate the limitations on SHS reaction initiation and propagation due to green compact thermal conductivity (TC) and the extent to which these limitations can be regulated by variations in green compact density. This task was performed in two steps. First the variation in green compact TC with compaction density was measured for the titanium-graphite powder system. Using this information, the SHS process was then modeled to predict the effect of green compact density and TC on the initiation and propagation of the SHS reaction. Extension of this modeling allowed the dependence of post synthesis temperature-time profiles on containment vessel TC to be investigated. By tailoring both the reacting sample and containment vessel to the requirements of individual compaction schemes, it is hoped that SHS processing may yield economical, low porosity ceramic materials.

II. Green Compact Thermal Conductivity Measurements

Samples were prepared by mixing stoichiometric mixtures of -325 mesh titanium* and oxidation resistant graphite† powders in a ball mill and compacting in a 1.27 cm diameter opposed anvil cylindrical die. The range of attainable green compact densities was limited on the low end by failure of the compacts to maintain structural integrity and on the high end by failure of the die. Cubic samples of approximately one centimeter on a side were cut from these cylinders with care being taken to orient one orthogonal axis normal to the anvil compaction surfaces. The known orientation of the samples with respect to the powder compaction direction allowed the anisotropy of the TC to be investigated.

The thermal conductivities of the green compacts were measured using a thermal wave propagation delay method.⁶ One end of a sample at ambient temperature was brought into thermal contact with a heat reservoir of known, elevated temperature while the temperature of the other end of the sample was recorded as a function of time. The TC of the compact was then determined by fitting the time-temperature response of the sample to the corresponding theoretical time-temperature profile⁷ using the sample's mass density, specific heat and linear dimensions. All temperatures were measured using thermocouples. Flat contact surfaces, thermally conducting grease and constant contact pressures ensured good thermal contact between the thermocouples, the sample and the heat reservoir. The accuracy for this TC

*Atlantic Equipment Engineers, Bergenfield, NJ (stated purity: 99.7%).

†Consolidated Astronautics, Smithtown, NY (stated purity: 99%).

measurement system was determined to be $\pm 10\%$.

Thermal conductivities of mixed titanium and graphite powder compacts, ranging in density from 58% to 81% of theoretical density, were measured in the directions parallel and perpendicular to the uniaxial compaction direction. Thermal conductivities of porous materials often exhibit a power series relation to the mass density.⁸ These TC data are also well fit by power series relations with the perpendicular data being fit by the expression:

$$k_{\perp}(\rho) = 9.12\eta^{4.48}; (W/m - K) \quad (1)$$

and the parallel data being fit by the expression:

$$k_{\parallel}(\rho) = 3.43\eta^{3.75}; (W/m - K) \quad (2)$$

where η is the powder compact mass density expressed as a fraction of the theoretical maximum density (3750 kg/m^3). The data and power series fits are plotted in Figure 1.

A pronounced anisotropy in the TC was observed between the directions parallel and perpendicular to the compaction direction. This anisotropy is predominantly due to the graphite component of this powder system. Under uniaxial pressure, graphite particles are preferentially oriented with their basal planes normal to the pressure axis.⁹ The high TC along the planes of the graphite particles enhances the TC of the bulk powder mixture in the direction perpendicular to the compaction direction.

Powder compact thermal conductivities were also measured at elevated temperatures. These TC values remained essentially constant from room temperature up to 500 C. Over this same temperature range the TC of graphite changes significantly¹⁰ suggesting that the bulk TC of these compacts is controlled by the high thermal resistance between contacting particles rather than the TC of the individual particle material.

III. Thermal Conductivity Effect Modeling

A numerical analysis computer model was developed to predict the limitations imposed on the SHS initiation and propagation process by the green compact thermal conductivity. The sample was represented as a matrix of cubic volume elements sized on the scale of individual powder particles which for the -325 mesh powders is approximately 44 microns. The time scale of the calculations was subdivided into 25 microsecond intervals which were small enough to allow for an accurate approximation to a continuous time evolution. Heat flow through the

sample was simulated by calculating the thermal interactions between all pairs of interacting volume cells during each interval of time. As a given volume element's temperature exceeded an assumed reaction ignition temperature of 1670 C (the melting point of Ti) for TiC, the release of the heat of reaction was simulated by increasing the volume cell temperature to a post synthesis value. For reaction initiation studies, the temperatures of the volume elements representing the igniting filament were increased with time at a rate which depended on the filament power density. This simulation model was verified against convenient test cases which were amenable to analytical solution.

Taking advantage of the symmetry of the linear filament geometry, the effects of green compact TC and filament power on the SHS reaction initiation process were modeled using a two dimensional array of volume cells. The size of this array was chosen to be large enough to avoid edge effects. A tungsten filament was assumed to be at the central position of the array supplying heat energy to the surrounding cells at a rate which depended on the filament power density. By turning off the filament after varying heating times and determining whether or not the SHS reaction continued to propagate, the minimum time for initiation of the self propagating reaction was determined. The temperatures of the volume cells representing the tungsten filament were also monitored for an increase above the tungsten melting point which would indicate filament failure.

Figure 2 shows the results of the SHS reaction initiation simulation for the titanium and graphite system with open symbols representing conditions leading to filament failure. The computed times required to initiate a self-sustaining reaction are plotted versus filament power density for a family of powder compact thermal conductivities. Both the power required to ignite a compact in a given period of time and the time to ignition at a given power level increase with the TC of the compact. Due to localization of the filament heat energy, filament melting and failure is seen to be more likely for the lower TC powder compacts.

SHS propagation velocities were modeled using an array of volume elements initially at room temperature. Heat energy was added to one row of cells to simulate a heating filament. This filament heated surrounding volume elements which eventually reached the assumed SHS ignition temperature triggering the temperature increase associated with the exothermic synthesis reaction. The additional heat energy from the reacted cells heated and ignited additional cells and this process worked its way through the entire array. Following the initial transient ignition process, the self-propagating reaction reached a steady state velocity which was taken as the

propagation velocity of the SHS reaction. Figure 3 shows the predicted propagation velocity as a function of powder compact density for this titanium and graphite system. This calculation assumes that the propagation velocity is controlled by heat transport and does not take into account any possible limitations that would be imposed by mass transport phenomena during the synthesis reaction. In addition, heat loss from the reacting sample to the surrounding environment, which has been shown to modify observed propagation velocities,¹¹ has not been considered.

Using nonadiabatic sample boundary conditions, the effect of containment vessel thermal conductivity on post synthesis sample temperatures has also been studied. Knowledge of post reaction temperatures and the length of time that a sample remains above the ductile-brittle transition temperature can be critical to the proper timing of compaction events. Figure 4 shows the predicted temperature contours for two samples 5 seconds after synthesis to a temperature of 2500 C. The enclosure for sample A was modeled with a TC corresponding to steel while the enclosure for sample B had a TC corresponding to gypsum wallboard. The 1500 C isotherm, representing an assumed ductile-brittle transition temperature, has been highlighted for emphasis. The sample in the steel container is seen to cool much more rapidly with significant regions of the outer portion of the sample below the transition temperature. A sample compacted under these conditions would be expected to yield low porosity material only at the central region with the edges being severely cracked. However the entire sample in the wallboard enclosure is predicted to remain well above the ductile-brittle transition temperature yielding a greater amount of low porosity final product following the compaction event.

Although the results of this study are directly applicable only to equivalent titanium and graphite systems, many of the characteristics and observations may be generally applicable. Instead of adding a diluent to SHS powder compacts as a means of reducing propagation velocities, the reduced thermal conductivity of low density powder compacts may serve the same purpose while maintaining the high sample temperatures required for post synthesis densification. For reaction apparatus where the energy for ignition is limited or fixed, the mass density of the sample's ignition region may be tailored to the available ignition energy source to ensure synthesis initiation. Powder systems with anisotropic thermal conductivities, such as uniaxially compacted powders containing graphite, offer additional control over the relevant green compact thermal conductivity. Proper choice of orientation between powder compaction direction, ignition geometry and synthesis propagation direction may yield more desirable SHS

ignition and reaction dynamics. All compaction schemes which require elevated post reaction temperatures can benefit from containment vessels fabricated from low specific heat and TC materials.

IV. Conclusions

Thermal conductivities of mixed titanium and graphite powder compacts have been measured as a function of compact mass density from 58% to 81% of theoretical density. An anisotropy in the thermal conductivity was observed between the directions parallel and perpendicular to the uniaxial powder compaction direction with conductivities in the perpendicular direction being approximately twice those in the parallel direction. This anisotropy is due to the orientation of graphite particles under uniaxial pressure. Over this range of powder compact densities, thermal conductivities increase with mass density by a factor of four. The limitations imposed by the green compact TC on SHS reaction initiation time and propagation velocity have been modeled for this titanium and graphite system. Initiation modeling predicts that the time required to start an SHS reaction using a resistively heated filament of a given power density is strongly dependent on the thermal conductivity of the powder compact. Low filament power levels can lead to unacceptably long ignition times due to excessive heat loss from the portion of the compact surrounding the filament to the remainder of the green compact. Conversely, overly high power levels will cause the filament to melt before the SHS reaction is initiated. Propagation modeling predicts that, over the range of easily obtained densities, propagation velocities in this system can increase monotonically with green compact density provided that additional limitations are not imposed by mass transport requirements and excessive heat loss from the sample. Post synthesis modeling of reacted samples surrounded by environments of different thermal conductivities reveals the importance of fabricating containment vessels from low conductivity materials.

References

- ¹ W. L. Frankhouser, M. C. Kieszek and J. A. Gogolewski, "Advanced Materials Technology Project-Semiannual Technical Report", System Planning Corporation report number 1059, Arlington, VA, 1984.
- ² M. Riley and A. Niiler, "Low Pressure Compaction of SHS Prepared Ceramics and Cermet," *Materials Processing by Self-Propagating High-Temperature Synthesis (SHS)*, MTL-SP-87-3, 1987.

³ J. B. Holt, G. Bianchini and D. Kingman, "Simultaneous Combustion Synthesis and Densification of Refractory Materials," *Materials Processing by Self-Propagating High-Temperature Synthesis (SHS)*, MTL-SP-87-3, 1987.

⁴ J. Wallace, G. Y. Richardson and D. Schrodt, "Simultaneous Densification and Reaction Synthesis in the Ti-C System Through Hot Rolling," *Materials Processing by Self-Propagating High-Temperature Synthesis (SHS)*, MTL-SP-87-3, 1987.

⁵ A. R. Sarkisyan, S. K. Dolukhanyan, I. P. Borovinskaya and A. G. Merzhanav, "Laws of the Combustion of Mixtures of Transition Metals with Silicon and the Synthesis of Silicides," *Fizika Goreniya i Vzryva*, 14 49-55 (1978).

⁶ T. Kottke and A. Niiler, "Thermal Conductivity Effects on SHS Reactions," Ballistic Research Laboratory report BRL-TR-2889, Aberdeen Proving Ground, MD, March, 1988.

⁷ H. S. Carslaw and J. C. Jaeger, "Operational Methods in Applied Mathematics"; pp. 94-95, Clarendon Press, Oxford, 1941.

⁸ B. Schulz, "Thermal Conductivity of Porous and Highly Porous Materials," *High Temperatures - High Pressures*, 13 , 649-60 (1981).

⁹ W. N. Reynolds, "Physical Properties of Graphite,"; pp. 27-8, Elsevier Publishing, New York, 1968.

¹⁰ R. Taylor, K. Gilchrist and J. Poston, *Carbon*, 6, 537 (1968).

¹¹ E. I. Maksimov, A. G. Merzhanov and V. M. Skiro, "Gasless Compositions as a Simple Model for the Combustion of Nonvolatile Condensed Systems," *Fizika Goreniya i Vzryva*, 1, 24-30 (1965).

FIGURE CAPTIONS

Fig. 1. Thermal conductivity of titanium and graphite powder compacts in the directions parallel and perpendicular to the direction of compaction as a function of mass density.

Fig. 2. Predicted TiC SHS reaction initiation time versus filament power density. Open symbols represent conditions leading to filament failure.

Fig. 3. Predicted dependence of SHS propagation velocity on powder compact density for a titanium and graphite system.

Fig. 4. Predicted temperature contours 5 seconds after SHS synthesis for samples in a steel (A) and a gypsum wallboard (B) containment vessel.

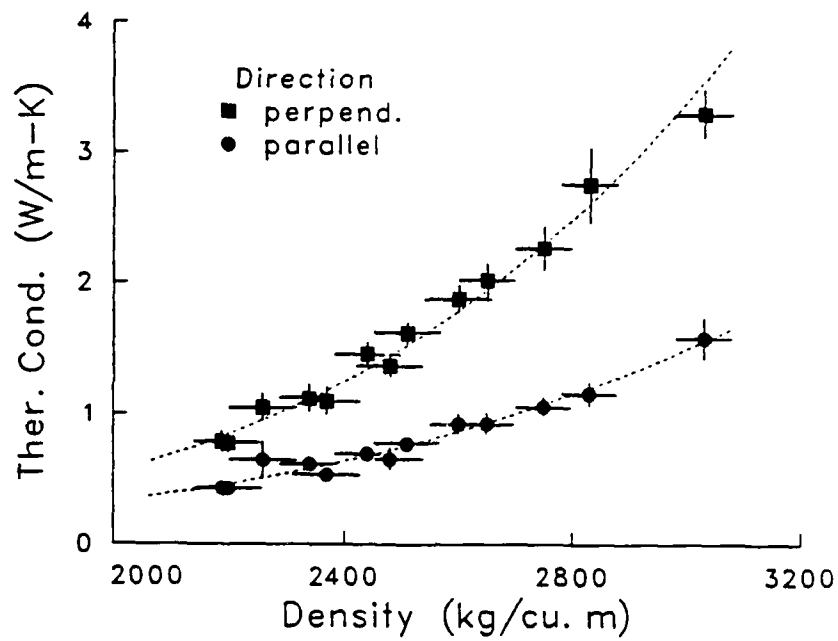


Fig. 1

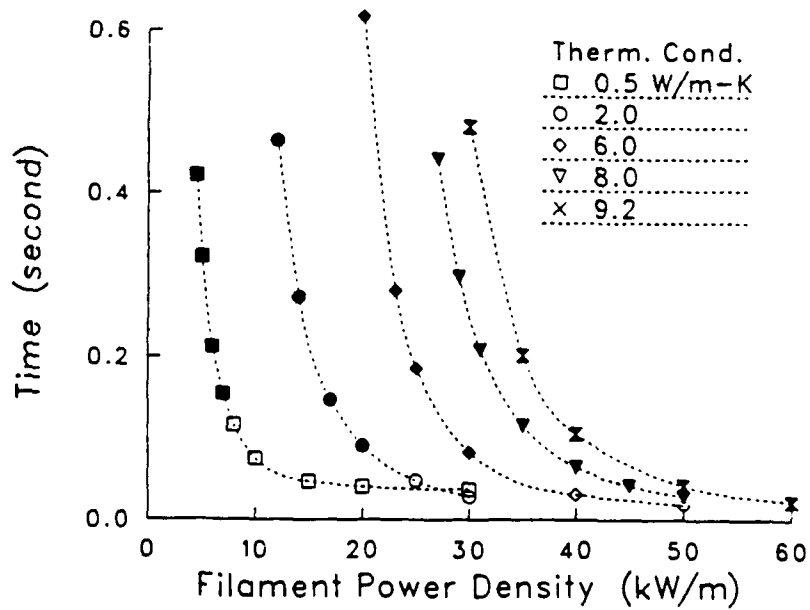


Fig. 2

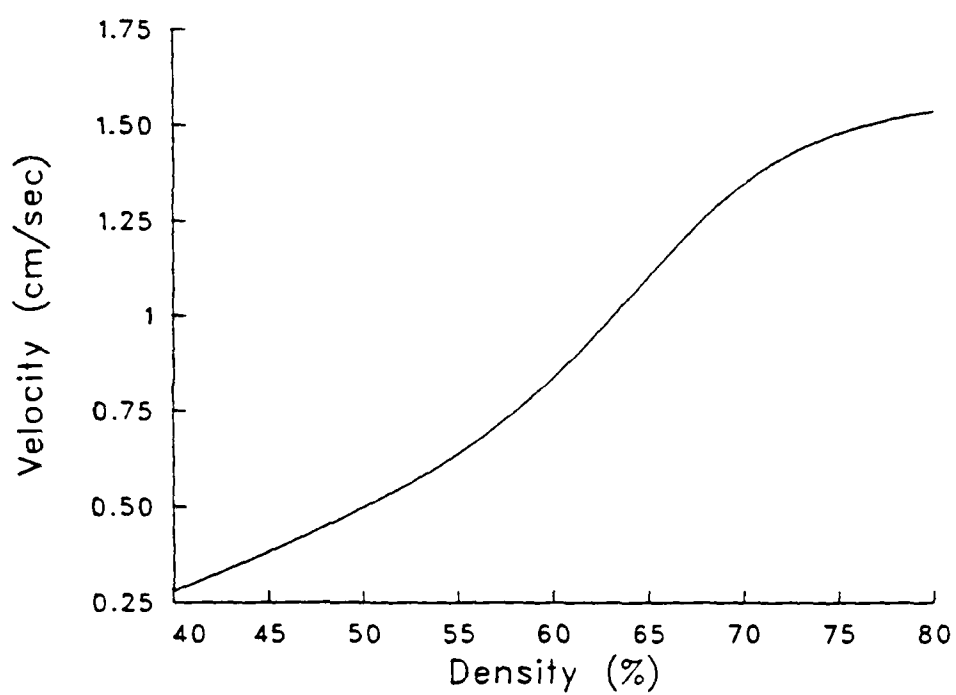
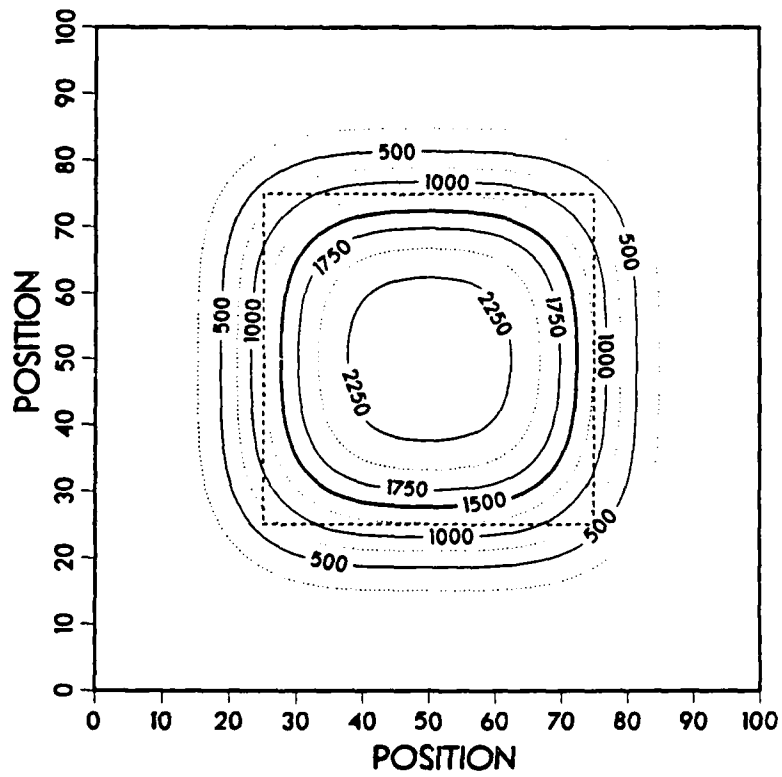
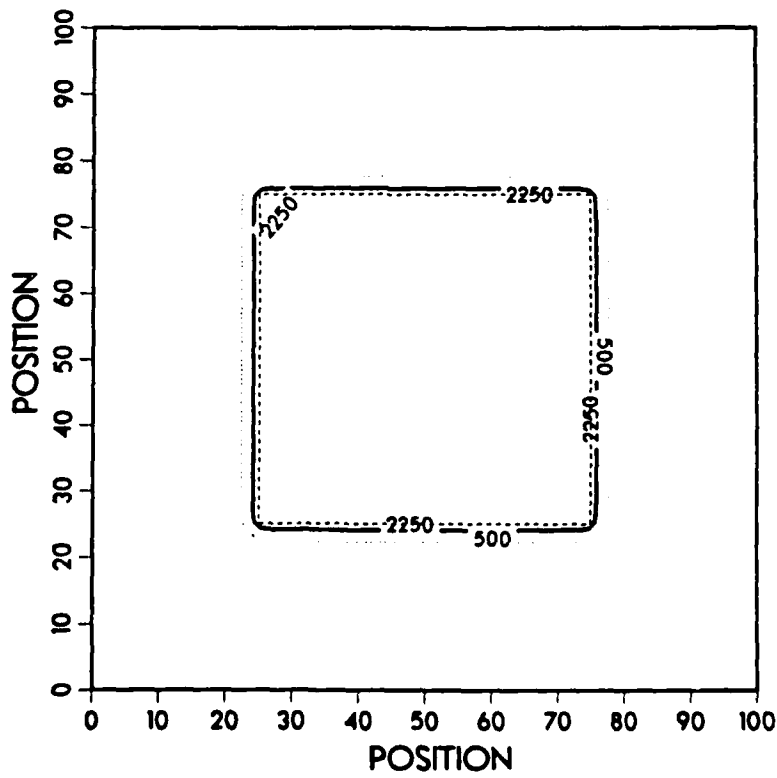


Fig. 3



A



B

Fig. 4

ELEMENTARY PROCESSES IN SiO_2 -Al THERMITE-TYPE REACTION ACTIVATED OR INDUCED BY MECHANOCHEMICAL TREATMENT

Abstract

Experimentally observed phenomena during grinding of the reactant mixture are presented. Mechanochemical activation - as pretreatment of the reactant mixture - strongly influences the kinetic parameters, the reaction mechanism and the composition and structure of the end-product. Intensive grinding of the reactant mixture induces processes consisting mainly of penetration of aluminum into the silica particle surfaces, leading both to "destoichiometrisation" of the surface and to formation of Al-O-Si bonds. Consequently, as was established, the process follows a new mechanism in its highly exothermic sequence, the "mechanolytic" mechanism.

The two mechanisms: "chain" and "mechanolytic", coexist in the general balance. Extension of the mechanochemical treatment reduces the share of the "chain" mechanism, involving the intermediate product as a gaseous phase, in favor of its "mechanolytic" counterpart.

Mechanochemical treatment activates the process up to onset of the highly exothermic sequence in the grinding vessel. Two phenomena result: a highly exothermic reaction initiated during grinding and termed "mechanothermitic", a pyrophoric ignition by opening the vessel and forming a bridge between the mechanochemical reactions during grinding and the highly exothermic sequence - "thermitophoric" reaction.

**ELEMENTARY PROCESSES IN $\text{SiO}_2\text{-Al}$ THERMITE-TYPE REACTION
ACTIVATED OR INDUCED BY MECHANOCHEMICAL TREATMENT**

by

G.T. Hida* and I.J. Lin**

INTRODUCTION

Investigations of the aluminothermic reduction of silicon dioxide [1-7], followed by a close observation of the aluminum-silica interface [8-11], led to the understanding of the mechanism of silica-thermite reaction [12] and, based on this, to the reformulation of the elementary processes in highly exothermic metallothermic reductions: oxides-suboxides [13,14].

The present work is devoted to studying the dependence of the combustion rate on the duration of intensive grinding of powdered mixtures and to the changes occurring in the mechanism of the highly exothermic sequence of the entire process. On the basis of the results obtained, a mechanochemically activated or induced thermite-type reaction mechanism is advanced with respect to the formation of aluminum monosilicates and subsilicates. This phenomenon is assumed to be due to the formation of Si-O-Al bonds found on the surface of the ground mixture.

* Dr. George T. Hida is Chief Scientist at the Combustion-Synthesis Dept. of Benchmark Ceramics Corp
2500 Walden Ave. Buffalo, NY 14225, U.S.A.

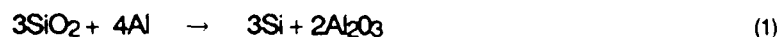
* To whom all correspondence should be sent.

** Dr. Israel J. Lin is Professor at the Minerals Engineering Dept. of Technion,
Israel Institute of Technology, Haifa 32000, Israel.

EXPERIMENTAL

The purpose of the experimental work was to obtain data on the silica-aluminum reaction parameters and structural information on the reaction intermediary and final products. The ignition method and the observation of the combustion front parameters are analogous to those described in [13]. The entire lab work consisted of two main operations: intensive grinding and ignition.

The experiments were made on cylindrically-compacted samples ground as a mixture of a 200 / 240 mesh of silica quartz-sand and aluminum powdered material, in the stoichiometric ratio, according to equation (1):



The weighed reactants were lightly mixed in petroleum ether and then subjected to intensive grinding in a high speed planetary ball mill equipped with a water-cooling system. (See Table 1). Ground samples were compacted into pellets by unidirectional pressing and ignited in the ignition assembly described in [13].

Results are shown in Figure 1. Characterization of the mixtures after different grinding durations, as reacted samples, was done by X-ray diffraction - XRD (see Figure 2). The product structure was analyzed by means of a Scanning Electron Microscope - SEM, equipped with an Energy Dispersive Spectrometer - EDS. The spectrometer data were compiled via T.N. Flextran 7-U computer program for qualitative element identification - QEI technique, and for Standardless Semi-Quantitative Analysis - SSQ. Patterns obtained are presented in Figure 3.

RESULTS

It was found that silicon dioxide reacts with aluminum under combustion conditions to form alumina and elemental silicon. Some silica, near small Al_2SiO_5 reflections, can be seen on XRD patterns of the product (Figure 2) suggesting formation of an intermediate product.

Intensive Grinding

The process parameters underwent significant modifications due to the intensive grinding. In the lightly mixed sample, ignition occurred at 600°C , while in the ground samples the ignition temperature was drastically lowered (see Figure 1). This means that the intensive grinding caused the mixture to deviate

from Tammany-Hedwall rules [15], i.e. the process is no longer a reaction between solid crystallites at the intimate contact points. Some chemical processes occurred during grinding, transforming the interface region to an entire zone of a complex phase which triggered combustion.

Intensive grinding induced "penetration" of aluminum atoms deep into the silica particle surface, leading to "destoichiometrisation" of SiO_2 and to the formation of Al-O-Si bonds, resulting in Al_2SiO_5 as a by-product even before the combustion process (see Figure 4).

Combustion Stage

Thermite reaction occurs at the silica particle surface (Figure 5) for lightly mixed samples. The calculated "reaction depth" (Table 2), is a consequence of oxygen transport by an intermediary product from the attacked surface to the adjoining, still unreacted aluminum unit. No aluminum diffusion occurs within the product layer but, on the contrary, the oxygen-bonded silicon induces a new aluminum unit to react. In the product zone the two main products, silicon and alumina, are in a wide range of concentrations (see Figure 5).

Intensive grinding led to the appearance of large agglomerates containing alumina, silicon and aluminum monosilicates (Figure 6). As the reaction depth increased over four microns, the amount of unreacted silica decreased significantly as the amount of agglomerates increased.

Induced Reactions

Intensive grinding extended beyond three hours led to the initiation of the reaction within the grinding vessel. On opening the lid between three and four hours of grinding, contact with outside air caused pyrophoric excitation of the thermite reaction - presumably by partial oxidation of the aluminum powder. The heat released triggered the thermite reaction. No such pyrophoric excitation was observed in Al- Al_2O_3 mixtures after the same time of intensive grinding.

For an intensive grinding time of more than four hours, the reaction started during grinding. The temperatures reached during the reaction combined with the specific conditions, favored an interesting microstructure - sphericity of the alumina particles, implying the possible existence of a molten phase (Figure 7).

DISCUSSION

As was expected, intensive grinding of the powdered mixture of reactants plays an important role in the initiation of aluminothermic reduction of silica.

I. The shift of the DTA exothermic peaks to lower temperatures, as a function of grinding duration, implies reduction of the ignition energy needed for the reaction to start. In other words, the intensive grinding activation - a mechanical one - through the accumulation of specific surface free-energy and stored elastic strain-energy, makes the system metastable, readily available to a process of energy relaxation, such as the ignition of the metallothermic reduction in our case. The fact that the mechanical activation has a considerable influence on thermite-type reactions shows that they should be characterized in the category of surface-chemistry phenomena.

II. It is shown (Figure 4) that considerable quantities of alumina, as well as small quantities of aluminum monosilicate were formed under intensive grinding prior to the onset of the thermite process. Blanks of aluminum powder alone, or mixed with different quantities of alumina, ground under ambient environmental conditions - (which had shown no difference in XRD following grinding) - now showed, after heat treatment in an inert atmosphere, alumina reflections in the pure aluminum samples, and an increase in the alumina content in mixed aluminum-alumina samples. All these led to the conclusion that during the intensive grinding the newly exposed surfaces of the aluminum adsorbed considerable quantities of oxygen and moisture from the immediate environment. The newly-exposed surfaces have a strongly enhanced sorption capacity compared with their unground counterparts. The adsorbed components may create chemical or pseudo-chemical bonds into the solid surface. The stressed aluminum surfaces sorbed oxygen and silicon suboxides, forming Al-O and Al-O-Si bonds during intensive grinding, thereby facilitating formation of alumina, and aluminum monosilicates. This is a chemical change through mechanical treatment - a mechanochemical activation.

III. SiO₂ particles tend to be coated and agglomerated by ductile aluminum. As a result of fracturing, interatomic bonds are severed, forming active interface molecular groups with open ligands which upon recombination change the initial coordination state. In fact, these active groups are instrumental in the

process of agglomeration, crystallization, mechanochemical synthesis, and chemisorption of environmental gaseous species.

The newly-exposed surfaces have a strongly enhanced sorption capacity compared with their stable counterparts. The adsorbed components, such as oxygen and silicon suboxides, form with the opened ligands Al-O and Al-O-Si bonds, near captured SiO_x ($x = 1-1.5$) groups. Due to the treatment, aluminum particles penetrated deep into the silica surface and generated point chemical reactions resulting in new chemical bonds. At the same time, the entire zone acquired surface-like properties reducing considerably the bulk properties share of the material.

IV. If gas is added after intensive grinding, the sorption of a considerable amount of gas in a very short period of time might lead to unexpected phenomena. In our case the "thermitophoric reaction" occurred when the vessel was opened after more than three hours of grinding. After that a large amount of oxygen was sorbed and uncompensated Al-O bonds were formed, leading to the release of sufficient energy (a pyrophoric action) to trigger the combustion process.

V. The aluminothermic reaction was triggered and took place within the unopened grinding vessel after more than four hours of grinding. This was a true mechanochemical reaction excited when particle size fell below the "Reaction Triggering Dimension - RTD" [16], the excess free-energy of the particulate system exceeding the activation level needed for triggering. Formation of "magma-plasma" pockets at the points of impact and friction between particles have nothing to do with the mechanochemical process. At most, they can enhance the rate of excitation of the metallothermic reaction as a kinetic effect, but only if the particulate system is readily available in the proper metastable (activation) state, namely - having approached the needed "RTD".

VI. So far, the findings of the mechanochemical effect upon the metallothermic reductions in the present study bring forward the reaction mechanisms that we believe can explain our experimental results as well as the results found by other investigators.

A. "Jump-Chain" Mechanism

Assume a stoichiometric mixture of silica and aluminum powders (without any former mechanochemical treatment). On heating, two main transformations occur:

1. Polymorphic transformation of β quartz into α -quartz - the plateau observed in the DTA diagram (Figure 1) - a very weak endothermic effect (partially compensated by formation of chemical bonds among the aluminum and oxygen adsorbed - an exothermic process):



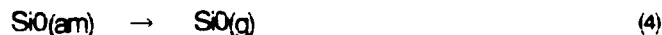
2. The oxygen adsorbed by aluminum forms chemical bonds. Around the above temperature, the thermite reaction sets in and creates a reaction zone in which the following set of thermochemical reactions commence:

- a. Reduction of silicon dioxide to silicon monoxide:



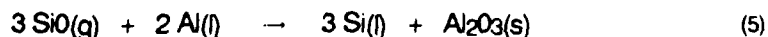
which takes place at the interface of intimate contact between reactant particles.

- b. Sublimation of silicon monoxide due to the temperature of the immediate environment:



The amorphous silicon monoxide is thermodynamically unstable, particularly vis-a-vis the ambient temperature; however, its sublimation temperature (2300-2500°K) and heat consumed lead to the conclusion that some of it remains in the amorphous state at this stage. It is worth mentioning that SiO could not appear directly in a gaseous phase, the corresponding calculated adiabatic temperature being over 5500°K - an impossibility.

- c. Sublimation is followed by another reduction:



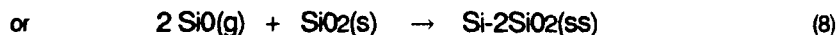
Here, the SiO acts as an oxygen carrier, "reactive transport," through the pores to aluminum particles

However, the probability of a SiO molecule landing on an aluminum surface is 1/3, while that of its landing on an inert surface (alumina or unreacted-yet silica) is 2/3. These surfaces catalyze the redox disproportionation of SiO, leading to by-products.

- d. Side reactions - disproportionation of SiO:



Reaction (6) has moderate endothermic characteristics. Its products will form compounds or solid-solutions with the medium:



- e. Another reduction of some silicon monoxide remaining in the amorphous phase may also occur:



- f. The same amorphous silicon monoxide will undergo a redox disproportionation process in absence of an aluminum unit to form with alumina, aluminum monosilicates:

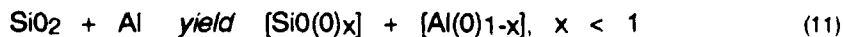


B. "Mechanochemical" Mechanism

As a consequence of intensive grinding, true chemical reactions occur during penetration of aluminum atoms through the silica surface. Based on these, one can divide the entire process into reactions during grinding, and reactions during combustion.

- The mechanochemical sequence consists of a "penetration-reaction" mechanism in which:

1. SiO₂ will suffer "destoichiometrization", the aluminum units will adsorb the freed oxygen atoms:

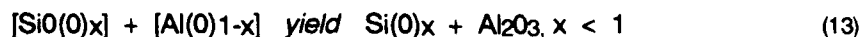


2. Aluminum atoms will penetrate into the silica surface, leading to formation of Si-O-Al bonds:



As a consequence of the mechanochemical "penetration-reaction" process, the reactants acquire a high activation level and the array of intimate contact points is replaced by a complex phase region which favors the onset and progress of combustion. From Figure 1 one can observe that the preignition and ignition exothermic peaks draw closer to each other until they coincide. The assumed mechanism for this is:

- Combustion sequence - reduction of the "destoichiometrized" silicon oxide by the "oxygenated" aluminum:



- Formation of Si-Al₂SiO₅ Solid-Solution:



These elementary reactions form part of the entire chemical process and their importance increases as a function of the duration of intensive grinding. Besides this, the mechanochemical effect induced by grinding will expose to the reaction interface, surface molecular groups so that there is little need for SiO gas, but the condensed phase reaction will follow. Thus, the amount of porosity in consolidated pellets of ground powder is much below that needed for only mixed powder pellets for proper aluminothermic reaction. The probability of intimate contact between reactant units becomes many folds higher in ground materials, so that the need for reactive transport of oxygen becomes less important. The products obtained are large agglomerations containing real solid-solutions with the possible formula:



CONCLUSION

The SiO₂-Al mechanochemically activated reaction mechanism proposed is the Mechanolytic model, comprising the mechanochemical Penetration-Reaction sequence during intensive grinding, and the Mechanolyzed-Reduction during combustion. Of course, this is combined with the Jump-Chain mechanism activated by the above model. The main features of the process are:

1. The process occurs in condensed phases.
 2. During intensive grinding aluminum penetrates the silica network, yielding silicon suboxides and aluminum-oxygen-silicon groups.
 3. The array of contact points between aluminum and silica is replaced by an entire zone comprised of active molecular groups - in a high degree of intimacy - with open ligands, which upon ignition - at a drastically reduced temperature - undergo chemical relaxation. The resulted heat ignites the thermite process.
 4. Zones comprised of active molecular groups transform in large agglomerations having the proposed (15) formula.
 5. The Jump-Chain and Mechanolytic mechanisms operate concurrently.
- Extension of intensive grinding time reduces the share of the Jump-Chain mechanism in the general process balance in favor of its Mechanolytic counterpart.

REFERENCES

1. Walton, J.D., and Poulos, N.E., "Cermets from Thermite Reactions", J. Amer. Cer. Soc., Vol. 42, No. 1, pp. 40-49 (1959).
2. Abramovici, R., and Enache, M., "Investigations Concerning the Use of Aluminothermic Reduction Ser. Chim., Vol. 18, No. 32, pp. 35-42 (1973).
3. Prabirputtaloong, K., and Piggott, M.R., "The Reaction between Silica and Aluminum", J. Electrochem. Soc., Vol. 121, No. 3, pp. 430-434 (1974).
4. Hida, G.T., Lin, I.J., and Nadiv, S., "Considerations on Self-Propagating Reactions in Solid State", Proc. 7th Conf. IAAME, Israel, PP. 73-82 (1984).
5. Holt, J.B., and Munir, Z.A., "The Fabrication of SiC, Si₃N₄ and AlN by Combustion Synthesis", Proc. Fir. Int. Sym. Cer. Comp. Eng., Japan, pp. 721-728 (1983).
6. Cutler, R.A., "Synthesis of Submicron Silicon Carbide", DARPA/ARMY SYM. SHS, FI, U.S.A. (1985).
7. Behrens, R.G., and Hansen, G.P., "Thermochemical Modeling of Thermite-Type Reactions", DARPA/ARMY Sym. SHS, FI, U.S.A. (1985).
8. Maki, K., and Shigeta, Y., "Surfaces of Vacuum-Deposited Silicon Oxide Films Studied by Auger Electron Spectroscopy", Japanese J. Appl. Phys., Vol. 20, No. 6, pp. 1047-1053 (1981).
9. Baner, R.S., Bachrach, R.Z., and Brillson, L.J., "Au and Al Interface Reactions with SiO₂", Appl. Phys. Lett. Vol. 37, No. 11, pp. 1006-1008 (1980).
10. Roberts, S. and Dobson, P.J., "Evidence for Reaction at Al-SiO₂ Surface", J. Phys. D: Appl. Phys., No. 14, pp. L17-L22 (1981).
11. Jung, T., and Titel, W., "Application of Auger Depth Profiling on Al-SiO₂ Surface", Phys. Sol. St., No. 74, pp. 85-90 (1982).
12. Hida, G.T., "Study of Solid-State Aluminothermal Reactions: Influence of Activation and Moderation Processes", Ph.D. Thesis, Israel, pp. 66 - 99 (1987).
13. Hida, G.T., Lin, I.J., and Nadiv, S., "Kinetics and Mechanism of the Reaction between Silicon Dioxide

- and Aluminum", AIChE Sym. Series, Vol. 84, No. 263, pp. 69-72 (1988).
14. Hida, G.T., "Metallothermic Reduction Mechanisms: Oxides-Suboxides- Elements", BSCC Report, NY, U.S.A., pp 7-9 (1988).
 15. Murgulescu, I.G., Oncescu, T., and Segal, E., "Introduction to Physical Chemistry" [in Romanian], Vol. II, 2, Romania, pp. 708-733 (1981).
 16. Nativ, S., and Lin, I.J., "Thermodynamic Concepts, Kinetics and Mechanisms Controlling Solid-State Mechano-Chemical Reactions in Particulate Systems", React. Sol., pp. 731-733 (1985).

Table 1: Ignition temperature as function of intensive grinding duration; for loose powder - DTA and for pellets in a 720°C preheated furnace.

No.	Sample Code	Intensive Grinding Duration (Hours)	Ignition Temperature (°C)	
			Ignition Assembly*	DTA**
1	SA ₀	0	630-670	600
2	SA ₁	1	580-600	520
3	SA ₂	2	535-550	480
4	SA ₃	3	495-500	450

SA = Silica & Aluminum

*Pellet

**Loose Powder

Close approximation of the ignition temperature was obtained by Differential Thermal Analysis - DTA

Table 2: "Reaction Depth"

No.	Code	Intensive Grinding Duration (Hours)	Giant SiO ₂ Particles ,mm (product layer included)	Reaction Depth Average(μm)			Al / Si Value
				Si	Al	Mean	
1	SA ₀	0	35.0*	1.5	2.0	1.75	0.521
2	SA ₁	1	25.2*	3.2	3.4	3.30	0.874
3	SA ₂	2	17.1*	4.1	4.5	4.30	0.983
4	SA ₃	3	14.5**	4.4	4.7	4.55	1.175

* Nine particles were measured and the extremes were eliminated.

** Only five particles over 10 microns were found.

FIGURES

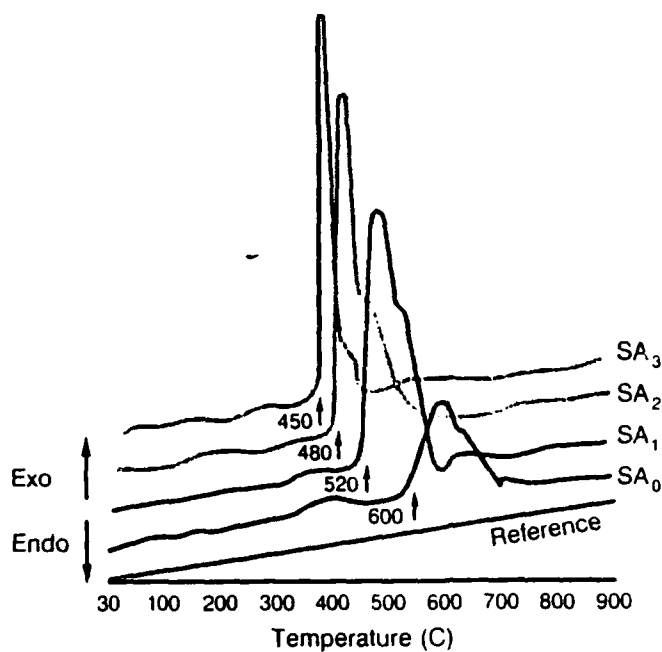


Figure 1. DTA patterns of mechanochemically activated samples and of blank (loose mixtures).

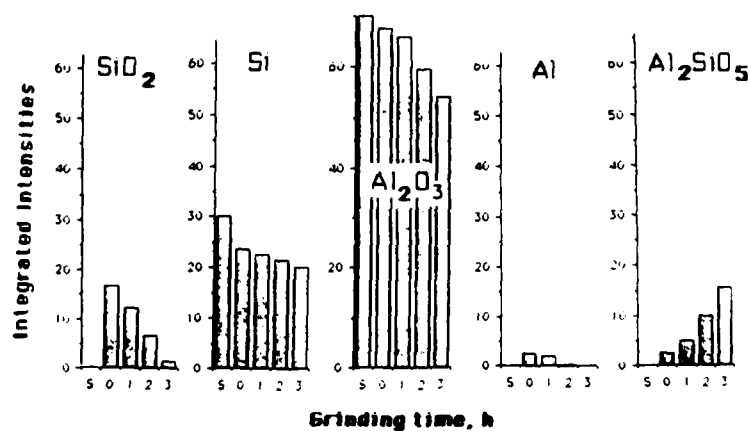


Figure 2. Integrated intensities of Al₂O₃, Si, Al₂SiO₅, SiO₂ and Al major reflections from XRD patterns for reacted samples in SiO₂-Al system. S refers to XRD pattern of the standard mixture of Si and Al₂O₃ made according to equation (1).

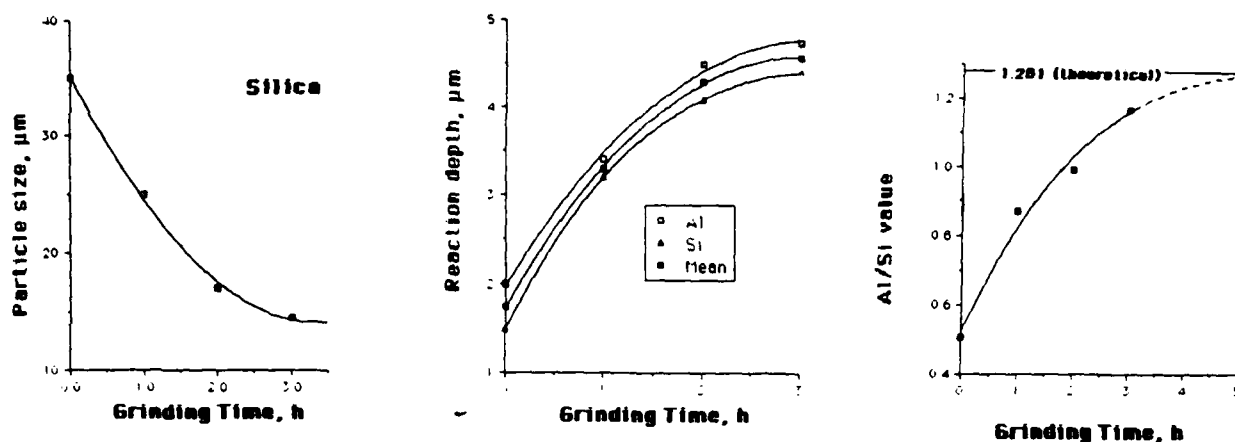


Figure 3. Reaction "Depth". Figures are showing the results obtained from SEM micrographs for each sample, choosing positions in as far as possible without unreacted SiO_2 particles. As a first step, the QEI technique was used. Data obtained allowed differentiation between silicon as metal (oxygen-free) and as SiO_2 , either as small particles or as part of agglomerations or of product layers on large SiO_2 granules. Thus, it was possible to perform SSQ. The computation errors being reduced to those due to analyzed surface imperfections: relief non-uniform distribution of pores and of their sizes, vesicles, etc. Based on SSQ data Al as Al_2O_3 and total Si concentration values were calculated. This diagram represents the reduction in size of the biggest SiO_2 core found, as function of intensive grinding duration (see also Table 3). It shows the so-called reaction depth; the product layer thickness found on the above giant SiO_2 granules. Note that much larger product agglomerates were found (see also Table 3). Based on SSQ values, it was possible to calculate the overall Al/Si value which now represents a measure of sample homogeneousness versus intensive grinding duration.

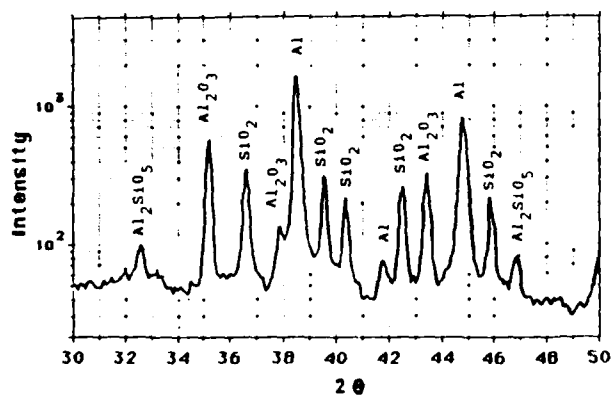
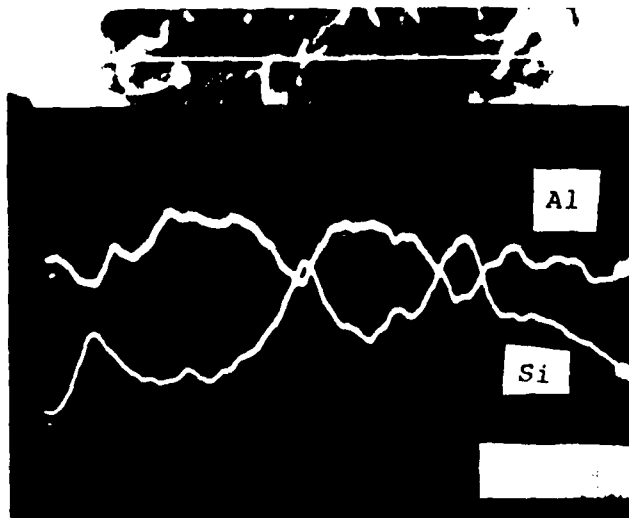


Figure 4. XRD pattern of SiO_2 -Al sample after three hours of intensive grinding; preheated in the ignition assembly under vacuum. The heat treatment was stopped before ignition



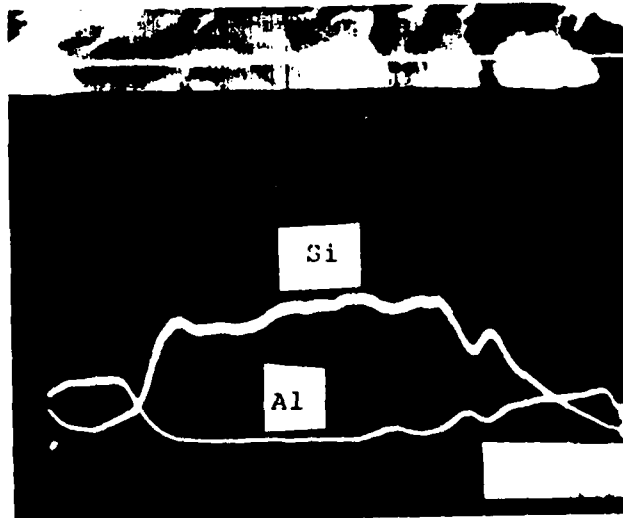
5.1A: SA0(10000x) SiO₂. Surface After Ignition



5.1B: X-ray Line Profile of 5.1A

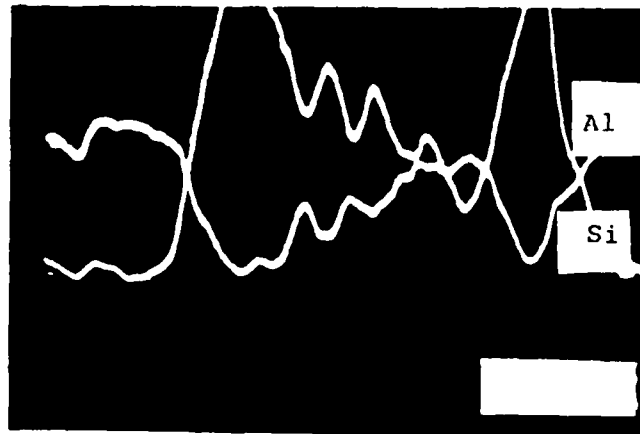


5.2A: SA0 (7500x). Section in a Surface Reacted SiO₂ Particle

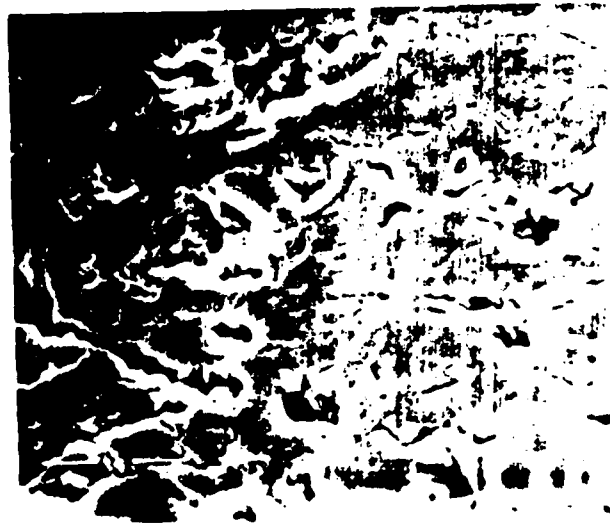


5.2B: X-Ray Line Profile of 5.2A

Figure 5 Blank sample - SA0 - micrographs of large silicon dioxide particles reacted at its surface. One can observe the "reaction depth"



6.1A: SA₃ (3500x). Extra-Large End-Product Agglomeration 6.1B: X-Ray Line Profile of 6.1A



6.2: SA₃ (1000x). Dense Zone - Reaction - Sintered Process

Figure 6 Micrographs taken from dense zones of samples ignited after three hours of intensive grinding

420



7.A: Alumina Spheres Micrograph (7500x)



7.B: X-Ray Analysis of 7.A. The dots represent aluminum

Figure 7 Alumina spheres in the end-product of the sample reacted during intensive grinding

COMBUSTION SYNTHESIS OF CERAMIC PREFORMS FOR MOLTEN-METAL INFILTRATION

Danny C. Halverson
Zuhair A. Munir

University of California
Davis, California, U.S.A.

- Beverly Y. Lum

Lawrence Livermore National Laboratory
Livermore, California, U.S.A.

ABSTRACT

Capillarity-thermodynamic studies were conducted to obtain contact-angle data of molten aluminum on boride (B_4C , TiB_2 , AlB_{12}) and carbide (TiC , SiC) substrates to illustrate the feasibility of infiltrating preforms containing these phases with aluminum. Techniques for increasing the exothermic potential of self-propagating high-temperature synthesis (SHS) reactions ("exothermic boosting") are suggested for the fabrication of B_4C -rich and SiC -rich composite-ceramic preforms for subsequent infiltration with molten aluminum. EXOBOOST, a computer program, has been developed to rapidly screen hundreds of ceramic preform combinations based on SHS thermodynamics and exothermic boosting. Preliminary studies on the SHS of TiC indicate that reactant-greenbody properties strongly influence uniformity in the preform microstructure.

INTRODUCTION

This is a progress report of continuing research in the area of developing porous-ceramic bodies to act as preforms for subsequent infiltration with liquid metals.

The overall research objectives are: (1) To fabricate boride (e.g., B_4C or TiB_2) and carbide (e.g., TiC or SiC) composite preforms using self-propagating high-temperature synthesis (SHS). (2) To infiltrate these preforms with molten aluminum or other suitable metal phase. (3) To investigate the practical application of thermodynamic principles for the selection of composite preforms. (4) To establish processing guidelines for the manufacture of these materials.

The technical approach will, first, confirm the capillarity-thermodynamic compatibility of potential ceramic preform phases with aluminum. Second, it will develop a computer program to rapidly check SHS thermodynamics of different two-phase ceramic preform combinations. And finally, it will systematically study reactant-greenbody processing parameters and their influence on combustion and preform microstructure. Work is still in progress on the latter, so results there are preliminary.

BACKGROUND

Capillarity-thermodynamic criteria for the infiltration of metal into a ceramic preform have already been established by Halverson et al.¹ Their application to the processing of B_4C -Al cermets has also been demonstrated.²⁻⁴ It is appropriate, therefore, to extend the use of wetting data for the infiltration of aluminum into alternative boride- and carbide-containing preforms.

The authors' previous work⁵ has shown that the fabrication of B_4C - TiB_2 preforms is possible because of the high exothermicity associated with the TiB_2 reactions. The authors also confirmed experimentally that the relative amount of B_4C in these preforms can be increased by simply increasing the pre-ignition temperature of the reactants. These preforms were subsequently infiltrated with aluminum.

Merzhanov⁶, in a general overview of the SHS process, indicates that the formation of weakly-exothermic compounds (B_4C , Al_4C_3 , SiC , $NbAl_3$, $NbGe_2$, $TaSi_2$, Mo_2C , MoB_2 , Mo_2B , Mo_3Si , WB , W_2B_5 , and WB_2) requires an additional heat source and that joint synthesis methods for strongly- and weakly-exothermic compounds can be worked out.

The present authors have developed a principle called "exothermic boosting" that is defined as follows: *Exothermic boosting* is increasing the exothermic potential of an SHS reaction by (1) raising the pre-ignition temperature of the reactants just prior to combustion and (2) by combining reactants that form low-exothermic-potential products (LEPPs) with reactants that form high-exothermic-potential products (HEPPs).

The application of wetting data and the principle of exothermic boosting are straightforward approaches to developing many novel compositions of matter. One severe problem still remains, however: achieving "total" uniformity in the SHS preform.

To fundamentally approach this problem, systematic analysis must be conducted of the intrinsic and extrinsic variables associated with precombustion processing. The synthesis of TiC was selected for these studies. Titanium carbide is probably one of the most-widely-studied SHS reactions; consequently, it offers researchers considerable information about its properties, structure, thermodynamics, and kinetics. With these data "in-hand," one can now focus on the processing parameters that influence and (hopefully) control uniformity.

EXPERIMENTAL PROCEDURE

Contact-angle data were obtained at Lawrence Livermore National Laboratory (LLNL) on the Advanced Sessile Drop Measurement System (ASDMS).⁷ High-purity aluminum^{Note 1} was placed atop hot-pressed ceramic substrates of B₄C, TiC, AlB₁₂, SiC, and TiB₂.^{Note 2} Each substrate and a small piece of the aluminum were heated in vacuum (10⁻⁵ to 10⁻⁶ Torr) in the ASDMS according to the temperature-time profile of Fig. 1. The wetting behavior was recorded on video tape, and contact angles were measured with a protractor during playback.

Titanium carbide processing experiments were performed using two grades of titanium powder^{Note 3} and two grades of carbon powder.^{Note 4} All powders were characterized at LLNL. Particle-size distributions for the titanium and carbon powders are shown in Figs. 2 and 3, respectively. BET N₂-gas adsorption analysis^{Note 5} indicated that the -325 mesh and 1-3 μ m Ti powders had surface areas of 0.5 and 13.3 m²/g, respectively, and that the -325 mesh graphite and carbon black powders had surface areas of 8.3 and 234 m²/g, respectively. Because of the wide size distributions, these powders will herein be referenced by their surface areas.

Helium-pycnometric densities^{Note 6} of the powders are as follows:

$$0.5 \text{ m}^2/\text{g Ti} = 4.46 \text{ g/cm}^3$$

$$13.3 \text{ m}^2/\text{g Ti} = 4.44 \text{ g/cm}^3$$

$$8.3 \text{ m}^2/\text{g C} = 2.40 \text{ g/cm}^3$$

$$234 \text{ m}^2/\text{g C} = 1.934 \text{ g/cm}^3$$

X-ray diffraction studies indicated both Ti powders and the 8.3 m²/g C (graphite) to be crystalline. The 234 m²/g C (carbon black) was shown to be completely amorphous.

SEM analysis showed the 0.5 m²/g Ti to be predominantly smooth-convoluted grains of titanium averaging 10-20 μ m in cross-section. Most appeared to be dense. The 13.3 m²/g Ti was more angular and less smooth

(probably because of oxidation) with dense grains averaging 1-8 μm in cross-section. The 8.3 m^2/g C showed a typical graphite structure (platey habit) with dense plates on the order of 2 μm across and 0.5 μm thick. The graphite had a uniform appearance with about 10% of the plates being sub- μm . The 234 m^2/g carbon black consisted of highly-agglomerated porous spheres about 1-10 μm in diameter. Closer examination showed what appeared to be dense, smooth, oval structures measuring less than 0.1 μm in diameter.

Table I shows powder impurity levels. Oxygen levels were measured using neutron activation,^{Note 7} so are representative of bulk and surface contamination. ESCA^{Note 8} indicated only slightly higher surface oxides in the finer Ti powders and negligible surface oxidation in both C powders. Carbon, hydrogen, and nitrogen were determined by combustion^{Note 9}; all other impurities were measured using mass spectrometry.^{Note 10}

Initial processing studies involved making low-magnification (20 \times) microscopic comparisons of SHS-produced TiC after:

- Varying the reactant particle mixtures by combining different grades of titanium powders with different grades of carbon powders;
- Comparing outgassing at room temperature (3.5 hours, 200 mTorr) to outgassing at 500 °C (3.5 hours, 200 mTorr) to no outgassing conditions;
- Changing the reactant-powder axial-compaction pressure from 5,000 psi to 10,000 psi (no binders, dry);
- Altering the mixing order of the reactant powders.

(Note: All powder mixtures consisted of 81 wt% Ti + 19 wt% total C to produce stoichiometric TiC products. Each was vibratory mixed for 5 minutes before pressing.)

-
- 1 Alfa 00526 aluminum pellets, 0.99999 pure.
 - 2 Cercom hot-pressed substrates.
 - 3 Alfa 00724 titanium powder (-325 mesh) and Alfa 99883 titanium powder (1-3 μm , packed in argon).
 - 4 Alfa 00641 graphite powder (-325 mesh) and Cabot Monarch 700 amorphous carbon black.
 - 5 Digisorb 2600 5-point BET calculation.
 - 6 Beckman autopycnometer.
 - 7 IRT Corporation, San Diego, Calif.
 - 8 Surface Science Laboratories, Mountain View, Calif.
 - 9 Leco combustion technique.
 - 10 Jarrell-Ash spectrographic analysis.

THERMODYNAMIC CONSIDERATIONS

Figure 4 shows the results of the capillarity-thermodynamic studies. These results indicate that contact angles less than 90 degrees (wetting) can be achieved for the ceramic-aluminum combinations shown. This is a necessary condition for the infiltration of aluminum into preforms containing these ceramic phases. Other factors (e.g., ceramic-metal capillarity kinetics, reaction thermodynamics, and reaction kinetics) must also be considered for microstructural enhancement¹⁻⁴; however, for successful infiltration, wetting must be achieved first.

Table II shows thermodynamic properties for the selection of product phases in B₄C-TiB₂, B₄C-TiC, and SiC-TiC composite preforms. This table also gives the theoretical density and reported hardness range for each phase. From the table, it is evident that both B₄C and SiC are LEPPs and that both TiB₂ and TiC are HEPPs. Although it would be very easy to form TiB₂-TiC preforms, a more practical application of exothermic boosting is evidenced by the following SHS reactions:



Previous work⁵ illustrated that a pre-ignition temperature of 1200 K exothermically boosted the first reaction shown above to a preform microstructure containing 81 vol% B₄C!

The previous research also resulted in a crude computer program for calculating adiabatic temperatures as a function of B₄C/TiB₂ ratios for different pre-ignition temperatures. During the past 3 months, considerable effort was spent developing a more "generic" form of the program.⁸ The new program (appropriately named EXOBOOST) has a sophisticated user interface (menu-driven, context-sensitive help, graphics, etc.); comes with a database containing commonly-synthesized borides, carbides, silicides, and sulfides; and offers the user a 62x62 matrix of LEPP/HEPP preform combinations.

Figure 5 shows a rendition of an EXOBOOST screen after performance of one of its high-speed iterative-trapezoid-rule integrations. Also shown is the ability to select adiabatic-temperature output as a function of LEPP/HEPP ratios for different values of the pre-ignition temperature (T₀), or as a function of T₀ for different LEPP/HEPP ratios.

Figures 6 through 8 are renditions of EXOBOOST's high-resolution graphical output. Each is a plot of adiabatic temperature as a function of LEPP/HEPP ratios up to 3.0 (i.e., to a yield of slightly greater than 80 vol% LEPP) for pre-ignition temperatures of 298 K, 600 K, 900 K, and 1200 K for the fabrication of B_4C -TiB₂, B_4C -TiC, and SiC-TiC preforms.

EXOBOOST output is based on the thermodynamic values input by the user. Thermodynamic data vary from source to source. For example, enthalpies of formation (298 K) for TiB₂ are reported in the literature as -70,260 cal/mole,⁹ -77,400±900 cal/mole,¹⁰ -77,400 cal/mole,¹¹ and -66,800 cal/mole.¹² Figure 6 was plotted using the value reported by Pankratz et al.¹¹ Using a lower enthalpy will result in the output of lower adiabatic temperature curves.

PRELIMINARY PROCESSING-STUDY RESULTS

Figure 9 shows the microstructural differences that occur from use of different size titanium reactant powders with three different carbon mixtures (all powders mixed together at the same time, axially pressed at 10,000 psi, and outgassed 3.5 hours at 500 °C, 200 mTorr). Regardless of the carbon mixture used, the 0.5 m²/g Ti compacts always showed more laminar (exfoliated) microstructures than did the 13.3 m²/g Ti compacts.

Figure 10 illustrates the microstructural change resulting from variation in outgassing conditions. This figure compares the conditions of no outgassing to outgassing at 20 °C (3.5 hours, 200 mTorr) to outgassing at 500 °C (3.5 hours, 200 mTorr). Reactant powders were 13.3 m²/g Ti and 234 m²/g C (all mixed together at once and axially pressed at 10,000 psi). Elevated-temperature outgassing appeared to inhibit lamination with these reactants. A similar experiment using 0.5 m²/g Ti and 234 m²/g C did not eliminate lamination as much as did the 13.3 m²/g Ti, but it did significantly reduce the degree of exfoliation during SHS.

It was not possible to ignite the compacts when 8.3 m²/g graphite was the only source of carbon. The maximum graphite:carbon black ratio that could sustain combustion was 50:50 by weight. Figure 11 compares the effect on microstructure of changing the graphite:carbon weight ratios from 0:100 to 25:75 to 50:50. No change is readily evident at low magnification, but higher magnification reveals different morphologies. It is suggested that the greater thermal conductivity associated with the graphite powder may be drawing heat from the combustion zone. This localized heat-transfer phenomenon would affect the kinetics associated with TiC grain growth and could account for these microstructural differences. Further study is needed to confirm this, however. Compacts were

prepared using both 0.5 m²/g and 13.3 m²/g Ti reactants. These morphological changes appeared regardless of the Ti used. All reactants were mixed at the same time, outgassed at 500 °C (3.5 hours, 200 mTorr), and axially pressed at 10,000 psi.

Two other preliminary observations were noteworthy. When the graphite:carbon mixtures were premixed (i.e., separately vibratory mixed for 5 minutes) and then combined with the Ti reactant powder, the time to ignition was considerably longer. In addition, the microstructure appeared "graded," probably partly due to the partial sintering of the ignition surface prior to combustion.

Finally, compacts that were axially pressed at 10,000 psi appeared to exfoliate more than did samples pressed at 5,000 psi. This may be caused by increased pressure-buildup resulting from smaller channels in more compacted parts that make the escape of volatiles more difficult.

CONCLUSIONS

Capillarity-thermodynamic compatibility studies indicate that infiltration of aluminum into composite-ceramic preforms containing B₄C, TiB₂, AlB₁₂, SiC, and/or TiC is feasible. Exothermic boosting can be used to produce composite preforms rich in either B₄C or SiC (>80 vol%). EXOBOOST computer program calculations indicate that SHS of B₄C-TiB₂, B₄C-TiC, and SiC-TiC preforms is possible. Preliminary SHS-processing studies of TiC suggest that preform microstructure is strongly influenced by reactant-greenbody properties and processing.

ACKNOWLEDGMENTS

Work performed under the auspices of the U.S. Department of Energy by the Lawrence Livermore National Laboratory under Contract W-7405-Eng-48.

REFERENCES

- [1] D.C. Halverson and R.L. Landingham, U.S. Patent No. 4,718,941, *Infiltration Processing of Boron Carbide-, Boron-, and Boride-Reactive Metal Cermets*, Jan. 12, 1988.
- [2] D.C. Halverson, A.J. Pyzik, and I.A. Aksay, "Processing and Microstructural Characterization of B₄C-Al Cermets," *Ceram. Eng. Sci. Proc.* 6(7-8), 736 (1985).
- [3] D.C. Halverson, A.J. Pyzik, I.A. Aksay, and W.E. Snowden, "Processing of Boron Carbide-Aluminum Composites," *J. Amer. Ceram. Soc.*, 72(5) (1989).

- [4] D.C. Halverson, A.J. Pyzik, and I.A. Aksay, U.S. Patent No. 4,605,440, *Boron-Carbide-Aluminum and Boron-Carbide-Reactive Metal Cermets*, Aug. 12, 1986.
- [5] D.C. Halverson, B.Y. Lum, and Z.A. Munir, "The Combustion Synthesis of Boride Composites," in *Proceedings of the Symposium on High Temperature Materials Chemistry—IV*, Eds. Z.A. Munir, D. Cubicciotti, and H. Tagawa (The Electrochemical Society, Inc., Pennington, 1988), p. 613.
- [6] A.G. Merzhanov, "Self Propagating High Temperature Synthesis of Refractory Compounds," *Vestnik Akad. Nauk USSR* [10] 76-86 (1976).
- [7] W.A. Stuttler and B.Y. Lum, Lawrence Livermore National Laboratory, Private Communication (1987).
- [8] D.C. Halverson and K.H. Ewald, *EXOBOOST Combustion Synthesis Computer Program* (D.C. Halverson and K.H. Ewald, Modesto, 1988). Copies available from the authors.
- [9] *Thermodynamics of Certain Refractory Compounds, Vol. I: Discussion of Theoretical Studies*, Ed. H.L. Schick (Academic Press, New York, 1966), p. 491.
- [10] O. Kubaschewski and C.B. Alcock, *Metallurgical Thermochemistry* (Pergamon Press, Oxford, 1979), p. 316.
- [11] L.B. Pankratz, J.M. Stuve, and N.A. Gokcen, *Thermodynamic Data for Mineral Technology*, U.S. Department of the Interior, Bureau of Mines Bulletin 677, p. 101 (1984).
- [12] M.W. Chase, Jr., C.A. Davies, J.R. Downey, Jr., D.J. Frurip, R.A. McDonald, and A.N. Syverud, *JANAF Thermochemical Tables, Third Edition, Part I, Al-Co* (American Chemical Society and American Institute of Physics, Midland, 1985), p. 274.

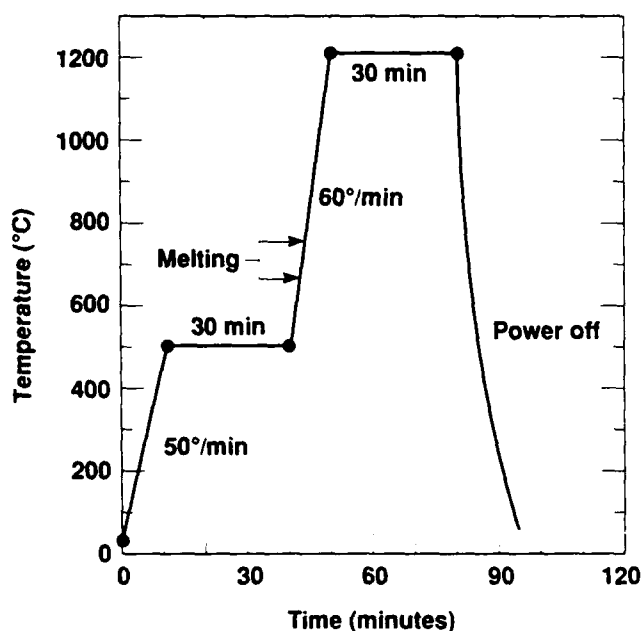


Figure 1. Temperature-time profile used on the ASDMS to obtain the contact-angle data of Fig 4.

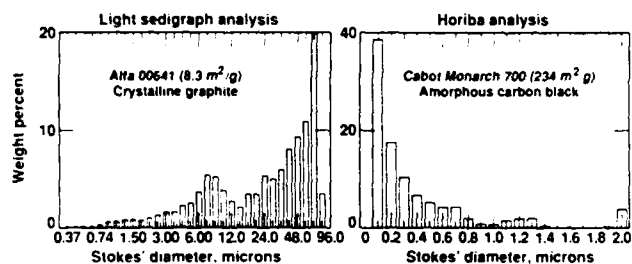


Figure 3. Particle-size distributions for carbon powders.

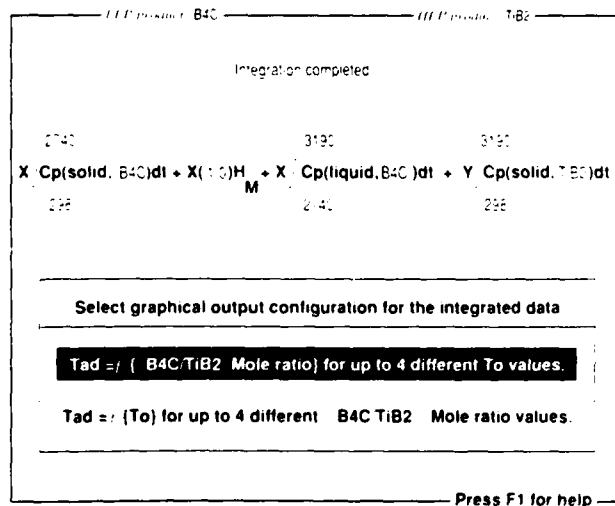


Figure 5. EXOBOOST integration screen offering different data output choices.

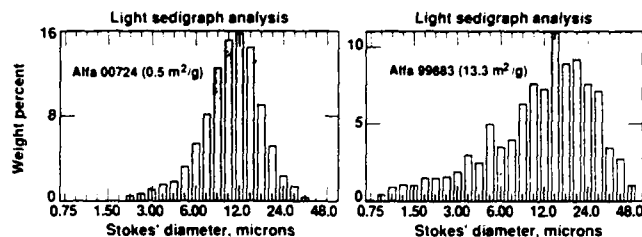


Figure 2. Particle-size distributions for titanium powders.

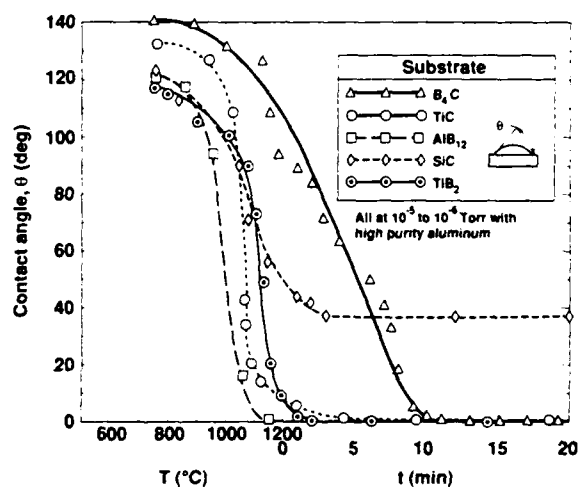


Figure 4. Contact-angle data of aluminum on hot-pressed B_4C , TiC , AlB_{12} , SiC , and TiB_2 .

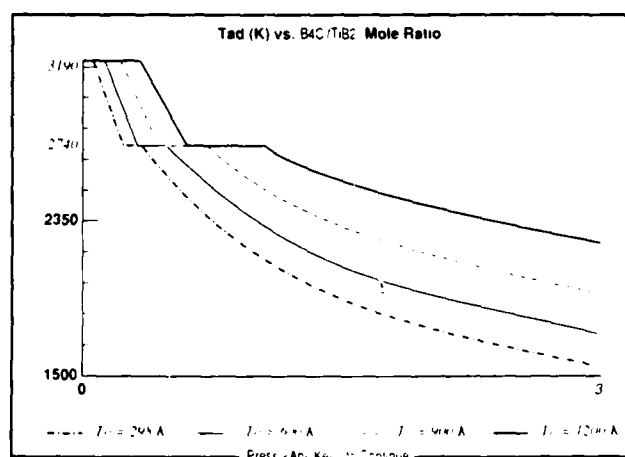


Figure 6. EXOBOOST output for fabricating B_4C - TiB_2 preforms.

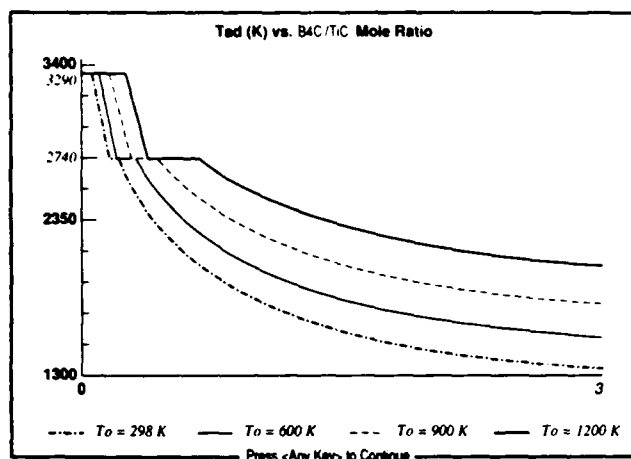


Figure 7. EXOBOOST output for fabricating B_4C -TiC preforms.

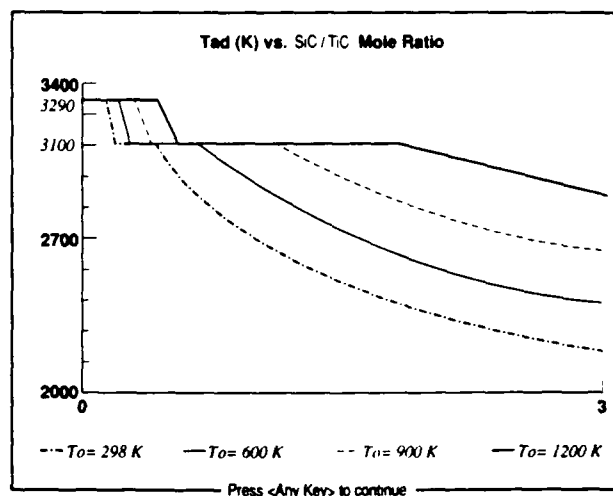


Figure 8. EXOBOOST output for fabricating SiC-TiC preforms.

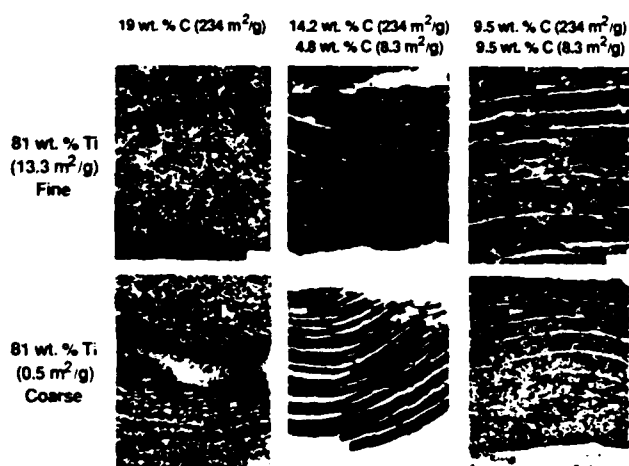


Figure 9. Influence of titanium reactant particle size on SHS-produced TiC microstructures. All samples were vibratory mixed 5 minutes, axially pressed at 10,000 psi, and outgassed at 500 °C, 200 mTorr for 3.5 hours. (Scale bar = 0.5 mm.)

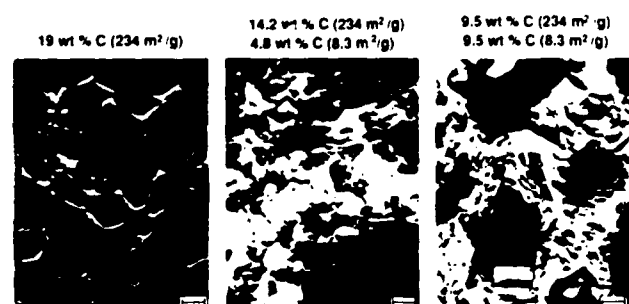


Figure 11. Influence of carbon reactant type on SHS-produced TiC microstructures. All samples contained 81 wt. % Ti (13.3 m²/g), were vibratory mixed for 5 minutes, axially pressed at 10,000 psi, and outgassed at 500 °C, 200 mTorr for 3.5 hours. (Scale bar = 5.0 μ m.)

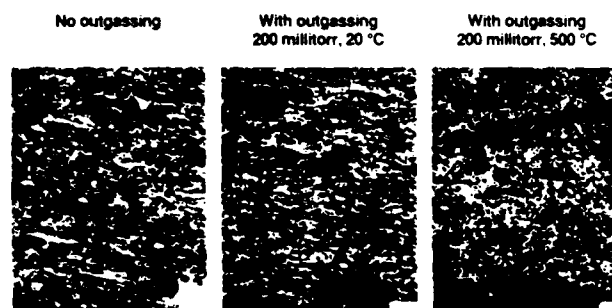


Figure 10. Effect of precombustion outgassing on SHS-produced TiC microstructures. All samples were 81 wt. % Ti (13.3 m²/g) plus 19 wt. % carbon black (234 m²/g), vibratory mixed for 5 minutes and axially pressed at 10,000 psi. (Scale bar = 0.5 mm.)

TABLES

Table 1. Powder impurity levels (> 0.1 wt%).

	Titanium		Carbon	
	0.5 m²/g	13.3 m²/g	8.3 m²/g	234 m²/g
O	0.5	0.8	0.7	6.5
N	0.8	-	0.6	0.6
H	0.2	0.2	-	0.7
C	-	0.2	-	-
Zr	0.5	0.5	-	-
Ca	0.4	-	-	-
Al	0.2	-	0.2	-
Si	-	-	0.1	-
Fe	-	-	0.1	-

Table 2. Thermodynamic properties, theoretical densities, and typical hardness ranges for the LEPP and HEPP phases studied.

Phase	T_{melt} (K)	T_{deg} (K)	ΔH_f^0 (cal/mol)	ρ_{th} (g/cm³)	H (kg/mm²)
B_4C	2740	1000	-17,000	2.52	2750-4950
TiB_2	3190	3190	-77,400	4.50	3000-3600
SiC	3100	1800	-16,000	3.17	2100-3300
TiC	3290	3290	-44,100	4.93	1550-3200

COMBUSTION CHARACTERISTICS OF SOLID - SOLID SYSTEMS

EXPERIMENT AND MODELING

S. Kumar, J.A. Puszynski and V. Hlavacek

CHEMICAL ENGINEERING DEPARTMENT

STATE UNIVERSITY OF NEW YORK AT BUFFALO

AMHERST, N.Y. 14260

ABSTRACT

The combustion characteristics of molybdenum - silicon system have been studied both experimentally and theoretically. The simple surface reaction controlled model has been proposed for the systems in which the product layer exhibits a porous microstructure.

The combustion front velocity, the maximum combustion temperature as well as the axial temperature distribution for different degree of dilution and average molybdenum particle sizes are in good quantitative agreement with experimental measurements.

INTRODUCTION

There is a significant number of the theoretical [1-5] and experimental [6-8] papers on the combustion processes of both gas - solid and solid - solid systems. However, there are only a few papers [9-11] comparing experimental observations with numerical simulation. Quantitative simulation of solid - solid reactions in the combustion regime is very difficult due to the lack of information on the reaction mechanism as well as physical properties of solid reactants and products at elevated temperatures.

In this paper we have made an attempt to i) understand the reaction mechanism in a system where one of the reactants does not melt and the product formed in this reaction exhibits porous microstructure.
ii) compare the experimental observations of the reaction front propagation with the numerical results.

As a modeling reaction we have chosen molybdenum - silicon system which was previously studied experimentally [12-14].

EXPERIMENTAL APPARATUS AND PROCEDURE

The synthesis of molybdenum disilicide from molybdenum powder of different particle sizes and silicon was carried out in the reactor chamber (see Fig. 1) at atmospheric pressure of argon. The cylindrical specimens were formed from well mixed reactant powders in a cold-pressing operation and latter ignited by a resistively heated grafoil filament.

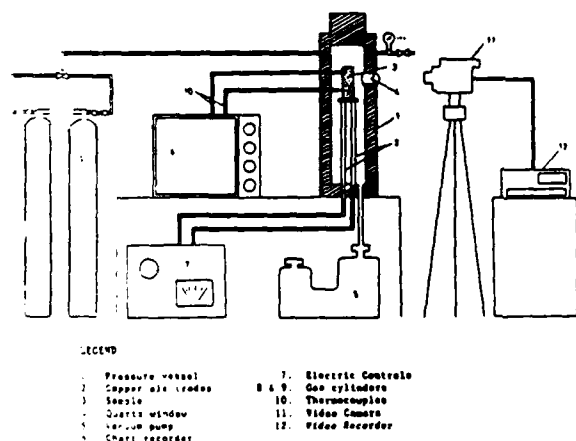


Figure 1. Experimental set-up.

The uniformity of the dispersion was varified by SEM micrographs. Thermal conductivity was measured using a steady state technique. The reactant powders were analyzed for the particle size, shape and structure using scanning electron microscope. The reactants and product were also analyzed

for elemental composition using emission spectroscopy and X-ray diffraction. Both axial and radial temperature profiles were measured by using tungsten/ 5% rhenium - tungsten/ 26% rhenium thermocouples that were inserted in the cylindrical pellets. The propagation of the combustion front was recorded using RCA video camera/ recorder system. Frame by frame analysis of the combustion front propagation was done to characterize the mode of combustion and the combustion front velocity.

EXPERIMENTAL RESULTS

The effect of a set of parameters such as reactant composition, specimen density and diameter, initial temperature, reactant particle size and degree of dilution on the combustion wave propagation and product composition has been studied.

Molybdenum powders with different particle sizes obtained from Van Lac Oid Co., N.J. of minimum purity 99.98% and amorphous silicon from ROC/RIC of minimum purity 99% were used in these experiments. The dilution of the reactant mixture was achieved by using excess of silicon or molybdenum disilicide. Reactants, when mixed, in stoichiometric proportions after reaction always gave tetragonal single phase molybdenum disilicide. The phase composition remained unchanged even when the reactant mixture was diluted by excess of silicon or/and molybdenum disilicide. The micrographs (see Fig. 2a) show the reactant metal particles which appear to be largely spherical and porous. The product particles obtained also appear to be porous and retained the spherical shape (see Fig. 2b).

Molybdenum disilicide produced by SHS technique exhibits also significantly (more than two times) higher specific surface area than molybdenum powder.

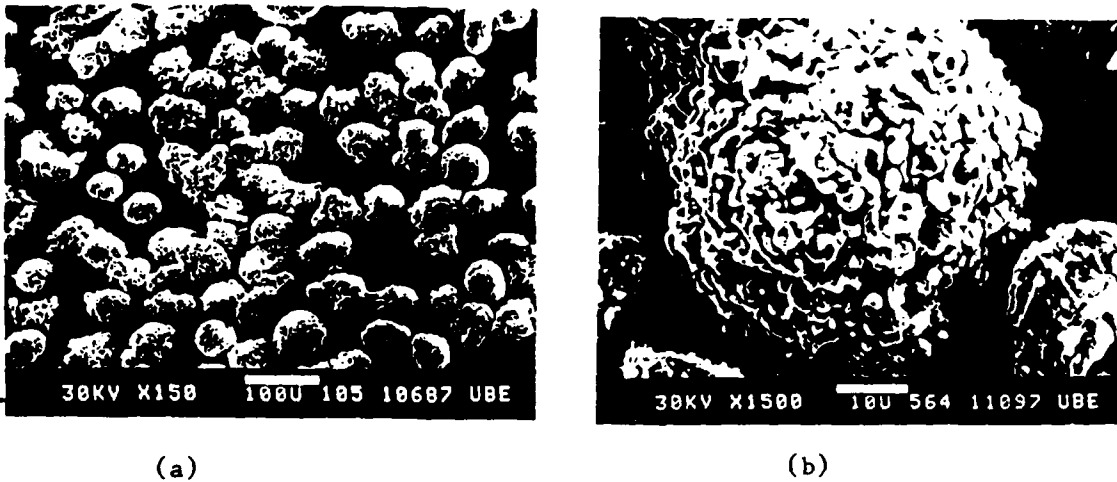


Figure 2. The micrographs of the molybdenum and molybdenum disilicide particles.

It indicates that the product formed in this reaction has porous microstructure. The effect of dilution by molybdenum disilicide, and the effect of average molybdenum particle size on the combustion front velocity and comparison with numerical simulations are presented in Figures 3 and 4.

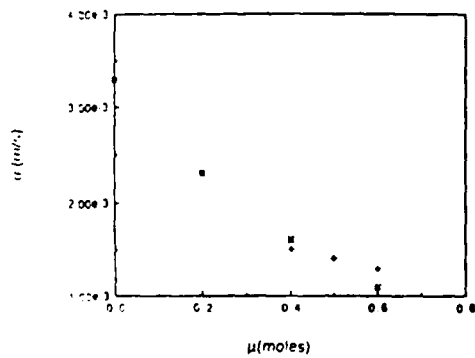


Figure 3. Effect of dilution on combustion front velocity

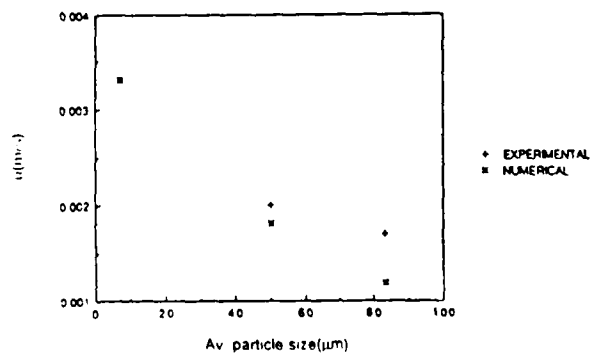


Figure 4. Effect of average Mo particle size on combustion front velocity

MODEL FORMULATION

The analysis of solid - solid combustion reactions in the SHS regime is quite difficult due to the complex interaction between solid reactants.

A majority of reaction models describing reaction between two solid compounds, assumes that the diffusion process of one or both reactants through the product layer is the rate determining step. These models also assume that the chemical reaction and nucleation of the new phase are significantly faster than diffusion through the product layer. Such assumption is valid for many solid - solid as well as solid - gas systems where the solid product is formed as a continuous film which separates both reactants. However, in many cases the morphological structure of the nonmelting reactant as well as a formed product is porous due to the nature of a reaction or due to the crack development caused by large microthermal stresses. In such cases the more "mobile" solid reactant has quite good access into the unreacted core of a second reactant. The effect of diffusion through the product layer is limited to the diffusion through the submicron product layers formed on micrograins of a porous particle. This type of diffusion should not be affected by particle size of a nonmelting reactant.

Based on the above analysis we have assumed in our model that the reaction rate is proportional to the surface area of the fraction of unreacted nonmelting compound.

The reaction between two reactants where one of them does not melt during reaction and a product exhibits a porous microstructure is described by:



The reaction rate at the interface reads:

$$-\frac{dN_A}{dt} = k_s e^{-E/RT} 4\pi r_c^2 c_{AR} M_A \quad /1/$$

The molar rate of consumption can be expressed as follows:

$$\frac{dN_B}{dt} = \frac{1}{a} \frac{dN_A}{dt} = \rho_B M_B 4\pi r_c^2 \frac{dr_c}{dt} \quad /2/$$

where: M_A, M_B - molecular weight of reactants, kg/kmol

ρ_B - density of nonmelting reactant, kg/m³

k_s - pre-exponential factor, m/s

E - activation energy, J/kmol

R - universal gas constant, J/kmol.K

a - stoichiometric coefficient

R_p - average particle radius, m

r_c - reaction front interface position, m

C_{AR} - initial concentration of more "mobile" reactant kg/m³

Defining the extent of conversion of the solid particle as:

$$\eta = 1 - \left(\frac{r_c}{R_p}\right)^3 \quad /3/$$

and rearranging the equations /1/ and /2/ we obtain:

$$\frac{d\eta}{dt} = \frac{M_A k_s e^{-E/RT} C_{AR}}{a M_B \rho_B R_p} (1 - \eta)^{0.667} \quad /4/$$

The kinetic constant k_s and the activation energy E have been determined experimentally using the Merzhanov's approach [2] and from DTA measurements [16]. A good agreement between both techniques was found.

The numerical simulations of combustion wave propagation in the cylindrical specimen were performed using one-dimensional model. The heat and material balances for the semi-infinite cylindrical body are:

$$\frac{\partial T}{\partial t} = \frac{\lambda}{\rho_p c_p} \frac{\partial^2 T}{\partial x^2} + (-\Delta H)_m \frac{1}{c_p} w_m \frac{\partial \eta}{\partial t} - \frac{4h}{\rho_p c_p D} (T - T_0) \quad /5/$$

$$\frac{\partial \eta}{\partial t} = f(\eta, T) \quad /6/$$

The initial conditions are:

$$t = 0 \quad 0 < x < \infty : T = T_0, \quad \eta = 0$$

The boundary conditions are:

$$\begin{aligned} t > 0 \quad x = 0 & : T = T_p \\ x \longrightarrow \infty & : T = T_0 \end{aligned}$$

where:

- ρ_p - pellet density, kg/m^3
- λ - thermal conductivity, W/m.K
- c_p - heat capacity, J/kg.K
- $(-\Delta H)_m$ - heat of reaction/ mass of the limiting reactant, J/kg
- w_m - mass fraction of the limiting reactant
- h - heat transfer coefficient, $\text{W/m}^2\text{K}$
- D - specimen diameter, m
- T_0 - ambient temperature, K

The equations /5/ and /6/ were solved using the parameter values given in Table 1. A fourth order finite difference technique has been used to approximate the governing equations [4].

DISCUSSION AND CONCLUSION

The experimental results of the combustion front propagation as a function of dilution by final product or by silicon together with those numerically calculated are presented in Fig.3. The velocity of the reaction front, the maximum combustion temperature as well as the temperature distribution and the extinction point are in a very good quantitative agreement.

The effect of the average particle size on the rate of propagation has shown slightly higher discrepancy between the experimental observations and the numerical results for larger molybdenum particles (see Fig. 4). This discrepancy might be explained by the fact that the average product particle size was smaller than the molybdenum particle size, apparently due to the enormous intraparticle thermal stresses during the combustion synthesis. It has been also demonstrated that the simple surface reaction controlled model might be a very useful approximation in the case of solid - solid reactions where a product exhibiting porous microstructure is formed. Such a porous structure allows relatively easy access of one, usually low melting component, to the surface of the second reactant. However, a more extensive study, including the analysis of other systems, is required in order to fully justify the use and applicability of this model.

TABLE 1

Kinetic and physico-chemical data for molybdenum - silicon system [16].

Heat capacity	J/kg.K	607.0
Thermal conductivity	W/m.K	1.8
Pellet density	kg/m ³	2520.0
Heat of reaction	J/kg	1.38 10 ⁶
Heat transfer coefficient	W/m ² .K	75.0
Activation energy	J/mole	99,722.
Pre-exponential factor	m/s	2.349
Mo average particle radius	m	5.0 - 50.0 10 ⁻⁶
Degree of dilution		0 - 60%

REFERENCES

1. Shkadinsky K.G., Khaikin B.I. and Merzhanov A.G.: Propagation of Pulsating Exothermic Reaction Front in the Condensed Phase; Combustion, Explosion and Shock Waves 7, 15-22, (1971).
2. Merzhanov A.G.: SHS Process: Combustion Theory and Practice; Archivum Combustionis 1, 23-48, (1981).
3. Matkowsky B.J. and Sivashinsky G.I.: Propagation of a Pulsating Reaction Front in a Solid Fuel Combustion; SIAM J Appl. Math 35, 465, (1978)
4. Puszynski J.A., Degreve J. and Hlavacek V.: Modeling of Exothermic Solid-Solid Noncatalytic Reactions; Ind. Eng. Chem. Res. 26, 1422-1434, (1987)
5. Puszynski J.A., Jayaraman V.K. and Hlavacek V.: A Stefan Problem for Exothermic Noncatalytic Reactions; Int. J. Heat Mass Transfer 28, 1237-1239, (1985)
6. Merzhanov A.G., Filonenko A.K. and Borovinskaya I.P.: New Phenomena in Combustion of Condensed Systems; Dokl. Phys. Chem. 208, 122-125, (1973)
7. Holt J.B. and Munir Z.A.: The Fabrication of SiC, Si₃N₄, and AlN by Combustion Synthesis; Proceedings of the First International Symp. on Ceramics for Engine 721-728, (1983)
8. Merzhanov A.G., Shkiro V.M. and Borovinskaya I.P.: Method of Producing Refractory Carbides, Borides, Silicides, Sulfides and Nitrides of Metals of Group IV, V, and VI of the Periodic System; US 3,726,643
9. Holt J.B., Kingman D.D. and Bianchini G.M.: Kinetics of the Combustion Synthesis of TiB₂; Materials Science and Engineering 71, 321-327, (1985)
10. Booth F.: The Theory of Self-Propagating Exothermic Reactions in Solid Systems; Trans. Faraday Soc. 44, 790, (1953)
11. Hardt A.P. and Phung P.V.: Propagation of Gasless Reactions in Solids - Analytical Study of Exothermic Intermetallic Reaction Rates; Combustion

- and Flame 21, 77-89, (1973)
- 12 Sarkisyan A.R., Dolukhanyan S.K., Borovinskaya I.P. and Merzhanov A.G.:
Laws of the Combustion of Mixtures of Transition Metals with Silicon and
the Synthesis of Silicides; Fiz. Goreniya i Vzryva 14, 49-55, (1978).
- 13 Kostikov V.I., Levin N.P. and Levin B.Ya.: Reaction of Liquid Silicon
with Refractory Metals; Neorg. Materialy 5, 152-154, (1969)
- 14 Novikov N.P., Borovinskaya I.P. and Merzhanov A.G.: Thermodynamic
Analysis of Reactions of Self-Propagating High-Temperature Synthesis (in
Russian) Preprint, Branch Institute of Chemical Physics Academy of
Sciences of the USSR, Chernogolovka (1975)
- 15 Beek J.: Design of Packed Bed Reactors; Adv. in Chem. Engng. 3, (1962)
- 16 Kumar S.: Self-Propagating High Temperature Synthesis of Ceramic
Materials; PhD Dissertation, State University of New York (1988)

Microstructure of TiB_2 Sintered by Self Combustion Method

by K. Urabe, Y. Miyamoto*, M. Koizumi and H. Ikawa**
Faculty of Science and Technology, Ryukoku University, Oe-cho Seta
Otsu-sity 520-21, Japan

*Institute of Scientific and Industrial Research, Osaka University
Ibaraki, Osaka 567, Japan

**Tokyo Institute of Technology, Ookayama Meguro-ku
Tokyo 152, Japan

Abstract

The simultaneous formation and sintering of TiB_2 was investigated. The resulting material showed an equi-granular structure with grain sizes $>1\mu m$. Coherent grain boundaries were frequently observed. A new phase was found in grain boundaries and b-axis of the base was as long as $3/2$ times that of TiB_2 .

Introduction

Recently, a self combustion synthesis has been applied to produce sintered bodies of high temperature materials without any additives (1). Takano, et al., have succeeded in producing TiB_2 sintered bodies by the self combustion reaction between Ti and B in an HIP apparatus. The sintered bodies consisted of fine-grained TiB_2 crystals. Densities of the sintered bodies reached more than 98% of the theoretical value, although they depended on the Ti/B mole ratio in starting mixtures. However, the reason the mole ratio affects the densities still remains unsolved.

The purpose of the present study is to describe the microstructure of a TiB_2 sintered body and provide new information which will contribute to solving the mechanism of the simultaneous sintering with a self combustion reaction.

Specimen used and Preparation of Thin Foil

Starting materials were powders of Ti (purity, 99.5%) and B (purity 95.0%) which were mixed with a Ti/B mole ratio of 0.58. The value was the optimum one to form sintered bodies with high density. The starting materials were mixed with ethanol in an agate mortar. The mixture was dried, then pressed into a pellet 15 mm in height and 17 mm in diameter. The surface of the pellet was coated with BN powder and was isostatically pressed at room temperature at 100 MPa, followed by degassing at 500°C for two hours in a pyrex glass tube. After degassing, the specimen was sealed into the glass tube. The sealed specimen was placed in a carbon crucible which was filled with a mixture of Ti and B powders, was put into a pressure vessel, and was heated to 700°C. After the pyrex glass tube was softened, pressure was loaded by injecting argon gas into the vessel until the pressure increased to 100 Mpa.

The powders in the crucible were ignited by passing a current of 100 ampere for 2 or 3 seconds through a carbon ribbon heater which was placed at the top of the crucible.

The bulk density of the sintered body was measured by the Archimedes method.

Thin sections were prepared for the TEM observations. A section cut out from the specimen was ground to a thin foil with a thickness of about 30 μm and was thinned by ion bombardment using argon gas.

The thinned specimen was observed by high resolution type TEM (HITACH H-1250) equipped with a double tilt goniometer operating at 1,000 kV.

Results and Discussion

The specimen was observed at low magnification at the beginning (Figure 1). Almost all of the grains were less than 1 μm in size and no grain boundary

phase was observed. Traces of grain boundaries often appeared as straight segments of lines which were marked with open circles in this Figure. These characteristic grain boundaries were considered to be closely related to the crystal habit of TiB_2 .

Figure 2 shows details of the grains. An electron diffraction pattern from one of the grain was also shown in the inset in this figure. The grain was identified as TiB_2 from the diffraction pattern which was consistent with the reciprocal plane normal to $[101]^*$ of TiB_2 . The trace of the grain boundary marked by an arrow in the figure was parallel to (001) of TiB_2 . These facts indicate that the grains often retain idiomorphic faces of the TiB_2 crystal.

An X-ray diffraction pattern of the sintered body indicated the existence of a small amount of Ti_3B_4 . The phase was observed as large particles under the TEM observation. Figure 3 shows a Ti_3B_4 grain with irregular form. The inset of this figure is an electron diffraction pattern from the grain which could be indexed with the reciprocal lattice of Ti_3B_4 .

No grain boundary phase was observed except in the case where an unidentified phase existed in the marginal zones of grains. Figure 4 shows an example of the fact that different electron diffraction pattern could be observed in a grain. The central part of the grain gave an electron diffraction pattern which could be identified as a TiB_2 crystal. The marginal zone gave a quite similar diffraction pattern to that observed in the center of the grain, but the repeat distance along the c-axis was different. These two electron diffraction patterns are shown in the insets of Figure 4. The latter diffraction pattern could be indexed by a new lattice which has $3/2$ times the repeat distance along the c-axis of TiB_2 . The result is shown in Figure 5, which represents the fact that the two phases maintain an axial relationship to

each other.

There were many cases in which two TiB_2 grains contacted directly at a grain boundary giving rise to a coherent structure.

Figure 6 shows a coherent grain boundary between two TiB_2 grains. The two grains are in an orientation similar to each other. The insets in Figure 6 are optical transforms for the corresponding regions. The orientation of the bright region in this figure deviates slightly from that of the dark region, the $[110]$ axis being common in the two grains. The orientation relationship is shown schematically in Figure 7.

The characters of the microstructure of the TiB_2 sintered body prepared by self combustion reaction could be summarized as follows:

1. The specimen shows an equi-granular structure with grain sizes less than $1\ \mu\text{m}$.
2. The grain often retains idiomorphic crystal faces.
3. There are many grain boundaries where coherent grain boundary structures are maintained.
4. These characteristic microstructures should originate from processing in which the specimen reach more than 3000°C .

References

1. Y. Miyamoto and M. Koizumi, "Potentiality of High Pressure Combustion Sintering to Produce Ceramic Based Multi-Phase Components," Proc. Int. Symp. on "sintering '87," Tokyo, 1987, in printing.
2. Y. Takano, S. Ohmura, Y. Miyamoto and M. Koizumi, "New Application of HIPing to Combustion Sintering of TiB_2 ," Proc. 3rd Int. Conf. on Isostatic Pressing, MPR Publishing Services Ltd., London (1986) pp. 21-1-11.

Figures

- Fig. 1 Microstructure of a TiB_2 sintered body.
- Fig. 2 Microstructure of a TiB_2 sintered body.
- Fig. 3 A grain of Ti_3B_4 in TiB_2 sintered body.
- Fig. 4 Microstructure of a marginal zone of a grain showing the existence of an unidentified phase.
- Fig. 5 Reciprocal lattice and electron diffraction patterns of an unidentified phase.
- Fig. 6 Coherent grain boundary between two TiB_2 grains.
- Fig. 7 Schematic illustration of an orientation relation between two grains.

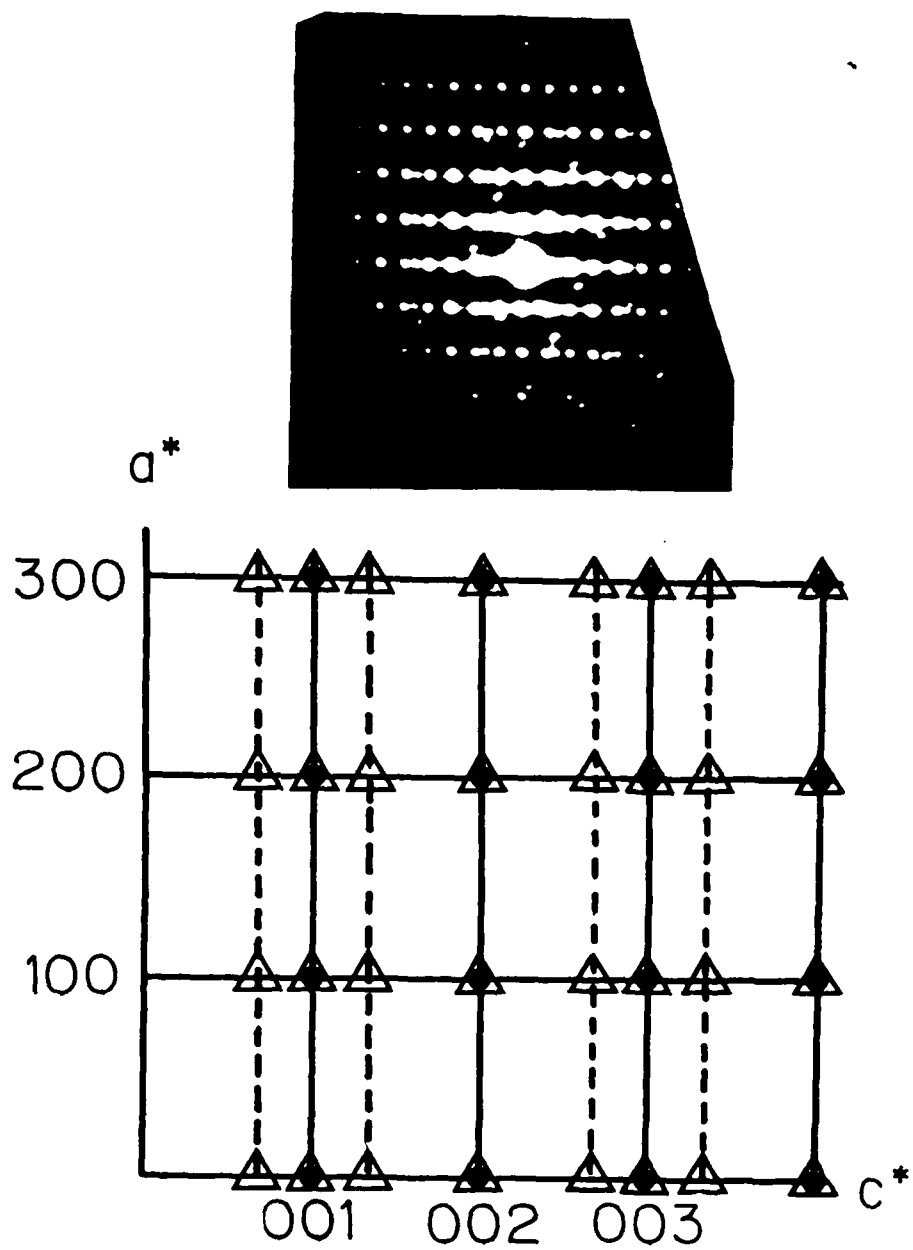
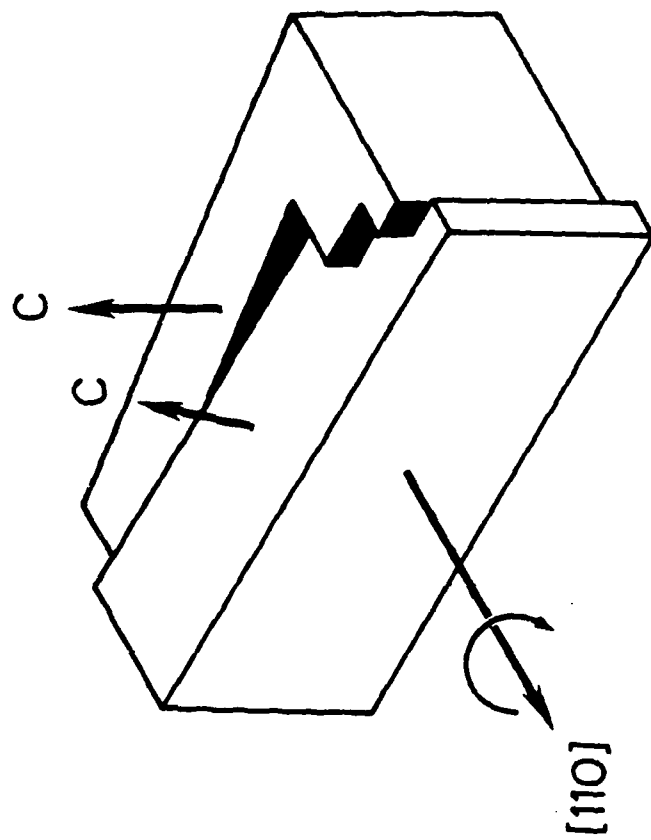


Figure 5

5

877

Fig. A
7



677

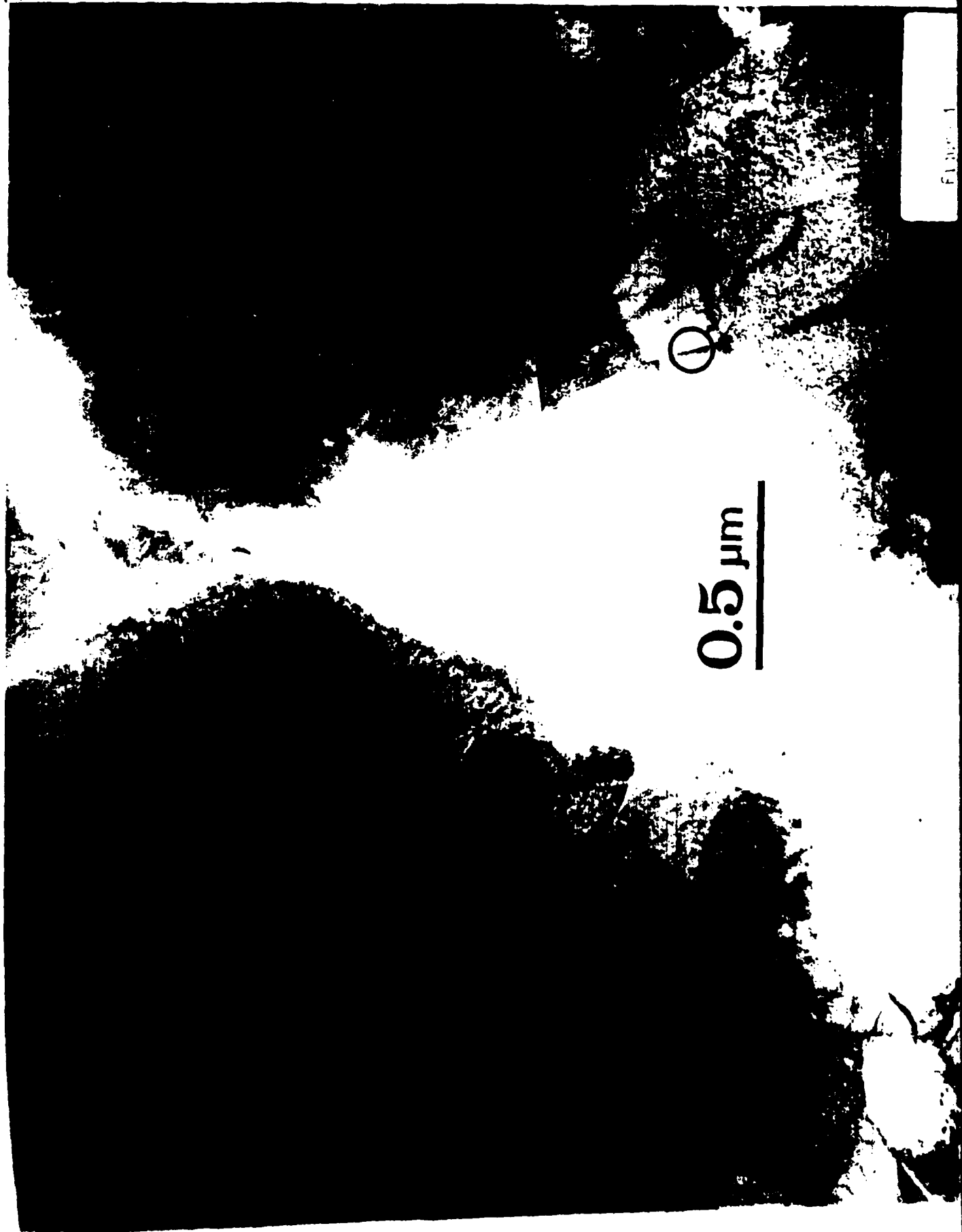


Figure 1

0517

Figure 2



1a.

45h

1 μm

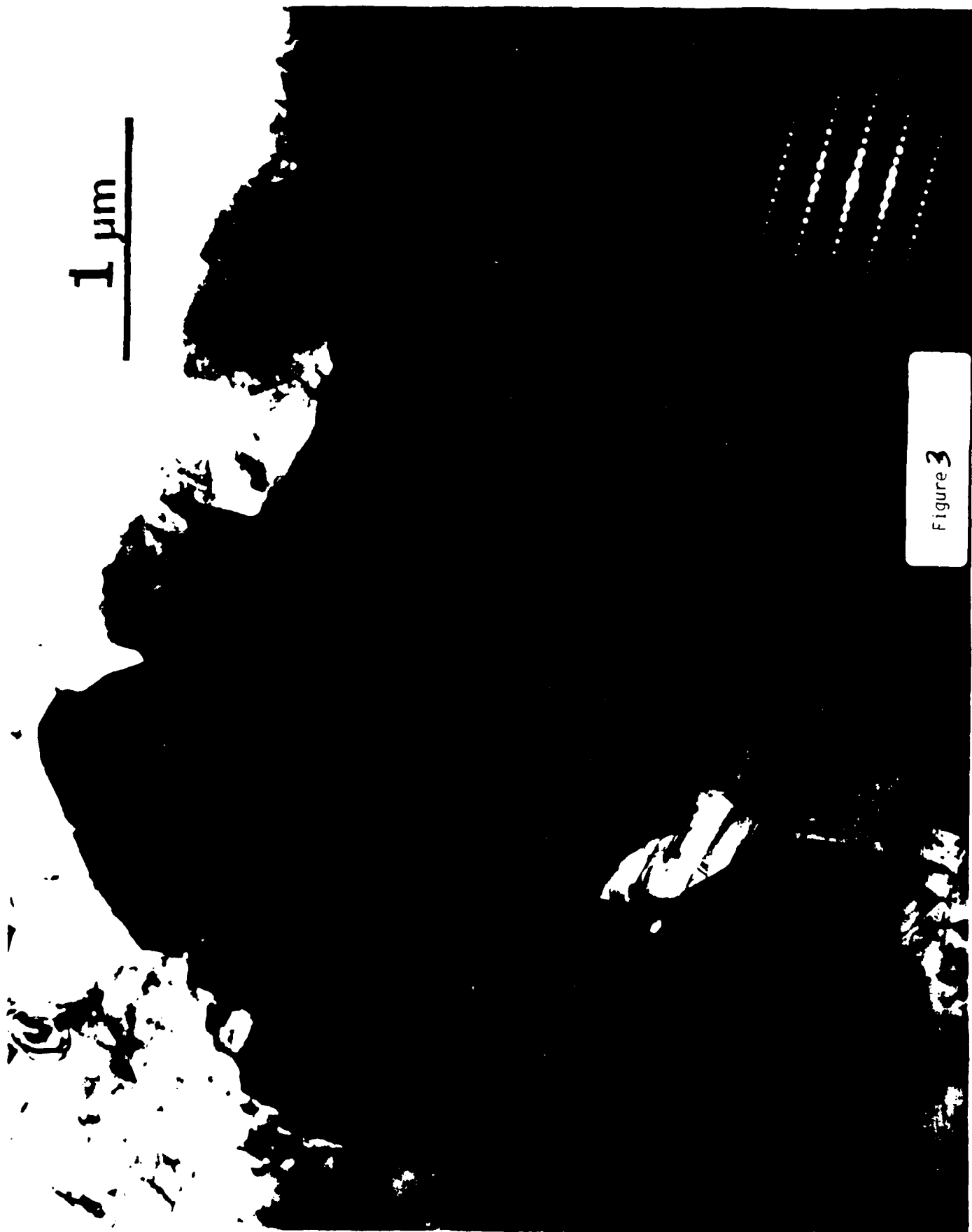
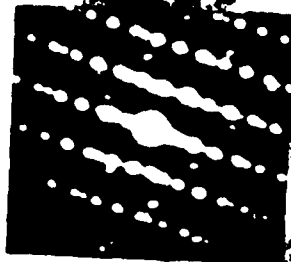


Figure 3

Fig 3

15h



0.1 μm

Figure 4

Fig 4

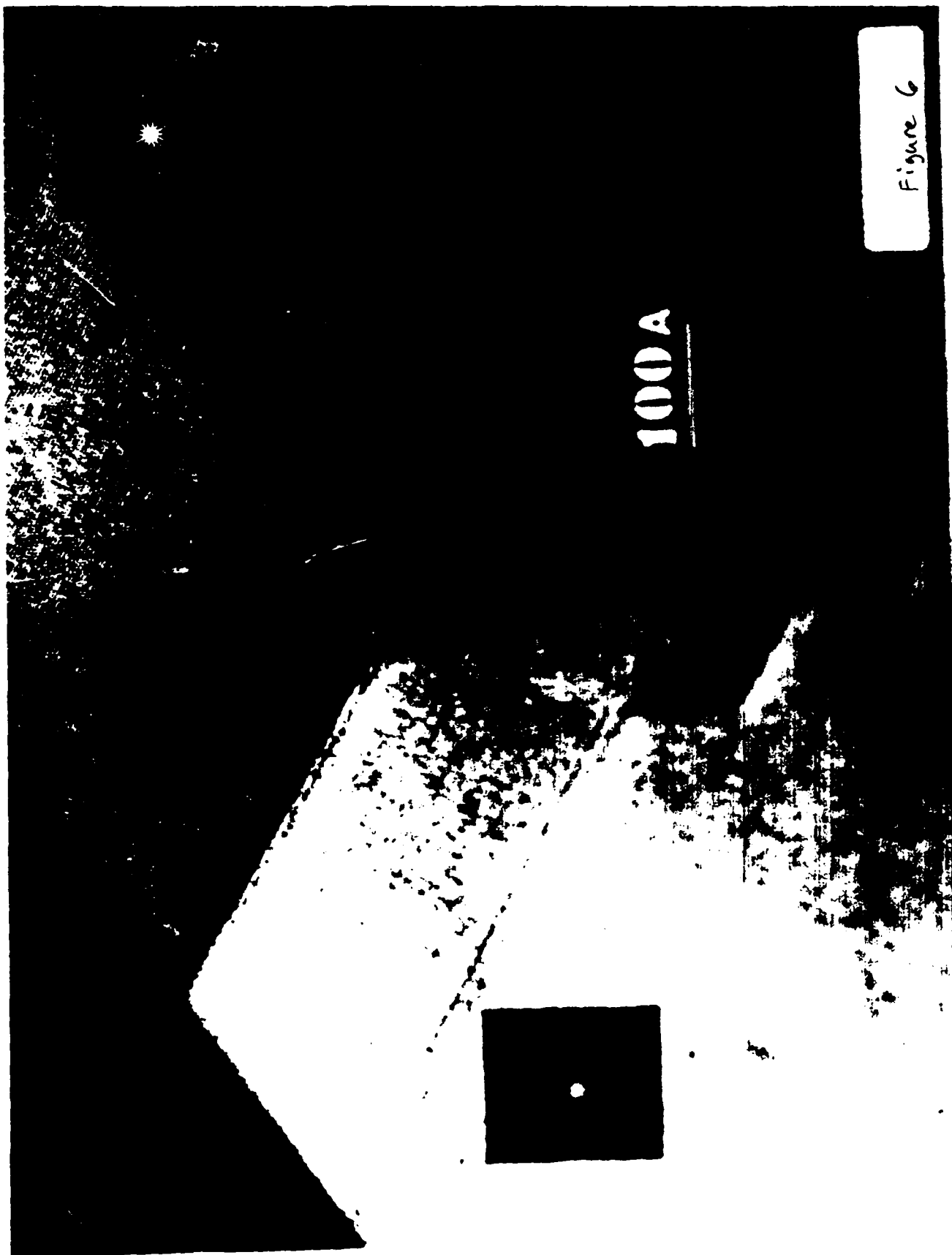


Figure 6

100A

452

452

A Laser Ignition Study of Gasless
Reactions Using Thermography

Charles T. S. Chow
Lawrence Livermore National Laboratory
Livermore, California

Jonathon H. Mohler
EG&G Mound Applied Technologies, Inc.*
Miamisburg, Ohio

Abstract

The utilization of a laser for the ignition of gasless combustion reactions is demonstrated. Practical experimental methods and data reduction techniques are discussed.

*EG&G Mound Applied Technologies, Inc. is operated for the U. S. Department of Energy under Contract No. DE-AC04-89DP43495.

A Laser Ignition Study of Gasless Reactions Using Thermography

INTRODUCTION

Lasers provide many distinct advantages for studying the dynamics of pyrotechnic ignition. The beam is readily controlled, allowing one to apply a known power density to a precise location for an accurately known time. From a knowledge of the absorption spectra of materials to be tested and the wavelength of the laser radiation, one should in principle be able to predict, with confidence, the amount of energy absorbed by a sample during laser radiation. Several complications can spoil this ideal picture - sample surface finish, vaporization, decomposition, beam fluctuations and even air current. With some samples and at high power densities radiative losses can be significant as well.

Even under ideal conditions, a knowledge of the amount of energy absorbed alone may not be sufficient. One also needs to know the distribution of energy in the sample at ignition. This becomes a difficult experimental challenge in samples that are relatively poor thermal conductors, in which the temperature gradients are large and the effective heated spot size is small. Optical techniques, which are fast, non-obtrusive, and which can be arranged to give ample spatial resolution and which are capable of measuring very high temperatures, would seem to be ideally suited to observe the temperature distribution in a laser heated sample. Infrared scanning systems which can produce complete surface temperature records at video display and recording rates are commercially available. Using such a system to monitor a laser heated sample during ignition is a powerful experimental technique.

We have reported the initial results from the application of this method to the study of thermite ignition.^{1,2} The emphasis in these reports was on the application of standard ignition theory to interpretation of our data. Practical experimental methods and data reduction will be emphasized in this report.

TEST APPARATUS

A schematic view of the test system is shown in Figure 1. The beam from the 80w CO₂ laser is combined with the He Ne laser at the beam splitter and a minor portion of the CO₂ laser beam is split off to a small detector to monitor the length and shape of the laser pulse applied to the sample. The main portion of the beam is directed through a 10 inch focal length, zinc selenide lens, and then through a hole in a tungsten mirror mounted at 45 degrees to the beam axis. The beam passes through the sodium chloride window of the sample housing and impinges on the 3/4 inch diameter sample pellet. The sample housing is protected by a graphite sample cup. The power meter head mounted behind the sample housing is used to measure the power of the beam, prior to testing. Infrared radiation emitted from the test sample is reflected from the tungsten mirror into the thermographic scanner.

The small size of the sample housing, 2" x 2" x 3", permits mounting on translation stages for accurate location of the sample. The housing is fitted with a flexible high pressure tube for introduction of special gases or for evacuation or pressurization. ~~A photograph of the experimental apparatus is shown in Figure 2.~~
~~The standard scanner lens is shown in Figure 2, but~~ By use of a 3X lens and a six inch close-up lens, spatial resolution is improved to .0091 cm/pixel.

INSTRUMENTATION

used here
The scanner ~~seen in Figure 2~~ is part of the Inframetrics, Model 600 system. It is fitted with a selection of filters that can be inserted into the optical path within the scanner. Filter selection is controlled from the system console. A 6.9 micron cutoff filter blocks 10.6 micron energy reflected from the laser beam.

Two mirrors in the scanner provide for horizontal and vertical scanning. In one mode, the vertical scan mirror is stopped, causing repetitive horizontal scanning of a single line across the sample surface. The resulting video image in which the vertical axis is time and the horizontal axis is radial distance is shown in Figure 2~~1~~. An update of the temperature distribution along this line is provided every 125 microseconds. Ignition times ranging from a few milliseconds to a second or more can be obtained by judicious control of beam power.

The transiency of the ignition period makes it necessary to record the thermographic response. A high quality video tape recorder is important since noise, distortion or intensity shifts can have a severe effect on the accuracy of the temperature readings obtained during play back. We use a Sony 5800, 3/4 inch recorder. While it is often convenient to use search and freeze frame to locate and fix a selected field, the resulting intensity shift and/or distortion is often unacceptable. One should also be aware that video frames consist of two interlaced fields and that some recorders are not capable of freezing sequential fields. To avoid these problems, it is necessary to capture selected video frames in digital memory while the recorder is in play mode. Time encoding and time code reading capability is needed to identify and freeze a selected field. The digital freeze frame unit converts the intensity record back to an analog signal for transfer to the display monitor and/or PC-AT based data analysis system. During the complete process, from initial scan to final analysis, the intensity record goes through three analog to digital conversions. The first A/D conversion occurs in the scanner where microprocessor controlled gain is applied to correct the detector signal, which is reconverted for analog video output. A second A/D conversions is done to capture two video fields (one frame) in digital memory. The digitally stored fields are reconverted to an analog signal for transfer to the video processor board in the

PC-AT computer where the third A/D conversion occurs in preparation for digital processing of the intensity-space-time data. The integrity of the intensity scale is maintained by a gray scale at the bottom of each field. If needed, a gain and offset adjustment can be made at the frame store unit before the final A/D conversion.

DATA ANALYSIS

The final digitized image field can be processed using software supplied by Thermoteknix Systems Ltd. For the purpose of this project, only the data file formation function is used. This function stores experimental parameters such as sample emissivity, external optics transmission factors and reflected radiation along with instrument calibration and image intensity data. User programming is required to read and convert these data to temperature, distance and time values.

Final data analysis, which accomplishes smoothing and makes extraction of heat rise and thermal properties possible, involves fitting a function that accurately reproduces the observed thermal distribution. Ideally, the theoretically expected distribution function should be fitted to the experimental data. For a point source, this function is:

$$T(r) = T_0 + A/r \operatorname{erfc}(Br)$$

where $\operatorname{erfc}(r)$ is the conjugate error function of r , and $A=q/4k$ and $B = 1/2 \sqrt{\alpha t}$

The parameter T_0 is initial temperature, q is heat input in cal/s, k is thermal conductivity in cal/cm.deg and α is thermal diffusivity in cm/s. Unfortunately, $1/r \operatorname{erfc}(r)$ is not an explicit function that can be fitted to temperature - distance data. We have found that, for the range of r of interest in our experiments,

$1/r \operatorname{erfc}(r)$ can be accurately represented by the function:

$$V/r e^{-C(r)}$$

where V and C are adjustable parameters. Figure 3 illustrates the accuracy of this function for values taken from standard tables, over the range $r = 0.1$ to $r = 2$

Obviously, this function cannot represent real data at small values of r since it approaches infinity and since real laser beams cannot be focused to an infinitesimal spot radius. By setting $r = r_0 + r$ the simulant function can accurately represent real temperature distributions. Figure 4 indicates that the parameters of the simulant function can be adjusted to accurately represent an experimentally observed temperature distribution. An iterative Newton-Raphson approximation procedure is used to fit the temperature distribution function to experimental data.

It is interesting to note that the calculated beam radius at the sample, for our experimental setup, is 0.04 cm and the spot radius measured from the mark left by the laser beam in a MACOR sample is approximately 0.06 cm. The values r_0 obtained from fitting the simulant function to real data are in the range of $0.1 \pm .05$ cm.

The precision achieved by using the equipment and procedures described here are illustrated by the thermal rise data recorded for an inert sample, shown in Figure 5.

SUMMARY

Thermographic monitoring of laser ignition comprises a powerful experimental technique. Implementation of this technique requires careful attention to experimental detail and data handling procedures.

References

1. J. H. Mohler and C. T. S. Chow, Proc. 11th International Pyrotechnics Seminar, Vail CO, 1986, pp 789-800.
2. C. T. S. Chow and J. H. Mohler, Proc. 12th International Pyrotechnics Seminar, Juan-Les-Pins France, 1987, pp 55-60.

Figures

- Fig. 1 Laser ignition system
- Fig. 2 System display showing system responses in the horizontal direction
 as a function of time, vertical axis
- Fig. 3 Simulant function $v/r e^{-C(r)}$ fitted to value for $1/r \operatorname{erfc}(r)$ taken
 from standard tables
- Fig. 4 Simulant function fitted to real data points for an inert laser
 heated pellet
- Fig. 5 Thermal rise observed for an inert, $\text{Fe}_2\text{O}_3/\text{Al}_2\text{O}_3$ pellet

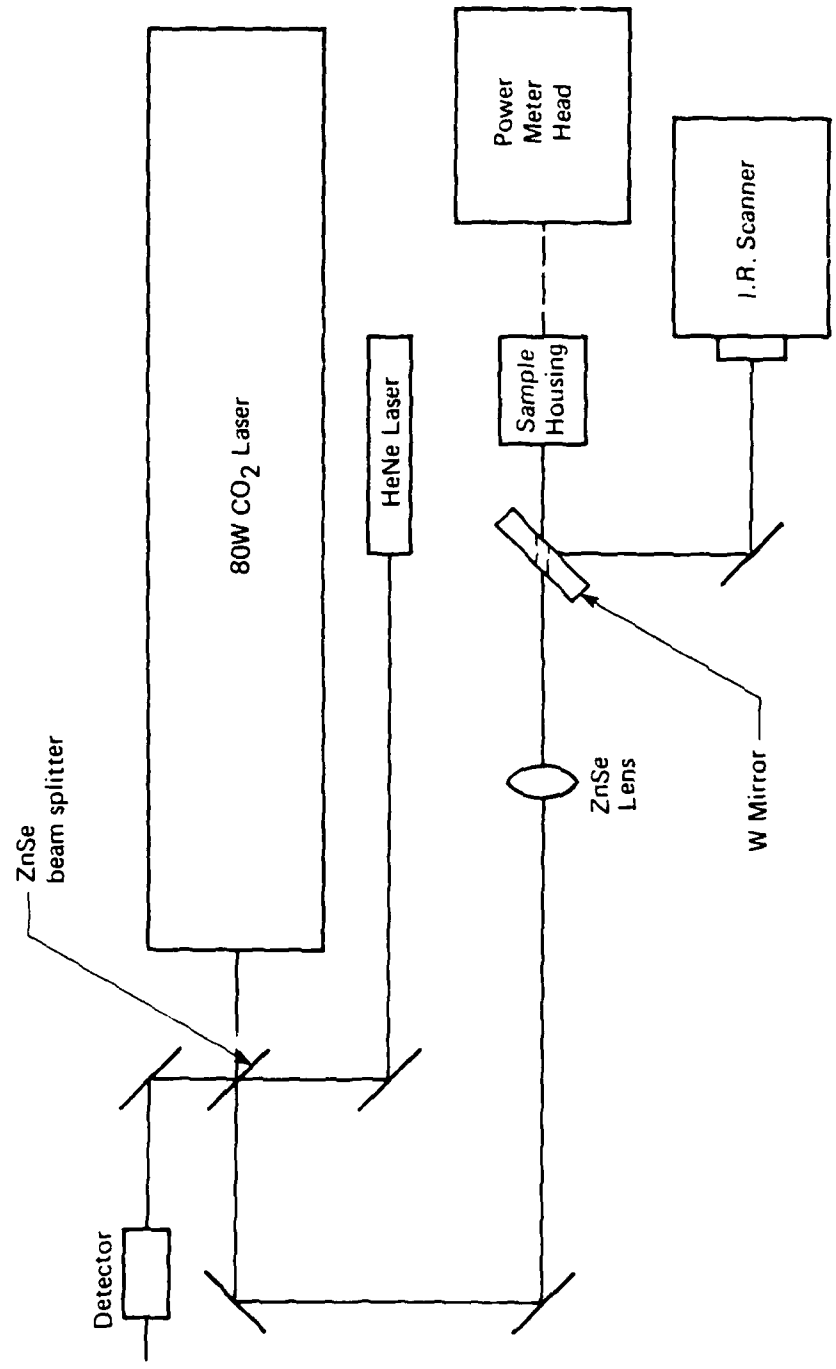
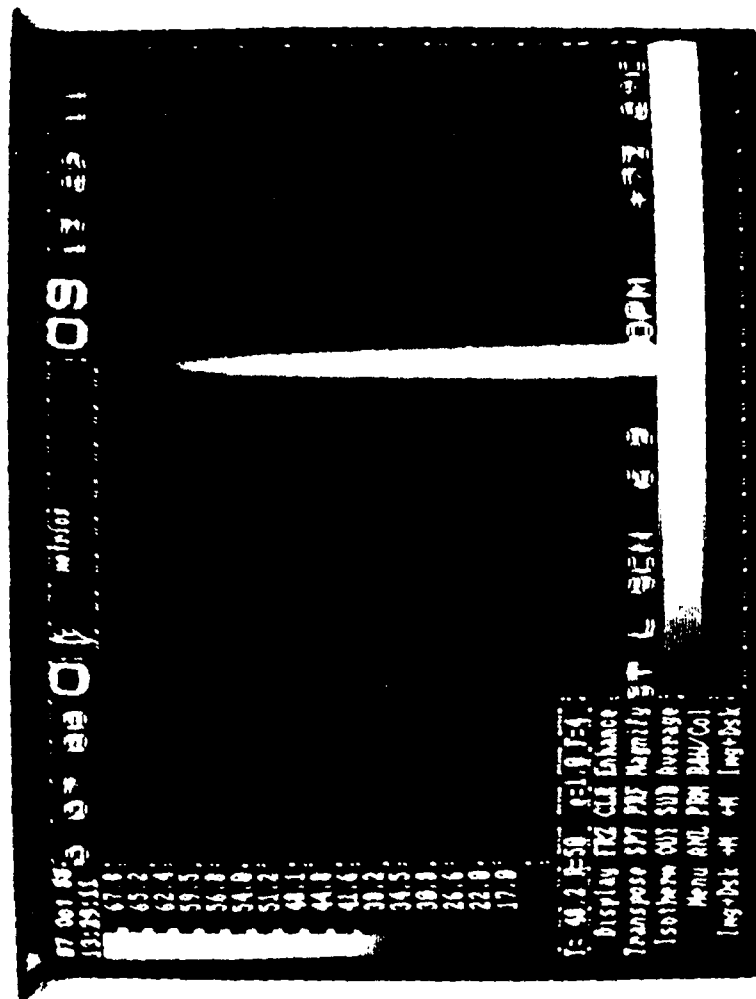


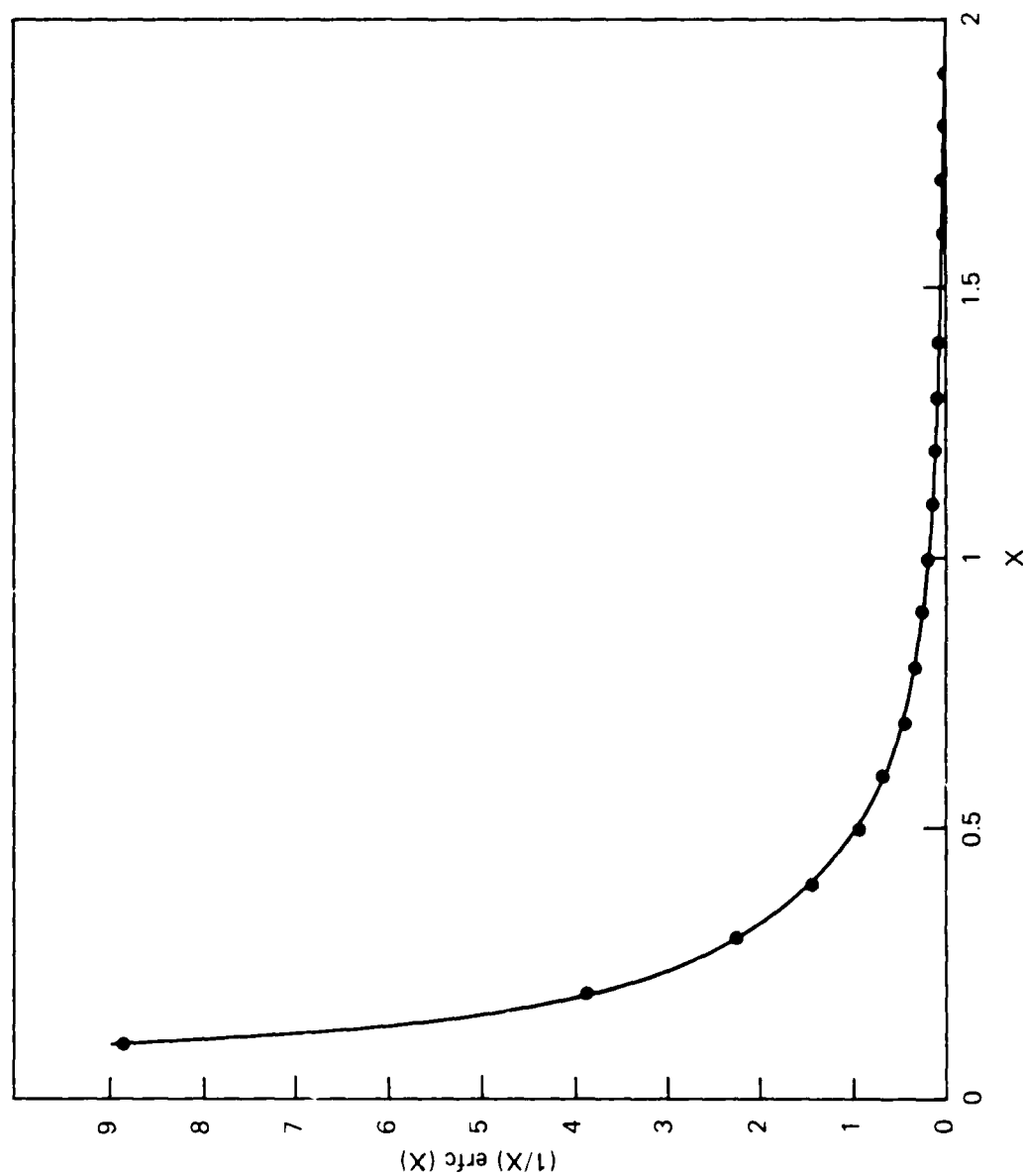
Figure 1 - Laser ignition system

Figure 2 System display showing system response (response = $f(T,s)$) in the horizontal direction as a function of time, vertical axis.



hgh

Figure 3 - Simulant function $V/r e^{-C(r)}$ fitted to values for $1/r \operatorname{erfc}(r)$ taken from standard tables



59h

Figure 4 Simulant function fitted to real data points for an inert laser heated pellet

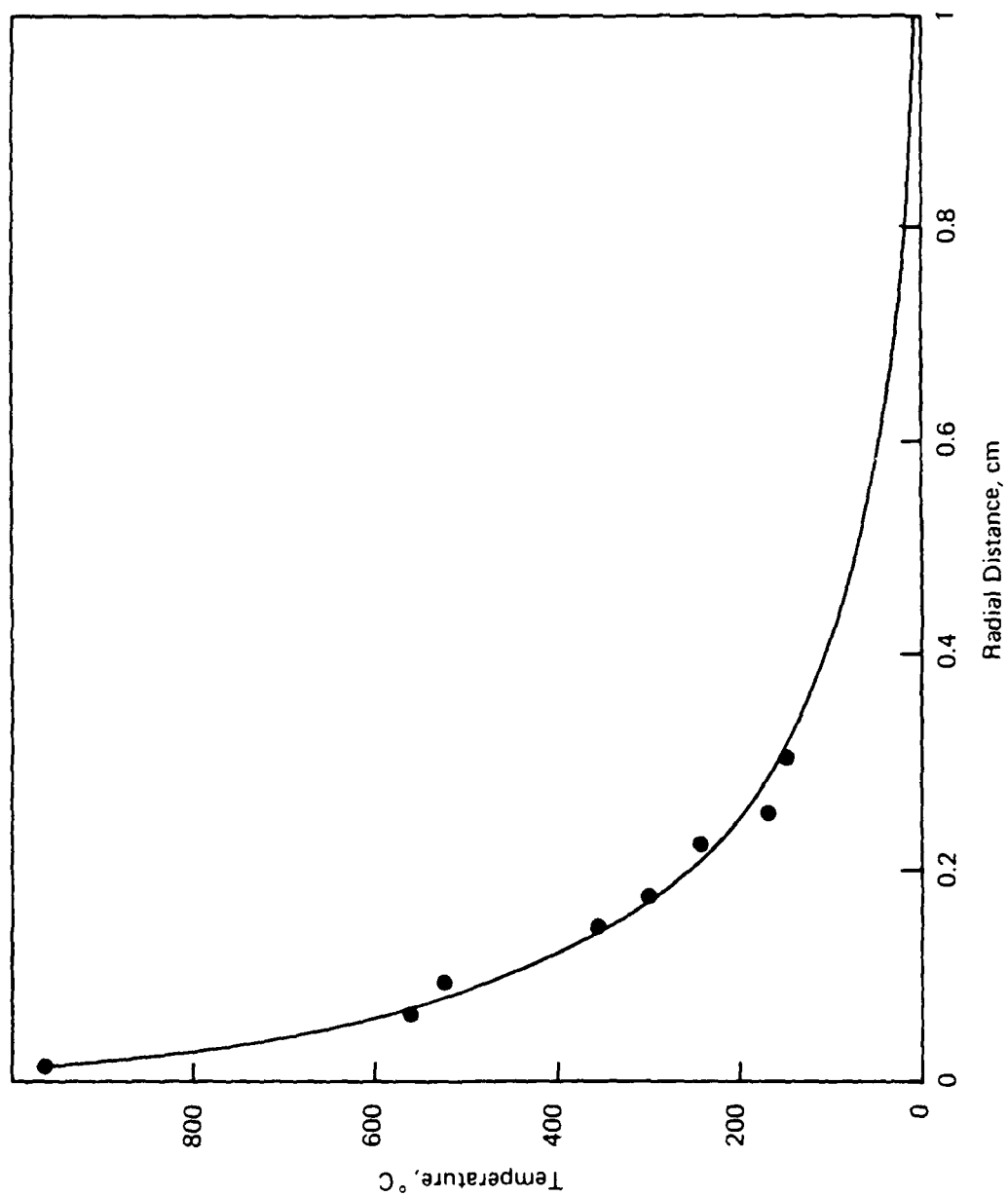
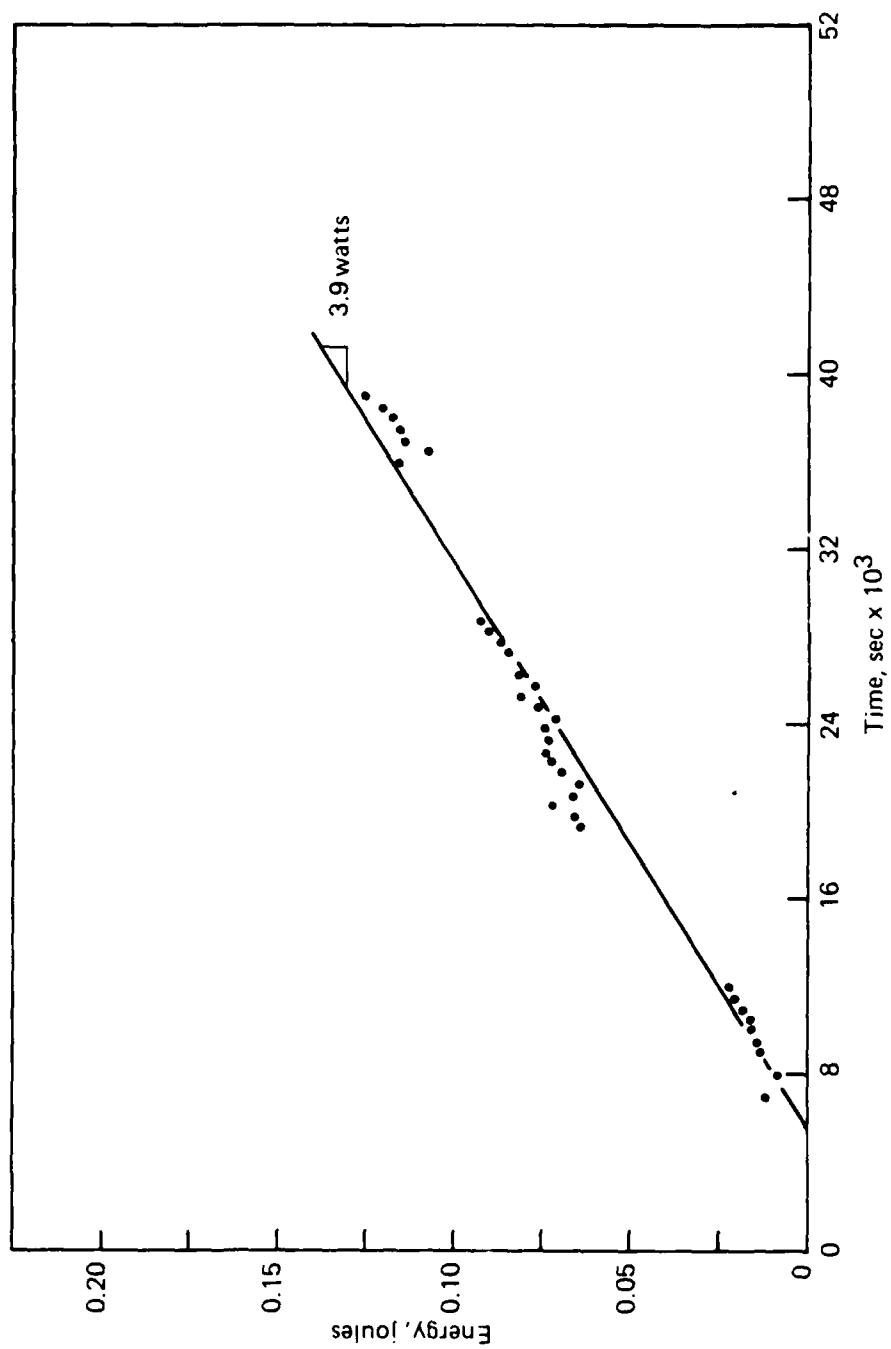


Figure 5 - Thermal rise observed for an inert, $\text{Fe}_2\text{O}_3/\text{Al}_2\text{O}_3$ pellet



MS #30

SHOCK-INDUCED REACTION SYNTHESIS ASSISTED PROCESSING OF CERAMICS

Ronald Ward, Naresh Thadhani, and Per-Anders Persson

CENTER FOR EXPLOSIVES TECHNOLOGY RESEARCH
NEW MEXICO INSTITUTE OF MINING AND TECHNOLOGY
SOCORRO, NEW MEXICO 87801

for publication in Proceedings of

INTERNATIONAL SYMPOSIUM ON COMBUSTION AND PLASMA SYNTHESIS OF
HIGH-TEMPERATURE MATERIALS, SAN FRANCISCO, OCTOBER 23-26, 1988.

APPROVED FOR PUBLIC RELEASE
DISTRIBUTION UNLIMITED

SHOCK-INDUCED REACTION SYNTHESIS ASSISTED PROCESSING OF CERAMICS

Ronald Ward, Naresh Thadhani, and Per-Anders Persson

Center For Explosives Technology Research
New Mexico Institute of Mining and Technology
Socorro, New Mexico 87801 (U.S.A.)

KEY WORDS:

shock compaction
energy localization

exothermic reaction
microscopic analysis

ABSTRACT

Shock-induced reaction synthesis (SRS) is used to assist in the consolidation of ceramic powders of TiB_2 , B_4C , SiC , and $Al_2O_3 + B_4C(A*B)$. The passage of a shock wave triggers an exothermic, self-sustaining reaction between elemental powder mixtures of Ti and B, and Ti and C. The ceramic-based reaction products and the heat generated aid in consolidation of otherwise difficult-to-compact ceramics. Almost crack-free compacts with better than 96% density and hardness $\sim 2000 \text{ kg/mm}^2$ (at 1000 g load) have been produced.

1. INTRODUCTION

The process of shock compression loading places a material in a highly unusual combination of states. Very high pressures and significant increases in temperatures, achieved in few microseconds can cause deformation and forced relative mass motion of individual particles, exposure of fresh surfaces and cleansing of existing surfaces, leading to interparticle bonding. Given the conditions of this process, shock compression processing can be used to fabricate new materials unattainable by conventional processing techniques. Various processes being developed that utilize these concepts are: dynamic compaction [1-2]; shock-induced chemical synthesis [3-5];

shock enhanced sintering or shock conditioning [6,7]; and shock-induced structural transformations [8-10].

In this work, shock-induced reaction synthesis (SRS) was used to assist in the consolidation of TiB_2 , B_4C , SiC , and $A*B$ ceramics. The SRS technique was originally developed by Akashi and Sawaoka [11] for consolidation of very hard and otherwise difficult-to-bond c-BN powders. The basic concept of the SRS technique is shown schematically in Figure 1. Here, elemental reactants 'C' and 'D' (e.g., Ti and B or Ti and C) are blended in different proportions with an ' A_xB ' inert ceramic powder, and subjected to shock loading. The passage of a shock wave through this porous mixture triggers an exothermic reaction between the reactants 'C' and 'D'. The heat released and the ceramic binder phase provided by the reaction product ' C_yD ' help in consolidating the ' A_xB ' ceramic powder.

2. EXPERIMENTAL PROCEDURE

In the present work, 80-90, volume percent of inert ceramic powder (TiB_2 , B_4C , SiC , or $Al_2O_3*B_4C$) was mechanically mixed with 10-20 volume percent of an exothermically reacting elemental mixture of Ti and B or Ti and C (in 7:3 ratio) powders. The mixing of the powders was conducted in an inert atmosphere to avoid oxidation and possible hazardous reactions of fine Ti powder. The twelve capsule Sawaoka recovery fixture (Figure 2) was used for performing shock processing experiments. The detonation of the explosive (PBX 9501), initiated by a conical plane-wave lens, accelerates a steel flyer plate which impacts the powders at velocities of 1000-3000 m/s generating 15-100 GPa peak pressures.

SHOCK SYNTHESIS AND CONSOLIDATION

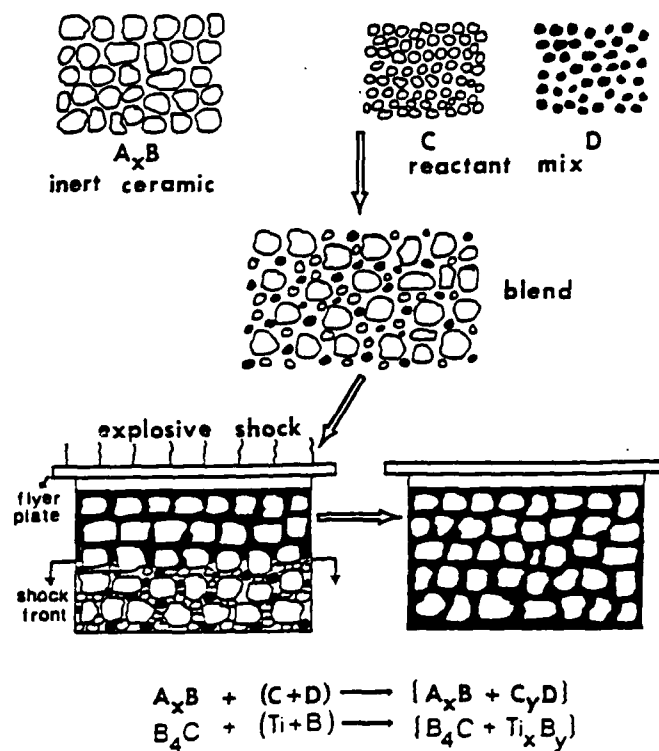


Fig. 1. Schematic illustrating principle of SRS assisted consolidation of very hard ceramic powders.

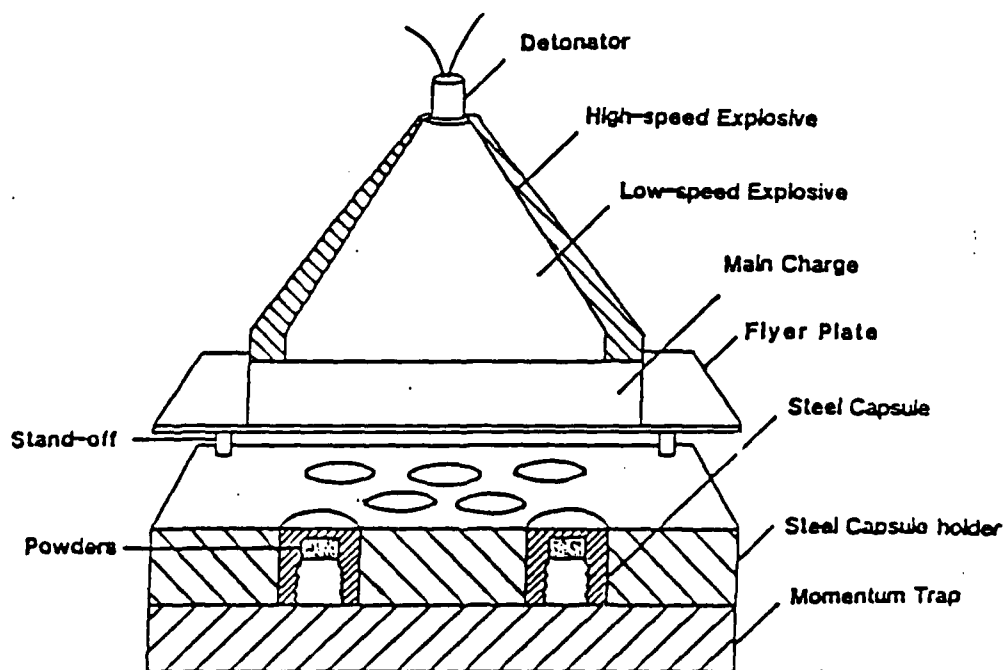


Fig. 2. Schematic of the 12-capsule Sawaoka shock recovery fixture and explosive loading assembly.

The powders (packed at approximately 65% density) are in 12 steel capsules embedded in the cavities in the steel fixture backed by another momentum trapping plate. The ceramic and reactant powder proportions, respective particle sizes, powder mixture packing densities, and impact velocities at which the shock experiments were conducted are listed in Table I. The elemental powder mixtures react exothermically, generating heat of the order of 750-1000 cal/gm. After shock loading, the capsules were machined to recover 12 mm diameter by 5 mm thick compacted disks, which were subsequently characterized by various analytical techniques.

TABLE I: STARTING POWDER CHARACTERISTICS AND EXPERIMENTAL PARAMETERS

CERAMIC INERT (I)	PARTICLE SIZE (um)	REACTANT* (R1+R2)	VOL% RATIO (I:R1:R2)	PACKING DENSITY(%)	IMPACT VEL km/s
TiB ₂	4-6, 7-10 & 4-10	Ti + B	90:7:3 & 80:14:6	55 to 65%	1.3-2.37
B ₄ C	2-14, 5-25 & 16-49	Ti + B Ti + C	90:7:3 & 80:14:6	55 to 65%	1.3-2.37
SiC	240, 320, 400 & 600 mesh; & 7um	Ti + B Ti + C	90:7:3 & 80:14:6	65%	1.6-1.98
Al ₂ O ₃ *B ₄ C	-100 to -325 mesh, 2-49 um	Ti + B Ti + C	90:7:3 & 80:14:6	65%	1.6-1.98

*Ti(5 um); crystalline B(-325 mesh); amorphous B(1 um); C(~15 um).

3. RESULTS AND DISCUSSIONS

3.1 Physical characteristics of shock processed compacts

Small scale compacts of TiB₂, B₄C, SiC, and (A*B) were successfully consolidated. Representative macrophotographs of unpolished surfaces of the recovered compacts (impact and non-impact surfaces) of the four ceramic systems are shown in Figure 3.

The major crack in the TiB_2 compact is due to the fracture produced during diamond indentation hardness testing. The remaining compacts have some circumferential cracks along the periphery or very fine radial microcracks, apart from which they are virtually crack-free. The final compact densities ranged between 89-96% for TiB_2 , 90-97% for B_4C , 93-98.4% for SiC , and 94-98% for A*B . In general, the compact density increased with higher impact velocity, with larger ceramic powder particle size, and with an higher initial powder packing density. Between the two different proportions of inert ceramic and reactant powders used, the 80 volume percent ceramic and 20 volume percent reactant yielded better compacts.

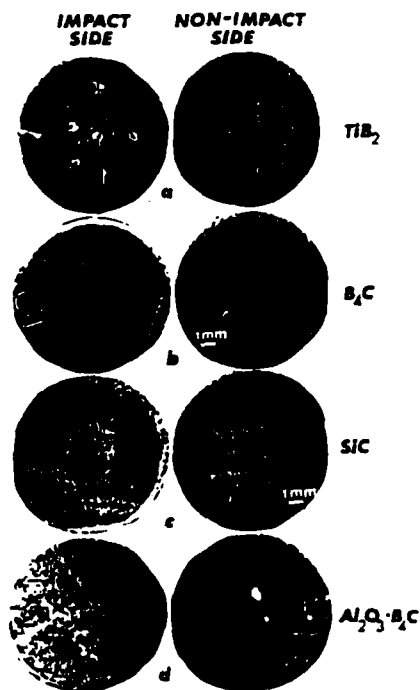


Fig. 3. Macrographs of impact and non-impact surfaces of (a) TiB_2 , (b) B_4C , (c) SiC , and (d) $\text{Al}_2\text{O}_3*\text{B}_4\text{C}$ compacts.

This was due to a better mechanical mixing attained with a larger amount of the reactant mixture. Microhardness measurements were conducted on the recovered compacts using a 1000 g load which ensured that the indentation encompassed more than one powder particle. The microhardness values were observed to be affected most severely by the type of boron powder. In the TiB_2 compacts using crystalline boron instead of the amorphous boron, the microhardness values increased by as much as 500 kg/mm^2 . The optimum density and microhardness values obtained for each of the shock processed ceramic systems are as follows: TiB_2 - 96% dense and 1728 kg/mm^2 ; B_4C - 97% dense and 2168 kg/mm^2 ; SiC - 98% dense and 1568 kg/mm^2 ; and A*B - 98% dense and 1387 kg/mm^2 .

3.2 Microscopic characterization of compacts

Optical and scanning electron microscopy were used to (a) obtain a general idea of the different features of bonding in the compacts and (b) a semi-qualitative estimate of the nature of the shock-induced reaction products. Optical micrographs of cross-sectional surfaces of the TiB_2 , B_4C , SiC , and $\text{Al}_2\text{O}_3*\text{B}_4\text{C}$ (A*B) compact are shown in Figure 4 (a), (b), (c) and (d), respectively. Intraparticle cracking is observed in the micrograph of the TiB_2 compact (Fig. 4(a)), with the cracks running across the dark contrast crystalline boron particles. This indicates that the large boron particles, which have remained unreacted, bond well with the matrix ceramic material. The clean featureless area seen in this micrograph (marked 'R') is evidence of a reaction region. Spherical voids (indicated by arrows) formed due to solidification shrinkage of the reacted and melted material can be seen in the reaction

region. The micrograph in Fig. 4(b) reveals different aspects of the bonding that occur in the case of the B_4C compact. The featureless grey-contrast regions in the micrograph (marked 'B') correspond to the crystalline boron powder particles. The small white areas (marked 'T') are the unreacted Ti (5 μm) particles. The narrow region running from top to bottom in the micrograph (marked 'R') appears to be a reaction area containing a fine dispersion of unreacted Ti particles. The optical micrograph of the SiC compact is shown in Figure 4(c). The large grey particle along with the other grey regions in the micrograph are -325 mesh SiC particles.

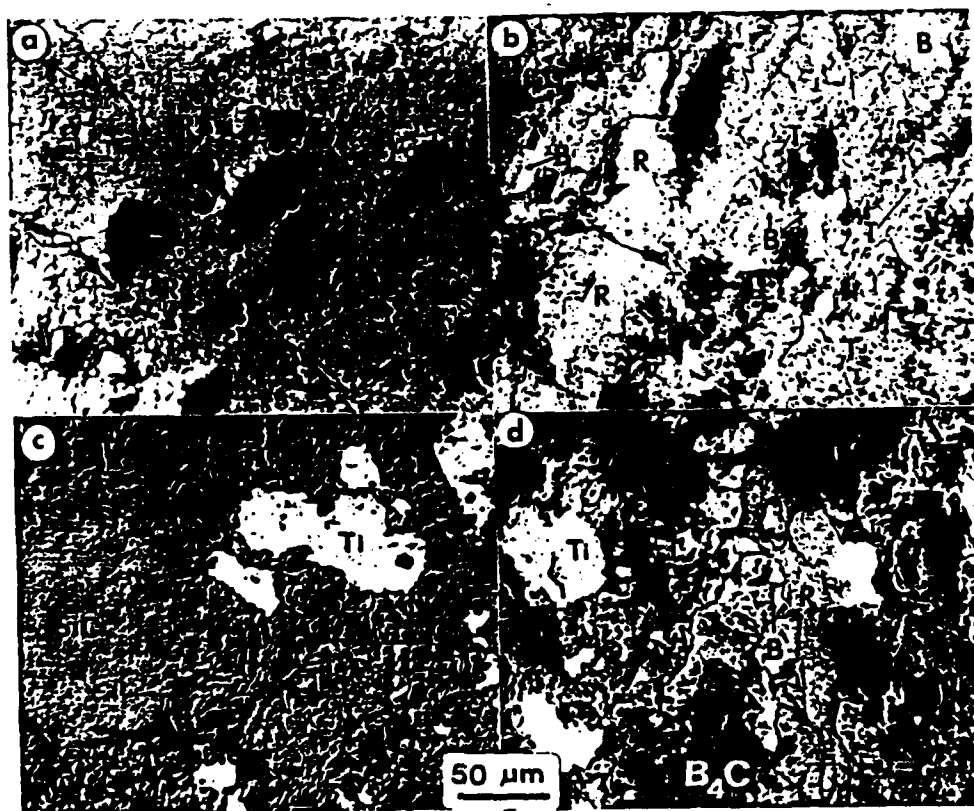


Fig. 4. Optical micrographs of cross-sectional surfaces of (a) TiB_2 , (b) B_4C , (c) SiC, and (d) $Al_2O_3 \cdot B_4C$ compacts.

Some of the SiC particles appear to have been fractured during the shock loading process. The white contrast regions in the micrograph are Ti agglomerates formed upon dynamic consolidation of 5 μm particles. The presence of a spherical void in the Ti agglomerate region in micrograph (c) indicates partial melting of the Ti powders leading to subsequent welding and retention of shrinkage voids. Although the real dark regions in the micrograph appear to be pores, some of these may in fact correspond to very fine boron particles. Excellent bonding between the powder particles was also seen in the case of the A*B compact. The micrograph of the non-impact surface of the A*B compact is shown in Figure 4(d). The different constituent phases (Al_2O_3 , B_4C , Ti and B) can be identified in this micrograph mainly by the contrast and particle size. In this compact, 1 μm amorphous boron powder (seen as fine, very dark precipitate-like) and 5 μm Ti powder (white contrast regions) were used. The Al_2O_3 and B_4C powders had an average particle size of 40 μm . The grey regions in the micrograph correspond to Al_2O_3 and the somewhat darker regions are B_4C particles. The narrow region in the center of the micrograph running from the top to the bottom appears to be a reaction region.

SEM and EDX were also conducted on each of the four shock processed ceramic systems. Figures 5 (a) to (d) and 6 (a) to (d) are SEM photographs and corresponding EDX analysis results obtained on the TiB_2 , B_4C , SiC, and A*B compacts, respectively. In essence it was observed that some of the reactant constituents remained unreacted. Although, elemental boron could not be detected with the EDX machine, the retention of unreacted Ti was confirmed by the presence of nitrogen in the EDX spectrums. Nitrogen in the

unreacted Ti particles is due to its adsorption during the powder manufacturing process. During shock processing nitrogen is retained in the unreacted Ti particles. On the other hand, spectra obtained from possible reaction regions (marked 'R' in SEM images do not reveal any trace of nitrogen. This may be because of loss of nitrogen during the reaction between Ti and B or C. Based on this analysis, it was deduced that in the case of the TiB_2 compact (Fig. 5(a) and 6(a)) some of the Ti reacted with B forming a TiB compound (trace (i)), and some Ti particles remained unreacted (trace (ii)). The very dark regions in the SEM image (Fig. 6(a)) correspond to agglomerates of very fine amorphous boron powders. In the B_4C compact (Fig. 5(b) and 6(b)) a TiC reaction region was also observed. Here Ti appears to have reacted with the C (trace (ii)) from B_4C . Some unreacted elemental Ti is also observed (trace (i)). The aluminum peak in the EDX scan in Fig. 6(b) is due to the impurity from sample polishing. The bottom trace (iii) in Fig. 6(b) corresponds to the B_4C particles in the matrix. Ti and C were used as the reactants for consolidating SiC powder. EDX analysis (Fig. 6(c)) from different regions in the SEM micrograph (Fig. 5(c)) show a TiC reaction region and some unreacted Ti powder (trace (i)). In the SEM image (Fig. 5(d)) of the A*B mixture compact, a reaction area containing Ti and B was observed along with some white contrast unreacted Ti particles as shown in the EDX spectrum in Fig. 6(d). The grey regions in the SEM image are Al_2O_3 particles, as confirmed by the EDX trace (i) in Figure 6(d), whereas the dark regions in the SEM image are B_4C particles (trace (ii) in Fig. 6(d)). The EDX scans of the TiB reaction region and unreacted Ti particles are shown in traces (iii) and (iv) in Fig. 6(d).

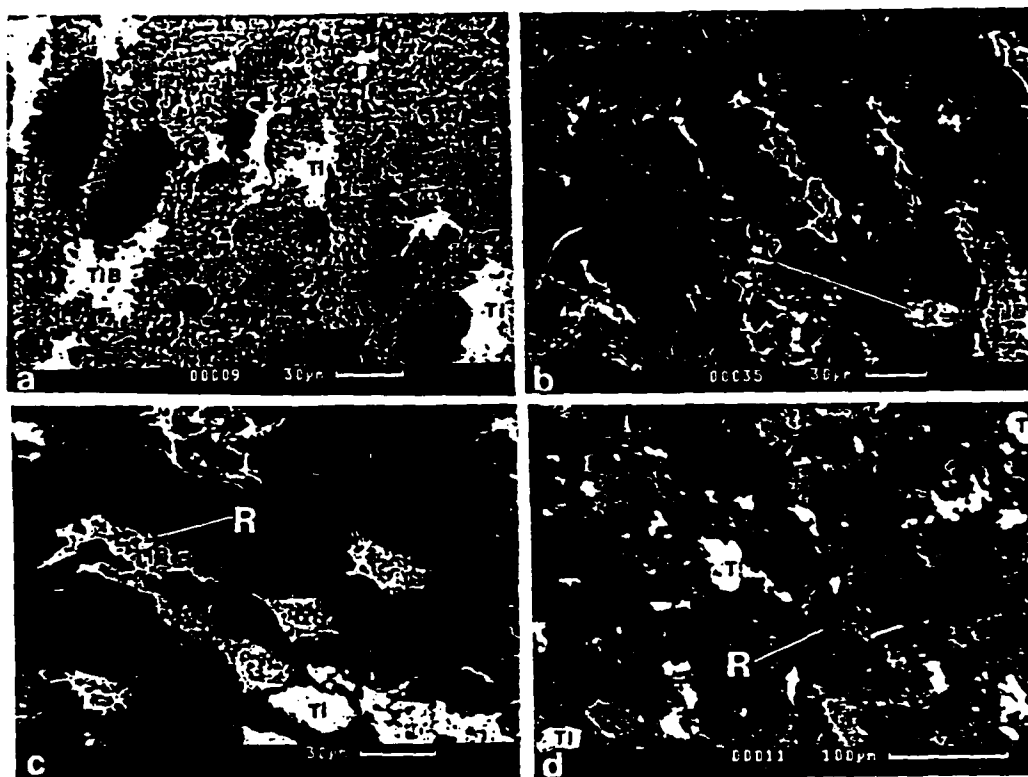


Fig. 5. SEM photographs showing reacted and unreacted regions in (a) TiB_2 ; (b) B_4C ; (c) SiC ; and (d) A^*B compacts.

It was evident from the SEM and EDX analysis that an insignificant amount of Ti and B had remained unreacted, due to the improper mixing and agglomeration of fine powder particles.

4. SUMMARY OF RESULTS

Shock-induced reaction synthesis (SRS) is used to assist in the consolidation of ceramic powders of TiB_2 , B_4C , SiC , and A^*B . Almost crack-free compacts of these ceramics with better than 96% density and hardness close to 2000kg/mm^2 (at 1000 g load), have been produced with this technique.

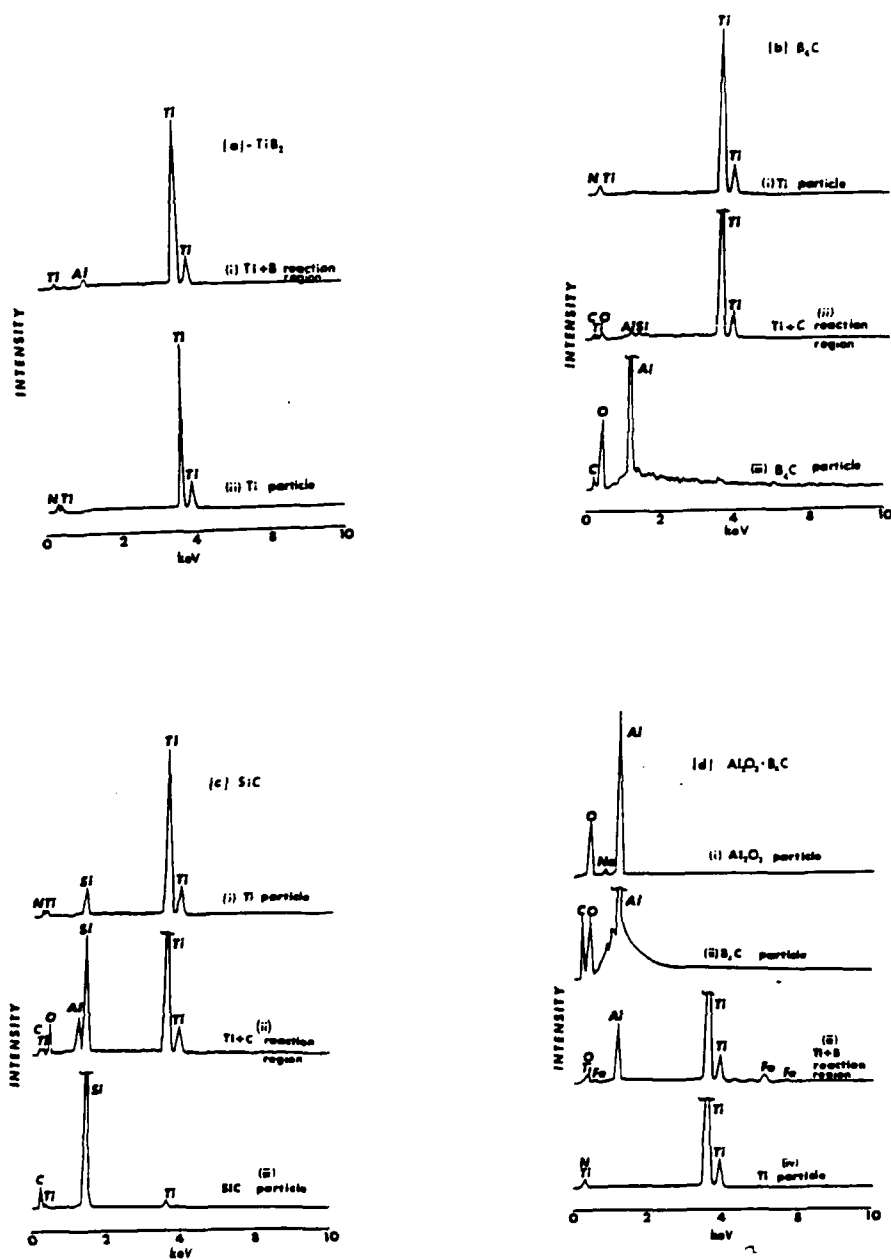


Fig. 6. Energy dispersive x-ray analysis from different regions of (a) TiB_2 , (b) B_4C , (c) SiC, and (d) A*B compacts in Fig. 5.

ACKNOWLEDGMENTS

This research has been supported by DARPA under Contract No. DE-AC04-87AL4326. The explosive shock experiments were conducted at the CETR Eagle firing site crew. The help of Mr. Jim Smith with the SEM work at LANL, and valuable suggestions provided by Drs. Marc Meyers and Paul Lessing are acknowledged.

REFERENCES

1. "Dynamic Compaction of Metal and Ceramic Powders", National Materials Advisory Board, NMAB-394, National Academy, Washington, D.C., 1983.
2. Gourdin, W.H., Prog. in Mater. Science, V. 30, 1986, p. 39.
3. "Shock Compression Chemistry in Materials Synthesis and Processing", NMAB Report No. 414, National Academy Press, Washington, D.C., 1984.
4. Graham, R.A., Morosin, B., Venturini, E.L., Beauchamp, E.K., Hammetter, W.F., in Emergent Process Methods for High Technology Ceramics, eds. Davis, R.F., Palmour, H., and Porter, R.L., Plenum Press, 1984, p. 719.
5. Graham, R.A., Morosin, Venturini, E.L., and Carr, M.J., Ann. Rev. Materials Science, V. 16, p. 315.
6. Cline, C.F., ed. Final Report of the DARPA Dynamic Materials Synthesis and Consolidation Program, LANL Report No. UCID-19663-85, Vols. I and II, LLNL, Livermore, 1985.
7. Bergmann, O.R. and Barrington, J., Journal of American Ceramic Society, V. 49, 1966, p.502.
8. DeCarli, P.S., "Method of Making Diamond", U.S. Patent No. 3,238,019, March 1, 1966.
9. DeCarli, P.S. and Jamieson, Science, V. 133, 1961, 821.
10. Olinger, B. and Newkirk, L., Sol. St. Comm., V. 37, 1981, 613.
11. Akashi, T. and Sawaoka, A.B., U.S. Patent 4,655,830, 4/7/87.

**SUMMARY ASSESSMENT OF THE APPLICATION OF SPS AND
RELATED REACTION PROCESSING TO PRODUCE DENSE CERAMICS**

by

Roy W. Rice
W. R. Grace & Co.-Conn.
7379 Route 32
Columbia, Maryland 21044

ABSTRACT

A summary assessment of directly producing relatively dense ceramic products by SPS/SHS processes, based upon evaluation of basic materials phenomena, SPS and other ceramic reaction processing and economics seriously questions many of the broad, i.e., generic, advantages claimed for SPS processing. However, probable economic advantages for some composites made by processing using mainly non-propagation reactions and hot pressing is indicated.

KEY WORDS

Economic, Economics Microstructures, and Hot Pressing

I. INTRODUCTION

Reacting powder compact constituents to directly produce a body of different composition from the starting constituent has a substantial history and future in ceramics. Self-propagating (high-temperature) synthesis (SPS or SHS), the focus of this paper, involves reactions that are sufficiently exothermic such that if the reaction is initiated in some area of the compact it will, under proper conditions propagate as a narrow, high-temperature reaction zone through the compact, e.g., at velocities of a few mm/sec-cm/sec. Broad claims of unique compositions and

microstructures obtainable in a diversity of materials, sizes and shapes at low cost have been made. This paper summarizes more detailed⁽¹⁾ evaluating reaction processing experience to put such processing for dense ceramics in a more realistic perspective.

II. GENERAL CLAIMS AND BASIC MATERIALS BEHAVIOR

The basic concept of directly making dense ceramic bodies by SPS has been to form and ignite a reactant compact to directly yield a final product. This implies great versatility in size and shape, and has been specifically cited as a very energy efficient and, hence, cost effective process since it produces its own temperature; potentially implying no furnace or other facilities may be necessary. It has also been claimed that the very high temperatures and rapid movement of the reaction front with resultant local quenching, can yield unique compositions and microstructures.

Unfortunately, the above generic claims and hopes for the process are not particularly consistent with intrinsic or extrinsic aspects of basic material and processing behavior. Rice and McDonough⁽²⁾ have previously pointed out that SPS is associated with intrinsic increases in product density (which generally increases with increasing reaction energy release); i.e., the product has a smaller intrinsic volume than that of the reactants. Thus, even in a fully dense compact, reactions generate porosity (e.g., 20% or more) which must be eliminated during or following the reaction. In view of sintering kinetics typically being much slower than reaction kinetics, Rice and McDonough⁽²⁾ and subsequently Munir⁽³⁾ observed that substantial external pressure will commonly be required to yield dense products, restricting sizes and, especially, shapes and

to some extent costs (discussed later). Extrinsic limitations also arise, especially from outgassing due to boiling adsorbed species off the surface reactant particles, again indicating the need for externally applied pressure. The potential for novel compositions and microstructures from SPS is limited in dense ceramic bodies by transport processes necessary for densification.

III. COMPARISON WITH OTHER CERAMIC REACTION PROCESSING

A variety of other ceramic processing reactions provide valuable insights to both constraints and opportunities for SPS. Thus, reaction of Si with C to give SiC (which can, over a considerable range of solid Si and C particulate and compact characteristics, be self-propagating) is used industrially in a non-SPS mode to give nearly fully dense bodies by infiltrating molten Si to compacts of SiC (or alternatively other materials such as B_4C) and carbon powders. The substantial reduction in volume (~35%) in forming SiC is counteracted not by pressure, but by:

- 1) significant dilution of the overall reaction (an approach which will often be important in making SPS processing more practical);
- 2) the compact typically being in contact with the molten Si so, as molten Si within the body reacts with the C to form SiC, additional Si can be wicked into volume left by reacted Si; and 3) Si being one of the few materials having a lower solid than liquid density (i.e., solid Si floats on liquid Si similar to H_2O , so solidifying Si can either fill remaining void spaces or if the process is carried out right, actually squeeze residual Si out of the body). That both a molten Si reservoir is beneficial to high densities and reaction volume changes can be a serious problem as shown by Telly and

Petzow's⁽⁴⁾ work on densifying B_4C with Si. While near theoretical densities could be achieved by hot pressing, sintering typically yielded bodies with 15% or more porosity, apparently due to intrinsic volume changes direction from reaction and from wetting changes of the solid by the molten phase, as well as volatilization of Si.

A more recent process for producing relatively dense ceramic composites by reaction of B_4C with molten Al, again involves exothermic reactions and resultant intrinsic generation of porosity.⁽⁵⁾ In earlier work it was found necessary to apply pressure to accelerate densification faster than the kinetics of phase transformation which is the major hindrance to rearrangement during "pressureless sintering". However, subsequent work reports full densification by pressureless infiltration of molten Al due apparently to: 1) wicking of more molten Al from the reservoir into the body to compensate for the ~20% volume decrease on reaction, as well as the retention of residual Al in the final product; and 2) significantly reducing the rate of reaction of the molten Al with the B_4C .

A major development in reaction processing of ceramics from molten metals has been the development of the Lanxide process,⁽⁶⁾ apparently entailing wicking of molten metal through fine channels in the reaction product to the reaction front, resulting in controlled product growth. Again, a key to the high density of the resultant product appears to be both the slow, very controlled nature of the reaction (orders of magnitude slower than SPS reactions), as well as the retention of some residual metal.

Partially related to the above reaction processing to form SiC is the reaction sintering (or bonding) of Si_3N_4 , as well as more recent limited work on Si_2ON_2 . The key to successful processing of Si_3N_4 from Si metal powder and a nitrogen source, e.g., N_2 (usually with some H_2) or NH_3 , is the opposite of its possibilities as a SPS reaction, i.e., a very slow and controlled reaction rate to allow the internal transport necessary for this somewhat unique process to be successful. This reaction provides considerable information on microstructural aspects of the processing that may be pertinent to SPS processing of Si_3N_4 , as well as related materials.

Another related and important example is recent reaction processing of zirconia-toughened ceramics. Processing of zirconia-toughened mullite composites by in-situ reaction of zircon (the lowest cost source of ZrO_2) and Al_2O_3 shows achieving fully dense bodies depends upon two key factors: 1) achieving most densification before the reaction commences, i.e., use of fine reactant particles since densification rates vary as D^{-3} to D^{-4} (D = particle size) vs. D^{-1} to D^{-2} for reaction rates; and 2) use of undissociated as opposed to dissociated ZrSiO_4 to avoid formation of free SiO_2 before mullite formation and volume change problems accompanying phase changes. The importance of 1) is shown by attempts to reaction process fosterite- ZrO_2 composites. The reaction could not be prevented from occurring simultaneously with densification, yielding ~60% of theoretical density by sintering alone (but high densities by hot pressing).

Dense mullite-BN particulate composites have been made by hot pressing and in-situ reactions of Si_3N_4 , B_2O_3 , and Al_2O_3 and by Coblentz⁽⁷⁾ yielding composites superior to those hot pressed from

mixtures of mullite and BN powder. It is not all clear that these composites can be sintered before, during, or after the reaction despite their non-SPS character.

The overall lessons from other ceramic reaction processing are: 1) reaction processing is often favorable to making composites, and at low to moderate cost; 2) low reaction rates are typically important to densification by sintering, otherwise hot pressing (or HIPing) is generally necessary; 3) large reaction volume changes are typically a serious problem, but may be accommodated by hot pressing, or with molten metals, use of a liquid reservoir to allow continued wicking into the reacting body; and 4) microstructure of the reacting compact can be quite important.

IV. CERAMIC SPS EXPERIENCE

Although limited, some key evaluations of ceramic microstructures and compositions in dense bodies produced by SPS reactions are now becoming available. A recent study, as well as evaluation of the literature⁽⁸⁾, shows that SPS processing of TiC and TiB₂ generally produced similar but somewhat coarser grains than conventional processing of similar density bodies. SPS processing of TiC + TiB₂ composites significantly reduces the product grain size, but again with no clear evidence that resultant grains structures are finer than those produced by conventional processing, e.g., hot pressing, of TiC + TiB₂.

Work by Cameron, et al,⁽⁹⁾ comparing dense, hot pressed bodies of various oxide, carbide, or oxide- boride composites made by hot pressing compacts consisting of either: 1) ingredients to form the resultant composite by in-situ reaction mostly by SPS; or 2) a

mixture of the composite constituents to yield as nearly identical composites as possible. Evaluation of microstructures and physical properties of the four different composites showed no generic advantage to either processing approach. In some cases, finer microstructures were achieved by SPS processing, while in other cases finer microstructures were achieved by conventionally hot pressing the resultant composite constituents. Overall physical properties were similar for both types of processing, with some composites made by SPS showing possible advantages or disadvantages as did those made by conventional hot pressing. A key observation was that in scaling up reactions (e.g., to ~ 8 cm diameter) SPS reactions left various shaped cavities (depending upon the direction of reaction propagation) in the reacting bodies and resultant densification irregularities and difficulties.

V. ECONOMICS AND OTHER PRACTICAL FACTORS

The low cost claims for SPS processing based on energy considerations are readily seen to be at best on shaky grounds. First, the direct energy cost of either sintering (e.g., oxide ceramics) or hot pressing (e.g., non-oxide ceramics) is typically less than 5% of the resultant selling price, thus eliminating the "fuel bill" for processing ceramics, results in little economy. Further, an inherently counterproductive trade-off can be seen in that the reactions that typically produce the most heat, hence implying the greatest freedom from external energy requirements, typically involve elements which are more energy consuming (and hence typically more expensive) in winning them from their ores. Further, elimination of heating facilities and possibly some floor

space by eliminating heating rates is probably unrealistic, since even moderate scale up, e.g., to ~4 cm in diameter, shows that the absence of any heating frequently results in thermal shock cracking of the body on cooling, especially with hot pressing as commonly required.

There does, however, appear to be some potential economic advantage to at least some aspect of SPS processing, namely processing composites from low cost raw materials. While expensive elements such as Ti and, especially, B need to be avoided, a variety of oxide-non-oxide composites can be made from ingredients such as Al, TiO_2 , B_2O_3 and C, which are less expensive than the average cost of resultant composite constituents, e.g., $\text{Al}_2\text{O}_3 + \text{TiC}$, $\text{Al}_2\text{O}_3 + \text{TiB}_2$.

VI. SUMMARY AND CONCLUSIONS

A brief review of basic materials behavior, other reaction processing, as well as recent SPS processing, of ceramics leads to the following general conclusions:

1. Substantial intrinsic volume reductions of SPS reactions will commonly require application of external pressure for densification.
2. Unique compositions and microstructures are unlikely in dense bodies due to the diffusional changes typically needed to achieve high densities.
3. Claimed low costs due to energy efficiency are misleading, since a) direct energy costs of making ceramics are a small portion of their final cost, and b) both external

pressurization and cooling control, e.g., heating, are likely to be required to achieve quality dense products.

4. SPS processing does appear to offer useful opportunities for making various ceramic composites. Although there appears to be no generic advantage to some composites, there may be special advantages in certain composite systems. A broader advantage appears to be the opportunity of making useful composites from cheaper raw materials.

5. Production of dense ceramic composites by both SPS and non-SPS reactions strongly suggests that weakly or more likely non-propagating reactions are desired in order to achieve better, more homogeneous densification by hot pressing or sintering to nearly full densification before reaction commences. This does not preclude possible use of a variety of SPS reactions, since frequently microstructural control of the reactant compact via particle size, density control, as well as dilution with the product can frequently make them sufficiently non-propagating to be more useful.⁽¹⁰⁾

ACKNOWLEDGEMENT

The support of the Office of Naval Research in the preparation of this paper is gratefully acknowledged.

REFERENCES

1. Rice, R. W., "Assessment of the Application of SPS and Related Reaction Processing to Produce Dense Ceramics", to be published.

2. Rice, R. W., and McDonough, W. J., "Intrinsic Volume Changes of Self-Propagating Synthesis", J. Am. Ceram. Soc., Vol. 68, No. 5, pp C-122-C-123 (1985).
3. Munir, Z. A., "Synthesis of High Temperature Materials by Self-Propagating Combustion Methods:", Ceram. Bull., Vol. 67, No. 2, pp 342-349 (1988).
4. Telle, R., and Petzow, G., "Mechanisms in the Liquid Phase Sintering of Boron Carbide with Silicon Based Melts", High Tech Ceramics, edited by P. Vincenzini, Elsevier Science Publishers, pp 961-973 (1987).
5. Halverson, D. C., Pyzik, A. J., and Aksay, I. A., "Born-Carbide-Aluminum and Boron-Carbide-Reactive Metal Cermets", U. S. Patent No. 4,605,440 (August 12, 1986).
6. Newkirk, M. S., Urquhart, A. W., Zwicker, H. R., and Breval, F., "Formation of LanxideTM Ceramic Composite Materials", J. Mater. Res., 1 (1), pp 81-89 (Jan/Feb. 1986).
7. Coblenz, W. S., and Lewis, D., III, "In Situ Reaction of B_2O_3 with AlN and/or Si_3N_4 to Form BN-Toughened Composites", J. Am. Ceram. Soc., 71 [2], pp 1080-1085 (1988).
8. Rice, R. W., "Reactant Compact and Product Microstructures for TiC, TiB_2 , and TiC/ TiB_2 from SPS Processing", to be published.
9. Cameron, C. P., Enloe, J. H., Dolhert, L. E., and Rice, R. W., "A Comparison of Reaction Versus Conventionally Hot Pressed Ceramic Composites", to be published.
10. Rice, R. W., "Microstructural Aspects of Fabricating Bodies by Self-Propagating Synthesis", to be published.

SHOCK CONSOLIDATION OF COMBUSTION SYNTHESIZED CERAMICS

by

A. Niiler, L.J. Kecskes, and T. Kottke

Ballistic Research Laboratory
Aberdeen Proving Ground, MD 21005

ABSTRACT

A process whereby full density, monolithic ceramic materials are fabricated is described. This method utilizes combustion synthesis to convert elemental powders into hot, porous ceramics which are then compacted to high density by a pressure wave produced by a high explosive. This technique has been used to produce TiC and TiB_2 at greater than 98% of theoretical density.

1. INTRODUCTION

High-technology, structural ceramics are becoming utilized in an ever larger range of applications which require light-weight, high-temperature, high performance materials. These ceramics are typically the borides, carbides, nitrides, and oxides of a variety of metals and are fabricated in such a way as to eliminate most of the porosity and impurities from the bulk. Commercial processing of these materials is generally done by hot pressing or hot isostatic pressing. Both of these methods require expensive starting materials, are very energy, labor, and capital intensive and so result in very high final product costs.

Ceramic materials can also be produced by Self-Propagating High-Temperature Synthesis (SHS). This process involves combustion synthesis reactions between component powders; reactions which are characterized by high exothermicities, reaction temperatures of about 3000 C, and reaction front velocities on the order

of a few centimeters per second. The powder mixtures can be ignited with very small amounts of energy after which the released heat sustains further reaction until the whole sample has been synthesized. The advantages and drawbacks of fabrication by SHS are well documented by Frankhouse¹, who has compiled a comprehensive listing of the early work in the Soviet Union in this area and Munir², who has written an excellent, recent, review article.

There are a number of causes for porosity in combustion reacted samples, the major ones being impurity evolution and the difference in the specific volumes of precursor powder compact and reacted ceramic product. In the absence of significant liquid phase in the product, it is necessary to use external pressure after the synthesis reaction is complete to achieve full density. At the Ballistic Research Laboratory (BRL), a processing method has been developed which utilizes the SHS reaction to form porous ceramic bodies which, while still hot, are compacted to high density by explosively generated pressure waves. This SHS/Explosive or Dynamic Compaction process will be called SHS/DC henceforth. No external heat is applied to the system and the fixture in which both the reaction and compaction take place is made of relatively common, inexpensive materials. A detailed description of this work is given by Niiler et al.³

2. EXPERIMENTAL PROCEDURE

The green compact of the mixed component powders was placed in the fixture shown in Figure 1. This arrangement served to contain the sample during reaction and compaction, allowed any volatile gases to escape during the reaction, provided a degree of insulation for the hot sample, and served to prevent impurities from diffusing into the hot reacted sample. Once the SHS reaction is complete, the explosive is initiated by a linewave generator resulting in a sweeping shock

wave and grazing incidence compaction. The heat from the reaction not only propagates the reaction through the whole sample, but also heats the sample to temperatures in excess of 2000 C. Experiments done on samples reacted in containment fixtures as described above show temperatures in excess of 1200 C for at least one minute, allowing an extended time window during which the compaction pulse can be initiated.

The experiments reported here consisted of investigating the effects on final product density and hardness on the explosive charge thickness (measured in terms of charge mass to compression plate mass c/m) and lateral dimension scaling. Most samples were 1.2 cm thick with diameters of 5.0 cm, 10.0 cm, and 15.0 cm but several 15.0 cm TiB_2 discs were 2.1 cm thick. Only -325 mesh titanium powder with a 99+% specified purity was used. The boron powder was crystalline -325 mesh, 99.5% specified purity and the carbon was 90.5% pure, .05 micron carbon black.

3. RESULTS AND DISCUSSION

The highest density, as a percentage of full theoretical density (TD), and microhardness results for the various sizes of samples that have been made by SHS/DC are summarized in Table 1. Commercial hot pressed materials are also included for comparison. As expected, a strong dependence was found between the density and c/m with larger c/m resulting in a denser product, up to a point. At values of c/m beyond that point, the density was reduced while increased fracturing and delamination indicated more edge effects and stronger rarefaction waves from the shock. The maximum TiB_2 density of 99+% was reached at c/m=0.22 while for TiC , the maximum of about 98% was reached at c/m=0.44.

Table 1. TiC and TiB₂ Results

Material	Dimensions (dia x thk)	Density (% of TD)	C/M	Hardness HK(100g) (kg/mm ²)
TiC	5cm x 1.3cm	98+	.44	2000
TiC	5cm x 2.5cm	90	.22	1400
TiC	10cm x 1.3cm	90	.16	1500
TiC	15cm x 1.3cm	90	.16	1500
TiC	Commercial Hot Pressed	98+		2500
TiB ₂	5cm x 1.3cm	99+	.22	3200
TiB ₂	10cm x 1.3cm	92	.16	2000
TiB ₂	15cm x 1.3cm	99+	.22	3200
TiB ₂	15cm x 2.1cm	98+	.44	
TiB ₂	Commercial Hot Pressed	98+		3300

The requirement of a higher c/m for TiC indicates that it is harder to compact than the TiB₂. At 1800 C, the compressive yield strength of TiC is 50 MPa⁴ while that of TiB₂ is 441 MPa.⁵ Thus if yield strength, or plasticity, were the only factor involved in compactability, TiC should compact more easily than TiB₂. Since it does not, another mechanism must be invoked to explain the difference. This other mechanism, it is speculated, is that the TiB₂ melting point of 2800 C was exceeded. Continuing the speculation, melting did not occur in TiC because its melting point, 3150 C, was not reached even with the additional energy provided by the shock. Thus, TiB₂ compacted more easily than TiC because it contained at least some liquid phase while the TiC did not.

This hypothesis about the TiB₂ melting is supported by the backscatter SEM micrographs of polished surfaces of the TiB₂ and TiC samples prepared by SHS/DC shown in Fig. 2. The TiB₂ surface shows grain shapes which are consistent with a section cut through randomly oriented, hexagonal single crystal grains. This single crystal formation could only occur during cool-down from a liquid phase

of TiB_2 . Figure 2a and similar micrographs of reacted but uncompacted TiB_2 indicate that melting temperatures were reached in parts of the sample during the reaction and throughout the whole sample when the energy from the shock was added to the reaction heat. On the other hand, the TiC surface shows no evidence of grain shapes that might be associated with a cut through randomly oriented face centered cubic single crystals. Rather, the morphology of TiC surface resembles squeeze packing of plastic grains, a structure which is consistent with the TiC grains being plastic but at temperatures below its melting point.

X-ray analysis of these surfaces shows an average concentration of iron at about 2 wt%. An x-ray map, however, shows that all of this iron is in the grain boundaries with none in the grains. An analysis of both the titanium and boron precursor powders by Inductively Coupled Argon Plasma Spectroscopy shows that both contain about 3 wt% of iron impurity. Thus, the source of the grain boundary iron is shown to be the precursor powder contamination at a level several orders of magnitude greater than allowed by the manufacturer's purity specification. X-ray diffraction of a TiB_2 sample shows all the peaks from TiB_2 along with several small peaks due to Fe_2B and Fe . Although these x-ray diffraction data indicate the presence of iron, the 3 wt% iron shown to exist in the precursor powders cannot be quantitatively verified. X-ray diffraction of the analyzed TiC sample identifies the presence of only TiC , the absence of iron explained by the fact that a different batch of titanium powder was used in preparing this sample.

The capability to upscale the size of samples produced by the SHS/DC method was tested. TiB_2 samples with diameters of 5.0 cm, 10.0 cm, and 15.0 cm were made keeping all parameters except the diameter constant. Good results were obtained with all these sizes and the densities of the central test cores from

the larger samples were higher than for the smaller samples. It is felt that because of a reduced surface to volume ratio, the increased size improves heat retention and thus plasticity at the sample center.

Knoop microhardness test results on a representative set of SHS/DC TiC and TiB₂ samples for both 100 gm and 400 gm loads are shown in Figure 3. For comparison, results on commercially available, hot-pressed TiC and TiB₂ are also shown. As can be seen, the microhardness clearly improves with density for both TiC and TiB₂. However, whereas the highest density SHS/DC TiB₂ has a value comparable to the equivalent hot-pressed sample, this is not the case for TiC. The reason for the lower values for the SHS/DC TiC is not clear. The possibilities are poor grain bonding because of some intergrain iron, the presence of the remaining 2% of porosity or carbon vacancies in the crystal lattice caused by the substoichiometric Ti:C ratio of 1:.8 that has been used in these experiments. These data also show significant differences between the 100 gm and 400 gm loads. This indicates the importance of making microhardness measurements at a high enough load so that grain boundaries and not only the single grains are involved.

The high cost of ceramics such as TiC and TiB₂ has been a significant deterrent to their widespread use in large quantity. Their current price of more than \$90/kg would have to drop to less than \$25/kg to be widely used. A model developed by Frankhouser⁶ was used to estimate the costs of producing TiC and TiB₂ by the SHS/DC method. If a reduction in materials cost from a combination of experience curve reductions and some new technologies for producing clean boron powders are assumed, then the estimates show costs of both TiB₂ and TiC could drop to the desired range.

LIST OF REFERENCES

1. W.L. Frankhouser, "Materials Fabrication by Self-Propagating High-Temperature Synthesis in the Soviet Union, Vol.II," System Planning Corporation Report 81-4082, 1982.
2. Z.A. Munir, "Synthesis of High Temperature Materials by Self-Propagating Combustion Methods," Ceramic Bulletin, V. 67, No. 2, 342-349, 1988.
3. A. Niiler, L.J. Kecskes, T. Kottke, P.H. Netherwood, Jr., and R.F. Benck, "Explosive Consolidation of Combustion Synthesized Ceramics: TiC and TiB₂," Ballistic Research Lab Report BRL-TR-2951, Aberdeen Proving Ground, MD, 1988.
4. L.E. Toth, Transition Metal Carbides and Nitrides, Academic Press, New York, NY, 1971.
5. J.R. Ramberg and W.S. Williams, "High Temperature Deformation of Titanium Diboride," Journal of Materials Science, V. 22, No. 5, 1815-1826, 1987.
6. W.L. Frankhouser, "Advanced Materials Technology Project; Final Technical Report," System Planning Corporation Report 1121, May 1986.

LIST OF FIGURES

1. A schematic diagram of the reaction, shock compaction assembly showing the sample, container and the explosive charge.
2. Polished surface of 99+% dense TiB₂ on the left, and of 98+% dense TiC on the right, both made by SHS/DC. The brighter phase in the grain boundaries contains iron.
3. Knoop microhardnesses at 100g and 400g loads vs. density for SHS/DC TiC and TiB₂. Values for hot-pressed TiC and TiB₂ are shown also for comparison.

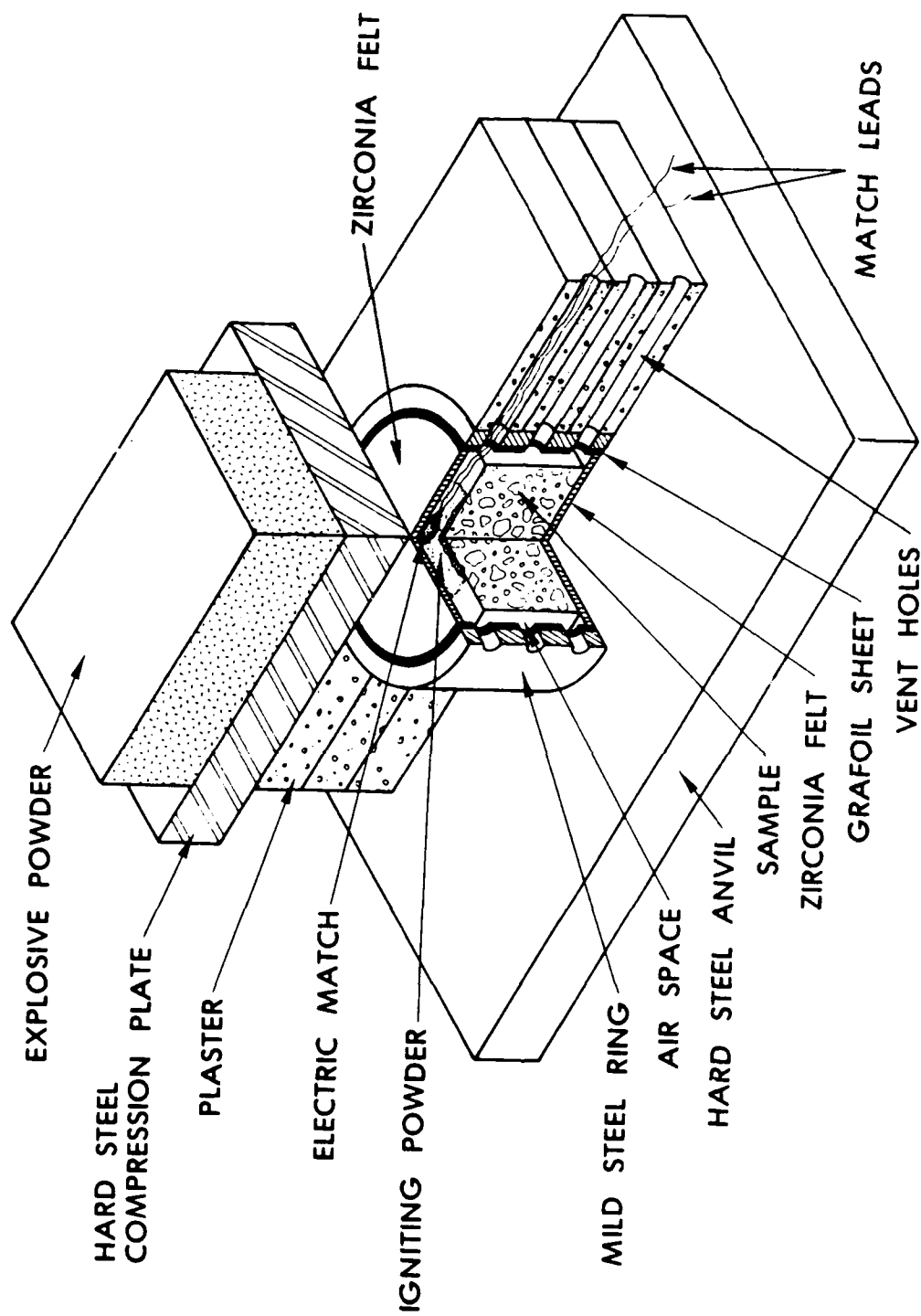


Figure 1

TiB₂



TiC



Figure 2

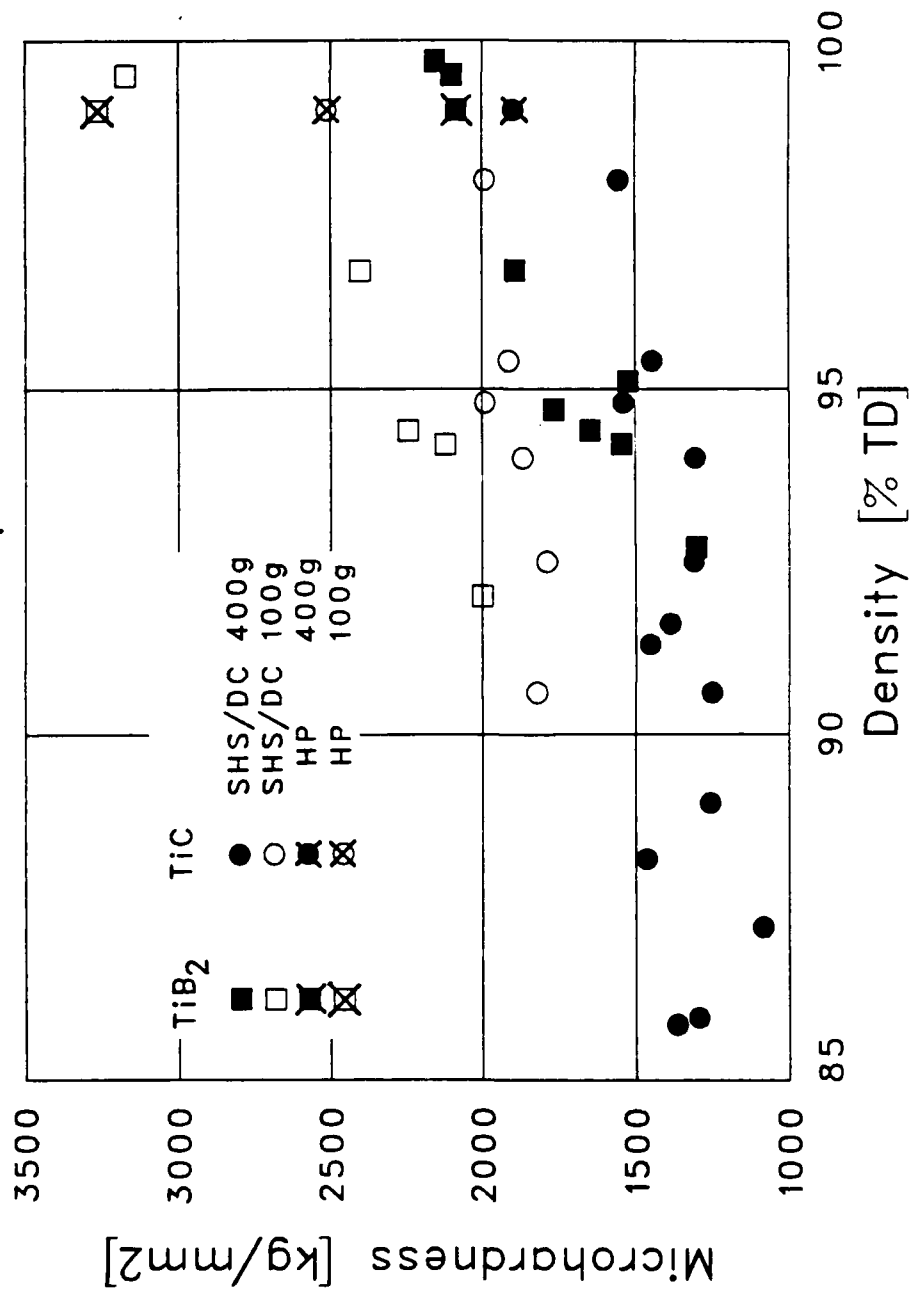


Figure 3

MS #33

High Pressure Burning Rate of
Silicon in Nitrogen

Marc Costantino

and

J. Birch Holt

Chemistry and Materials Science Department
Lawrence Livermore National Laboratory
Livermore, CA 94550

ABSTRACT

We report measurements of the speed of the combustion front in the self-sustaining high temperature synthesis (SHS) of Si_3N_4 under high nitrogen pressure. We performed replicate experiments at two pressures, 10 and 100 MPa with dilutions of 25, 35, and 50 weight percent Si_3N_4 . Porosities of the starting material ranged from 0.59 to 0.66. Combustion speed was measured by detecting the melting of .04 mm diameter copper wires imbedded along the 75 mm long sample. At 10 MPa, the combustion speed is linear with weight per cent dilution by Si_3N_4 , in good agreement with Mukas'yan, et.al.¹ At 100 MPa, the speed has a maximum near a dilution of about 40 w/%. We attribute this to the balance between the excess heat generated in the combustion zone

KEYWORDS: Combustion Synthesis, Silicon Nitride, Silicon, High Pressure, Combustion Speed, Ceramics.

and the heat lost by convection and conduction in the dense nitrogen. At 10 MPa there is adequate excess heat at all dilutions to drive the combustion wave. However, at 100 MPa, the heat loss owing to convection competes with the heat generated by Si combustion. As the amount of silicon available for reaction decreases with increasing dilution, the net heat energy to drive the combustion wave decreases, and the combustion speed is slower.

INTRODUCTION

Recent results presented by Mukas'yan, et. al.¹ on the combustion of silicon in high pressure nitrogen show a strong dependence of the combustion speed, u_c , on the dilution of the silicon with silicon nitride, α , while the combustion temperature, T_c , remains constant. This is unexpected in the context of most solid-gas self-sustaining combustion, in which T_c decreases with dilution by an inert compound or by the combustion product. Mukas'yan, et.al. explain this effect by considering the melting of the pure Si and the dissociation of the Si_3N_4 . When the temperature in the thermal wave ahead of the combustion zone reaches 1707 K, the Si melts and flows in the porosity around the Si_3N_4 , increasing substantially the surface area of the unreacted Si. At about 2200K an equilibrium is established between the heat generated by the Si-N reaction, and the heat lost in dissociation and by transfer to the rest of the system. This thermal balance in the combustion zone results in a relatively constant T_c . The increase in the combustion speed, u_c , owes to the increase in surface to volume of the pure Si component as the volume fraction of Si_3N_4 increases. At

high values of α , there is relatively less Si between the Si_3N_4 particles. When the Si melts, the typical volume that must be reacted, ie., the volume of the molten Si in the porosity of the Si_3N_4 , becomes smaller and the surface to volume ratio larger. This faster reaction generates heat at a higher rate and increases the thermal gradient, resulting in a larger u_c . Mukas'yan, et. al.¹ report temperature and combustion speed measurements to 12 MPa (1700 Psi) using one apparatus and combustion in another to 200 MPa (28000 Psi).

We undertook this work as an initial step in a program to provide data that are useful in establishing the phenomenology of solid-gas, self-sustained high temperature synthesis (SHS) and in providing data for input and for tests of models. We report here combustion speeds of Si in N_2 as a function of N_2 pressures to 150 MPa and dilution by $\alpha\text{-Si}_3\text{N}_4$ of 25, 35, and 50 weight percent.

EXPERIMENTAL AND RESULTS

Samples were formed by stacking 7 to 10 disks 19 mm dia by 7 mm thick, made from a mixture of 2 micron Si and 3 micron $\alpha\text{-Si}_3\text{N}_4$. The speed of the combustion front was measured by detecting the melting of a 0.038 mm Cu wire placed between each disk.²

The experimental matrix and a summary of the results are in Table I. The fully-burned samples showed distinct differences in appearance, depending on the N_2 pressure. Regions of nearly-complete conversion to $\beta\text{-Si}_3\text{N}_4$, as determined by x-ray diffraction, appeared white to greyish-white, while those with substantial fractions of unreacted starting material, $\alpha\text{-Si}_3\text{N}_4 + \text{Si}$, appeared grey. The results of the

x-ray diffraction for starting pressures near 10 MPa are shown in Figure 1. The conversion from the $\text{Si} + \alpha\text{-Si}_3\text{N}_4$ mixture to the product, $\beta\text{-Si}_3\text{N}_4$, was substantially complete throughout most of the sample except for the case $\alpha = 0.25$, for which there remained a considerable amount of the original $\alpha\text{-Si}_3\text{N}_4$. At the surface of the cylinder, there was less complete reaction, with only partial conversion of the Si and $\alpha\text{-Si}_3\text{N}_4$ to $\beta\text{-Si}_3\text{N}_4$.

As seen in Figure 2, this was not the case for experiments with starting pressures near 100 MPa. Internally, the conversion of the $\text{Si} + \alpha\text{-Si}_3\text{N}_4$ mixture to $\beta\text{-Si}_3\text{N}_4$ was above 90%. However, in a shell 1-2 mm thick at the surface of the cylinder, the color of the product indicated a composition gradient, with x-ray analysis of material at the surface showing almost no reaction.

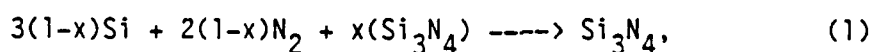
Data for the burning speed vs. weight per cent dilution with Si_3N_4 are shown in Figure 3 and listed in Table 1. The curves drawn through the data are guides to the eye.

DISCUSSION

A. Nitrogen density

In SHS the reaction rate must be fast enough so that the exothermic heat generated equals or exceeds the heat required to ignite the reactants plus the heat lost to the environment. In solid-solid SHS, reactants in stoichiometric quantities are mixed intimately, usually with particle sizes of the order of a few microns. However, in solid-gas systems the gaseous reactant must flow into the reaction zone from, ultimately, the volume outside the sample. As a consequence, the permeability of the sample volume is important, especially if a melt

phase exists. This requirement for mass transport can be relaxed somewhat if the gas density in the porosity near the combustion zone is adequate to provide enough gas to complete the reaction. For the present discussion, we can divide the sample into three regions: 1) the unreacted volume far ahead of the combustion front, 2) the volume ahead of the combustion front that is affected by the thermal gradient created by the combustion, and 3) the volume behind the combustion front. We will ignore the last, and discuss the effect of N_2 pressure on the first two. For the reaction



the nitrogen density, in a homogeneous volume containing Si and porosity, required for complete reaction is

$$\tilde{\rho}(N_2) > \frac{2}{3} \cdot \frac{(1-\phi)}{\phi} \cdot \frac{1}{1 + \left(\frac{\alpha}{1-\alpha}\right) \frac{\rho(Si)}{\rho(Si_3N_4)}} \cdot \tilde{\rho}(Si) \quad (2)$$

where ϕ , as before, is the porosity, α the weight per cent Si_3N_4 , and $\tilde{\rho}$ are molar densities ($kmol/m^3$). We ignore the change in the density of silicon with temperature, pressure, and change of phase, and plot in Figure 4 the nitrogen density required for complete reaction vs w/% dilution with Si_3N_4 for two porosities. For example, the N_2 density required for a sample having a porosity of 0.6 and diluted with 50 w/% Si_3N_4 is about $22 kmol/m^3$. At room temperature, this corresponds to an N_2 pressure of about 120 MPa. If the porosity is 0.65, the N_2 pressure required for complete reaction is about 70 MPa. On the other hand, for $\alpha = 0.25$, the required pressure is about 340 MPa for $\phi = 0.60$; and

for $\alpha = 0.35$, the value is about 230 MPa. We conclude that there is inadequate N_2 contained in the porosity for complete combustion without mass flow in all cases for the 10 MPa experiments. For the 100 MPa experiments, the density is high enough for some combinations of dilution and porosity, but not others.

Of course, the N_2 density relevant to the combustion is that at the pressure-temperature conditions in and near the combustion zone. Assuming pressure equilibrium in the porosity, these are the measured pressure and the combustion temperature. We can estimate T_c from Mukas'yan, et. al.,¹, who find $dT_c/dP \approx 4.5K/MPa$, and $T_c(P=6 MPa) \approx 2200K$. Thus, at $P=150 MPa$, $T_c \approx 2850K$. To find the N_2 density at this P, T we use the second virial equation, with constants from Hirschfelder, Curtiss, and Bird³

$$Pv = RT [1 + B(T)/v], \quad (3)$$

where $R = 8.3147(10^3) J-K^{-1}-Kmol^{-1}$, $B(T)$ is the temperature dependent second virial coefficient and v is the molar volume. For $T=2850K$, $B(T) = 0.527b_0$ where $b_0=63.78(10^{-3})m^3/Kmol$. Evaluating Eqn (3) for $P = 150 MPa$ and $T = 2850K$, $v = 0.187 m^3/Kmol$ and the N_2 density is $5.35 Km^3/m^3$.

Since this is about a factor of five less than is required for complete combustion, there must be some transport from nearby, cooler porosity into the combustion zone. Assuming $dT/dt=10^4K/s$ in the combustion wave and a combustion speed of $1mm/s$, the spatial temperature gradient is about $10^4K/mm$. Solving Eqn (3) for $P=150 MPa$ and $v=.04m^3/Kmol$ (corresponding to nominal values for the dilution and porosity for this work), we find $T \approx 500K$. For a temperature gradient of $10^4K/mm$, this means gas must flow about $0.05mm$ to reach the combustion front or, for a

mean particle size of 2 microns, about a distance of 25 particles. Thus it is not surprising that the combustion does not seem to be limited by the permeability of the reactant mixture. In this rough analysis, we have ignored the presence of a melt which may decrease the permeability significantly near the combustion zone.

Combustion Speed

Our combustion speed results for starting pressures near 10 MPa agree reasonably well with those of Mukas'yan, et.al..¹ The speed increases nearly linearly with dilution, with little or no scatter in the replicated experiments. Hirao, et. al.,⁴ report combustion speeds at 10 MPa N_2 pressure that decrease strongly with decreasing porosity for dilutions of about 30 and 47 weight percent Si_3N_4 . Our data can be compared only at their lowest porosity of about 60%, where the combustion speeds agree within the scatter in their data. Their data do not show a dependence of the combustion speed on dilution. At starting pressures near 100 MPa we find that the combustion speed has a maximum at a dilution of 30-40 w/% $\alpha-Si_3N_4$. With the limited data available, we can only speculate that the maximum owes to a balance between the increase with α of the reaction surface area of the melted Si, as postulated by Mukas'yan, et.al., and the decrease in the heat balance in the combustion zone.

We examine the effect of pressure and dilution by Si_3N_4 on the combustion speed (Fig. 3) by considering the heat balance in the combustion zone. High N_2 density increases the reaction rate owing to higher fugacity and to the ready availability of N_2 in the porosity

near the combustion zone. For Arrhenius reactions, it decreases the reaction rate owing to a decrease in combustion temperature resulting from better heat transfer away from the combustion zone. We also note that the heat generation rate may be constrained by both the amount of Si available for reaction ($1-\alpha$) and its surface area, as proposed by Mukas'yan, et. al.¹ The combustion speed, then, depends on the balance between these heat source and sink mechanisms. At 10 MPa, neither the heat loss nor the flux of Si into the combustion zone dominate, and the combustion speed increases with α because of the increase in reactive surface area. Since the starting porosity in our study was nominally constant near 62%, we cannot draw conclusions about the effect on the combustion speed of preheating, owing to radiation, of the material ahead of the combustion front, as suggested by Hirao, et. al..⁴

However, at high N_2 density the heat loss owing to conduction and convection and the relative decrease in heat generation owing to the decrease in the amount of Si available for reaction evidently become important. At 470K the thermal conductivity of N_2 increases by about 20% over the pressure range 1 to 28 MPa.⁵ Thus, at 100 MPa, we expect the heat loss out of the combustion zone to increase significantly. In addition, the higher combustion speeds at 100 Mpa increase the flux of unreacted Si into the combustion zone. As long as the weight per cent of Si is adequate, the combustion speed increases with α , with the initially higher slope at 100 MPa owing to the increased fugacity. However, as α increases, the heat source owing to the Si reaction decreases (since the amount of Si available for reaction is $1-\alpha$) and

finally is overtaken by the heat loss owing to conduction and convection. At 100 MPa and dilutions near 40%, the mechanisms tending to decrease the heat balance in the combustion zone begin to dominate, and the combustion speed decreases.

REFERENCES

1. A.S. Mukas'yan, V.M. Martynenko, A.G. Merzhanov, I.P. Borovinskaya, and M.Yu. Blinov, *Fizika Goreniya i Vzryva*, 22, 43-49(1986).
Translated in *Combustion, Explosion, and Shock Waves*, 22, 534(1986).
2. M. Costantino and D. Ornellas, 23d JANNAF Combustion Meeting, 20-24 October 1986; Hampton, VA.
3. Joseph O. Hirschfelder, Charles F. Curtiss, and R. Byron Bird, Molecular Theory of Gases and Liquids, John Wiley and Sons, 1967
4. K. Hirao, Y. Miyamoto, and M. Koizumi, *Advanced Ceramic Materials*, 2, No. 4 p. 780, 1987.
5. A.I. Johns, S. Rashid, L. Rowan, J.T.R. Watson, and A.A. Clifford, *Int. J. Thermophysics*, 9, 3(1988)

Table 1. Sample characterization and combustion speeds for the combustion of Si in N₂.

Exp't	P(MPa)	Weight %	Density	Porosity (%)	u _c (mm/s)
		Si ₃ N ₄	(gm/cm ³)		
14	10	25	1.022	59.7	.54
15	10	25			.50
10	10	35	.975	62.9	.67
11	10	35	.967	63.2	.67
16	10	50	.961	65.4	.87
17	10	50	.953	65.6	.87
12	100	25			1.10
13	100	25	1.0	60.4	1.07
8	100	35	.943	64.0	1.23
9	100	35	.964	63.3	1.32
18	100	50	.966	65.2	1.12
19	100	50	.944	66.0	1.01

Captions to the figures.

Figure 1. Composition of the SHS product after combustion of Si in N_2 , diluted with x wt% Si_3N_4 , with a nominal starting pressure of 10 MPa. The balance for each sample is unreacted Si.

Figure 2. Composition of the SHS product after combustion of Si in N_2 , diluted with x wt% Si_3N_4 , with a nominal starting pressure of 100 MPa. The balance for each sample is unreacted Si.

Figure 3. Combustion speed vs. dilution by Si_3N_4 . The chain-dot line is from Mukas'yan, et.al.¹

Figure 4. Molar density of N_2 required such that there is full reaction of Si diluted by x wt% Si_3N_4 using only the N_2 in the sample porosity.

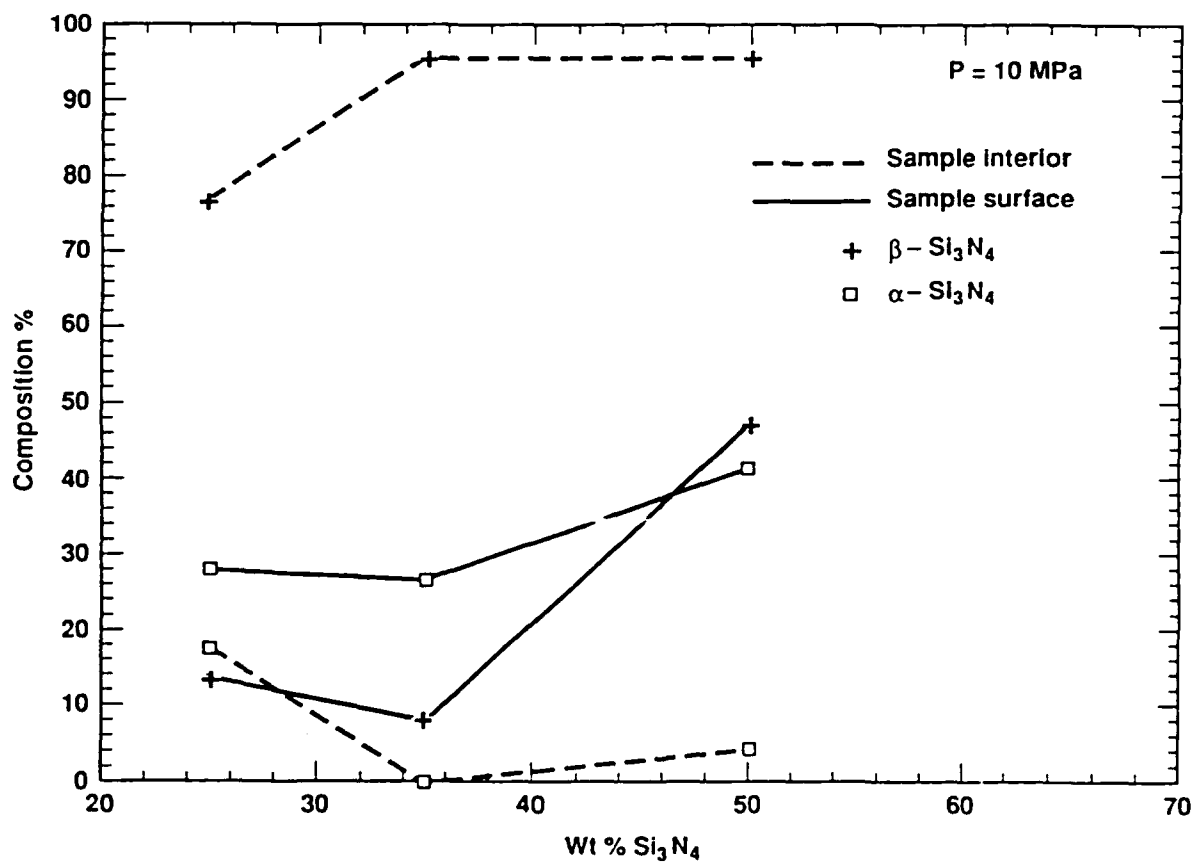
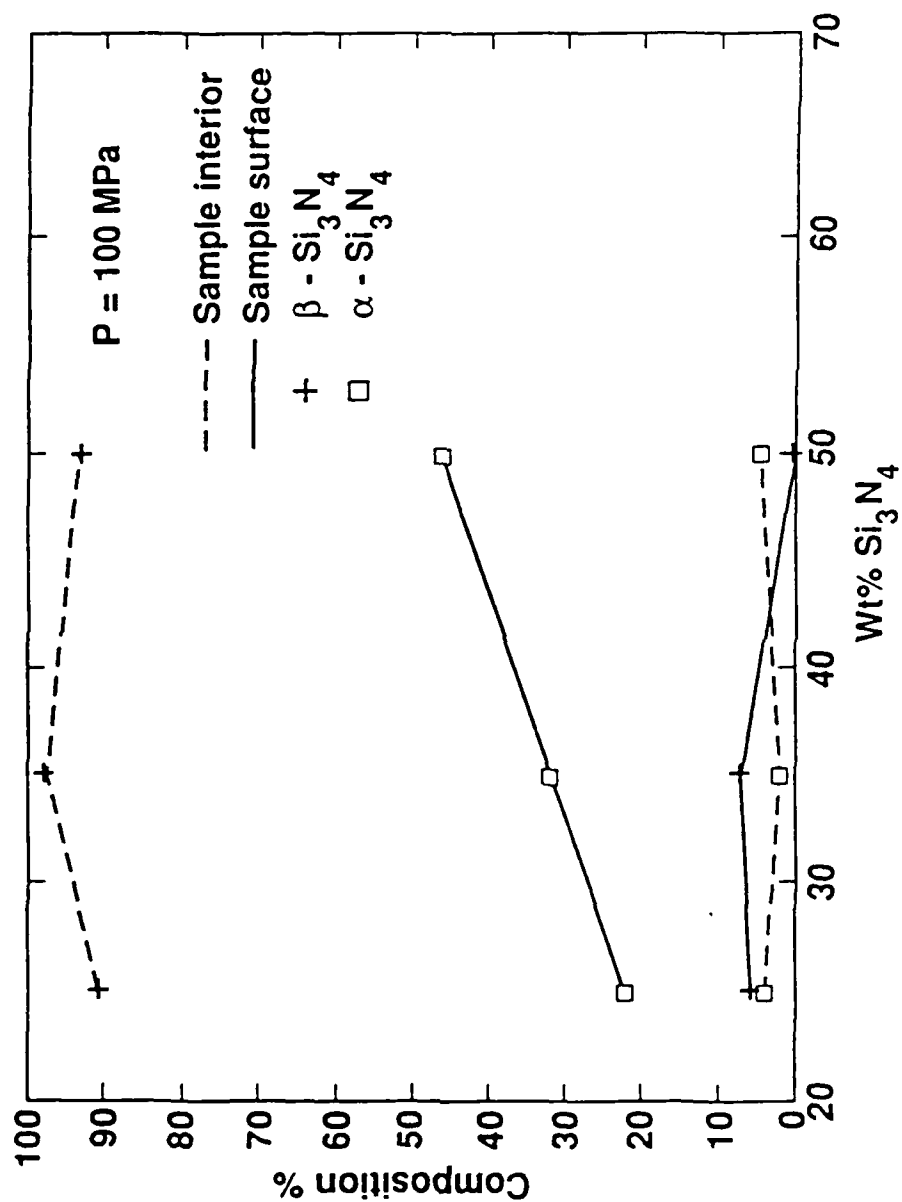


Fig. 1

Fig. 2



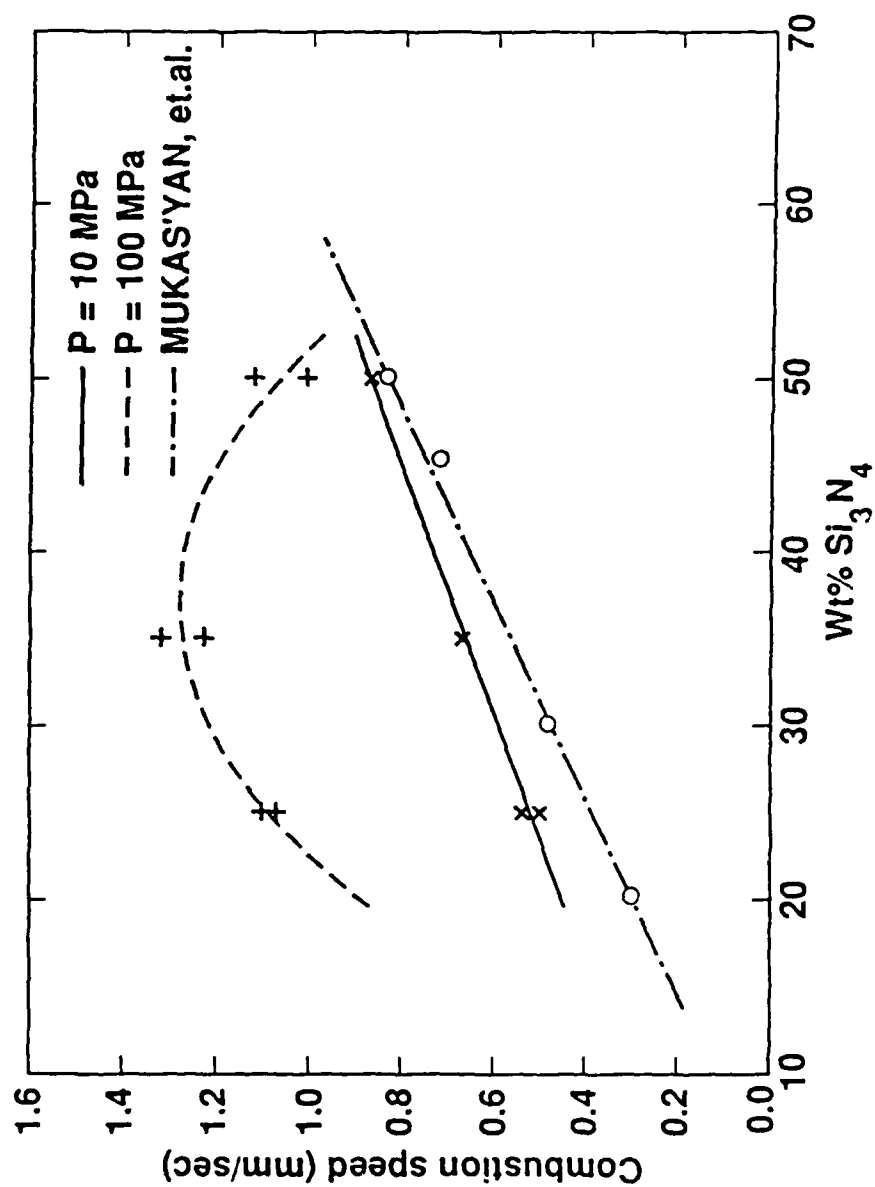


Fig. 3

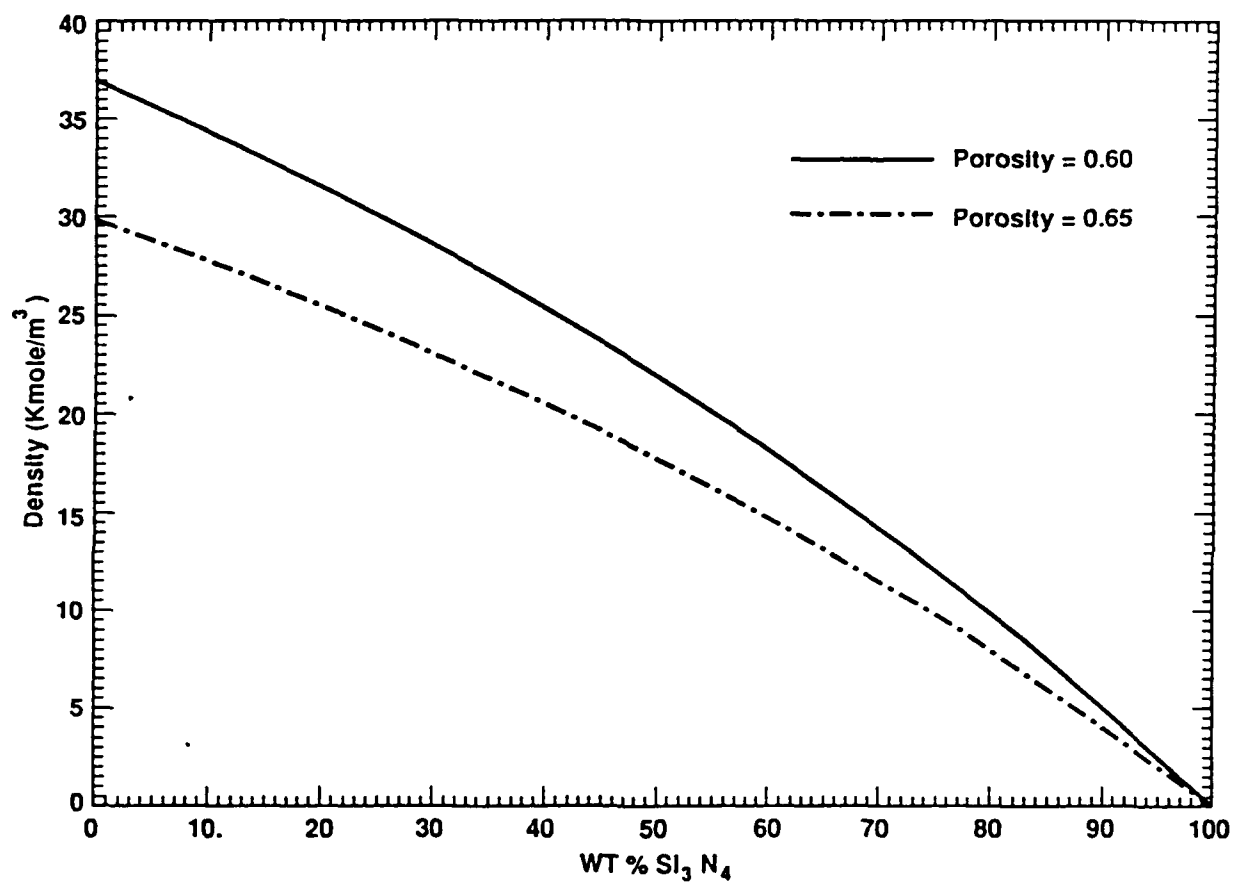


Fig. 4

Preparation of TiC Single Crystal from Self-Combustion Rod
by Floating Zone Method

Shigeki OTANI, Takaho TANAKA and Yoshio ISHIZAWA
National Institute for Research in Inorganic Materials
1-1, Namiki, Tsukuba, Ibaraki 305, Japan

ABSTRACT

The use of the SHS process to provide pure materials for subsequent single crystal preparation is demonstrated. From an SHS product, TiC single crystals were prepared by the floating zone method.

Introduction

The single crystals of TiC are of interest as new field emitters because their electron beam is stable, without noise or drift [1,2]. As a field emitter, a high purity single crystal with nearly stoichiometric composition is needed.

The single crystals prepared from the commercial powder contains 0.05 - 0.5 wt% of a tungsten, W, impurity [3,4]. The W impurity often causes troubles during a zone pass, such as difficulties in the seeding process and polycrystalization due to sudden spurious nucleation. The impurity can not be removed at all by a zone pass, in spite of a high growth temperature (2900°C) because W has a lower vapor pressure than TiC and its distribution coefficient is higher than unity [3,5].

Therefore, in order to remove the impurity from the starting material, we tried the synthesis of the carbide by the self-combustion reaction of Ti metal and carbon [6,7], and, using a self-combustion rod prepared at the same time, prepared TiC single crystal by floating zone method.

2. Experimental

The raw materials used were Ti metal powder with -350 mesh, and carbon black which had been heated in advance at 2000 °C in vacuum (10^{-4} torr) to remove the oxygen and nitrogen impurities. The starting materials with various compositions were produced by mixing them with a small amount of acetone. After putting the mixture in the rubber bag and shaping it cylindrically, it was isostatically pressed (100 MPa) at room temperature to form a rod 9 mm in diameter and 15 cm long.

The rod was put in the graphite susceptor, and the end of the susceptor was put into the heater (1300 °C) in vacuum (10^{-2} torr) to start the self-combustion from the end of the rod. The combustion temperature was determined from the rod surface temperature during self-combustion, using a two color pyrometer, which was calibrated up to 2800 K and extrapolated above 2800 K[8,9]. After the self-combustion, the susceptor was taken off from the heater and cooled down.

The contents of carbon, oxygen and nitrogen were determined by analyzers (LECO, WR-12 and TC-136). The densities of the rods were determined from the measurement of the volume and the weight after cutting it to 2 cm long rods.

Using these rods, the single crystals were prepared by a floating zone technique in a radio frequency induction heating furnace. The molten zone was passed under 9 atm of helium, using a 3 turn-2 step coil 18 mm in diameter. The details are given elsewhere[3,4,10].

3. Results and discussion

The important things for the preparation of the feed rod are the composition control, the purity, its density and the preparation of a straight cylindrical rod. Therefore, we examined the influence of the self-combustion preparation.

The composition change due to the self-combustion synthesis is shown in fig. 1. The composition tended to change to the carbon rich composition in the composition range of less than $C/Ti=0.8$. On the other hand, in the range of a higher ratio than $C/Ti=0.9$, the composition tended to change to the carbon poor composition. The composition deviations were not so large, at most, 3 at% in spite of self-combustion in vacuum. This is because the combustion time is short in spite of the high combustion temperature. However, the reaction between Ti and carbon proceeded enough in the entire composition range, judging from the splitting of the $K\alpha_1$ and $K\alpha_2$ peaks on the x-ray diffraction chart. According to fig.1, the composition of the feed rod could be controlled within 1 at%.

The combustion temperature is shown as a function of the rod composition in fig.2(a). The combustion temperature was maximum, 2980 K, at a composition (C/Ti) of 0.95. The cross section of the self-combustion rod with $C/Ti=0.98$ is shown in fig.2(b). The rod had many small cavities inside. It was found from the observation under a microscope that the interior of the rod partially melted and the cavities were formed by melting. Therefore, the inside temperature during the self-combustion

reaction was found to be the TiC-C eutectic temperature (3049 K)[12]. On the other hand, the peripheral part of the self-combustion rod had no cavities, as shown in fig.2(b), which indicates the combustion temperature at the peripheral part was lower than the eutectic temperature. Therefore, the measured temperature of the rod surface, 2930 K, was reasonable.

The contents of oxygen impurity in the rod decreased from 0.55 to 0.15 wt% with increasing carbon content. This oxygen came from the Ti metal powder which contained 0.5 wt% of oxygen. The oxygen contents were at the same level, compared with the rod sintered from the commercial TiC powder. The nitrogen contents decreased from 0.04 to 0.01 wt% with increasing carbon content, like the case of oxygen. The nitrogen contents were much lower, compared with that in the sintered rod. The metal impurities in the rod were examined by x-ray fluorescence spectroscopy. Only iron impurity, which came from the Ti powder (120 ppm), was detected as a trace. The iron contents may be less than 10 ppm, but this impurity can be refined perfectly due to evaporation during a zone pass[3,4]. Therefore, the impurity contents in the rod are low enough for preparation of the TiC crystal.

The relative density of the self-combustion rod decreased from 50 to 40 % with increasing carbon content when the density of TiC was assumed to be 4.87 g/cm^3 . The cross section of the feed rod was already shown in fig. 2(b). These densities are fairly low, compared with that of the rod sintered from the TiC powder(70 %). This comes from the facts that the green rod does

not have such a high density (55 %), that the rod did not shrink due to self-combustion, and that the volume decreased by 23 % due to the reaction of titanium and carbon. Because of the low density, we had to prepare a longer feed rod, compared with the desired length of the crystal.

It was not difficult to prepare the rod with a desired shape and size by the self-combustion method, controlling the temperature of the heater and the position of the graphite susceptor.

The features of the self-combustion rod were low density and high purity.

4. Preparation and characterization of the crystal

The single crystal of $\text{TiC}_{0.96}$ was prepared by the modified zone leveling method[4]. The feed rod with the composition of $\text{C/Ti}=0.98$ was attached to the upper shaft in the furnace. The $\langle 100 \rangle$ seed crystal was attached to the lower shaft. A carbon disk was put between them to control the composition of the initial molten zone so as to reach a zone leveling condition on initial melting. The initial zone was formed by melting the seed crystal and the carbon disk because the density (43 %) of the feed rod was too low to form the initial molten zone. The crystal growth rate was 1.5 cm/h, and the feed rod was melted into the molten zone at a rate of 3.5 cm/h to compensate for its low density.

Using the self-combustion rod as a feed rod, the heating

power during a crystal preparation was decreased by 10 %, compared with the case of a usual sintered rod with 70 % of the relative density[13]. This is because the heat flow from the molten zone to the feed rod decreased due to the low density of the feed rod (43 %). To decrease the heating power is profitable for the preparation of crystals with high melting points.

The grown crystal is shown in fig.3(a). The crystal is 9 mm in diameter and 4 cm long. The smoothness of the crystal surface indicates that the zone could be passed stably in spite of the low density.

The crystal composition (C/Ti) were determined to be 0.946, 0.956 and 0.958 at the initial, middle and final parts of the crystal rod, respectively. The composition was controlled within the accuracy of 1 at%. The oxygen impurity was not detected (less than 20 ppm) and the nitrogen impurity content was 30 ppm, which is one order lower than the previously grown crystal[5]. W and other metal impurities could not be detected by x-ray fluorescence spectroscopy. The purity of the crystal was increased by more than one order of magnitude, that is, >99.99 %, compared with the crystal prepared from the commercial powder.

The influence of the W impurity on the crystal growth was examined. Fig.4 shows the longitudinal cross sections of the initial parts of the crystal rods, which were prepared by spontaneous nucleation. The initial grains in the W-free rod were large, which indicates that the grain easily grows large, that is, the single crystal can be prepared easily.

In the case of using a commercial powder, the growth rate had to be lower than 0.5 cm/h in order to prevent perfectly the troubles caused by the W impurity[4]. However, using a self-combustion rod, the preparation at higher growth rate, 1.5 cm/h, was made possible, and the crystal quality was increased. This is because the decrease in crystal quality after growth due to the strong thermal stress was suppressed by increasing the growth rate[14]. The (100) cleavage plane of the prepared crystal is shown in fig.3(b). Compared with the conventional crystal prepared at 0.5 cm/h[4], the misorientation of higher than one degree was removed over the cross section. The density of the subgrain boundary, which is observed as lines on the (100) etching plane, also decreased from 1400 to 850 cm^{-1} ($=\text{cm}/\text{cm}^2$).

5. Conclusion

Using the self-combustion rod, the crystal purity was increased by more than one order of magnitude. The high purity led to removal of the troubles during a zone pass. Consequently, the preparation of the single crystals was made possible in the optimum growth conditions, and the crystal quality was improved.

Self-combustion has been found very useful for the preparation of materials for single crystals with high melting points because it is difficult to obtain the high purity materials.

References

- [1] Y.Ishizawa, S.Aoki, C.Oshima and S.Otani, J. Vacuum Soc. Japan, 29(1986)578.
- [2] Y.Ishizawa, M.Koizumi, C.Oshima and S.Otani, J. DE Physique C6(1987)9.
- [3] S.Otani, T.Tanaka and Y.Ishizawa, J. Less-Common Metals, 82(1981)63.
- [4] S.Otani, S.Honma, T.Tanaka and Y.Ishizawa, J. Crystal Growth 61(1983)1.
- [5] S.Otani, ~~Y.Ishizawa~~, T.Tanaka and Y.Ishizawa, J. Crystal Growth (in press).
- [6] J.B.Holt and Z.A.Munir, J.Mater.Sci. 21(1986)251.
- [7] O.Yamada, Y.Miyamoto and M.Koizumi, J.Am.Ceram.Soc. 70(1987)C-206.
- [8] S.Otani, T.Tanaka and Y.Ishizawa, J.Crystal Growth 66(1984)419.
- [9] S.Otani, T.Tanaka and Y.Ishizawa, J.Less-Common Metals 113(1985)205.
- [10] S.Otani, T.Tanaka and Y.Ishizawa, J. Crystal Growth 83(1987)481.
- [11] A.P.Hardt and F.J.Valenta, Proc. of 8th Int. Pyrotechic Seminar, Steamboat Spring, Colorado, July 1982, p297.
- [12] L.E.Toth, Transition Metal Carbides and Nitrides, (Academic Press, New York, 1971).
- [13] S.Otani, T.Tanaka and Y.Ishizawa, J. Crystal Growth 87(1988)175.

- [14] S.Otani, T.Tanaka and Y.Ishizawa, J. Crystal Growth
92(1988)8.

Figure captions

Fig.1 Composition change due to self-combustion.

Fig.2 (a) Self-combustion temperature. The dashed line[6] and dash-dotted line[11] show the calculated adiabatic temperature. The arrow shows the TiC-C eutectic temperature(3049 K)[12]. (b) Cross section of the self-combustion rod with composition of C/Ti=0.95.

Fig.3 (a) $\text{TiC}_{0.96}$ single crystal rod and (b) the (100) cleavage plane. Marker represents 1 cm.

Fig.4 Longitudinal cross sections of the initial parts of (a) the W-free crystal and (b) the W-contained crystal, which were prepared by spontaneous nucleation.>

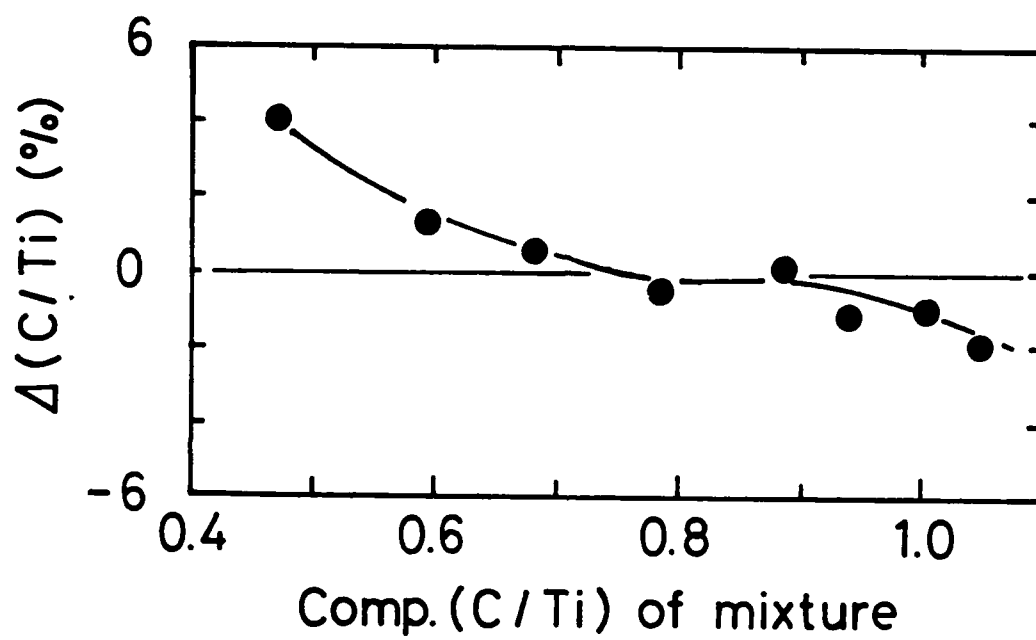
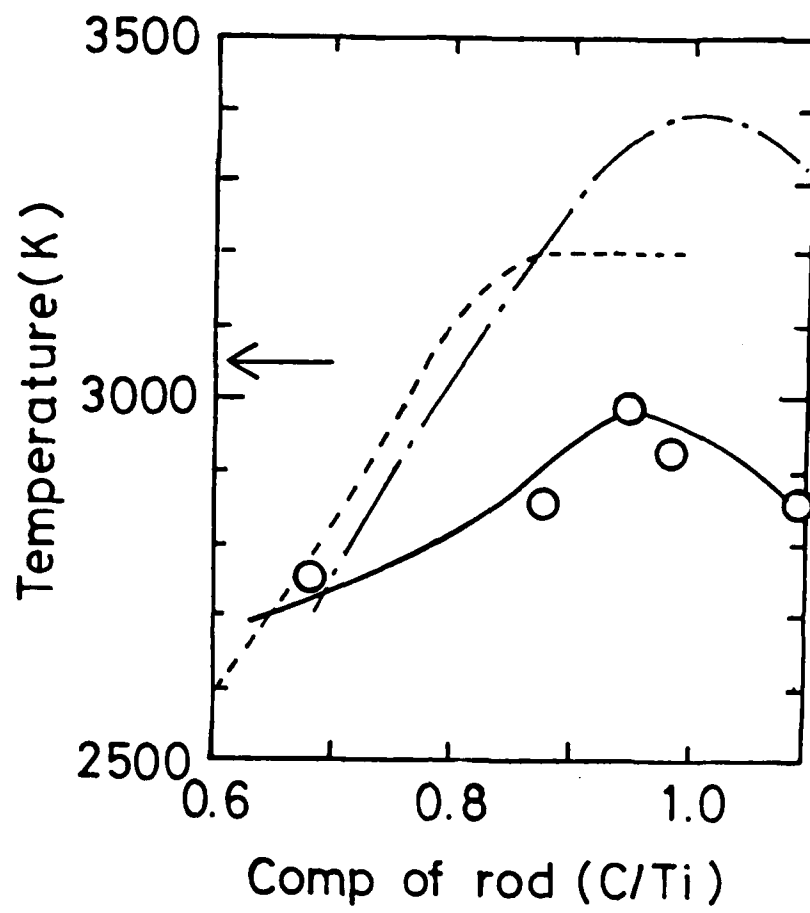
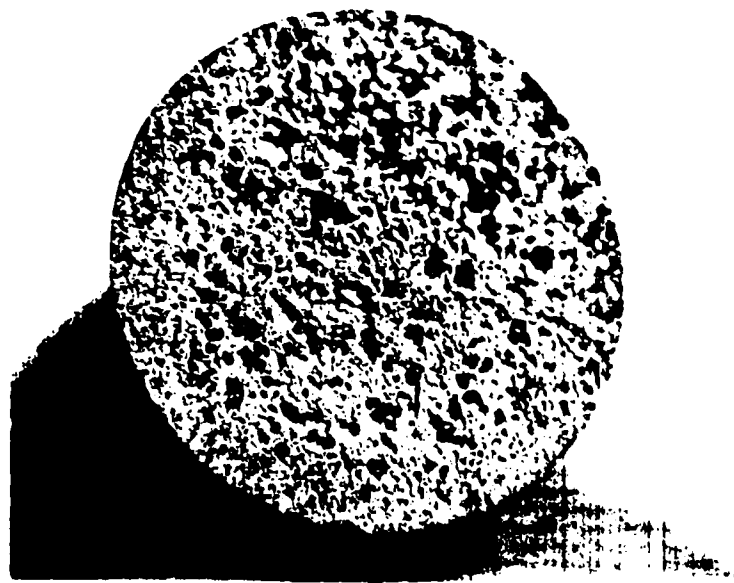


Fig. 1.

S. Otani



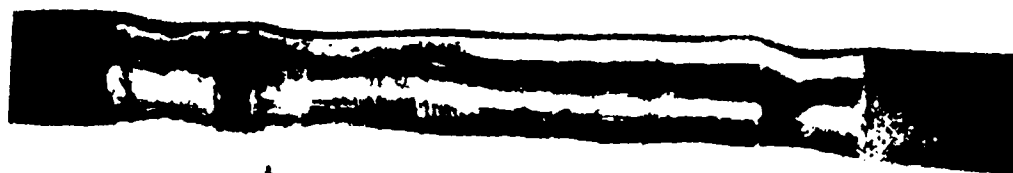
(a)



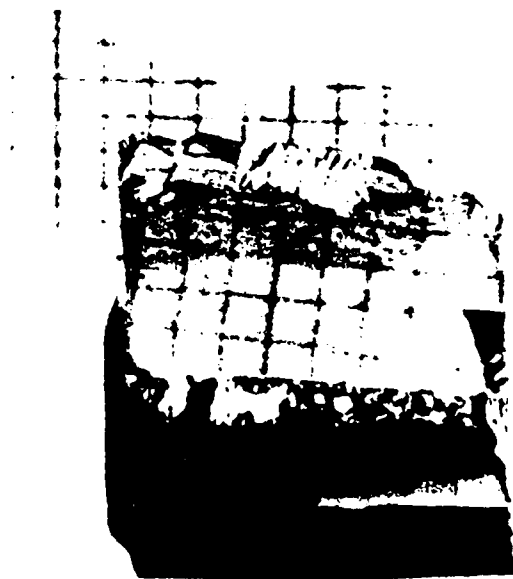
(b)

Fig.2

S. Otani.



(a)



(b)

Fig. 3. S. Otani



(a)



(b)

Fig. 4. S. Otani

THERMAL PLASMA SYNTHESIS OF CERAMIC POWDERS AND COATINGS

Toyonobu Yoshida

Department of Metallurgy and Materials Science
Faculty of Engineering, The University of Tokyo
Hongo, Bunkyo-ku, Tokyo 113, JAPAN

Abstract

In this paper, we characterize three types of injection plasma processing (IPP) and review the problems relating to IPP. In order to demonstrate the feasibility and prominent features of IPP, special attention will be given to radio-frequency(rf) and hybrid plasma processing, which will be discussed in conjunction with our recent research concerning the synthesis of ceramic powders and coatings. "Super-high rate deposition of ceramics" and "rf plasma spraying of ceramics" will be proposed as two distinctive candidates for the future development of IPP in the field of ceramic technology.

key words: thermal plasma synthesis, ceramic powders and coatings, RF plasma, Hybrid plasma

1. Introduction

Over the past two decades, thermal plasmas have been used for processing of materials and chemicals. However, the development of plasma technology, especially in the fields of inflight or injection plasma processing(IPP), was commercially successful only in a few cases. The major reason is that the direct current(dc) plasma jet has been used exclusively for generating thermal plasmas because of its ease of operation and installation. Unfortunately, however, the dwell time of the injected materials in the plasma is usually less than 1msec, which is insufficient to be used for the majority of synthesis by IPP. Moreover, the steep temperature gradients occurring in the plasma generally result in non-uniform heating and reactions. In these respects, rf

and hybrid plasmas are highly recommended. The most important characteristics of these plasmas are their large volume and low velocity. Moreover, they may allow central feeding of materials to minimize trajectory and reaction variations. From the viewpoints mentioned above, we have been developing rf and hybrid plasma processing. Fig.1 shows the promising fields for thermal plasma processing, which are now under study in our laboratory.

II.Characterization of IPP

The present thermal plasma technology can be roughly classified into two fields, which originated from batch-type arc heating technology and combustion flame technology. Injection plasma processing may be classified into a new branch of the latter case.

Fig.2 shows a conceptional drawing of IPP. As shown in the figure, IPP can be divided into the following four stage. In zone (A), it is crucial to inject reagents properly into the plasma without disturbance, in competition with the high viscosity and magneto-hydrodynamic characteristics of the plasma. In zone (B), thermal and reaction histories, and trajectories must be effectively controlled and homogenized. In zone (C), homogeneous and controlled reactions are essential. Especially, in the case of fine powder synthesis, nucleation and growth processes must be highly controlled by effective devices based on fluid dynamics as well as electromagnetics. In zone (D), it is now highly expected to develop an efficient collection method, which should not destroy the unique characteristics of the prepared powder. If these subjects could have been overcome by future research, many industrialized IPP should be developed to meet the need for the chemical synthesis of powders and coatings.

IPP can be divided into three main categories as shown in Fig.3. The thermal plasma CVD is characterized by the injection of gaseous reactants into the plasma. This processing may be considered to be the modification of usual

CVD. However, the axially injected reactants are completely dissociated to the elements, which is different from the usual CVD. Frequently, the second reactant such as CH_4 or NH_3 is injected into the tail flame in order to use radicals generating during heating process. In the thermal plasma flash evaporation method, powders are used as reagents. It may fairly be said that the ability to cause vaporization is a most important feature in this method. In order to expect perfect evaporation of the powders, the size less than 30 μm must be used⁽¹⁾. By this method, multicomponent composition controlled vapors can be easily generated in a plasma flame^(2,3). Frequently, reactive plasma is used for the reaction with the vaporized elements⁽⁴⁾. The advantages of this processing are its simplicity, flexibility, and that by-products can be minimized. The last one shows plasma spraying. In this case, injected powder size must be large enough not to be vaporized, and small enough to be completely melted. Each droplet is flattened on impact at the substrate and solidified, and the coating consists of many layers of the flattened particles. Essentially, the structure of the coating is determined by the viscosity of the droplet just before the collision rather than the velocity as will be shown in section IV-3.

III. Plasma torches for IPP

As mentioned in the pervious chapter, the most important key to success for IPP in various applications depends to a large extent upon the development of plasma torches which make it possible to generate relatively large size plasma, and to sustain a stable plasma, in particular, when reagents are being axially injected. In these respects, an rf plasma torch and a hybrid plasma torch are strongly recommended. Fig. 4 shows the schematic diagrams of these two torches, which have been used for IPP in our laboratory. And Fig. 5 shows the calculated temperature and flow fields in Ar plasmas, which will be

generated in the torches shown in Fig.4, with coil current of 4MHz-100A, sheath gas flow rate and swirl velocity of 40SLM and 10m/s, carrier gas and dc plasma jet flow rate of 5 SLM, and dc jet power of 0.6kW at inlet boundary. The rf input power level is about 6.6kW in each case. Principally, the rf plasma is electrodeless discharge and the plasma is free from electrode contamination. Accordingly, reactive gases such as O_2 and Cl_2 can be used as plasma gases for special cases. The residence time is the order of 10ms and this torch is very fit for powder processing in IPP. On the other hand, the main feature of the hybrid plasma is that the large recirculation flow existing in the rf plasma is extinguished by the presence of the high-velocity channel caused by the dc arc jet. Therefore, if the reactants can be carried by the arc jet flow, they can be expected to pass through the high temperature region higher than 9000K, with the dwell time of about 5 ms. The applications of the two-types torches to the thermal plasma synthesis of ceramic powders and coatings will be shown in what follows.

IV. Review of our recent research

IV-1 Hybrid plasma CVD

IV-1-1 Synthesis of ultrafine Si_3N_4 and SiC powders(5-8)

Fig.6 shows the reactor chamber designed for powder processing, schematically. Typical operating conditions are shown in Table I.

Silicon nitride

As shown in our previous papers(5-7), ultrafine amorphous Si_3N_4 with the nitrogen content of about 37 wt% and the size of 10 to 30 nm could be prepared successfully by a reaction of $SiCl_4$ with NH_3 . It was also shown that the nitrogen content did not depend on the $NH_3/SiCl_4$ molar ratio over the range of

the experimental conditions, but depended upon the absolute NH_3 injection flow rate. Recently, the influences of $\text{NH}_3/\text{SiCl}_4$ molar ratio and the injection linear velocity on the nitrogen content in the product and on the particle size were investigated. In Fig.7 nitrogen content are plotted as a function of $\text{NH}_3/\text{SiCl}_4$ molar ratio. D_s and V_s mean the diameter of the ring slit and the linear velocity at the exit of the slit. As might be expected, it was found that the nitrogen content depended on the quenching rate as well as the molar ratio. In each case, the powder was essentially amorphous ultrafine Si_3N_4 .

Silicon carbide

SiC synthesis was carried out by injecting CH_4 diluted with H_2 into the tail flame⁽⁸⁾. In this case also, the effects of the quenching rate on the carbon content in the product and on the particle size were investigated under two different conditions. The quenching rate was controlled by regulating the H_2 flow rate. In Fig.8, carbon content are plotted as a function of $\text{CH}_4/\text{SiCl}_4$ molar ratio. The data shown by open and filled symbols correspond to the cases for the H_2 flow rate of 50 SLM and 20SLM, respectively. In each case, the carbon content increased with the molar ratio of the reactants up to about 1.5, and approached a saturation value depending upon the H_2 flow rate. Nearly stoichiometric powder prepared here showed the color of whitish gray and consisted mainly of β - SiC . Fig.9 shows electronmicrographs of typical powders. These results clearly show that the particle size distribution and the composition can be controllable by changing the injection flow rate of the quenching gas.

It was confirmed that pure ultrafine amorphous Si_3N_4 and crystalline β - SiC could be prepared effectively by the processing developed here. Moreover, it was suggested that the effective "REACTIVE QUENCHING" is one of the key to success for the preparation of ideal ultrafine ceramic powders in this

processing.

IV-1-2 Super-high rate deposition of SiC layers

As shown in our recent paper⁽⁹⁾, thick and dense SiC layers were successfully deposited at a rate of 10 $\mu\text{m}/\text{min}$ on a graphite substrate from SiCl_4 and CH_4 under soft vacuum of about 200 Torr, by using a 25kW level hybrid plasma reactor. The best process conditions were typically under flow rates of $\text{SiCl}_4=1.5\text{ g/min}$ and $\text{CH}_4=0.3\text{ SLM}$, and deposition temperatures of 1000 $^\circ\text{C}$ to 1100 $^\circ\text{C}$. Fig.10 shows the cross section of the film deposited on a graphite substrate under optimum conditions for 30 min, which clearly show the high quality of the film. The density and the Vickers hardness of the film were 3.2 g/cm^3 , and higher than 3000 Kg/mm^2 . XRD showed that the film consisted of pure β -SiC with the preferred orientation of (100), which is different from the usual CVD cases. There might be some driving force caused by plasma-surface interaction for the presence of (100) orientation in this process, although the reason is not evident at this stage. Anyhow, this process may be easily applicable to another ceramics, and will be expected to play an important role in the future ceramic technology. Very recently, we have actually succeeded in depositing thick Si_3N_4 layers at a rate of above 10 $\mu\text{m}/\text{min}$ ⁽¹⁰⁾.

IV-2 RF plasma flash evaporation

As an example of rf plasma flash evaporation processing, the deposition of as-grown superconducting Y-Ba-Cu-O films using the rf plasma torch (Fig.4) will be shown here⁽¹¹⁾. A mixture of Y_2O_3 , BaCO_3 , and CuO powders of 1 μm in size or a co-precipitated powder of 1 μm in size with the same composition as that of the superconductor were fed into Ar- O_2 plasma, and co-evaporated completely. And the ternary composition controlled high-temperature metallic vapors were co-deposited onto (100) MgO single crystal substrates placed in a Ar- O_2 plasma

tail flame. The deposition rate of more than 10 $\mu\text{m}/\text{min}$ could be achieved. The crystal structures were identified to be orthorhombic oxygen-deficient layered perovskite $\text{Y}_1\text{Ba}_2\text{Cu}_3\text{O}_{7-x}$. It is also found that the c-axis-oriented films can be obtained. Fig.11 shows the superconducting transition temperatures of 92K(onset) and 83K(offset). These results confirmed that the reactive plasma flash evaporation method is very effective for the preparation of the mixed oxide superconducting films.

IV-3 RF plasma spraying

Fig.12 shows schematic illustration of (A) dc plasma spraying and (B) rf plasma spraying. Considering the features of an rf plasma, relatively large powders in size have to be used to prevent evaporation. The large heat capacity of such powders will reveal different spraying characteristics⁽¹²⁾ from those of the established spraying technology.

With these points as background, rf plasma spraying of Al_2O_3 and ZrO_2 ⁽¹³⁾ was tried by using the rf plasma torch shown in Fig.4. Typical experimental conditions are as follows: rf plate power, 4MHz-55kW; gas flow rate, 60 SLM(Ar) and 8 SLM(H_2); powder feeding rate, 5-10 g/min. Fig.13 shows the influence of the initial powder size(d) of Al_2O_3 on the sprayed and flattened particle diameter(D) at the distance(L)=5cm from the torch exit. This clearly shows that the powder of $d=80-100\mu\text{m}$ is suited to be sprayed in this case. Fig.14 shows the cross section of the sprayed Al_2O_3 layer under optimum conditions, which reveals that dense Al_2O_3 coating could be obtained by rf plasma spraying. Moreover, the coating mainly consisted of α -phase, which is different from the usual case and is considered to be favorable. Note that the use of such large size powders made it possible to deposit adhesive Al_2O_3 and ZrO_2 coatings of 300 μm on as-rolled SUS304 stainless steel without grit blasting treatment. This excellent adhesive characteristic seems to be due to the increase of the

heat flux from the larger particles to the substrate. These experimental results have proved that the rf plasma spraying must be a strong candidate to open new fields of spraying applications.

V. Summary

In this paper, we reviewed the problems relating to IPP and the promising fields for the future development of IPP. As shown in section IV-1, plasma synthesis of ultrafine ceramics powder by IPP has been, in a sense, well-established. However, because of the peculiar characteristics of ultrafine powders(UFP) such as high activity and surface area, UFP is too difficult to be processed with a conventional ceramic technology. Accordingly, for the future development of this field, considerable efforts from both sides of plasma technology and ceramic technology, must be directed toward opening the way to use the essential properties of such a peculiar powder. At this stage, "Super-high rate deposition of ceramics" proposed here is considered to be one of the solutions to overcome the above-mentioned problems. Without a doubt, another promising IPP relating to ceramic technology exists in the field of plasma spraying. The novel spray coating technique with an rf plasma torch or a hybrid plasma torch will open new spraying fields in the near future.

VI. Acknowledgments

The author is deeply indebted to the staff and many graduate students who have passionately engaged in research relating to each root and branch of the tree shown in Fig.1.

References

- (1) T.Yoshida and K.Akashi, J.Appl.Phys., 48 (1977) 2252
- (2) T Harada, T.Yoshida, T.Koseki, and K.Akashi, J.Japan Inst.Metals, 45(1981)1138
- (3) Y.Anekawa, T.Koseki, T.Yoshida, and K.Akashi, J.Japan Inst.Metals, 49 (1985) 451
- (4) T.Yoshida, A.Kawasaki, K.Nakagawa, and K.Akashi, J.Mater.Sci., 14 (1979) 1624
- (5) T.Yoshida, T.Tani, H.Nshimura, and K.Akashi, J.Appl.Phys., 54 (1983) 640
- (6) T.Yoshida, Y.Tamou, K.Eguchi, and K.Akashi, Proc.8th-ICVM,linz, Austraila (1985) 437
- (7) T.Tani, T.Yoshida, and K.Akashi, J.Ceram.Soc.Japan, 94 (1986) 11
- (8) Y.Tamou, T.Yoshida, and K.Akashi, J.Japan Inst.Metals, 51 (1987) 737
- (9) H.Murakami, T.Yoshida, and K.Akashi,Advanced Ceram.Mater., 3 (1988) 423
- (10) H.Murakami, H.Ngai, T.Irokawa, T.Yoshida, and K.Akashi, J.Ceram.Soc.Japan, 97 (1989) 49
- (11) K.Terashima, K.Eguchi, T.Yoshida, and K.Akashi, Appl.Phys.Lett., 52 (1988) 1274
- (12) S.Takeuchi, T.Okada, T.Yoshida, and K.Akashi, J.Japan Inst.Metals, 52 (1988) 711
- (13) T.Okada, H.Hamatani, and T.Yoshida, J.Am.Ceram.Soc. (in press)

Figure captions

- Fig. 1 Promising fields for thermal plasma processing.
- Fig. 2 Conceptual drawing of IPP.
- Fig. 3 Three main categories of IPP.
- Fig. 4 Schematic diagrams of rf and hybrid plasma torches.
- Fig. 5 Stream-line patterns and temperature distributions for rf and hybrid plasmas.
- Fig. 6 Schematic diagram of the reactor chamber designed for the preparation of ultrafine ceramics.
- Fig. 7 Nitrogen content in the products as a function of $\text{NH}_3/\text{SiCl}_4$ molar ratio with different quenching conditions.
- Fig. 8 Carbon content in the products as a function of $\text{CH}_4/\text{SiCl}_4$ molar ratio with different quenching conditions.
- Fig. 9 Typical electron micrographs of silicon carbide particles.
(left: higher quenching rate, right: lower quenching rate)
- Fig.10 Cross section of SiC film deposited on a graphite substrate under optimum conditions. (left:as-fractured, right:polished)
- Fig.11 Temperature dependence of the electrical resistance for an as-grown Y-Ba-Cu-O film.
- Fig.12 Schematic illustration of (A) dc plasma spraying, and (B) rf plasma spraying.
- Fig.13 Influence of the initial powder size(d) of Al_2O_3 on the sprayed and flattened particle diameter(D) at the distance of $L = 5$ cm from the torch exit.
- Fig.14 Cross-sectional SEM of sprayed Al_2O_3 layer.

Table I. Typical operating conditions

(1) Gas flow rate

Arc jet gas = 10 L/min(Ar)

Sheath gas = 30 - 40 L/min(Ar) + 1.5 - 2.0 L/min(H₂)

Carrier gas = 1.5 - 2.0 L/min(Ar)

Quenching gas = 20 - 50 L/min(H₂)

(2) Reactants injection rate

SiCl₄ = 1.6 - 4.6 g/min

NH₃ = 1.0 - 20 L/min

CH₄ = 0.1 - 0.8 L/min

(3) RF plate power input : 20 kW

(4) DC power supply : 5 kW

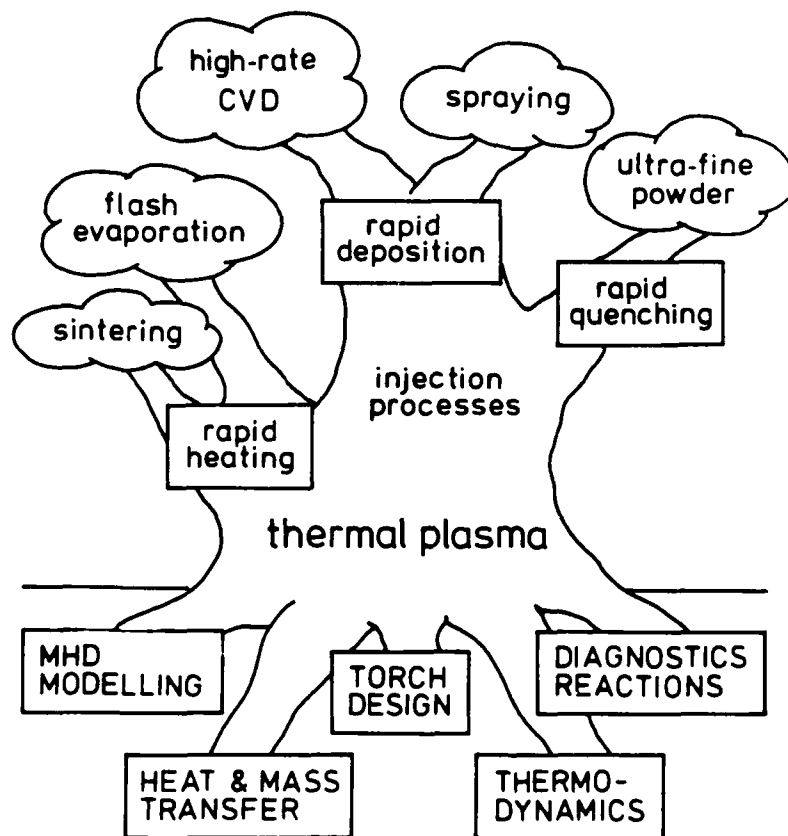


Fig. 1 Promising fields for thermal plasma processings

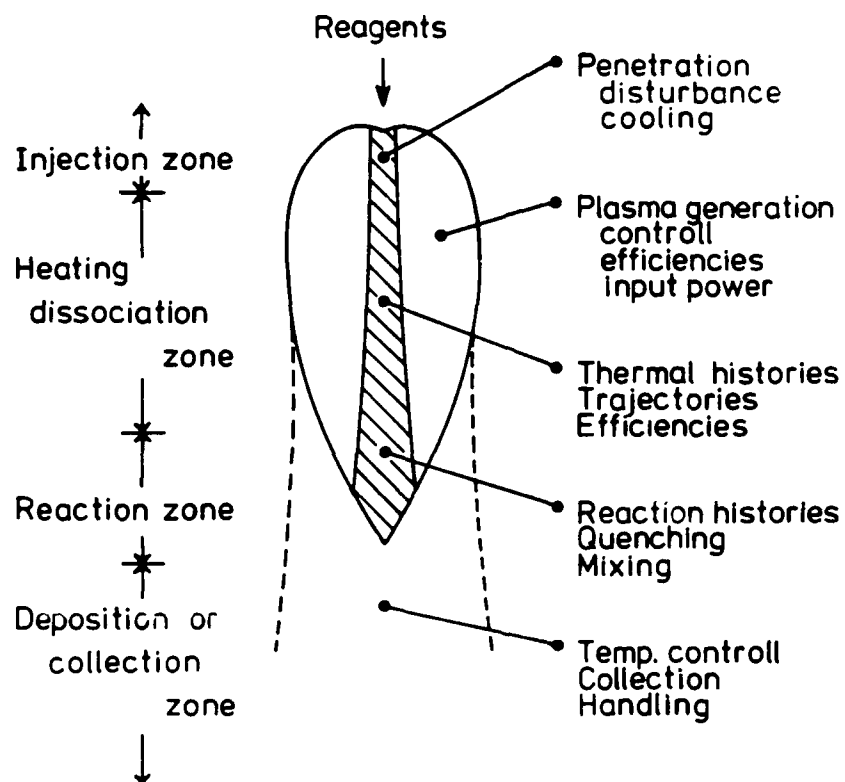


Fig. 2 Conceptual drawing of IPP.

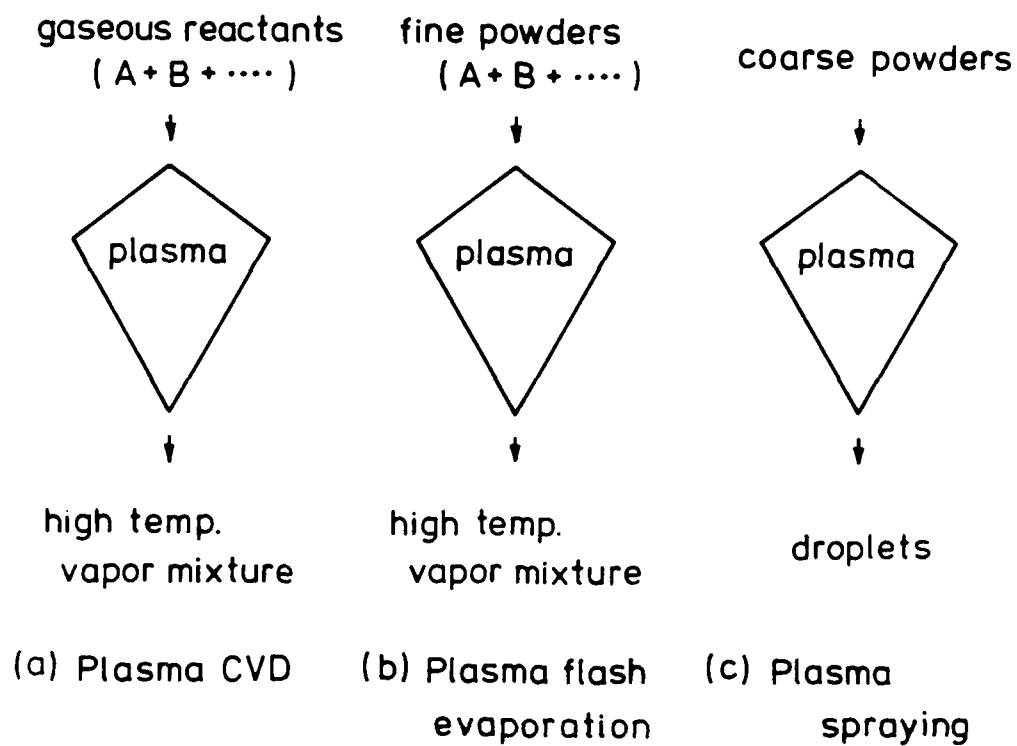


Fig. 3 Three main categories of IPP.

548

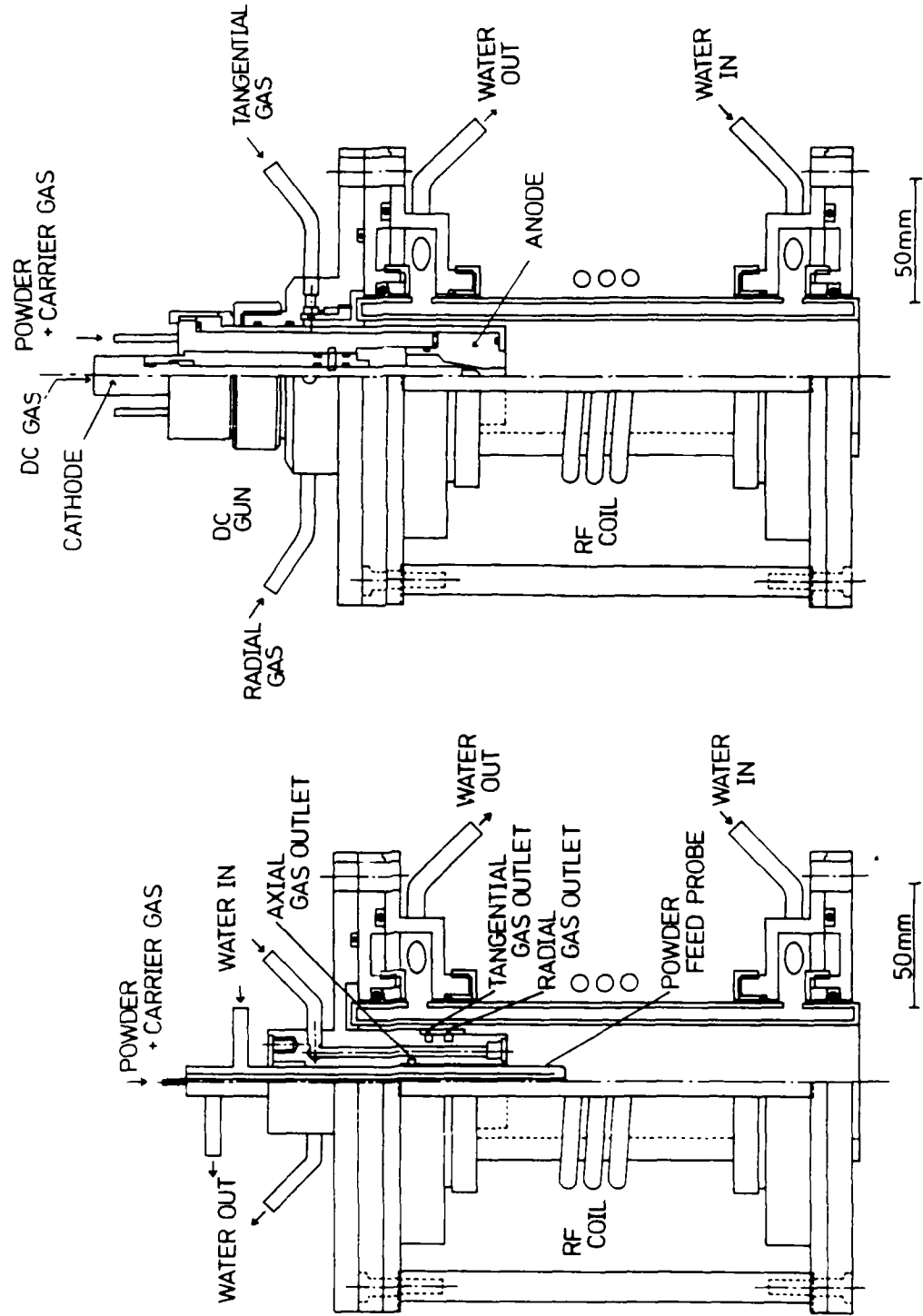


Fig 4 Schematic diagrams of rf and hybrid plasma torches.

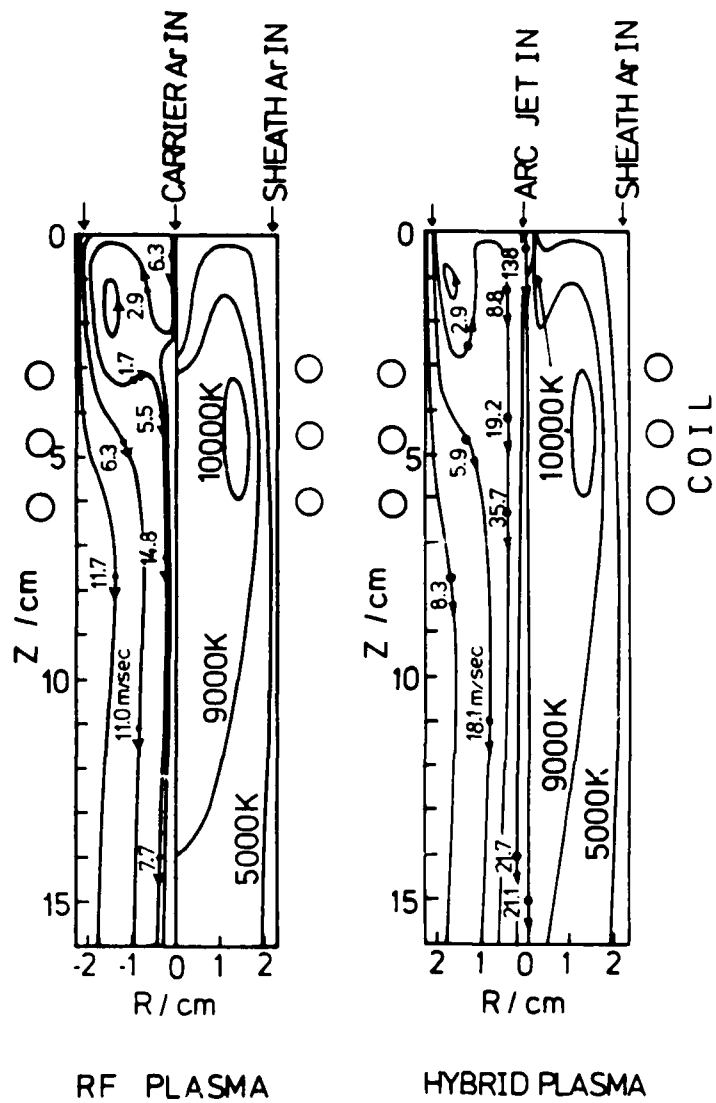


Fig. 5 Stream-line patterns and temperature distributions for rf and hybrid plasmas.

1. 2

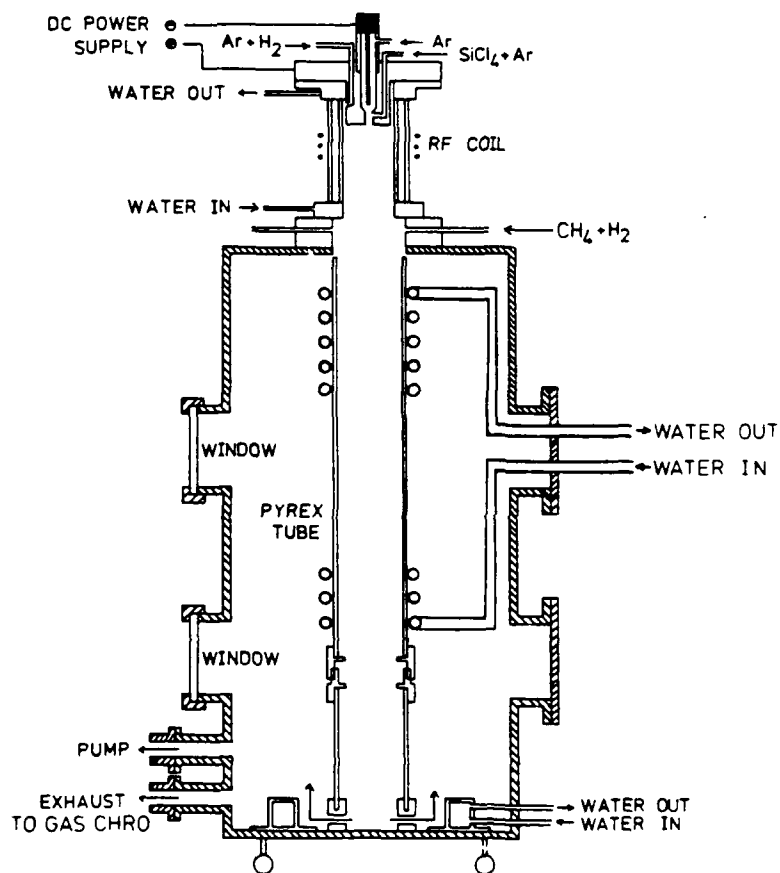


Fig. 6 Schematic diagram of the reactor chamber designed for the preparation of ultrafine ceramics.

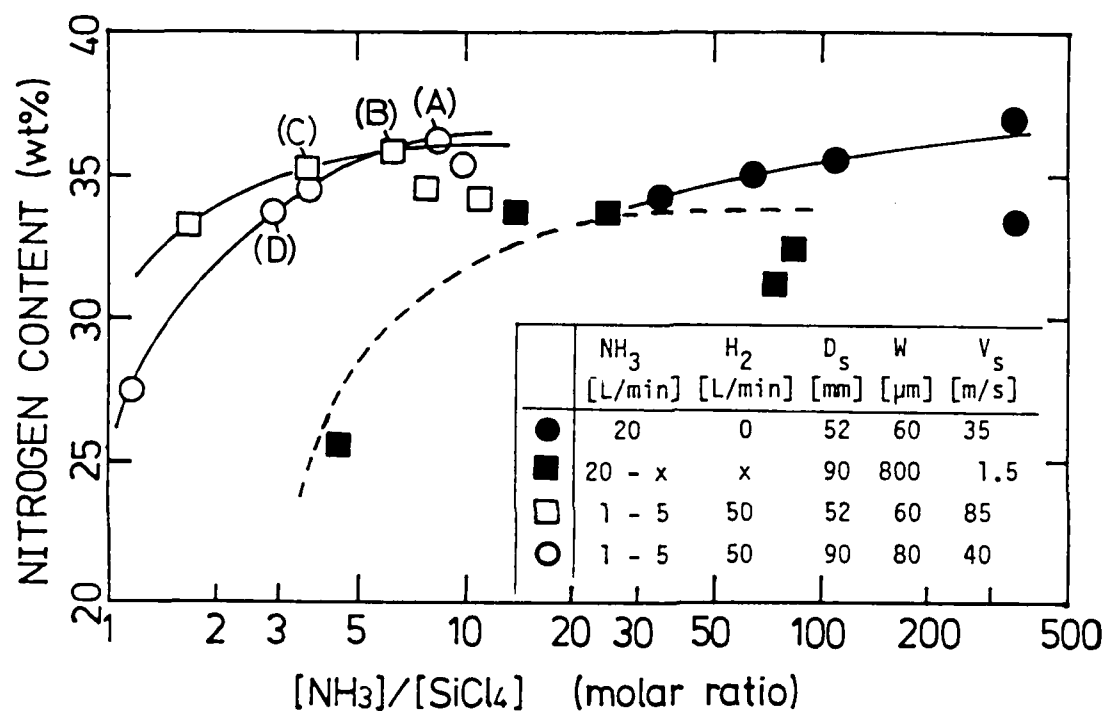


Fig. 7 Nitrogen content in the products as a function of $\text{NH}_3/\text{SiCl}_4$ molar ratio with different quenching conditions.

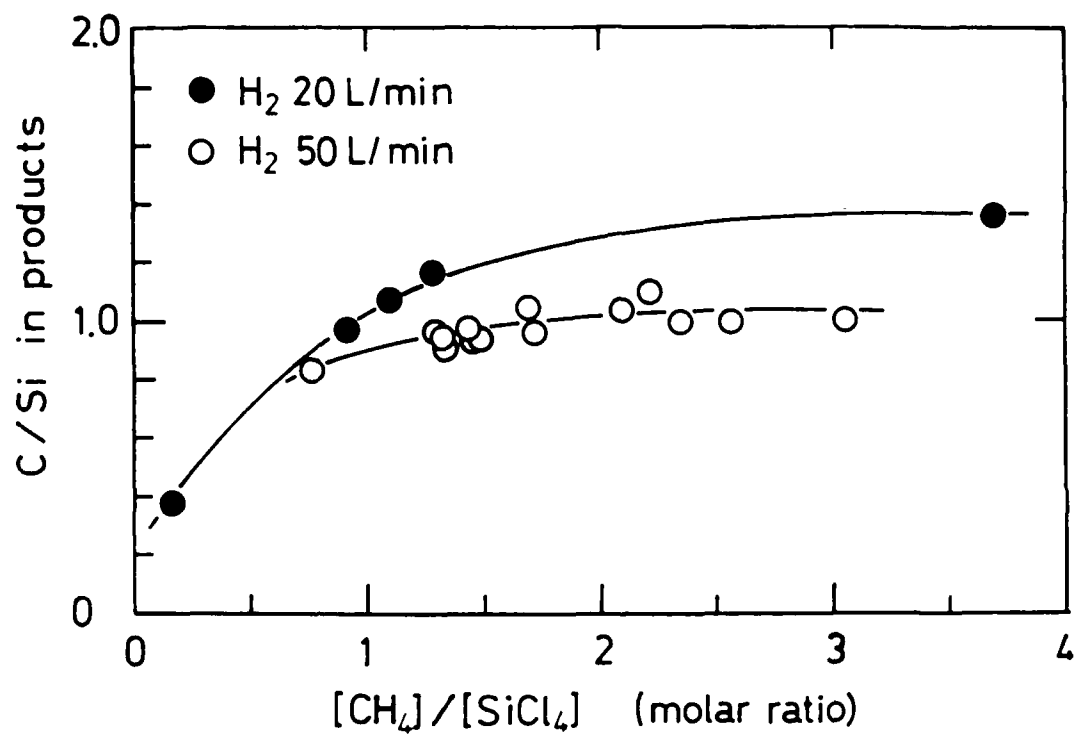


Fig. 8 Carbon content in the products as a function of CH₄/SiCl₄ molar ratio with different quenching conditions.

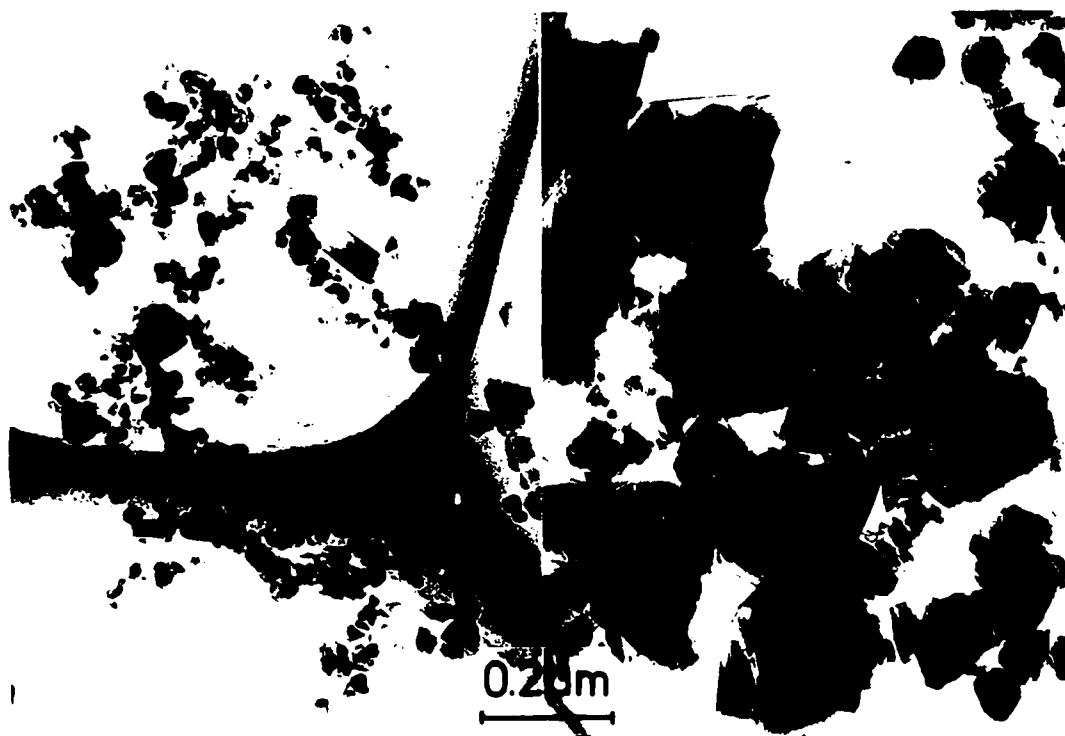


Fig. 9 Typical electron micrographs of silicon carbide particles.
(left: higher quenching rate, right: lower quenching rate)

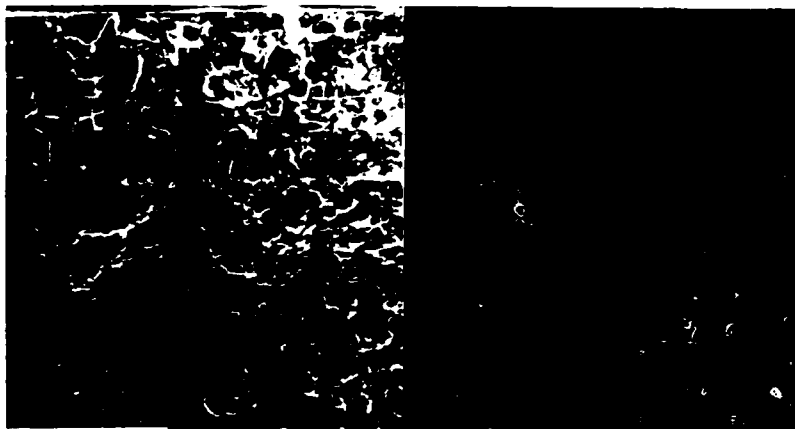


Fig. 10 Cross-section of SiC film deposited on a graphite substrate under optimum conditions.
(left: as-fractured, right: polished)

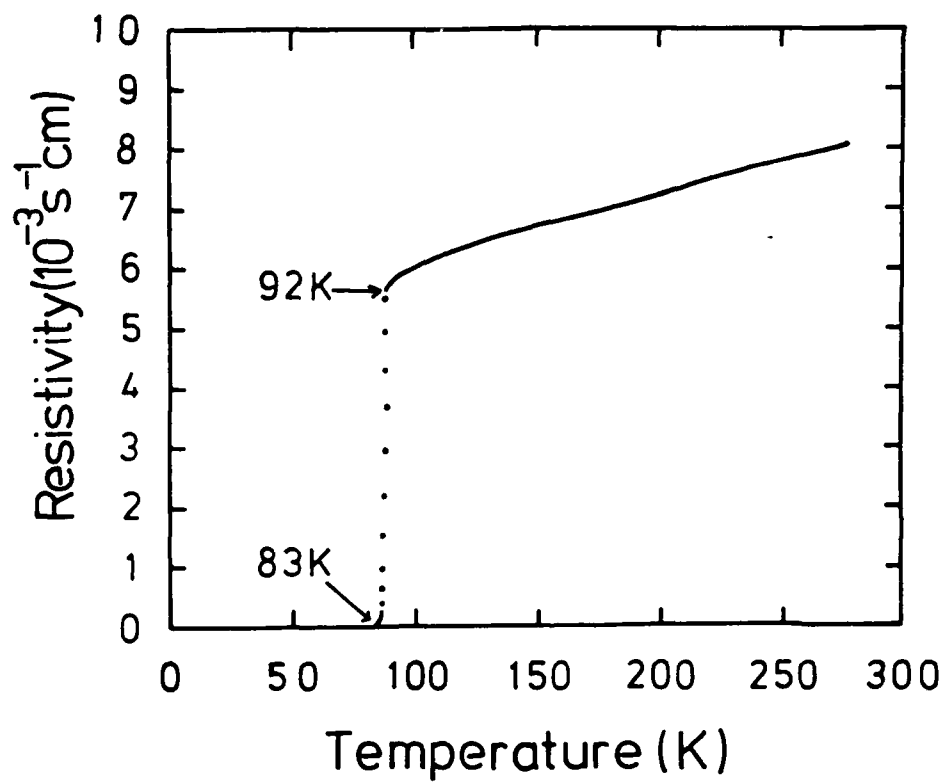


Fig. 11 Temperature dependence of the electrical resistance for an as-grown Y-Ba-Cu-O film.

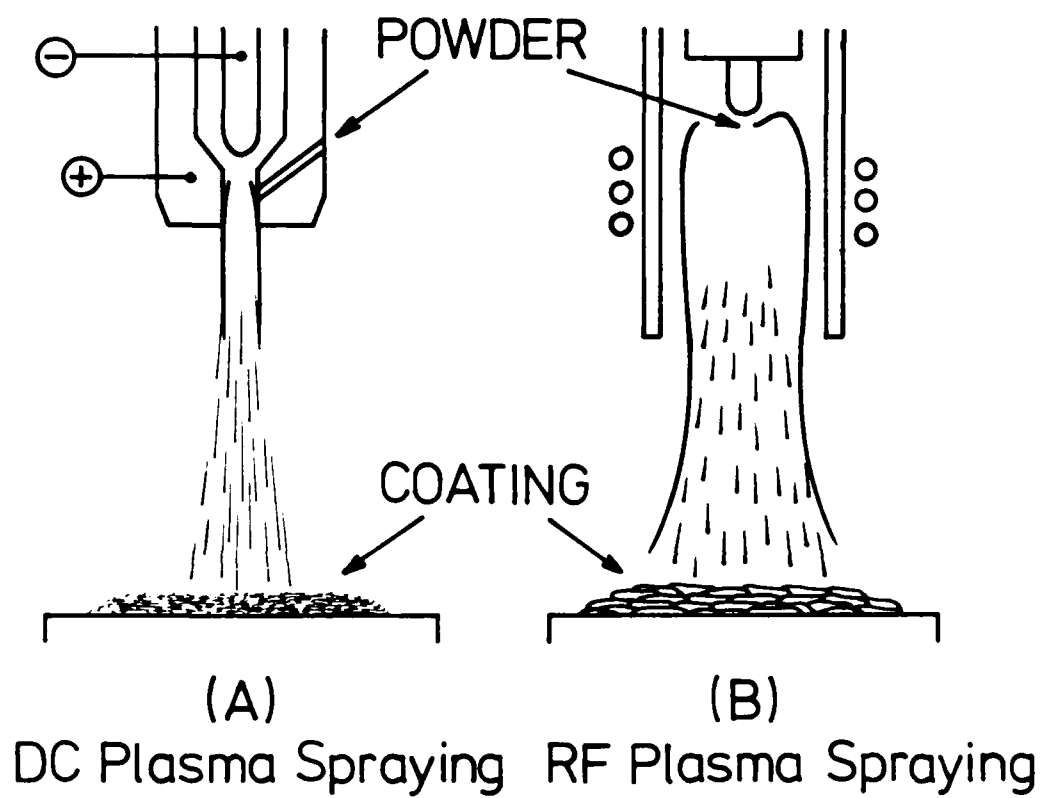


Fig. 12 Schematic illustration of (A) dc plasma spraying, and (B) rf plasma spraying.

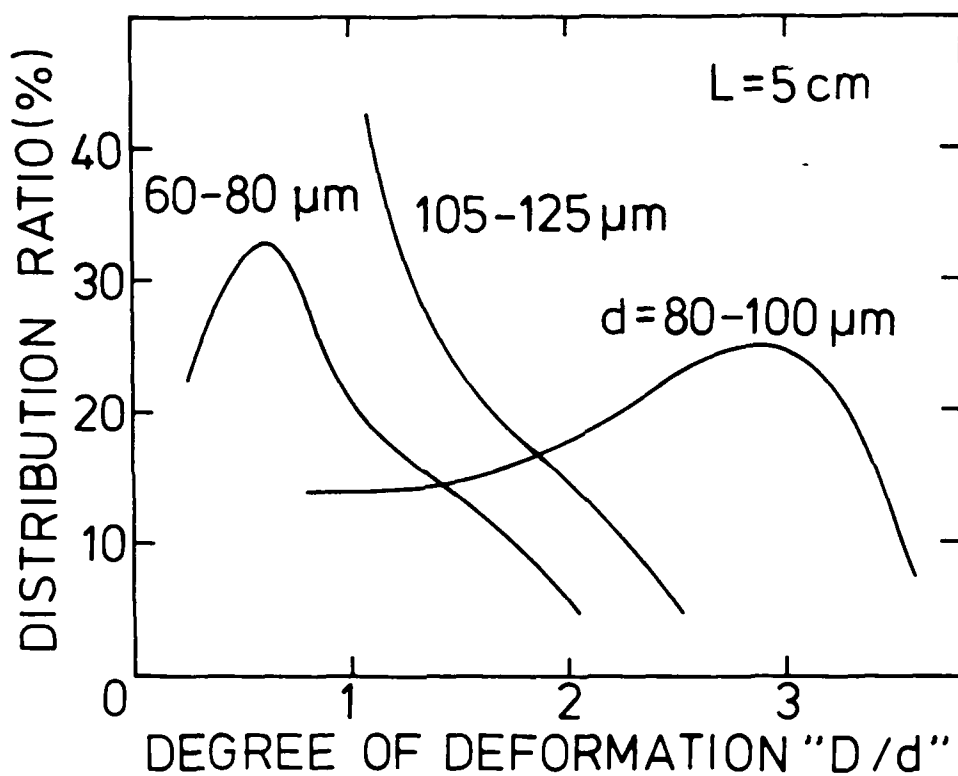


Fig. 13 Influence of the initial powder size(d) of Al_2O_3 on the sprayed and flattened particle diameter(D) at the distance of $L = 5$ cm from the torch exit.

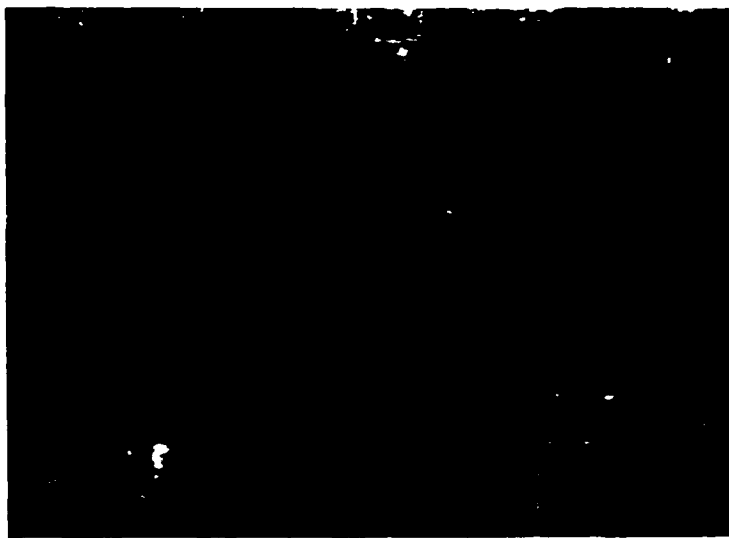


Fig. 14 Cross-sectional SEM of sprayed Al_2O_3 layer.

A THEORETICAL COMPARISON OF CONVENTIONAL AND HYBRID RF PLASMA REACTORS

JOHN W. MCKELLIGET, Dept. of Mechanical Engineering
University of Lowell, Lowell, MA 01854.

NAGY EL-KADDAH, Dept. of Materials and Metallurgical Engineering
The University of Alabama, Tuscaloosa, AL 35486.

ABSTRACT

A Mathematical model for the analysis and design of hybrid plasma reactors for advanced materials synthesis has been developed. The model is used to study the thermal decomposition of silicon tetrachloride and it is demonstrated that the hybrid system possesses superior characteristics for materials synthesis over conventional DC or RF systems.

1. INTRODUCTION

In 1971 Poole and Vogel/1/ developed the concept of using a low power DC plasma torch augmented by an RF induction coil for plasma chemical synthesis. The first application of this 'hybrid' plasma was by Yoshida et al/2/ who successfully synthesized amorphous silicon nitride particulates. The improved performance of the hybrid reactor compared to the conventional RF system is thought to be due to the modification of the temperature and flow fields caused by the superposition of the DC plasma jet/2/. The objective of the present paper is to provide a fundamental understanding of the interaction between the DC and RF components of the hybrid reactor through the development of a quantitative description of the electromagnetic, heat, and fluid flow phenomena, and the chemical reaction kinetics. The model is used to investigate the thermal decomposition of silicon tetrachloride and the predicted performance of the hybrid reactor is compared to that of conventional RF and DC systems.

2. MODEL FORMULATION

The electromagnetic field is calculated using a technique developed by the authors for RF plasma systems/3,4/. Maxwell's equations are expressed in

terms of the electromagnetic vector potential, A , by the equation;

$$\nabla^2 A = \sigma \mu_0 \partial A / \partial t \quad (1)$$

where σ is the electrical conductivity, and μ_0 is the magnetic permeability in vacuum. The boundary condition for the solution of equation (1) is;

$$A(r) = (\mu_0/4\pi) \left(\int J/|r - r_c| d^3 r_c + \int J/|r - r_p| d^3 r_p \right) \quad (2)$$

where J is the current density, r is a position vector, and the subscripts c and p refer to the coil and to the plasma respectively.

The equations governing the flow field are the continuity equation,

$$\nabla \cdot (\rho V) = 0 \quad (3)$$

and the turbulent Navier-Stokes equation,

$$\rho V \cdot \nabla V = -\nabla P + \nabla \cdot \tau + F \quad (4)$$

Here, ρ is the plasma density, P is the pressure, V is the plasma velocity, τ is the effective stress tensor, and F is the Lorentz force ($J \times B$). The model uses the K- ϵ turbulence model/5/ to evaluate τ .

The conservation of energy may be expressed as;

$$\rho V \cdot \nabla h = \nabla \cdot (k \nabla T) + S_J - S_R + S_C \quad (5)$$

where k is the effective thermal conductivity, and T and h are the plasma temperature and specific enthalpy respectively. The temperature field is influenced by the Joule heating, $S_J = J \cdot E$, the radiation loss, S_R , and the heat required for chemical reaction, S_C .

The mass conservation equation for a general reacting species i may be expressed as;

$$\rho V \cdot \nabla C_i = \nabla \cdot (D_i \nabla C_i) + R_i \quad (6)$$

where C_i , D_i , and R_i are the mass concentration, effective diffusivity, and volumetric rate of formation of species i respectively.

The thermal decomposition of silicon tetrachloride in plasmas was studied by Vurzel and Polak/6/. They determined that the volumetric rate of depletion of $SiCl_4$ in kilograms per cubic meter is;

$$R_{\text{SiCl}_4} = -\rho C_{\text{SiCl}_4} 5 \times 10^7 \exp(-1.26 \times 10^5 / RT) \quad (7)$$

All calculations are performed for argon at 1 atmosphere and it is assumed that the concentration of the other gases is low enough not to affect the properties of argon. The density is, however, allowed to vary with the mass fraction of SiCl_4 . In order to obtain an estimate of the silicon recovery at the torch exit it is assumed that the walls act as perfect silicon sinks and that, consequently, the concentration of silicon there is zero.

3. RESULTS AND DISCUSSION

Calculations are described for a hybrid torch similar to the one described by Yoshida et al/2/, sketched in Figure. 1. The combined flow rate of argon carrier gas and SiCl_4 (10% by volume) is 10 l/min and the sheath gas flow rate is 20 l/min. Results are presented for the five cases summarized in Table I.

TABLE I SUMMARY OF MODEL RESULTS

Reactor	RF Current (A)	RF Power (kW)	DC Power (kW)	% of SiCl_4 converted	% Si recovery
DC	0.0	0.0	0.56	58	67
RF	115.0	14.0	0.0	100	30
HYBRID	115.0	16.1	0.56	100	48
HYBRID	70.0	3.56	0.56	100	76
LEVITATION	51.0	3.56	0.56	100	72

The predicted flow fields for the conventional DC and RF torches are shown in Figure 2. The flow in the DC torch behaves as a classical confined, turbulent jet, while the flow in the RF torch exhibits the characteristic recirculating loop driven by the Lorentz force. The corresponding temperature fields are shown in Figure 3. For the DC torch the high temperature region is restricted to the very center of the reactor, while the interior of the RF

system is almost completely filled by the plasma. Figure 4 shows the corresponding mass concentration distribution of silicon. As suggested by the temperature field, the reactions in the DC torch occur in a narrow region around the periphery of the high temperature jet. This is reflected in the small percentage of silicon tetrachloride decomposition. Furthermore, the computed silicon recovery, which is only about 67%, suggests that the recirculating flow near the torch exit causes significant deposition on the walls. The silicon distribution in the RF torch shows that the injected SiCl_4 is entrapped by the recirculating flow and is thermally decomposed mainly at the top of the reactor along the periphery of the fireball. The silicon produced is then transported by the flow towards the wall of the reactor. Although the reaction is 100% complete, a very large fraction (70%) of the silicon condenses on the walls.

The predicted flow and temperature fields for a hybrid torch operating at the same coil current as the conventional RF torch are shown in Figure 5. The extent of the recirculating flow is considerably reduced, and the gases from the DC torch penetrate through the center of the fireball. Except for the very center of the reactor the nature of the fireball is similar to that of the RF plasma. Figure 6 shows the concentration distribution of silicon, which is produced in a region much deeper within the fireball than is possible with the RF reactor. Although some of the silicon is caught up in the back flow, the fraction deposited on the walls drops to 52% compared with 70% for the conventional RF torch.

The flow and temperature fields for a hybrid torch operating with a reduced coil current are shown in Figure 7. The extent of the recirculating flow and the plasma fireball are significantly reduced with the plasma fireball displaced away from the side wall. Despite the decrease in power the general characteristics of the high and the low power fireballs are very

similar. The corresponding silicon distribution is shown in Figure 8 and the concentration immediately adjacent to the walls is seen to be lower than in the high power case. It is important to note that the conversion efficiency is unaffected by the power reduction while the amount of silicon deposited on the walls is halved, to 24% of the silicon produced.

Figure 9 shows the predicted flow and temperature fields for a levitation coil/3/ augmented by a DC torch. The magnitude of the recirculating flow is reduced and, as expected, the upper edge of the fireball is shifted down, away from the top wall, and into the coil region. Figure 10 shows the corresponding silicon concentration. The chemical reaction occurring around the periphery of the DC jet now extends much deeper into the reactor before being entrapped by the recirculating flow. As in all the RF systems studied, the reaction is 100% complete. The predicted silicon recovery is almost the same as for the low power hybrid reactor operating with a conventional coil. This final case introduces the important concept of flow and temperature field modification through changes in the coil design.

Acknowledgments

This work was supported by NSF-Alabama EPSCoR Program, and by GTE, Mass.

REFERENCES:

1. J.W. Poole and C.E. Vogel, NASA Report #CR-1765, (1971).
2. T. Yoshida, T. Tani, H. Nishimura, K. Akashi. J. of Applied Physics, 54 (1983), 640-646.
3. J.W. McKelliget, N. El-Kaddah, J. Appl. Phys., 64 (1988), 2948.
4. J.W. McKelliget, N. El-Kaddah, MRS Symp. Proc. Plasma Processing and Synthesis of Materials, vol. 98 (1987), 21-27.
5. N. El-Kaddah, J. McKelliget, J. Szekely, Met.Trans. B, 15B (1984), 59-70.
6. F.B. Vurzel, L.S. Polak, Khim. Vys. Energ., 1 (1967), 268.

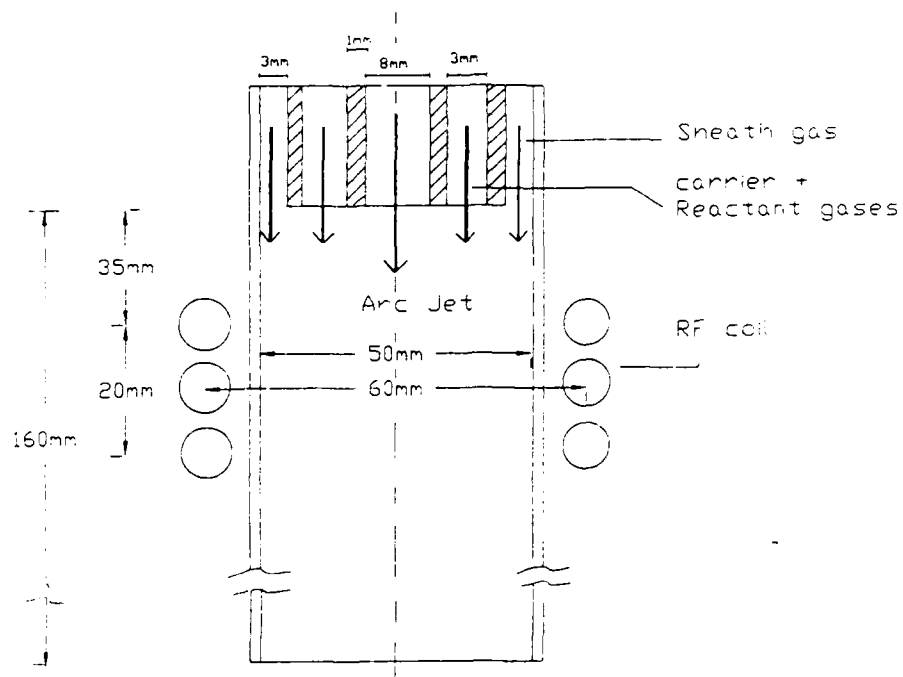


Figure 1. Sketch of the hybrid plasma reactor including dimensions.

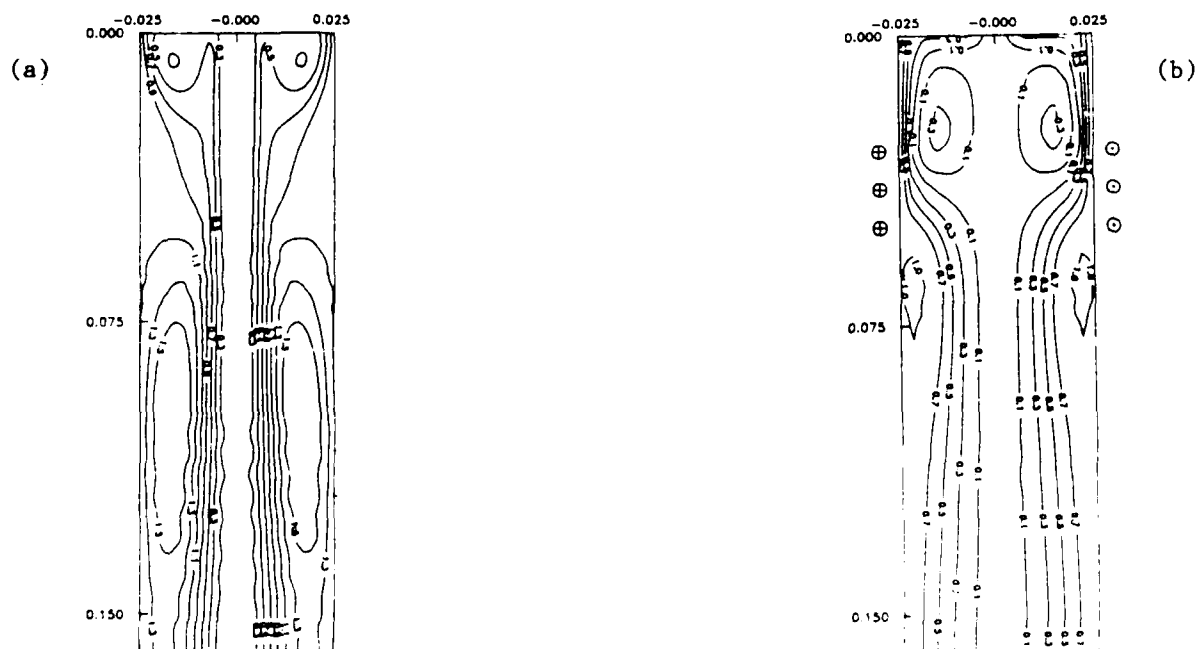


Figure 2. Computed stream lines for (a) DC plasma torch and (b) RF plasma torch..

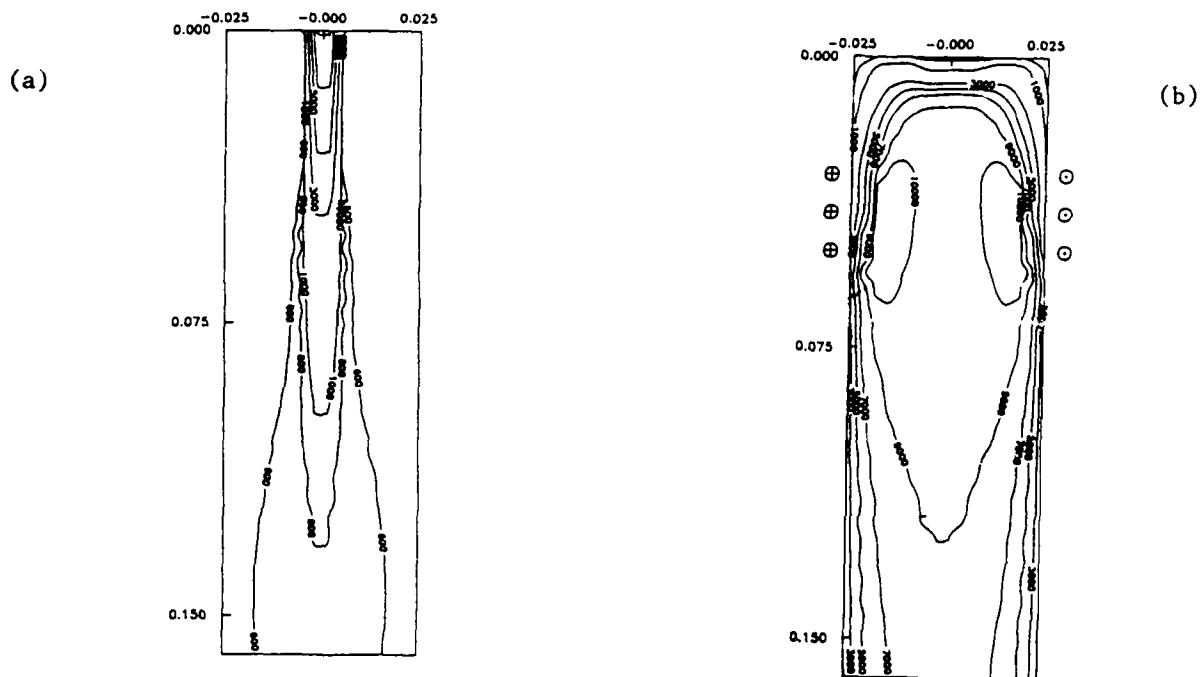


Figure 3. Computed temperature field for (a) DC plasma torch and (b) conventional RF plasma torch.

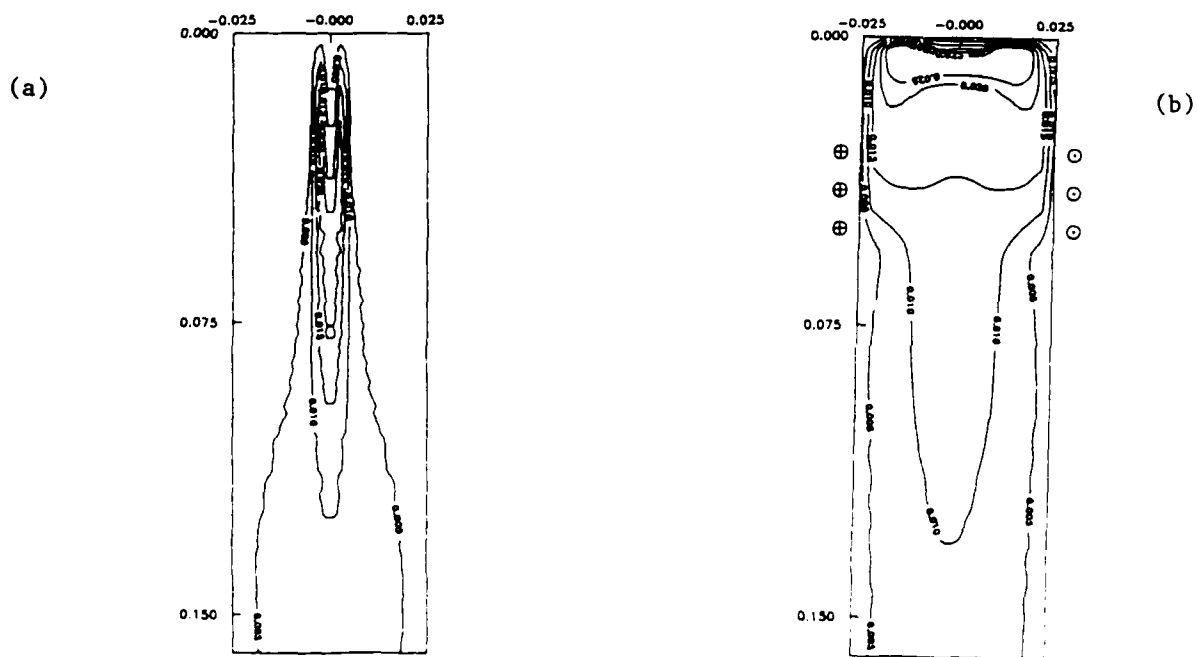
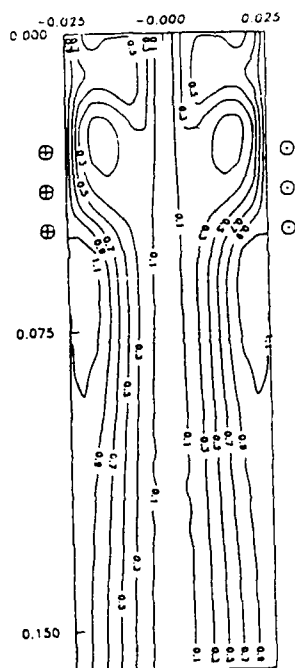


Figure 4. Computed mass fraction of silicon in the (a) DC reactor and (b) Conventional RF reactor.

(a)



(b)

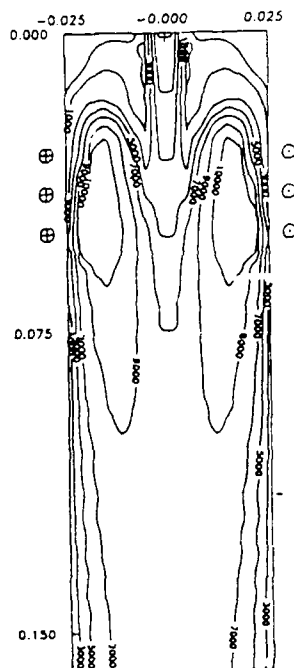


Figure 5. Computed (a) stream lines and (b) temperature field for the high power Hybrid reactor.

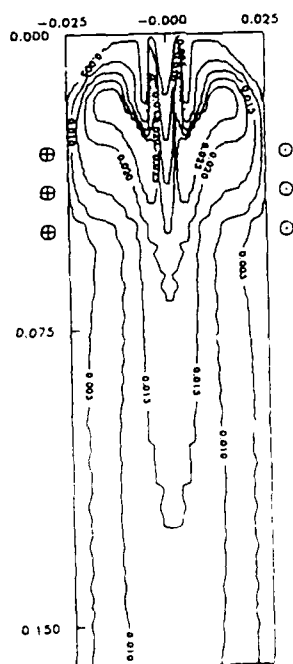


Figure 6. Computed mass fraction of silicon in the high power Hybrid reactor.

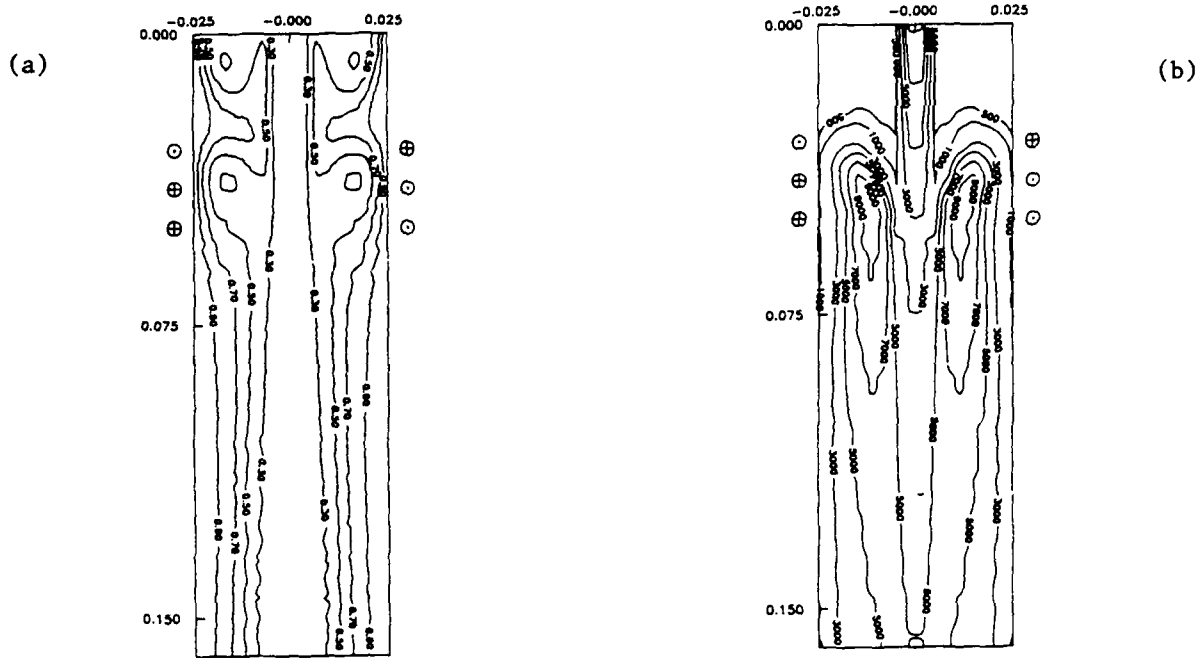


Figure 9. Computed (a) stream lines and (b) temperature field for the levitation Hybrid reactor.

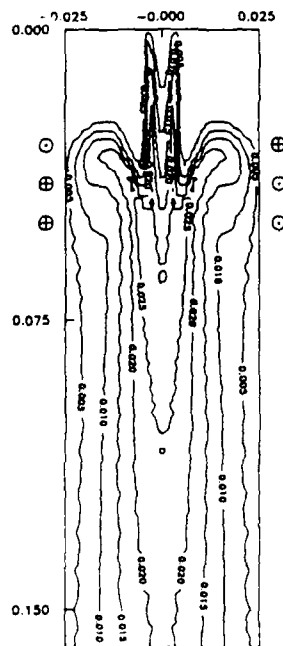


Figure 10. Computed mass fraction of silicon in the levitation Hybrid reactor.

HOMOGENEOUS NUCLEATION AND PARTICLE GROWTH IN THERMAL PLASMA SYNTHESIS

S. L. Girshick and Chia-Pin Chiu

Department of Mechanical Engineering, University of Minnesota, Minneapolis, MN

Abstract

Particle nucleation and growth in a plasma reactor are modeled under the assumptions of plug flow and that the gas-phase chemistry is decoupled from the aerosol dynamics. The aerosol dynamics equations are solved for the case of elemental iron, including both evaporation and coagulation terms in the cluster-balance rate equations. The size of nucleated particles is found to be significantly affected by the cooling rate and by the initial monomer concentration.

Introduction

The dynamics of particle formation in a thermal plasma reactor is an important problem in plasma synthesis of ultrafine powders of advanced materials. A number of factors can be present which make analysis of this problem extremely complicated, even aside from the aerosol dynamics: for example nonuniform temperature and velocity profiles, imperfect mixing of reactants, and finite-rate chemical kinetics. However considerable insight can be gained by focusing on the aerosol dynamics, considering an idealized plug flow reactor in which the relevant gas-phase chemistry is completed upstream of particle nucleation. We treat the effect of gas-phase chemistry concurrent with particle nucleation and growth in a separate paper¹.

Reactants in a thermal plasma reactor, whether it is of the DC or RF type, may be introduced upstream of the plasma, or injected directly into the plasma, or injected into the tail flame. If the reactants pass through the plasma core they are exposed to temperatures on the order of 10,000 K. The tail flame region is cooler, but typically still above about 5000 K. We assume that reactants are completely vaporized. Molecular gases are largely dissociated in the hottest regions, but as the

gas cools chemical reactions generate one or more condensable species. For simplicity we assume that there is only one condensable species. In the absence of preexisting particles, particle nucleation would not be expected to occur until the gas became significantly undercooled with respect to the condensable species.

In previous work Girshick, Chiu and McMurry² applied a collision-controlled model to the nucleation and growth of iron powder in a plasma reactor. In this approach cooling rates are assumed to be so high that cluster evaporation can be neglected. Unfortunately an *a priori* assumption is then required regarding the supersaturation at which nucleation occurs. Recently efficient numerical techniques for solving the aerosol dynamics equations, including simultaneous evaporation and coagulation, have been developed. We have found these techniques to be effective for handling monomer concentrations and cooling rates typical of plasma reactors.

Theory

The particle size distribution function is conventionally represented by $n_i(t)$, $i = 1, 2, 3, \dots$, which gives the number of particles per unit volume of gas which are comprised of i monomers. In the non-isothermal case it is more convenient to follow the number of particles per unit mass of gas, \hat{n}_i . Accounting for coagulation and evaporation the monomer population rate equation following a fluid streamline can be written

$$\frac{D\hat{n}_i}{Dt} = -\rho_g \hat{n}_i \sum_{j=1}^{\infty} \beta_{ij} \hat{n}_j + \sum_{j=2}^{\infty} (1 + \delta_{2j}) E_j \hat{n}_j \quad (1)$$

where ρ_g is gas density, β_{ij} (m^3s^{-1}) is the collision-frequency function for collisions between i -mers and j -mers, δ_{2j} is the Kronecker delta function and E_j (s^{-1}) is the evaporation coefficient. The mass accommodation coefficient is assumed to equal unity.

For dimers and larger particles the population balance equations can be written

$$\frac{D\hat{n}_k}{Dt} = \frac{1}{2}\rho_t \sum_{i+j=k} \beta_{ij} \hat{n}_i \hat{n}_j - \rho_t \hat{n}_k \sum_{j=1}^{\infty} \beta_{jk} \hat{n}_j + E_{k+1} \hat{n}_{k+1} - E_k \hat{n}_k, \quad k \geq 2 \quad (2)$$

As these calculations pertain to ultrafine particles in a hot gas with relatively long mean free paths, the coagulation coefficient was modeled by the free-molecule expression³,

$$\beta_{ij} = \left(\frac{3v_1}{4\pi} \right)^{1/6} \sqrt{\frac{6k_B T}{\rho_p} \left(\frac{1}{i} + \frac{1}{j} \right)} (i^{1/3} + j^{1/3})^2 \quad (3)$$

Here v_1 is the monomer volume, k_B is Boltzmann's constant, T is absolute temperature and ρ_p is the particle mass density. This expression assumes spherical, electrically neutral particles and neglects London-van der Waals forces. Sphericity is a reasonable assumption for the early stages of nucleation and growth examined here. Electrical neutrality depends on the absence of preexisting particles, which would carry negative charge from the plasma. The neglect of dispersion forces probably causes collision frequencies to be somewhat underestimated.

The evaporation coefficient is given by⁴

$$E_j = \beta_{1j} n_s \exp \left\{ \frac{A_1 \sigma}{k_B T} \left[j^{2/3} - (j-1)^{2/3} \right] \right\} \quad (4)$$

where n_s is the saturation monomer concentration, A_1 is the monomer surface area and σ is surface tension.

The calculation is started at a temperature where the saturation ratio equals unity, at which point the aerosol is assumed to exist entirely as monomers. This choice of initial condition may be justified by the observation that while a distribution of subcritical clusters develops rapidly in the calculations, a relatively long time elapses before homogeneous nucleation occurs.

As in Ref. 2 the present calculations are based on elemental iron. Data on surface tension and vapor pressure were obtained from the literature^{5,6}.

Numerical method

We solved Eqs. (1) and (2) by modifying the discrete-sectional computer code written by Rao and McMurry⁷. Depending on input parameters, the total set of equations consisted of 10-15 equations for the discrete regime (smallest sizes), plus 25-30 equations to represent size sections logarithmically spaced by particle volume. At each time step the temperature was updated according to the given cooling rate, and all temperature-dependent terms were recalculated.

Results and discussion

We focus on the results for a single base case, followed by cases in which either the cooling rate or the monomer concentration was varied.

Base case

For the base case we consider an iron vapor partial pressure of 5×10^{-4} atm and a cooling rate of 30 K/ms. Figure 1 shows the calculated value of the saturation ratio as the gas cools, where the saturation ratio S at each point is defined by $S = n/n_s$. The line in the figure labelled "nucleation suppressed" indicates how the supersaturation would increase if particles larger than monomers were not allowed to form. The calculated saturation ratio follows this line closely until the gas cools to about 1600 K, corresponding to a supersaturation of about 280. At that point the calculated saturation ratio peaks and then drops rapidly; by 1400 K the calculated monomer concentration has relaxed to its equilibrium value.

To understand this behavior it is instructive to consider the critical size for a stable nucleus, which is the size for which the condensation rate balances the evaporation rate: smaller particles tend to evaporate and larger ones to grow. In terms of particle diameter the critical nucleus size can be written³

$$d^* = \frac{4\sigma v_1}{kT \ln S} \quad (5)$$

Figure 2 shows the calculated variation in the critical cluster size k^* (number of monomers comprising the critical size nucleus). In early times the critical cluster size is very large, and only monomers and smaller clusters are present, so no stable particles can form and the supersaturation mounts. But the rapid rise in the supersaturation eventually causes k^* to drop to a small value, in this case equal to 12. When the critical size becomes this small, there finally are clusters present whose size is equal to or larger than k^* . Most of the highly supersaturated vapor condenses to these particles in a remarkably short time, producing a "nucleation burst." This result is seen clearly in Figure 3. In a very short temperature span the mean particle size $\langle k \rangle$ jumps from essentially unity up to about 60,000. Thereafter growth follows the almost linear trend produced by coagulation⁸, for which $\langle k \rangle \sim t^{1/5}$.

The detailed result of these calculations is the evolution of the particle size distribution, as shown in Figure 4, in which the distributions in the neighborhood of the nucleation burst are emphasized. At $T = 1647$ K the distribution consists mostly of monomers, with a monotonically decreasing distribution of subcritical clusters. At 1620 K, less than one millisecond later, the distribution has changed dramatically, showing the sudden presence of stable particles. By 1567 K the distribution has the mature appearance of an aerosol which is growing by pure coagulation. At a considerably lower temperature, 1090 K, the distribution has shifted by coagulation towards larger particles with a correspondingly smaller total number density.

Effect of cooling rate

The time response of the aerosol to the rise in supersaturation and resulting decrease in critical cluster size is governed by collision rates, and thus varies inversely as the monomer concentration. Our calculations confirm that if the cooling rate is increased for a given monomer concentration, the supersaturation shoots to a higher value before the nucleation burst occurs. Shooting to a higher supersaturation causes a decrease in the critical nucleus size before the onset of nucleation. The result is that a larger number of mostly smaller stable nuclei are made available for condensation. Therefore we would expect a higher cooling rate to produce more and smaller parti-

cles. The calculations support this conclusion, as seen in Figure 5, in which all three cases assume the same monomer concentration as in the base case.

It is worth re-emphasizing that we have assumed a constant cooling rate. In fact the cooling rate in a plasma reactor would typically be expected to decrease in the flow direction: it can be on the order of 10^6 K/s in the plasma core and less than 10^3 K/s at the reactor exit. Since the cooling rate effect on nucleation appears to be strong, we conclude that the local cooling rate at the location of the nucleation burst is an important determinant in the final size. -

Effect of monomer concentration

The discussion above suggests that increasing the monomer concentration should have an effect opposite to increasing the cooling rate. Comparing the base case to a case with the same cooling rate but twice the monomer concentration, our calculations show that the base case supersaturation peaks at a value of about 280, whereas the higher concentration case peaks at about 190. Therefore increasing the monomer concentration results in the nucleation of larger particles, as seen in Figure 6.

Conclusions

We have considered an idealized view of a plasma reactor in which the flow field is one-dimensional, the relevant chemistry is completed before homogeneous nucleation occurs, and there is only one condensing species. We found that homogeneous nucleation from the vapor phase in a plasma reactor can be expected to occur as a rapid event in which a large number of particles are suddenly formed by condensation to stable clusters and particles. The size and number of nucleated particles can be significantly affected by two factors, the cooling rate at the location of nucleation and the monomer concentration. Lower local cooling rates and higher concentrations both favor the nucleation of larger particles. The nucleation burst is followed by steady growth by coagulation.

Acknowledgements

The authors gratefully acknowledge our colleague P. H. McMurry for his comments and suggestions regarding the work reported in this paper. This work was supported by the National Science Foundation, Grant CBT-8805934, by the University of Minnesota Graduate School, and by the Minnesota Supercomputer Institute.

References

- ¹Chiu, C.-P. and Girshick, S. L., *Proc.*, 9th International Symposium on Plasma Chemistry, Pugnuchiuso, Italy, Sept. 4-8, 1989.
- ²Girshick, S. L., Chiu, C.-P. and McMurry, P. H., *Plasma Chem. Plasma Process.* **8**, 145-157 (1988).
- ³Friedlander, S. K., *Smoke, dust and haze; fundamentals of aerosol behavior*, New York, Wiley, 1977.
- ⁴Frankel, J., *Kinetic Theory of Liquids*, Dover, 1955.
- ⁵Sahoo, P. and Debroy, T., *Met. Trans. B* **18B**, 597-601 (1987).
- ⁶Hultgren, R. et al., *Selected Values of Thermodynamic Properties of the Elements*, American Society for Metals, 1973.
- ⁷Rao, N. P. and McMurry, P. H., *Aerosol Sci. Tech.*, in press.
- ⁸Lai, F. S., Friedlander, S. K., Pich, J. and Hidy, G. M., *J. Coll. & Interface Sci.* **39**, 395-405 (1972).

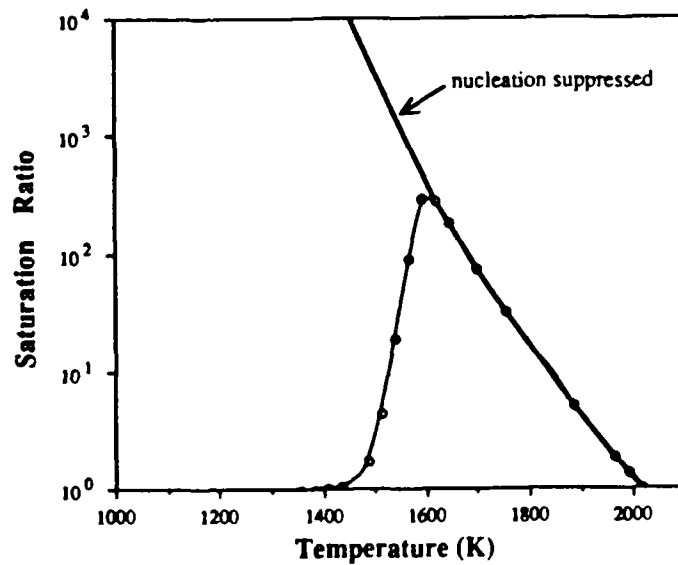


Figure 1

Calculated variation of the saturation ratio with temperature for the base case: iron vapor, $P_{Fe} = 5 \times 10^{-4}$ atm, $b = 30$ K/ms. The curve labeled "nucleation suppressed" shows how the saturation ratio would vary if all particles were constrained to stay as monomer.

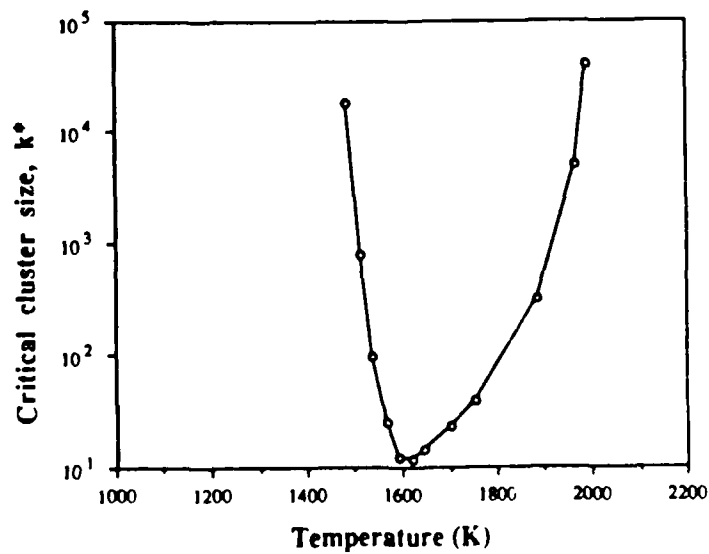


Figure 2

Calculated variation of the critical size for a stable nucleus, base case.

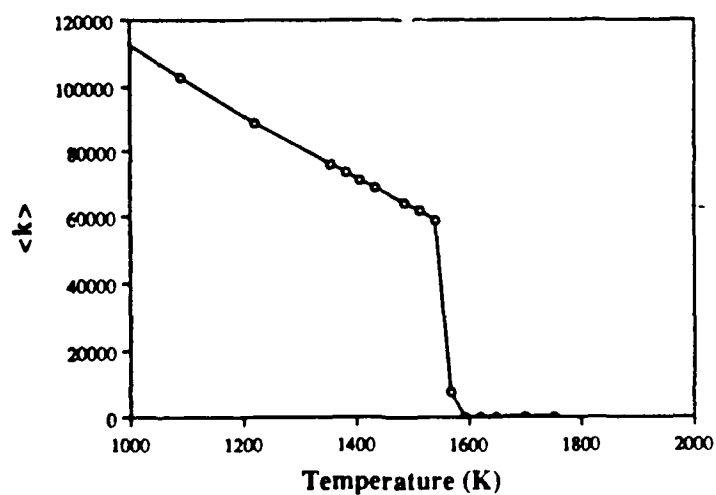


Figure 3
Calculated mean cluster size, base case.

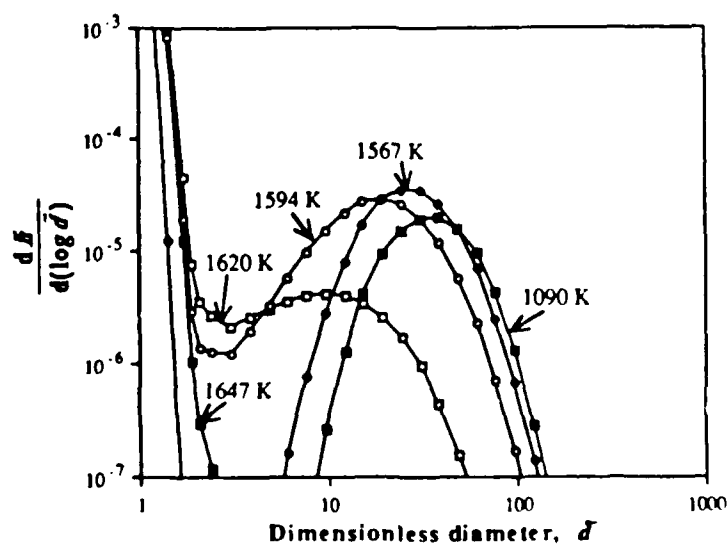


Figure 4
Calculated evolution of the particle size distribution, base case.
The dimensionless diameter \bar{d} is normalized by the monomer diameter.

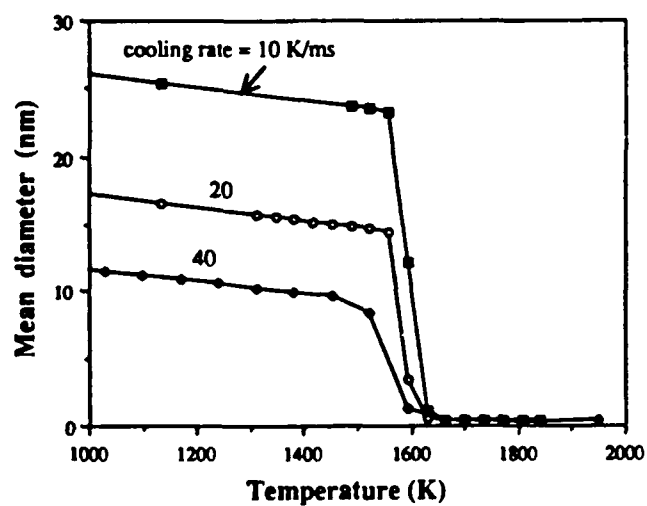


Figure 5
Comparison of mass-mean diameters for three values of the cooling rate.
Monomer concentration is same as in base case.

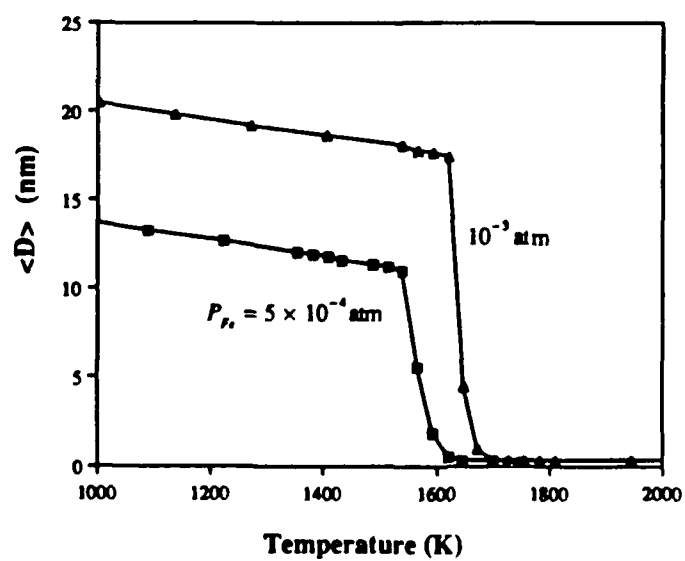


Figure 6
Effect of monomer concentration on mass-mean diameter.
Cooling rate is same as in base case.

FORMATION OF REFRACTORY AEROSOL PARTICLES

*Richard C. Flagan, Hung V. Nguyen, and Steven N. Rogak
California Institute of Technology 138-78
Pasadena, CA 91125*

Abstract

The formation of refractory particles by gas phase chemical reactions in high temperature systems is examined using thermal decomposition reactions as sources of vapor species which nucleate forming small particles that grow by coagulation and vapor deposition. Particles are formed from the products of gas phase reactions by homogeneous nucleation. Aggregate particles formed by coagulation have a fine structure that is determined by the aggregation kinetics and the rate at which the aggregates coalesce or sinter within the reactor.

Introduction

Refractory particles are frequently synthesized through gas phase processes that lead to the formation of an aerosol of fine particles. The nature of the particles depends strongly upon the processing environment and the properties of the product material. While considerable effort has been invested in the synthesis of the ideal powder, i.e., one consisting of nonagglomerated spherical particles of controlled composition and particle size, such particles remain an elusive objective. In particular, the product particles frequently consist of hard agglomerates. The dynamics of such agglomerate particles are not fully understood.

Recent efforts in our laboratory have demonstrated that nucleation can be suppressed by careful control of the reaction kinetics during the growth of seed particles, although the particles thus produced were not the dense spheres sought, but rather were low density flocs¹. The origin of these agglomerates was attributed to the deposition of small clusters of less than a few nanometers diameter during the growth process. Sintering or coalescence of the deposited clusters were apparently so slow that the particle density could not be maintained during the growth process.

Materials with low melting points form dense particles much more readily than do more refractory particles. Haggerty and coworkers²⁻⁴ have demonstrated that dense particles of silicon could be grown by laser induced reactions, but agglomerate particles were likely to be formed when silicon carbide or silicon nitride were generated. Dense silicon nitride particles could, however, be generated if ammonia were introduced after the particles were formed by silane pyrolysis. In this mode of particle synthesis, the dense silicon particles formed by sintering of agglomerated formed by Brownian coagulation are subsequently reacted with ammonia to form the nitride, thereby eliminating the need to achieve reaction conditions under which the refractory silicon nitride particles would coalesce.

The evolution of the particle structure in ceramic powder synthesis is only partially understood. The processes involved include gas phase chemical reactions which produce condensable products and intermediates that can undergo surface reactions, particle inception or nucleation, particle growth by condensation, surface reactions, and coagulation, and the coalescence of agglomerate particles formed by coagulation. The nature of the particles synthesized can be confused depending upon the analytical methods employed to determine size distribution and particle structure. Microscopic examination of refractory particles synthesized by aerosol routes frequently reveals the presence of small spherules of approximately uniform size, whereas direct measurement of particles in suspension in the carrier gas will reveal that the separately identifiable particles are low density agglomerates of the small spherules. Resuspension of collected particles in liquid for sedimentation or optical analysis does not necessarily recover this structure.

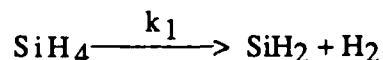
Erroneous interpretation of particle formation mechanisms have resulted from reliance on the scales observable in aggregate samples of the powders. Ulrich and coworkers⁵⁻⁷ made observations of silica particle growth in flame synthesis of fume silica using gas adsorption measurements of the surface areas of collected powder samples. These observations led to the conclusion that the well established expressions describing the coagulation of particles that are comparable in size to the mean free path of the gas molecules are not valid, at least for the environment of flame synthesis. This conclusion was disproved in the later papers in which direct *in situ* observations of particle size were made using light scattering methods. More recently, Flint and Haggerty⁹ have suggested that collisions between particles in the laser synthesis of silicon powders become elastic once the particle temperatures drop below the melting point, an attempt to resolve the abrupt transition in particle fine structure that occurs at that point.

In this paper, we examine some of the facets of particle formation that determine the ultimate structures of the product particles, and attempt to resolve some of the confusion that has developed in description of ceramic powder synthesis by aerosol processes beginning with gaseous precursors. Some of the processes discussed are also important in atomization-based powder synthesis, but the special problems associated with liquid precursors will not be discussed here.

Chemical Kinetics

To produce a powder by reaction of a gaseous precursor, the reaction is initiated by heating the gases, mixing reactants, photolysis, etc. The chemical processes involved in the formation of condensable species are rarely understood in detail. One reaction system that has received considerable attention and can, therefore, be used as an example is the thermal decomposition of silane gas, a reaction that is used in the laser driven synthesis of silicon, silicon carbide, and silicon nitride powders as well as the production of those

powders in thermal reactors. Coltrin and coworkers¹⁰⁻¹¹ have published a detailed reaction mechanism for this system. The mechanism begins with the unimolecular decomposition of silane,



Twenty six other reactions leading to the formation that contribute significantly to the formation of silicon have been identified, and rates for these individual reactions have been measured or estimated. Rate equations can be written for each of the many species involved and integrated to follow the time varying gas composition although, in the chemical vapor deposition environment they examined, it has been found that the silane decomposition could be described by a constrained equilibrium which shifts relatively slowly at a rate determined by the kinetics of the unimolecular decomposition reaction.¹⁰ Thus, only the progress of this initial reaction need be followed in detail to reproduce the essential features of this reacting system.

This reaction is highly temperature dependent due to its 62 kcal/mole activation energy, proceeding slowly at low temperatures and more rapidly at high temperature. In order to cause the silane to decompose, it is necessary to heat the reactant. Plasma, laser, and convection heating have all been applied to this system. In the plasma and laser reaction systems, the reactants are heated to sufficiently high temperature that the silane is quickly consumed, but slower heating in thermal reactors leads to a more gradual conversion of silane to silicon. Instantaneous reaction may be a reasonable approximation in the former cases, but the reaction kinetics must be followed to describe the latter system accurately.

For many systems of interest, the reaction kinetics are not well understood. Even for the silane system, the kinetics are incompletely known when additional reactants are introduced to produce the carbide or nitride powders. Metal alkoxide vapors are well known as sources for high purity metal oxide particles, but the thermal decomposition kinetics are not understood. A qualitative understanding of the reaction process can, however, guide the identification of reactor operating conditions that lead to the formation of high quality powder, and reactor optimization is greatly facilitated by the generation of even approximate reaction rate expressions.

Aerosol Dynamics

(i) Particle Inception

Particle inception, the formation of new particles directly from the vapor phase, is frequently modeled using the classical theory of homogeneous nucleation, although for the conditions encountered in aerosol reactors, key assumptions of this model are frequently inappropriate. This theory describes the growth of clusters by the condensation of

monomers. The smallest clusters are thermodynamically unstable due to their large surface free energies, hence they tend to evaporate as rapidly as they are formed. Only a few survive long enough to grow to larger sizes. Eventually some of the clusters become large enough to become thermodynamically stable. The critical cluster radius is

$$r^* = \frac{2\sigma v_m}{kT \ln S} \quad (1)$$

where σ is the surface tension, v_m is the monomer volume, and $S = P_v/P_{\text{sat}}$ is the saturation ration. Clusters larger than this size grow rapidly. This critical cluster size and the populations of clusters of various sizes are generally calculated using the macroscopic surface tension to describe the thermodynamics of clusters down to atomic dimensions, a highly questionable assumption.

In the synthesis of refractory powders by gas phase reactions, the critical cluster size is frequently estimated to be of atomic dimensions because the reactions produce condensable vapors at concentrations far above the equilibrium vapor pressure. For such high supersaturations, the evaporation of even the smallest clusters is unlikely, at least once the excess energy of the colliding molecules is exchanged by collisions with the background gas. In this circumstance, the classical nucleation theory is inappropriate. Instead, one may model cluster growth as a kinetic process involving cluster-monomer and cluster-cluster coagulation.

(ii) Particle Growth

The growth of aerosol particles involves two major processes, coagulation and condensation or vapor deposition. Coagulation describes the collision and sticking together of particles. The primary mechanism of coagulation of fine particles is Brownian coagulation which occurs when the random Brownian motions of the particles brings two particles into contact with one another. When particles in the micron size range come into contact, van der Waals forces bind them strongly together, so the sticking probability of uncharged particles is generally very near unity. Condensation and vapor deposition refer to the special processes of particle growth by diffusion of molecular species to the particle surfaces.

For refractory particles, the distinction between these two mechanisms becomes vague since the critical cluster or smallest particle that is thermodynamically stable approaches atomic dimensions. In this case, particle growth by monomer addition can be treated as an irreversible process of monomer-particle coagulation. Wu and Flagan¹² have recently presented a computationally efficient description of such cluster growth in which the smallest clusters were represented as discrete particle sizes (monomer, dimer, trimer, etc.) and the larger particles were represented using a sectional (or histogram) approximation to a continuous particle size distribution function. With this model, the suppression of nucleation by growing seed particles and the abrupt transition to

catastrophic nucleation in the silane pyrolysis system was accurately predicted. Several simplified models of particle dynamics have been proposed. For the special case of very rapid reaction, particle growth can be described as a coagulation process which is well described by the so-called self-preserving particle size distribution model¹². Moments of the particle size distribution function can be used for efficient calculation of aerosol evolution in the more general case of finite reaction kinetics^{13,14}.

(iii) Particle Structure

The structure of solid particles undergoing coagulation has been the subject of numerous theoretical and experimental studies, but many questions remain unresolved. We consider first the coagulation of small spheres that retain their integrity as the particles grow. When two particles collide, they form a doublet. Subsequent coagulation events add more spherules to the growing cluster in a random way, but certain patterns evolve. Figure 1 illustrates an agglomerate particle that has undergone several generations of growth by addition of previously formed clusters, indicated as alternating light and dark structures. The particle that results is a low density aggregate because the outermost spheres shield the interior of the aggregate reducing the probability that new particles can diffuse into the core of the particle. Such aggregates are frequently fractal in nature, with the mass within a distance R from the center of mass of the aggregate scaling as

$$m \propto R^D \quad (2)$$

where D , the so-called fractal dimension, is smaller than the geometric dimension of 3. The precise value of D depends upon the physical processes that govern the growth of the aggregate and on any rearrangements (such as sintering) that occur after the aggregate begins to form. Numerous theoretical studies of diffusion limited aggregation (growth of the aggregate by addition of individual spheres) and of cluster-cluster aggregation have been reported.¹⁵⁻¹⁷ The former mechanism leads to relatively dense particles with $D=2.4$, while the latter mechanism typically results in $D=1.8$. When aerosols produced in high temperature systems are carefully sampled to retain the integrity of the individual aggregates, such fractal structures are invariably observed. The structures of soot, fume silica, ceramic powders, and other refractory materials generally appear to be low density and low fractal dimension flocs typical of cluster-cluster aggregation, although dramatically different structures can be produced under special circumstances. A notable example is the growth of very large aggregates of higher apparent fractal dimension in aerosol reactors in which new particle formation was suppressed as seed particles were grown.¹ Those particles were formed by deposition of clusters that were smaller than about 10 nm diameter onto particles that ultimately approached 100 μm in extent, closely approximating the conditions of the diffusion limited aggregation model.

Aggregate particles do not have an invariant structure. At high temperatures, the aggregates can sinter, increasing the fine structure scale and the aggregate density. At temperatures above the melting point, the particles may coalesce into dense spheres as

observed in both laser and plasma synthesis of silicon powders. At the extreme temperatures of plasma reactors, evaporation of the particulate material is also possible.¹⁹ Thus, a spectrum of particle structure parameters can be expected in the growth of refractory particles as aerosols, depending upon the details of the thermal processing environment and growth kinetics.

Experimental Investigations

The evolution of particles formed under conditions of coagulation dominated growth has been studied using silicon aerosols formed in a nonisothermal silane pyrolysis reactor, operated with sufficiently rapid temperature increase that most of the reactant contributed to new particle formation, and in pyrolysis of metal alkoxide vapors under a variety of temperature ramps. Experimental observations included electron microscopy of aggregate samples of the product powder and analysis of the aerosols while still entrained in the carrier gas.

Measurement of the sizes of particles as they are present in the reactor gases is necessary if one is to assure that large agglomerates are not present. Agglomerates that are formed during high temperature processing can be expected to be strong agglomerates due to sintering or bonding by vapor deposition, while those formed in collection systems at low temperatures are much more likely to be readily dispersed. Methods for the measurement of particles entrained in a gas include in situ optical methods from which one can estimate mean concentrations, moments of the particle size distribution, and structure parameters such as the fractal dimensionality of the mass distribution in the particles. Optical measurements of the sizes of individual particles can be made, at least for particles larger than about 0.3 μm , provided the number concentration is low enough that the probability of more than one particle being present in the view volume at any time. This limits the number concentration to less than about 10^9 m^{-3} , a level that is exceeded in most aerosol-based particle synthesis. To obtain high resolution measurements of the particle size distribution, one must generally extract a portion of the gas flow and pass that through an aerosol measuring device. With extractive sampling, one can dilute the aerosol sample to facilitate optical sizing of individual particles. Instruments capable of sizing particles ranging from a few nanometers to 1 μm in size measure the electrical mobility of the particles. In this method, the charged particles are classified according to their drift velocities in an electric field. Mobility analyzers are generally calibrated using dense spherical particles, so the size inferred by this method may differ significantly from that that would be measured using electron microscopy.

Figure 2 shows the particle size distributions estimated using the TSI Differential Mobility Classifier with a TSI Condensation Nuclei Counter as a detector for a silicon aerosol produced by silent pyrolysis. The same temperature profile along the reactor wall was used for all experiments. Two observations are reported for each of the silane concentrations in nitrogen carrier, indicating the reproducibility of the data from day to day. For a relatively low silane concentration, Particles with a mean size of about 50 nm were

generated. Increasing the silane concentration to 0.1%, the mean size increases to about 100 nm, and the number concentration increases somewhat. Figure 3 compares the mean sizes determined by the mobility method with the spherule size inferred using transmission electron microscopy. While the agglomerate size increases with reactant concentration, the agglomerate fine structure size actually decreases somewhat, from 18 nm for 0.01% silane to 14 nm for 1% silane.

The inferred agglomerate sizes differ from the size that would be inferred by electron microscopy. Schmidt-Ott¹⁹ recently reported observations of the thermally induced rearrangements of silver agglomerates that provide insights into the relationship between the mobility size (R_o) and mass (dense sphere) equivalent size (R_v) for agglomerate particles. His results suggest that R_o and R_v can be related through a simple model of the drag forces acting on aggregate spheres.

Conclusions

Aerosols are central to a number of processes for the synthesis of ceramic powders including plasma, laser, and thermal reaction systems. The nature of the particles generated is determined by chemical kinetics, particle inception or nucleation, coagulation to form agglomerate particles, and coalescence of those agglomerate particles. While the reaction kinetics are rarely known in detail, the essential features are frequently understood. The dynamics of refractory aerosols is also incompletely understood. A distinction must be drawn between the size of the particle present in the aerosol phase and the size of the smaller structures present in agglomerate particles. The former relates to the total mass of the particle that would be formed if the particle were completely densified, although this relationship depends on the fractal structure of the agglomerate. The latter is an indication of the extent to which sintering or coalescence has taken place during particle formation.

In order to understand the formation of powders by aerosol processes, the particle properties must be measured while the particles are still entrained in the carrier gas flow. The formation of hard agglomerates by sintering or vapor deposition is quite likely as long as such agglomerates are maintained at temperatures at which reactions continue or which approach the melting point of the material in question.

Acknowledgements

This work was supported in part by the Program in Advanced Technologies of the California Institute of Technology, sponsored by Aerojet General, General Motors, and TRW.

References

1. Wu, J.J., and Flagan, R.C., "Onset of Runaway Nucleation in Aerosol Reactors," *J. Appl. Phys.* **61**, 1365-1371 (1987).
2. Cannon, W.R., Danforth, S.C., Flint, J.H., Haggerty, J.S., and Marra, R.A., "Sinterable Ceramic Powders from Laser Driven Reactions, Part I: Process Description and Modeling," *J. Amer. Ceram. Soc.*, **65**, 324-330 (1982).
3. Cannon, W.R., Danforth, S.C., Haggerty, J.S., and Marra, R.A., "Sinterable Ceramic Powders from Laser Driven Reactions, Part II: Powder Characteristics and Process Variables," *J. Amer. Ceram. Soc.*, **65**, 330-335 (1982).
4. Aoki, M., Flint, J.H., and Haggerty, J.S., "Synthesis of Non-Agglomerated Si_3N_4 Powder," *Proceedings of the First International Conference on Ceramic Powder Processing Science*, pp. 253-260 (1988).
5. Ulrich, G.D., "Theory of Particle Formation and Growth in Oxide Synthesis Flames," *Combust. Sci. Technol.* **4**, 47 (1971).
6. Ulrich, G.D., Ines, B.A.M., and Subramanian, N.S., "Particle Growth in Flames II: Experimental Results for Silica Particles," *Combust. Sci. Technol.* **14**, 243 (1976).
7. Ulrich, G.D., and Riehl, J.W., "Aggregation and Growth of Submicron Oxide Particles in Flames," *J. Colloid Interface Sci.* **87**, 257-265 (1982).
8. Flint, J.H., and Haggerty, J.S., "Models for Synthesis of Ceramic Powders by Vapor Phase Reactions," *Proceedings of the First International Conference on Ceramic Powder Processing Science*, pp. 244-252 (1988).
9. Coltrin, M.E., Kee, R.J., and Miller, J.A., "A Mathematical Model of the Coupled Fluid Mechanics and Chemical Kinetics in a Chemical Vapor Deposition Reactor," *J. Electrochem. Soc.: Solid-State Sci. Technol.* **131**, 425-434 (1984).
10. Coltrin, M.E., Kee, R.J., and Miller, J.A., "A Mathematical Model of Silicon Chemical Vapor Deposition: Further Refinements and the Effects of Thermal Diffusion," *J. Electrochem. Soc.: Solid-State Sci. Technol.* **133**, 1206-1213 (1986).
11. Wu, J.J., and Flagan, R.C., "A Discrete-Sectional Solution to the Aerosol Dynamic Equation," *J. Colloid Interface Sci.* **123**, 339-352 (1988).
12. Lai, F.S., Friedlander, S.K., Pich, J., and Ildiy, G.M., "The Self-Preserving Particle Size Distribution for Brownian Coagulation in the Free-Molecule Regime," *J. Colloid Interface Sci.* **39**, 395-405 (1972).
13. Wu, J.J., Nguyen, H.V., Flagan, R.C., Okuyama, K., and Kousaka, Y., "Evaluation and Control of Particle Properties in Aerosol Reactors," *AIChE J.* **34**, 1249-1256 (1988).
14. Pratsinis, S., "Simultaneous Nucleation, Condensation, and Coagulation in Aerosol Reactors," *J. Colloid Interface Sci.* **124**, 416-427 (1988).
15. Medalia, A.I., and Heckman, F.A., "Morphology of Aggregates - II. Size and Shape Factors of Carbon Black Aggregates from Electron Microscopy," *Carbon* **7**, 567-582 (1969).
16. Forrest, S.R., and Witten, T.A., Jr., "Long-range Correlations in Smoke Aggregate Particles," *J. Phys. A: Math. Gen.* **12**, L109-L117 (1979).
17. Mountain, R.D., Mullholland, G.W., and Baum, H., "Simulation of Aerosol Agglomeration in the Free Molecular and Continuum Regimes," *J. Colloid Interface Sci.* **114**, 67-81 (1986).
18. Girschick, S.L., Chiu, C-P., and McMurtry, P.H., "Modeling Particle Formation and Growth in a Plasma Synthesis Reactor," *Aerosol Sci. Technol.* (in press).
19. Schmidt-Ott, A., "In Situ Measurement of the Fractal Dimensionality of Ultrafine Aerosol Particles," *Appl. Phys. Lett.* **52**, 954-956 (1988).

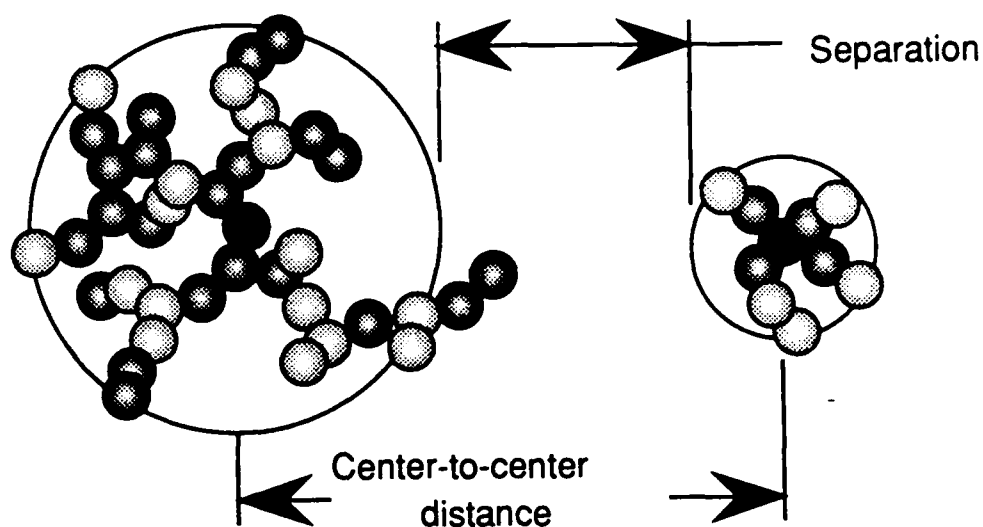


Figure 1. Illustration of the agglomerate structure that results by successive agglomeration events between clusters.

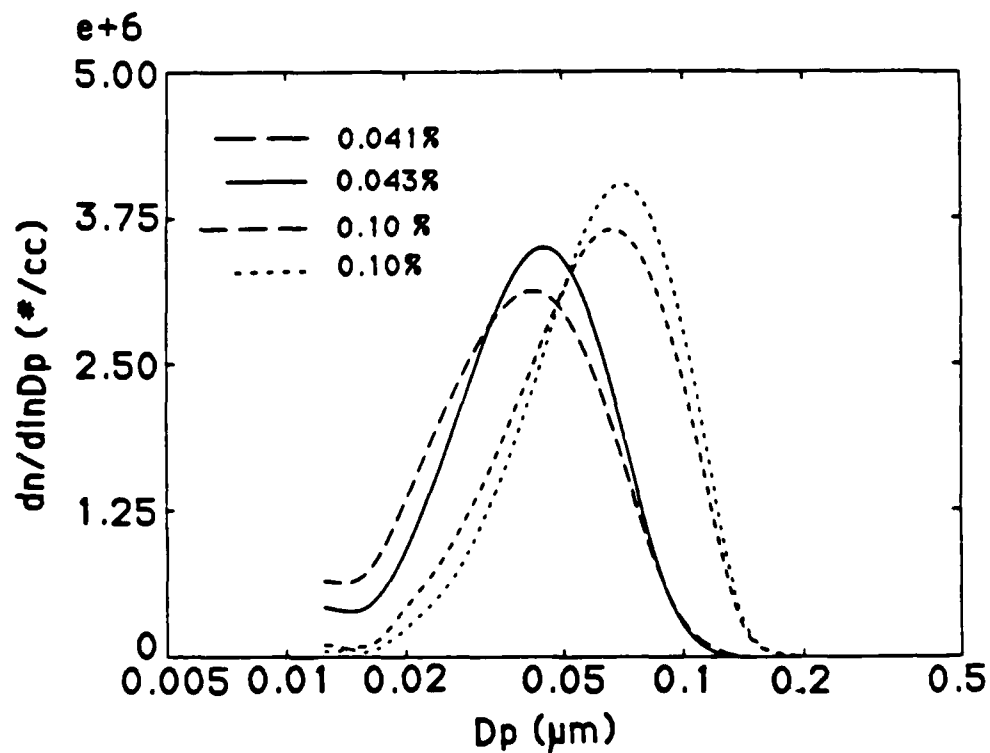


Figure 2. Size distributions measured using TSI Condensation Nuclei Counter as a detector at the outlet of the silane pyrolysis reactor. The reported diameter is the mobility equivalent diameter, i.e., that of a dense sphere with the same charge to aerodynamic drag ratio.

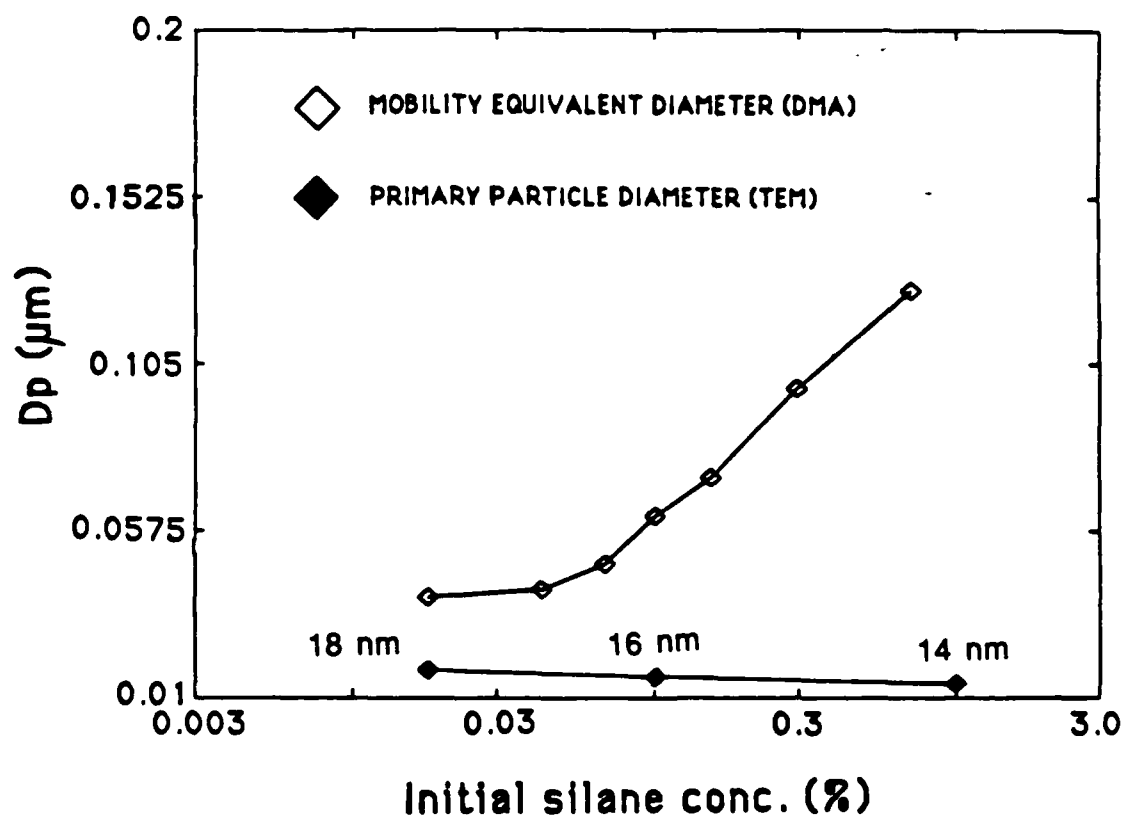


Figure 3. Comparison of mobility equivalent diameters of Fig. 1 with the fine structure scales determined by transmission electron microscopy on samples obtained from the same experiments.

CERAMIC POWDER SYNTHESIS IN AN AEROSOL REACTOR

M. K. Alam, C. Wiseman and Q. Azeez

Dept. of Mechanical Engineering
Ohio University, Athens, OH 45701

ABSTRACT

A flow reactor has been used to produce ceramic powders from gas or vapor phase reactants. Experiments have been carried out to produce powders of silicon, silicon nitride and aluminum nitride. The product powder was characterized in terms of particle size and chemical composition. The powders were typically submicron in size; the chemical composition of the powders was observed to be sensitive to processing parameters. An analytical model for aerosol growth has been used to simulate the particle growth in the reactor.

INTRODUCTION

One of the simplest forms of an aerosol flow reactor is a heated tube into which gas reactants are metered. Typically, the product of the reaction has a very low vapor pressure which leads to the nucleation of new particles. These particles remain dispersed in the gaseous medium, and are called aerosols. The aerosol particles collide and form clusters or larger spheres. This process reduces their number, while increasing the size of each unit. The operating conditions of the flow reactor can be varied to control the gas phase chemical reactions and ultimately the characteristics of the product particles.

In the present study, an aerosol flow reactor has been used to produce powders of silicon, silicon nitride and aluminum nitride. The size distributions of the product particles were then measured. The chemical composition of silicon nitride has been analyzed by x-ray fluorescence. Preliminary

The following are the keywords for the paper "Ceramic Powder Synthesis in an Aerosol Reactor" by Alam, Wiseman and Azeez:

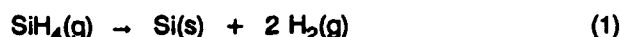
Flow Reactor, Silicon, Silicon Nitride, Aluminum Nitride

experiments also indicate that it is feasible to produce aluminum nitride in this reactor.

RATIONALE AND BACKGROUND

Silane and silicon-chlorine compounds are commonly used in silicon and silicon nitride production. In this study silane was used for the production of silicon powder. Silane and ammonia were used for the production of silicon nitride. Aluminum compounds with ammonia, nitrogen and hydrogen gases were used in the production of aluminum nitride powders.

The overall reaction involving the thermal pyrolysis of silane is:



while that for synthesizing silicon nitride is:



Conversion of silane to silicon is rapid at temperatures above 800 K [1]. In regard to Equation 2, 550°C is the lowest temperature which gives an appreciable yield of silicon nitride. 700° to 900°C is a typical temperature range for the conversion of silane and ammonia to silicon nitride.

Alam and Flagan [1] designed an aerosol reactor to produce silicon particles. Wu [2] studied the synthesis of silicon powder in a flow reactor from the perspective of ceramic application. The objective was the production of uniform, spherical, nonagglomerated submicron particles with high purity. The basic reactor design was similar to that used by Alam and Flagan [1].

Prochazka and Greskovich [3] experimented with the production of high purity silicon nitride. Their reactor consisted of a 3.8 cm ID, fused silica tube heated over a 25 cm length by a single zone resistance furnace. Silane, ammonia, and argon (diluent gas) were metered into the reactor. No appreciable reaction was observed below 500°C. Maximum temperature in the experiments was 920°C. For NH_3/SiH_4 ratios less than 10 (by volume) the product was brown to orange, indicating some free

silicon. With NH_3/SiH_4 ratios over 10, the powders were white to tan. The composition of the product, and the powder size distribution, were not analyzed extensively. It was observed that the diameters were of the order of 1 μm and typical oxygen content was 2% or more.

No studies have been reported in synthesis of aluminum nitride by a flow reactor. Mitomo et al. [4] investigated the reduction of alumina by carbon in the presence of nitrogen to produce aluminum nitride. For an aerosol reactor, the reactants must be in the vapor phase. Organometallic compounds can be volatilized easily, but such compounds contain oxygen, which is undesirable in the product. Aluminum chloride is a suitable volatile compound for the flow reactor. The complementary reactants are ammonia and/or nitrogen.

EXPERIMENTATION

The reactor (Figure 1) consists of a 2.2 cm ID quartz tube passing through two electric furnaces. The first furnace is a 34 cm long resistance furnace (Lindberg model 55031). It is followed by a 93 cm long, single zone furnace (Lindberg vertical tube furnace, model 54453-V). The reactor tube is followed by a filter collector for separating the powder from the flow. The gases for the flow reactor were first purified by removal of oxygen and water vapor. In some runs a molecular sieve was also used for purification. All joints in the flow system were checked with a leak detector (Gow Mac, model 21-250).

Typical operating temperatures and resulting product colors are shown in Table 1. The residence times in the reactor varied from 1 to 5 seconds. For silicon powder production, excess of argon was used as diluent. In producing nitride powders, excess of ammonia and/or nitrogen were used. In addition, aluminum organometallic compounds and aluminum chloride were used in the production of aluminum nitride. Experiments in production of Aluminum Nitride are still in progress; results presented here are obtained from the first set of experiments.

PARTICLE CHARACTERISTICS

Particle diameters were measured by a centrifugal particle size analyzer (Horiba, CAPA-300) and then checked against the sizes indicated by transmission electron microscopy (TEM). An additional

benefit of TEM is that it shows particle morphology.

Table 1 Operating Conditions for production of Powders

Powder		Set Temperatures(°C)		Product color
		Seed furnace	Primary Furnace	
Si	1	450	1000	brown
	2	450	1000	brown
	3	500	1200	brown
	5	500	1300	dark brown
	6	500	1475	grey brown
Si ₃ N ₄	1	500	900	white/tan
	2	500	1150	white/brown
	3	600	1150	white/grey
	4	500	750	tan/white
	5	600	850	brown/white
	6	500	800	brown/rust
	7	900	900	uniform brown
	8	800	800	tan
	9	800	800	tan/brown
	10	775	775	uniform tan

Figures 2a through 2d show the volume distribution of silicon, silicon nitride and aluminum nitride powders produced in the reactor. It can be seen that the particle sizes are typically in the submicron size range. From the two results for silicon nitride (run #8 and run #10), it can be deduced that processing parameters are extremely important in determination of particle size distribution. The higher temperature tends to produce a smaller particle size.

The size and morphology is also determined by presence of trace impurities such as oxygen. TEM pictures show that, when trace amounts of oxygen are present in the reactants used in these experiments, chain-like structures of very small particles are produced. When the reactants are properly processed to remove impurities, and the temperatures are optimized, the powders tend to be clean and spherical. Figures 3a & 3b show TEM pictures of silicon and silicon nitride. Some geometrical defects (dislocations) can also be observed in the powders. These defects are not indicative of the process, but are governed by the material and shape.

The variation of the product particle characteristics is a function of the reaction kinetics, measured parameters such as temperature, and flow rates; impurities such as oxygen in the reactant gases also change the particle properties. Reaction kinetics of the system are not always available. Analytical modeling of this system is, therefore, rather difficult.

ANALYTICAL PREDICTIONS

A number of approaches have been adopted to calculate the formation and growth of aerosol particles in a flow reactor. The solution tends to be cumbersome since the general case of aerosol dynamics is described by a nonlinear, partial integro-differential equation [5]. One model which simplifies the aerosol dynamics was developed by Wu [2] and is called the Simplified Reaction - Coagulation (SRC) model.

The SRC model divides the full range of particles - small nuclei cluster through larger aerosol particles - into two modes: (i) particles or clusters newly formed as a result of homogeneous nucleation and (ii) those which are growing by condensation and/or coagulation. The information that can be obtained from this model is the number concentrations, mass concentrations, and the average diameters. The conservation equations for these modes are solved to obtain an estimate of the particle size that could be expected in the reactor. Results for a silicon nitride powder production experiment is shown in Figure 4. In this simulation, a first order reaction was assumed; with an estimate for the reaction constant obtained by observing the reaction termination time experimentally [2].

The results indicate that the final diameter of the particle is expected to be 0.66 microns. This

is quite comparable to the experimental value of 0.5 microns average diameter shown by centrifugal aerosol analyzer (run #10). The TEM pictures, however, show primary particles mostly in the size range of 0.2 - 0.4 microns. This indicates agglomeration of particles without subsequent fusion.

CHEMICAL ANALYSIS

IR spectroscopy was used to determine the presence of impurities in silicon and aluminum nitride. It was not particularly useful for silicon nitride since the O-H and N-H energy bands overlap. Quantitative results were obtained by using x-ray fluorescence techniques on silicon nitride powders. It was observed that the initial runs in the production of silicon powder showed significant amounts of oxygen. With greater control on the reactant purity and flow system, the oxygen contamination was reduced to trace amounts. Similar behavior was observed in the aluminum nitride product. Initial samples showed large amounts of oxygen, while the latter samples showed no oxygen peaks. Additional experiments in the synthesis and analysis of aluminum nitride are currently in progress.

Silicon nitride samples were analyzed by x-ray fluorescence to determine the composition. It was observed that the product powder tended to be rich in silicon. The compositions were particularly poor when the reactor was operated at higher temperatures. The theoretical atomic ratio of silicon to nitrogen is 0.75. The following ratios were observed in the product from the different runs:

Run Number	Atomic Weight %		[Si]/[N]
	Si	N	
7	53.5	39.8	1.344
8	43.8	48.9	0.895
10	41.1	52.3	0.786

The gradual improvement in the composition was due to process control by improving the flow purification and the temperature of the reactor. The amount of oxygen in the sample was seen to vary

from 2% to 6%. From the above results it can be concluded that, for this flow reactor system, the optimum temperature for production of silicon nitride is approximately 775°C.

CONCLUSIONS

Silicon, silicon nitride and aluminum nitride powders have been synthesized from gas phase reactants in an aerosol flow reactor. The production of clean, spherical powder of silicon from silane is achieved best by using a high sintering temperature in the final stages of the reactor.

The production of silicon nitride seems to be best achieved at lower temperatures, approximately 775°C. Higher temperatures result in the production of free silicon. Preliminary experiments in the production of aluminum nitride have indicated that it should be possible to produce aluminum nitride powders by using an aerosol reactor. The characteristics of the product powders depend strongly on the processing parameters, and are extremely sensitive to reactant impurities such as oxygen.

Aerosol growth models can predict the particle sizes reasonably well. It would be extremely useful to have predictive capabilities for particle morphology. Present analytical models, however, cannot simulate such details of particle growth.

ACKNOWLEDGEMENTS

This work was supported by NSF Grant CPE-84044712, by Research Challenge funds of Ohio University, and by Stocker Funds of the College of Engineering and Technology, Ohio University. The authors would also like to acknowledge help from Mr. Bob White of EDAX International in x-ray analysis.

REFERENCES

- 1) Alam, M.K. and Flagan, R.C. (1986). Aerosol Sci. and Tech., 5:237-248.
- 2) Wu, J.J. (1986). Powder Synthesis in Aerosol Reactors. Doctoral thesis, California Inst. of Tech., Pasadena, Ca.
- 3) Prochazka, S. and Greskovich, C. (1978). Ceramic Bulletin, 57:579-581.
- 4) Mitomo, M., Yoshika, Y. (1987). Advanced Ceramic Materials, 2:253-256
- 5) Friedlander, S.K. (1977). Smoke, Dust, and Haze. Wiley, New York.

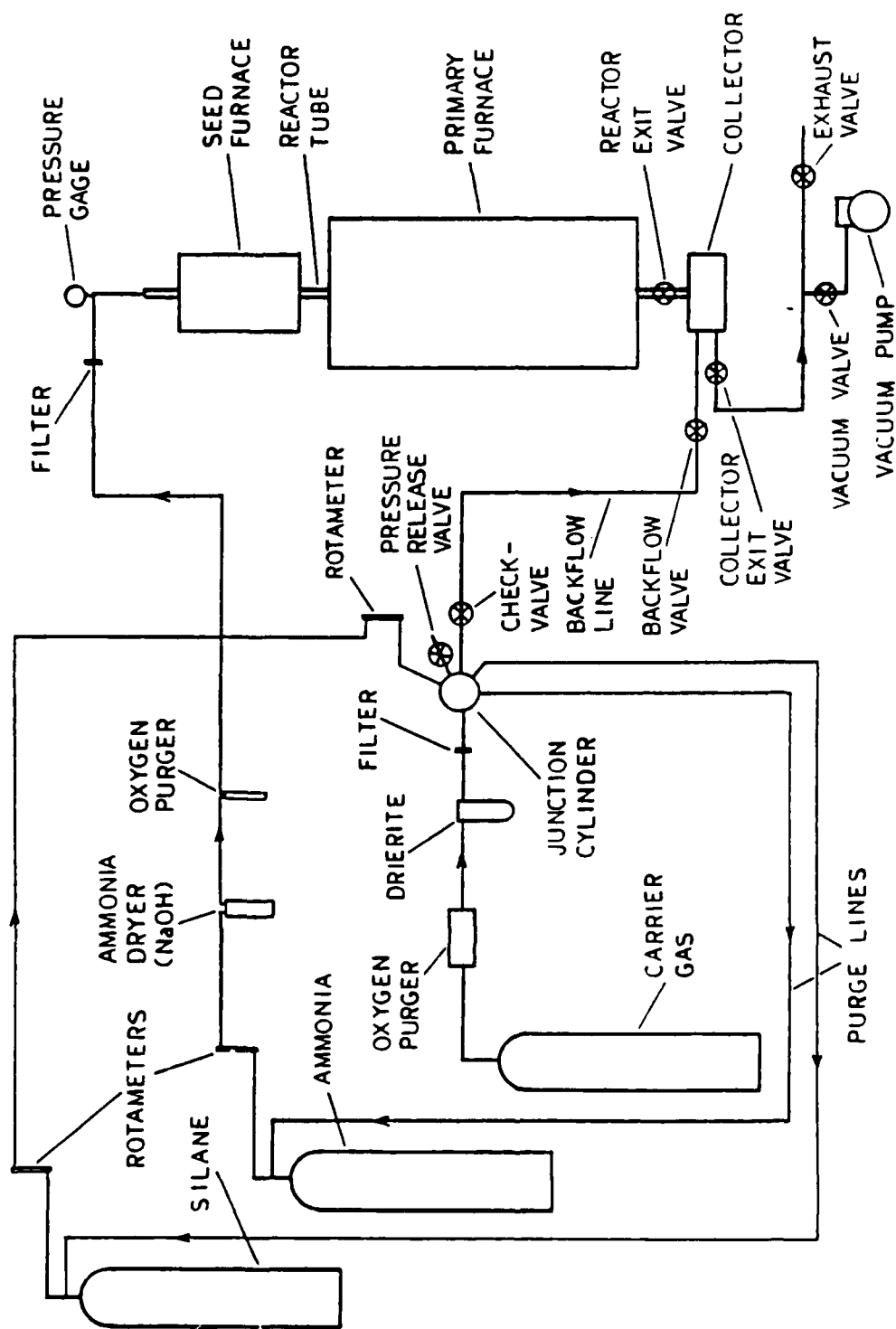
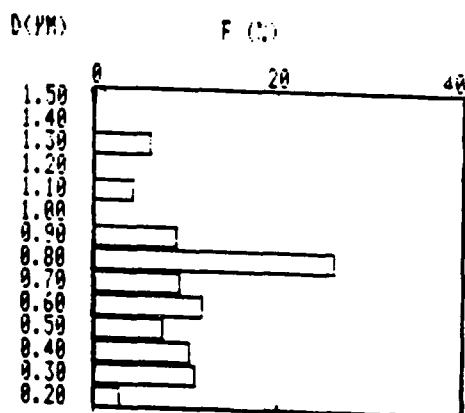
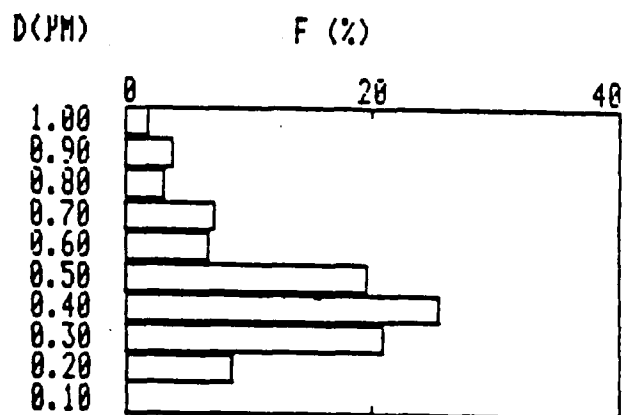


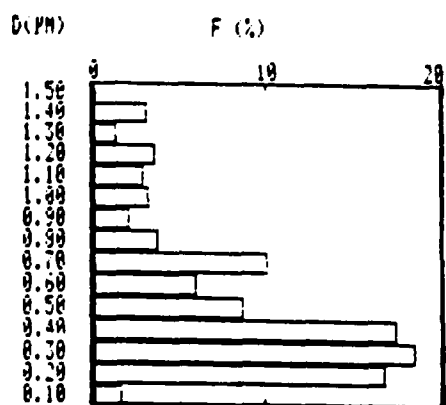
Figure 1 Schematic of experimental Reactor System



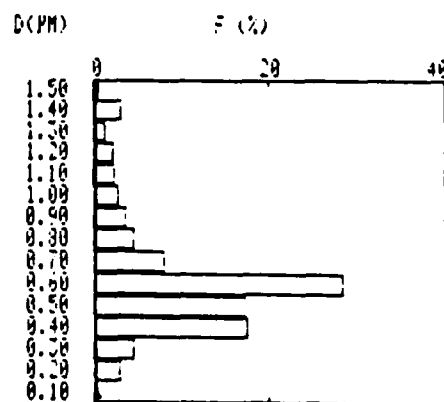
(a) silicon run #6



(b) aluminum nitride powder



(c) silicon nitride run #8



(d) silicon nitride run #10

Figure 2 Volume distributions of powders as obtained from HORIBA CAPA-300



(a) Silicon nitride

(b) silicon

Figure 3 TEM pictures of powders

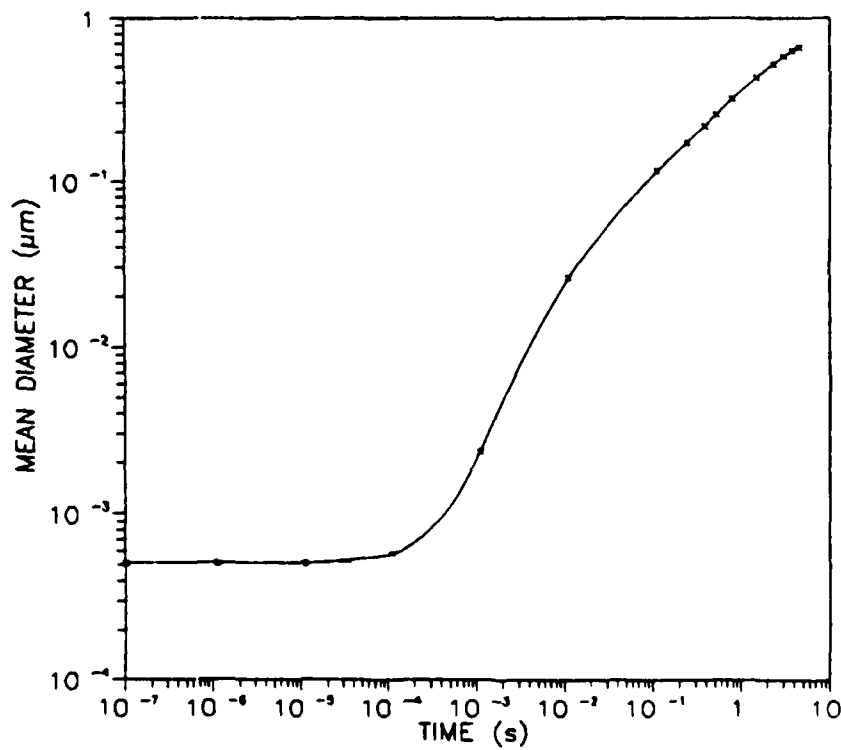


Figure 4 Average diameters of the 'seed' particles as predicted by SRC model for silicon nitride run #10

SILICA PARTICLE FORMATION USING THE COUNTERFLOW
DIFFUSION FLAME BURNER

Joseph L. Katz, Douglas Chin[†], Shyan-Lung Chung^{*}

Department of Chemical Engineering
The Johns Hopkins University
Baltimore, MD 21218

and

Michael R. Zachariah, Hratch G. Semerjian

Center for Chemical Engineering
National Institute of Standards and Technology
Gaithersburg, MD 20899

Keywords: Silica, SiO_2 , Nucleation, Ceramic Powders, Flame, Counterflow
Diffusion, Light Scattering

Abstract

A rectangular version of the counterflow diffusion flame burner has been developed and used to study the formation, nucleation, and growth of SiO_2 particles. Spectroscopic methods were used to measure temperatures and concentrations of stable intermediates. Both dynamic light scattering and two angle light scattering was used to measure particle size.

A number of refractory materials are produced as fine particles by combustion of appropriate precursors. In the pigment and reinforcing agent industries, tens of thousands of tons of SiO_2 , TiO_2 , and Fe_2O_3 , are produced annually in this way (1-3). A recent use of flame generated particles which has become commercially important is in the production of optical fibers. They are produced by generating SiO_2 - GeO_2 fumes which are deposited as a preform, treated to remove water and other undesirable substances, melted, and drawn (4,5). Another exciting use of flame generated refractory particles is in the production of starting materials for the manufacture of high-tech ceramics. These ceramics are needed in extreme environments such as internal combustion, gas turbine, jet, and rocket engines (6,7). They are lighter and able to withstand much higher operating temperatures than the best superalloys currently available.

We are studying the processes controlling the flame generation of refractory particles using the counterflow diffusion flame burner (8-13). This burner (see Fig. 1) differs from traditional counterflow burners (14-17) by its rectangular instead of cylindrical geometry, its separate side sections, and its fused silica side windows. With this burner, the chemical and physical processes controlling particle formation, growth, and agglomeration can be studied in a uniform and highly controllable flame environment.

Our counterflow diffusion flame burner consists of two vertically opposed tubes of rectangular cross section. Each tube consists of three channels, a central main channel, and two side channels. Fused silica plates are fitted to the ends of the two side channels, thus forcing the combustion gases to flow out through the front and back. Oxidizer (oxygen diluted by argon) flows downward from the top tube, while fuel (hydrogen diluted by argon and also

containing a low concentration of the appropriate precursor gas, e.g., silane (SiH_4) flows upward from the bottom tube. No precursor gas is added to the mixtures which are fed to the side channels. Flanges fitted to both top and bottom of the burner minimize entrainment of surrounding air and keep the gas outflow parallel to the burner surfaces. A flame is generated in the region where the two opposed gas streams impinge. This flame appears very flat and uniform in the horizontal plane. Temperature measurements made using thermocouples (8) (see Figs. 2 and 3) and species concentration profiles measured by light absorption (9) (see Fig. 4) confirm this uniformity.

There are significant advantages to the use of the rectangular counterflow diffusion flame burner for studies of the mechanisms of particle formation and generation. They are:

- Both temperature and concentration distributions are uniform in a horizontal plane. Hence one is able to use non-intrusive measurement techniques, (e.g., emission and absorption spectroscopy, laser light-scattering and extinction, laser induced fluorescence) to measure temperature, species concentrations, particle size, and particle concentration. (The separate end sections of the burner are very important for these purposes. They not only keep the temperature uniform, they also do not contain the condensable species. Thus light beams that pass down the long axis traverse uniform conditions.)

- Formation of the condensing species by chemical reaction, the nucleation of particles, and the subsequent growth of these particles all occur in an essentially one-dimensional flow region.

- Pyrophoric compounds such as SiH_4 and $\text{Al}(\text{CH}_3)_3$ can be used. One is thus free to choose precursor materials on the basis of other criteria, e.g., rates of reaction, cost, safety, toxicity.

- Three key factors that determine refractory particle characteristics (temperature, species concentration, and residence time) can be controlled almost independently of one another. Temperature can be controlled by changing the concentrations of the fuel and the oxidant in their respective gas streams (i.e., by changing the amount of diluent in either stream). Species concentrations can be controlled by changing the concentrations of the precursor compound (e.g., SiH_4) in the fuel stream. Residence time can be controlled by changing the flow rates of the fuel and the oxidant gas streams.

We have used the rectangular counterflow diffusion flame burner to study the formation of silica particles. Hydrogen (diluted by argon) and oxygen (diluted by argon) were used as the primary fuel and oxidant, respectively. Small volumes of silane (SiH_4) were added to the fuel stream. The oxidation of silane generated the particle forming species (i.e., SiO_2). Particle formation was monitored using laser light scattering. SiO and O_2 concentrations were measured by analyzing their respective ultraviolet absorption spectra. Temperatures were measured by two techniques: measuring UV absorption spectra to determine the ground state distribution of hydroxyl radicals and thus their rotational temperature; using Pt-10%Rh thermocouples and correcting for radiation losses. More detailed discussion of these techniques will now be presented.

Light scattering intensities as functions of vertical position in the burner for various silane fuel ratios ($\text{SiH}_4 \text{ flow} / [\text{H}_2 + \text{SiH}_4 \text{ flow}]$) are shown by dashed curves in Figure 5 (taken from ref. 8; see it for a fuller explanation). No scattering is observed until the silane fuel ratio is increased to 0.00109

(the dashed curve with squares). This fuel ratio corresponds to a silane flow fraction ($\text{SiH}_4 \text{ flow} / [\text{H}_2 + \text{Ar} + \text{SiH}_4 \text{ flow}]$) of 0.00065. The higher the silane fuel ratio, the stronger is the light scattering. (The progressively higher dashed curves in Figure 5 correspond to silane fuel ratios of 0.00403, 0.00441, 0.00474, and 0.00592, respectively.) Note that these are total scattering intensities and are not broken down into information about particle sizes and concentrations.

We have measured the concentrations of various vapor phase species as a function of their vertical position in the burner. Figure 6 shows the partial pressure profiles of SiO and hot O_2 (see ref. 8). The SiO profile is for a silane fuel ratio of 0.00474 (i.e., a flow fraction of 0.0028). One sees that at $Z = -7\text{mm}$ (i.e. 1/2mm above the lower mouth of the burner), a barely detectable amount of silane has been converted to SiO. Higher up in the flame, the SiO partial pressure rapidly increases then decreases slightly and then increases again. The O_2 partial pressure profile drops very rapidly in the main flame region as it is consumed by combustion with the hydrogen.

OH concentration can also be measured. However OH has an additional important use. The relative intensities of the various lines can be used to determine the temperature. Figure 7 is an example of the relevant portion of the OH spectrum, taken with the aid of our microcomputer. Using such spectra one obtains the temperatures shown as x in Figure 6. The temperatures denoted by o were measured using a thermocouple (and radiation corrected). Note their good agreement at those temperatures where both techniques were used.

In 1986, J. L. Katz, while on sabbatical leave at the National Bureau of Standards (today known as the National Institute of Standards and Technology) duplicated the burner and began a collaborative research program involving his colleagues there and also, his student, Douglas Chin. After verifying that both burners gave identical results, the availability of the appropriate lasers, FFT spectrum analyzer, etc., and existing expertise on 2 angle scattering suggested concentrating the effort at the Bureau on obtaining particle sizes by in-situ techniques.

Techniques utilizing light scattering from particles to obtain size and number densities include scattering to extinction ratio, two color measurements, polarization ratio, and angular dissymmetry (18,19). These techniques are generally referred to as ensemble elastic light scattering (ELS) methods. Dynamic light scattering (DLS) methods (quasi-elastic) are a relatively new development in particle measurement (20). We will compare the results of measurements obtained from DLS and light scattering angular dissymmetry (LSD) for the in-situ characterization of silica particle formation in counterflow diffusion flames after a brief description of each measurement method.

Dynamic light scattering (20-23), also known as diffusion broadening spectroscopy, has been used as a means of noninvasive particle sizing, particularly in the measurement of soot formation (24,25). The Brownian motion of particles illuminated with monochromatic light will cause fluctuations in the scattering field. One can correlate these fluctuations to the mean speed or to the particle diffusion coefficient, which, in turn, can be related to a particle diameter. The fluctuating interference pattern, when imaged on a

photomultiplier, produces a corresponding fluctuating photocurrent (homodyne) which can be processed directly by correlation methods (21), or low pass filtered to remove sum frequencies and then Fourier transformed to the frequency domain spectrum centered at 0 Hz.

For monodisperse spherical particles undergoing no mean motion, the resulting power spectra in frequency space is a Lorentzian in form, centered at 0 Hz:

$$P(\omega) = \frac{2I^2 K^2 D/\pi}{(2K^2 D)^2 + \omega^2} + \text{Shot noise} \quad (1)$$

Here I is the intensity of scattered light, D is the particle diffusion coefficient and K is the magnitude of the scattered wave vector as defined by, $K = 4\pi/\lambda_0 \sin \theta/2$, where λ_0 is the wavelength of the illuminating source and θ is the scattering angle measured relative to the forward scattering direction. Diffusion coefficients for the particles is obtained from the frequency at half maximum (HW = half width @ half max), $f_{HW} = D K^2/\pi$. For spherical particles, $D = kT/f$. For particles in the continuum regime ($\ell/d \ll 1$), the friction coefficient f for particle drag takes on the familiar Stokes law form, $f = 3\pi\eta d$, where η is the gas viscosity, and d the particle diameter. If the particles are in the free molecular regime ($\ell/d \gg 1$), the drag on a particle is less than that predicted by Stokes' Law, and expressions derived from kinetic theory becomes more appropriate (26). Under these conditions:

$$f = \frac{2 d^2 \rho}{3} \left[\frac{2\pi kT}{M} \right]^{1/2} \left[1 + \frac{\pi\alpha}{8} \right] \quad (2)$$

where ρ is the gas density, M is the molecular weight and α is the accommodation coefficient ($\alpha \approx .9$). Note that in going from a particle in continuum flow to one in free molecular flow the friction coefficient's dependence on particle diameter changes from d to d^2 . In this transition regime, an empirical interpolation formula is usually used, $f = 3\pi\eta d/C$, where C is a slip correction factor(27), $C = 1 + [2\ell/d] (1.257 + 0.400\exp[-0.55d/\ell])$.

Our dynamic light scattering system is shown in Fig. 8. The light source is a 4 W Argon-ion laser operating at 514.5 nm with an incident power of 1.5 W. A polarization rotator is used to polarize the light perpendicularly relative to the measurement plane. The laser is weakly focused into the scattering volume by a 500 mm lens, resulting in a beam waist of approximately 0.2 mm. Scattered light is collected at shallow angles ranging from 6 to 10° from the forward direction; spatial filters are used to define the probe volume. The scattered light is focused by a 10 cm focal length lens through a polarizer and laser line filter and then onto a photomultiplier.

If mean particle motion were significant, instead of the Lorentzian used above, the resulting Doppler effect would change the scattering into a Voigt profile (23). The criteria for selecting the appropriate fitting profile is the ratio of the two characteristic times, τ_d (diffusion time, $\tau_d = 1/2K^2D$) and τ_v (transit time through laser beam). For our experimental conditions, a Lorentzian fit is appropriate since typical transit times are 2 msec and

typical diffusion times are 0.02 msec.

By measuring the angular dependence of scattered (LSD) radiation one can infer particle size. The method requires one to know the refractive index of the scatterer, which can be a limitation when the optical properties of the scatterer are not well established. In order to observe angular dependence in the scattered light, the size of the particle must be larger than the Rayleigh limit as defined by the Mie parameter $X > 0.3$ ($X = \pi d/\lambda$). Also, the particles are assumed spherical.

The scattering intensity at an angle θ is:

$$Q_{vv}(X, \theta) = C_{vv}(X, \theta) N SR(\theta) \quad (3)$$

where $C_{vv}(X, \theta)$ is the Mie scattering cross-section for monodisperse spheres and the subscripts refer to the state of polarization of the incident and detected scattered light ($v = \text{vertical}$). N is the total number of scatterers and SR is the system response function of the optical and electronics system; it is obtained by calibration with a molecule of known scattering cross-section (ethene). The dependence on number density is eliminated by ratioing Q_{vv} at two different angles. C_{vv} itself is obtained from Mie theory (28). Once a particle diameter is determined, the scattering intensity and corresponding scattering cross-section for any one of the scattering angles may be used in equation (3) to obtain the number density. This number density, in turn, may be related to a particle volume fraction, ϕ , $\phi = \pi N d^3/6$.

The light scattering system consisted of a 4 W argon-ion laser operating on the 514.5 nm line. Incident laser power was set at 0.5W and modulated with a mechanical chopper at 1018 Hz. A polarization rotator was used to orient the direction of polarization perpendicular to the measurement plane. The beam was focused using the same optical arrangement used in the DLS experiment, with scattered light detected at 45° and 135° relative to the forward scattering direction. The detection optics at each angle consisted of a polarizer to reject cross-polarization effects, a collection lens, a pinhole aperture which defined the length of the sample volume to be 1 mm, and a laser line filter centered at 514.5 nm ($\Delta\lambda = 1\text{nm}$). Three lock-in amplifiers, one each for the two scattering angles and the third for the extinction leg, were used. The outputs from the lock-ins were digitized at 10 Hz for 10 sec and then sent to a microcomputer.

We have varied a number of process parameters (temperature, H_2 - O_2 ratio, silane loading, and flow velocity) and observed the resulting particle growth. Figure 9 is an example of the power spectrum obtained from a DLS experiment, along with the associated Lorentzian fit (solid curve). The vertical dotted line corresponds to the frequency at half maximum, from which the particle size is calculated. The spectrum is a 32-point average of power current fluctuation profiles. A least-squares fit to a Lorentzian profile was made and is also plotted as the solid smooth line. From the half-width of this fit, one calculates a value for the diffusion coefficient of $4.45 \times 10^{-5} \text{ cm}^2/\text{sec}$, resulting in a particle diameter of 0.185 μm .

To verify this result, a sample was taken of the silica that was flame-generated at this location. A carbon-coated grid placed on a thin brass holder was rapidly inserted and then withdrawn from the flame zone. The sample was analyzed by transmission electron microscopy. Comparison of the particle sizes determined from dynamic light scattering and from physical sampling show good

agreement.

Figure 10 presents a comparison of particle diameter measurements obtained using the DLS and LSD techniques for a set of flame conditions resulting in a peak temperature of about 2500K. In addition, the calibrated scattering intensity Q_{45} (45°) is plotted for comparison. Agreement between the two techniques is extremely good in the central portion of the particle field. However, near the entrance to the burner and also near the center, there is a marked difference in the diameters obtained. The LSD measurements, where they differ from DLS, always measure larger particle sizes. Note that in those regions where particle scattering intensity was large, agreement between the two techniques was good.

These differences can be understood by considering some factors which affect the results. The diffusion coefficient of a particle is highly temperature dependent (for free molecular flow $D \propto T^{3/2}$) and under flame conditions can be considerably larger than those of aerosols at ambient temperatures. Since the measured half-width is directly proportional to the diffusion coefficient, which under flame temperatures can be very large, small scattering angles ($\theta < 10^\circ$) are necessary to avoid overflowing the frequency range of the spectrum analyzer (100 KHz). Small particles, and particles with high diffusion coefficients (due to high temperatures), will spread the scattering signal over a wider range of frequency space, thus lowering signal to noise and enhancing the shot noise contribution to the power spectrum, which is frequency independent. This results in a broader power spectrum, which translates into an artificially large diffusion coefficient and therefore smaller particle size. At small scattering angles, decreasing the scattering angle by a factor of two will decrease the half width four fold. However, this results in decreased spatial resolution, necessitating a stopping down of the apertures to define an equivalent scattering volume, and coherence area, and resulting in a lower signal at the detector. The lower signal intensity manifests itself as a contribution of the shot noise term and lower signal/noise. To obtain a half width accuracy of 10%, a signal-to-noise ratio of about 100 is required. But when the scattering intensity was low, we were unable to obtain signal-to-noise ratios better than 5.

Dissymmetry measurements, and other elastic light scattering methods, need not work only at shallow angles, and also are not constrained by the coherence limitations which decrease the amount of light collected. Furthermore, since total scattering intensity (without frequency discrimination) is measured, these techniques provide significantly higher signal-to-noise ratios, and therefore are more reliable measurements at lower scattering intensities. However, they are limited to particles whose diameters are larger than $\approx 0.3\lambda/\pi$, and one must also know their index of refraction. This latter requirement can cause significant uncertainty since, under some conditions, it may be SiO or some other non-equilibrium silicate (e.g., Si_2O_3) which is condensing. Furthermore, since scattering intensity is a very strong function of particle size, a few, very large particles will dominate the total scattering. The strong rise in size near the burner mouth is probably due to large particles which were driven there by thermophoresis.

Figure 11 shows the effect of increasing silane loading on particle size. Relative to the results attained using a loading of 0.073%, increasing the loading by a factor of 2.5 resulted in a reduction of the half-width by a

factor of 4, and an approximate doubling of the maximum particle size. Increasing the loading by a factor of 5 resulted in a reduction of measured half-width by a factor of 7, and an approximate tripling of the maximum particle size. (The DLS curve in Fig. 10 is also curve D in Fig. 11)

A second set of flame conditions, with 1.75 times the flow rate of the first set also was analyzed (Figure 12). The gas phase temperature profile was about the same as that of flame 1. The increased flows made streamline velocities higher, thereby pushing particles out of the burner mouth faster, i.e., reducing particle residence times in the flame, resulting in smaller particle sizes. The region of detectable scattering was also reduced, i.e., the region of nucleation and growth was made narrower by the decreased residence times.

Both of these sets of high temperature flame conditions show similar trends in particle formation. Particles go through four regions: particle inception, surface growth, melting, and expulsion from the flame zone near the stagnation plane.

Sets of flame conditions also were constructed such that the maximum temperature of each was approximately 2000K, while the equivalence ratios varied between 0.757 and 1.310. Particle size measurements are given in Figures 13-15. The momentum ratios of the flames were chosen to be in the narrow region 0.767-0.880 and the total flow rates were kept approximately constant to insure that the residence times of the particles in the flames would be approximately the same. Our results indicate that increasing the equivalence ratio (while maintaining a maximum temperature of 2000K) has the effect of: narrowing the region of particle growth; causing particle inception to occur higher in the flame; producing a bimodal distribution with the second mode caused by particles agglomerating while falling back through the fuel-rich region; and increasing the maximum particle size. We also saw that the melting stage which occurred at higher temperature flames did not occur here.

The effect of momentum ratio was studied by maintaining a constant equivalence ratio of 0.757 and varying the momentum ratio from 0.849 to 0.309. Flame position and temperature profiles were not significantly affected by changing the momentum ratio. Variation of the momentum ratio, however, moved the stagnation plane in the flame region. Lowering the momentum ratio caused the initial particle inception to occur lower in the flame, i.e., in a cooler temperature region. The region of initial particle inception and growth was made narrower when the stagnation plane was in the cooler flame region. Conversely, pushing the stagnation plane into the hotter region of the flame broadened the region where particle inception followed by growth occurred. A bimodal distribution occurred at the lower momentum ratio as some particles which grew high in the flame were pushed back into the lower region of the fuel-rich region.

CONCLUSIONS

The sizes of silica particles were measured in a rectangular counterflow diffusion flame burner using a dynamic light scattering technique. The effects of silane loading, temperature, equivalence ratio, and residence times on particle formation were investigated. Choice of a flame with a maximum temperature of 2500K resulted in the silica undergoing a melting stage in the

flame. Increasing the residence time limited the size of particles grown. Increased silane loadings resulted in larger particles with broadened regions of particle growth.

Under conditions of high signal-to-noise ratio both DLS and LSD compare very favorably. In fact it is quite surprising that the two techniques, which rely on completely different physical principles for particle sizing should compare at all, since the underlying theory assumes that the particles are spherical and monodisperse. This suggests that for most aggregates the hydrodynamic radius (measured by DLS) and the Mie scattering volume (measured by LSD) are very nearly equivalent. This would not be the case were we able to make the same measurements on single particles; however, by making an ensemble measurement we obtain orientation and shape averaged spherical scattering and hydrodynamic volumes.

These results show the capabilities of the rectangular counterflow diffusion burner as a valuable tool in studying fundamental particle processes. They show that we can measure in-situ precursor concentration and temperature profiles. We can also obtain, in-situ, good measures of particle size and concentration. Our research goal is to interrelate the experimental measureables, i.e., temperature, concentrations of the precursor, intermediate and final species, O_2 and OH concentrations, onset of nucleation, particle size, and particle morphology. Using these measurements, in combination with nucleation theory and growth models, will enable us to extract the relevant experimental parameters. Thus one will be able to apply these results to many different geometries and experimental conditions. Furthermore, we hope to use these results to decipher the mechanisms behind the nucleation and growth processes occurring during refractory particle formation, answering questions such as: When are processes diffusion limited? When are they surface reaction limited? Do the oxidation steps themselves occur at the surfaces of the growing particles? Is the nucleation process auto-catalytic (29)?

ACKNOWLEDGEMENTS

We thank Dr. Robert J. Santoro for suggesting the DLS technique. Support for the research of Joseph L. Katz by Division of Materials Research, Office of Basic Energy Sciences, U. S. Dept. of Energy grants DE-AC02-79ER10456 and DE-FG02-88ER45356 is acknowledged.

† Present Address : United Technologies Corporation Research Center
Silver Lane
East Hartford, CT 06108

* Present Address : Department of Chemical Engineering
National Cheng Kung University
Tainan, Taiwan R.O.C.

REFERENCES

1. Mezey, E.J., "Pigments and Reinforcing Agents", in Powel, C.H., Oxley, J.H., and Bocker, J.M. Jr. (eds.), Vapor Deposition, Wiley, New York, 1966.
2. Wiseman, T.J., "Inorganic White Pigments", in Parfitt, G.D., and Sing, K.S.W. (eds.), Characterization of Powder Surfaces, Academic Press, New York, 1976.
3. Herman, E., "Inorganic Colored Pigments", in Parfitt, G.D., and Sing, K.S.W. (eds.), Characterization of Powder Surfaces, Academic Press, New York, 1976.
4. Ulrich, G.D., "Flame Synthesis of Fine Particles", Chemical and Engineering News, 62 (32), 22 (1984).
5. Kawachi, M., Sudo, S., and Shibata, N., "Deposition Properties of SiO_2 - GeO_2 Particles in the Flame Hydrolysis Reaction for Optical Fiber Fabrication", Jap. J. Appl. Phys., 19, L69 (1980).
6. Bowen, H.K., "Basic Research Needs on High Temperature Ceramics for Energy Application", Materials Science and Engineering, 44, 1 (1980).
7. Sanders, H.J., "High-Tech Ceramics", Chemical and Engineering News, 62 (28), 26 (1984).
8. Chung, S.L., Katz, J.L., "The Counterflow Diffusion Flame Burner: A New Tool for the Study of the Nucleation of Refractory Compounds", Combustion and Flame, 61, 271 (1985).
9. Chung, S.L., The Counterflow Diffusion Flame Burner: A New Tool for the Study of the Nucleation of Refractory Compounds, Ph.D. Thesis, The Johns Hopkins University, Baltimore, 1985.
10. Chin, D., A Study of Silica Formation in a Counterflow Diffusion Flame, Master's Essay, The Johns Hopkins University, Baltimore, 1987.
11. Katz, J.L., Chin, D., and Chung, S.L., "Refractory Particle Formation using the Counterflow Diffusion Flame Burner", in High Temperature Materials Chemistry IV, proceedings vol. 88-5, p. 555 (Electrochemical Society, 1988).
12. Zachariah, M.R., Chin, D., Semerjian, H.G., and Katz, J.L., "Dynamic Light Scattering and Angular Dissymetry for the In-Situ Measurement of Silicon Dioxide Particle Synthesis in Flames", Applied Optics (accepted for publication).
13. Zachariah, M.R., Chin, D., Semerjian, H.G., and Katz, J.L., "Silica Particle Synthesis in a Counterflow Diffusion Flame Reactor", Combustion and Flame (accepted for publication).
14. Pandya, T.P., and Weinberg, F.J., "The Structure of Flat, Counter-flow Diffusion Flames", Proc. Roy. Soc., 279, 544 (1964).
15. Patel, N.K., and Chu Chieh, "Studies of Opposed Jet Diffusion Flames. I. Temperature Distribution", Combustion and Flame, 14, 137 (1970).

16. Pandya, T.P., and Srivastara, N.K., "Structure of Counterflow Diffusion Flame of Ethanol", Comb. Sci. Tech., 11, 165 (1975).
17. Tsuji, H., "Counterflow Diffusion Flames", Prog. Energy Combustion Science, 8, 93 (1982).
18. Dobbins, R.A., Santoro, R.J. and Semerjian, H.G., "Interpretation of Optical Measurements of Soot in Flames", in Combustion Diagnostics by Nonintrusive Methods, T.D. McCray and J.A. Roux, Eds., Progress in Astronautics and Aeronautics, 92, 208 (1983).
19. D'Allesio, A., "Laser Light Scattering and Florescence Diagnostics of Rich Flames Induced by Gaseous and Liquid Fuels", Particulate Carbon-Formation During Combustion, Ed. Siegl, D.C. and Smith, G.W. p. 207, Plenum Press, New York, 1981.
20. Hinds, W. and Reist, P.C., "Aerosol Measurement by Laser Doppler Spectroscopy II, Operational Limit, Effects of Polydispersity, and Applications", Aerosol Science, 3, 501 (1972).
21. Chu, B., Laser Light Scattering, Academic Press, New York 1974.
22. Pedora, R., Dynamic Light Scattering, Plenum, New York 1985.
23. Cummins, H.Z. and Swinney, H.L., "Light Beam Spectroscopy", in Progress in Optics VIII Wold, E. Ed. p. 135, North-Holland Amsterdam, 1970.
24. Driscoll, J.F., Mann, D.M., and McGregor, W.K., "Submicron Particle Size Measurements in an Acetylene-Oxygen Flame", Combustion Science and Technology, 20, 41 (1979).
25. Flower, W.L., "Optical Measurement of Soot Formation in Premixed Flames", Combustion Science and Technology, 33, 17 (1983).
26. Hidy, G.M., and Brock, J.R., The Dynamics of Aerocolloidal Systems, Pergamon, Oxford 1970.
27. Friedlander, S.F., Smoke Dust and Haze, John-Wiley, 1977.
28. Dave, J.V., Subroutines for Computing the Parameters of the Electromagnetic Radiation Scattered by a Sphere, IBM Scientific Center Report No. 320-3237 (1968).
29. Katz, J.L., and Donohue, M.D., "Nucleation with Simultaneous Chemical Reaction", J. Colloid Interface Sci., 85, 267 (1982).

FIGURES

- Fig. 1. The Rectangular Counterflow Diffusion Flame Burner. Note the X, Y, and Z coordinate scales and that their zero is at the geometric center of the burner.
- Fig. 2. Temperature Profile Along the Length of the Burner, i.e. the X Direction.
- Fig. 3. Temperature Profile Across the Width of the Burner, i.e. the Y Direction.
- Fig. 4. Concentration Profile Across the Width of the Burner.
- Fig. 5. Scattering Intensity as a function of Height in the Burner. $Z=0$ is located at its geometric center.
- Fig. 6. Partial Pressures and Temperature as a function of Height in the Burner.
- Fig. 7. The OH Absorption Spectrum
- Fig. 8. Schematic representation of the dynamic light scattering system. M, mirror; PR, polarization rotator; L, lens; BD, beam dump; S_1, S_2, S_3 , spatial filter; f, narrow band filter; PMT, photomultiplier.
- Fig. 9. Example of a dynamic light scattering power spectrum and an associated lorentzian fit.
- Fig. 10. Axial profiles of DLS and light scattering angular dissymmetry (LSD) particle diameters and corresponding $Q_{\downarrow\downarrow}(45)$ scattering cross-sections. The Vertical bar corresponds to the particle stagnation plane.
- Fig. 11. Particle Diameters as a function of Height in the Burner, for different Silane Concentrations.
- Fig. 12. Particle Diameters as a function of Height in the Burner, for different Silane Concentrations.
- Fig. 13. Particle Diameters as a function of Height in the Burner, for different Silane Concentrations.
- Fig. 14. Particle Diameters as a function of Height in the Burner, for different Silane Concentrations.
- Fig. 15. Particle Diameters as a function of Height in the Burner, for different Silane Concentrations.

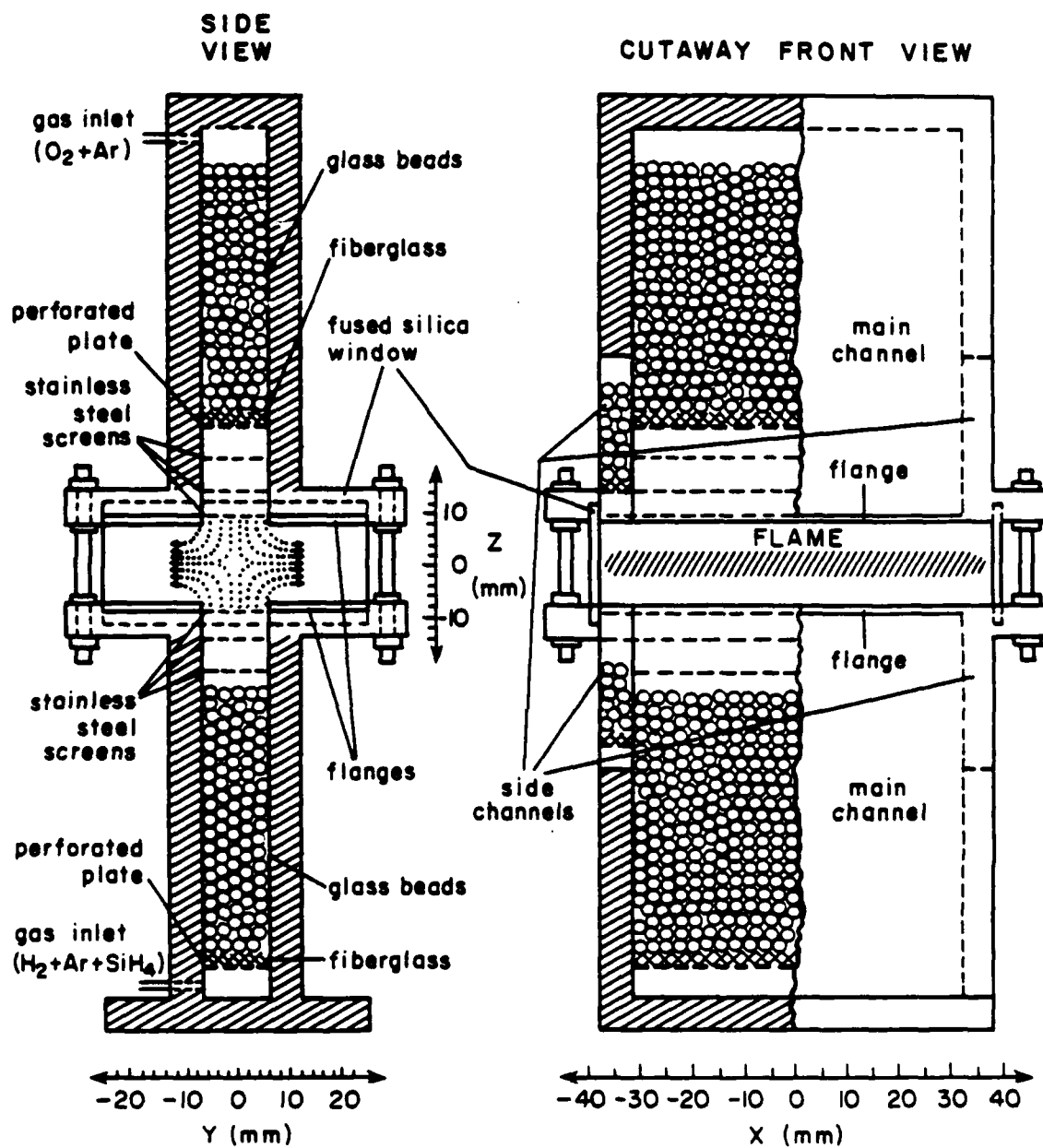


Fig. 1

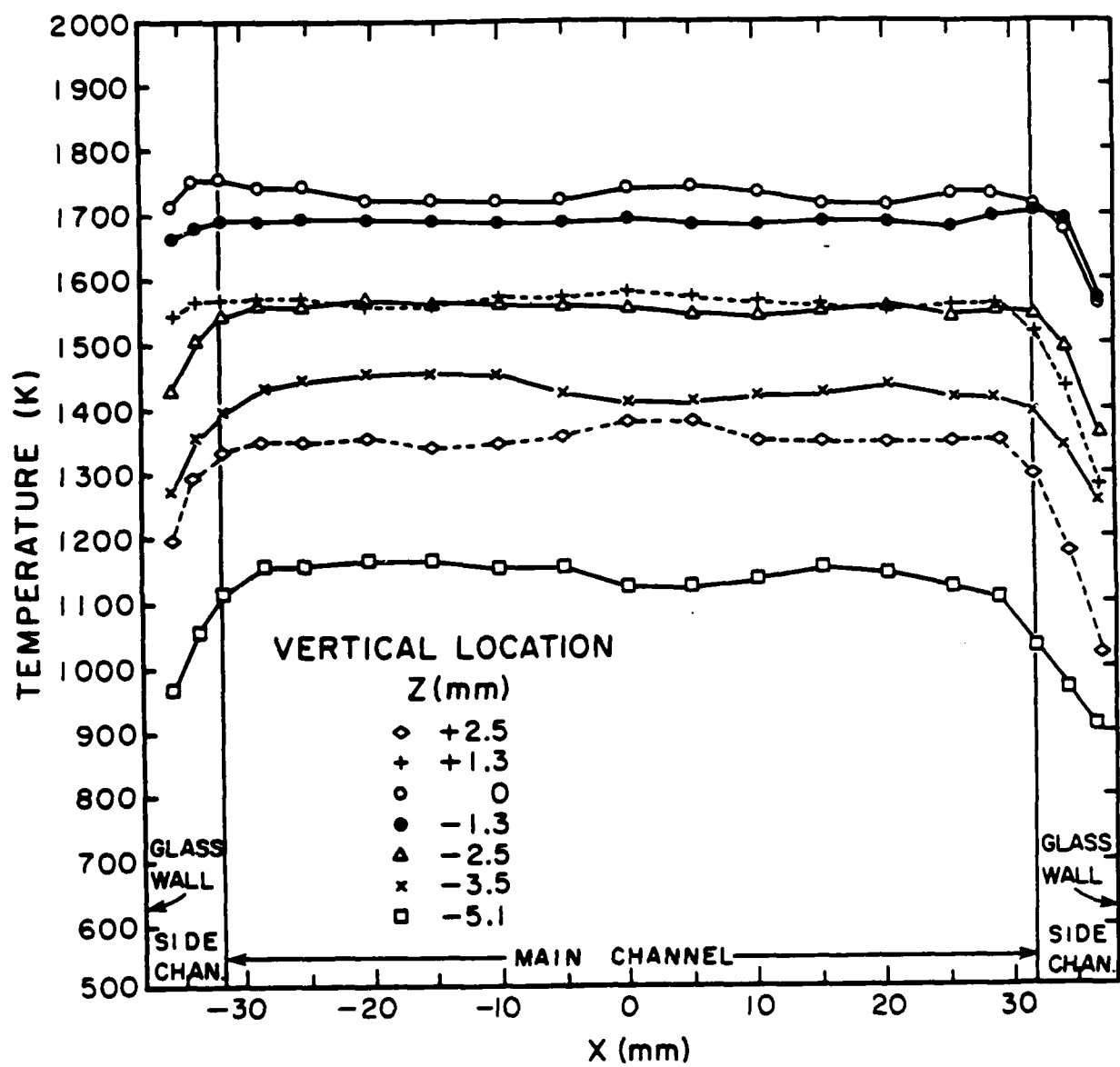


Fig. 2

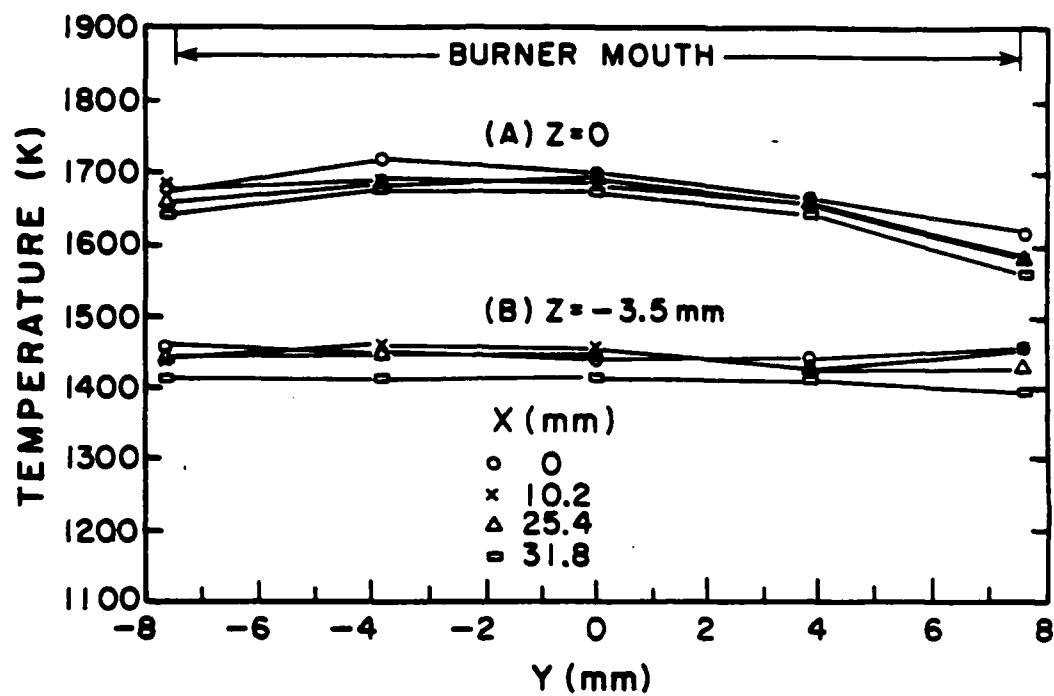


Fig. 3

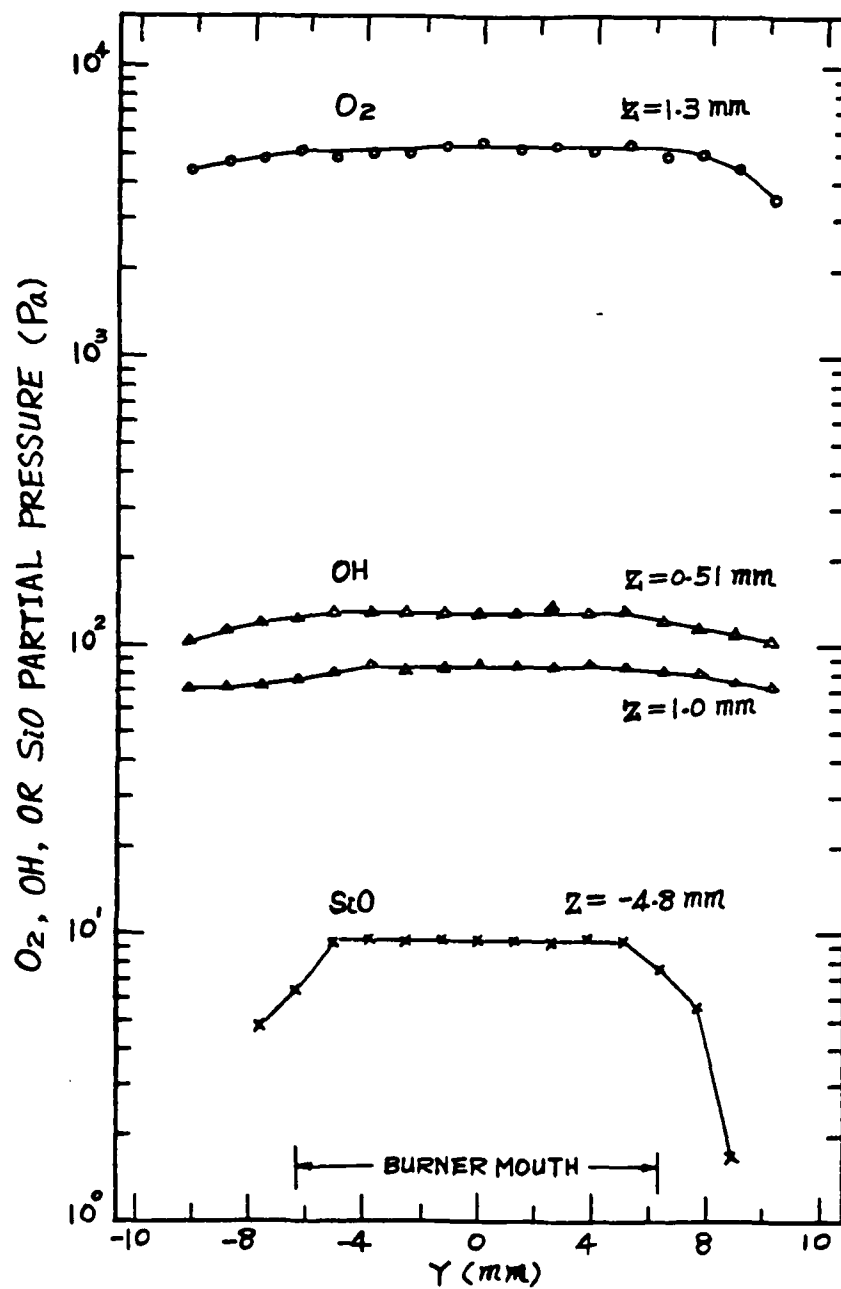


Fig. 4

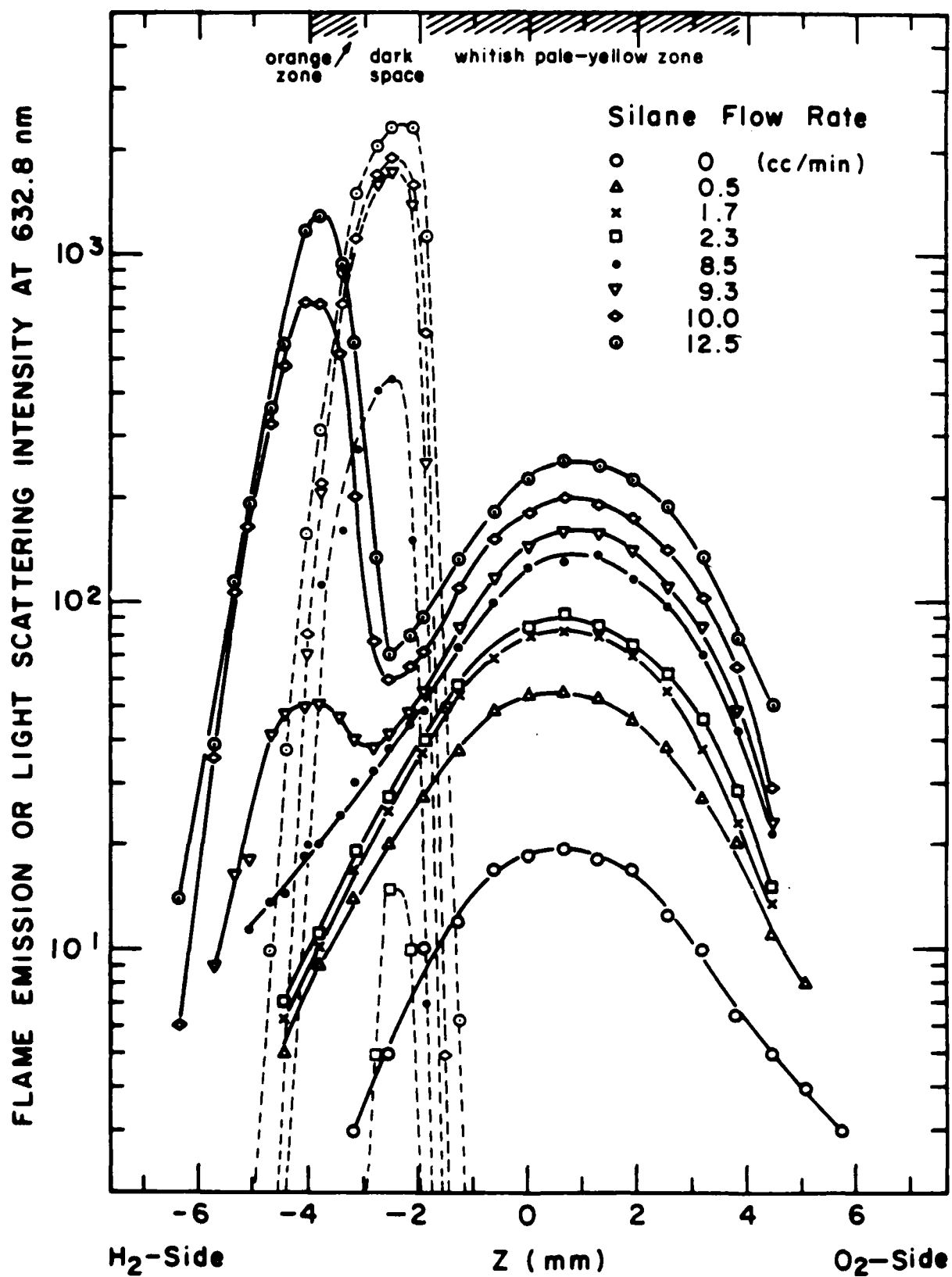


Fig. 5

611

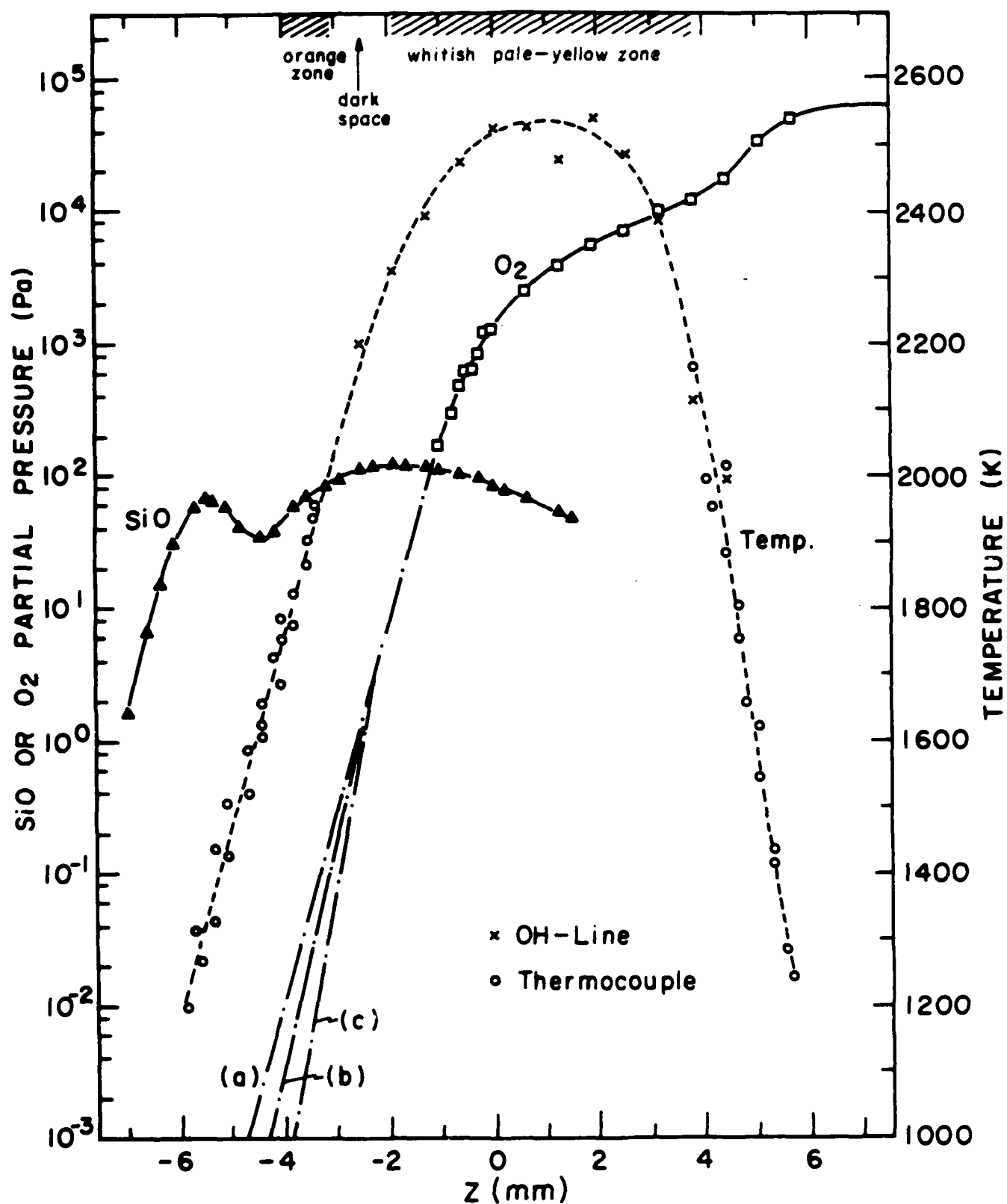


Fig. 6

612

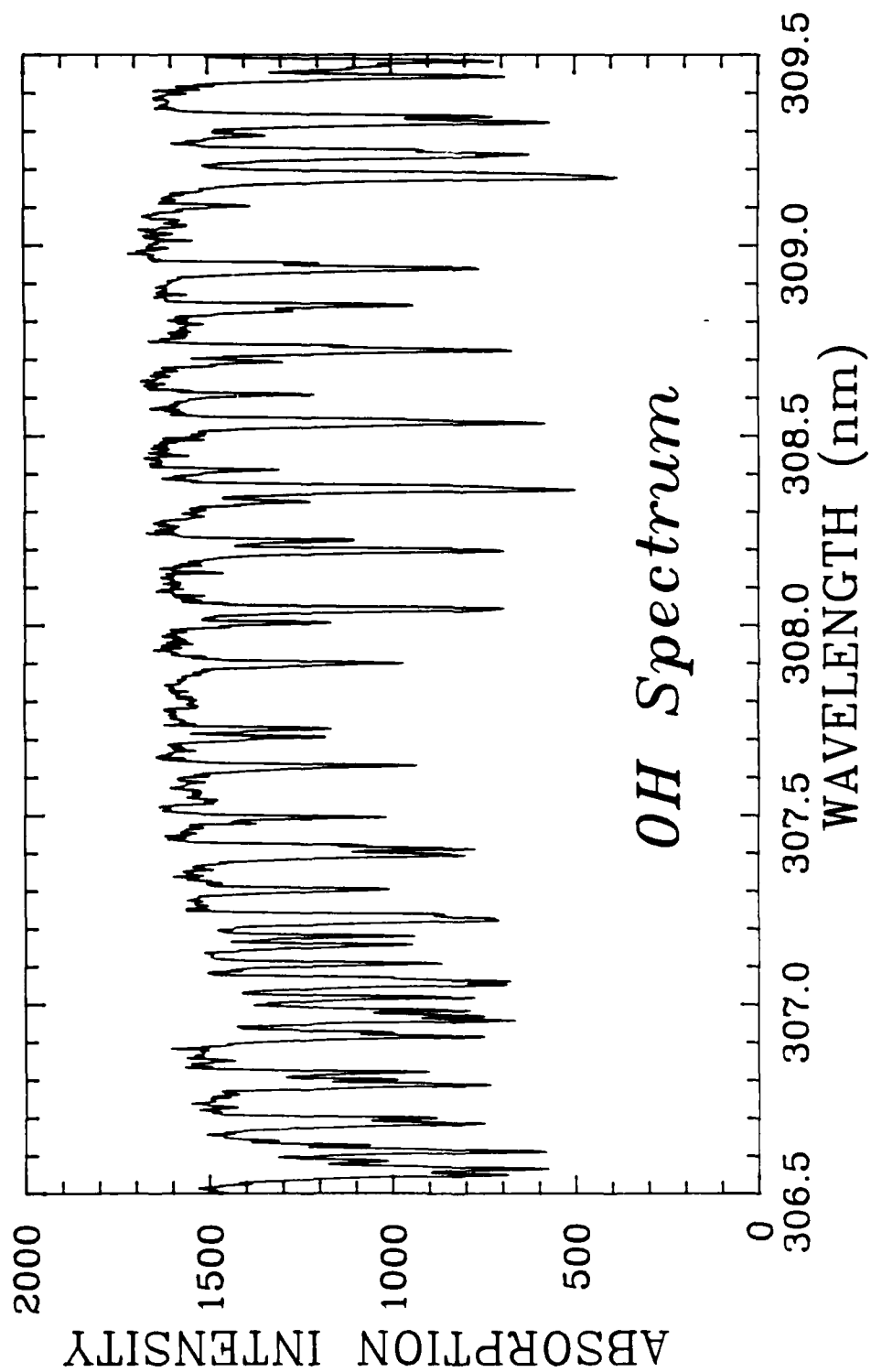


Fig. 7

Dynamic Light Scattering System

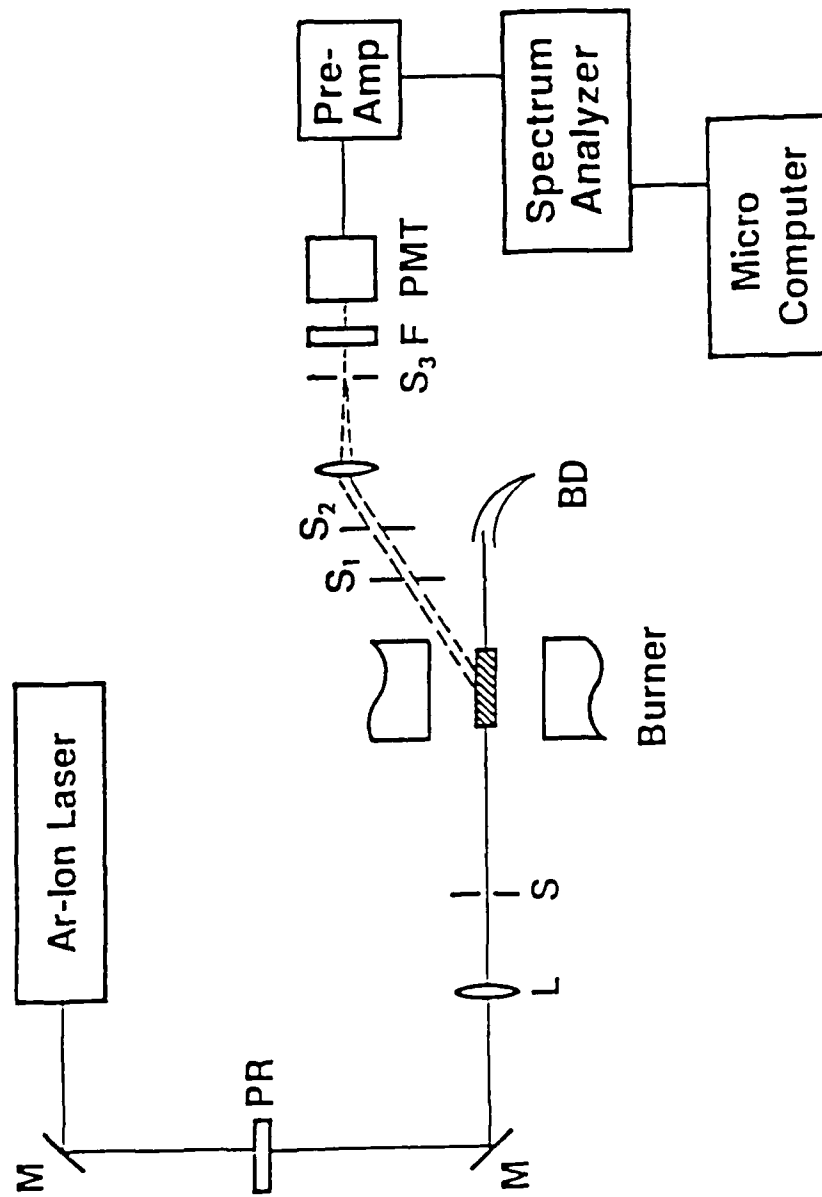


Fig. 8

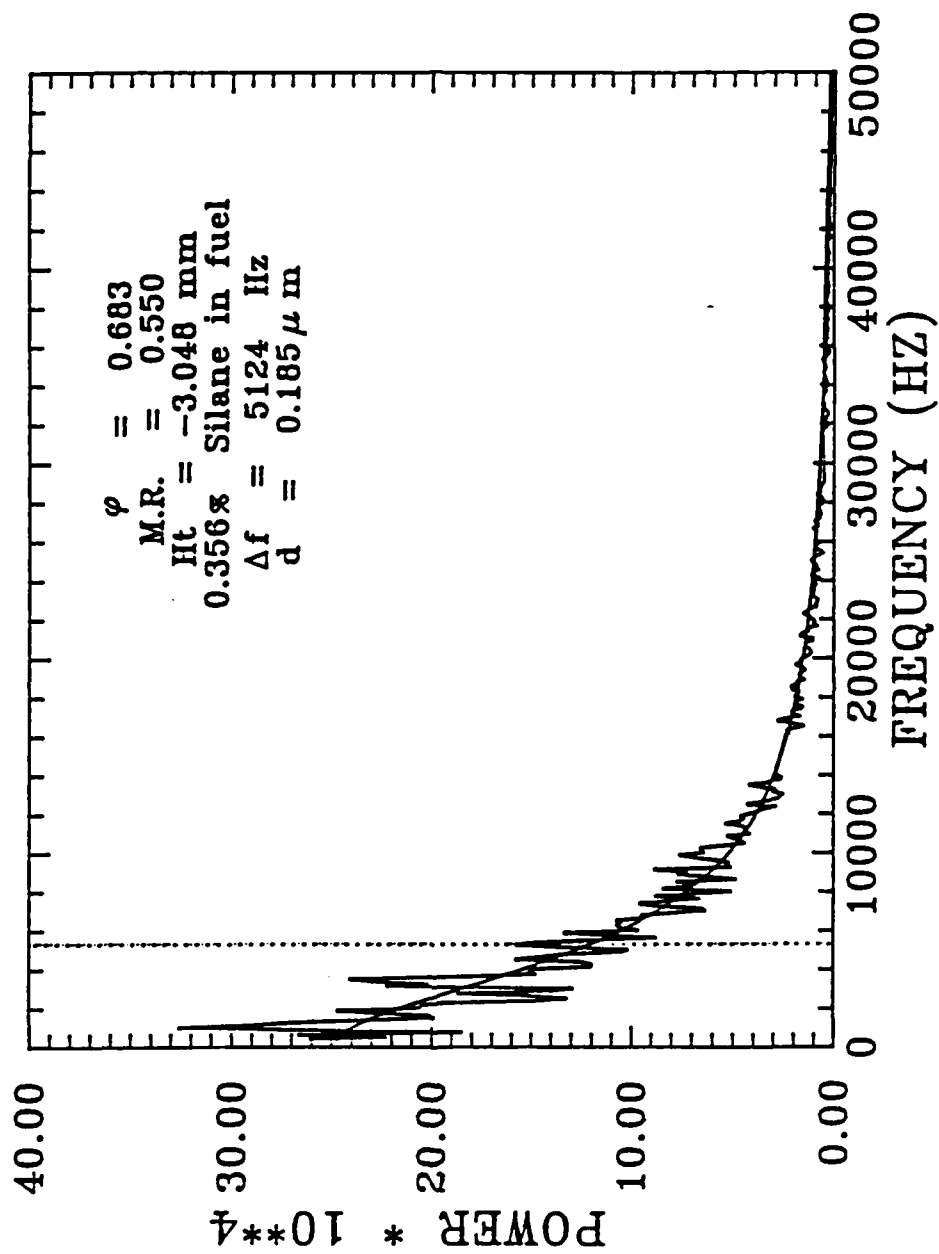


Fig. 9

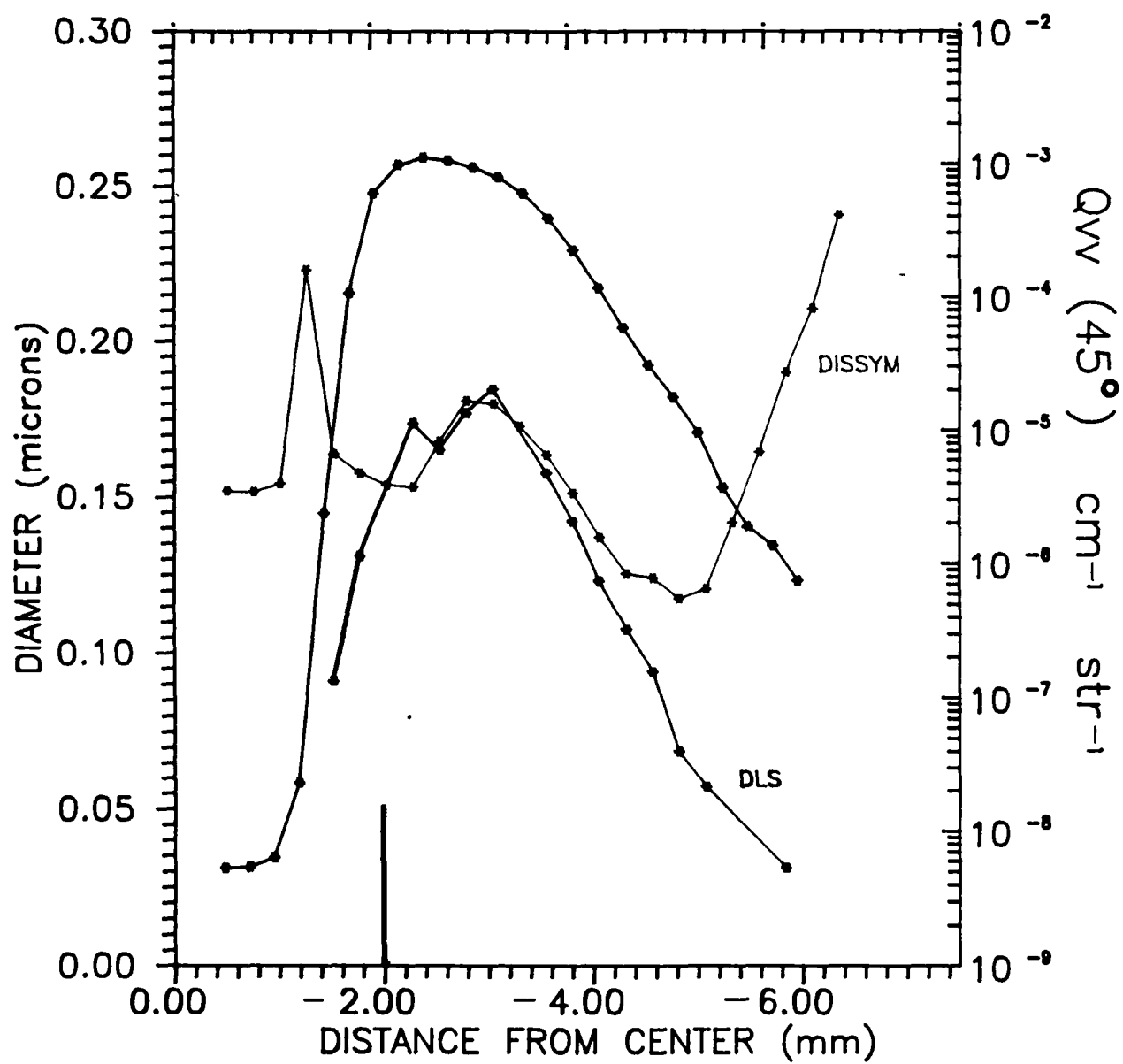
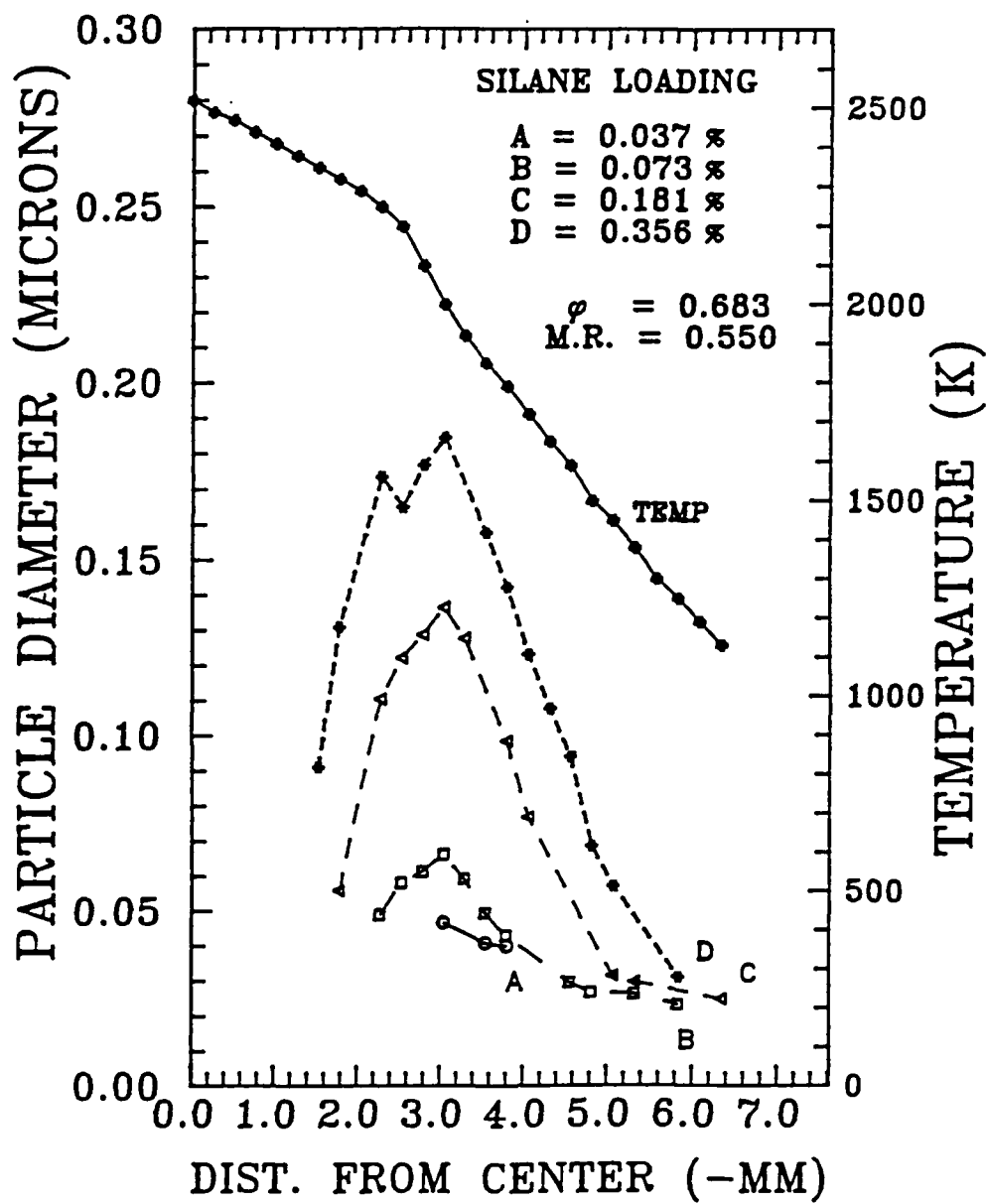
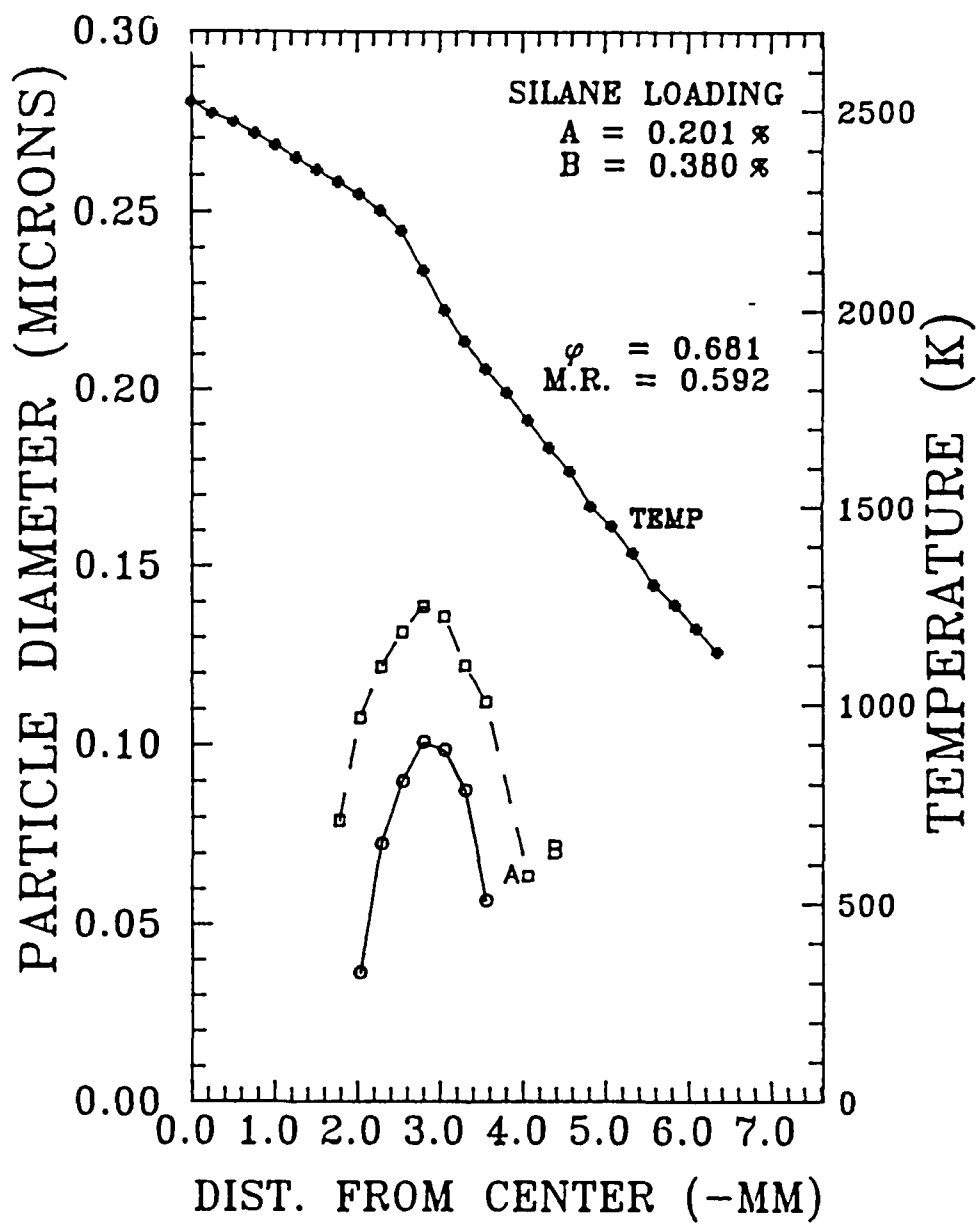


Fig. 10

6.16

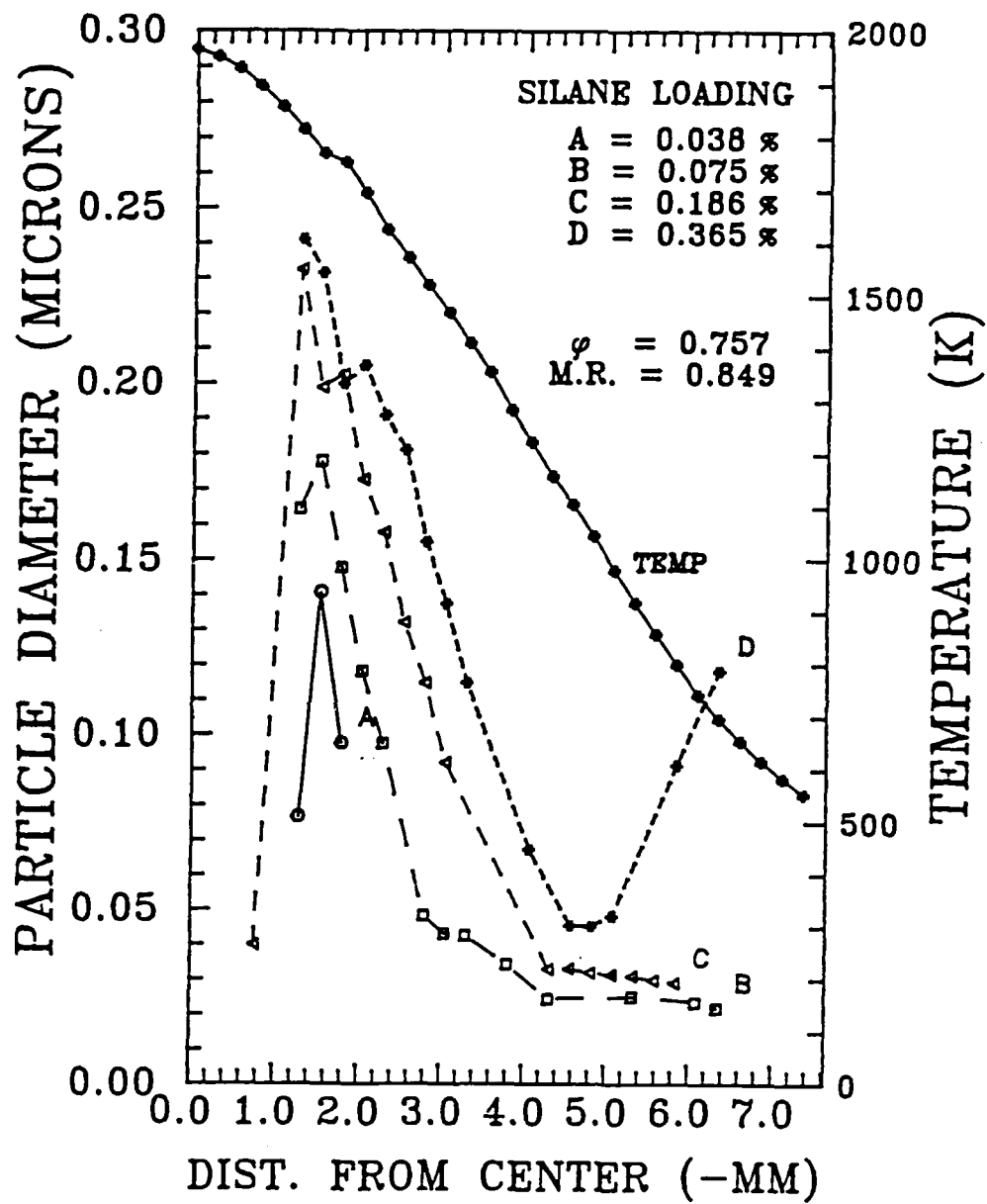
Fig 10





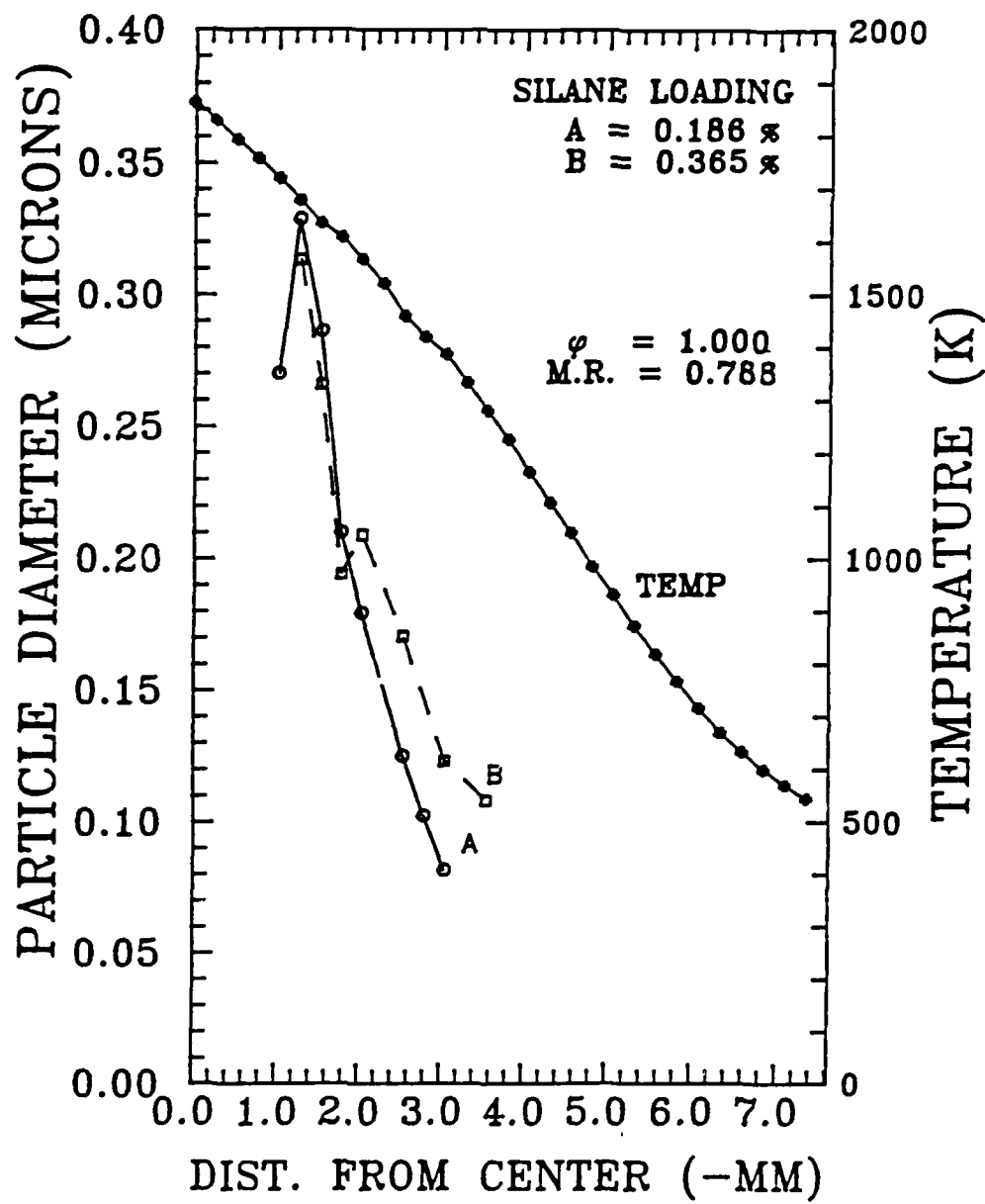
618

Fig. 12



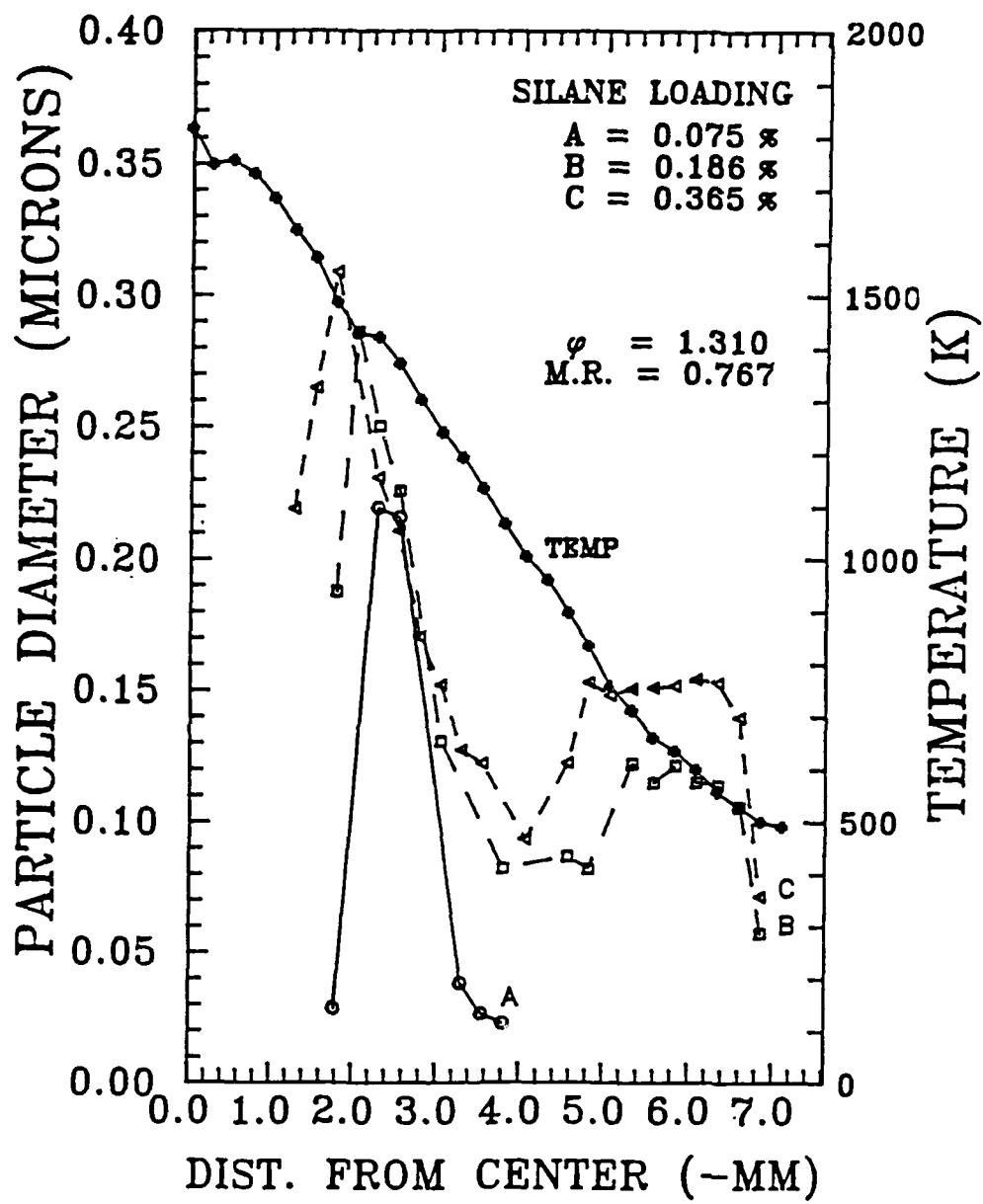
619

Fig. 13



620

Fig. 14



SYNTHESIS AND PROPERTIES OF LOW CARBON BORON CARBIDES

C. L. J. Adkins*, A. N. Campbell, and T. J. Headley
Sandia National Laboratories, Albuquerque, NM 87185

ABSTRACT

Boron carbides of low carbon content (<10%) were produced from BCl_3 and CCl_4 at 1273 - 1673 K in a CVD reactor. TEM revealed that phase separation had occurred and tetragonal boron carbide was formed along with β -boron or α -boron carbide under carbon depleted gas-phase conditions. At temperatures greater than 1390°C, graphite substrates served as a carbon source, affecting the phases present. Microstructure typical of CVD-produced α -boron carbide was observed. Plan view TEM of tetragonal boron carbide revealed a blocky structure.

INTRODUCTION

Rhombohedral boron carbides are refractory materials of unique structure and unusual thermal, electronic, and mechanical properties. Their use as high temperature semiconductor or thermoelectric materials has been suggested. Several different boron carbide phases are known. The unit cell of the thermodynamically stable " α -rhombohedral" form is composed of B_{12} or B_{11}C icosahedra at the corners of a rhombohedron with a central chain of three atoms, CBB or CBC (Fig. 1).¹ The distribution of the two types of icosahedra and chains is a function of carbon content. This phase has a large homogeneity range from approximately 8 to 20 at.% carbon. Under nonequilibrium, carbon depleted conditions, a metastable tetragonal phase may be formed. Tetragonal boron carbide ($\text{B}_{48}\text{B}_2\text{C}_2$) (see Fig. 2) is made up of four icosahedra within a tetragonal unit cell. Upon heating, the tetragonal phase decomposes into α -rhombohedral boron carbide and β -rhombohedral boron.² Little is known about the properties, electrical or thermal, of tetragonal boron carbide.

The interest in low carbon boron carbides follows from the prediction that the normally p-type conduction in rhombohedral boron carbide will become n-type at a carbon contents less than 8 at.%. This paper describes a study of low carbon boron carbides produced using a chemical vapor deposition (CVD) process. The various phases and microstructures obtained at given operating conditions are discussed.

EXPERIMENTS

Boron carbide specimens were prepared by atmospheric pressure CVD from an inlet gas mixture of BCl_3 , CCl_4 , and H_2 that was passed perpendicularly over a heated substrate of either POCO graphite or pyrolytic boron nitride (see Fig. 3). The substrate was set on an inductively heated graphite holder. Deposition temperatures were measured using an optical pyrometer and ranged from 1273 to 1673 K. It is estimated that no more than a 5 K temperature variation existed across the substrate during deposition. CCl_4 vapor was delivered to the reactor by bubbling argon through a reservoir of liquid CCl_4 . The reservoir was placed in a water bath to maintain a constant temperature. The amount of CCl_4 vapor was controlled by adjusting either the temperature of the water bath or the argon flowrate. CCl_4 and BCl_3 flowrates used ranged from 0.5 to 5 sccm and 16 to 46 sccm, respectively, and the hydrogen flowrate was maintained at 1000 sccm for all runs. These flowrates correspond to gas-phase B:C ratios of 9 to 90 and B:H ratios of 0.03 to 0.05. Sample thicknesses ranged from 50 to 500 μm .

Both X-ray and electron diffraction were used to determine the phases present in the deposit. Because boron and boron carbides are poor X-ray absorbers, film thicknesses on the order of 100 - 1000 μm are required if the substrate background signal is not to dominate the spectrum. Consequently, X-ray diffraction was only able to give qualitative phase analysis information. For those samples studied using TEM combined with selected area electron diffraction, it was also possible to estimate the percentage of each phase present. Auger electron spectroscopy (AES) was used to determine the average carbon content of the specimen. The most reproducible results were obtained by analysis of well-polished samples. While using this method to assign an absolute composition to a boron carbide sample results in a large error, comparisons between samples can be made with small error.

RESULTS

Equilibrium thermodynamic calculations can be used to study a reaction system as a function of composition, temperature, and pressure. While a CVD reactor typically does not operate at equilibrium, the general trends determined by the calculations can prove useful in interpreting the experimental results. Thermodynamic calculations were performed using a free-energy minimization technique (computer program SOLGASMIX³). The following species were included in the calculations: $\text{Cl}_2(\text{g})$, $\text{H}_2(\text{g})$, $\text{H}(\text{g})$, $\text{BCl}(\text{g})$, $\text{BCl}_2(\text{g})$, $\text{BCl}_2\text{H}(\text{g})$, $\text{BCl}_3(\text{g})$, $\text{BH}(\text{g})$, $\text{BH}_2(\text{g})$, $\text{BH}_3(\text{g})$, $\text{B}_2(\text{g})$, $\text{B}_2\text{Cl}_4(\text{g})$, $\text{B}_2\text{H}_6(\text{g})$, $\text{B}_3\text{H}_9(\text{g})$, $\text{B}_{10}\text{H}_{14}(\text{g})$, $\text{HCl}(\text{g})$, $\text{B}(\text{g})$, $\text{C}(\text{g})$, $\text{CCl}_4(\text{g})$, $\text{CH}_4(\text{g})$, $\text{C}_2\text{H}_2(\text{g})$, $\text{C}_2\text{H}_4(\text{g})$, $\text{B}_4\text{C}(\text{s})$, $\beta\text{-B}(\text{s})$, $\text{C}(\text{s})$.⁴ Thermochemical data are not available for the entire homogeneity range of rhombohedral boron carbide or the metastable tetragonal phase. Therefore, the data for B_4C (20 at.% carbon) was used to approximate the entire boron carbide composition range. This should be considered when evaluating the results. Calculations were performed at the conditions used in the experiments: 85 kPa (635 torr) total pressure, 1000 sccm H_2 carrier gas, BCl_3 and CCl_4 source gases, temperatures of 1173 to 1673 K, B:C ratios greater than 4, and B:H ratios of 0.02, 0.05 and 0.10. The results are presented in the deposition diagrams shown in Fig. 4. Note that the single-phase B_4C region is narrow and occurs only for B:C ratios greater than stoichiometric. This region broadens at lower temperatures and increased B:H ratios. Calculations were also performed using CH_4 since it is a commonly used carbon source gas. If the B:H ratio is held constant and 1000 sccm H_2 carrier gas is still assumed, the main difference between deposition using CH_4 and CCl_4 occurs in the H:Cl ratio of the inlet gas mixture. This results in a narrowed B_4C single-phase region. On the basis of a relative comparison, keeping in mind that the boron carbide phase modelled is carbon-rich, CCl_4 would appear to allow for more latitude in the deposition conditions required to produce single-phase material. In either case, taking the entire rhombohedral boron carbide homogeneity range into account would broaden the single-phase rhombohedral boron carbide region.

The experimental conditions used, and the phases and compositions of the boron carbides produced are given for selected runs in Table I. Several trends may be noted in the data. First, the tetragonal boron carbide phase was formed in all but four of the runs indicating that deposition takes place under nonequilibrium conditions. Rhombohedral boron carbide and β -rhombohedral boron

Table I. Selected Deposition Data and Results

Run	Temp (K)	Deposition Rate ($\mu\text{m/hr}$)	B:C (gas)	B:C (solid)	Phases*
155	1423		9.8	11.4	$\alpha + t$
1	1393	25	12	6	α
2	1293	16	12	8	
3	1323	20	24	7.4	$\alpha + t$
4	1473	38	24	8.2	$\alpha + t$
5	1423	70	90	30	$\beta + t$
25	1273	54	86	70	$\beta + t$
29	1663	160	88		$\beta + t$
37	1663	175	22		$\alpha + \beta$
71	1623	127	28		$\alpha + \beta$
72	1623	150	30		$\beta + t$

* α = α -rhombohedral boron carbide, β = β -rhombohedral boron, t = tetragonal boron carbide (B_{10}C_2)

Note: All depositions were made on a POCO graphite susceptor except for Run 72, which was made using pyrolytic BN.

would be expected to form at equilibrium. Second, in general the deposition rate is greater for those runs at high temperatures and/or high B:C ratios in which β -boron was deposited. This is consistent with the findings of Jansson⁵ and Vandenbulke and Vuillard⁶ that suggest a kinetic barrier to carbon deposition in the $\text{BCl}_3/\text{CH}_4/\text{H}_2$ reaction system. Whether this is a surface or gas-phase effect is unknown at this point. However, a sensitivity of the deposit composition to substrate shape has been noticed in this laboratory, and higher carbon uptake has been noted with the use of hot-wall versus cold-wall reactors by other workers.⁵ These observations point to the importance of homogeneous reactions in the gas-phase. Finally, it was observed that the graphite substrate appears to serve as a carbon source in high temperature deposition. Reaction of BCl_3 and CCl_4 at 1623 K over a graphite substrate produced α -rhombohedral boron carbide and β -rhombohedral boron. By contrast, deposition under the same conditions, but using a pyrolytic boron nitride substrate, led to the formation of a more carbon-depleted film, in which tetragonal boron carbide and β -boron were found. As further evidence, at temperatures in excess of 1623 K, passing BCl_3 over a heated graphite substrate causes rhombohedral boron carbide to form rather than the expected boron deposit.

The boron carbide deposits were examined microstructurally. Fig. 5a-d show the effect on the microstructure of decreasing carbon content. Fig. 5a (Run 1) shows the microstructure typically observed for single-phase α -rhombohedral boron carbide produced in this CVD reactor. This sample had an average carbon content of 14 at.% carbon. The large grains are oriented and twinned. Smaller, randomly oriented grains surround the larger grains. The microstructure of the deposit produced in Run 3, containing 12 at.% carbon, is shown in Fig. 5b. Both rhombohedral and tetragonal boron carbide phases were found in this specimen. The tetragonal material is essentially defect-free, blocky in appearance, and surrounded by the rhombohedral matrix (~ 95% by volume). In cross-section, the rhombohedral grains are feathery or dendritic in appearance. These grains are single crystals, the "feather-axis" being oriented in the direction of growth. It has been postulated that the fine needle structure within the grains is caused by strain contrast.⁵ This growth structure appears to be characteristic of CVD-produced rhombohedral boron carbides since it has also been observed in material deposited at low pressure (6.7 kPa, 50 torr) from BCl_3 and CH_4 on refractory metals.⁵

The effects of further carbon depletion are shown in Figs. 5c and 5d (Runs 155 and 5, respectively). The overall carbon content of the deposit in Fig. 5c is 8 at.% ($\text{B}_{11.4}\text{C}$). The tetragonal phase is again blocky in appearance and accounts for approximately 10-15 vol.%. The surrounding matrix is α -rhombohedral boron carbide. When the carbon content is further decreased (3 at.% carbon, B_{30}C), as in Fig. 5d, the matrix phase becomes β -rhombohedral boron with tetragonal boron carbide (~ 25 vol. %) as the remaining phase. The defects in the tetragonal phase appear to be stacking faults.

CONCLUSIONS

Low carbon boron carbide deposits have been made using a chemical vapor deposition process. The lowest carbon, single-phase, α -rhombohedral boron carbide material deposited was $\text{B}_{6.5}\text{C}$. At increasingly carbon-poor conditions the metastable tetragonal boron carbide phase was formed along with β -rhombohedral boron or α -rhombohedral boron carbide, indicating nonequilibrium deposition conditions in the reactor. Reaction of carbon from the graphite substrate at deposition temperatures greater than 1623 K affects the phases present in the deposit. Finally, the behavior of the

reaction system indicates that gas-phase reactions may play a role in the deposition of boron carbide and should be studied.

ACKNOWLEDGEMENTS

The authors gratefully acknowledge the contributions of J. F. Smatana in the preparation of the boron carbide specimens, R. G. Tissot in the X-ray diffraction analysis, and P. W. Mott and W. O. Wallace in the AES analysis. This work performed at Sandia National Laboratories was supported by U. S. Department of Energy Contract No. DE-AC04-76DP00789.

REFERENCES

1. B. Morosin, A. W. Mullendore, D. Emin, G. A. Slack, "Rhombohedral Crystal Structure of Compounds Containing Boron-Rich Icosahedra"; pp. 70-86 in Boron-Rich Solids. Edited by D. Emin, T. Aselage, C. L. Beckel, I. A. Howard, C. Wood. Amr. Inst. Physics, New York, 1986.
2. S. Lartigue, G. Male, "Contribution to the Study of Tetragonal Compounds in the Boron Carbon System," J. Mat. Sci. Letters, 7, 153-156 (1986).
3. G. Eriksson, "Thermodynamic Studies of High Temperature Equilibria. III. SOLGAS, a Computer Program for Calculating the Composition and Heat Condition of an Equilibrium Mixture," ACTA Chemica Scandinavica, 25, 2651-2658 (1971).
4. M. W. Chase, Jr., C. A. Davies, J. R. Downey, Jr., D. J. Frurip, R. A. McDonald, A. N. Syverud, JANAF Thermochemical Tables 3rd Edition. Amr. Chem. Soc., New York, 1985.
5. U. Jansson, Chemical Vapour Deposition of Boron and Boron Carbides - Aspects of Kinetics, Mechanism and Selective Deposition; PhD. Thesis, Uppsala University, Uppsala, Sweden, 1988.
6. L. Vandenbulcke, G. Vuillard. "Kinetics in the Chemical Vapor Deposition of Boron Carbide"; pp. 95-103 in Proc. 8th Intl. Conf. CVD. Edited by J. M. Blocher, Jr., G. E. Vuillard, G. Wahl, Electrochem. Soc., Inc., Princeton NJ, 1981.

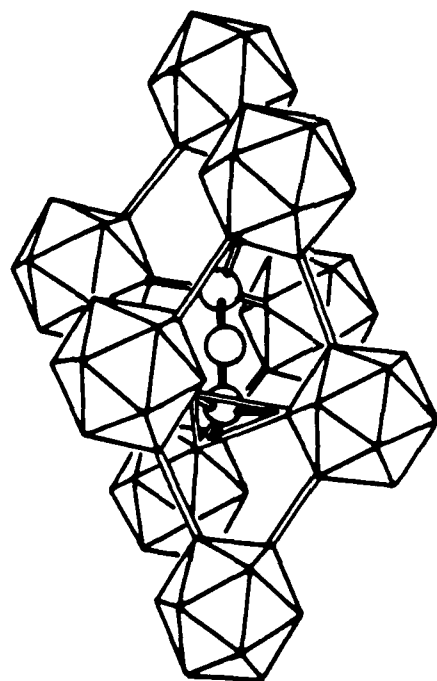


Figure 1. Structure of α -rhombohedral boron carbide.

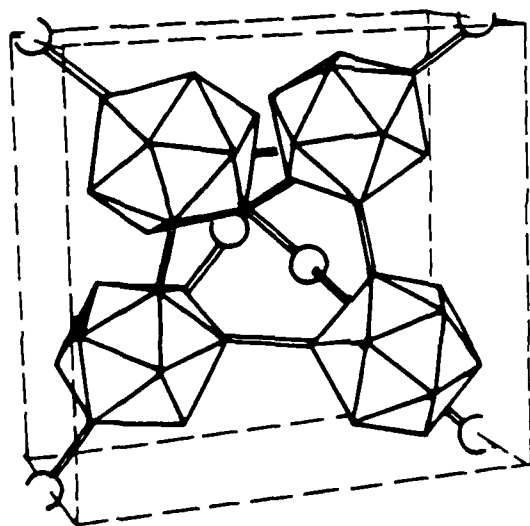


Figure 2. Structure of tetragonal boron carbide.

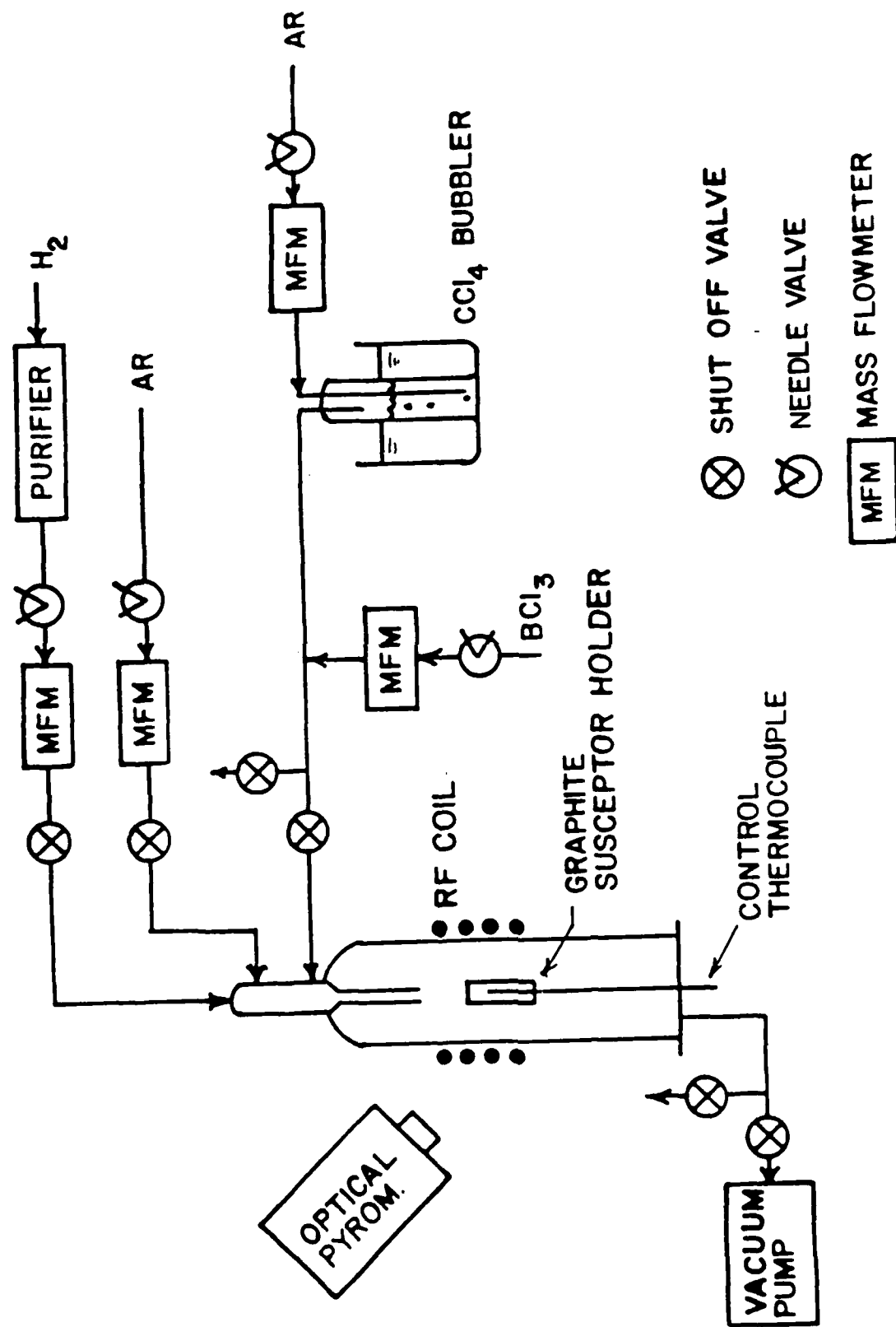


Figure 3. Boron carbide CVD apparatus.

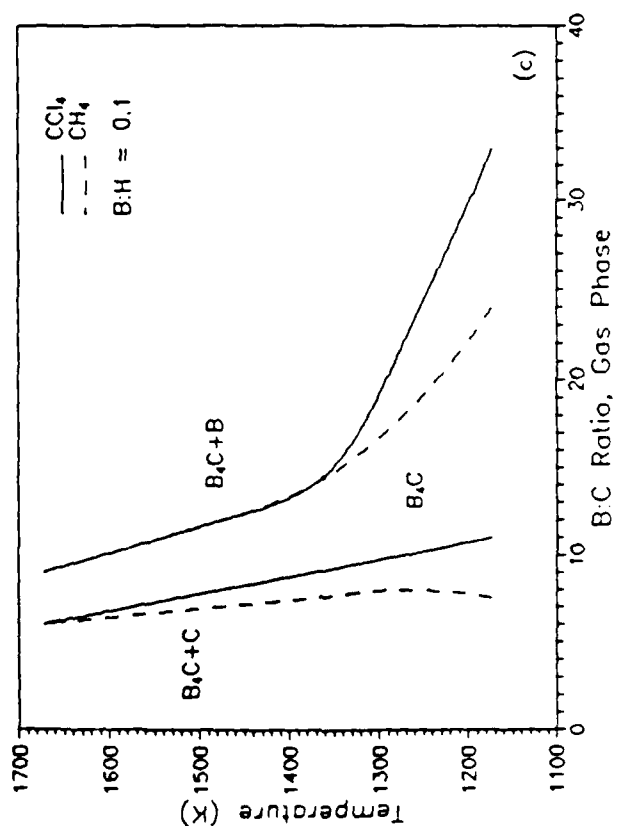
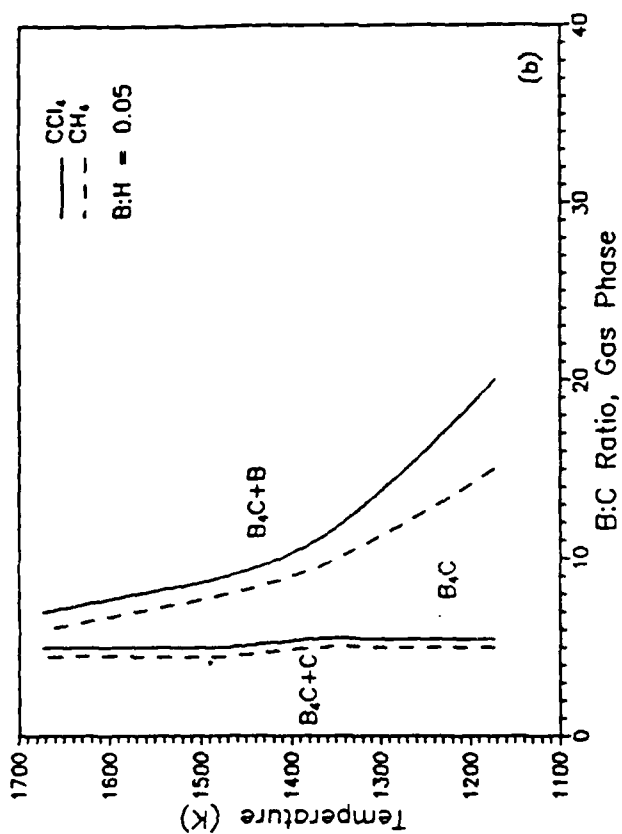
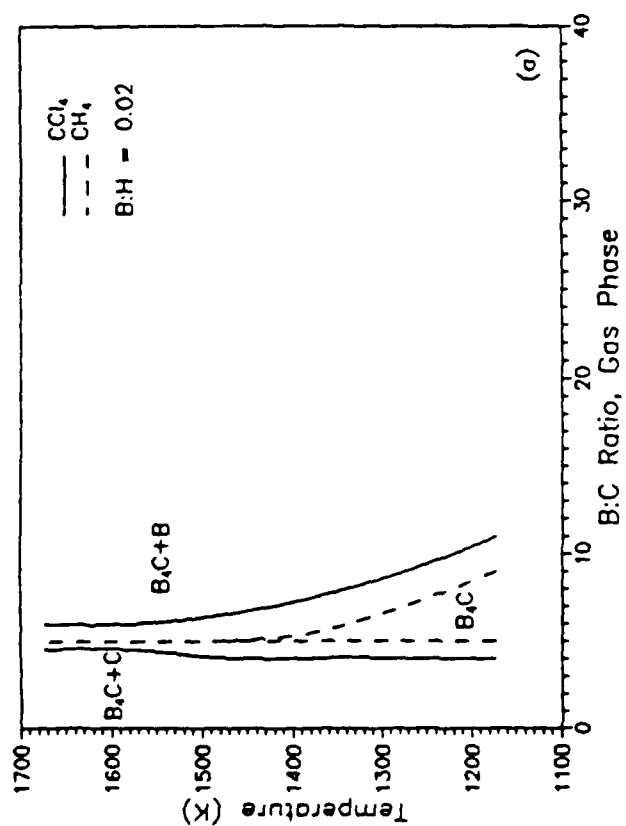


Figure 4. Thermodynamically predicted deposition diagrams for CVD of boron carbide. Total pressure of 85 kPa (635 torr) and B:H ratios of (a) 0.02, (b) 0.05, and (c) 0.10.

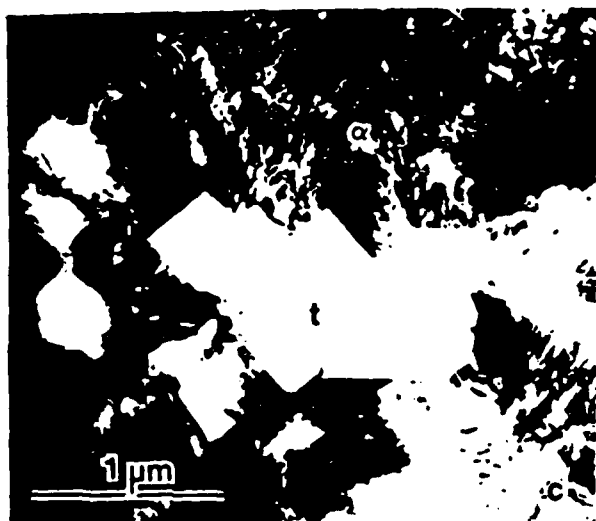
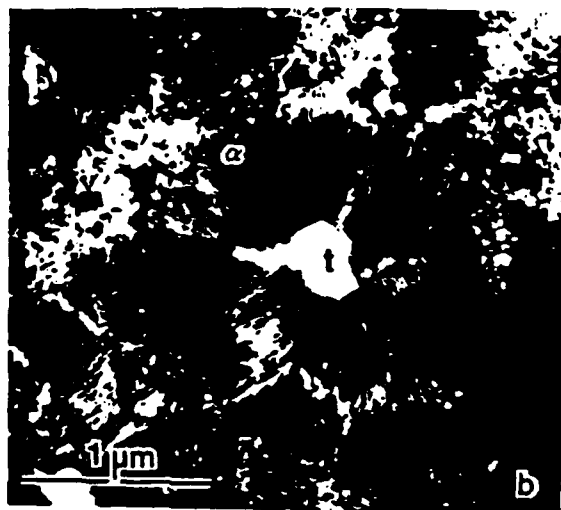
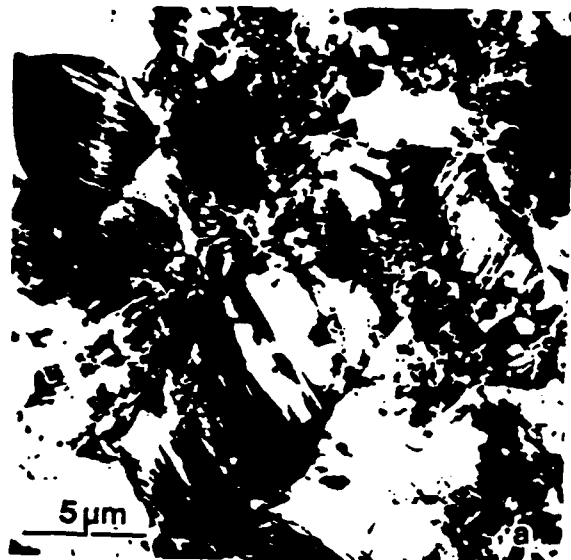


Figure 5. Plan views of the deposit microstructure for (a) Run 1, (b) Run 3, (c) Run 155, and (d) Run 5.

FIGURE CAPTIONS

- Figure 1. Structure of α -rhombohedral boron carbide.
- Figure 2. Structure of tetragonal boron carbide.
- Figure 3. Boron carbide CVD apparatus.
- Figure 4. Thermodynamically predicted deposition diagrams for CVD of boron carbide. Total pressure of 85 kPa (635 torr) and B:H ratios of (a) 0.02, (b) 0.05, and (c) 0.10.
- Figure 5. Plan views of the deposit microstructure for (a) Run 1, (b) Run 3, (c) Run 155, and (d) Run 5.

SYNTHESIS OF Si, SiC AND Si₃N₄ POWDERS UNDER HIGH NUMBER DENSITY CONDITIONS

John S. Haggerty and John H. Flint
Massachusetts Institute of Technology
Cambridge, MA 02139

INTRODUCTION

Because a ceramic part can be no better than its constituent powders, we developed a new powder synthesis process. The requisite powder characteristics are small and uniform size, spherical shape, purity and freedom from agglomerates. Although some feel that uniform particle sizes are not desirable, all agree that optimum powders will require precisely controlled particle size distributions. For commercial applications, cost issues are as important as the technical attributes of the powders.

For Si, SiC, and Si₃N₄ powders made from laser-heated SiH₄ based chemistries (7.2 kg/h per nozzle and a SiH₄ cost of \$10/kg assumed), we found¹ that approximately \$2.50/kg of the total manufacturing costs (nominally \$12.50/kg) resulted from a set of costs that were inversely proportional to the production rate. Although each reactor configuration and chemistry will have different detailed cost structures, production rates in controlled-atmosphere, hermetic reactors cannot drop much below the levels that we assumed before the rate-proportional costs preclude the powders from the marketplace. Based on these assumptions, the manufacturing cost would rise to ~ \$35/kg at a production rate of 0.72 kg/h. In our view, this conclusion dictates the type of powder formation and growth mechanisms that should be considered for a commercial powder synthesis process.

Figure 1 summarizes an important consequence of making small diameter powders; decreasing particle number density and increasing growth time both proportionally reduce a reactor's specific production rate (kg/h/liter of reactor volume). Typical operating conditions for the laser process we developed are indicated by the "collision-coalescence" area, and the conditions reported for CVD growth of uniform size Si powders² are shown

by the "CVD" area. Growth by CVD requires low number densities to avoid interparticle collisions during the long exposures to slow growth rate conditions that are needed to suppress nucleation of new particles. One must conclude that the factor of 10^8 difference between the specific production rates of the two types of processes favors synthesis by collision-coalescence mechanisms.

Based on these conclusions, we developed a powder synthesis process that employs collision-coalescence mechanisms. Although laser heating has been used to date, other heat sources can be employed now that the necessary synthesis conditions have been defined.

POWDER SYNTHESIS

The ceramic powders are synthesized by rapidly heating a reactant gas stream with a CW CO₂ laser beam in a cold wall reactor.^{3,4} The reactant gas stream flows from the nozzle into the laser beam, where it is heated at $\approx 10^6$ K/second until the gas reacts and the particles form and grow. A concentric flow of argon injected around the reactant stream stabilizes the reaction zone and helps the powder flow smoothly through the chimney into a filter where the particles are trapped. Because of rapid heating, there is little mixing between the reactant gas and the argon so the reactant concentration is uniform throughout most of the reaction zone.

Silane (SiH₄) is used to make Si powders, and SiH₄ mixed with methane (CH₄) or ethylene (C₂H₄) is used to make SiC.⁵ Ammonia (NH₃) mixed with SiH₄ is used to make Si₃N₄.⁶ We have also used a variety of chlorides^{7,8,9} to make TiB₂, B, TiO₂, and SnO₂, as well as Si and SiC. The effects of process variables have been studied experimentally using a light scattering-transmission technique¹⁰ and also analytically.^{11,12}

High quality Si powders are formed by the collision and coalescence of liquid silicon droplets.^{12,13} The process begins when SiH₄ gas heated by the laser decomposes into Si dimers and trimers. As shown in Figure 2, the number density of these "initial" particles decreases rapidly from 10^{12} - 10^{13} cm⁻³ to the 10^{10} cm⁻³ range as particles grow to $\sim 0.1\mu\text{m}$ through interparticle collisions. Collision rates that start as high as $10^7/\text{sec}$, also

decreasing as the particles grow. We have found that solid particles grow to 10-20 nm in less than 1ms before non-dispersible aggregates begin to form, once sintering rates can no longer spheroidize dense particles in the time interval between collisions. If temperatures exceed the silicon melting point (1410°C), the agglomerates rapidly coalesce into spherical particles by a viscous flow process, and particle growth can continue. The coalescence process stops with solidification, either by freezing or by forming solid compound particles. Cooling rates must be rapid relative to interparticle collision rates.

Along a specific flow stream, Si particle growth continues until the temperature decreases below 1410°C. A variation in exposure times to $T > 1410^\circ\text{C}$ produces a distribution of particle sizes in the powder. Flow streams that never reach 1410°C produce agglomerates of small particles. If the cooling rate from 1410°C is not fast enough to reduce the particle temperature several hundred degrees in the period between interparticle collisions, aggregates of large particles can be produced. Therefore, the particle size and morphology distributions are directly attributable to the temperature and velocity distributions in the reaction zone. Uniform powder is produced only when all flow streams experience similar, and correct, time-temperature-concentration histories.

Using the aerosol growth law developed by Lee,¹³ we have calculated the particle size and size distribution expected from the collision and coalescence of molten particles in the laser heated silane temperature and velocity fields. Figure 3 compares calculated and observed Si particle size distributions. The agreement between the average sizes and the shape of the distributions is excellent. The achieved geometric standard deviation (1.48) is only slightly larger than the minimum value achievable by a collision-coalescence process (1.35).¹³

High quality silicon carbide is formed from premixed streams of SiH_4 and CH_4 via a two-step reaction mechanism.^{5,12} The reactant gas mixture is heated by conduction as it approaches the CO_2 laser beam. At approximately 1050°C, the SiH_4 is fully decomposed and solid Si particles start to grow in a H_2/CH_4 atmosphere. The temperature of the particle- CH_4 - H_2 mixture continues to increase as the laser beam is approached. If the

maximum temperature does not exceed $\sim 1200^{\circ}\text{C}$, the resulting powder is mostly ($>82\%$) unreacted, small diameter ($\sim 50\text{ nm}$), agglomerated Si.

Any combination of process conditions that increases the temperature further results in a sudden change in reaction zone temperature, structure and turbidity. Under these conditions, the maximum temperature jumps to at least 1600°C , and two bands appear in the reaction zone. Silicon particles form and grow in the lower band. The temperature at the boundary between the lower and upper bands is just over 1410°C , allowing the silicon particles to coalesce just before carburization becomes rapid. The temperature increases rapidly to the maximum value in the upper band; the sudden rise is caused by the combined effects of the exothermic carburization reaction and by increased CO_2 laser absorption by the SiC particles.

The onset of the carburization reaction terminates the particle growth process since SiC is a solid at these temperatures. The short time available between the beginning of Si particle formation and the onset of carburization is responsible for the SiC particle size being $\sim 100\text{ nm}$ instead of $\sim 300\text{ nm}$ as in the case of silicon. Only very small ($\sim 40\text{ nm}$) agglomerated particles are produced when SiH_4 and C_2H_4 are used. This results because C_2H_4 starts to carburize the Si particles at temperatures below 1410°C , preventing their coalescence into spherical particles.

The laser synthesis of useful SiC powders depends on the correct combination of several temperature-dependent reaction rates. Carburization of liquid Si must be rapid since only a few milliseconds are available, but it must be delayed until the Si particles have had a chance to grow. Fortunately, the premixed $\text{SiH}_4\text{-CH}_4$ system satisfies these requirements and high-quality powder can be produced.

The synthesis of high-quality Si_3N_4 powder is more difficult than for Si or SiC powders.⁶ Premixed streams of SiH_4 and NH_3 can produce stoichiometric Si_3N_4 but the particles are very small ($20\text{-}30\text{ nm}$) and are usually highly agglomerated. As is the case with $\text{SiH}_4\text{-C}_2\text{H}_4$ mixtures, NH_3 begins to react with solid Si particles at temperatures only slightly higher than the silane decomposition temperature, preventing the formation of large particles by coalescence.

Larger Si_3N_4 powders have been synthesized successfully⁶ by injecting ammonia into SiH_4 reaction zones. The physical separation of the NH_3 source from the SiH_4 decomposition region permits the required Si particle growth by collision-coalescence prior to nitridation. The Si_3N_4 particle size distribution is broader than the other optimized powders since the NH_3 is injected from outside of the reaction zone. Powder on the outer edge of the zone is nitrided while still small. The silicon particles in the center continue to grow, reaching a larger size as the NH_3 diffuses inward. Growth stops when nitridation begins.

Test parts of reaction bonded silicon nitride (RBSN) and sintered SiC (SSC) were made to demonstrate that superior consolidation kinetics and properties result from using laser synthesized powders.¹⁴ In both cases, the resulting parts exhibited superior characteristics. The average strengths of 75% RBSN samples have been as high as 590 MPa and maximum strengths as high as 870 MPa; these strength levels have never been observed with this level of porosity. Improved nitriding kinetics¹⁶ have reduced nitriding schedules from typical values of 100h at 1500°C to levels like 1h at 1150°C or 10m at 1250°C. Oxidation resistance of the RBSN at 1000 and 1400°C is 10-20 times better than high quality hot pressed Si_3N_4 and strengths do not decrease with the exposures.¹⁷ The SSC samples densified to essentially full density in 1h at 2050°C and exhibited an average strength of 645 MPa.¹⁴ These results support our original premise; the use of superior powders will make possible superior properties and processing characteristics.

CONCLUSIONS

Powder synthesis conditions needed to produce 0.1-0.3 μm , non-agglomerated Si, SiC and Si_3N_4 particles have been defined for powders produced under the high number density conditions needed for acceptable mass flow rates. During at least one stage, growth must proceed by collisions between molten particles. With Si, this is accomplished simply by raising the reaction temperature above the melting temperature for an appropriate time interval. For the Si-compounds, the reactions must be made to occur in two steps; Si

particles form and grow in the first, and compounds form in the second. The separation of the two steps can be made to occur in both premixed and injected reactant streams.

Superior consolidation kinetics and properties can result if powders having the specific characteristics we achieved are employed in combination with careful post-synthesis handling procedures. Powders must be small, equiaxed, fairly uniform in size, pure and free of agglomerates. Of these criteria, freedom from agglomerates is the most important because agglomerates lower the achievable green density to unacceptably low levels and introduce large, localized defects.

REFERENCES

1. J.H. Flint and J.S. Haggerty, *Ceramic Powders from Laser Driven Reactions, Applications of Lasers to Industrial Chem.*, SPIE, Vol. 458, 1984.
2. R.C. Flagan, *Aerosol Routes for Powder Synthesis*, Proceedings of the First International Conference on Ceramic Powder Processing Science, Orlando, FL, November 1987, Ceramic Transactions, 1, 229-243 (1988).
3. W.R. Cannon, S.C. Danforth, J.H. Flint, J.S. Haggerty, R.A. Marra, *Sinterable Ceramic Powders from Laser Driven Reactions, Part I; Process Description and Modeling*, J. Am. Ceram. Soc., 65 [7], 324-30 (1982).
4. W.R. Cannon, S.C. Danforth, J.S. Haggerty, R.A. Marra, *Sinterable Ceramic Powders from Laser Driven Reactions, Part II; Powder Characteristics and Process Variables*, J. Am. Ceram. Soc., 65 [7], 330-5 (1982).
5. K. Sawano, J.S. Haggerty, and H.K. Bowen, *Formation of SiC Powder from Laser Heated Vapor Phase Reactions*, YOGYO-KYOKAI-SHI (J. of Ceram. Soc. Japan), 95 [1], 64-9 (1987).
6. M. Aoki, J.H. Flint, and J.S. Haggerty, *Laser Synthesis of Silicon Nitride Powders for Ceramic Processing*, Proceedings of the First International Conference on Ceramic Powder Processing Science, Orlando, FL, November 1987, Ceramic Transactions, 1, 253-260 (1988).
7. J.D. Casey, and J.S. Haggerty, *Laser-Induced Vapor-Phase Syntheses of Boron and Titanium Diboride Powders*, J. Mat. Sci., 22, 737-744 (1986).
8. J.D. Casey and J.S. Haggerty, *Laser-Induced Vapor-Phase Synthesis of Titanium Dioxide Powder*, J. Mat. Sci., 22, 4307-12 (1987).

9. A. Lightfoot, MIT, unpublished results.
10. J.H. Flint, R.A. Marra, and J.S. Haggerty, *Powder Temperature, Size, and Number Density in Laser Driven Reactions*, *Aerosol Sci. and Tech.*, **5**, 249-261 (1986).
11. I.S. Akmandor, Theoretical and Computational Models of Reacting Silane Gas Flows: Laser Driven Pyrolysis of Subsonic and Supersonic Jets, Ph.D. Thesis, MIT, 1985.
12. J.H. Flint, and J.S. Haggerty, *Models for Synthesis of Ceramic Powders by Vapor Phase Reactions*, Proceedings of the First International Conference on Ceramic Powder Processing Science, Orlando, FL, November 1987, *Ceramic Transactions*, **1**, 244-252 (1988).
13. K.W. Lee, H. Chen, and J.A. Gieseke, *Log-Normally Preserving Size Distribution for Brownian Coagulation in the Free-Molecule Regime*, *Aerosol Sci. and Tech.*, **3**, 53-62 (1984).
14. J.S. Haggerty, G.J. Garvey, J.H. Flint, B.W. Sheldon, M. Aoki, M. Okuyama, J.E. Ritter, and S.V. Nair, *Processing and Properties of Reaction Bonded Silicon Nitride and Silicon Carbide made from Laser Synthesized Powders*, Proceedings of the First International Conference on Ceramic Powder Processing Science, Orlando, FL, November 1987, *Ceramic Transactions*, **1**, 1059-1068 (1988).
15. A. Lightfoot, F.M. Yee, C. Ker, B. Sheldon and J.S. Haggerty, *Processing of Reaction Bonded Si_3N_4 - SiC Composites*, presented as paper No. 54-SI-89 at the 91st Annual Meeting and Exposition of the American Ceramic Society, Indianapolis, IN, April 1989.
16. B.W. Sheldon, and J.S. Haggerty, *The Nitridation of High Purity, Laser-Synthesized Silicon Powder to Form Reaction Bonded Silicon Nitride*, to be published in the Proceedings of the 12th Annual Conference on Composites and Advanced Ceramics, Cocoa Beach, FL, 1988.
17. J.S. Haggerty, A. Lightfoot, J.E. Ritter, S.V. Nair, and P. Gennari, *Properties of Reaction Bonded Silicon Nitride made from High Purity Silicon Powder*, to be published in the Proceedings of the 12th Annual Conference on Composites and Advanced Ceramics, American Ceramic Society, Cocoa Beach, FL, January 1988.

FIGURES

1. Hourly mass flow rates per unit volume as a function of residence (growth) time for $0.2\mu\text{m}$ diameter spherical powders. The collision-coalescence domain is typified by number densities on the order of 10^{10} cm^{-3} and growth times between 1-10ms. The CVD domain requires much lower number densities ($\sim 10^5 \text{ cm}^{-3}$) to avoid

interparticle collisions during the long growth times (~ 5 s) required under low supersaturation conditions.

2. A description of particle growth by a collision-coalescence mechanism. As particles collide, stick to one another and coalesce into spherical particles having twice the volume of the colliding particles, the number density decreases and both the diameter and the time between collisions increase. For the case shown ($P_{\text{SiH}_4} = 1.3 \text{ atm}$), Si particles grow to $0.15 \mu\text{m}$ diameter in ~ 10 ms at which time the interparticle collision time is approximately 2ms. To avoid formation of agglomerates, particles must be cooled $\sim 500^\circ\text{C}$ in a time period corresponding to the interparticle collision rate (cooling rate $\sim 2.5 \times 10^5 \text{ }^\circ\text{C/s}$).
3. Calculated and observed particle size distributions for Si powers synthesized from laser heated SiH_4 gas. The calculated distributions, resulting from a collision-coalescence mechanism, were based on measured residence times in 5 concentric rings having approximately equal mass flows. One of the calculated distributions assumes no mixing with the annular Ar stream; the other assumes 70% dilution of the Si mass density in only the exterior ring.

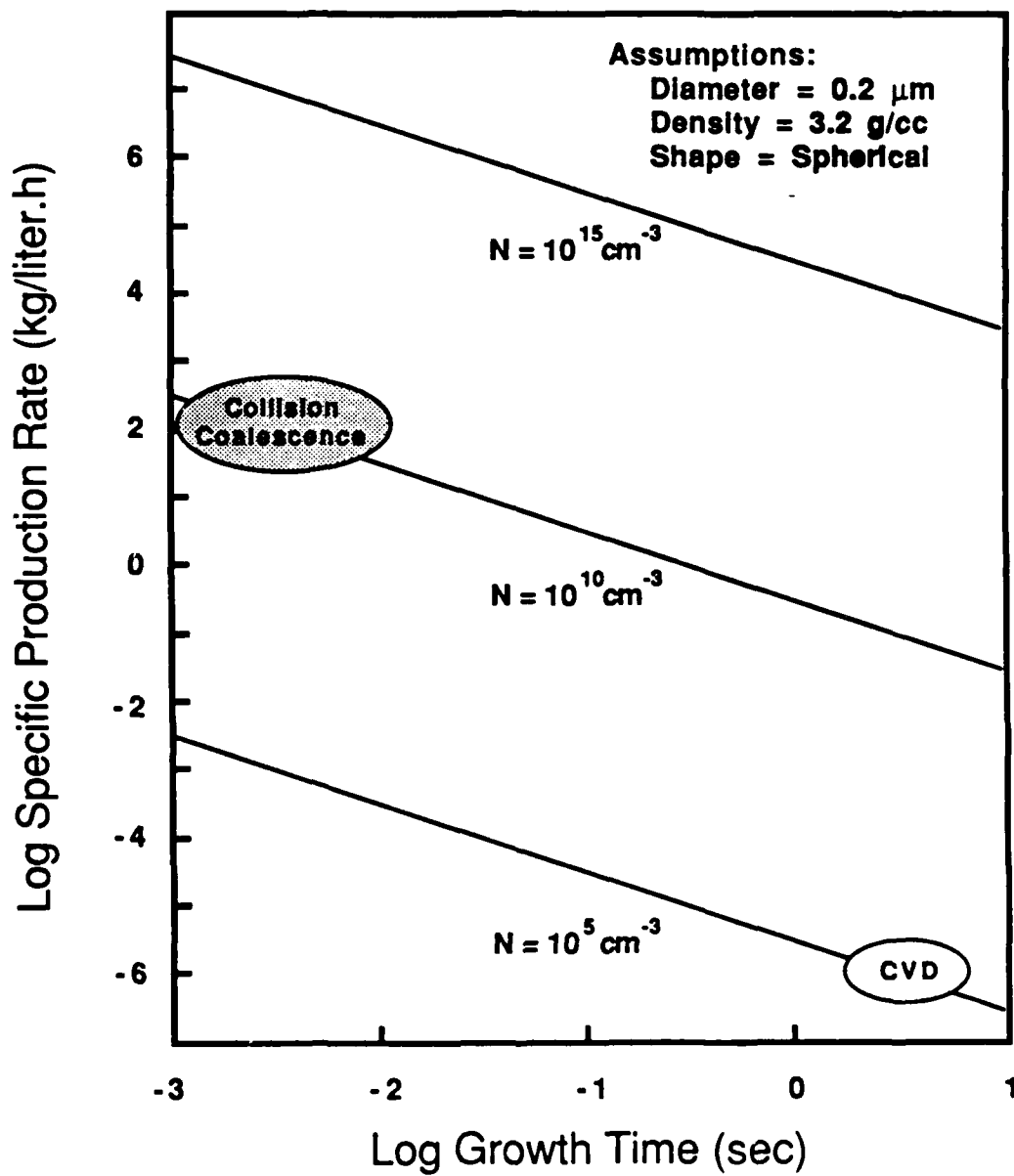


Fig. 1

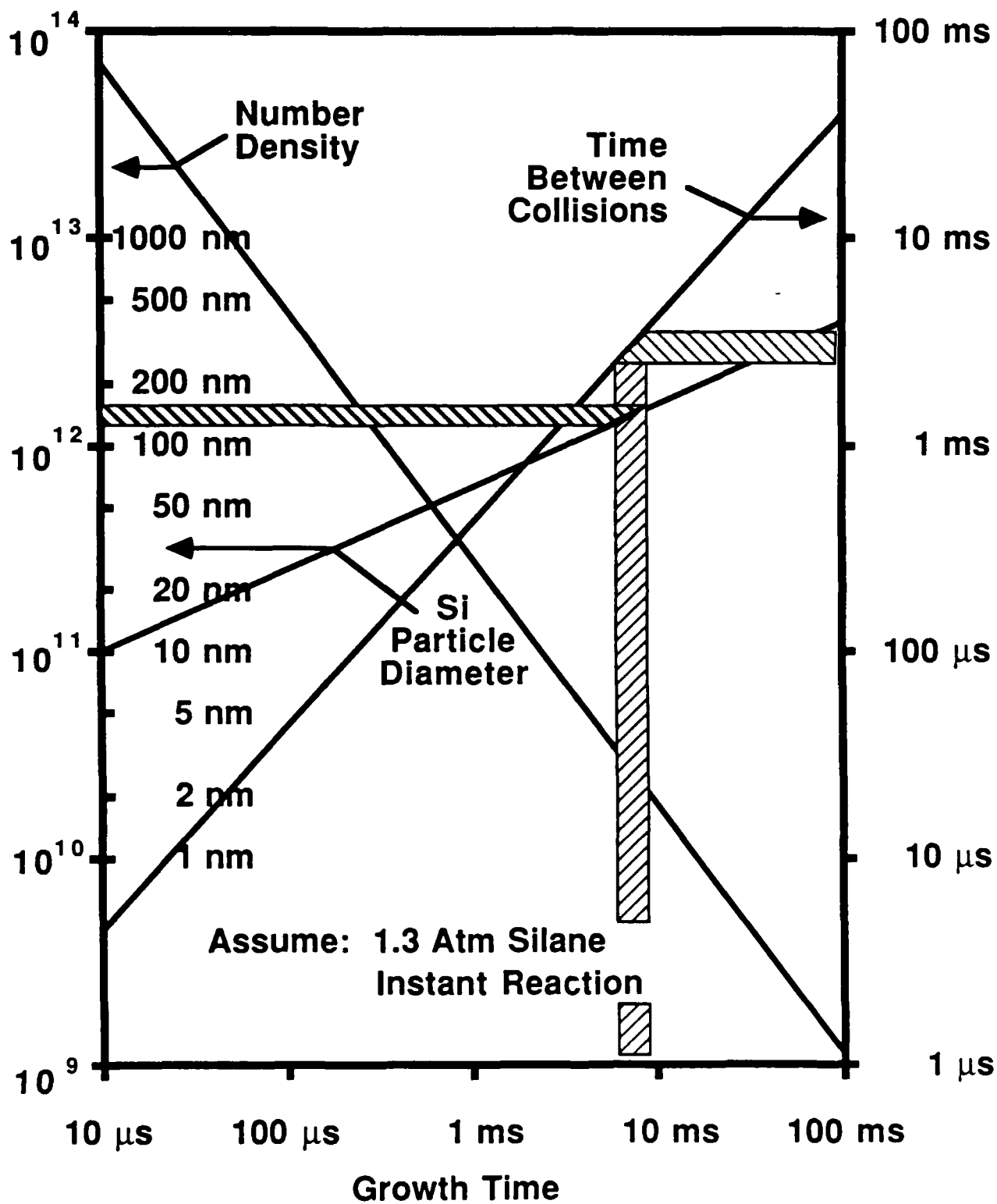


Fig. 2

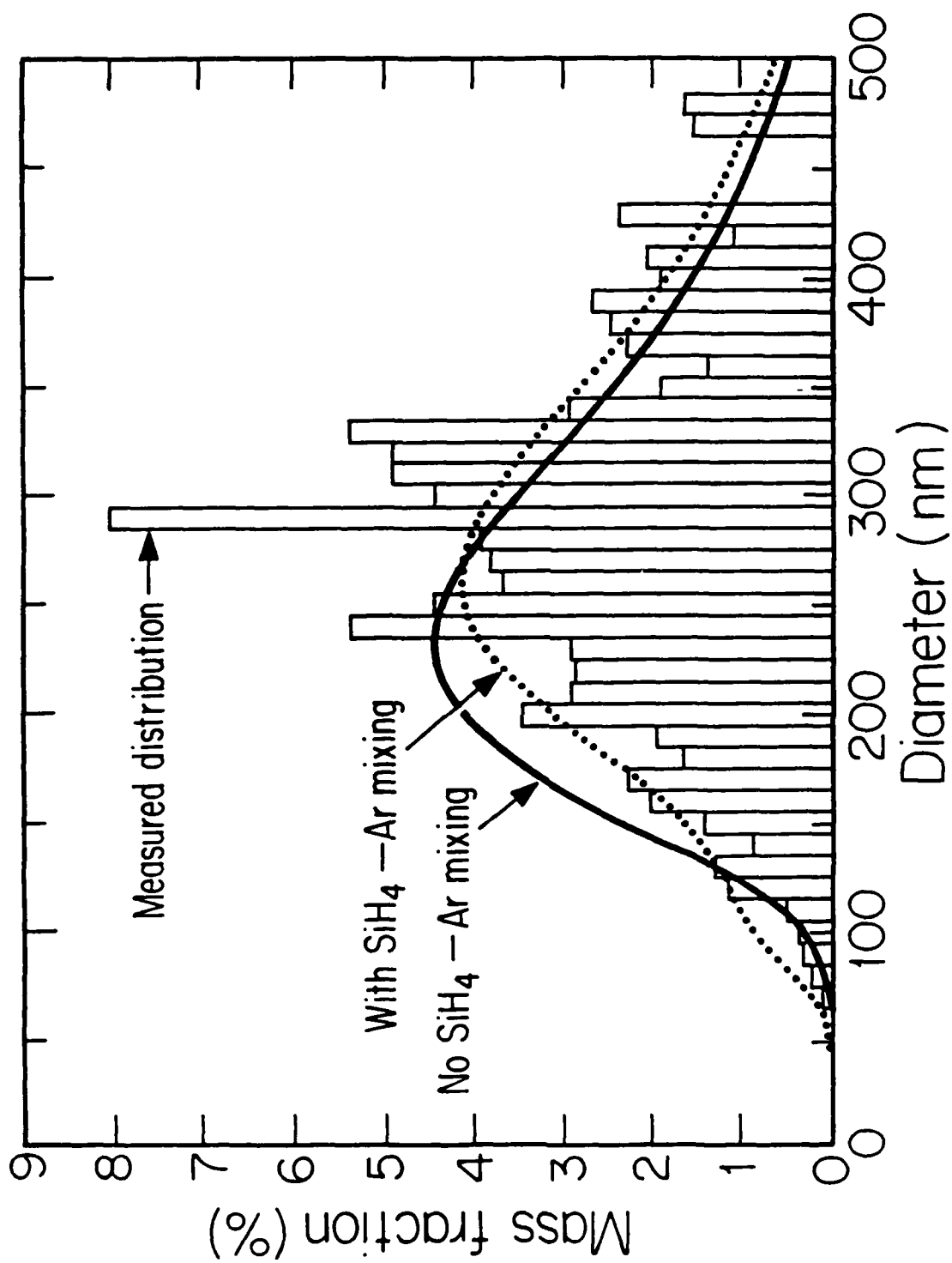


Fig. 3

F3
643.

**RAPID PREPARATION OF TITANIUM AND OTHER TRANSITION METAL NITRIDE AND
CARBIDE POWDERS BY A CARBO-REDUCTION METHOD USING ARC IMAGE HEATING**

Masahiro YOSHIMURA, Masao NISHIOKA and Shigeyuki SŌMIYA

Research Laboratory of Engineering Materials, Tokyo Institute of
Technology, 4259 Nagatsuta, Midori, Yokohama 227 Japan

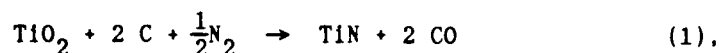
1 ABSTRACT

Titanium nitride, titanium carbonitrides, titanium carbide and other transition metal (Nb, Ta, V and W) nitrides and carbides powders were synthesized in a very short period of heating time of about 30 sec by the arc-image heating from a mixture of the transition metal oxides and graphite in 1 atm nitrogen or argon flowing gas. TiN and $\text{TiC}_x\text{N}_{1-x}$ ($x \leq 0.63$) powders were obtained as single phase in the nitrogen atmosphere. Carbon content in the $\text{TiC}_x\text{N}_{1-x}$ could be controlled directly by the mixing ratio of C/TiO₂ in the starting sample. The lattice parameter of the $\text{TiC}_x\text{N}_{1-x}$ increased linearly with carbon content (x) as predicted by Vegard's law. VN and Nb₄N₃ powders were also prepared as single phase, whereas the other nitride products could not be obtained as single phase but contained a small amount of the other phases such as Me₂N (Me = transition metal) and/or remaining oxide. AlN was synthesized in the case of longer heating of >120 sec with excess graphite. Whereas beta-SiC was formed instead of Si₃N₄ in the carbo-reduction in 1 atm N₂.

The tendency for the formation of each phase was supported by the calculation of Gibbs' free energy. TiC and NbC were obtained as single phase in Ar atmosphere, whereas the other carbide products contained a small amount of Me₂C and/or graphite.

2 INTRODUCTION

Transition metal nitride and carbide powders are used for cermet or cutting tools due to their hardness. These powders are conventionally prepared by the carbo-reduction of oxide powder with subsequent nitridation in nitrogen atmosphere or carbonization in inert gas such as argon[1,2]. For example, titanium nitride and carbide powders are prepared by the following reaction;



These methods produce fine grain products using low-cost materials, however they require high temperature and long heating times[3] if a conventional electric furnace is used [4]. On the other hand, using an arc imaging furnace[5], we have studied the rapid preparation of TiN, TiC and their solid solution, TiC_xN_y , powders from the mixture of TiO_2 and graphite powders[6]. Thermochemical investigation of the titanium carbonitride indicated that a large negative interaction parameter of the TiC_xN_y solid solution would result in homogeneous powders in spite of the steep temperature gradient of arc image heating[7]. Other transition metal nitrides and carbides have similar properties as titanium nitride and carbide[1,2]. Therefore, arc image heating seems to be applicable to the rapid preparation of those powders using the carbo-reduction method. In the present study, we examined the rapid synthesis of the transition metal (Ti,V,Nb,Ta,W) nitrides and carbides by the arc image heating. We also tried to prepare AlN and Si_3N_4 powders as an example of non-transition metal nitride for comparison.

3 EXPERIMENTAL

Figure 1 shows a schematic diagram of the optical system of an arc

imaging furnace (UF-10001, Ushio Inc., Tokyo Japan). The light generated by the Xe arc lamp is collected by mirrors, and then makes an arc image on the sample stage made of water-cooled Cu plate.

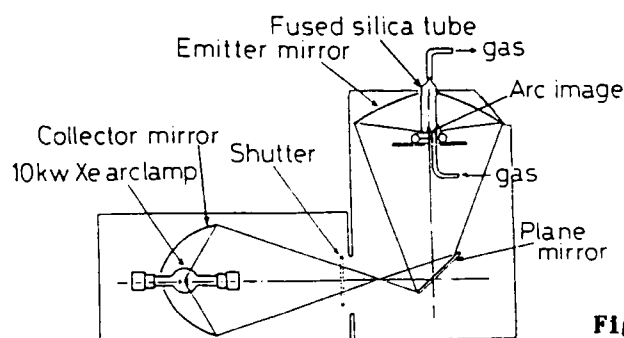
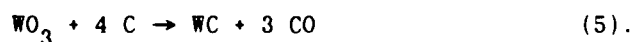
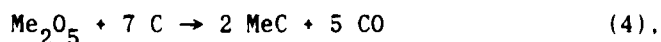
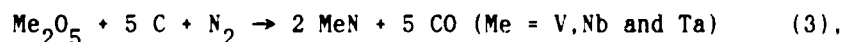


Figure 1 Schematic diagram of the optical system of the arc imaging furnace.

TiO₂ powder (99.5%, approximately 1 micron diameter) and graphite powder (99.5%, approximately 5 micron diameter) were mixed thoroughly in an agate mortar with CH₃OH for 1 hour to prepare starting mixtures of various C/TiO₂ molar ratios from 2 to 3. The other transition metal oxide powders were mixed with the graphite powder in the same way. The oxide powders were V₂O₅ (99%, a few micron in diameter), Nb₂O₅ (99.9%, approximately 1 micron diameter), Ta₂O₅ (99.9%, 0.78 micron diameter in average) and WO₃ (99.9% 1 to 10 micron diameter). The mixing ratios of graphite to each of the oxides were made according to the following equations;



We also tried to prepare AlN and Si₃N₄ powders from the starting mixture of C/Al₂O₃ = 3 and 5 and C/SiO₂ = 2. The metal oxide/graphite mixture was dried in air at 120°C. Then it was formed into columnar pellets (5 mm diameter x about 6 mm high, with a packing density of

approximately 40%) and then put onto the sample stage. After a fused silica tube was set up, a gas was introduced into the chamber with the flow-rate of 1 l/min. The gas was N_2 for the synthesis of nitride and carbonitride, while Ar was used for carbide. After the air in the chamber was sufficiently exchanged for the gas, the pellet was irradiated by the arc image at the lamp power of 5 kW. The sample pellet was heated upto ca. 1800K or higher in several seconds. The heating period was varied from 30 to 300 sec to complete the reactions. A W3%Re-W25%Re thermocouple was inserted into the sample pellet for measuring the sample temperature in several pellets. The heated pellet was subsequently cooled in the flowing gas after the light was shut off, and then the product was taken out of the chamber. The powders produced were investigated by X-ray diffraction analysis to identify phases and to measure their lattice parameters. Titanium carbonitride powders were also chemically analyzed to determine the total carbon (by a combustion infrared-absorbing method), the oxygen (by a thermal decomposition method using LECO TC-136), the titanium and the nitrogen (by a wet chemical method).

4 RESULTS AND DISCUSSION

4.1 Synthesis of Titanium Nitride and Carbonitride [6, 7]

Figure 2 shows the X-ray diffraction profiles of the products obtained from the starting mixture of $C/TiO_2 = 2$ in a nitrogen atmosphere at various heating times. As TiO_2 was completely reduced, single phase TiN was synthesized within 30 sec. The products had golden-yellow color, characteristic of TiN, and could be easily ground into powders. The products consisted of fine grains approximately 1 micron diameter according to the scanning electron micrograph as seen in Fig.3.

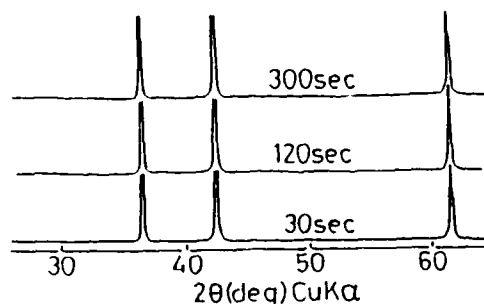


Figure 2 X-ray diffraction profiles of products obtained from the sample of $C/TiO_2=2$ in a nitrogen atmosphere at various heating periods.



Figure 3 Scanning electron micrograph of TiN powders obtained from the sample of $C/TiO_2=2$ in nitrogen atmosphere after heating for 120 sec.

The single phase of titanium carbonitrides (TiC_xN_y) with controlled x values were obtained from the sample with $C/TiO_2 = 2.1-2.7$ in the nitrogen atmosphere. Excess graphite remained in the sample of $C/TiO_2 = 2.7$ or above, increasing with the C/TiO_2 ratio.

The lattice parameter increased linearly with the C/TiO_2 ratio of the starting sample, and then became constant ($a = 4.297 \pm 0.003$ Å) at C/TiO_2 of 2.7 or above because of the coexistence with carbon under 1 atm nitrogen gas. This phase should be the most thermochemically stable titanium carbonitride at equilibrium in the nitrogen atmosphere at the irradiated temperature: 2210 ± 40 K [7].

The chemical analysis indicated the composition of the equilibrium titanium carbonitrides as $TiC_{0.63}N_{0.37}$ with maximum oxygen content of 0.02 [6, 7].

4.2 Synthesis of Transition Metal Nitrides

Table 1 shows the results of the X-ray diffraction analysis of the

products obtained from each of the starting mixtures of transition metal oxide and graphite in the nitrogen atmosphere with various heating times. The produced phases were MeN , Me_2N and/or MeN_x ($x < 1$) containing less nitrogen than the stoichiometric nitride. The carbo-reduction was completed almost within 30 sec to synthesize nitrides. The produced powders consisted of rather fine grains of a few microns in all cases.

Table 1 Crystalline phases in the products obtained in the nitrogen atmosphere for various heating time determined by X-ray diffraction method.

starting sample	produced phases		
	heating time (sec)		
	30	120	300
$\text{C/TiO}_2=2$	$\text{TiN}(\text{vs})$	$\text{TiN}(\text{vs})$	$\text{TiN}(\text{vs})$
$\text{C/Nb}_2\text{O}_5=5$	$\text{Nb}_4\text{N}_3(\text{vs})$ $\text{NbN}_{0.90.1}(\text{s})$ Graphite(t)	$\text{Nb}_4\text{N}_3(\text{vs})$	$\text{Nb}_4\text{N}_3(\text{vs})$
$\text{C/V}_2\text{O}_5=5$	$\text{VN}(\text{vs})$	$\text{VN}(\text{vs})$	$\text{VN}(\text{vs})$
$\text{C/Ta}_2\text{O}_5=5$	$\text{Ta}_2\text{N}(\text{s})$ $\text{TaNss}(\text{w})$ $\text{Ta}_2\text{O}_5(\text{vw})$	$\text{Ta}_2\text{N}(\text{s})$ $\text{TaNss}(\text{vw})$ $\text{Ta}_2\text{O}_5(\text{vw})$	$\text{Ta}_2\text{N}(\text{s})$ $\text{TaNss}(\text{t})$ $\text{Ta}_2\text{O}_5(\text{t})$

intensity; vs=very strong, s=strong, w=weak, vw=very weak
t=trace

4.3 Formation of Non-Transition Metal Nitride

AlN was synthesized but Al_2O_3 , AlON and other Al-related phases were also formed from the starting sample of $\text{C/Al}_2\text{O}_3 = 3$. When using the starting sample of $\text{C/Al}_2\text{O}_3 = 5$ containing excess graphite for completely reducing the Al_2O_3 , single-phase AlN was formed with remaining graphite. Beta-SiC was formed instead of Si_3N_4 from the starting sample of $\text{C/SiO}_2 = 2$. These reactions proceeded after 120 sec or longer and were not completed in whole with the sample at a lamp power of 5 kW. When

increasing the lamp power, the sample showed evaporation with smoking. The smoke deposits contained the same crystalline phases as the products.

4.4 Synthesis of Transition Metal Carbides

Carbides were synthesized in an argon atmosphere. Table 2 shows the identified phases in the products obtained from the starting sample prepared with the theoretical ratio at which stoichiometric carbides should be formed. The produced phases were MeC, Me₂C and/or MeC_x (x<1).

Table 2 Crystalline phases in the products obtained in the argon atmosphere for various heating time determined by X-ray diffraction method.

starting sample	produced phases		
	heating time (sec)		
	30	120	300
C/TiO ₂ =3	TiC(vs)	TiC(vs)	TiC(vs)
C/Nb ₂ O ₅ =7	NbC(vs)	NbC(vs)	NbC(vs) Nb ₂ C(t)
C/V ₂ O ₅ =7	V ₈ C ₇ (vs) Graphite(w) V ₂ C(vw)	V ₈ C ₇ (vs) Graphite(w) V ₂ C(vw)	V ₈ C ₇ (vs) Graphite(w) V ₂ C(vw)
C/Ta ₂ O ₅ =7	TaC(vs) Ta ₂ C(t) u.k.(vw)	TaC(vs) Ta ₂ C(t) u.k.(vw)	TaC(vs) Ta ₂ C(t) u.k.(vw)
C/WO ₃ =4	WC(vs) W ₂ C(w)	WC(vs) W ₂ C(vw)	WC(vs) W ₂ C(vw)

intensity; vs=very strong, s=strong, w=weak, vw=very weak
t=trace

u.k.= unknown phase, d=2.85, 1.74, 1.62, 1.48

The TiC powder had grey color and a lattice parameter of $a = 4.327$ Å, in good agreement with the value reported for stoichiometric TiC[8].

The oxides were completely reduced within 30 sec, carbides were synthesized as rapidly as the nitrides. At longer heating times, the produced phases were almost identical with those at 30 sec. The grain sizes of vanadium carbide and tungsten carbide were larger than those of tantalum carbide and niobium carbide corresponding to those of the source materials.

4.5 Thermochemical Calculation

The sample temperature rose very rapidly and reached to a maximum value within almost 20 sec. That was 2450 ± 80 K, 2140 ± 80 K and 2210 ± 40 K for the sample of $C/TiO_2 = 3$ in argon atmosphere, 2 and 2.7 in nitrogen atmosphere respectively. The differences between these heating temperatures seem to be caused by the different effective emissivities and heat conductivities of the samples.

We calculated thermochemical energy to understand why the transition metal nitrides are easily formed by the arc image heating but AlN or Si_3N_4 are not. The variation of Gibbs' free energy (ΔG) for the chemical reactions to form nitrides by the carbo-reduction and nitridation is plotted in Fig.4, where ΔG was calculated given to unit molar carbon monoxide production using data from MALT[9]. The equilibrium partial pressure of carbon monoxide (P_{CO}) is also plotted in Fig.4. One can consider if each of the reactions proceeds or not by comparing ΔG with $-RT \ln P_{CO}$. P_{CO} during carbo-reducing reaction could not be measured, although, we estimated it as less than 0.3 atm from the mass of pellet, gas-flow rate and reaction duration. The heating temperature in the present work was estimated to be in the range of 2000 to 2500 K. Fig.4 indicates that ΔG for the reaction to form AlN and

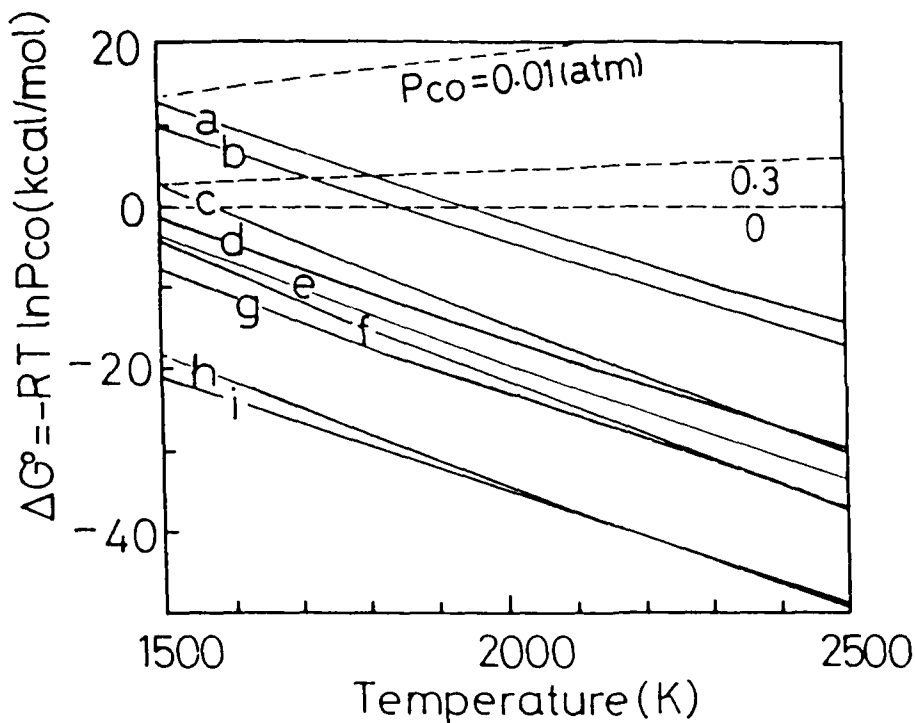


Figure 4 Gibbs' free energy of carbo-reducing reaction as a function of temperature. The dashed lines are the equilibrium partial pressure of carbon monoxide.

- a: $1/3\text{Al}_2\text{O}_3 + \text{C} + 1/3\text{N}_2 \rightarrow 2/3\text{AlN} + \text{CO}$
- b: $1/2\text{SiO}_2 + \text{C} + 1/3\text{N}_2 \rightarrow 1/6\text{Si}_3\text{N}_4 + \text{CO}$
- c: $1/5\text{Ta}_2\text{O}_5 + \text{C} + 1/10\text{N}_2 \rightarrow 1/5\text{Ta}_2\text{N} + \text{CO}$
- d: $1/2\text{TiO}_2 + \text{C} + 1/4\text{N}_2 \rightarrow 1/2\text{TiN} + \text{CO}$
- e: $1/5\text{Ta}_2\text{O}_5 + \text{C} + 1/5\text{N}_2 \rightarrow 2/5\text{TaN} + \text{CO}$
- f: $1/5\text{Nb}_2\text{O}_5 + \text{C} + 1/10\text{N}_2 \rightarrow 1/5\text{Nb}_2\text{N} + \text{CO}$
- g: $1/5\text{Nb}_2\text{O}_5 + \text{C} + 1/5\text{N}_2 \rightarrow 2/5\text{NbN} + \text{CO}$
- h: $1/5\text{V}_2\text{O}_5 + \text{C} + 0.993\text{N}_2 \rightarrow 2/5\text{VN}_{0.465} + \text{CO}$
- i: $1/5\text{V}_2\text{O}_5 + \text{C} + 1/5\text{N}_2 \rightarrow 2/5\text{VN} + \text{CO}$

Si_3N_4 are close to zero while the other transition metal nitrides have ΔG values sufficiently large for the reaction to proceed. Furthermore, the melting or decomposition temperatures for AlN and Si_3N_4

are close to the present heating temperature so that it is difficult to synthesize rapidly these nitrides by the arc-image heating when using the carbo-reduction method. While the transition metal nitrides have higher melting temperatures so that the arc image heating method is very suitable for the synthesis of those powders.

We could not always obtain single-phase stoichiometric nitrides or carbides. At those temperatures, ΔG of the formation for Me_2N is close to that for MeN . This is one of the reasons why a single phase of these nitrides could not be obtained. Some part of the starting materials also remained. A small amount of Ta_2O_5 remained in the produced tantalum nitride powders. The lattice parameter of TaN_{ss} was larger than that of the stoichiometric TaN and close to that of TaC . It indicates that the tantalum nitride dissolved some carbon to form a solid solution. Therefore, the carbon content became insufficient to reduce all of the oxide. The carbo-reducing reaction and/or carbonizing reaction must occur between solids. When non-stoichiometric carbides and nitrides containing carbon are formed, these products are not contact with the reactants and oxide and/or graphite remain separately, because carbon monoxide is formed between them. Furthermore, the diffusion rate of carbon is very low in the tantalum carbonitride, thus it takes much longer time for the reduction of Ta_2O_5 by the carbon contained in TaN_{ss} than by graphite in direct contact with oxide in the starting sample. Similarly, since carbon diffuses very slowly in the carbides, non-stoichiometric carbides could not be completely carbonized once a stoichiometric carbide was formed between graphite and the non-stoichiometric carbide. For the purpose of better contact between oxide and graphite, the fine powders of graphite are desirable to use in these carbo-reduction processes.

ACKNOWLEDGMENTS

The authors thank to R & D Lab.-I, Nippon Steel Corporation, Kawasaki, Japan for the chemical analysis of the products.

REFERENCES

1. L.E.TOTH, "Transition Metal Carbides and Nitrides", p.12, Academic, New York and London, (1971).
2. E.K. STORMS, "The Refractory Carbides", p.1. Academic, New York and London, (1967).
3. E. FRIEDRICH and L. STTIG, Z. Anorg. Allgem. Chem., 143, 293 (1925).
4. Z. ARAI, Nagoya-Kogyogijutsushikenjo-Hōkoku, 5, 454 (1956).
5. M. YOSHIMURA and S. SŌMIYA, Proceedings 4th International Conference on Rapidly Quenched Metals, Vol.1, p.23, Japan Inst. of Metals, Sendai, (1981).
6. M. YOSHIMURA, M. NISHIOKA and S. SŌMIYA, J. Mater. Sci. Lett., 6, 1463 (1987).
7. M. YOSHIMURA, M. NISHIOKA and S. SŌMIYA, Proceeding of MRS International Meeting on Advanced Materials, May 31-June 3, 1988, Tokyo, and 2nd International Conference on Ceramic Powder Processing Science, Oct. 12-14, 1988, Berehtesgaden, FRG, to be published.
8. J. V. SMITH et al.(eds.), "JCPDS X-ray Powder Data File", (ASTM, Philadelphia, (1967) No.32-1383.
9. Y. YAMAUCHI and H.YOKOKAWA, "Materials-oriented Little Thermodynamic Data Base for Personal Computers", Netsu Sokutei, 12, (1985) 142.

MICROWAVE PLASMA DENSIFICATION OF ALUMINUM NITRIDE

Susan M. Knittel* and Subhash H. Risbud

Department of Materials Science and Engineering
and Arizona Materials Laboratory
University of Arizona
Tucson, Arizona 85721

Abstract

Microwave induced plasma (MIP) sintering of pure and Y_2O_3 doped aluminum nitride (AlN) was investigated. Processing parameters (nitrogen gas pressure, power level, and time) were optimized to achieve densification in less than 15 minutes at temperatures estimated to be 1500° to 1800°C.

Densities of only 81% of theoretical were obtained in undoped AlN, while densities in excess of 95% of theoretical were achieved for yttria doped AlN. Microstructural investigations revealed a smaller grain size in the plasma sintered specimens ($\approx 2 \mu m$) compared with conventionally sintered AlN ($\approx 8 \mu m$).

*Now at Allied Signal Corp., Garrett AiResearch Division, Tucson, Arizona.

Key Words: sintering, grain size, Y_2O_3 doped AlN, electronic packaging substrate

11/1/65

11/1

22

21

661

200
1000

22

212

665

I. Introduction

AlN is an emerging electronic packaging substrate material due to its attractive electrical and thermal properties. As in other covalent compounds, limited atomic mobility prevents complete densification of pure AlN at reasonable temperatures. At higher temperatures ($>1600^{\circ}\text{C}$) decomposition of AlN is a major problem in achieving a sintered dense solid from powders.¹ Thus, sintering of AlN is usually performed either at relatively high pressures or via the use of additives that assist densification by liquid phase formation at the firing temperature.

Densification of ceramic materials in high temperature plasmas is a rapidly developing processing technique which promises the achievement of high density, smaller grain size, and enhanced sintering kinetics in several systems. While successful plasma densification has been obtained in oxide ceramics,²⁻⁴ applications of this method of non-oxide materials have only recently been considered. For example, densities of 96-99% of theoretical were obtained⁵ in RF plasma sintering of boron doped SiC while "pure" SiC showed only morphological changes with little or no shrinkage.⁶

In the present work we have studied the sinterability of AlN with and without additives using a microwave induced plasma (MIP). The focus of the research was on optimization of the processing parameters in MIP sintering and parallel characterization of the microstructure of the densified material.

II. Experimental Procedures

Commercially available aluminum nitride powders were used for MIP sintering: (a) Powder D (Denka) which contained the following major impurities: Si (0.14%), C (0.22%) and O (1.2%). The specific surface area of this powder was 3.1 gm/m^2 with an average particle size of $\approx 1.02 \mu\text{m}$.

(b) Powder T (Tokoyama Soda) which contained the following impurities: C (0.04%) and O (1.35%). This powder had a specific surface area of 3.46 gm/m^2 with an average particle size of $1.08 \text{ }\mu\text{m}$. (c) Powder K was a spray dried mixture of powder D and 2 wt% of Y_2O_3 additive commonly used in AlN sintering. Cylindrical pellets 0.63 cm diameter by about 2.5 cm high were uniaxially pressed in a steel die at 135 MPa yielding a green density of about 2.2 gm/cm^3 (67% of theoretical) for powders D and K, and about 1.9 gm/cm^3 (57% of theoretical) for powder T.

Microwave induced plasma (MIP) processing was conducted in a unit driven by a magnetron power source consisting of a 2.45 GHz microwave generator. Power (from 0 to 3 kW) was delivered through a waveguide to an aluminum microwave applicator into which a fused silica tube had been inserted.

The plasma reactor consisted of a fused silica tube inserted into the applicator and connected to a pressure regulator system for introducing a nitrogen gas atmosphere. Samples were inserted into the plasma system via a vacuum tight aluminum fixture placed at the bottom of the microwave applicator. An alumina rod inserted through the fixture provided support for the BN sample holder and the AlN specimen. It was connected to a device which provided rotation of the specimen and movement into and out of the plasma zone. The plasma was ignited by reducing the pressure to $<1 \text{ torr}$ ($\approx 1.33 \text{ mbar}$) and introducing nitrogen gas flow as the power was turned on. After the plasma was ignited, gas flow and pressure were increased and the green sample was moved into the plasma zone for sintering.

III. Results and Discussion

(1) Density of MIP Sintered AlN

Samples of powder K were processed at a variety of gas pressures and power levels for short times (minutes). Apparent temperatures of $\approx 1500^{\circ}\text{C}$ were measured by an optical pyrometer when the plasma was confined in a 12 mm diameter fused silica tube; lower temperatures ($\approx 1200^{\circ}\text{C}$) were measured in a 25 mm tube. The apparent temperature, which increases with gas pressure, might be underestimated⁷ by as much as 300°C because of the difficulties in making optical pyrometry measurements on the sample contained in the luminescent plasma. Nonetheless, the optical pyrometer temperatures do provide a comparative guide in MIP processing of AlN.

A representative plot of experimentally measured bulk densities as a function of power level is shown in Figure 1, for powder K densified under a gas pressure of 60 torr for ≈ 7 minutes. No densification was observed at power levels below 0.4 kW, while power levels of 1 kW caused melting of the fused silica tube. Power levels of 0.6 to 0.8 kW were found to be optimum for achieving $>90\%$ theoretical densities in powder K. The increased density with higher power is consistent with the higher temperature expected as electron concentration and plasma density increase with greater applied power. The densities obtained in MIP sintered AlN were also improved by higher gas pressures during processing. Most of the densification of AlN was completed in less than 15 minutes. Powders K, D, and T attained their highest densities in 10 to 15 minutes when held in the plasma at a gas pressure of 100 torr and a power level of 0.6 kW. Highest densities (92 to 95% of theoretical) were obtained in powder K in less than 15 minutes.

(2) Microstructure and Chemistry

One of the major advantages of plasma sintering is the finer grain size in comparison with conventionally sintered specimens. SEM micrographs of the fracture surface of a plasma sintered doped AlN sample (powder K) and that of the same powder conventionally sintered are shown in Figure 2. The micrographs show a clear reduction in grain size ($\approx 2 \mu\text{m}$) in the plasma sintered sample in comparison with the same powder fired conventionally at 1810°C for 4 hours in N_2 (grain size $\approx 8 \mu\text{m}$). The plasma sintered sample also shows a uniform microstructure with a small amount of evenly distributed porosity.

X-ray photoelectron spectroscopy (XPS) data of plasma sintered samples (powder K) were compared with conventionally sintered samples (98% theoretical density). Analyses were performed on freshly fractured surfaces, and are shown in Figure 3. The expected peaks for Al, N, O, and Y were observed in both spectra. The oxygen content in the plasma sintered sample appears to be qualitatively higher, perhaps due to the unavoidable presence of air in the plasma tube as discussed earlier.

IV. Summary and Conclusions

- (1) Y_2O_3 doped AlN was densified in less than 15 minutes in a microwave induced plasma (MIP) to a density of $\approx 3.13 \text{ gm/cm}^3$ (95% of theoretical value) while undoped AlN could be densified to only 81% of theoretical density.
- (2) A finer, uniform grain size of $\approx 2 \mu\text{m}$ was obtained in MIP sintering compared with a grain size of $\approx 8 \mu\text{m}$ in the same powder sintered conventionally in N_2 at 1810°C for 4 hours.

- (3) The presence of air in the plasma tube during MIP processing influences densification behavior because of the formation of an Al_2O_3 layer which can be easily flaked off.

Acknowledgement

This work is based on a M.S. thesis by Susan M. Knittel and was partially supported by the Keramont Research Corporation in Tucson, Arizona.

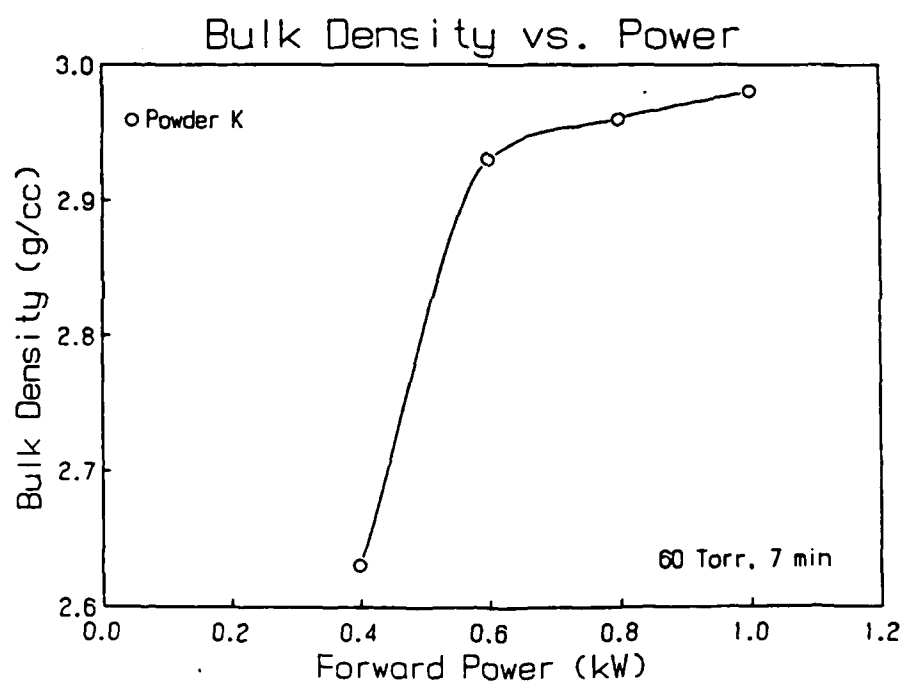
References

- ¹K. Mitchell and A. Hendry, "Sintering of Non-Oxide Ceramics," in *High Tech Ceramics*, edited by P. Vincenzini, pp. 901-910 (Elsevier, Amsterdam, 1987).
- ²E. L. Kemer and D. L. Johnson, "Microwave Plasma Sintering of Alumina," *Am. Ceram. Soc. Bull.*, 64[8], 1132-36 (1985).
- ³G. Thomas and J. Freim, "Parametric Investigation of the Glow Discharge Technique for Sintering UO_2 ," *Trans. Am. Nucl. Soc.* 21, 182 (1975).
- ⁴K. Upadhy, "Sintering Kinetics of Ceramics and Composites in the Plasma Environment," *J. Metals*, 39, 11-13 (1987).
- ⁵K. Kijima, "Plasma Sintering of Ceramic Materials," *7th International Symposium on Plasma Chemistry Proceedings*, vol. 2, edited by C. J. Timmermans, pp. 662-667 (1985).
- ⁶R. L. Porter, "Plasma-Induced Morphological Changes in α Silicon Carbide," *J. Am. Ceram. Soc.*, 70[2], C26-C28 (1987).
- ⁷E. L. Kemer, "Microwave-Induced Plasma Sintering of Alumina," M.S. Thesis, Northwestern University (1984).

Figure Captions

- Figure 1. Bulk density as a function of forward power for densification of powder K. Optimum power level is in the range of 0.6 to 0.8 kW.
- Figure 2. SEM micrographs of (bottom) plasma sintered AlN with Y_2O_3 additive (grain size $\approx 2 \mu m$) and (top) conventionally sintered ($1810^\circ C$, 4 hours in N_2) AlN with Y_2O_3 additive (grain size $\approx 8 \mu m$).
- Figure 3. XPS patterns for plasma sintered AlN (top) versus conventionally sintered AlN (bottom).

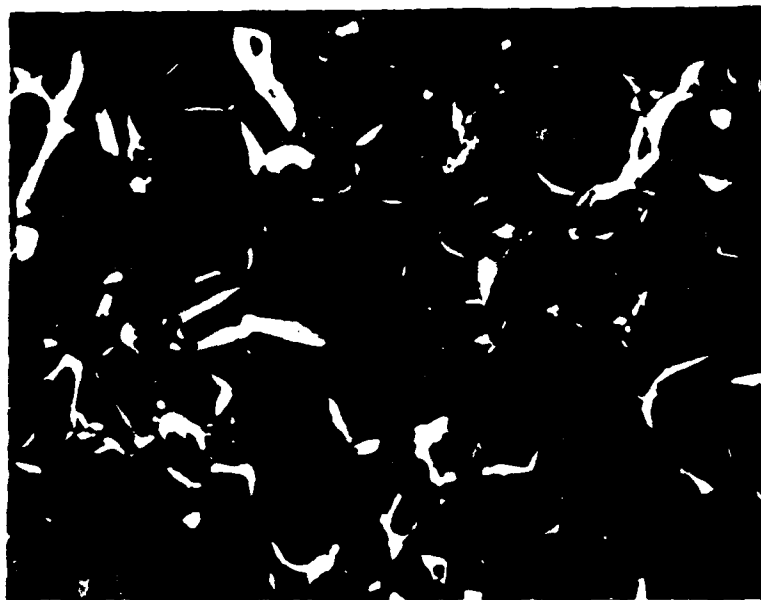
Fig.1



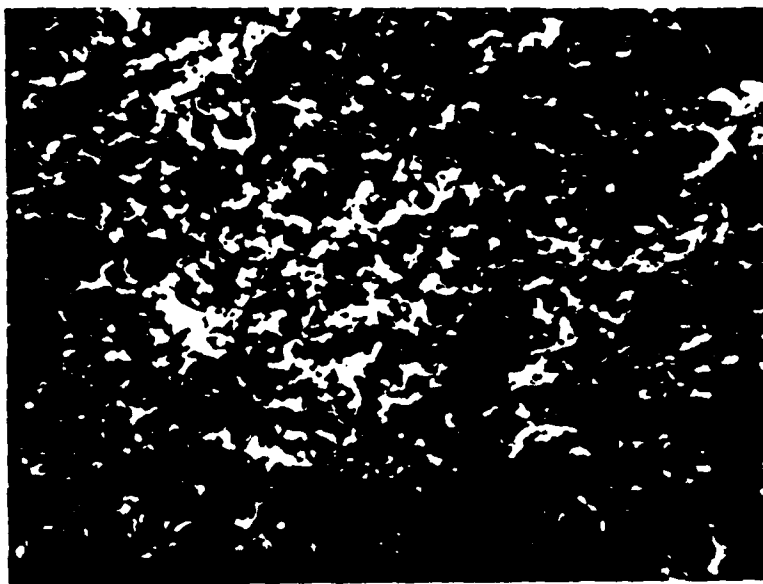
NOTE TO PUBLISHER

The pages that follow are original photographs of figures already included in manuscript.

Fig. 2

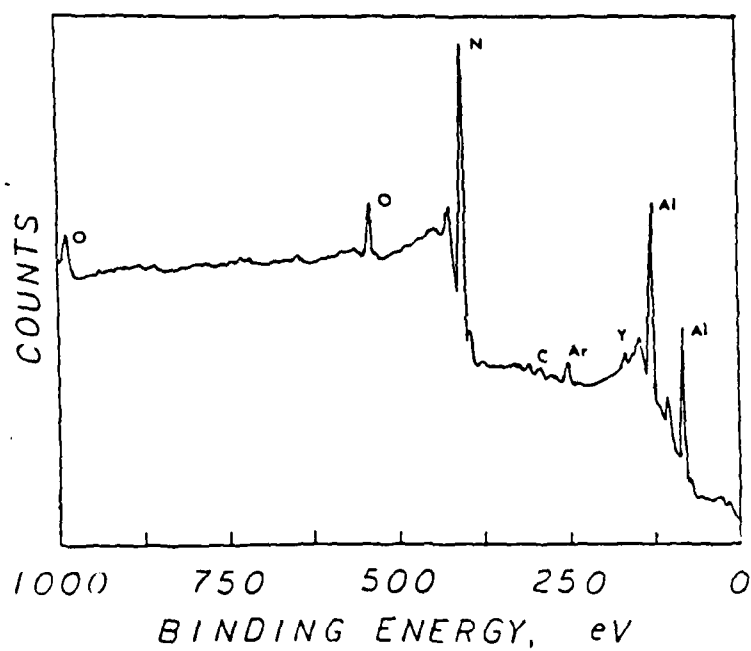
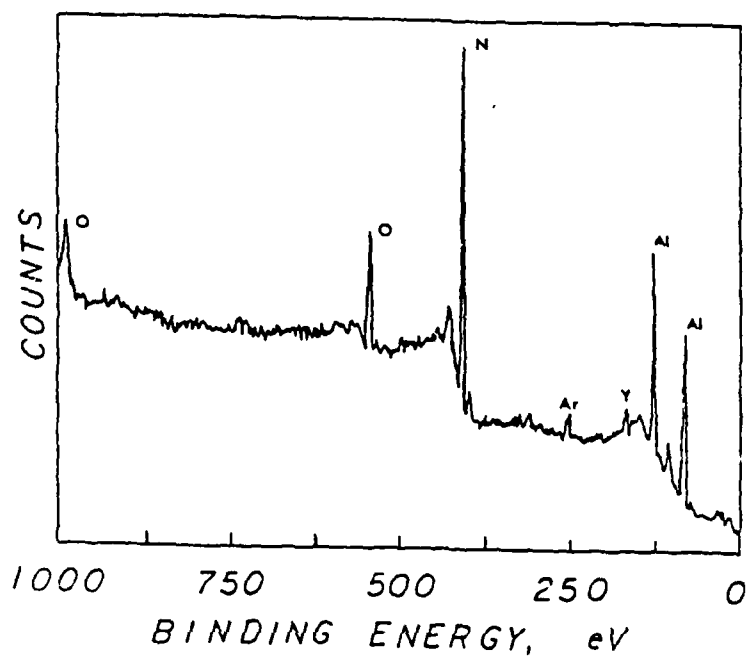


10 μm



10 μm

Fig. 3



PLASMA SYNTHESIS OF FINE POWDERS

BY

COUNTER-FLOW LIQUID INJECTION

**PETER C. KONG AND E. PFENDER; ENGINEERING RESEARCH CENTER FOR
PLASMA-AIDED MANUFACTURING; DEPARTMENT OF MECHANICAL ENGINEERING;
UNIVERSITY OF MINNESOTA, MINNEAPOLIS, MINNESOTA 55455**

ABSTRACT

Ceramic powder of carbides, oxides and oxide solid solutions have been successfully synthesized in a DC thermal plasma jet reactor using a liquid injection method. This procedure has been developed to overcome the problems associated with solid injection and to realize the benefits of gaseous reactants. This paper presents recent results based on liquid injection plasma synthesis with a brief comparison of gas and solid injection plasma synthesis. The materials characterization makes use of standard techniques.

INTRODUCTION

In thermal plasma synthesis the reactants may be gases, liquids, or solids before injection into the plasma. The injection process is not trivial; in fact it can be a serious problem due to the high viscosity of the plasma. The most common route for synthesizing fine powders in thermal plasmas starts with at least one solid precursor. The reactants undergo chemical or physical changes in the plasma and chemical reactions induced on or within the particle itself or in the gas phase after evaporation. After the desired chemical reactions are completed, a fast quench is necessary to preserve the product. Fast quench rates ($> 10^5$ K/s [1]) will lead to homogeneous nucleation, resulting in ultrafine particles with sizes down to 10 nm. If heterogeneous nucleation processes prevail, larger particles ($>> 100$ nm) may be formed. Over the past decade, the thermal plasma group at the University of Minnesota has synthesized a large number of refractory carbides and nitrides [1-14] using transferred arcs, convective stabilized free burning arcs, and DC plasma jets. In these processes solid reactants and reactive carrier gases were used as the starting materials.

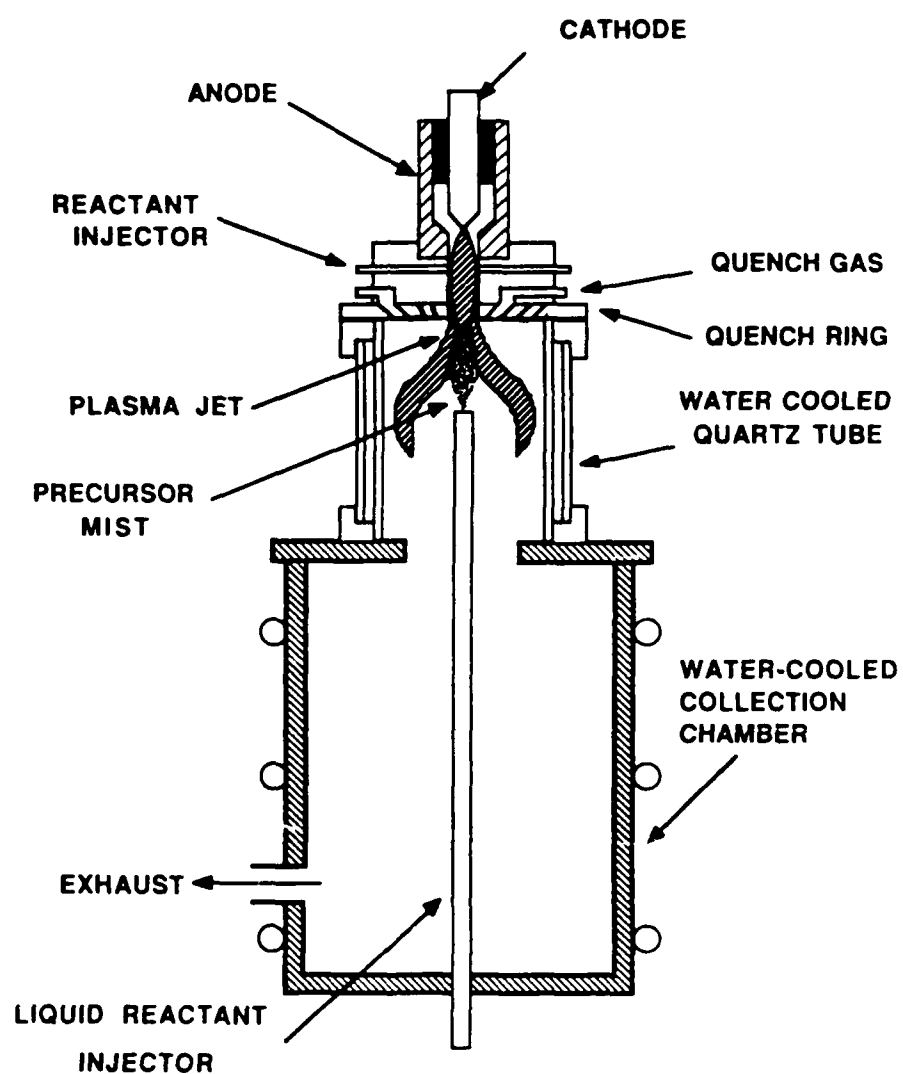
Gas phase reactants are the most desirable and beneficial starting materials for plasma synthesis. But unfortunately, gaseous reactants for metals are severely limited. As a consequence, plasma synthesis depends largely on solid precursors. However, solid feeding and particle injection is a serious problem in plasma powder synthesis. There are major problems [14,15] associated with uniform particle injection and processing in thermal plasmas.

In view of the solid injection problems, another approach has been developed for achieving the benefits of gaseous reactants, but avoiding the problems associated with powder injection. This approach is termed Liquid Injection Plasma Synthesis (LIPS). There are two methods for LIPS, injection parallel to the flow and the counter-flow injection. Parallel injection into RF plasmas for synthesis is not a new approach and has been studied by Kagawa et.al. [16-19], by Lau, Kong and Pfender [20,21] and is also widely used in spectrochemical analysis [22]. LIPS has a number of advantages when compared to the solid injection method [23]. Counter-flow LIPS is a new approach which provides significant advantages over the parallel-flow LIPS method. (1) In counter-flow LIPS, the heat transfer between the plasma and the liquid droplets is substantially higher due to the higher relative velocities between droplets and the plasma. (2) The residence time for the liquid droplets in the plasma is longer. This ensures complete evaporation of the liquid precursors, i.e. a gas phase reaction in the plasma.

The feasibility of producing ceramic powders by this counter-flow LIPS has been demonstrated by the synthesis of pure oxides, oxide solid solutions, and carbides. The pure oxides include alumina, ceria, cobalt oxide, lithia, magnesia, nickel oxide, ferric and ferrous oxides, yttria, zinc oxide and zirconia. The synthesis of solid solutions have been restricted to the fully stabilized zirconia system. The stabilizing oxides include 9 mole % yttria and 1 mole % ceria plus 9 mole % yttria. The carbides include silicon carbide and boron carbide. X-ray diffraction and electron microscopy have been used for powder characterization.

EXPERIMENTAL PROCEDURE

The experimental setup for the counter-flow LIPS is shown schematically in Fig 1. The reactor contains a high power, swirl stabilized, DC plasma torch. The plasma torch is operated with argon at a flow rate of 30 g/min at atmospheric pressure. The arc voltage assumes values



Counter flow DC Plasma Synthesis

Fig. 1a

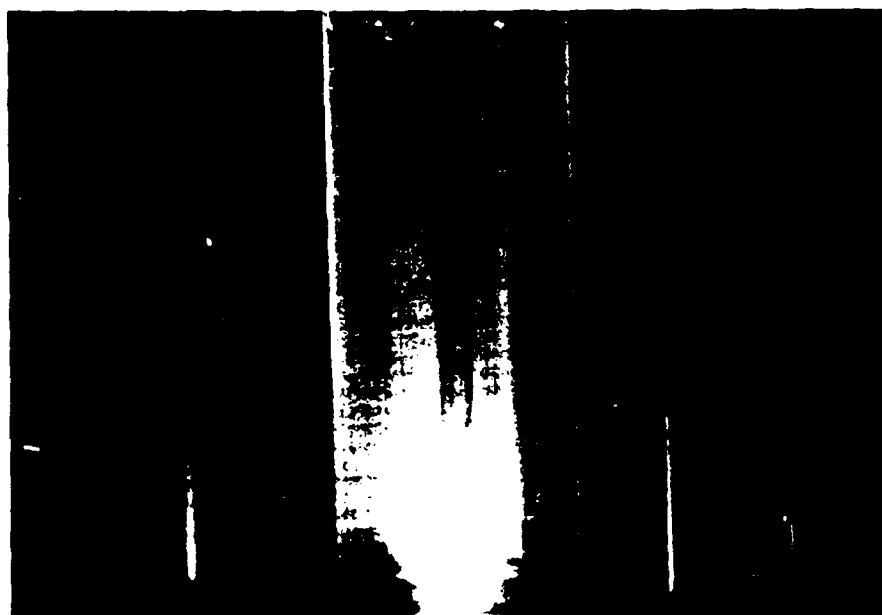


Fig. 1b

around 30 V for pure argon and the arc current may be varied between 300 to 1000 A. Therefore, the typical power input for a pure Ar plasma ranges from 9 to 30 kW. The power of the plasma torch may be increased to higher values if diatomic gases such as hydrogen or nitrogen are added to the main flow. The torch is attached to a water cooled reactant and quench gas injection flange, followed by a double wall, water cooled quartz reaction tube. A water cooled collection chamber is placed directly beneath the quartz reaction tube. A four-channel water cooled stainless steel liquid injection probe is inserted into the plasma flame through the bottom flange of the collection chamber. Precursors together with atomizing gases are injected against the plasma flow for vaporization. A well defined stagnation region is formed at the confluence of the two flows as shown in Fig. 1. At the outflow of the confluence, fine particles nucleate from the supersaturated vapor. For single phase oxide synthesis soluble metal acid salts, such as nitrates, are dissolved in distilled water to prepare standard (1 M) stock solutions. Appropriate amounts of the stock solutions are well mixed to prepare homogeneous precursors for solid solutions and multi-component compound synthesis. For all cases, either oxygen or argon served as the atomizing gas.

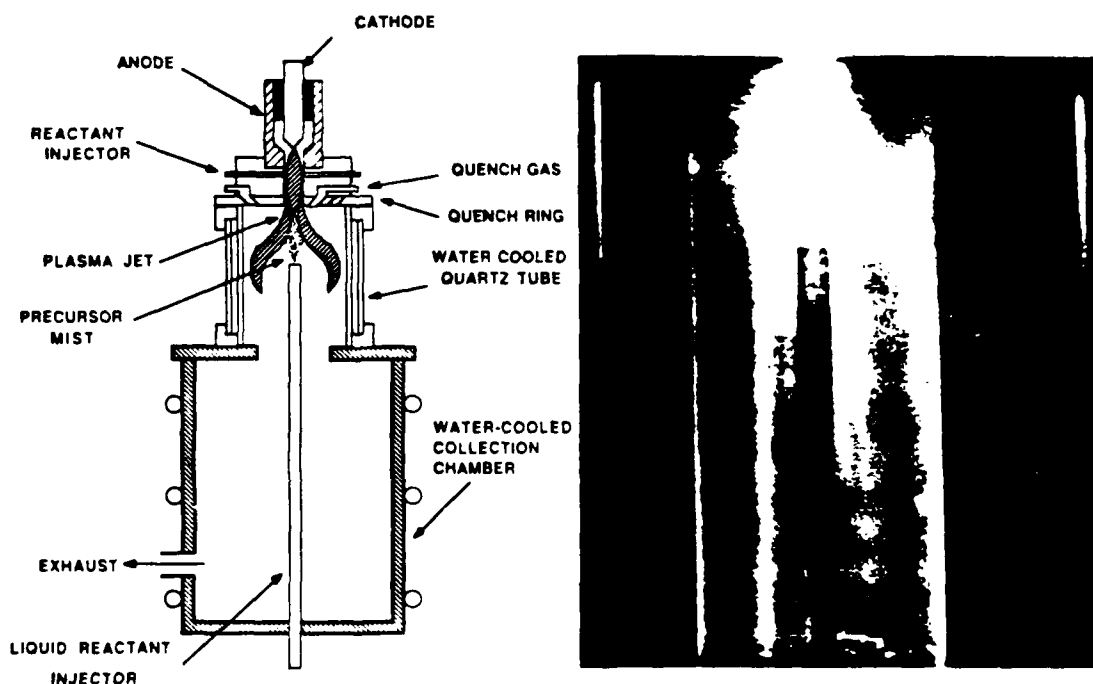


Fig. 1. Experimental set-up

For carbide synthesis, liquid organometallics are used as precursors. The oxygen content in these organometallics is quite high which would hamper the carbide formation if it is not totally controlled. Therefore, liquid hydrocarbons are used to adjust the metal/carbon ratio in the solution mixture to maintain a high carbon content and to ensure complete carbonization of the metal. Instead of liquid hydrocarbons, methane can be used as an atomizing reactive gas in the reaction to keep the carbon/metal ratio high. The excess amount of carbon is controlled by using hydrogen in the plasma.

For all experiments the liquid flow rate is set at 20 ml/min and the atomizing gas flow rate at 110 ml/min.

RESULTS AND DISCUSSION

In the formation of oxides, whether they are compound oxides or solid solutions, single phase products have been formed. X-ray diffraction patterns of compound oxides such as NiO, MgO, CeO₂ and Y₂O₃ are shown in Fig. 2. All these X-ray diffraction patterns show single phase, pure oxide formation without impurities. The X-ray line profiles indicate that the powder size of the oxides produced by the counterflow LIPS method is comparable for all oxides. During dispersion these powders form non-settling colloidal suspensions indicating that the powders are ultrafine. The effects of solute concentrations, solution feed rates, atomizing gas flow rates and velocities, initial droplet sizes and quenching of vapor on the final particle size distribution are still under investigation. In the synthesis of MgO, the fine particles will partially hydrolyze to the hydroxide if the collection chamber is water cooled. When the collection chamber runs hot, no hydrolysis of oxides occurs.

The X-ray diffraction patterns of yttria and ceria/yttria stabilized zirconia solid solutions are shown in Fig. 3. The 9 mole % yttria stabilized zirconia forms a cubic solid solution and the X-ray lattice parameter is 0.5138 nm. The solid solution of zirconia stabilized with 1 mole % ceria and 9 mole % yttria also forms a face-centered cubic structure with a X-ray lattice parameter of 0.5160 nm. The unit cell of this new solid solution expands by 1.3 % when compared to that of yttria stabilized zirconia. This is equivalent to 15.5 mole % yttria in zirconia. After the addition of 1 mole % ceria into the solid solution the powder turns from white to pink.

The X-ray diffraction patterns of SiC and B₄C are shown Fig. 3. The carbide powders are made from precursors which contain a high amount of oxygen. The reaction of SiC is almost complete except for a minute quantity of SiO and Si formed as impurities. Conversion of the silicon precursor to the carbide should improve if the C/Si ratio is adjusted to higher values. β -SiC represents the major phase product with a small amount of the α -SiC. The precursor for the B₄C reaction is an aqueous organoboron which contains an exceptionally high amount of oxygen. The C/O ratio in the system is deliberately set very high for controlling oxygen and to allow for boron carbide formation. No attempt has been made to control the excess carbon in this particular reaction. Future work will be focused on the optimization of all carbide reactions to produce single phase and pure products.

The particle morphologies of CeO₂, NiO, MgO, and Y₂O₃ are shown in Fig. 4. The powders, with the exception of ceria, have comparable particle size and the size distribution is extremely narrow while the particle size ranges from 0.05 to 0.2 μ m. Occasionally, a small number of spheres larger than 1 μ m in size are observed. These larger particles are probably formed by incomplete evaporation and then drying of the initially large liquid droplets which is an indication of nonhomogeneous initial spray droplets size. The roundness of the submicron particles suggests a liquid phase nucleation process. These submicron particles formed loose agglomerates. Interestingly, CeO₂ forms nice spheres in a particle size range from 1 to 13 μ m. The majority of the particles forms in a narrow particle size distribution ranging from 1 to 2.5 μ m. Some particles show a completely smooth surface which indicates that the particles form a total liquid phase before solidifying.

The particle morphology of yttria stabilized zirconia solid solution is shown in Fig. 5. The particle size distribution is quite narrow ranging from 0.5 to 2 μ m. Similar to the ceria particle the yttria stabilized zirconia forms spherical particles. Besides spherically smooth surfaces, some particle nucleation on the surface have been observed. This indicates that the newly formed particles act as nucleation centers for the incoming vapor.

SUMMARY

Counter-flow LIPS is a new promising process for powder synthesis. This process holds substantial advantages over both the parallel flow LIPS and the solid injection plasma

synthesis. Synthesis of carbides, oxides and oxide solid solutions has been demonstrated. Synthesis of other materials, including composites, nitrides, borides, silicates, appears to be feasible.

ACKNOWLEDGEMENTS

This material is based upon work supported by NSF under grant number CDR-8721545. The government has certain rights in this material.

REFERENCES

1. P. C. Kong, Ph. D. Thesis, University of Minnesota, (1985).
2. B. Mitrofanov, A. Mazza, P. Ronsheim, L. E. Toth and E. Pfender, Mat. Sci. and Eng., Vol. 48, p.21(1981).
3. P. Ronsheim, L. E. Toth and E. Pfender, Proc. 5th Int. Symp. on Plasma Chem. (ISPC5), Vol. 2, p.844(1981), HeriotWatt University, Edinburg, Scotland.
4. P. Ronsheim, L. E. Toth, A. Mazza, B. Mitrofanov and E. Pfender, J. of Mat. Sci., Vol. 16, p.265(1981).
5. P. Ronsheim, L. E. Toth and E. Pfender, J. Mat. Sci. Lett., Vol. 1, p.343(1982).
6. P. C. Kong, T. T. Huang and E. Pfender, Proc. ISPC6, Vol. 1, p.219(1983), Universite de Sherbrooke and McGill University, Canada.
7. P. C. Kong, M. Suzuki, R. Young and E. Pfender, J. Plasma, Chem. and Plasma Processing, Vol. 3, No. 3, p.351(1983).
8. P. C. Kong, R. Young, T. T. Huang and E. Pfender, Proc. ISPC7, Vol. 2, p.674(1985), Eindhoven, Netherland.
9. P. C. Kong, T. T. Huang and E. Pfender, IEEE Transaction on, Plasma Sci., Vol. PS14, No. 4, p.357(1986).
10. P. C. Kong and E. Pfender, Langmuir, Vol. 3, p.259(1987).
11. P. C. Kong and E. Pfender, Proc. MRS Spring Meeting, Vol. 98, p.337 (1987), Anaheim, CA.
12. R. Young, Yl Chang, B. Lecerf and E. Pfender, Proc. ISPC8, Vol. 4, p.2028(1987), Tokyo, Japan.

13. YI Chang, R. Young and E. Pfender, J. Plasma Chem. and plasma Processing, Vol. 7, No. 3, p.299(1987).
14. YI Chang, P. C. Kong and E. Pfender, J. Plasma Chem. and Plasma Processing, to be Vol. 9, No. 1, p.73 (1989).
15. D. S. Phillips and G. J. Vogt, MRS Bull. Vol. XII, No.7, October, p.54(1987).
16. M. Kagawa, M. Kikuchi, Y. Syono and T. Nagae, J. Am Cer. Soc. Vol. 66, No.11, p.751(1983).
17. M. Kagawa and T. Nagae, Science Report of the Res. Inst. Tohoku University, Sr.A, Vol. 31, No.2, p.216(1983).
18. M. Kagawa, H. Ohta, H Komatsu and Y. Syono, Jap. J. App. Phys., Vol. 24, No.4, April, p.477(1985).
19. T. Ono, M. Kagawa, Y. Syono, M. Ikebe and Y. Muto, J. Plasma Chem. and Plasma Processing, Vol. 7, No.2, p.201(1987).
20. Y. Lau, P. C. Kong and E. Pfender, Proc. ISPC8, Vol. 1, p.101 (1987), Tokyo, Japan.
21. Y. Lau, P. C. Kong and E. Pfender, Ceramic Transactions, Vol.1, p.298(1988).
22. H. Hiroki, H. Tetsuya and A. Mohamed, Pure and App. Chem. Vol. 6, No. 5, p.685(1988).
23. P. C. Kong and E. Pfender, Proceedings of the 2nd Int. Conf. on Cerm. Powder Processing Sci., Oct. 1214, 1988. Berchtesgaden, FRG (in press).

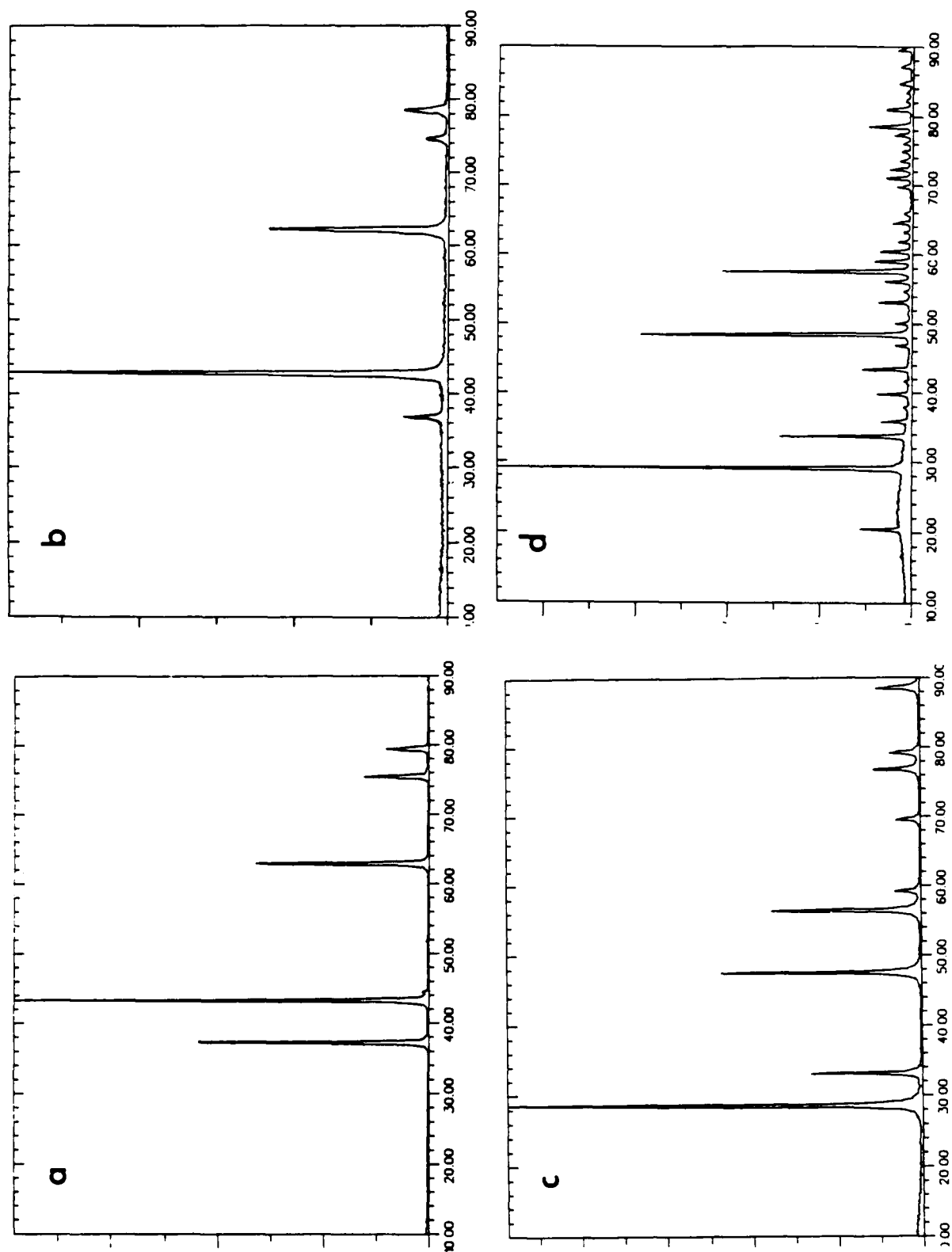


Fig. 2. X-ray diffraction profiles for (a) NiO, (b) MgO, (c) CeO₂, (d) Y₂O₃.

NOTE TO PUBLISHER

The pages that follow are original photographs of figures already included in manuscript.

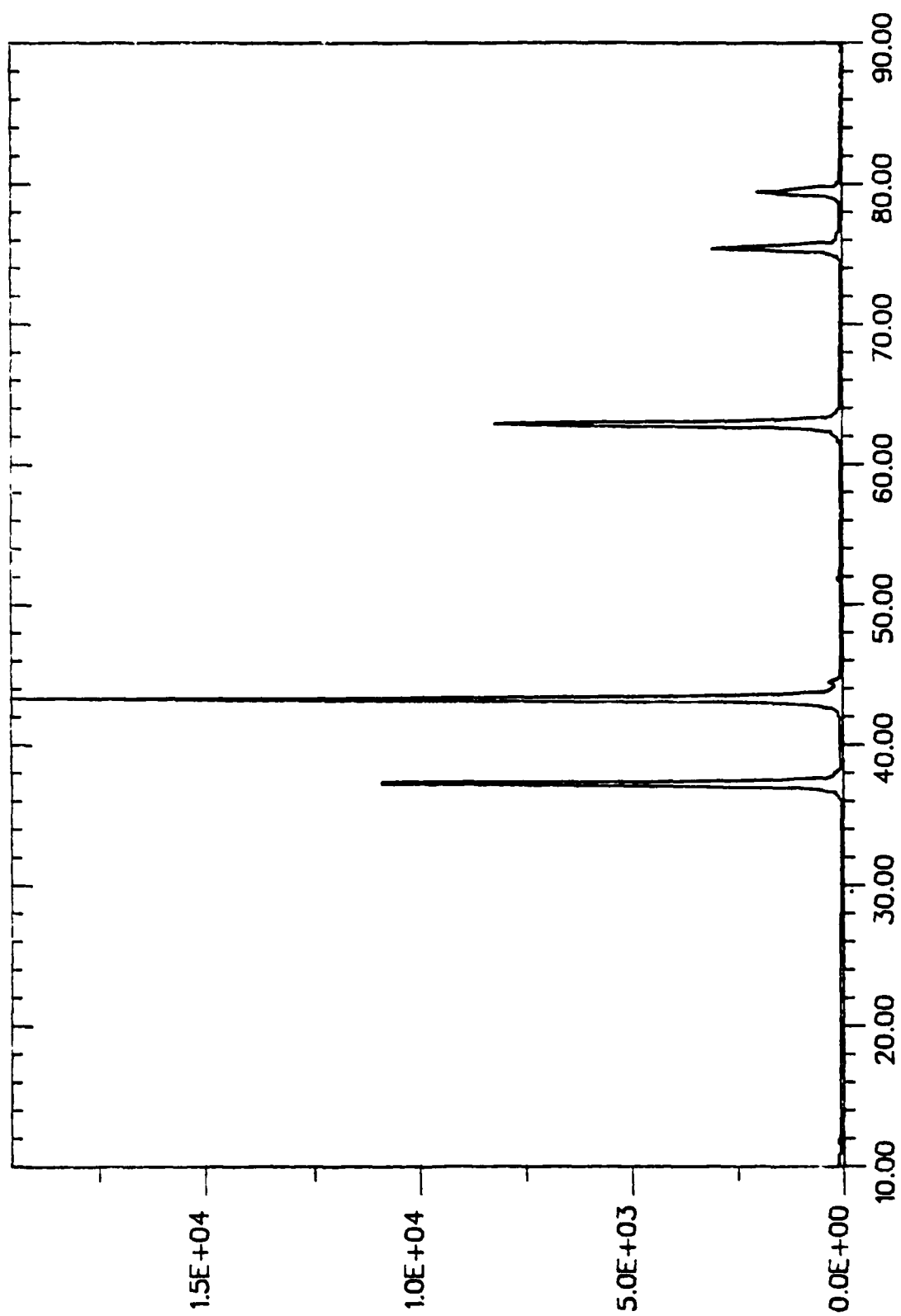


Fig. 2a

689

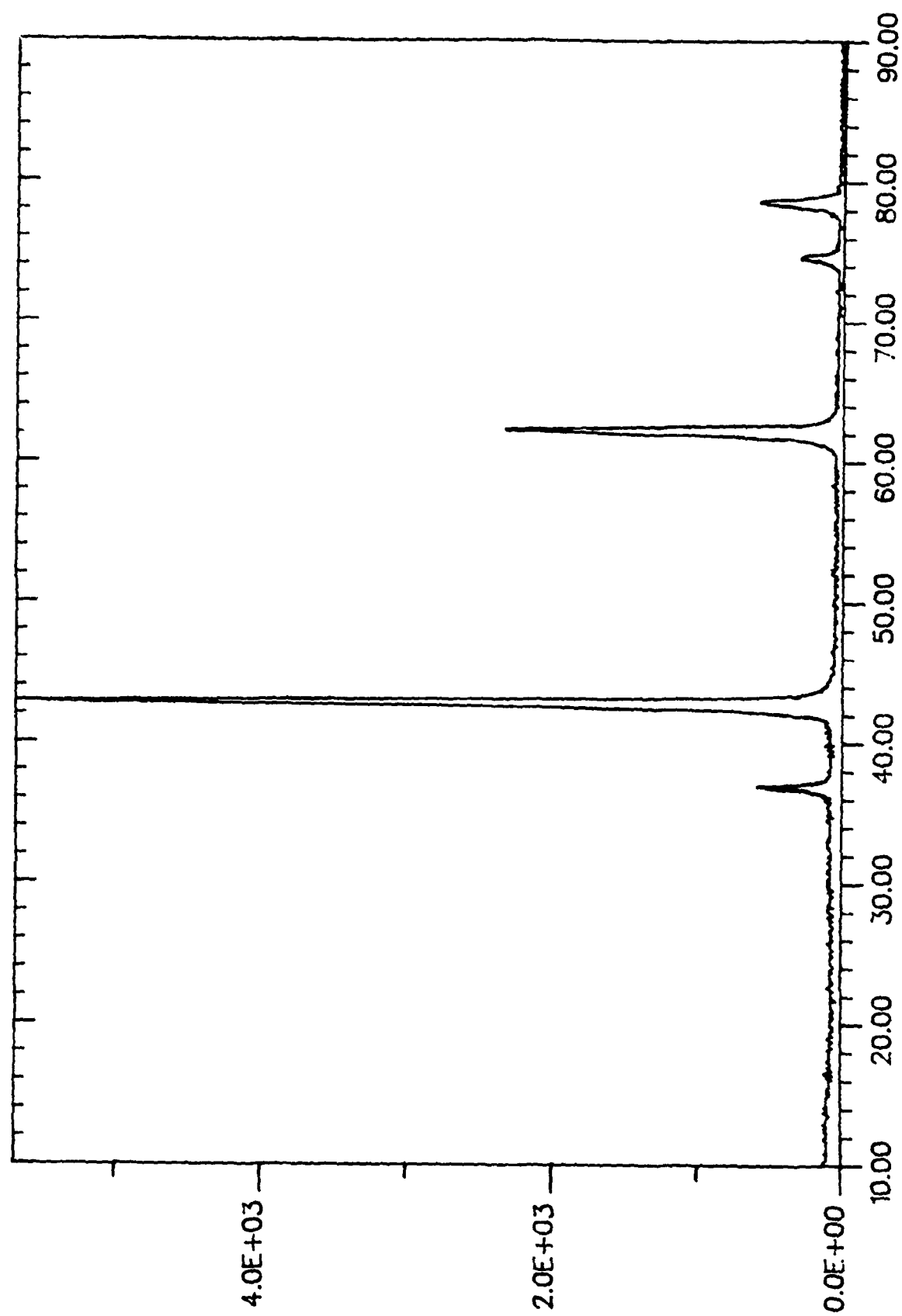


Fig. 2b

069

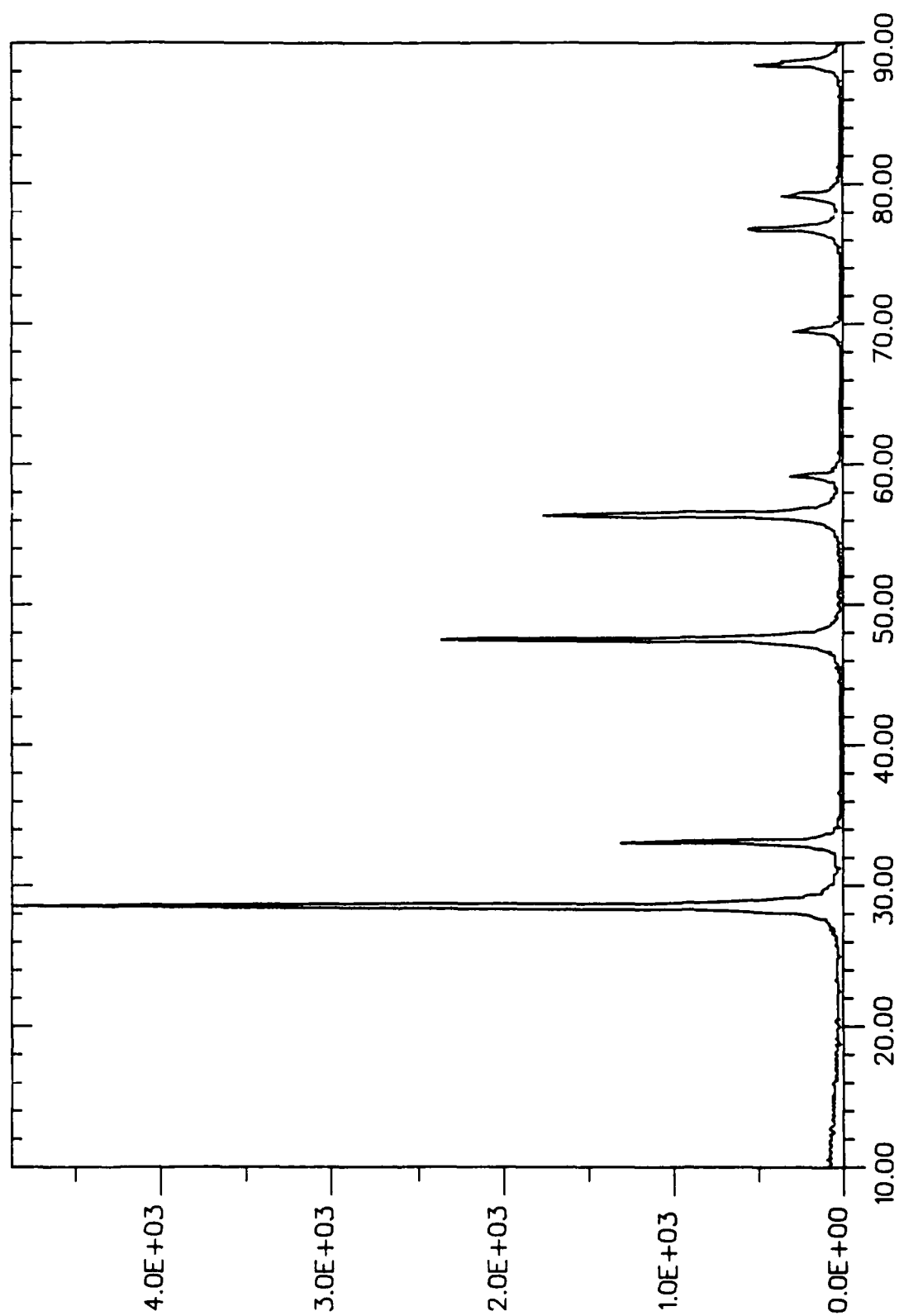


Fig. 2c

169

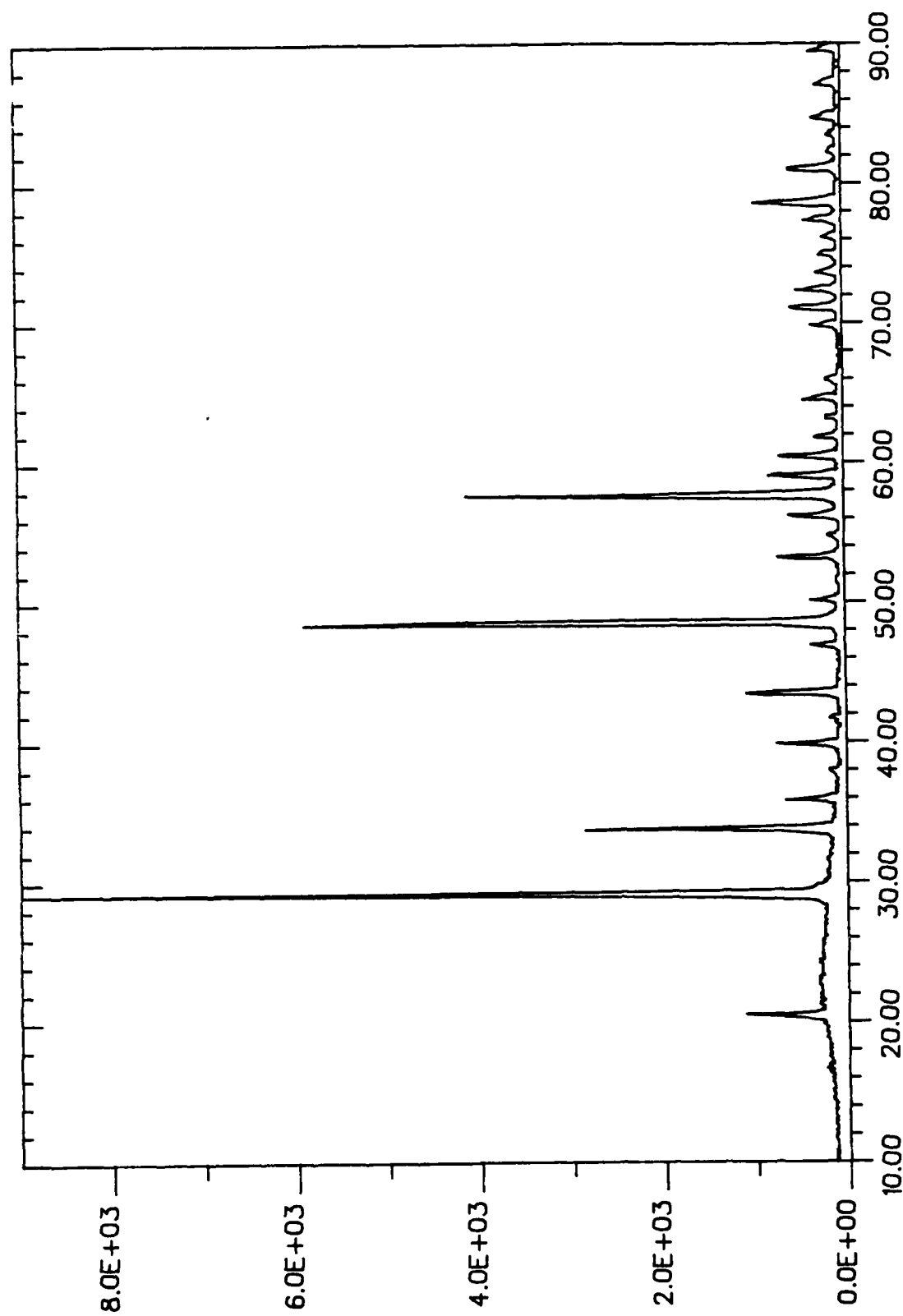


Fig. 2d

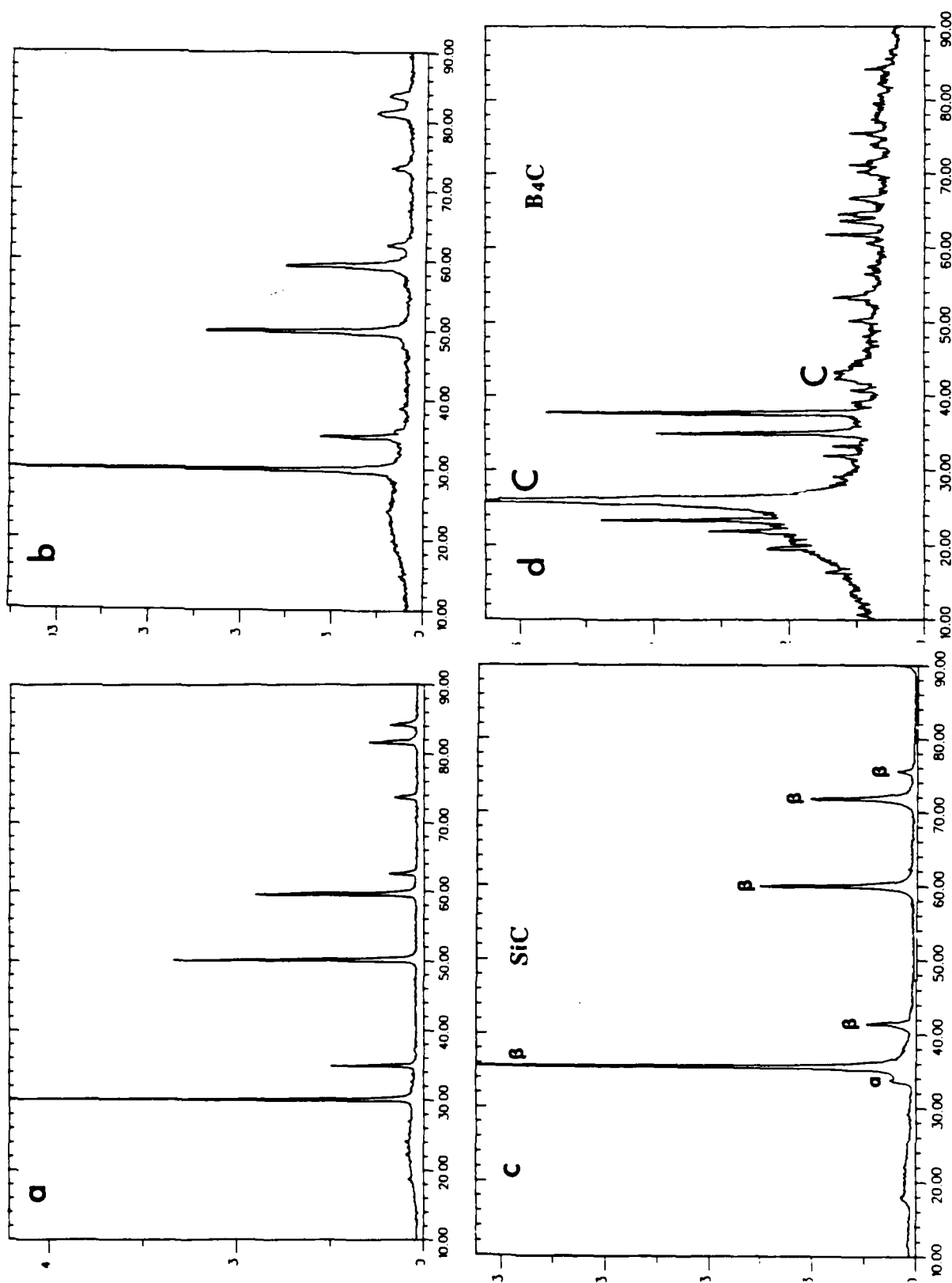


Fig. 3. X-ray diffraction profiles for (a) 9 mole % Y_2O_3 , (b) 1 mole % CeO_2 / 9 mole % Y_2O_3 stabilized zirconia solutions, (c) SiC and (d) B_4C .

NOTE TO PUBLISHER

The pages that follow are original photographs of figures already included in manuscript.

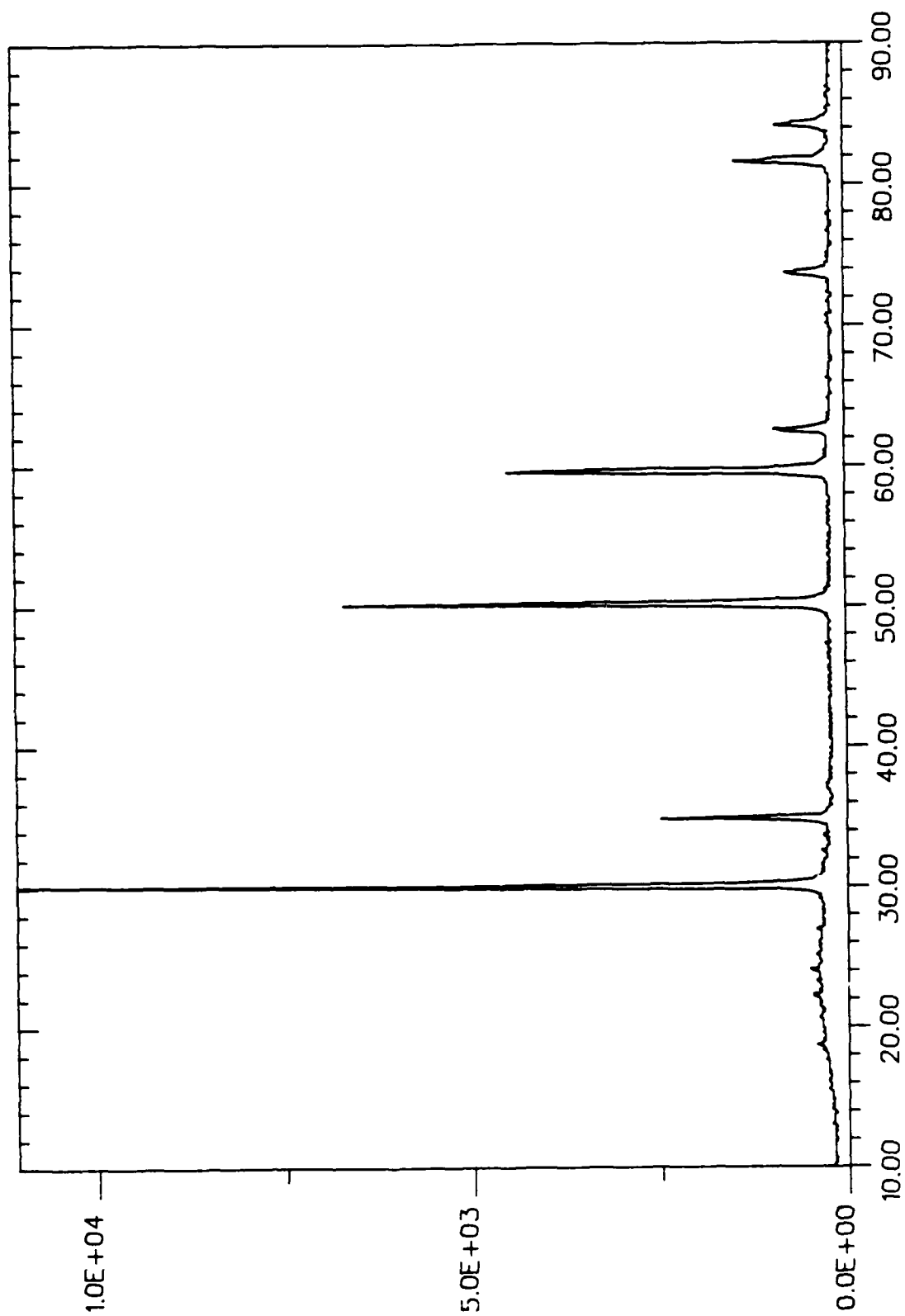


Fig. 3a

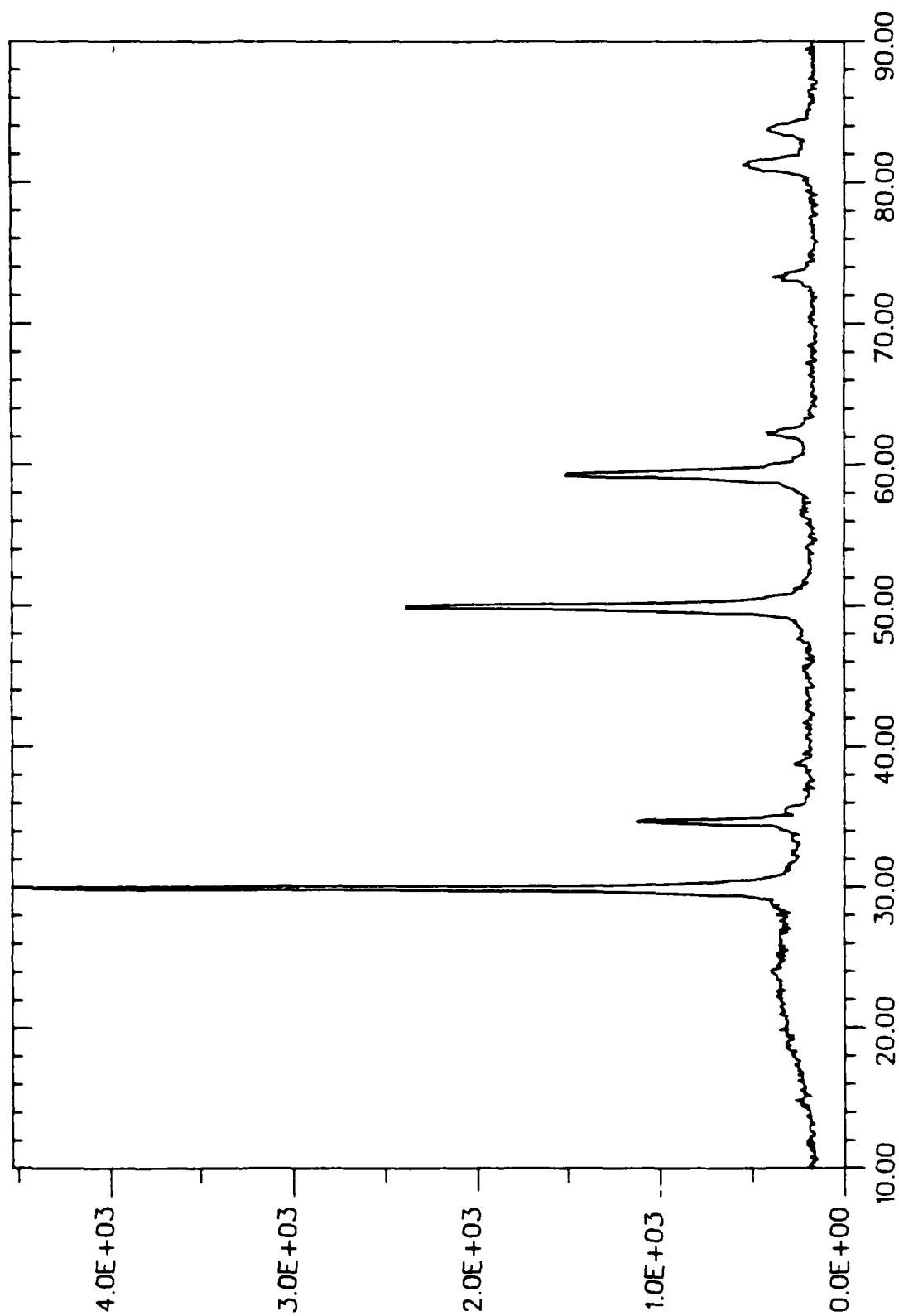


Fig. 3b

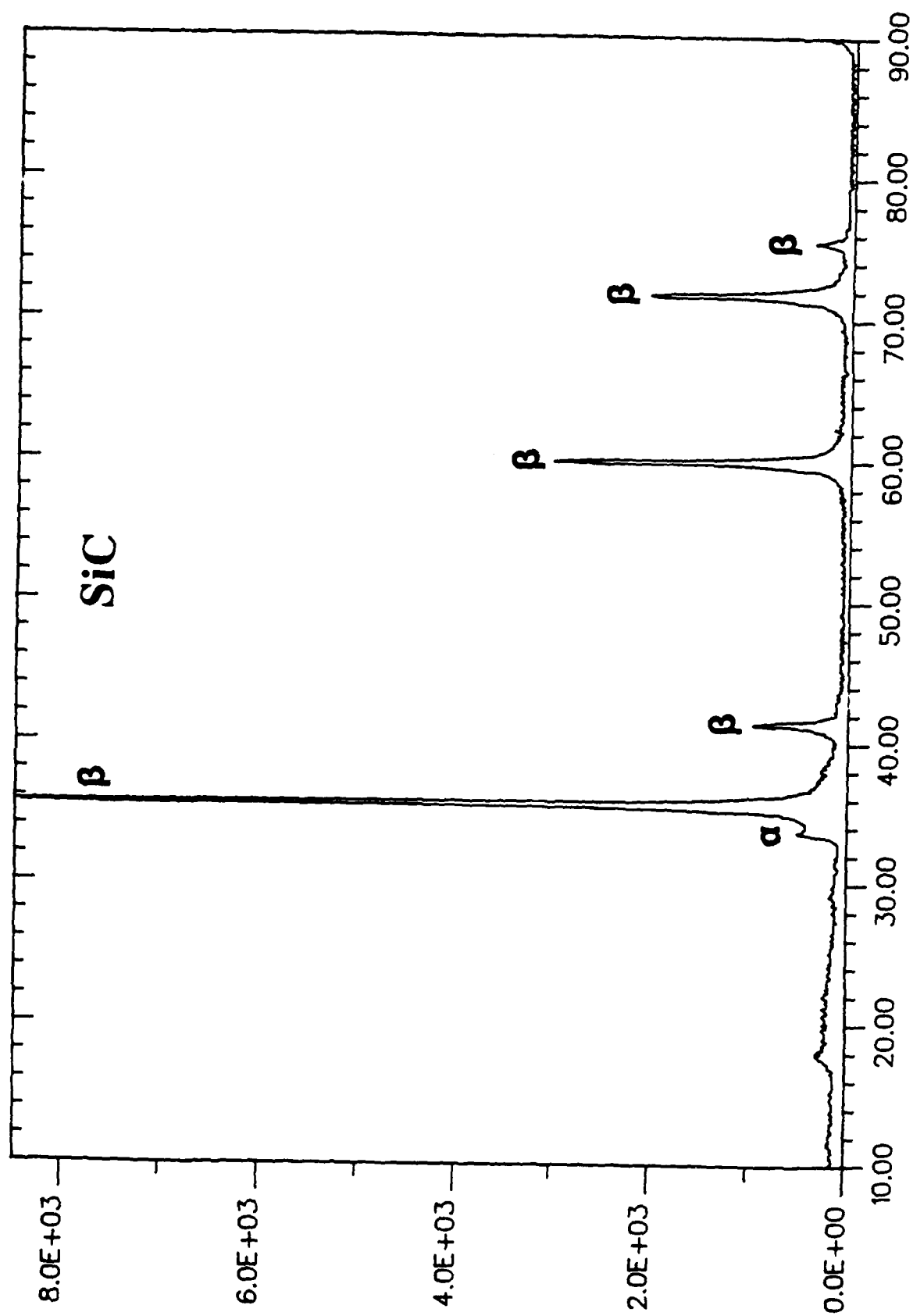


Fig. 4a

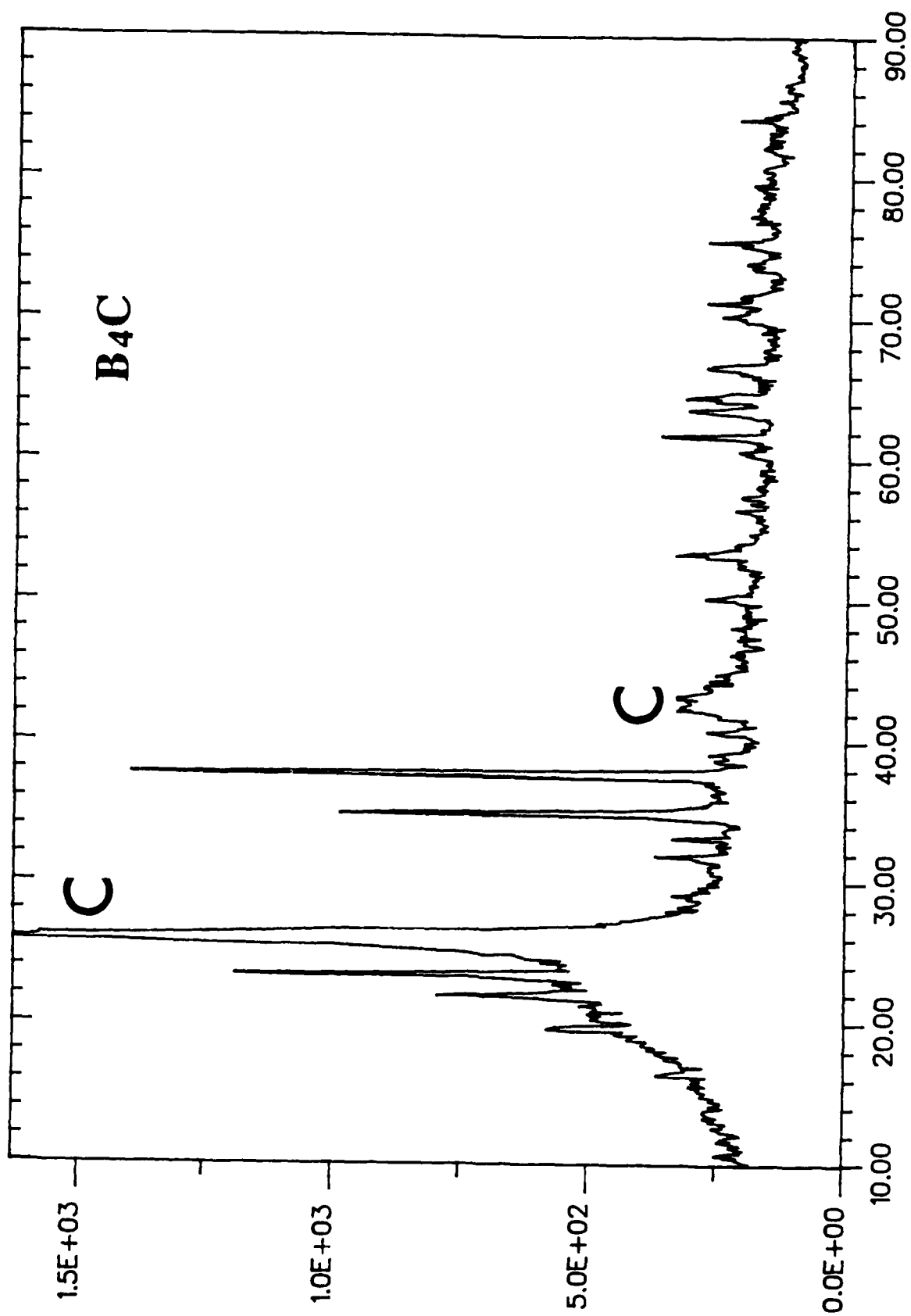


Fig. 4b

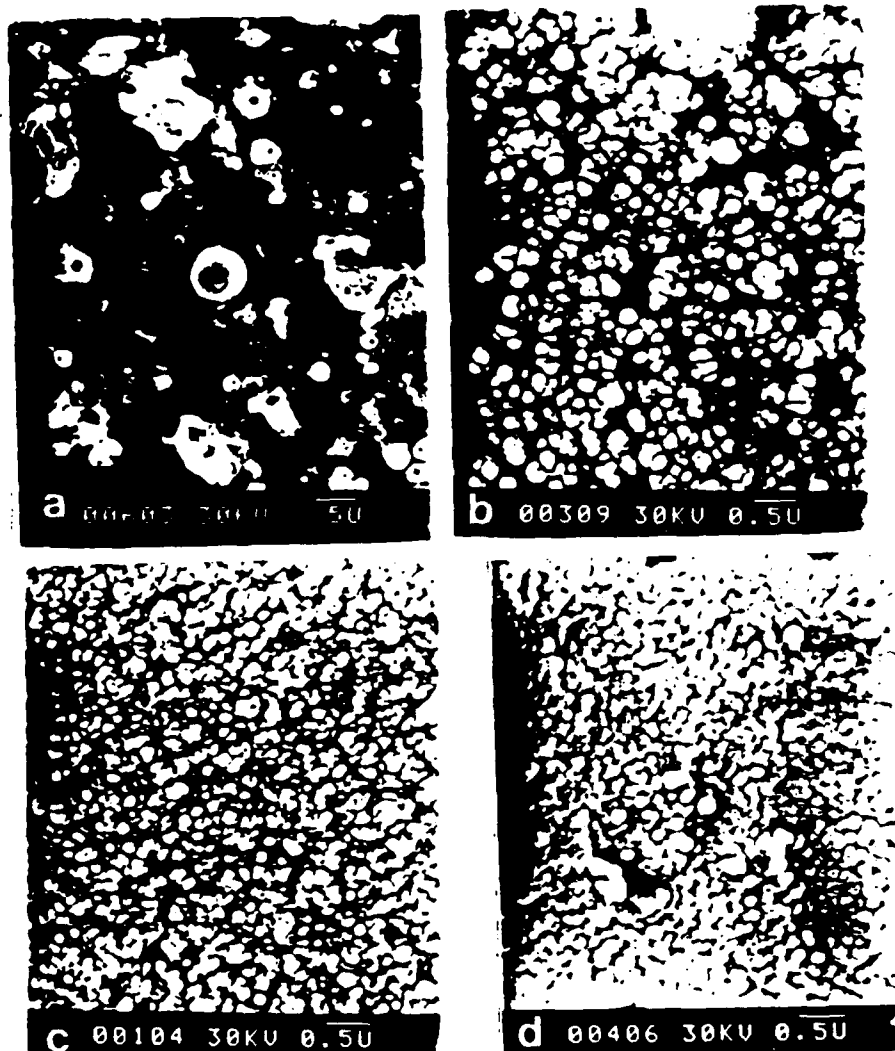
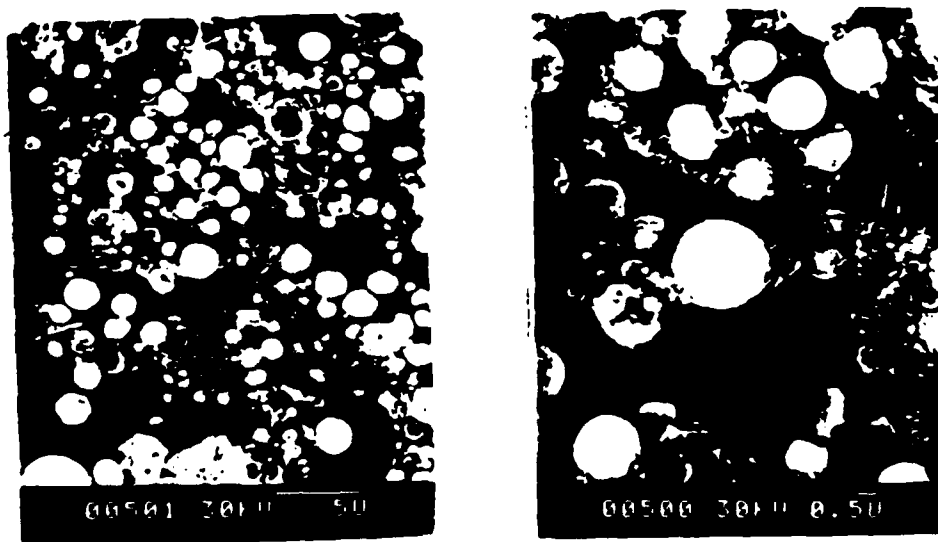


Fig. 4. SEM micrographs for CeO , NiO , MgO , and Y_2O_3 .



5b

Fig 5a SEM micrographs of fully stabilized zirconia.

APPLICATION OF NON-EQUILIBRIUM GAS DYNAMIC TECHNIQUES TO THE PLASMA SYNTHESIS OF CERAMIC POWDERS

John S. McFeaters¹ and John J. Moore²

¹ Mechanical Engineering Department, University of Auckland, Auckland, New Zealand

² Chem. and Mat. Engineering Department, University of Auckland, Auckland, New Zealand

ABSTRACT In some plasma processing applications the products can be meta-stable with regard to stoichiometry and phase structure. The key to the formation of these products is a rapid rate of cooling which essentially freezes in the desired stoichiometries and phases. The required cooling rates are on the order of 10^6 K/s. Theoretical work suggests that it may be possible to use gas dynamic techniques on plasma synthesized products to achieve these rates of cooling. At such high rates of cooling non-equilibrium effects strongly influence chemical reaction rates, molecular energy transfer, nucleation, condensation and heat transfer processes. A theoretical model has been developed to account for these effects and implemented into a computer program to model the process.

1. INTRODUCTION There has been much recent work which demonstrates that it is possible to use plasma processing in a wide variety of areas including the synthesis of engineering ceramics, spheroidization of particles and extractive metallurgy. In some applications the products can be meta-stable with regard to stoichiometry and phase structure. An example of such a product would be the reduction of tungsten oxide in an Ar/CH₄ plasma to beta-phase tungsten carbide^{1,2}. While these products may be thermodynamically favored at high temperatures, they are meta-stable at room temperature and, consequently during cooling from the reaction temperature, may suffer unacceptable degradation in quality. The key to the production of these meta-stable products is a rapid rate of cooling from formation temperatures to temperatures at which there is no degradation. This cooling essentially freezes in the desired stoichiometries and phases. The cooling rates required are on the order of 10^6 to 10^8 degrees Kelvin per second^{1,3-6}.

There are many potential advantages to using this type of process. The rapid cooling inhibits reverse reactions so that metal oxides could be used directly as reactants to produce metal nitrides, borides and carbides. The rapid cooling also allows for the production of particles with unusual phases and geometries^{1,3,4,6,7} and it has also been proposed that the rapid cooling could also be used as a means of preventing reverse reactions in the extractive metallurgy of elements such as aluminum and magnesium⁸.

Theoretical work suggests that it may be possible to use gas dynamic techniques, i.e. expansion through a nozzle, on plasma synthesized products to achieve the required rates of cooling in a process that has the potential for a high throughput. At these high rates of cooling, non-equilibrium effects strongly affect the progress of chemical reactions as well as molecular energy transfer and nucleation, condensation and heat transfer processes. A theoretical model has been developed to account for these effects and implemented into a computer program to model the process. An example has been done using methane to reduce titanium dioxide and form titanium carbide.

2. BACKGROUND In many of the plasma processing experiments, the technique has been to pass the reactants and an inert carrier gas through either a transferred arc plasma or an RF plasma. The source of the metal is often a powdered metal, a metal oxide or a gaseous metal halide. The metal is usually a transition metal. Carbon is generally used as the reducing agent and the most common source is methane. Excess methane or an alternative source of carbon can be used to produce metal carbides, or a source of nitrogen or boron can be used to produce metal nitrides and borides^{4,9,10}. The reactant stream also usually includes a substantial

mass fraction of an inert gas. The reactant mixture is heated to high temperatures where the process is dominated by gas phase reactions. The gas temperatures in the hottest parts of the plasma are usually in the 5,000 K to 10,000 K range. While these temperatures are higher than needed for the desired reactions to occur, they are necessary to maintain the plasma and also, in the case of powdered reactants, to help vaporize the particles during the short residence time in the plasma flame. The reactions continue after leaving the plasma and a considerable fraction of the product formation occurs when the product stream begins to cool after passing through the hot spot of the plasma. Many materials, such as titanium carbide in the presence of oxygen, are metastable at room temperature and pressure. Often, however, these materials are effectively highly stable because of large activation energies and concomitantly low reaction rates. The problem in the processing of these materials arises during cooling from plasma temperatures. Reverse reactions may become thermodynamically favored while temperatures are still relatively high. In this case reaction rates can be high enough to cause a significant degradation of the desired product and it becomes necessary to properly handle the products to preserve their integrity. In experiments, this is accomplished by rapid cooling using such techniques as impingement on a cooled copper plate, dilution by an inert gas or free expansion into a vacuum.

Experimental results suggest, that for many products, a cooling rate on the order of 10^6 K/s may be sufficiently rapid to quench undesirable reactions. Cooling rates up to 10^8 K/s can be achieved in practical systems by the use of cold gas entrainment, flow in cold wall tubes or by injection into fluidized beds^{11,12}. It may not, however, be possible for these techniques to be used in some applications because the exceptionally high rates of cooling are only achieved while the gases are at high temperatures. Extrapolation of results suggests that the actual cooling rates may be well below 10^6 K/s when the temperature of the product stream falls below 2000 K.

It is proposed here that adiabatic expansion through a converging-diverging, (De Laval), nozzle could be used as an alternative means to produce the high rates of temperature change required to preserve meta-stable products. In this process, the reactants are heated in a plasma and then expanded through a converging-diverging nozzle to freeze in the desired products. Theoretical work shows that it should be possible to achieve high enough rates of cooling to allow the use of metal oxides directly as reactants for the production of nitrides, borides and carbides and that it may also be possible to produce ceramic particles which are coated with a dissimilar metal in the same one step process^{13,14}.

A nozzle is essentially an adiabatic device. The total enthalpy of the flow does not change through the nozzle, rather energy is given up from the molecular modes of energy storage to the kinetic energy of the bulk flow. In a nozzle, the velocity of the gas increases continually from the inlet, reaches the sonic point near the throat and becomes supersonic in the diverging section. As the velocity increases the temperature and pressure drop. The average rate of cooling in a supersonic nozzle is on the order of 10^7 K/s and near the throat an order of magnitude higher than that. Because of this rapid cooling, there may be a large departure from chemical equilibrium and it becomes possible to freeze in chemical species which would normally be consumed by chemical reactions if the temperature change were to occur on a slower scale. At the end of the cooling process in the nozzle, the product stream will be moving at supersonic speed. In order to avoid reheating the products by shocking the flow back to subsonic, care must be taken in product recovery. It is proposed to exhaust the product stream into an expansion chamber maintained at a pressure lower than the exhaust pressure of the nozzle. A co-flowing stream of a cold gas which is inert with respect to the desired products can be used to lower the total enthalpy of the product stream.

Although in application, the materials used to construct the device would limit the pressures and temperatures, these limits may be quite high. Experimental work¹⁵ shows that it is possible to run a reactor/nozzle system continuously with supply pressures on the order of 100 atmospheres and temperatures near 6,000 K by cooling the reactor and the nozzle walls. Short component life would be offset by the characteristically high mass flow rates in nozzles. It may also be possible to separate the nozzle from the

plasma by some distance to increase the residence time of the reactants and overcome some of the problems associated with solid reactants and short residence times. This method would separate the recovery of products from the plasma process itself and could conceivably be applied to any type of plasma reactor.

In any non-equilibrium system, the state of the system at any given time is a function of its entire history. Species concentrations in a non-equilibrium system depend not only on the temperature and pressure of the system, but at what rate the temperature and pressure were changed from the time the system is initially disturbed from equilibrium until the time in question.

At the high cooling rates associated with nozzle flows it is necessary to consider energy transfer on a molecular level. In molecules, energy is distributed in translational, rotational, vibrational and electronic modes. As the temperature of a gas is lowered, the distribution of energy in the system will move towards a new equilibrium in accord with the ambient temperature and pressure. Translational and rotational modes equilibrate quickly, typically within several molecular collisions¹⁶⁻²¹. The transfer of energy from vibrational modes is usually an inefficient process and may require 10^1 to 10^{10} times as many collisions for relaxation to occur. Because of this, when the temperature of a gas is changed rapidly, there is often residual energy left in the vibrational modes. In this case, the vibrational temperature is higher than the ambient temperature of the gas, (temperature being a measure of the energy of a system). Because chemical reaction rates are strongly dependent on the vibrational temperature²²⁻²⁴, reaction rates can be much higher than would be expected at the given ambient gas temperature. If relaxation is slow for the vibrational modes, then even though the ambient temperature is reduced, there may still be an unacceptably high rate of reverse reactions¹³. Consequently, the rate of cooling of the vibrational modes is as important as the rate at which the overall gas temperature is lowered and slow vibrational relaxation can affect product yields^{13,22-24}.

The rate at which energy is transferred away from vibrational modes is strongly dependent on the mass of the collision partner¹⁶⁻²¹, with light molecules being far more effective than heavy ones. In systems with a high mole fraction of light molecules, the vibrational relaxation can be fast enough so that the vibrational temperatures are effectively the same as the ambient temperature. In the proposed process, the use of methane as a reducing agent has a two-fold purpose. It provides a source of carbon to reduce the oxide and form the carbide and it also provides a high mole fraction of hydrogen which is essential to cool the vibrational modes and quench reaction rates. Previous work¹³ shows that in these flows the vibrational temperatures are maintained within a few degrees of the ambient temperature. The presence of light molecules is also important during condensation to cool the droplets as they grow because of the high enthalpies of vaporization of ceramics. This allows for high condensation rates and rapid cooling of the condensed mass which can result in meta-stable phases.

3. MODEL Flow in the nozzle was assumed to be quasi-one-dimensional, steady state and adiabatic and transport effects were not considered. The gas was assumed to behave as an ideal gas and local properties were calculated from spectroscopic data under a rigid rotor-harmonic oscillator approximation. Initially a chemical reaction mechanism of 64 reactions and 21 species was considered. However, this was reduced to a system of 12 reactions and 12 species. Comparison of results indicated that this smaller system could adequately describe the reactions at temperatures above 1600 K. The process was designed to finish all condensation and reaction processes above this temperature. Argon was included as an inert gas to increase the heat capacity of the system per mole of reactant species. The increase in thermal mass by addition of the inert gas allowed for the condensation process to occur faster and to finish at a higher pressure. Chemical reaction rates were taken from existing data wherever possible. The rates for the reactions involving gas phase titanium and titanium carbide were estimated using transition state theory^{13,25}. The set of reactions and reaction rates are given in Table I.

Nucleation in the system was modeled using the classical theory which is based on the capillarity approximation²⁶. The classical theory assumes that the thermodynamic properties of the microclusters formed during nucleation have similar thermodynamic properties to the bulk fluid. It was assumed that the classical rate of nucleation is correct to within a multiplicative factor^{27,31} referred to as the replacement factor, Γ . The range of values suggested for the replacement factor vary over 17 orders of magnitude, however, several researchers^{26,28,31} suggest a moderate value of 10^3 . Direct experimental values were not available for the system under study. However, comparison with tables²⁹ of experimental values for species with similar degrees of supersaturation, critical nuclei size and mass fraction of condensing species suggested a correction factor of between 10^{-2} and 10^{+5} . The actual value was shown to be relatively unimportant in this system and a value of 1.0 was used for most cases. The classical rate of nucleation is given as³⁰,

$$J_{cl} = 5.4 \cdot 10^{33} \left[\frac{P_v}{T} \right]^2 \frac{(\sigma - \mu_v)^{1/2}}{\rho_c} \exp \left[\frac{-n^* \ln(S)}{2} \right] \frac{\#nuclei}{m^3 s} \quad (1)$$

Where the critical number of molecules and radius are given by

$$n^* = \left[\frac{4\pi}{3} \right] \rho_c \left[\frac{N_A}{\mu_v} \right] (r^*)^3 \quad r^* = \frac{2\sigma\mu_v}{\rho_c RT \ln(S)} \quad (2) (3)$$

Because of the high surface tension of titanium carbide a significant degree of supersaturation is required for the formation of nuclei. As a result, it is possible for the gas in the plasma to become highly supersaturated with titanium carbide before nucleation occurs. This is important because the vapor pressure of titanium dioxide is much higher than that of titanium carbide. When titanium dioxide is vaporized with a source of carbon, gas phase reactions occur to form gaseous titanium, titanium carbide and carbon monoxide. The partial pressure of titanium carbide is then much higher than could be achieved by direct vaporization of titanium carbide. This supersaturated concentration is maintained without nucleation and subsequent condensation until a significant degree of undercooling occurs and raises the supersaturation to a critical level.

In this model, nucleation was considered only for titanium carbide. This species reached critical supersaturation at a temperature well above any other species. It was assumed that the other species then condensed onto the existing titanium carbide nuclei in a heterogeneous process. As the other species, i.e., gaseous titanium and carbon, condensed on to the existing nuclei, their partial pressures were lowered enough so that they never reached sufficient supersaturation for homogeneous nucleation.

The presence of a large mole fraction of hydrogen was important during the condensation process. The high mole fraction of light molecules and the concomitantly high heat transfer rate maintained the droplet temperature at or near the ambient gas temperature during the condensation process.

The rate at which a species condenses to a droplet depends on the partial pressure of the condensing species in the atmosphere surrounding the droplet and the equilibrium vapor pressure of that species over the droplet. The vapor pressure of a species over a droplet depends on the temperature and also the radius of the droplet because of surface tension effects. If the vapor pressure of a species over the droplet is greater than its partial pressure in the surrounding atmosphere, the species will not condense. The ratio of these pressures can be used to estimate the effective number of condensing to non-condensing collisions for a species.

The stoichiometry of a droplet can greatly influence the vapor pressures of its individual component species over the droplet. This can affect the rate at which each species condenses to the droplet from the surrounding atmosphere and thus can affect droplet stoichiometry by allowing preferential condensation of one species over another. This applies to titanium and carbon. Figure 1 show that any deviation from a one to one ratio of carbon to titanium will result in lowered vapor pressure of the lesser species

over the droplet. The resulting effect tends to maintain the stoichiometry of the particle near a one to one ratio. This stoichiometric influence on vapor pressure may explain why some experimental results¹ show products with stoichiometries near a one to one ratio of metal to carbon even though these stoichiometries are favored over only a very narrow range of conditions.

For an ideal gas flow in a nozzle the fluids equations may be written as³²,

$$\text{Continuity} \quad \rho u A = \text{Constant} \quad (4)$$

$$\text{Momentum} \quad \rho u \left(\frac{du}{dx} \right) = - \left(\frac{dP}{dx} \right) \quad (5)$$

$$\text{Energy} \quad h + u^2/2 = h_0 \quad \text{where, } h = h(T) + h_f^0 \quad (6)$$

$$\text{State} \quad P = \rho R T \quad (7)$$

The coupling between fluid motion, chemical reaction and condensation is through the properties of the fluid. In the final form the governing equations may be written as¹³,

$$\frac{du}{dx} = \frac{u}{(M^2 - 1)} \frac{1}{A} \frac{dA}{dx} + \frac{u}{(M^2 - 1)} \sum_i^{\text{vap}} \left\{ \left(\frac{h_i}{C_{pT}} - \mu_i \right) \frac{d\phi_i^v}{dx} \right\} + \frac{u}{(M^2 - 1)} \sum_k^{\text{con}} \frac{h_k}{C_{pT}} \frac{d\phi_k^c}{dx} \quad (8)$$

$$\begin{aligned} \frac{dT}{dx} = & \frac{-u^2}{(M^2 - 1)C_{pT}} \frac{1}{A} \frac{dA}{dx} - \frac{u^2}{(M^2 - 1)C_p} \sum_i^{\text{vap}} \left\{ \left(\frac{h_i}{C_{pT}} - \mu_i \right) \frac{d\phi_i^v}{dx} \right\} \\ & - \frac{u^2}{(M^2 - 1)C_p} \sum_j^{\text{con}} \frac{h_j}{C_{pT}} \frac{d\phi_j^c}{dx} - \sum_k^{\text{vap}} \frac{h_k}{C_p} \frac{d\phi_k^v}{dx} - \sum_m^{\text{con}} \frac{h_m}{C_p} \frac{d\phi_m^c}{dx} \end{aligned} \quad (9)$$

$$\frac{dp}{dx} = \frac{-p_T}{A} \frac{dA}{dx} \left(1 + \frac{1}{(M^2 - 1)} \right) - \frac{p_T}{(M^2 - 1)} \sum_i^{\text{vap}} \left\{ \left(\frac{h_i}{C_{pT}} - \mu_i \right) \frac{d\phi_i^v}{dx} \right\} - \frac{p_T}{(M^2 - 1)} \sum_k^{\text{con}} \frac{h_k}{C_{pT}} \frac{d\phi_k^c}{dx} \quad (10)$$

$$\text{Where } M^2 = \frac{u^2}{(\gamma R T)} \quad R = R \sum_i^{\text{vap}} \phi_i^v \quad \sum_i^{\text{vap}} \phi_i^v = \frac{1}{\mu_T} \quad (11) (12) (13)$$

And the rate of change of chemical species in the gas phase is given as,

$$\frac{d\phi_i^v}{dx} = \left(\sum_m^{\text{Chem Rx}} \{ [A_m] [B_m] k_f - [\phi_i] [D_m] k_b \} - l(\phi, T, g) \right) \cdot \frac{1}{u} \quad (14)$$

Where $l(\phi, T, g)$ is the rate of loss to the condensed phase which includes both nucleation and condensation and the summation is over all chemical reactions involving the i^{th} species. Condensation rates are given as,

$$Z_{\text{mol-nuc}} = \eta_{\text{con}} \pi r_{\text{nuc}}^2 \left(\frac{8kT}{\pi \mu_{\text{mol}}} \right)^{1/2} \left(\frac{N_{\text{nuc}}}{m^3} \right) \left(\frac{N_{\text{mol}}}{m^3} \right) \frac{\text{molecules}}{m^3 s} \quad \eta_{\text{con}} = \left(1 - \frac{P_d}{P_v} \right) \quad (15) (16)$$

Which is the rate of molecular collisions based on kinetic theory using the radius of the nucleus, the speed of the molecule and an efficiency of condensation based on the ratio of the equilibrium vapor pressure of the species over the droplet to the partial pressure of the species in the atmosphere surrounding the droplet.

The nozzle geometries were modeled as axisymmetric hyperbolic with the variation in area following the relation,

$$A/A^* = (1.0 + x^2/L^2) \quad (17)$$

where A^* is the area of the throat, x is the distance from the throat and L is the ratio of the throat radius to the tangent of the half angle of the asymptotic cone. Inlet values for L were taken as 1.0 and exit values used varied between 5.0 and 14.0. The rate of temperature change in a nozzle is inversely proportional to the L value of the nozzle.

4. NUMERICAL SOLUTION The mathematical nature of the equations which describe the flow change from mixed hybrid-elliptic to hyperbolic³³ with a singularity at the sonic point which occurs near the throat. This means that downstream conditions affect the solution in the converging section of the nozzle. Reaction rates and nucleation are exponential functions of temperature which makes the set of equations numerically stiff.

Because it is a boundary value problem, there is only one admissible solution which will give supersonic flow in the diverging section of the nozzle. For a specified nozzle geometry and inlet conditions, the unknown parameter is the inlet velocity. This velocity is not known a priori because of the non-equilibrium nature of the flow. Instead a shooting method is used where an initial velocity is guessed and the equations integrated through the nozzle to see if the boundary conditions are met at the sonic point. In general this required a number of iterations to find the inlet velocity corresponding to the admissible solution. Numerical integration techniques have difficulties with singularities. To cross the sonic point, which is singular, the integration was stopped, an extrapolation made and the integration then restarted. In general, integrations were continued very close to the sonic point, about $M = 0.998$, and the extrapolation distances were on the order of 0.01 mm.

A 6th order multi-step predictor-corrector integration technique was used³⁴. During the integrations, mass flow, total system enthalpy and the ratio of species were monitored as a check on accuracy. The average relative variation of any of these quantities throughout the integration was on the order of one part per ten thousand.

5. RESULTS As this was a first investigation into the feasibility of a process, only the main physical parameters were varied to search for a set of conditions where this process could be effective. Because of the computational intensive nature of the problem and available computer time, only a limited number of cases could be considered. The physical parameters varied were nozzle geometry, initial temperature of the reactants and degree of inert gas dilution.

The program was run until the gas temperature in the nozzle had dropped to 1600 K. It was assumed that at this point the gas would be exhausted into the expansion chamber and the total enthalpy lowered by dilution with an inert gas. Although the cooling rates are still high at this point and the gas could be further expanded to lower temperatures quickly, the pressure starts to fall rapidly and the velocity of the gas increases. Both of these effects would serve to make the product stream more difficult to handle. On this basis it is desirable to complete all processes at the highest pressure possible.

The initial conditions were determined by assuming sufficient TiO_2 had been vaporized to reach its equilibrium vapor pressure at the specified temperature and that this was mixed with the specified mole fraction of methane and argon.

At 3900 K a stoichiometric quantity of TiO_2 and methane yields a gaseous mixture containing TiC and Ti at partial pressures of about 0.5 atm each with the remaining carbon bound as CH_x , C and C_2 and virtually no oxides of titanium. The supersaturation of TiC is about 11, however the nucleation rate is negligible. It is not until the reactants are highly supercooled that nucleation becomes significant. It was found that the presence of a high mole fraction of hydrogen inhibited the polymerization of carbon and the resulting concentrations of C_3 and higher carbons were negligible¹³. The initial concentrations at 3900 K and 13.9 atm pressure are given in Table II.

Figure 2 shows a plot of the natural logarithm of nucleation rate versus distance along the nozzle. The plot is for the region near the throat where the rate of temperature change is on the order of 10^8 K/s. The nucleation rate rises by a factor of 10^7 from 4 mm before the throat to a peak rate of 10^{24} nuclei/m³-s right at the throat. Over this distance the supersaturation rises from 20 to 100 and the minimum number of molecules to form a stable nucleus drops from 20 to about 10. Almost all nucleation occurs between 1 mm before and 1 mm after the throat. The loss of material from the gas phase lowers the supersaturation enough so that the rate of nucleation drops 20 orders of magnitude and no further nucleation occurs. Plotted along the bottom of the graph is the mass fraction condensed which begins to grow as condensation occurs to the existing nuclei. The only significant effect of varying replacement factor was to move the point at which peak condensation occurred in the nozzle by about a millimeter.

The effect of initial temperature on the process was considered. Lower initial temperatures are desirable from both an energy and a materials point of view. However, the temperature must be high enough that there is a significant partial pressure of reactants. Equilibrium calculations indicated that a minimum temperature of approximately 3800 K would be needed to provide a sufficient partial pressure of titanium bearing species. A comparison of results between 3800 K and 3900 K is given in Table III. Higher initial temperatures which have higher initial pressures result in larger particle sizes. An initial temperature of 3900 K gave satisfactory results and was used throughout the rest of this study.

Figure 3 shows a plot of temperature and mass fraction condensed versus distance along the nozzle. The temperature rises during condensation because of the high enthalpy of vaporization for titanium carbide. This temperature rise slows the condensation process. Table IV shows a comparison of dilution by Argon at 0, 3 and 6 moles per mole of titanium. The effect of dilution is to increase the heat capacity of the product stream which limits temperature rise during condensation. This allows condensation to occur more quickly in the nozzle and finish at a higher total pressure. This is important because higher exhaust pressures represent less pump work required in the process. A dilution of 3 to 1 appeared to give satisfactory results. No dilution allowed for too high a temperature rise during condensation and higher dilutions increase the energy required to heat the reactants.

The third physical parameter considered was the nozzle geometry in the diverging section. Inlet nozzle geometry has only a secondary effect because little happens until just before the throat. The exit nozzle geometry has the largest effect on the cooling rates in the nozzle. The steepest exit cone angles gave an average cooling rate of approximately 20×10^6 K/s while the shallowest angle had an average cooling rate of 7×10^6 K/s. Table V shows a comparison of different nozzle exit geometries. The main effect is the fraction of titanium which remains uncondensed. The nozzle with the highest L value, (shallowest angle), has the least amount of titanium which remains uncondensed at about 0.2 percent while particle size is relatively unaffected by the angle. A nozzle with a shallow exit cone would be preferable in order to allow for more complete condensation.

Deviation from an initial carbon to titanium ratio of 3.0 was not considered. A lower ratio may not provide enough carbon to completely reduce the metal oxide and a higher ratio could result in the polymerization of carbon and soot formation.

6. CONCLUSIONS The results obtained indicate that this technique could be a viable process for the treatment of product streams in plasma processing. Although there were a number of assumptions made in the modeling of this process, the largest unknown was the replacement factor for the nucleation rate and this parameter was shown to be of only secondary importance. An initial temperature in the range of 3800 to 4000 K was found to produce good results and is typical of the average temperature of flow from a plasma since only a part of the reactants actually pass through the hot spot and are heated to the 10,000 K range.

The use of methane as a reducing agent was shown to be important because it also provided a source of hydrogen. A large mole fraction of hydrogen was necessary to cool both the vibrational modes of energy storage and droplets during condensation. Without this source of hydrogen, chemical reaction rates would remain high even though the ambient gas temperature is reduced and the

condensation process would take an order of magnitude longer because of heating due to the high enthalpy of vaporization of titanium carbide. The hydrogen also inhibits the polymerization of carbon to form soot.

The by products of this process are primarily CO, H and H₂ which could be catalyzed into a number of secondary products. The high cooling rates and rapid condensation suggests that this process could also be applied to extractive metallurgy. By addition of only enough carbon to reduce the metal oxide and the addition of a source of nitrogen or boron it may also be possible to produce metal nitrides and borides directly from metal oxides.

It was assumed that titanium and carbon atoms would condense onto existing TiC particles when their partial pressures were above their equilibrium partial pressure. This always occurred before either species reached a critical supersaturation for homogeneous nucleation to begin. This suggested that it may be possible to produce particles with coatings of dissimilar materials. For example in the TiC system, the addition of copper, which has a relatively high vapor pressure, would have little effect until an almost complete condensation of titanium and carbon has occurred. After the titanium and carbon have condensed onto the TiC particles and the temperature of the system is lowered further, the copper would condense onto the existing TiC particles in a heterogeneous process. This would produce copper coated titanium carbide particles. As with the titanium and carbon atoms, the copper will not reach a critical supersaturation because of the heterogeneous condensation. This process could apply to any species with relatively high vapor pressures such as silver, gold, indium or zinc. More than one coating species could be used in this process to produce alloyed coatings or coatings with concentrations which vary with the radius of the particle. Coated particles produced in this manner could have important applications, for example, where ceramics are used in a metal matrix.

REFERENCES

- 1.) P.C. Kong, M. Suzuki, R. Young, E. Pfender, *Plasma Chem. Plasma Process.*, 3, (4), (1982)
- 2.) R. Ronsheim, L.E. Toth, A. Mazza, E. Pfender, B. Mitrofanov, *J. Mat. Sci.*, 16, (1981), pp.2665
- 3.) R. M. Young, E. Pfender, *Plasma Chem. Plasma Process.*, 5, (1), (1985)
- 4.) O. Matsumoto, M. Konuma, Y. Kanzaki, *Proc. 4th Intl. Symp. on Plasma Chem.*, (1979)
- 5.) M. Moss, D.L. Smith, R.A. Lefever, *Appl. Phys. Lett.*, 5, (6), (1964)
- 6.) R. McPherson, *J. Mat. Sci.*, 8, (1973), pp. 851
- 7.) R. McPherson, *J. Mat. Sci.*, 8, (1973), pp. 859
- 8.) B. Karlovitz, U.S. Patent number 4,146,389
- 9.) O. Matsumoto, M. Konuma, Y. Kanzaki, *J. Less Common Met.*, 60, (1978), pp. 147
- 10.) O. Matsumoto, T. Asakura, M. Konuma, Y. Kanzaki, *High Temp. Sci.*, 10, (1978), pp.175
- 11.) W.M. Goldberger, J.H. Oxley, *A.I.Ch.E.J.*, 9, (6), (1963), pp.778
- 12.) M.P. Freeman, *Chem. E. Prog. Symp.*, vol. 67, num. 112, (1971), pp.85
- 13.) J.S. McFeaters, Ph.D. Thesis, Carnegie-Mellon University, Pittsburgh, Pa., 1986
- 14.) J.J. Moore, 1st Intl. Symp. on Comb. and Plasma Synthesis of High Temperature Materials, San Francisco, Oct., 1978
- 15.) D. Zonars, *AIAA*, 5, (1), (1967) pp.57
- 16.) J.W. Rich, Technical Report, CALSPAN Corp., June 1974
- 17.) V.D. Rusanov, A.A. Fridner, G.V. Sholin, *Vsp. Fiz. Nauk.*, 134, June 1981, pp185-235
- 18.) J.W. Rich, *Appl. Atomic Phys.*, 3, (1982)
- 19.) C.E. Treanor, J.W. Rich, R.G. Rehm, *J. Chem. Phys.*, 48, (4), (1978)
- 20.) J.T. Yardley, "Introduction to Molecular Energy Transfer" Academic Press, 1980
- 21.) C.B. Moore, *J. Chem. Phys.*, 43, (9), (1965)
- 22.) N. Basov, E. Belonov, V. Isalov, E. Markin, A. Praevskil, V. Romanenko, N. Ferapentov, *Sov. Phys. JETP* 41, (6), (1975), pp1017
- 23.) V.D. Rusanov, A.A. Fridman, *Sov. Phys. Dokl.*, 21, (12), (1976), pp.739
- 24.) V.D. Rusanov, A.A. Fridman, G.V. Sholin, *Sov. Phys. Dokl.*, 22, (12), (1977), pp.757
- 25.) J.W. Moore, R.G. Pearson, *Kinetics and Mechanism*, Wiley and sons, New York, (1981)
- 26.) A.C. Zettlemoyer ed., *Nucleation Phenomena*, Elsevier, 1977, pp.1
- 27.) ref. 26 pp. 325
- 28.) ref. 26 pp. 131
- 29.) ref. 26 pp. 390
- 30.) ref. 26 pp. 367
- 31.) P.P. Wegener, "Non-Equilibrium Flows, Part 1, Marcel Dekker, New York, 1969
- 32.) W.G. Vincenti, C.H. Kruger Jr., *Physical Gas Dynamics*, Robert E. Krieger, Huntington, New York, 1965
- 33.) J.A. Essers, *Computational Methods for Turbulent, Transonic and Viscous Flows*, Hemisphere Pub., 1983
- 34.) C.W. Gear, *Math. of Comp.*, (21), pp.97

TABLE I. Reactions and Reaction Rates

Reaction	Rate $m^3/mol \cdot s$
$CH_4 + M = CH_3 + H + M$	$k_f = 1.3 \cdot 10^{11} \cdot e^{-44,485/T}$
$CH_4 + H = CH_3 + H_2$	$k_f = 6.3 \cdot 10^7 \cdot e^{-5990/T}$
$H_2 + M = H + H + M$	$k_f = 2.2 \cdot 10^8 \cdot e^{-48,300/T}$
$CH_2 + Ti = TiC + H_2$	$k_f = 1.2 \cdot 10^3 \cdot T^{1.16} \cdot e^{-2500/T}$
$CH_2 + H_2 = CH_3 + H$	$k_f = 3.2 \cdot 10^6 \cdot e^{-3525/T}$
$CH_2 + H = CH + H_2$	$k_f = 3.2 \cdot 10^5 \cdot T^{0.7} \cdot e^{-2500/T}$
$CH + H = C + H_2$	$k_f = 6.3 \cdot 10^5 \cdot T^{0.5} \cdot e^{-4000/T}$
$CH_4 + CH = CH_2 + CH_3$	$k_f = 2.5 \cdot 10^5 \cdot T^{0.7} \cdot e^{-3000/T}$
$TiC + M = Ti + C + M$	$k_f = 6.8 \cdot 10^6 \cdot T^{0.5} \cdot e^{-64,071/T}$
$Ti + CH = TiC + H$	$k_f = 1.2 \cdot 10^4 \cdot T^{0.81}$
$Ti + C_2 = TiC + C$	$k_f = 1.2 \cdot 10^{12} \cdot T^{1.48} \cdot e^{-7035/T}$
$C + CH = C_2 + H$	$k_f = 6.3 \cdot 10^5 \cdot T^{0.5}$

TABLE II. Initial Concentrations

$T_0 = 3900 \text{ K}$, $P = 13.15 \text{ atm}$, $\rho = 0.737 \text{ kg/m}^3$
 $CH_4/TiO_2 = 3.0$, $Ar/TiO_2 = 3.0$

Species	Concentration
TiC	2.05 mol/kg
Ti	1.99
C	0.31
C ₂	0.75
H ₂	17.82
H	12.45
CH	0.085
CH ₂	0.021
CH ₃	0.066
CH ₄	0.007
CO	8.07
Ar	12.11

TABLE III. Effect of Initial Temperature on Condensing Flow

$L_{in} = 1.0$ $L_{exit} = 10.0$ $CH_4/TiO_2 = 3.0$
 $Ar/TiO_2 = 0.0$ Replacement Factor, $\Gamma = 1.0$

Initial Temperature	3800 K	3900 K	
Initial pressure, P_0	6.55	10.3	atm
Partial pressure TiC	0.305	0.483	atm
Supersaturation TiC	12.8	11.2	
Initial density, ρ_0	0.2477	0.3810	kg/m ³
Final particle size	0.026	0.039	μm
Ti (g)1600	2.0	1.7	%
(A/A [*])1600	25	26	
Final pressure, P_{1600}	0.0232	0.0344	atm

Note: The subscript 1600 refers to the point in the nozzle where the temperature of the gas was 1600 K. Ti(g) is the percentage of uncondensed titanium remaining in the gas phase.

TABLE IV. Effect of Inert Gas Dilution on Condensing Flow

$L_{in} = 1.0$ $L_{exit} = 10.0$ $CH_4/TiO_2 = 3.0$
 $T_0 = 3900 \text{ K}$ Replacement Factor, $\Gamma = 1.0$

Ar/TiO ₂	0.0	3.0	6.0	
Initial mass fraction Ar	0.0	0.483	0.652	
Initial mole fraction Ar	0.0	0.218	0.363	
Final particle size	0.039	0.035	0.034	μm
Ti (g)1600	1.7	0.38	0.15	%
(A/A [*])1600	26	15	11	
Final pressure, P_{1600}	0.0344	0.078	0.141	atm

TABLE V. Effect of Nozzle Exit Geometry Factor, L_e

$L_{in} = 1.0$ $CH_4/TiO_2 = 3.0$ $Ar/TiO_2 = 0.0$
 $T_0 = 3900 \text{ K}$ Replacement Factor, $\Gamma = 1.0$

Nozzle Geometry	$L_e = 5.0$	$L_e = 10.0$	$L_e = 14.0$	
Final particle size	0.0345	0.035	0.035	μm
Ti (g)1600	1.77	0.38	0.185	%
(A/A [*])1600	16	15	16	
Length throat to exit	19.4	37.4	54.2	cm
Final pressure, P_{1600}	0.075	0.078	0.076	atm

SYMBOLS

A	area
C_p	constant pressure specific heat
g	condensed mass fraction
h	enthalpy
J_{cl}	nucleation rate
k	Boltzmann constant
k_f, k_b	reaction rates
L	nozzle geometry factor
M	Mach number
n [*]	number of molecules in nucleus of critical size
N	number of molecules
P	thermodynamic pressure
P_d	equilibrium vapor pressure over a droplet
P_v	partial pressure of a species in the vapor phase
r^*	critical nucleus radius
R	gas constant
S	supersaturation
T	temperature
u	axial velocity in nozzle
x	distance along nozzle
Z	collision rate
ϕ	chemical concentration moles/kg
Γ	replacement factor
γ	ratio of specific heats
μ	molecular weight
ρ_v	density vapor phase
ρ_c	density condensed phase
α_{∞}	surface tension of bulk liquid

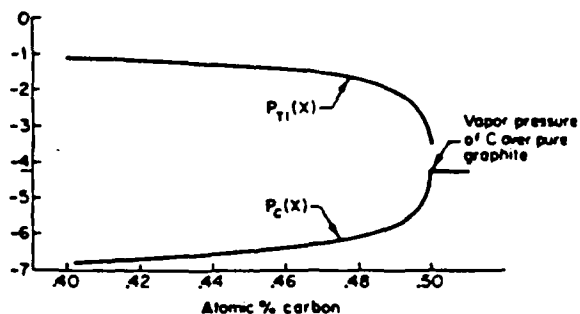


FIGURE 1A. Calculated vapor pressures of titanium and carbon over titanium carbide at 3000 K. (Reference - Transition Metal Carbides and Nitrides, L.E. Toth, Academic Press, pp. 136-137, 1971)

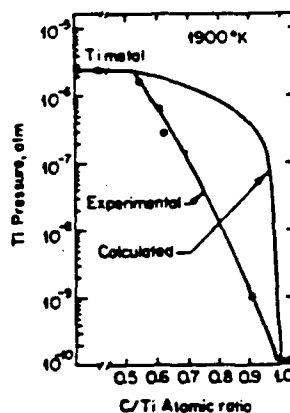


FIGURE 1B. Calculated vapor pressures of titanium over titanium carbide at 1900 K. (Reference - Transition Metal Carbides and Nitrides, L.E. Toth, Academic Press, pp. 136-137, 1971)

FIGURE 2. Nucleation data versus distance from the throat. $T_0 = 3900$ K, $L_{in} = 1.0$, $L_{exit} = 14.0$, $CH_4/TiO_2 = 3.0$, $Ar/TiO_2 = 3.0$, $\Gamma = 1.0$

- Δ \ln Nucleation rate $\#/m^3\text{-sec.}$
- \circ Supersaturation of TiC
- \square mass fraction condensed $\times 200$
- \times n^*

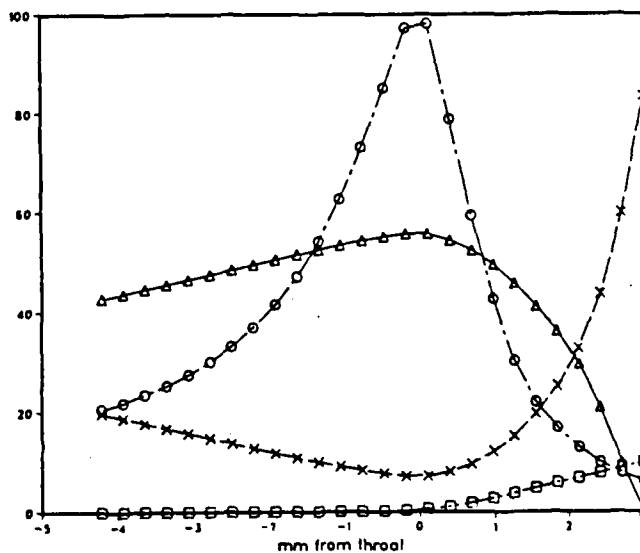
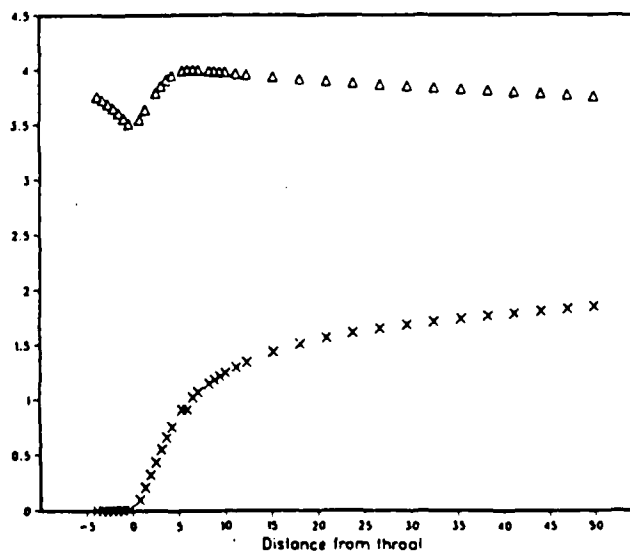


FIGURE 3. Temperature and mass fraction condensed versus distance from the throat. $T_0 = 3900$ K, $L_{in} = 1.0$, $L_{exit} = 14.0$, $CH_4/TiO_2 = 3.0$, $Ar/TiO_2 = 3.0$, $\Gamma = 1.0$

- Δ Temp $^{\circ} 10E-03$
- \times $g \cdot 10$



DEVELOPMENT OF TIN OXIDE COATINGS FOR USE AS ELECTRODES
IN MERCURIC IODIDE PHOTODETECTOR APPLICATIONS

A.K. Hays
R.C. Hughes
Sandia National Laboratories
Albuquerque, NM 87185

ABSTRACT

Plasma processing parameters and reactor configurations were evaluated for the production of visibly transparent, conductive tin oxide films at low temperatures. High-quality, mercuric iodide photodetectors were constructed having tin oxide electrodes deposited under more and less severe conditions. The relative quantum efficiencies of these detectors were measured.

INTRODUCTION

In this paper we determine plasma processing parameters for depositing thin, conductive, tin oxide films on HgI_2 substrates at relatively low temperatures. By developing low-temperature electrode deposition techniques, we hope to eliminate the adverse effects that heating has on both the transient and steady-state charge collection properties of the crystal under illu-

mination (trapping and polarization effects). In addition, we report relative quantum efficiency measurements as a function of wavelength for HgI_2 photodetectors possessing plasma-deposited electrodes.

EXPERIMENTAL

A schematic diagram of the plasma deposition apparatus is shown in Figure 1. Tetramethyltin, oxygen, and argon were admitted to the plasma chamber through calibrated leaks. Oxygen and argon were obtained from Matheson at stated purities of 99.997 and 99.999 %, respectively. Both gases were used without further purification. Tetramethyl tin was obtained from Fluka Chemie AG at a stated purity of 99.5 %. It was degassed prior to use by three freeze-pump-thaw cycles. The room temperature vapor pressure of liquid $\text{Sn}(\text{CH}_3)_4$ (120 Torr) was sufficient to provide gaseous $\text{Sn}(\text{CH}_3)_4$ for the experiments.

A radiofrequency (13.56 MHz) electric field was capacitively-coupled to the gaseous reactants through 14 cm-in-diameter, aluminum electrodes. The electrode spacing was 4.0 cm. Radiofrequency power densities of 0.065-0.975 watts/cm², were used to deposit the tin oxide coatings. Substrates, to be coated, were placed on the grounded, water-cooled, bottom electrode.

Two reactor configurations were used: (1) $\text{Sn}(\text{CH}_3)_4$ and O_2 mixed in the glow region (configuration A) and (2) $\text{Sn}(\text{CH}_3)_4$ and O_2 mixed prior to entering the glow region (configuration B). Tetramethyltin, oxygen, and argon flow rates were on the order of 0.5, 5, and 15 sccm, respectively. Gas pressures were measured using a variable capacitance manometer. The total pressure in the chamber was typically 91 Pascals (0.7 Torr). Under

these conditions film deposition rates of 2.5 nm/min and 75 nm/min were recorded for configurations A and B, respectively. It should be noted that it was necessary to use substantial amounts of argon back-ground gas in order to produce reasonably conductive coatings ($1-10 \Omega^{-1}\text{cm}^{-1}$). Other researchers¹ have reported the successful production of non-conductive, tin oxide films at room temperature using plasma deposition and gaseous mixtures of $\text{Sn}(\text{CH}_3)_4$ and O_2 . Using their plasma processing parameters we always produced copious amounts of powder (see Figure 2) with an average particle size of 0.25μ . This difference can probably be attributed to the fact that their substrates were placed outside of the glow region.

Mercuric iodide photodetectors were constructed by: (1) coating a sapphire substrate with carbon (Aquadag), (2) plasma-depositing a 5 mm-in-diameter tin oxide electrode on a HgI_2 crystal ($10 \times 10 \times 1$ mm), (3) attaching the coated HgI_2 crystal to the coated sapphire substrate with RTV silicone at two diagonal corners, and (4) attaching thin gold leads to the top and bottom electrodes with more Aquadag.

Photodetectors were coated under two sets of conditions chosen to be representative of more and less severe environments. In the most severe case a HgI_2 crystal (specimen C1) was thermally isolated from the water-cooled bottom electrode on a quartz pad. The crystal was under vacuum for 30 minutes and exposed to the rf plasma for 20 minutes. Furthermore, the stainless steel mask above the HgI_2 crystal was heated by ion and electron bombardment in the plasma resulting in crystal heating to $\sim 100^\circ\text{C}$. In the less severe case a HgI_2 crystal (specimen C2) was thermally connected to

the water-cooled electrode by a sapphire pad. The crystal was under vacuum for 10 minutes and exposed to the plasma for 2 minutes. The mask was made out of teflon and the crystal reached a temperature of $\sim 30^{\circ}\text{C}$.

The relative quantum efficiencies of the HgI_2 photodetectors were measured as a function of wavelength by comparing the photoresponse of the HgI_2 detectors to the calibrated responsivity as a function of wavelength of an EG&G SGD 200 photodiode. An Ealing 100 tungsten halogen light source was passed through a CVI Laser Digikrom 240 monochromator and focussed by a Newport F-917T multimode fiber coupler into a multimode fiber (50μ core) that was routed to a light-tight sample chamber. The detectors were mounted on a stage within the sample chamber to allow the measurement of their quantum efficiency as a function of position at a fixed wavelength. Photodetector outputs were measured using a Keithley 617 electrometer interfaced to an HP 300 series computer.

RESULTS AND DISCUSSION

In an attempt to determine the appropriate plasma processing parameters for the low-temperature deposition of tin oxide films, we began with reactive gas mixtures containing only $\text{Sn}(\text{CH}_3)_4$ and O_2 . In both reactor configurations (A and B) and over a range of $\text{Sn}(\text{CH}_3)_4:\text{O}_2$ ratios (1-4) and rf power densities ($0.065\text{--}0.422\text{ watts/cm}^2$) we obtained copious quantities of powder. We were able to obtain visibly transparent, conductive ($20\text{--}0.2\ \Omega^{-1}\text{cm}^{-1}$) films by the addition of argon to the reactive gas mixture. At a fixed rf power density and $\text{Sn}(\text{CH}_3)_4:\text{O}_2$ ratio the conductivity of the

films was seen to increase as the $\text{Ar}:\text{Sn}(\text{CH}_3)_4$ ratio was increased. At the same time the film deposition rate was observed to decrease. Recent studies² of the rf plasma deposition of thin SiO_2 on Si have shown that the use of a large inert gas to reactive gas ratio can produce films with few defects and excellent electrical properties. It is postulated that in these discharges energy is primarily channeled into the production of inert gas ions and metastables. The ions recombine with electrons producing UV radiation while the metastables collisionally excite the reactive gas molecules. These excited molecular species then dissociate at the solid/gas interface, as opposed to in the gas phase, aided by considerable UV irradiation.

It was also observed that at a fixed $\text{Sn}(\text{CH}_3)_4:\text{O}_2:\text{Ar}$ ratio, an increase in rf power density caused an increase in film deposition rate, a decrease in film conductivity, and a decrease in the optical transmission of the film in the visible region of the spectrum (the films were yellow). Examination of the infrared spectra of films deposited at a $\text{Sn}(\text{CH}_3)_4:\text{O}_2:\text{Ar}$ ratio of 1:9:25 and rf power densities of 0.45 watts/cm² (Figure 3(a)) and 0.58 watts/cm² (Figure 3(b)) revealed a large organic component in the film deposited at the higher power level. The ir spectrum of the film deposited at the lower power exhibits two broad features at 3330 and 540 cm⁻¹ that can be attributed¹⁶ to O-H stretching and Sn-O stretching, respectively. The IR spectrum of the film deposited at the higher power exhibits these features and four additional bands at 1610, 1370, 1290, and 990 cm⁻¹. These bands can be attributed³ to the C=O stretching, C-H in-plane bending, C-O stretching, and COO out-of-plane bending modes, respectively, in tin formate. It is postulated that the increased film

deposition rate at higher rf power levels buries the tin formate in the growing tin oxide film. At slower deposition rates Sn-C bond scission occurs and carbon is removed as CO₂.

Tin oxide electrodes were deposited using two different reactor configurations. Originally the reactive gases were mixed in the glow region. In this configuration film deposition rates were on the order of 2.5 nm/min and a crystal coating time of 20 minutes was used. When it was discovered that premixing the reactive gases, Sn(CH₃)₄ and O₂, gave deposition rates of 75 nm/min, it was possible to reduce the crystal coating time to 2 minutes and, in this way, reduce substrate heating.

Figure 4 shows the visible spectra of tin oxide films deposited on KBr substrates under conditions identical with those used to coat specimens C1 (Figure 4a) and C2 (Figure 4b). The transmissions of the films on specimens C1 and C2, at the peak (590 nm) of the HgI₂ photoresponse spectrum and normalized for the absorption of the KBr, were 88.8% and 95.4%, respectively.

Electron microprobe analysis of films deposited on Si substrates placed on the mask during HgI₂ crystal coating showed large quantities of iodine and lesser amounts of mercury incorporated in the films deposited under the more severe conditions. Both the I and Hg contents were substantially reduced in films deposited under the less severe conditions.

Figure 5 shows the relative quantum efficiency as a function of wavelength of a photodetector prepared from specimen C1. The observation of a peak photocurrent for this detector of ~1 nA, coupled with its low dark current (~10 pA), demonstrates that we have produced a

high-quality photodetector with a much better signal-to-noise than the best silicon detectors available in the 600 nm region of the spectrum. The relative quantum efficiencies of specimen C1 and a HgI_2 crystal having a transparent, liquid electrode were measured and were found to be comparable.

The quantum efficiency of both specimens C1 and C2, at a fixed wavelength, were observed to decrease with increasing irradiation time and increase with decreasing photon flux (polarization effect). Low-temperature photoluminescence experiments are planned to determine the nature of the defects giving rise to this effect.

SUMMARY

A range of plasma processing parameters and reactor configurations were evaluated for their suitability for producing visibly transparent, conductive tin oxide films at low temperatures. High-quality, mercuric iodide photodetectors were constructed having tin oxide electrodes deposited under more and less severe conditions. The relative quantum efficiencies of these detectors as a function of wavelength were measured. The quantum efficiencies of these detectors were found to be comparable to that of a photodetector having a transparent, liquid electrode. The polarization effects that we observed at high light intensities are also found for detectors having other electrode materials and are undoubtedly related to chemical or mechanical surface damage. A future goal of this program is to determine the deposition conditions that give the lowest surface damage and, hence, a detector with both high and laterally-uniform quantum efficiency.

ACKNOWLEDGEMENTS

The authors would like to acknowledge the invaluable technical assistance of G. Cordes, G. Gentry, and K. Pfeifer, as well as, many fruitful technical discussions with M. Butler and R. James. We would also like to thank EG&G, Santa Barbara Operations, for supplying us with HgI_2 crystals.

REFERENCES

1. S.K. Ghandi, R. Sivi, and J.M. Borrego, "The Growth of Tin Oxide Films at Room Temperature", *Appl. Phys. Lett.*, 34, 834 (1979).
2. J. Batey, E. Tierney, and T.N. Nguyen, "Electrical Characteristics of Very Thin Silicon Dioxide Deposited at Low Substrate Temperatures", *IEEE Electron Device Lett.*, 8, 148 (1987).
3. J.D. Donaldson, J.F. Knifton, and S.D. Ross, "The Vibrational Spectra of Some Tin (II) Carboxylate Complexes", *Spectrochim. Acta*, 21, 1043 (1965).

FIGURE CAPTIONS

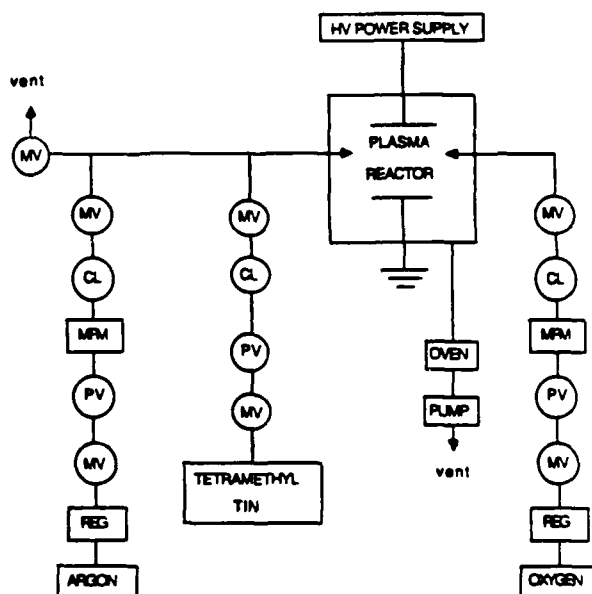
Figure 1. Schematic diagram of experimental apparatus: MV-manual valve, PV-pneumatic valve, CL-calibrated leak, REG-regulator, MFM-mass flow meter.

Figure 2. SEM micrograph of tin oxide powder. Plasma parameters: $\text{Sn}(\text{CH}_3)_4$ pressure-12.1 Pascals, O_2 pressure-52.0 Pascals, rf power density-0.42 watts/cm².

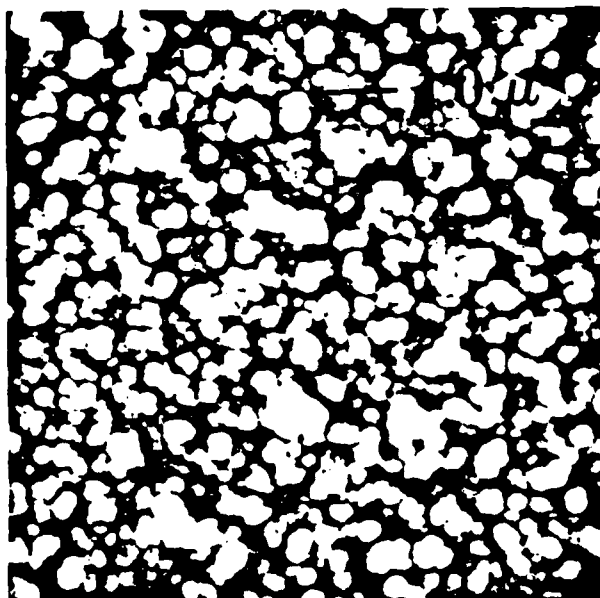
Figure 3. Infrared spectra of films deposited at a $\text{Sn}(\text{CH}_3)_4:\text{O}_2:\text{Ar}$ ratio of 1:9:25 and rf power densities of: (a) 0.45 watts/cm² and (b) 0.58 watts/cm².

Figure 4. Visible spectra of films deposited on KBr substrates under conditions identical with those used to coat specimens: (a) C1 and (b) C2.

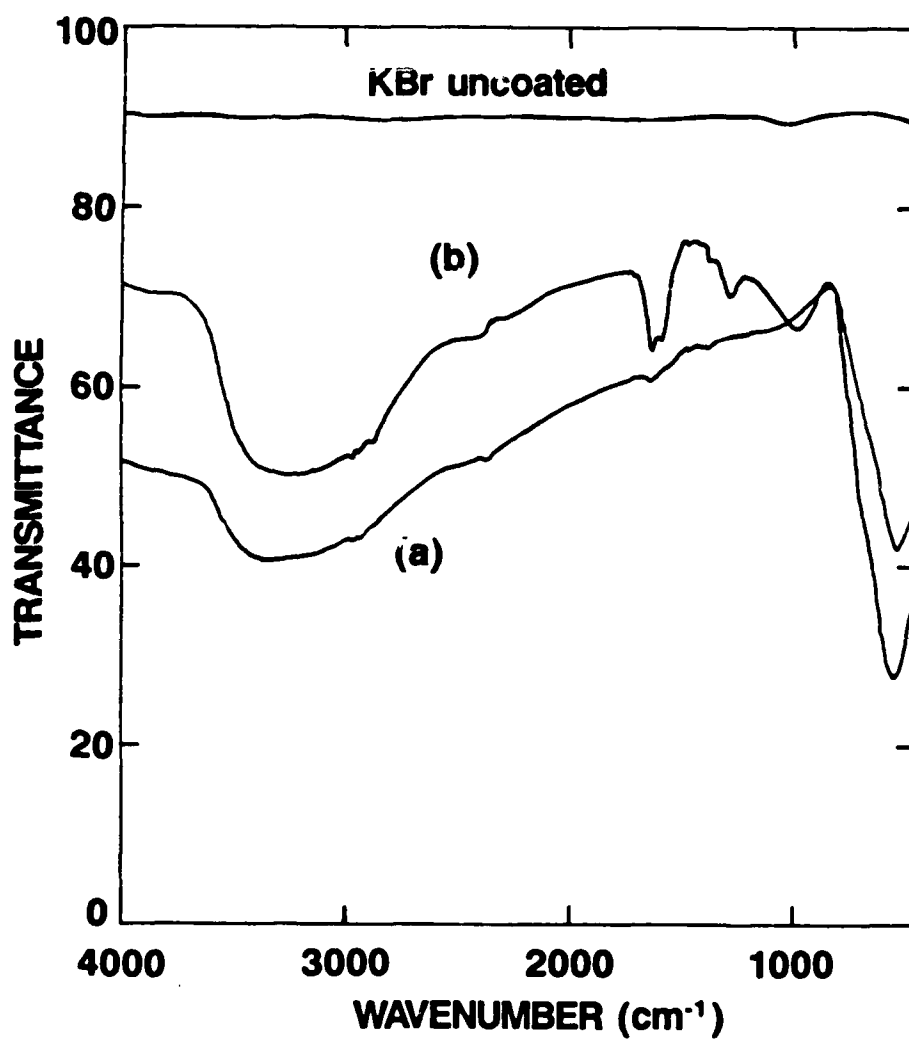
Figure 5. Relative quantum efficiency as a function of wavelength of a HgI_2 photodetector prepared from specimen C1.



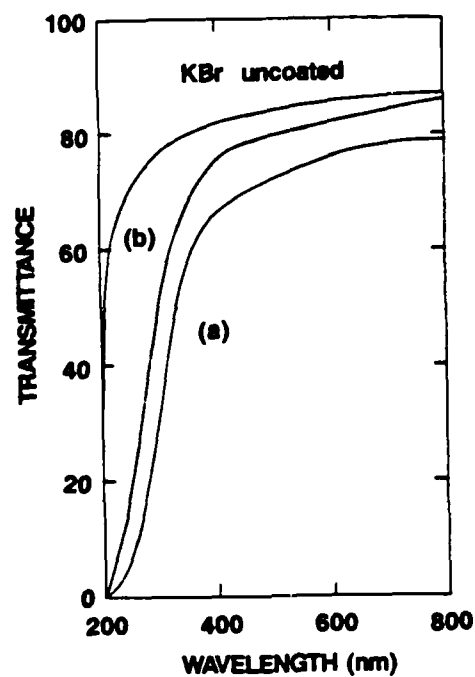
1. Schematic diagram of experimental apparatus:
 MV-manual valve, PV-pneumatic valve, CL-calibrated leak, REG-regulator, MFM-mass flow meter.



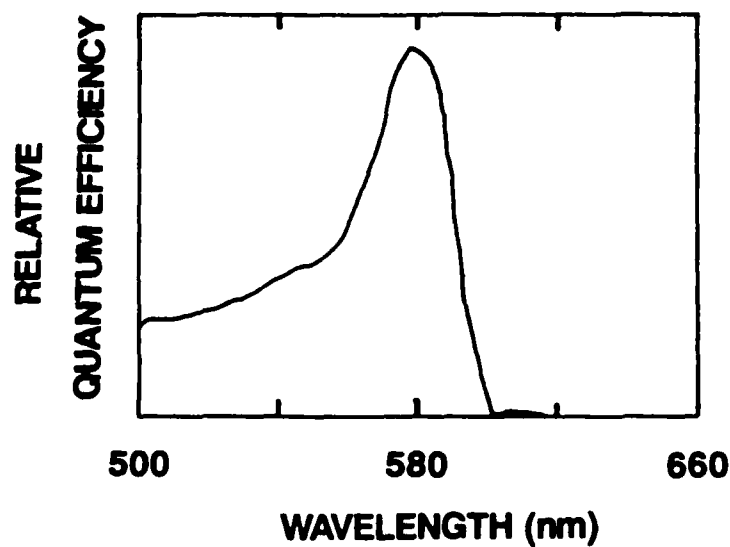
2. SEM micrograph of tin oxide powder. Plasma parameters: $\text{Sn}(\text{CH}_3)_4$ pressure-12.1 Pascals, O_2 pressure-52.0 Pascals, rf power density-0.42 watts/cm².



3. Infrared spectra of films deposited at a $\text{Sn}(\text{CH}_3)_4:\text{O}_2:\text{Ar}$ ratio of 1:9:25 and rf power densities of: (a) 0.45 watts/cm² and (b) 0.58 watts/cm².



4. Visible spectra of films deposited on KBr substrates under conditions identical with those used to coat specimens: (a) C1 and (b) C2.



5. Relative quantum efficiency as a function of wavelength of HgI_2 photodetector.

original figure

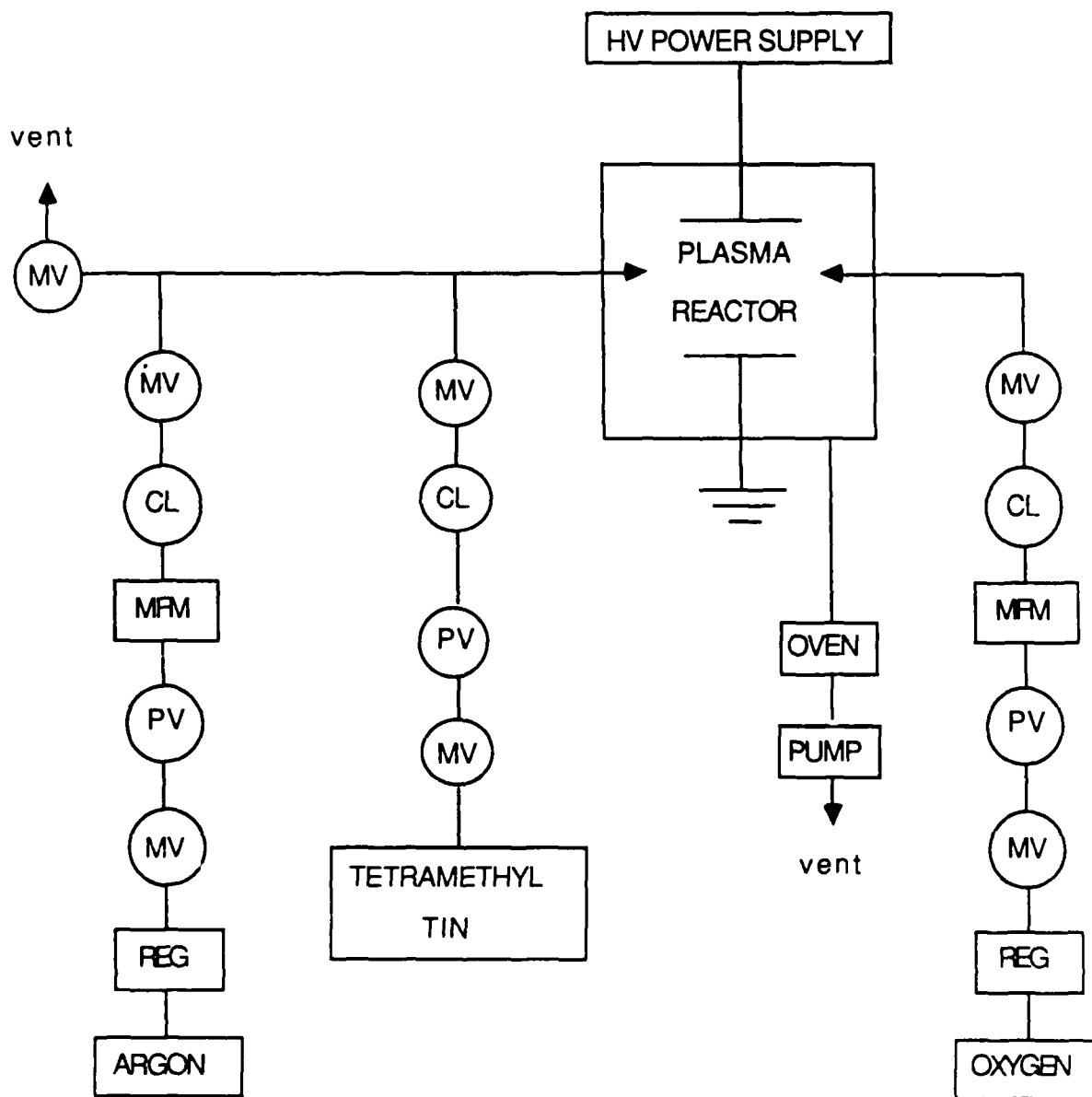


Fig. 1

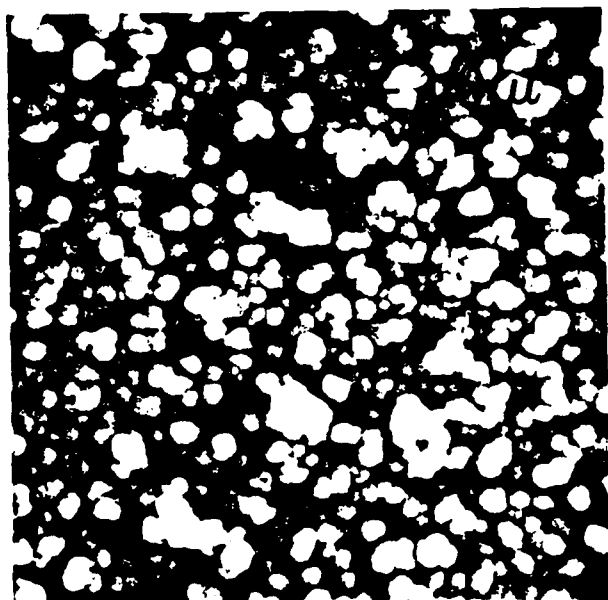


Fig. 2

47

722

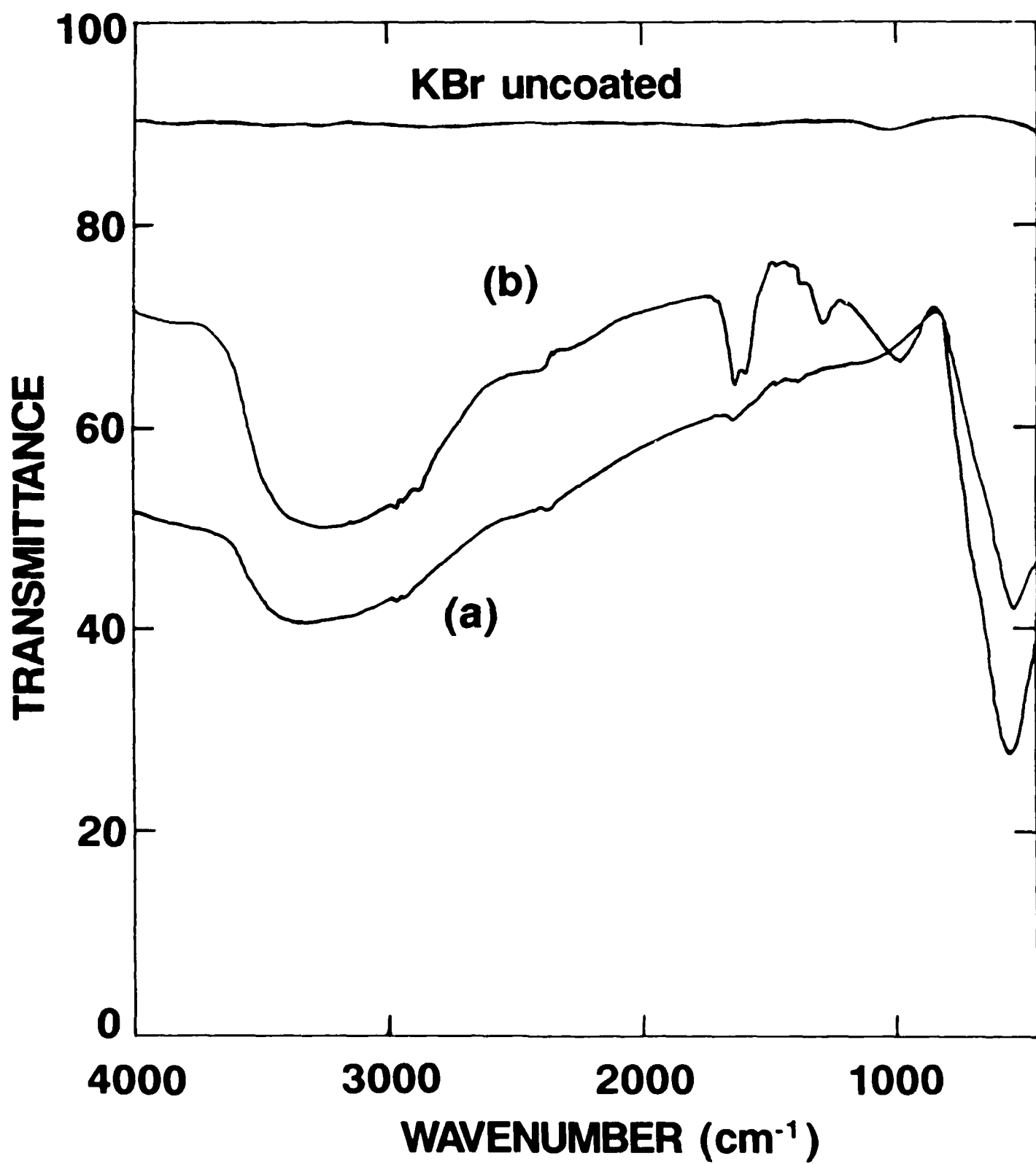


Fig. 3

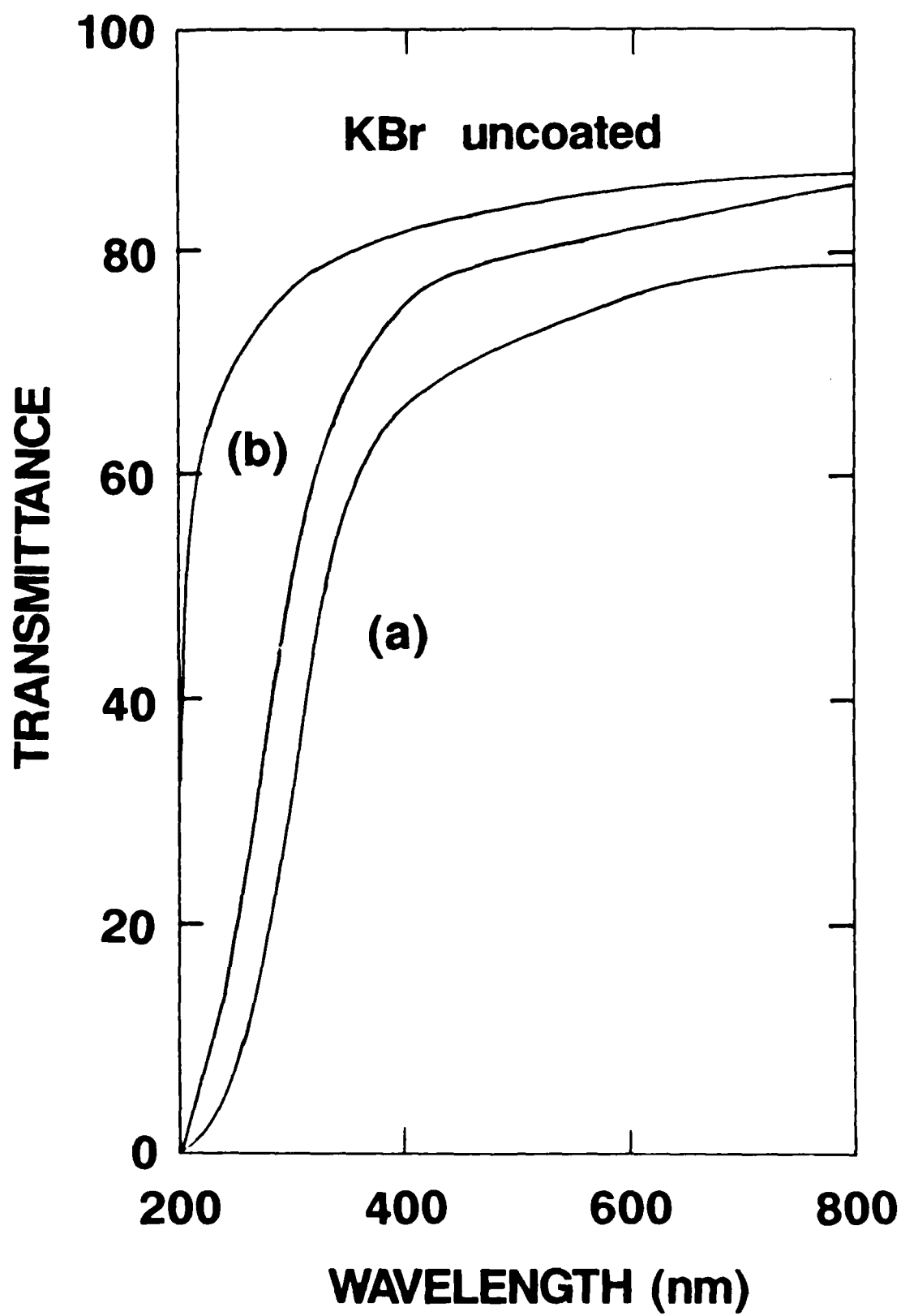


Fig. 4

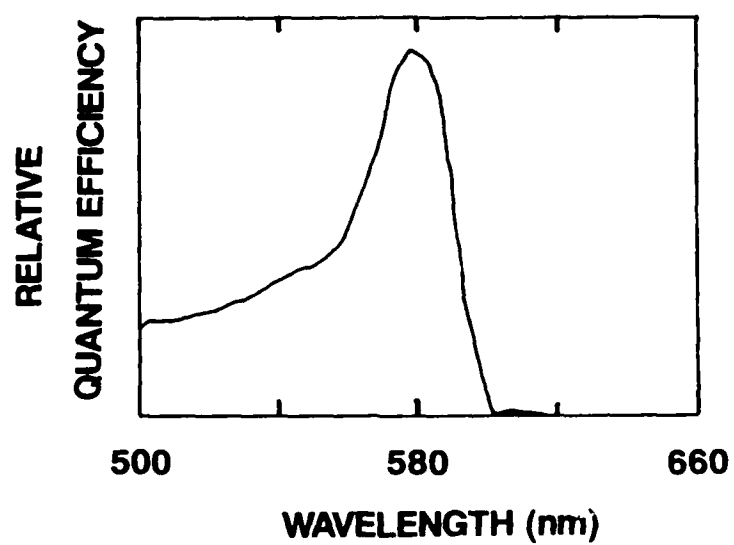


Fig. 5

P. HUMBERT*, D. MORVAN, J.F. CAMPION, P. JOLIVET, J. AMOUREUX
 Laboratoire de Chimie des Plasmas - Université Pierre et Marie Curie
 Ecole Nationale Supérieure de Chimie de Paris
 11 rue Pierre et Marie Curie - 75231 PARIS Cedex 05 FRANCE

Abstract : This paper describes mainly the synthesis of ultrafine Si_3N_4 and TiN powders, from Si and Ti particles in the size range of $10\ \mu\text{m}$, with a Ar-N_2 thermal plasma. Nitride powders have been prepared in a radio-frequency plasma reactor (this reactor has been used for silicon refining, and leads to very good results - the purification technique will also be described). The present work describes some of the main parameters responsible for the synthesis process, in order to optimize the design of a reactor for the synthesis of high purity ceramic powders with a good production rate. **Key words :** R.F. thermal plasma, ultrafine powders, ceramic synthesis, TiN , Si_3N_4 .

INTRODUCTION :

For over a decade, ceramic synthesis and processing have occupied an important place in material engineering technology because of the attractive properties and applications of ceramics (metal coating, heat barrier, hardness, corrosion protection, electrical insulation, tribology, etc.).

Conventional processes for ceramic synthesis are quite numerous : these include sol-gel process, solid-gas reaction, and gas-gas reaction.

If we consider the example of TiN and Si_3N_4 ^[1] synthesis, we can find three main routes :

- nitriding of Si or Ti (by a combustion reaction for example^[2])
 - carbothermic reduction of the oxide. Unfortunately, in this case most of the time the final product contains carbide or oxinitride.
 - reaction of ammonia with the halide. The by-products are removed by heating.
- Other routes also exist such as calcination of organo-metallic compounds with a nitriding agent.

Recently, thermal plasma processes have been used for substitution for conventional processes. In some cases, plasma is the only way for obtaining ceramic powders^[3]. Moreover, ceramic powders such as AlN , SiC , TiC are easily produced by thermal plasma and have a high yield efficiency. Ceramic powders synthesized by a plasma mean are ultrafine (in the range of $10\ \text{nm}$). The high surface area of these powders leads to lower sintering temperatures and no sintering additive addition.

In general thermal plasma reactors are characterised by :

- a very short residence time of reactives in the plasma plume with associated large thermal gradients
- the presence of high concentration of reactive species (ions, metastables atoms ...)
- the thermal plasma properties can give us a complete vaporisation, with associated gas phase chemistry
- high quenching rates leading in many cases to amorphous products.

The purpose of this paper is to expose some new results about plasma treatment of materials such as Si and Ti conducted in our laboratory.

We will examine silicon purification by plasma processing, in order to get very pure materials. Our goal is to correlate plasma properties and purification mechanisms.

We will also present the nitriding of Si and Ti particles in a R.F. thermal plasma by an Ar-N_2 mixture.

1 - EXPERIMENTAL APPARATUS :

The reactor used for our studies has been designed for silicon refining (Figure 1). The R.F. plasma is generated in a quartz tube of $30\ \text{mm}$ of diameter, by the mean of a cooled 4 turns work coil connected to a $4\ \text{MHz}$ generator (maximum power output : $20\ \text{kW}$). The powders are injected in the center, the treated products are collected in a water-cooled crucible. The gases are evacuated by the means of a pipe, without any vacuum pump. The powder feeder is composed of a closed vessel with a vibrating plate, and allows a distribution of particles with a feed rate lower than $0,01\ \text{g/min}$ and up to $10\ \text{g/min}$. The particles injected from the powder feeder are dragging along the plasma by means of a fluidizing gas ($0,4\ \text{l/min}$ argon). By using this device, it is possible to minimize the contamination of the gas by entrained air.

In order to study the chemical and thermal phenomena during the plasma treatment, we used an optical fiber to collect the emission photons produced at the interface of the plasma-sample. The emission signal is analyzed by an intensified diode array, with a wave range of $500\ \text{nm}$, while the computer analysis

gives us the atomic emission lines each 8 ms for high temporal resolution studies.

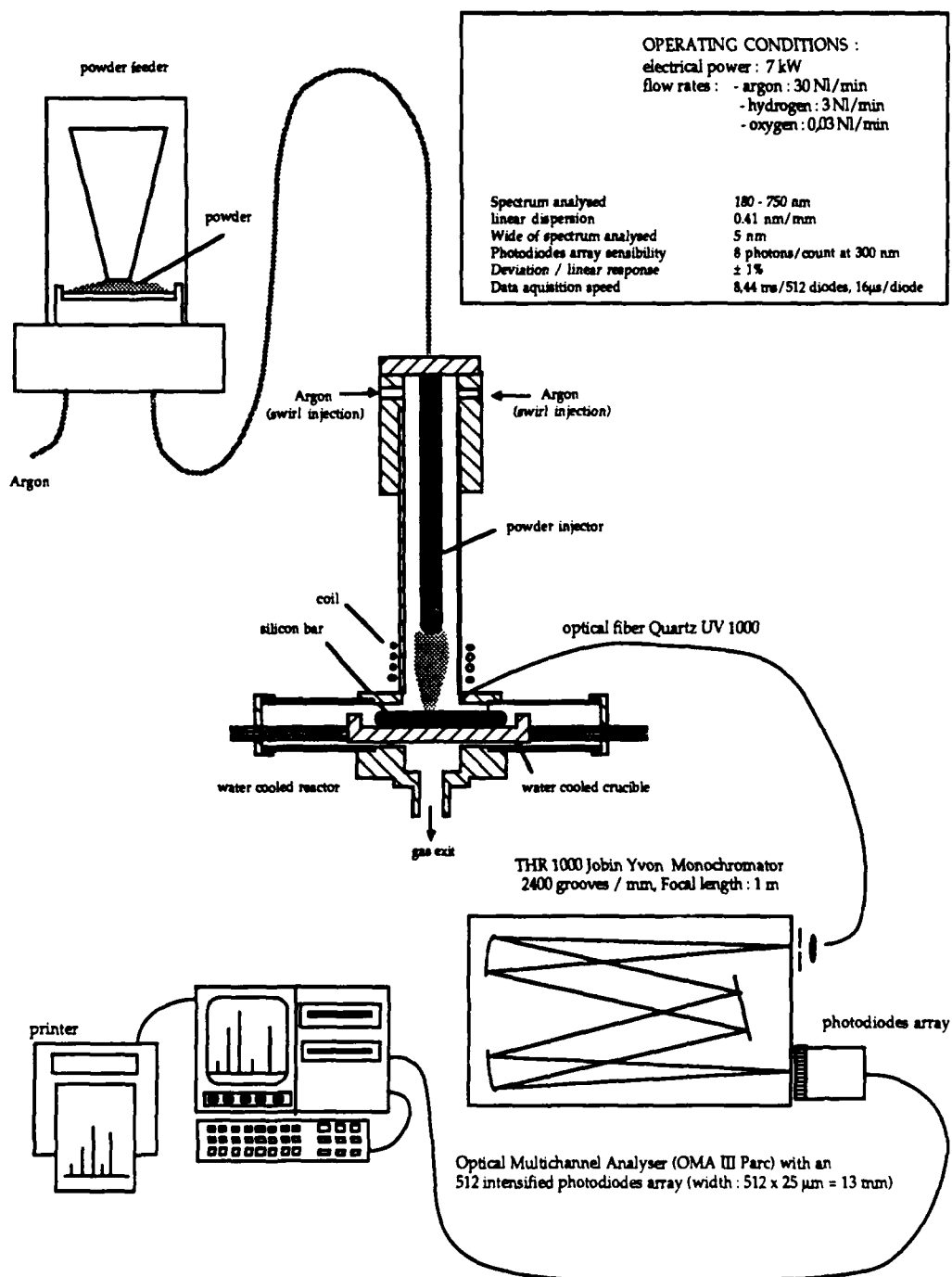


Figure 1 : R.F. plasma reactor and spectroscopic emission detection system

Two ways have been explored in order to study the mechanisms which occur during plasma treatment.
 - removing of impurities from a raw material. By using a method quite similar to a melting zone process, we achieved refining of silicon and titanium [4 - 8]. The products prepared are characterized by physical and chemical analysis, in order to check their properties and their chemical purity (neutron activation analysis N.A.A., E.S.C.A., X-rays, and electrical conductivity ...).

- addition of an element to a material for the preparation of ceramics or non-stoichiometric compounds. The fluidization argon feed rate is 0.4 l/min. This value has been chosen so as to get a good penetration of powder into the plasma plume. As soon as the plasma is stopped, N₂ supply in the swirl injection is removed. The ceramics powders prepared are characterized by S.E.M., X-rays, Infra-red spectroscopy and chemical analysis).

II - PURIFICATION OF MATERIALS :

Silicon refining of a metallurgical grade silicon by a reactive plasma (containing 2% of impurities) allows us to get relatively pure silicon (less than 1 p.p.m. impurities)[4] [5]. The resulting silicon can be used for solar cells production, with photovoltaic efficiencies reaching 10% [6].

The purification starts by the silicon melting while the second step needs the chemical reaction between the oxygen of the plasma gas Ar - H₂(1%) - O₂(0.1%) ; the silica layer which is formed on the surface traps the impurities by three ways (Figure 2) :

- 1 - liquid/liquid extraction between the liquid silicon and the slag
- 2 - evaporation at the plasma/slag interface of impurities
- 3 - segregation of impurities at the solidification interface.

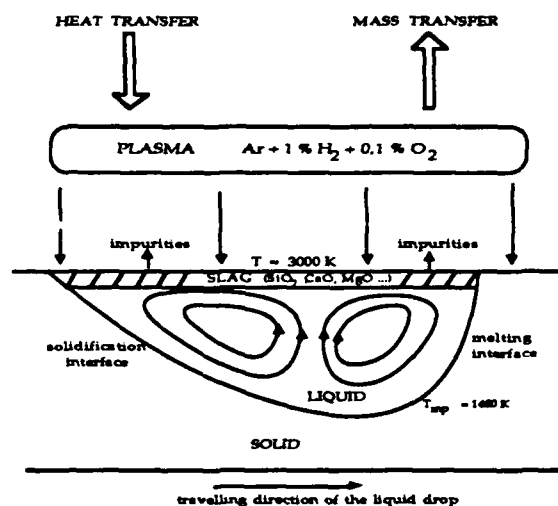


Figure 2 : Purification mechanisms in the case of plasma refining of silicon

This oxydation-reduction reaction at the plasma/slag interface explains the high purification rate, especially in the case of boron (indeed, boron is an impurity which can not be removed by a melting zone process). After evaporation from slag, oxides are decomposed in the plasma phase, the atomic emission of these impurities are correlated with the plasma properties (oxygen concentration, surface temperature, purity of the sample). Recently, we pointed out that evaporation processes of impurities from silicon could be continuous (Na, Mg, ...), discontinuous (Ca, Al, ...)[7], and reactive (B, As, P). Typical purification results are plotted in Table 1.

Refining of titanium with a R.F. plasma has been studied [8]. It appears that the purification phenomena are quite different from those involved for silicon. Oxygen is not used because of the formation of a barrier layer of TiO₂ on the surface of titanium and sintering when powders are used.

The gas mixture used for this study is Ar-0.1% H₂ or Ar-0.8% He. Indeed, it has been shown that these two mixtures have the same thermal conductivity [8], and thus allow the same purification rate. Because of the sensitivity of titanium for hydrogen, the second gas mixture has been chosen. Addition of KF, NaF or CaF₂ to the powder increases the purification process by elimination of fluorine compounds, thus impurities such as Fe, Co, Ca are removed.

Impurities	starting material	Oxygen free plasma	0.1% O2 plasma
Au	0.8	0.0003	0.0001
Ce	0.002	0.008	< 0.001
Co	4	0.14	< 0.01
Cr	87	0.3	< 0.01
Fe	742	57	< 0.8
Mn	250	3	0.0005
Mo	14	< 0.006	< 0.0002
Na	1	0.02	0.006
Pt	-	0.03	< 0.008
Ti	141	< 2	< 0.9
Zn	< 2	< 0.07	< 0.03
Zr	3	< 1	< 0.8
W	-	0.01	< 0.0002

Table 1 : Influence of the oxygen on the purification of metallurgical grade Silicon (concentration in p.p.m. weight, analysis by N. A. A.).

III - NITRIDING EXPERIMENTS :

The aim of the nitriding study, is to understand the phenomena which are responsible for either the formation or the destruction of a nitride under a thermal plasma. All experiments have been achieved with titanium and silicon as a starting material (powder and bulk material).

III-1- Thermodynamic considerations :

Ultrafine powders synthesis by plasma processing means proceeding from a vapor phase reaction. Because of the very short residence time of a particle in the plasma plume, a solid-gas or liquid-gas reaction is impossible, thus only a nucleation and growth process is allowed. Nucleation begins as soon as the supersaturation of a vapor exceeds a critical value. This phenomena is of very great importance because in Si_3N_4 synthesis it has been proved that liquid silicon formation stops the silicon nitride nucleation. Therefore, liquid silicon formation should be avoided in order to increase the yield of the reaction [1]. Because of the relatively high temperatures of a plasma plume, a large fraction of injected products are vaporized. The vapor phase is assumed to be in thermodynamical equilibrium.

A calculation of chemical equilibrium by minimization of the free energy has been performed in order to know the concentration of each species in the plasma. Data are available in JANAF [9]. Figure 3 shows the curves for a Si-N-O system. It appears that SiO_2 layer at the silicon particles surface is decomposed from 2500 K and leads to SiO(g) (SiO is stable below 5500 K). TiN is synthesized below 2760 K by a vapor phase reaction, according calculation for the Ti-N system [10].

The nitride formation by vapor-phase reaction assumes that the particle is completely vaporized. If not, the reaction proceeds from a nitrogen diffusion process through the particle. Thus it is important to know if the particle is vaporized in the plasma. Some models have been formulated in order to describe the temperature of a particle in a plasma plume versus the time [11-13]. By using Boulos' results [14] of flow and temperature fields in a R.F. plasma, the temperature history of a Si and Ti particle of 40 μm has been computed [15]. It appears that all particles injected in a Ar plasma with temperature plotted in Figure 4 and 5 are completely vaporized if the diameter is less than 20 μm . Because of the presence of nitrogen in the plasma, the thermal transfer and the vaporization process are increased. Some improvements are required with high powder feed rates [14].

III-2 - Results and discussion :

III-2-1 - Silicon nitride synthesis :

The silicon powder used is a good metallurgical grade silicon, supplied by P  chiney. Two parameters have been studied : the feed rate of Si powder and the position on the crucible for the collected product. It appears that final products have different characteristics, according to experimental conditions. Indeed, powders collected are white and very fine or brown/greenish.

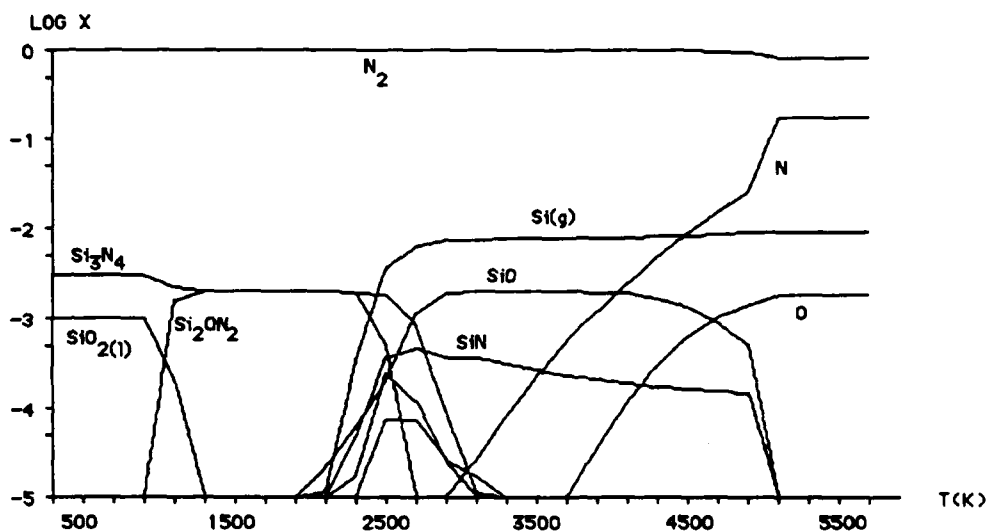


Figure 3 : Equilibrium composition of Si-N-O system
(Si = 0.005 - N = 1 - O = 0.001)

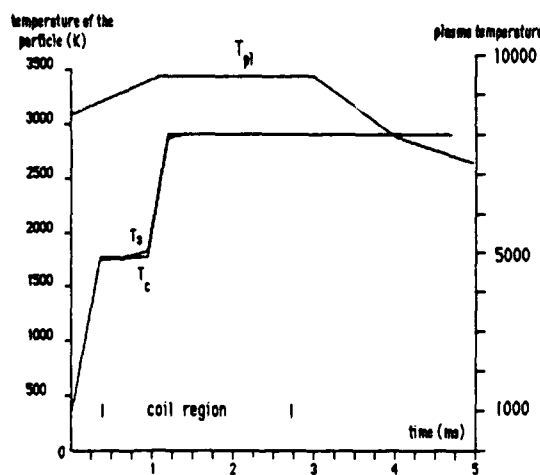


Figure 4 : Temperature history of a Si particle
in a Ar plasma

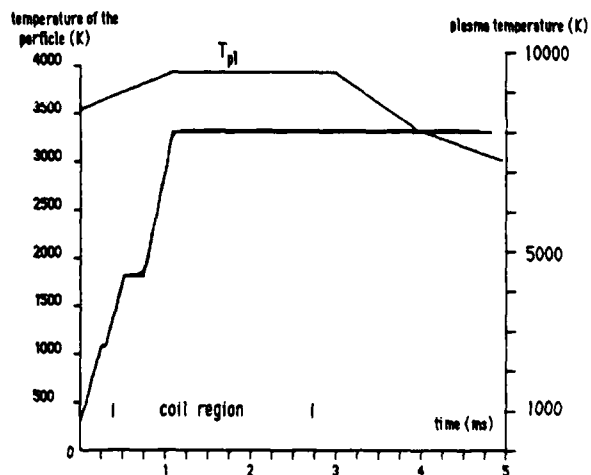


Figure 5 : Temperature history of a Ti particle
in a Ar plasma

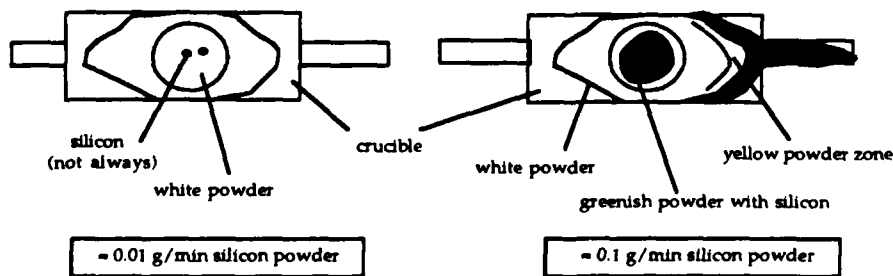


Figure 6 : Nature of the products on the water-cooled crucible versus powder feed rate

On one hand, it has been shown that an increasing of powder feed rate leads to a greater amount of brown/greenish products, whereas a low feed rate (≈ 0.01 g/min) gives a white and fine powder. On the other hand, the major amount of white powder was located at the top and on the walls of the water-cooled crucible, above the torch (Figure 6).

X-Ray diffraction : X-ray diffraction analysis of these two kinds of powders gives the following results :

- the greenish powder is crystalline silicon, without any Si_3N_4 peaks.
- The white powder is not well crystallized. So, the diffraction spectrum was carried out in using a metallic sample holder. It appears that the white powder contains $\alpha\text{-Si}_3\text{N}_4$ and $\beta\text{-Si}_3\text{N}_4$ (Figure 7). Peaks of Si are present. So we can conclude that there was a competitive silicon nucleation during quenching. The X-ray diffraction of another sample where $\alpha\text{-Si}_3\text{N}_4$ and $\beta\text{-Si}_3\text{N}_4$ peaks are visible did not show any detectable Si peak. Thus, silicon nucleation can be avoided if precautions are taken, but these experiments are not reproducible. We have concluded from these X-ray analyses that only the fine and white powder contains Si_3N_4 . Therefore only the white powder has been further investigated.

S.E.M. observations : The observation of white powder by S.E.M. shows a submicron structure: the mean size of particles is more or less 100 nm, with a lot of agglomerates (Figure 8).

I.R. Spectroscopy : The I.R. spectra were carried out on a BOMEM I.R.-F.T. Figure 9 gives the spectrum of the white powder. We can note the presence of Si-O and Si-N bonds in the product. On the same figure is plotted the I.R. spectrum of the Si powder before plasma treatment. It is obvious that the Si powder contains oxygen. Figure 10 shows the I.R. spectrum of a white by-product which was obtained during silicon particle treatment in a Ar plasma without nitrogen. It appears that only Si-O bounds are visible. This by-product is a consequence of the oxidant properties of the plasma. Since, SiO is produced simultaneously with Si_3N_4 , it is impossible to recover pure Si_3N_4 . Therefore, more accurate measurements are necessary in order to determine the yield of the reaction and on the purity of the product.

Chemical Analysis (O and N) : The sample is divided in two parts. One part is used for nitrogen, and the other for oxygen content determination. The powder is then placed in a carbon crucible where nickel is added. The crucible is degased and the mixture is heated at 2500°C with in a helium stream. Nitrogen is measured by a catharometric technique, and oxygen is measured with a I.R. device after it has reacted with the crucible to form CO_2 . Calibration is performed by melting of a standard.

A sample of 485 mg of white powder collected on the crucible yields :

O : 23.3% N : 19.2% (i.e. 48% weight of Si_3N_4)

The same measurements on the silicon powders yields :

O : 0.82% N : < 5 p.p.m.

The oxygen content in the starting material can not explain such a high content in the final product. A reasonable explanation of the high oxygen content in the product, is that the gases used during plasma synthesis are not very pure. This assumption is in good concordance with the presence of SiO by-product. Owing to some authors the oxygen found in the product should come from the treatment gases which is not pure [10] [16] [17]. Sometime, possibly leakages of air in the synthesis device may also be assumed to occur [18]. The gases we use in our laboratory are supplied by Air liquide. Argon is "Ar U" grade (less than 5 p.p.m. impurities) and nitrogen is "N₂ R" grade (200 p.p.m. impurities). These gases do not undergo further purification in our device, and the use of dryers and oxygen traps is necessary in further experiments. The difference between the total oxygen content of the sample and the oxygen content in the plasma gas is probably due to an oxidation after the plasma synthesis. Vogt [24] observed a decrease of the N, and an increase of the O content with time in the case of submicron Si_3N_4 powders. So, the product must be kept in Ar to prevent oxidation. The I.R. spectrum of the powder we synthesized, shows the presence of O-H bonds (Si-O-H groups at the surface of particles). This observation allows us to assume that there was an increase of the oxygen content in the product because of an exposure to air.

In general, nitriding processes using Si powders lead to products of relatively poor quality compared to processes using SiCl_4 . Indeed, silicon powders are coated with SiO_2 thus it is not possible to synthesize a nitride without any oxygen in it. On the contrary, SiCl_4 can be supplied with a very good purity, and the yield of the nitriding can reach 100%. Moreover, it appears that using NH_3 as a nitriding agent instead of N_2 gives much better results (Table 2).

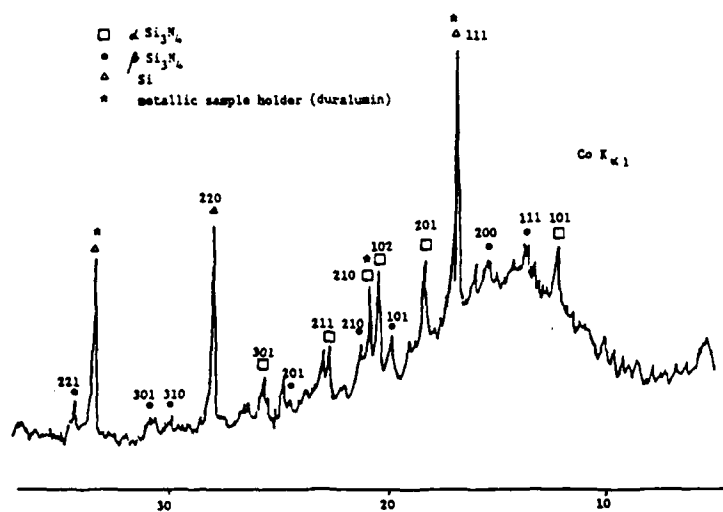


Figure 7 : X-Ray spectrum of the white powder produced during silicon nitriding

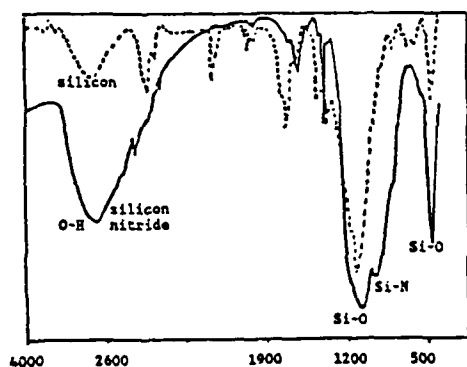


Figure 9 : I.R. spectrum of the starting silicon and of the product Si_3N_4

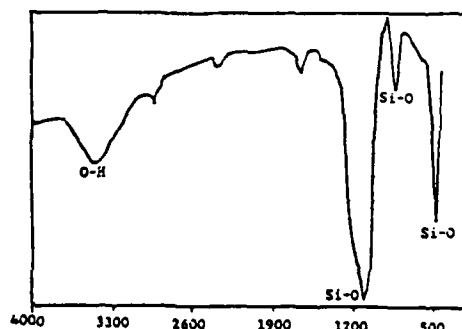


Figure 10 : I.R. spectrum of the by-product

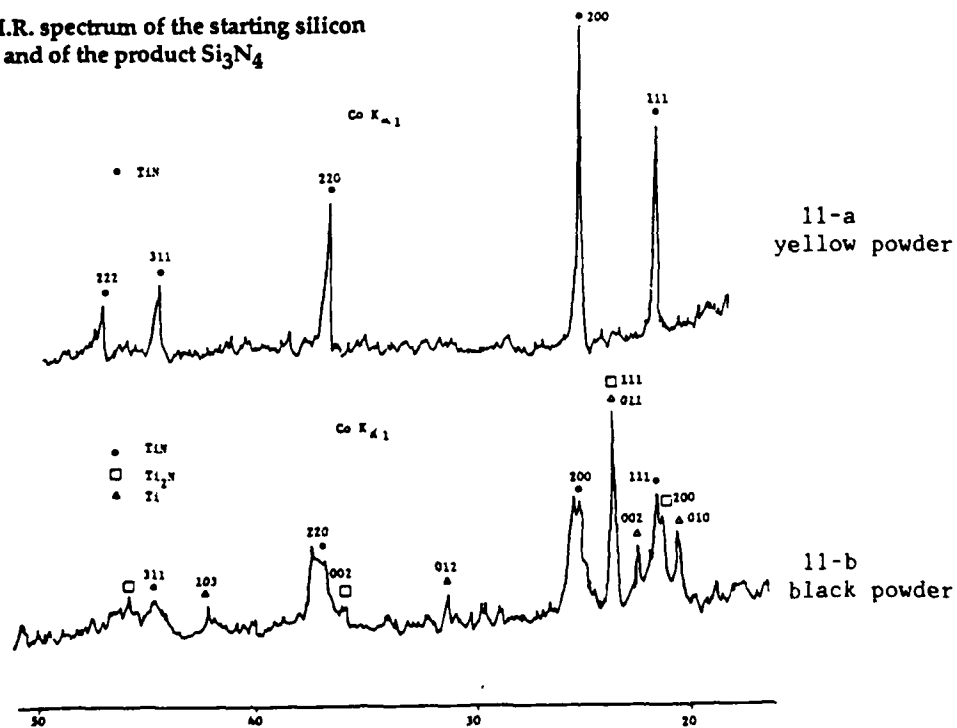


Figure 11 : X-Ray spectrum of the powder produced during titanium nitriding

REACTIVE	GAS	YIELD	REF.
Si powder (75% < 30 μ m)	N ₂ (33 l/min)	54 %	(16)
Si powder (25 μ m) 0.1 g/min	Ar (20 l/min) N ₂ (5 l/min)	22 % (chem. anal.)	(18)
Si powder (15-35 μ m) 0.4 g/min	NH ₃ (10.5 l/min)	85 %	(19)
Si powder (25 μ m) 0.1 g/min	Ar (20 l/min) NH ₃ (10 l/min)	22 %	(18)
Si powder (<5 μ m) = 1 g/min	NH ₃ / Si : 10/30	85 %	(20)
SiCl ₄ (2 l/min)	Ar (20 l/min) NH ₃ (10 l/min)	75 %	(18)
SiCl ₄ (13 g/min)	Ar (20-40 l/min) NH ₃ (2.2-4.6 l/min)	> 90 %	(21)
SiCl ₄ (0.4 g/min)	Ar (52 l/min) NH ₃ (20 l/min)	92.5 %	(22)
SiCl ₄ (5 l/min)	Ar, H ₂ NH ₃ (10 l/min)	80 %	(23)

Table 2 : Review of silicon nitriding science base

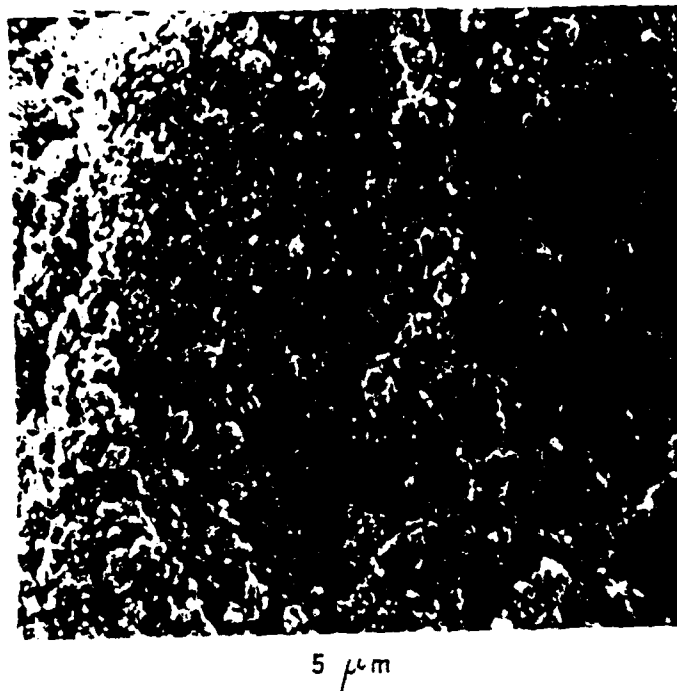


Figure 8 : photograph of the product silicon nitride

III-2-2 - Titanium nitride synthesis :

The titanium powder we used is supplied by Ventron. The mean size of particles is 10 μ m (S.E.M.). The experimental procedure used was the same than for Si₃N₄ synthesis.

When the titanium powder is injected with a low feed rate (≤ 0.03 g/min), the resulting powder is yellow. However, increasing of the feed rate leads to black fine powder in the crucible, with a small amount of yellow powder on the top, above the plasma plume.

X-ray Diffraction : Two samples of powders were studied by X-ray diffraction. The first sample is a gold-yellow powder obtained with a low Ti feed rate (Figure 11-a), whereas the second sample is the black fine powder (Figure 11-b). The X-ray diffraction spectrum of the black powder shows a mixture of Ti, TiN and Ti₂N. In contrast, in the X-ray spectrum of the yellow powder shows only the peaks of TiN, without Ti.

Since the yellow powder is observed above the plasma plume, we assume that the nitriding continues when the product in the crucible is on the axis of the plasma, because of the higher temperatures of the products. In order to check this thermal effect, a complementary experiment was performed. It consisted to comparing the nitriding rate of the powders recovered in the crucible after a short plasma with a high powders feed rate, with and without nitrogen in the cooling gas after the plasma has been stopped. A typical value is 75% TiN and 25% Ti with nitrogen in the cooling gas, whereas the powder was almost Ti without nitrogen in the gas (these values are calculated from X-Ray diffraction patterns).

This observation has been confirmed with bulk titanium samples. The sample was melted with pure Ar plasma, and cooled with and without nitrogen in the cooling gas. In the first case, a nitride layer appeared on the surface, in the second case the surface was not nitrided.

S.E.M. observation : Figure 12 shows a characteristic of the nitrided particles collected in the crucible. Instead of collecting particles in the crucible, an experiment was carried out involving collection of the particles at the surface of a molten bulk titanium sample. The purpose of this experiment was to increase the quantity of particles recovered. A surprising observation is that the morphology of the product (Figure 13) is very different from the aspect of particles collected in the crucible (Figure 12). Indeed, the product is well crystalized and the mean size of each crystal is 1 μ m.

Figure 14 is a photograph of the nitride layer at the surface of a bulk titanium sample tested under a Ar-N₂ plasma. The morphology of the nitride layer is quite similar to the surface of powders shown in Figure 12. Figure 15 shows the morphology of the nitride layer of bulk titanium treated by a Ar-NH₃ plasma. The nature of the nitriding gas seems to have a large importance on the morphology of nitride layer. A very similar condition of the surface is observed when a bulk titanium sample is exposed to a non-equilibrium NH₃ plasma^[25].

In summary, we have the following results :

- 1- With low Ti feed rates, TiN is synthesized, whereas with higher feed rates the nitride contains Ti_2N .
- 2- The nitriding continues when the powder is in the crucible, above the plasma plume.
- 3- The nitriding can occur during the cooling of the products if nitrogen is present in the reactor. This additional nitriding must be distinguished from the one during plasma treatment. For this reason, the cooling gas we used is Ar without N_2 .

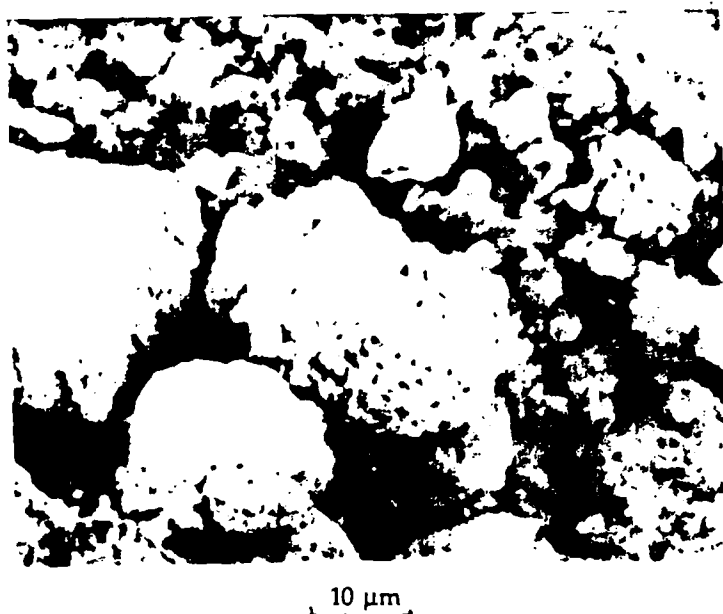


Figure 12 : photograph of largest particles of the yellow TiN powder collected in the crucible



Figure 13 : Crystals of TiN in the powder agglomerate on the molten titanium

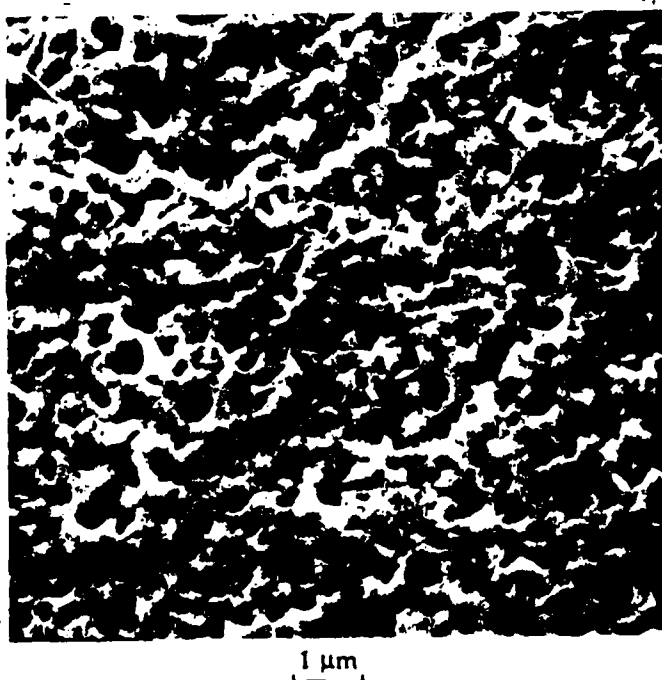


Figure 14 : Surface of a bulk titanium sample treated by Ar- N_2 plasma

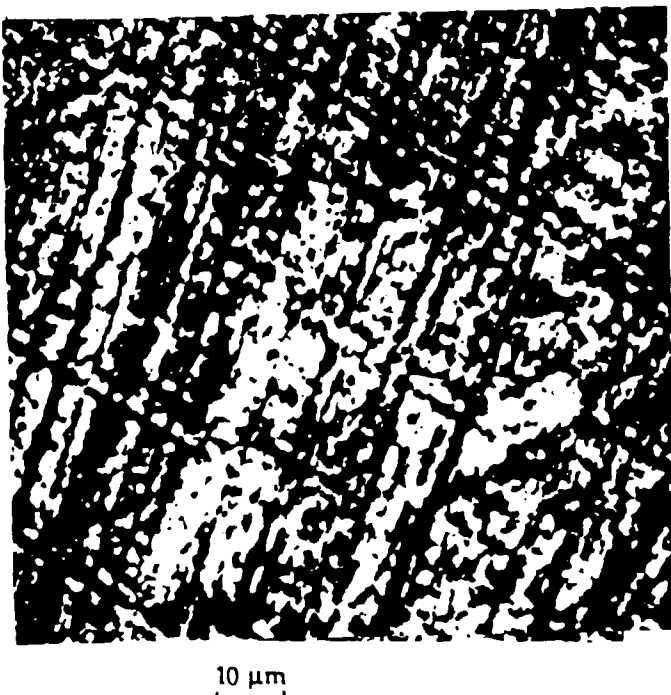


Figure 15 : Surface of a bulk titanium sample treated by Ar- NH_3 plasma

CONCLUSIONS :

It has been demonstrated that the synthesis of Si_3N_4 and TiN by vapor phase reaction from powders of Si and Ti (mean size : 10 - 20 μm) is possible in a radio-frequency reactor which is not specially designed for this purpose, if the efficiency of the quenching zone is adequate. In the case of Si_3N_4 , the final product is an ultrafine powder of mixed phases (mean size : 10 nm); for TiN , the mean size is 1 μm .

Chemical and thermal properties of plasma reactors simultaneously control the energy and mass transfer mechanisms versus the nature of treated materials.

The first part of the research underlines the role of chemical reactivity of oxygen introduced in a Ar-H_2 plasma so as to modify oxy-reductive phenomena responsible for silicon purification. The extraction mechanisms of boron proceeds in two steps : oxidation of boron in the silicon liquid bath and evaporation through the silica layer.

The second part of the research emphasizes the role of chemical reactivity of a Ar-N_2 plasma versus Si or Ti powders. The thermodynamical analysis and the thermal modelization of particles treatment points out that evaporation and instability of nitride leads to the formation of the nitride only in the plasma plume region. The study of the powders treated under different conditions confirms these hypothesis in vapor-phase with the addition of a nitriding of product in the cooled crucible. This latter step leads to growth phenomena by nucleation and agglomeration. It is important to emphasize the difficulty of removing oxygen in the product.

REFERENCES :

- 1 - Yi Chang, R.M. Young, E. Pfender Plasma Chem. and Plasma Proc. **7**(3), 299, (1987)
- 2 - K. Hirao, Y. Miyamoto, M. Koizumi, J. of the Amer. Ceram. Soc., **69**(4), C60, (1986)
- 3 - Yi Chang, E. Pfender, Plasma Chem. and Plasma Proc. **7**(3), 275, (1987)
- 4 - D. Morvan, Thèse de Doctorat d'Etat Université Paris VI "Mise en œuvre d'un procédé multiphase de purification du silicium sous plasma réactif haute fréquence" (1984) .
- 5 - J. Amouroux, D. Morvan, Plasma Chem. and Plasma Proc. **1**(4), 397, (1981)
- 6 - J. Amouroux, D. Morvan, H. Apostolidou, F. Sliotman, J.C. Rouchaud, M. Fedoroff, Proc. of 7th E.C. P.S.E.C. Sevilla 27 - 31 October p. 719-725 (1986)
- 7 - F. Sliotman, Thèse de Doctorat de l'Université de Paris VI "Etude des phénomènes d'évaporation lors de l'élaboration de silicium photovoltaïque à partir de poudres traitées par plasma thermique inductif" p. 118-133, (1988).
- 8 - T. Roger, Thèse de l'Université de Paris VI "Mise en œuvre d'un procédé de fusion et de purification du titane par un plasma inductif haute fréquence" (1988).
- 9 - JANAF Thermodynamical Tables. Third edition (1985).
- 10 - T. Yoshida, A. Kawasaki, K. Nakagawa, K. Akashi, J. of Mat. Sci., **14**, 1624, (1979)
- 11 - Xi Chen, E. Pfender, Plasma Chem. and Plasma Proc. **2**(3), 293, (1982)
- 12 - E. Bourdin, P. Fauchais, M. Boulos, Int. J. Heat Mass Transf., **26**(4), 567, (1983)
- 13 - A. Vardelle, Thèse de Doctorat ès Sciences Physiques Université de Limoges (1987)
- 14 - P. Proulx, J. Mostaghimi, M.I. Boulos, Plasma Chem. and Plasma Proc. **7**(1), 29, (1987)
- 15 - P. Humbert, D. Morvan, J. Amouroux, Proc. rencontre S.F.T. 1988 (Limoges), EMTT 14-1 (1988).
- 16 - A. Szymansky, A. Podgorski, A. Huczko, III^{ème} Symposium International de Chimie des Plasmas (I.U.P.A.C.) **3**, Limoges, p. S 4-13. July 13-19th 1977
- 17 - K. Akashi, Pure and Appl. Chem, **57**(9), 1197, (1985)
- 18 - T. Hussain, V.J. Ibberson, I.S.P.C. 7 Eindhoven, p. 692, July 1985
- 19 - J. Canteloup, A. Mocelin, "Special Ceramics 6" Ed. Papper 209, (1975)
- 20 - R.M. Young, Yi Chang, B. Lecerf, E. Pfender, I.S.P.C. 8 Tokyo, p. 2028, (1987)
- 21 - S. Futaki, N. Kubo, K. Shiraishi, I.S.P.C. 8 Tokyo, p. 2040, (1987)
- 22 - T. Yoshida, H. Endo, K. Saito, K. Akashi, I.S.P.C. 6 Montreal, p. 225, (1983)
- 23 - Ching-Wen Zhu, Jie-Peng Yan, I.S.P.C. 7 Eindhoven, p. 657, (1985)
- 24 - G.J. Vogt, R.S. Vigil, L.R. Newkirk, M. Trkula, I.S.P.C. 7 Eindhoven, p. 668, July 1985
- 25 - N. Laïdani, Thèse de l'Université de Paris VI "Etude des mécanismes de nitruration du titane massif et des films minces de titane, dans un réacteur plasma basse pression hors-équilibre, en atmosphère d'ammoniac".

Plasma Synthesis of Iron and Chromium Carbides by
Carbothermic Reduction of Their Mineral Oxides

J. J. Moore
Department of Metallurgical and Materials Engineering
Colorado School of Mines
Golden, CO 80401

ABSTRACT

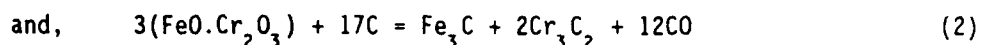
Magnetite, Fe_3O_4 , and chromite, $\text{FeO} \cdot \text{Cr}_2\text{O}_3$, concentrate fines were reacted in-flight with graphite fines in an expanded DC transferred plasma arc. The degree of conversion to Fe_3C and Cr_3C_2 is discussed with respect to the mineral chemistry, thermodynamics, kinetics and particle size. The degree of metastability of the products was also examined.

INTRODUCTION

Conventional synthesis techniques used for the production of carbides involves high temperature furnaces operating for several hours. Plasma technology offers a novel low volume- high throughput reactor¹ in which reactants and products are subjected to a highly reactive medium containing atomic and ionic species which are not available under conventional processing conditions. Rapid quenching of the products, provides a further potential for producing metastable or even amorphous products.

EXPERIMENTAL PROCEDURE

Fine magnetite, Fe_3O_4 , containing 6.2% SiO_2 (77% -44 μm), and a coarser chromite, $\text{FeO} \cdot \text{Cr}_2\text{O}_3$, containing 6.6% SiO_2 , 15.25% MgO and 15.49% Al_2O_3 (75% -300 μm +100 μm) were separately mixed with graphite fines, (-44 μm), in 100% and 200% stoichiometric proportions according to:



These mixtures were fed from a vibratory feeder, under gravity, into the arc of the DC transferred arc plasma (Figure 1). A hollow graphite cathode of 20mm diameter was used with a central bore of 2mm diameter through which was passed the argon plasma gas at approximately 0.8m³ per hour. A graphite ring of 130mm internal diameter was used as the anode. The tail flame from the plasma arc extended beneath the ring anode into a free fall (rapid quench) chamber of approximately 900mm length and 200mm internal diameter and the products collected in a refractory receptacle. The anode root of the arc was made to orbit around the anode ring by electromagnetic means and the whole reactor was enclosed. A more detailed description of this reactor has been given elsewhere³. Arc voltages of 140 to 220V and arc currents of 400-290amps, with arc rotations of 2,000-10,000rpm produced an optimum arc length of approximately 90mm. The reactant mix was fed into the arc at the cathode tip, taking advantage of the cathode pumping action, at an optimum feed rate of approximately 70 to 100 gms/min.

The plasma synthesised products were examined using optical metallography, scanning electron microscopy (SEM), with energy dispersive X-ray analysis (EDAX) and scanning Auger microprobe (SAM) analysis.

EXPERIMENTAL RESULTS

Large temperature and viscosity gradients within the plasma produced considerable variation in the extent of plasma-particle interaction

which, together with the range of stoichiometries used for reactions (1) and (2), provided a range in the extent of reduction. The efficiency of the plasma-particle interaction was measured as percent conversion or metallisation, e.g. Fe_3O_4 : wt% metallic iron/wt% of total iron in the product. For Fe_3O_4 , this was seen to depend on the degree of reduction of Fe^{3+} to Fe^{2+} (Figure 2) for reaction (1). No metallisation was achieved until 30% of Fe^{3+} had been reduced to Fe^{2+} , whereas the amount of Fe^{2+} remaining as FeO rather than Fe was relatively constant i.e. 25 to 35%. A maximum metallisation of 76% was achieved with 200% stoichiometric carbon. The reduced product was present as an iron-carbon metallic containing some internal porosity and surrounded by a slag which was determined by EDAX to be $\text{FeO} \cdot \text{Fe}_2\text{SiO}_4$ (Figure 3). The carbon content of the metallic particle varied from 1% to 3.5% C for the same experimental conditions at 200% carbon stoichiometry. The dark area in Figures 3(a) and (b) is pearlite and the inter-laminar pearlite spacing was subsequently determined (Figure 3c). A dendritic etch was used to determine the secondary, λ_2 , dendrite arm spacings (Figure 3(d)) which are presented in Table 1, together with SAM phase analysis.

The chromite reduced particles (Figure 4) were also surrounded by a silicate slag phase i.e. Mg_2SiO_4 . This product (Figure 4b) was largely primary carbides of Fe and Cr i.e. $\text{Fe}_3\text{C}, \text{Cr}_3\text{C}_2$. Some unreduced chromite particles were observed to have reduced particles (Fe,Cr,C) along intercrystalline boundaries (Figure 4c) in the unreduced mineral. These varied in Fe:Cr:C analysis from 50/50 Fe-Cr and with up to 12% carbon.

Table I
SAM Point Analysis of Plasma-Produced Particles
(Using internal standards)

Specimen/ Phase analysis	Fe (Wt%)	C (Wt%)	Cr (Wt%)	λ_2 (μm)	interlamellar spacing of Pearlite (μm)
Particles produced from plasma-processed magnetite (Fe_3O_4)					
Max. reduction: ~75%					
From	98.2	1.8			
To	96.2	3.8			
Phase analysis:					
(Fe-C eutectic)		5.1			
(Pearlite)		1.8		2.5	0.1
Particles produced from plasma-processed chromite ($\text{FeO} \cdot \text{Cr}_2\text{O}_3$)					
Max. reduction: ~65% FeO 55% Cr_2O_3	55.2	12.8	32.0		

Table II
Minimum Reduction Temperatures for
Carbothermic Reduction Reactions

Reaction	Min. Reduction Temp. ($^{\circ}\text{C}$)
$\text{FeO} + \text{C} = \text{Fe} + \text{CO}$	≈ 630
$3\text{FeO} + 4\text{C} = \text{Fe}_3\text{C} + 3\text{CO}$	≈ 630
$\text{Fe}_3\text{O}_4 + 4\text{C} = 3\text{Fe} + 4\text{CO}$	≈ 700
$\text{Fe}_3\text{O}_4 + 5\text{C} = \text{Fe}_3\text{C} + 4\text{CO}$	≈ 710
$1/2\text{Cr}_2\text{O}_3 + 3/2\text{C} = \text{Cr} + 3/2\text{CO}$	≈ 1330
$3/2\text{Cr}_2\text{O}_3 + 13/2\text{C} = \text{Cr}_3\text{C}_2 + 9/2\text{CO}$	≈ 1150

DISCUSSION

The minimum reduction temperatures for the carbothermic reduction (Table II) of Fe_3O_4 to produce either metallic Fe, or Fe_3C , are approximately the same, $\sim 700^{\circ}\text{C}$. However, Fe_3C formation is more strongly favoured above 1000°C and the formation of Cr_3C_2 is always more favourable than metallic Cr above 1150°C , (Figure 5). A thermodata software package, CSIRO-SGTE Thermodata System⁴, based on

minimisation of ΔG , was used to provide the data presented in Figures 6 and 7 for reactions (1) and (2) at stoichiometric carbon levels of 100% and 200% respectively. At 100% carbon stoichiometry for reaction (1) metallic iron is favoured above 1000°C with only a small amount of Fe_3C . Whereas, Fe_3C with an excess of carbon is formed between 1000°C to 2500°C. Cr_3C_2 and Fe_3C are the preferred product species for reaction (2) with an excess of carbon for the 200%C stoichiometry. An excess of 100% stoichiometry for reactions (1) and (2) has been found⁵⁻⁸ to be advantageous in achieving increased reduction within the plasma as was a small oxygen bleed into the system.

The required 30% reduction level of Fe^{3+} to Fe^{2+} (Figure 2) prior to metallisation is coincident with the reduction of Fe_2O_3 in the magnetite spinel ($\text{FeO} \cdot \text{Fe}_2\text{O}_3$) to FeO ; the subsequent reduction processes being: $\text{FeO} + \text{C} \rightarrow \text{Fe} + \text{CO}$ or alternatively, $3\text{FeO} + 4\text{C} \rightarrow \text{Fe}_3\text{C} + 3\text{CO}$ depending on carbon stoichiometry. The formation of Fe_2SiO_4 lowers the activity of FeO which is unlikely to be reduced under these 70kW, laboratory plasma conditions. This accounts for the 30% Fe remaining as unreduced FeO (Figure 2). It is apparent from Figures 2, 3, and 6 that a large proportion of the small magnetite particles were melted, dissociated and reduced within the plasma. The formation of the lower melting point $\text{FeO} \cdot \text{Fe}_2\text{SiO}_4$ slag subsequently condenses around the previously condensed $\text{Fe}-\text{Fe}_3\text{C}$ particles, thereby accounting for the slag envelope (Figure 3a).

Some of the particles in the chromite concentrate, due to their larger size and distribution remained unmelted (Figure 4(c)) but show evidence

of partial reduction. One possible explanation is that, owing to the violent plasma conditions, an outgassing of metallic species from the particle occurs producing microchannels of plasma along which reduction reactions can proceed favourable. Some evidence of this outgassing is given in Figure 8, in which the sodium in the chromite particle vaporized and transferred outwards since the Na levels were 0.23 (unreduced chromite) at particle centre, 5.23 (Mg_2SiO_4 -rich phase) at the particle surface and 2.11 (modified chromite) at mid radius position..

The secondary dendrite arm spacing (Table II) suggests a cooling rate of approximately $10^3 - 10^4$ K/sec, interlaminar spacing suggests a supercooling of approximately 180°C for the eutectoid transformation. These two data indicate considerable metastability, but are inconsistent since an average cooling rate of $10^3 - 10^4$ K/sec should result in more than a 180°C supercooling of the eutectoid temperature. Although the initial metallic particle could have achieved a cooling rate of $10^3 - 10^4$ K/sec once it is surrounded by a slag envelope, the heat transfer rate would decrease substantially, thereby decreasing the degree of supercooling through the subsequent eutectoid transformation.

Examination of the phase chemistries from the SAM analyses (Table I) i.e. 5% C eutectic carbide and 1.8% C pearlite, suggests that the pro-eutectic austenite was rapidly solidified (i.e. $10^3 - 10^4$ K/sec) from a super-saturated carbon liquid. This resulted in a higher than equilibrium carbon in the pearlite and a lower than equilibrium carbon in the subsequent formation of eutectic carbide. The 12-13% C recorded

in the Fe-Cr-C product from reaction (2) can also be explained using similar reasoning, while the very high volume of primary carbides (Figure 4b) is in agreement with that predicted by thermodynamics (Figure 7b) for a 200% carbon stoichiometry for reaction (2).

CONCLUSIONS

Commercial magnetite and chromite concentrates have been reduced in-flight within the DC transferred arc plasma medium to yield approximately 75% metallisation of the magnetite and approximately 60% metallisation of the chromite. Examination of the products indicated predominantly carbide, for the chromite-reduced particles and iron containing between 1-3.5% carbon for the magnetite-reduced samples. A considerable degree of metastability was achieved in the products. The presence of slag forming constituents in the concentrates decreased the metastability, and the level of reduction.

ACKNOWLEDGEMENT

The author extends his thanks to Dr K.J.Reid, Director, Mineral Resources Research Centre, University of Minnesota, for the provision of laboratory facilities.

REFERENCES

1. K.J.Reid, J.J.Moore: Proceedings The Reinhardt Schumann International Symposium on Innovative Technology and Reactor Design in Extraction Metallurgy. Ed by D.R.Gaskell, J.P.Hager, J.E.Hoffmann, P.J.Mackay, Pub. by TMS of AIME (1986) p87-112.
2. B.J. Berkowitz, R.O.Scattergood, Editor, Proceedings of Symposium on the Chemistry and Physics of Rapidly Solidified Materials, pub. by TMS of AIME (1983).

3. J.J.Moore, J.K.Tylko, K.J.Reid: Proceedings Extractive Metallurgy of Refractory Metals, Chicago, Feb, 1981 edited by H.Y.Sohn, J.T.Smith (TMS-AIME) p377-417.
4. CSIRO-SGTE Thermodata System: A.T.Turnbull, M.W.Wadsley "The CSIRO-SGTE thermodata system (version V)" CSIRO Inst. of Energy & Earth Resources, Div. of Mineral Chemistry, Port Melbourne, Australia (1987).
5. K.Upadhaya, J.J.Moore, K.J.Reid: Met. Trans, 17B (1986) pp192-207.
6. K.J.Reid, J.K.Tylko and J.J.Moore: Second World Congress of Chemical Engineering, Montreal Canada, October (1981) p1-11.
7. K.J.Reid, J.J.Moore and J.K.Tylko: Proceedings 5th ISPC, IUPAC, Edinburgh, August (1981).
8. K.J.Reid, J.J.Moore: Proc. 54th Annual Minnesota Sec. AIME Meeting, Duluth, January 1981, (University of Minnesota, 1982) p12-1.
9. J.J.Moore, K.J.Reid and J.M.Sivertsen, reference 2, p281-297.

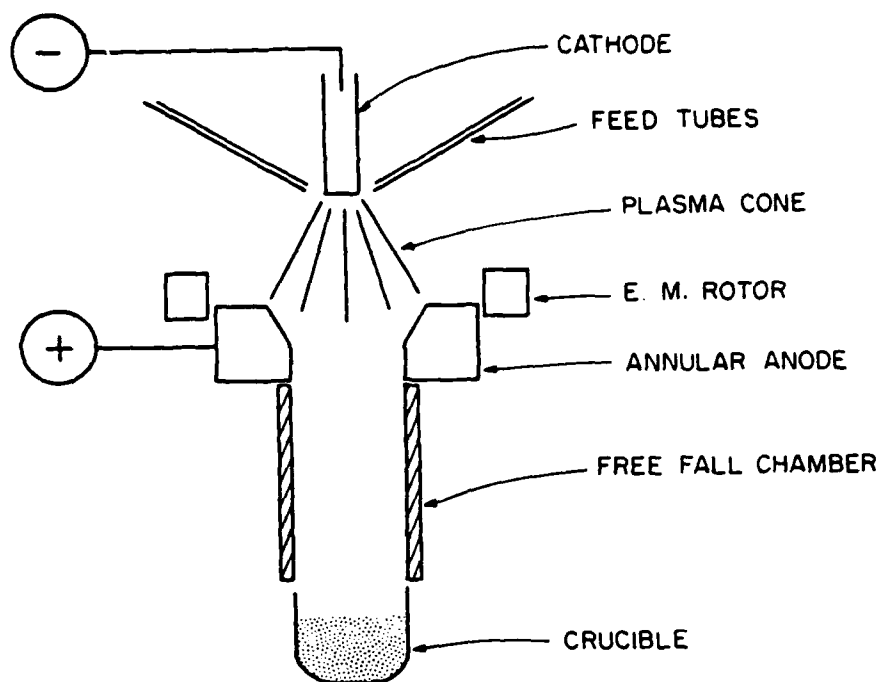


FIGURE 1. SCHEMATIC REPRESENTATION OF THE DC TRANSFERRED ARC PLASMA REACTOR

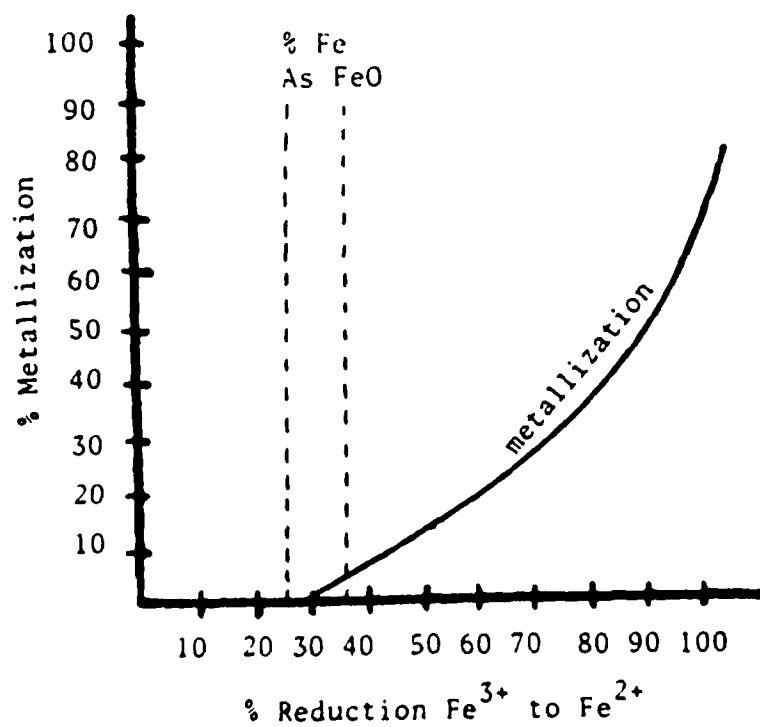
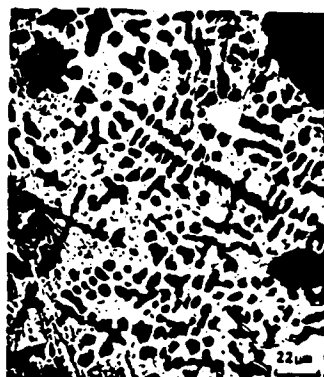


FIGURE 2. EXTENT OF METALLISATION ACHIEVED FOR THE CARBOTHERMIC REDUCTION OF MAGNETITE IN THE PLASMA AS A FUNCTION OF THE REDUCTION OF Fe^{3+} to Fe^{2+}



(a)



(b)



(c)



(d)

FIGURE 3. SCANNING ELECTRON PHOTOMICROGRAPHS OF A TYPICAL PRODUCT FROM THE CARBOTHERMIC REDUCTION OF MAGNETITE IN THE PLASMA REACTOR (ETCHED IN NITAL) USING 100% C WITH RESPECT TO REACTION (1).

a, b) Fe-C PARTICLE SURROUNDED BY $\text{FeO} \cdot \text{SiO}_2$ SLAG.

NOTE: (i) DARK PHASE IN SLAG ENVELOPE (a) IS Fe_2SiO_4 AND THE LIGHT PHASE IS FeO.

c) INTERLAMELLAR SPACING OF THE PEARLITE IN b)

d) DENDRITIC ETCH USED ON b)



(a)



(b)

FIGURE 4. SCANNING ELECTRON PHOTOMICROGRAPHS OF TYPICAL PRODUCTS FROM THE CARBOTHERMIC REDUCTION OF CHROMITE IN THE PLASMA REACTOR USING 200% C WITH RESPECT TO REACTION (2). a & b) Fe-Cr-C PARTICLE SURROUNDED BY Mg_2SiO_4 -RICH SLAG.

NOTE: HIGH VOLUME FRACTION OF PRIMARY CARBIDES IN ETCHED SPECIMEN (b).



c) UNMELTED CHROMITE PARTICLES SHOWING FINE REDUCED (WHITE) Fe-Cr-C PARTICLES SITUATED ALONG CERTAIN LINES IN THE PARTICLE

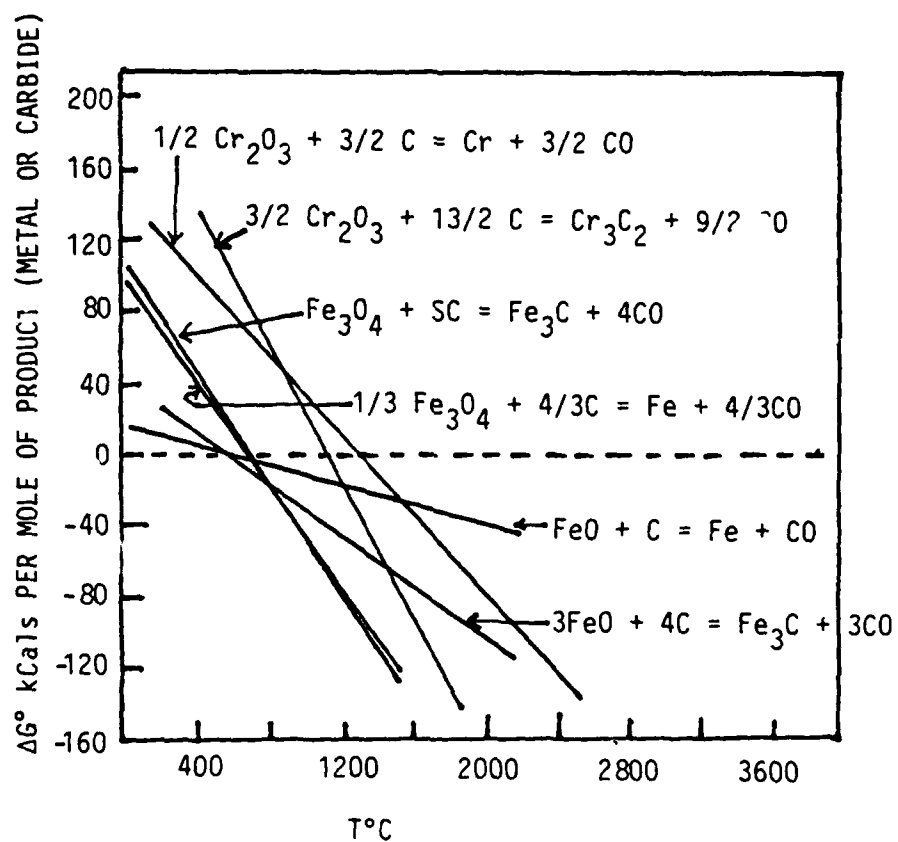
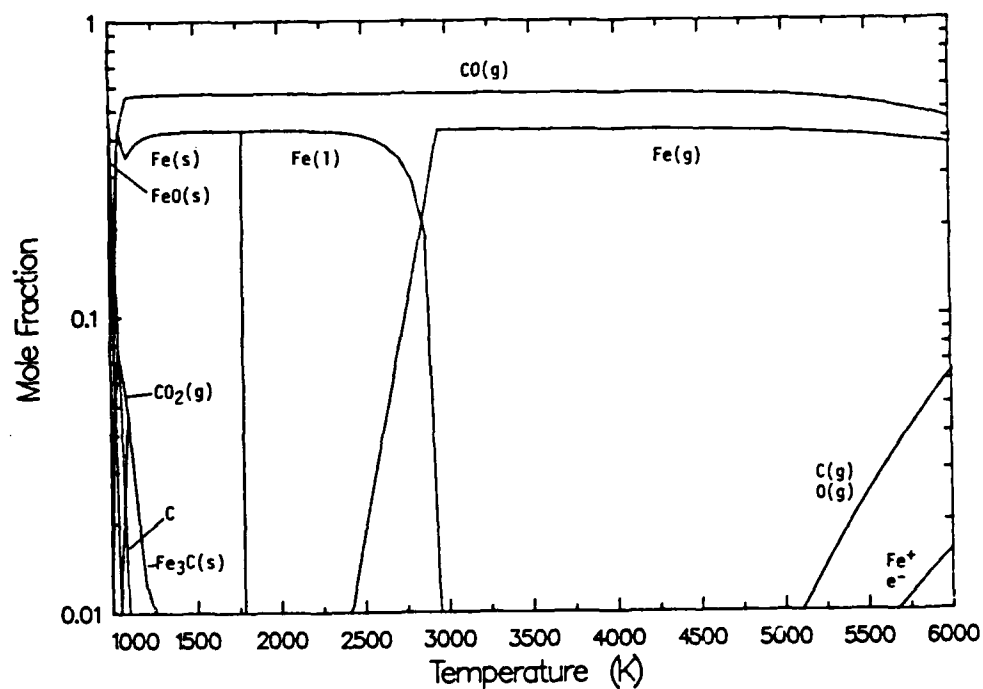
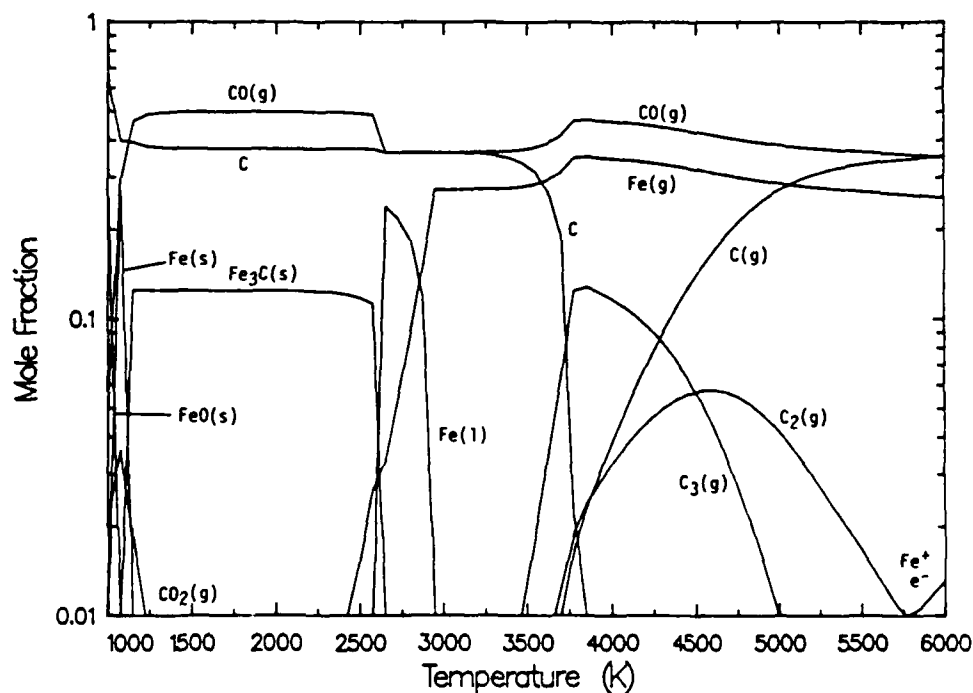


FIGURE 5. ΔG° - T DIAGRAM FOR THE CARBOTHERMIC REDUCTION OF FeO, Fe_3O_4 , Cr_2O_3

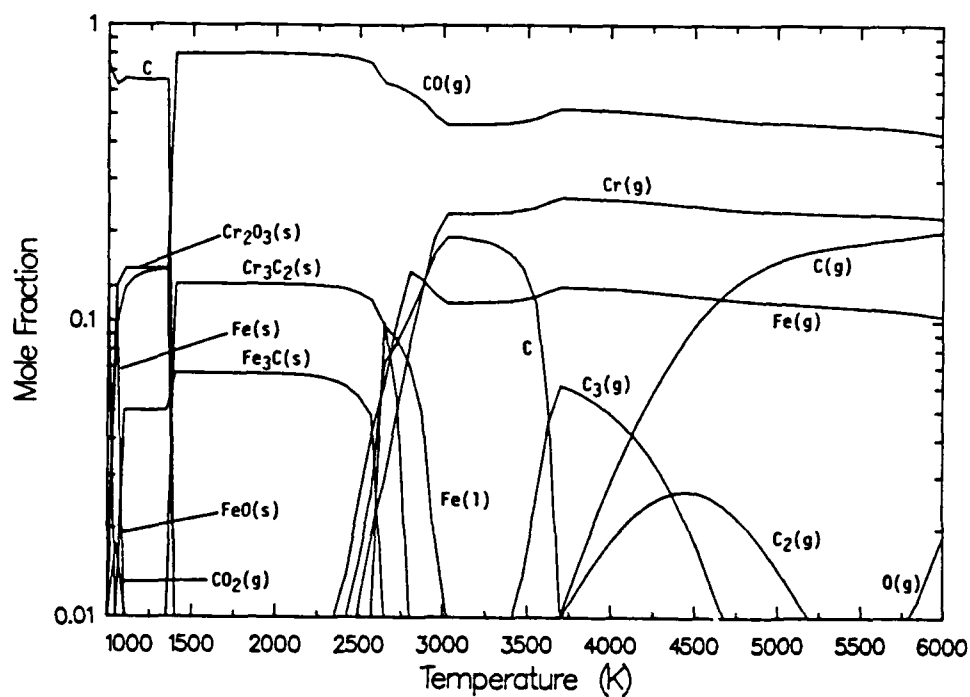


(a)

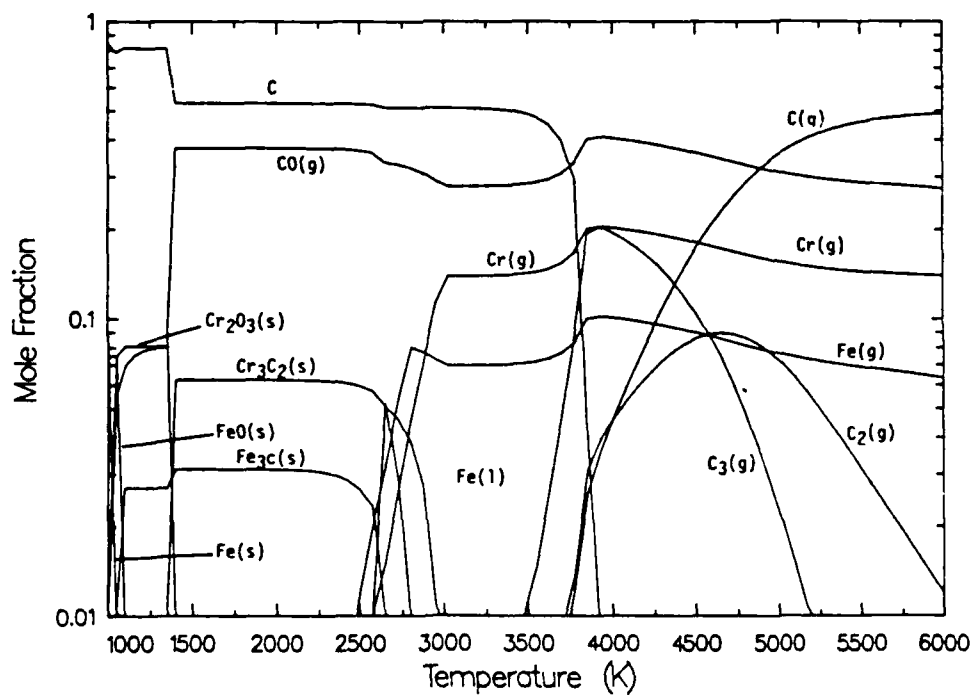


(b)

FIGURE 6. THERMODYNAMIC EQUILIBRIA DIAGRAMS FOR CARBOTHERMIC REDUCTION OF MAGNETITE BASED ON
 (a) $\text{Fe}_3\text{O}_4 + 4\text{C} = 3\text{Fe} + 4\text{CO}$, AND
 (b) 200% STOICHIOMETRIC CARBON COMPARED WITH (a)



(a)



(b)

FIGURE 7. THERMODYNAMIC EQUILIBRIA DIAGRAMS FOR CARBOTHERMIC REDUCTION OF CHROMITE BASED ON
 (a) $3(\text{FeO} \cdot \text{Cr}_2\text{O}_3) + 17\text{C} = \text{Fe}_3\text{C} + 2\text{Cr}_3\text{C}_2 + 12\text{CO}$, AND
 (b) 200% STOICHIOMETRIC CARBON COMPARED WITH (a)

EPMA ANALYSIS OF PARTIALLY REDUCED CHROMITE

	CHROMITE SPINEL (LIGHT GREY)	MODIFIED CHROMITE SPINEL (GREY)	Mg ₂ SiO ₄ - RICH PHASE (DARK GREY)
SiO ₂	0.28	1.52	18.9
Al ₂ O ₃	18.3	21.1	2.36
FeO	22.8	14.9	8.66
MgO	11.4	18.1	58.1
Cr ₂ O ₃	43.8	41.8	4.29
Na ₂ O	0.23	2.11	5.23
K ₂ O	0.01	0.06	0.02
TiO ₂	0.46	0.53	0.22
CaO	0.09	0.53	0.85
Total	97.37	100.6	100.0



FIGURE 8. SEM PHOTOMICROGRAPH OF PARTIALLY REDUCED CHROMITE PARTICLE SHOWING
 (a) REDUCED Fe-Cr-C PARTICLES (WHITE)
 (b) UNREDUCED CHROMITE (LIGHT GREY) IN CENTRE
 (c) MODIFIED CHROMITE SPINEL (GREY), BETWEEN CENTRE AND EDGE
 (d) Mg₂SiO₄ - RICH PHASE (DARK GREY), TOWARDS EDGE

LASER DIAGNOSTICS OF PLASMA SPECIES IN PACVD PROCESS
FOR HARD FACE COATING DEPOSITION*

W. C. Roman
J. H. Stufflebeam
A. C. Eckbreth
C. J. Ultee

UNITED TECHNOLOGIES RESEARCH CENTER
East Hartford, Connecticut 06108

ABSTRACT

In order to understand the complicated chemical and physical processes that occur during the deposition of hard face coatings such as diamond or Titanium Diboride, diagnostics that are sensitive to potential chemical species are necessary. Optical diagnostics are ideally suited because they are remote and nonintrusive. CARS measurements were conducted on a PACVD reactor used for depositing high quality diamond films. A mixture of acetylene (C_2H_2) and Argon operated over a range of total pressures down to 0.1 Torr was used to calibrate the CARS system. This paper includes details of the scanned narrowband colinear CARS system and examples of CARS spectra obtained for CH_4 and C_2H_2 species under PACVD diamond deposition conditions.

*Research supported in part by DOE Research Grant BES-ER 13560

INTRODUCTION

Nonequilibrium reactive plasmas are recognized as a novel approach for a wide variety of material coating applications.^[1] This type plasma provides a unique environment wherein deposition of thin, hard face, conformal coatings can occur at much lower temperatures (critical for inhibiting stresses) and within more complex chemical environments than are possible by conventional vapor deposition techniques. A need exists for in-situ nonintrusive techniques for diagnosing and controlling PACVD systems used for thin coating deposition.^[2] If improvements can be made in durable hard face coatings, increased utilization of lightweight materials under advanced development will follow. A complete understanding of the process requires information on a large number of physical and chemical processes involving gas phase and gas-surface interactions and the associated synergistic effects. Knowledge of plasma species concentrations and "temperature" is required for correlation with the corresponding physical and chemical properties of the coatings. CARS, a nonlinear optical laser technique, has high temporal and spatial resolution and is capable of major species concentration and temperature measurement for near atmospheric applications. It is also suited, because of its state specific nature, for the study of nonequilibrium phenomena. In temporally-stable situations, such as PACVD materials processing, it can also be configured to possess high detectivity capabilities.

Many compounds have potential for tribological hard coatings, but detailed inspection and study reveal that diamond and the titanium metalloids form an attractive group. The outstanding combination of unique material properties of diamond offers the potential for applying diamond coatings in many commercial applications ranging from protective coatings to films/heat

sinks for semiconductors to optical lenses to electronic devices for space environments. Because of its superior erosion and thermal shock resistance, TiB_2 was selected as the titanium metalloid hard face coating material together with diamond for initial investigation at UTRC.

Ti-6Al-4V was selected as the substrate material. It represents a critical alloy of paramount interest in many commercial/aerospace applications. Its strength to weight and low temperature oxidation/corrosion resistance are excellent, but erosion and wear occurs rapidly, thus the need for applying a durable hard face protective coating.

APPARATUS

Figure 1 is a schematic of the nonequilibrium PACVD reactor under current investigation at UTRC. The longitudinal, tube type geometry was selected as a design viable for later scale up to continuous production operation in addition to permitting high reactant gas flows and plasma power levels; increasing these parameters nominally results in enhanced deposition rates. The 4.0-cm-OD test section is constructed of high purity fused silica and high vacuum flanges for rapid disassembly. A 5 kW radio frequency (rf) power supply operating at 13.56 MHz is used to inductively couple the rf power into the plasma through a multiple-turn water-cooled copper work coil. Exploratory test results revealed the importance of minimizing contamination in the PACVD system. As a result, a completely oil-free, venturi, vacsorb, cryopump and vacion pump system is used, including a MKS flow metering system with special traps (e.g., GaInAl) and getters to remove water vapor and oxygen. To augment pumpdown time and provide operating range flexibility, a 380 ℓ/s turbomolecular pumping system, modified for corrosion resistant operation is used together with a residual gas analyzer to monitor trace impurities. This

system is capable of initial operating pressures down to 10^{-8} torr. The cleanliness of the substrate (1.3-cm-dia x 2 mm thick) prior to coating deposition is believed to be a key requirement for achieving good coating adherence to the substrate. Therefore, a test sample holder and isolated load-lock and transport system are interfaced with the PACVD system. This technique allows direct SIMS/ISS analysis of the substrates immediately following in-situ plasma cleaning and provides a unique capability not reported in the literature. To facilitate conducting optical/laser diagnostic measurements from the active plasma zone to the tailflame region and adjacent to the substrate, colinear optical ports and an automated traversing assembly are used. Additional advantages of this type system include the provision for graded composition control and independent biasing and temperature monitoring of the substrate.

As hardness and adhesion are critical parameters for characterizing thin, hard face coatings, a state-of-the-art ultramicrohardness tester and UTRC custom built adhesion test apparatus have been installed and preliminary calibration testing initiated. The ultramicrohardness tester (Nanoindenter) can resolve forces as small as 2.5 N and displacements of 0.4 nm. The adherence measurements are made on a computer-controlled pin-on-disc apparatus that has a 3-axis force transducer and a device to measure the advance of the pin into the coating. A modification to this device using an ultrasonic sensor allows for coating delamination detection. Reference 3 describes details of this equipment.

Figure 2 is a simplified schematic of the colinear phase-matched CARS system; the dye laser is scanned to generate the CARS spectrum. This scanned narrowband approach is used to get maximum species sensitivity by sacrificing

temporal resolution. In this way all of the available laser pump energy excites a single transition of the resonant molecule and increases the sensitivity by several orders of magnitude. The basic equipment includes an injector-seeded, single-mode, frequency-doubled (532 nm) Nd:YAG primary beam pump laser and a narrow bandwidth (0.4 cm^{-1}) Stokes beam scanned dye laser. The two laser beams are aligned colinearly and focused in the medium. The frequency-shifted CARS signal is formed in the laser focus and all three beams exit the reactor where a dichroic separates the CARS from the incident wave mixing beams. Digital acquisition of the CARS and reference signal are obtained from fast gated PMT detectors. The digital acquisition system also records the wavelength shift of the scanned dye laser for calibration of the CARS spectrum. All signals are digitized and processed in a computer. The result is a spectrum of the ro-vibrational manifold of the medium from which identification of species, their concentration and temperature (vibrational and rotational) can be obtained. With appropriate referencing, the molecular concentration can be measured to within 1% of the total gas density and the population in the vibrational and rotational states determined for assignment of temperatures.

RESULTS TO DATE AND DISCUSSION

In the exploratory experiments directed at diamond coatings, a mixture of 1% CH_4 in H_2 was used at a total pressure of 5 torr. The rf coils were located at the optical port location. Figure 3 is an example of the CARS methane (CH_4) molecular signal obtained for the ν_1 mode. It illustrates the effect of increasing rf power on depleting the methane concentration. Measurements were also made of the weaker $2\nu_2$ and ν_3 modes. Very little is known about the chemical mechanisms of diamond film growth. Global kinetic

theories have been proposed based on nucleation theory and equilibrium. Other proposed mechanisms rely on the presence of C_2H_2 or CH_3^+ . Frenklach and Spear at Pennsylvania State University [4] have proposed an alternative mechanism for diamond growth. It basically consists of two alternating steps. First, the surface is activated by H-atom removal of a surface-bonded hydrogen. The surface activated carbon radical then acts as a site for adding more carbons to the structure, by reacting with acetylene (C_2H_2) in the plasma. To provide more quantitative experimental information to verify these proposed theories and improve the basic understanding of the diamond growth process, a series of CARS experiments was conducted focused on measurement of the C_2H_2 molecular species. C_2H_2 is a linear molecule with five fundamental vibrations. Figure 4 illustrates a CARS spectrum of C_2H_2 (ν_1 band) measured using the CARS system shown in Figure 2. This measurement was made at room temperature and 10 torr reactor total pressure while flowing a mixture of 5% C_2H_2 in Argon. High purity C_2H_2 , as checked via a gas chromatograph, in concentrations of both 5% and 0.5% in Argon were used in these measurements. The measurements obtained using both concentrations indicate a C_2H_2 detectability of 5mtorr was achieved with the present system.

To determine the effect of rf plasma location on the ability to detect the C_2H_2 , a series of tests was conducted for the different configurations shown in Figure 5. In each case the total pressure was 3 torr. The 5% C_2H_2 in Argon was only detected when the rf plasma was located downstream of the laser optical ports. In the other locations, the concentration of C_2H_2 was less than 5mtorr. The next step was to investigate the configuration and test parameters under which high quality diamond coatings

have been deposited. The results for the CARS spectrum of C_2H_2, ν_1 mode observed at 3 torr, is shown in Figure 6. The rf plasma power was 300 watts and the H_2 and CH_4 flow rates were 99 and 1 sccm respectively. The rf coils were located at the optical port axis and the Ti-6Al-4V substrate was located within the plasma plume and 1-cm downstream of the optical centerline. For this configuration, no C_2H_2 CARS signal was observed in any of these tests. This would indicate, if C_2H_2 were present that it was at concentration levels less than the 5mtorr current detection limit of the CARS system. The quality of the deposited diamond films was determined from their Raman spectra. Figure 7 is an example of the test results obtained using Raman scattering on a Ti-6Al-4V substrate that was coated with the polycrystalline diamond film. In these measurements, a tunable cw dye laser operated in a single frequency configuration with a line width of <5 MHz, tuned to 16956.18 cm^{-1} , was used as the excitation source. Raman spectra reported by Matsumoto [5] for thin diamond films indicate only one sharp peak at about 1333 cm^{-1} . This is very close to the value 1332.5 cm^{-1} reported for natural diamond by Solin and Ramdas [6]. A feature of the UTRC diamond coating is that no graphite peak was detected in any of the Raman measurements. X-ray diffraction measurements indicated the observed interplanar spacings are in close agreement with reported values (2.065 and 1.262 Å) of natural diamond (ASTM 6-675) and UTRC reference natural diamond material.

Based on the above experiments, the following are the preliminary results: 1) a CH_4 CARS spectrum was observed in the rf plasma, 2) increasing the rf plasma power reduced the CH_4 CARS signal, 3) the rf plasma significantly reduces the C_2H_2 CARS signal in C_2H_2/Ar flow, 4) the

C_2H_2 CARS spectrum was not observed in rf plasma CH_4/H_2 diamond deposition tests to date. The present C_2H_2 detectability limit is 5mtorr.

Investigation of the CARS spectrum of the dominant species for the TiB_2 coating obtained using the reactant $TiCl_4$ and B_2H_6 is in progress.

SUMMARY

Novel laser/optical diagnostic (CARS) and coating surface analysis techniques (Nanoindenter and adhesion pin-on-disc with acoustic emission sensor) are candidates for application as plasma materials processing diagnostic tools, each with its own inherent advantages and associated limitations. Recognizing that no one diagnostic technique will suffice, it will only be through the complementary use of these techniques that a fundamental understanding of the relationship between plasma process variables and properties of the processed material will evolve. This may ultimately lead to simple process control strategies, including in-situ laser diagnostics and sensors, to ensure high quality, economic, reproducible plasma deposition of advanced coatings in a production scale environment. Research addressing these aspects is continuing.

REFERENCES

- [1] National Research Council, National Materials Advisory Board Report NMAB-415, Plasma Processing of Materials, National Academy Press, March 1985.
- [2] Roman, W., "Laser/Optical Diagnostic Techniques for Plasma Materials Processing." Invited Paper at Spring 1987 Materials Research Society Meeting, Anaheim, CA, Published in Proceedings of Symposium K - "Plasma Processing and Synthesis of Materials," April 20-24, 1987.
- [3] Roman, W., Stufflebeam, J., and Eckbreth, A., "Diagnostic Techniques for

PACVD Systems for Depositing Protective Coatings," Paper C2.2 -
 Proceedings of Materials Research Society Spring Meeting, Vol. 117,
 Process Diagnostics: Materials, Combustion, Fusion. Reno, NV, April
 1988.

- [4] Spear, K., and Frenklach, M., "Mechanistic Hypotheses on Diamond Growth from the Vapor." Presented at 3rd SDIO/IST - ONR Diamond Technology Initiative Symposium, Arlington, VA. July 1988.
- [5] Matsumoto, S., Sata, Y., Kamo, M., Tenaka, J., and Setaka, N., Proc. 7th International Conference on Vac. Metallurgy, page 386, Tokyo, Japan, 1982.
- [6] Solin, S., and Ramdas, A., Phys. Rev. B1 1687, 1970.

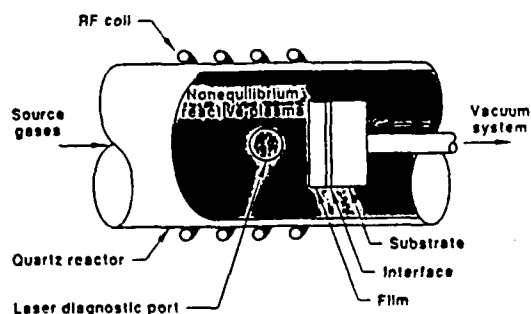


FIGURE 1. SCHEMATIC OF PACVD REACTOR

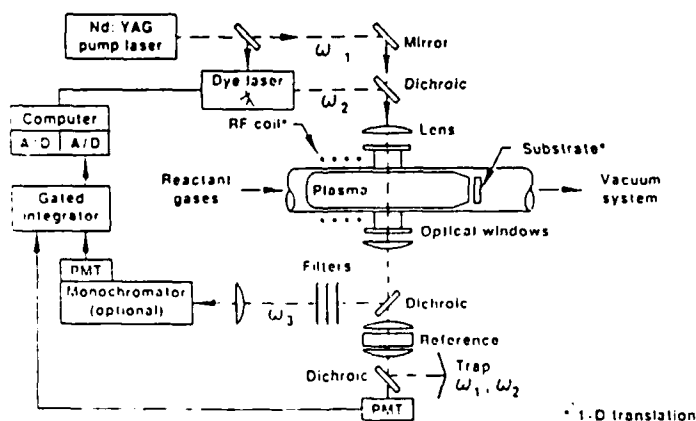


FIGURE 2. SCHEMATIC OF NARROWBAND, COLINEAR SCANNED CARS SYSTEM
 USED IN PACVD EXPERIMENTS

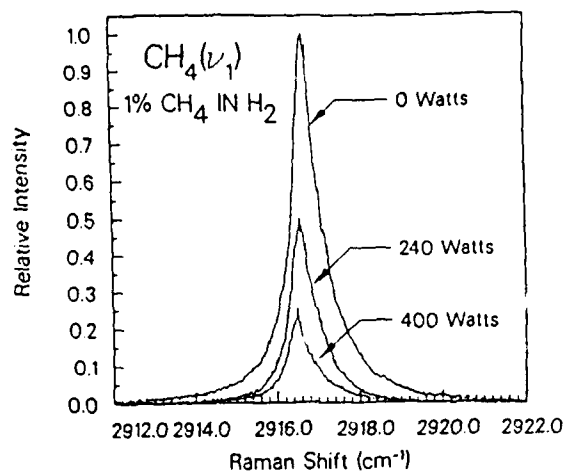


FIGURE 3. EFFECT OF RF PLASMA POWER ON CARS METHANE SPECTRUM

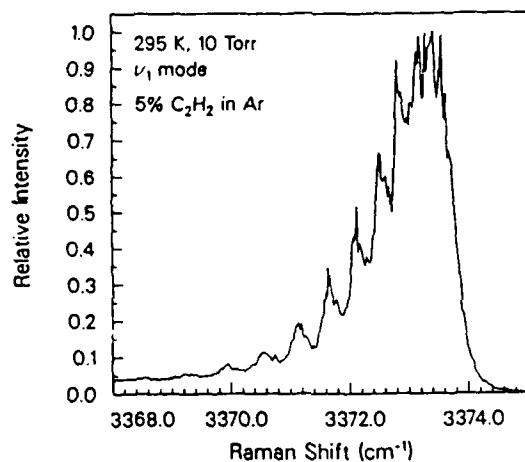


FIGURE 4. CARS SPECTRUM OF ACETYLENE

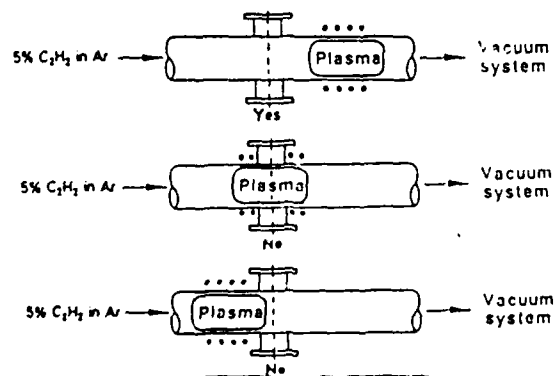


FIGURE 5. C_2H_2 DETECTION LOCATIONS

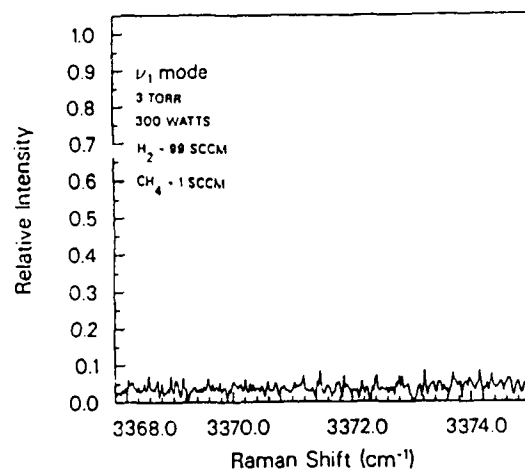


FIGURE 6. CARS SPECTRUM OF ACETYLENE IN PACVD DIAMOND COATING DEPOSITION

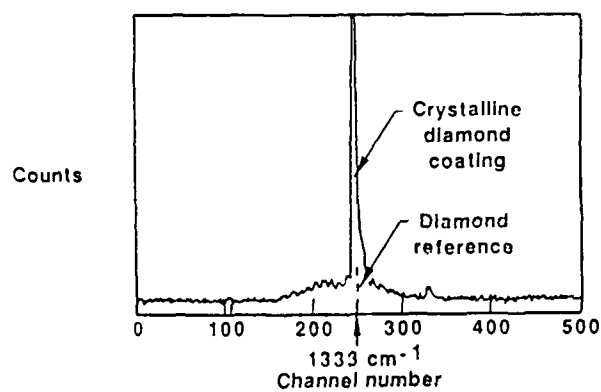


FIGURE 7. RAMAN SPECTRA OF DIAMOND COATING DEPOSITED VIA PACVD ON Ti-6Al-4V SUBSTRATE

AUTHOR INDEX

	<u>Paper Number</u>
Adkins, C. L. J.	41
Alam, M. K.	39
Amouroux, J.	48
Anselmi-Tamburini, U.	7
Armstrong, R.	6
Azeez, Q.	39
Bayliss, A.	3
Booty, M. R.	4
Bose, A.	9
Campbell, A. N.	41
Campion, J. F.	48
Chin, D.	40
Chiu, C. P.	37
Chow, C. T. S.	29
Chung, S. L.	40
Constantino, M.	33
DeAngelis, T. P.	12
Degreve, J.	5
Dimitriou, P.	5
Dunmead, S. D.	18, 23

	<u>Paper Number</u>
Eckbreth, A. C.	50
El-Kaddah, N.	36
Flagan, R. C.	38
Flint, J. H.	42
Gatti, A.	16
Gebhardt, J. J.	16
German, R. M.	9
Girshick, S. L.	37
Graham, R. A.	11
Haggerty, J. S.	42
Halverson, D. C.	26
Hammetter, W. F.	11
Hays, A. K.	47
Headley, T. J.	41
Hida, G. T.	25
Hirano, T.	19
Hlavacek, V.	5, 27
Holt, J. B.	18, 20, 23, 33
Hughes, R. C.	47
Humbert, P.	48
Ikeda, S.	13

	<u>Paper Number</u>
Ishizawa, Y.	34
Izawa, H.	13
Jolivet, P.	48
Kaieda, Y.	8
Katz, J. L.	40
Kecskes, L. J.	14, 24, 32
Kingman, D. D.	18, 23
Knittel, S. M.	44
Koizumi, M.	2, 13, 15, 28
Kong, P. C.	45
Koszykowski, M.	6
Kottke, T.	14, 24, 32
Kumar, S.	27
Lin, I. J.	25
Lis, J.	21
Logan, K. V.	22
Lum, B. Y.	26
Margolis, S. B.	4
Matkowsky, B.	3, 4
McFeaters, J. S.	46
McKelliget, J. W.	36
McLemore, W. J. S.	22
Merzhanov, A. G.	1
Meyers, M. A.	11
Miyamoto, Y.	2, 15, 28

Paper Number

Mohler, J. H.	29
Moore, J. J.	10, 46, 49
Morvan, D.	48
Munir, Z. A.	7, 20, 23, 26
Nguyen, H. V.	38
Niiler, A.	14, 24, 32
Niino, M.	19
Nishioka, M.	43
Odawara, O.	17
Oguro, N.	8
Otaguchi, M.	8
Otani, S.	34
Pampuch, R.	21
Persson, P. A.	30
Pfender, E.	45
Puszyński, J. A.	27
Rabin, B. H.	9
Rice, R. W.	31
Risbud, S. H.	44
Rogak, S.	38
Roman, W. C.	50
Sanada, N.	19
Sata, N.	19
Scholtz, J.	5
Semerjian, H. G.	40

Paper Number

Somiya, S.	43
Sparrow, J. T.	22
Stobierski, L.	21
Stufflebeam, J. H.	50
Tanaka, T.	34
Thadhani, N.	11, 30
Ultee, C. J.	50
Urabe, K.	13, 28
Wang, L. L.	20
Ward, R.	30
Weiss, D. S.	12
Wiseman, C.	39
Work, S. J.	11
Yi, H. C.	10
Yoshida, T.	35
Yoshimura, M.	43
Yu, L. H.	11
Zachariah, M. R.	40
Zavitsanos, P. D.	16

SUBJECT INDEX

	<u>Paper Number</u>
Al ₂ O ₃	20
Adaptive grid	5
Al/B ₂ O ₃	22
Al/TiO ₂	22
Aluminum nitride	17, 39
Aluminum	7
Aluminum oxide	22
Arc-image heating	43
B ₄ C	20
Bifurcation	4
Boron carbide	41
Bulk powder reaction	22
Carbide	49
Carbo-reduction method	43
Carbothermic reduction	49
Centrifugal force	17
Centrifugal-thermite process	2
Ceramic alloying	15
Ceramic superconductors	6
Ceramic synthesis	48
Ceramic powders and coatings	35

	<u>Paper Number</u>
Ceramics	33, 45
Ceramics processing	33
Ceramic powders	40
Cermets	12
Chemical vapor deposition	41
Combustion velocity	27, 33
Combustion synthesis	2, 4, 7, 14, 33
Combustion sintering	2
Combustion and densification	17
Composites	12, 17, 26
Condensed phase combustion	5
Counterflow	40
Cu/TiB ₂ Composite	19
Densification mechanisms	9
Diffusion	40
Diffusion flame	5
DTA characterization	10
Economics	31
Electronic packaging substrate	44
Elemental powder	8
Energy localization	30
Exothermic reaction	9, 17, 30
Experimental model	22
Explosive compaction	32

Paper Number

Flame	40
Floating zone	34
Flow reactor	39
Full density ceramics	32
Functionally gradient material (FGM)	19
Gas dynamics	46
Gas-pressure combustion sintering	15
Grain size	45
Heterogenous reactions	21
High pressure	33
HIP	8
Hot pressing	16, 23, 31
Hybrid plasma	35
Hybrid plasma reactors	36
Ignition	29
Intermettals	10
Iron powder	37
Laser heating	43
Laser diagnostics	50
Laser ignition	29
Light scattering	40
Long pipe production	17
Maximum temperature of products	19
Mechanism	20

	<u>Paper Number</u>
Mechanochemical reactions	25
Metal infiltration	26
Metal foils	6
MgO	20
Microscopic analysis	28
Microstructures	29
Mineral oxide	49
Modeling	6, 27, 36, 46
Molybdenum	27
Molybdenum-silicon system	27
Morphological effects	10
Multilayer materials	12
Multiple point combustion	3
Numerical computation	3
Nickel	7, 10
Nickel aluminides	10
Nickel-titanium	10
Niobium aluminides	10
NiTi	8
Non-equilibrium	46
Nonlinear stability	4
Nonsteady front propagation	3
Nucleation	40
Numerical simulation	6
PACVD	50

	<u>Paper Number</u>
Particle nucleation and growth	37
Particle-particle interactions	22
Plasma processing	48, 49
Plasma diamond deposition	50
Pulsating combustion	3
Quasi-periodic combustion	4
R. F. thermal plasma	48
Reaction mechanism	7, 21
Reaction propagation	17
Reaction hot-pressing	12
RF plasma	35
Shape memory alloy	8, 10
Shape-memory alloy	10
Shock compaction	30
Shock-induced mixing	10
Shock-synthesis	10
SHS method	1, 32
SHS product	14
SHS reactant impurities	14
SHS theory	1
SiO ₂	40
Si ₃ N ₄	48
Silica	40
Silicon	4, 27, 33
Silicon nitride	33, 41, 42

	<u>Paper Number</u>
Silicon carbide	13, 21, 42
Silicon carbide composite	13
Single crystals	34
Sintering	1, 28, 45
Solid solutions	45
Spinning combustion	3
Spring pressing method	19
Structural dynamics	1
Theory	6, 46
Thermal plasma synthesis	35
Thermite reactions	25
TiO ₂	14
TiB ₂	15
TiC	1, 15, 34
Tin oxide coatings	47
TiN	48
Titanium carbide	43
Titanium carbonitride	43
Titanium nitride	43
Titanium boride-boron carbide	26
Titanium carbide composites	23
Titanium diboride	16, 31, 28
T _{max}	19
Ultrafine powders	48
Water	22
Y ₂ O ₃ -doped AlN	44